

8-5-2010

## **Petrology and Geochemical Evolution of the East Hill Suite of the Mont Saint-Hilaire Alkaline Plutonic Complex**

Peter Tice  
*University of New Orleans*

Follow this and additional works at: <https://scholarworks.uno.edu/td>

---

### **Recommended Citation**

Tice, Peter, "Petrology and Geochemical Evolution of the East Hill Suite of the Mont Saint-Hilaire Alkaline Plutonic Complex" (2010). *University of New Orleans Theses and Dissertations*. 1229.  
<https://scholarworks.uno.edu/td/1229>

This Dissertation is protected by copyright and/or related rights. It has been brought to you by ScholarWorks@UNO with permission from the rights-holder(s). You are free to use this Dissertation in any way that is permitted by the copyright and related rights legislation that applies to your use. For other uses you need to obtain permission from the rights-holder(s) directly, unless additional rights are indicated by a Creative Commons license in the record and/or on the work itself.

This Dissertation has been accepted for inclusion in University of New Orleans Theses and Dissertations by an authorized administrator of ScholarWorks@UNO. For more information, please contact [scholarworks@uno.edu](mailto:scholarworks@uno.edu).

Petrology and Geochemical Evolution  
of the East Hill Suite  
of the Mont Saint-Hilaire Alkaline Plutonic Complex

A Dissertation

Submitted to the Graduate Faculty of the  
University of New Orleans  
in partial fulfillment of the  
requirements for the degree of

Doctor of Philosophy  
in  
Engineering and Applied Science  
Earth and Environmental Sciences

by

Peter E. Tice

B.Sc., McGill University, 1995  
M.Sc., University of New Orleans, 2009

August, 2010



Copyright 2010, Peter E. Tice

## ACKNOWLEDGEMENTS

Even a work with the name of one is touched by the hands of many. This study could not have been completed without the tireless assistance and encouragement of the author's colleagues and family.

Dr. Wm B. Simmons, Jr. gave thoughtful commentary on research methodology, analytical procedures, and petrological and mineralogical interpretations. At least as importantly, he constantly challenged the author to be a better student and scientist, and did more than he may know to help the author when he was far from home. Dr. Simmons gave the author a free hand in choosing the direction of this research, and, in spite of delays along the way, he never gave up.

Dr. Simmons and Mr. Alexander U. Falster, as joint operators of the analytical facilities in the Department of Geology and Geophysics at the University of New Orleans, deserve many collective thanks for providing a laboratory at which students are able, instrumentally and financially, to carry out analyses of both a broad scope and a deep extent. This work required a variety of instruments and a number of instrument-hours that would have made its proper development and completion unattainable at virtually any other institution. Dr. Simmons and Mr. Falster instructed the author on the theory and operation of the electron microprobe, the scanning electron microscope, the X-ray diffractometer, and the direct-coupled plasma spectrometer. Mr. Falster further assisted, when needed, in the author's operation of the latter three instruments. Also, Mr. Falster is responsible for maintenance, repairs, and upkeep of all of the instruments used by the author at the University of New Orleans.

Mr. Alexander U. Falster has been like a member of the author's family, there in good times and bad, ready to laugh or criticize, and always with the author's best interests in mind. As

an accomplished chemist, Mr. Falster offered wonderful insights into geochemistry. Mr. Falster operated the electron microprobe for over 1,000 hours to generate the vast majority of the mineral analyses for this work. Without his tremendous efforts, a work of this scope would have been impossible.

Dr. Karen L. Webber assisted in the recalculation and interpretation of electron microprobe analyses of mica group minerals and was a valuable participant in discussions of the petrology of the East Hill Suite. Dr. Webber was also a role model of scientific rigor, reasoning, and honesty and had the courage both to praise and also to be frank with the author when he least wanted to hear something but needed to most.

Dr. Bhaskar Kura, of the Department of Civil and Environmental Engineering, kindly served as faculty advisor and doctoral committee member from the College of Engineering. He was the instructor for the author's engineering classes and was extraordinarily encouraging in the author's academic and professional progress.

Dr. Martin T. O'Connell served as a doctoral committee member and, in his capacity as graduate coordinator for the Department of Earth and Environmental Sciences, was enormously helpful in facilitating the author's satisfaction of graduate school requirements, even while the author was living at great distance in Texas.

Dr. Robert F. Martin, of McGill University, first inspired the interest of the author in pegmatites, alkaline igneous rocks, and Mont Saint-Hilaire. As advisor for the author's undergraduate thesis, he provided instruction and engaged in delightfully illuminating and thought-provoking discussions that served as the nucleus for this current work.

Monsieur J.G. Poudrette of the Poudrette quarry graciously allows limited access to his property for the collection of aesthetic and research specimens. This beneficence is instrumental

in the continuing work by researchers to understand Mont Saint-Hilaire and is deeply appreciated.

Mr. László & Mrs. Elsa Horváth, Dr. Joseph Mandarino, Dr. Peter Tarassoff, and Monsieur Gilles Haineault kindly shared their collective long-standing expertise in the mineralogy of Mont Saint-Hilaire. This aided in the identification of minuscule phases or those that are otherwise difficult to analyze. It also helped to reinforce concepts of mineral associations and to better understand the field relationship of the lamprophyre with other rock types in the suite.

Monsieur Charles Normand, a Mont Saint-Hilaire collector since his youth, was also informative as to the mineralogy of the East Hill Suite. Furthermore, as leader of the author's first visit to the locality, he was invaluable in the realms of mineral occurrences and field identification of the minerals of Mont Saint-Hilaire

Dr. G. Nelson Eby participated in a lively and fruitful dialogue on the current nomenclature of alkaline igneous rocks and had useful suggestions for future petrologic work at Mont Saint-Hilaire.

Drs. Charles G. Gilbert and Eric Essene offered thoughtful advice on the electron microprobe analysis, recalculation, and interpretation of clinopyroxene compositions and structures and provided food for thought on the implications thereof.

Dr. Steve Nelson and Mr. Pierre Burnside are kindly thanked for allowing the use of the Inorganic Analysis Laboratory of the Coordinated Instrumentation Facility (CIF) at Tulane University for X-ray fluorescence (XRF) analyses of whole rock samples. In particular, Mr. Burnside provided much appreciated assistance in sample preparation and operated the XRF spectrometer.

The author's *Project Flowing Waters* colleagues from the Biology Department at Texas State University; in particular, doctoral candidate Alisa Abuzeineh, Dr. Weston Nowlin, and Dr. Timothy Bonner, gave constant support, friendship, and inspiration. Perhaps even more importantly, they provided the author with an environment of collegial fellowship and discussion, an intellectual "home away from home."

The faculty and staff and their families from PRIDE High School and the Phoenix Academy, most especially Judy & Lee Mitchell, Mary Williams, Hilda & Javier Arebalos, Peggy & Larry Hilburn, Betty Mayfield, and Brenda Voyles, were passionate about the author's goals for this project and for his academic life. Their true friendship and heartfelt good wishes eased the burden of this undertaking.

Deep appreciation is due to the author's friends and family, who gave steadfast support, love, and encouragement, especially Evelyn Rider, Melvin, Polly & John Lehman, Steve & Colleen Krupa, Richard, Betty, & Tammy Beltz, Joe & Judy Tamashasky, Rick & Kathy Lawry, Dominic & Eileen Rinaudo, Viet & Cúc Nguyen, and William C. Dowling.

The author's in-laws, Shannon and Melissa Edwards, regularly hosted his family and provided him with a quiet environment in which to work. Very special thanks are due to the author's wife, Sherri, who helped to carry his load in the home, and to the author's children, ages 4, 2, and newborn, who patiently missed out on playtime so that this work could be completed.

To anyone not mentioned by name who contributed to this project, many thanks.

This dissertation is dedicated to  
my father, Edward S. Tice (1935-2001), and my mother, Roseann D. Tice,  
who made a life for me in which I could be anything.

## TABLE OF CONTENTS

List of Tables .....	xiv
List of Figures .....	xviii
Abstract .....	xxvii
Introduction .....	1
Previous Work .....	4
Geologic Setting.....	5
Regional Geology .....	5
Tectonostratigraphy .....	5
Monteregian Province .....	7
Mont Saint-Hilaire – Physiography .....	10
Mont Saint-Hilaire – General Geology.....	12
Mont Saint-Hilaire – Age Relationships.....	13
Analytical Methods.....	15
Scanning Electron Microscopy .....	15
Background .....	15
Sample Preparation .....	15
Operating Conditions .....	15
X-ray Diffractometry .....	16
Background .....	16
Operating Conditions .....	16
Unit Cell Measurement .....	17
Analysis of Feldspar Structural States .....	17
Electron Microprobe Analysis .....	17
Background .....	17
Operating Conditions & Standards .....	17
X-ray Fluorescence .....	19
Background .....	19
Sample Preparation .....	20
Standards .....	21
Optical Microscopy.....	21
Background .....	21
Photomicroscopy.....	21
Mont Saint-Hilaire – Petrology.....	22
Overview .....	22
Sunrise Suite .....	22
Pain de Sucre Suite .....	22
East Hill Suite .....	22
East Hill Suite – Petrographic Descriptions.....	28
Introduction .....	28
Group 1: Host Rock .....	30
Nepheline Melasyenite.....	30
Group 2: Feldspathoidal & Rare-Element Syenites .....	33
Nepheline Leucosyenite.....	33
Eudialyte Syenite .....	36

Group 3: Dikes, Pegmatites & Various Syenoids .....	37
Feldspar-Aegirine Dikes .....	37
Annite Lamprophyre .....	38
Pegmatites & Various Syenoids.....	40
Perthite Syenite .....	41
Pyroxenite .....	41
Xenoliths .....	42
East Hill Suite – Whole-Rock Geochemistry .....	43
Alteration & Whole-Rock Geochemistry .....	43
Introduction.....	43
Estimation of Pre-Alteration Chemistry .....	43
Trace Element Behavior .....	44
Major Element Geochemistry .....	47
Post-Alteration .....	47
Pre-Alteration & Comparison .....	66
Trace Element Geochemistry.....	72
Overview .....	72
Geochemical Petrologic Classification .....	82
Tectonic Setting .....	89
Ga/Al Ratios.....	89
Tectonic Setting .....	89
Field Relationships Revisited & Differentiation Trends .....	99
Trace Element Variation .....	108
Mont Saint-Hilaire, East Hill Suite – Mineralogy .....	120
Introduction.....	120
Identified Mineral Species .....	124
Amphibole Group .....	124
Calcic Amphibole Group .....	124
Sodic-Calcic Amphibole Group.....	124
Sodic Amphibole Group .....	124
Overview of Speciation.....	125
Nepheline Melasyenite.....	126
Type 1 nepheline leucosyenite.....	139
Eudialyte Syenite .....	140
Annite Lamprophyre.....	145
East Hill Suite Amphiboles.....	145
Carbonates.....	155
Calcite .....	155
Type 2 Nepheline Leucosyenite.....	155
Type 3 Nepheline Leucosyenite.....	155
Eudialyte Syenite .....	157
Feldspar-Aegirine Dikes .....	160
Annite Lamprophyre.....	160
Dawsonite .....	164
Type 2 Nepheline Leucosyenite.....	164
Rhodochrosite .....	169

Annite Lamprophyre .....	169
Siderite .....	171
Type 2 nepheline leucosyenite .....	171
Rare-Earth Carbonates .....	175
Ancylite-(Ce) .....	175
Eudialyte Syenite .....	175
Feldspar-Aegirine Dikes .....	176
Calcioancylite-(Ce) .....	176
Type 3 Nepheline Leucosyenite .....	176
Eudialyte Syenite .....	176
Annite Lamprophyre .....	177
Synchysite-(Ce) .....	177
Type 2 nepheline leucosyenite .....	177
Annite Lamprophyre .....	178
East Hill Suite Rare-Earth Carbonates .....	178
Feldspar Group .....	179
Alkali Feldspar Group .....	179
Nepheline Melasyenite .....	179
Type 1 Nepheline Leucosyenite .....	183
Type 2 Nepheline Leucosyenite .....	186
Type 3 Nepheline Leucosyenite .....	189
Eudialyte Syenite .....	192
Feldspar-Aegirine Dikes .....	196
East Hill Suite Alkali Feldspars .....	200
Feldspathoids & Zeolites .....	207
Analcime .....	207
Eudialyte Syenite .....	207
Cancrinite .....	208
Nepheline Melasyenite .....	208
Type 3 Nepheline Leucosyenite .....	208
East Hill Suite Cancrinite .....	209
Natrolite .....	209
Nepheline Melasyenite .....	209
Type 1 Nepheline Leucosyenite .....	210
Type 2 Nepheline Leucosyenite .....	210
Type 3 Nepheline Leucosyenite .....	211
Eudialyte Syenite .....	211
Feldspar-Aegirine Dikes .....	212
Annite Lamprophyre .....	212
Nepheline .....	214
Nepheline Melasyenite .....	214
Type 2 Nepheline Leucosyenite .....	214
Type 3 Nepheline Leucosyenite .....	215
Eudialyte Syenite .....	215
East Hill Suite Nepheline .....	215
Sodalite .....	220



Nepheline melasyenite .....	220
Annite Lamprophyre .....	220
Sodalite ps. Nepheline .....	220
Type 1 nepheline leucosyenite .....	220
Type 2 nepheline leucosyenite .....	221
Type 3 nepheline leucosyenite .....	222
Eudialyte Syenite .....	223
Halides .....	224
Fluorite .....	224
Nepheline Melasyenite .....	224
Type 1 Nepheline Leucosyenite .....	224
Type 3 Nepheline Leucosyenite .....	224
Eudialyte Syenite .....	225
Halite .....	226
Type 2 Nepheline Leucosyenite .....	226
Oxides & Hydroxides .....	227
Baddeleyite .....	227
Annite Lamprophyre .....	227
Böhmite .....	227
Type 3 Nepheline Leucosyenite .....	227
Annite Lamprophyre .....	228
East Hill Suite Böhmite .....	228
Hematite .....	229
Feldspar-Aegirine Dikes .....	229
Hochelagaite .....	229
Eudialyte Syenite .....	229
Ilmenite .....	230
Nepheline Melasyenite .....	230
Magnetite .....	230
Nepheline Melasyenite .....	230
Pyrochlore .....	234
Type 2 Nepheline Leucosyenite .....	234
Type 3 Nepheline Leucosyenite .....	234
Eudialyte Syenite .....	235
Feldspar-Aegirine Dikes .....	235
Annite Lamprophyre .....	235
Pyrophanite .....	236
Feldspar-Aegirine Dikes .....	236
Rutile .....	236
Type 2 Nepheline Leucosyenite .....	236
Thorianite .....	237
Nepheline Melasyenite .....	237
Type 3 Nepheline Leucosyenite .....	237
Phosphates & Sulfates .....	238
Barite .....	238
Type 3 Nepheline Leucosyenite .....	238

Fluorapatite .....	238
Nepheline Melasyenite.....	238
Type 1 Nepheline Leucosyenite.....	239
Type 2 Nepheline Leucosyenite.....	239
Type 3 Nepheline Leucosyenite.....	240
Eudialyte Syenite .....	240
Annite Lamprophyre .....	241
Rhabdophane-(Ce) .....	241
Annite Lamprophyre .....	241
Pyroxene Group .....	242
Crystal Chemistry .....	242
Aegirine-Augite Recalculation Scheme.....	244
Titanaugite Recalculation Scheme.....	244
Nepheline Melasyenite.....	248
Type 1 Nepheline Leucosyenite.....	253
Type 2 Nepheline Leucosyenite.....	255
Type 3 Nepheline Leucosyenite.....	255
Eudialyte Syenite .....	258
Feldspar-Aegirine Dikes .....	262
Annite Lamprophyre .....	262
East Hill Suite Clinopyroxene .....	267
Sulfides .....	288
Acanthite .....	288
Eudialyte Syenite .....	288
Alabandite .....	288
Type 1 Nepheline Leucosyenite.....	288
Arsenopyrite.....	289
Type 1 Nepheline Leucosyenite.....	289
Chalcopyrite.....	290
Eudialyte Syenite .....	290
Covellite.....	290
Eudialyte Syenite .....	290
Galena .....	290
Nepheline Melasyenite.....	290
Type 2 Nepheline Leucosyenite.....	291
Eudialyte Syenite .....	291
Annite Lamprophyre .....	291
Feldspar-Aegirine Dikes .....	291
Molybdenite .....	292
Type 2 Nepheline Leucosyenite.....	292
Type 3 Nepheline Leucosyenite.....	292
Pyrite .....	292
Nepheline Melasyenite.....	292
Type 1 Nepheline Leucosyenite.....	293
Type 2 Nepheline Leucosyenite.....	293
Eudialyte Syenite .....	293

Annite Lamprophyre .....	294
Sphalerite .....	294
Nepheline Melasyenite.....	294
Type 1 Nepheline Leucosyenite.....	294
Type 2 Nepheline Leucosyenite.....	294
Type 3 Nepheline Leucosyenite.....	295
Eudialyte Syenite .....	295
Annite Lamprophyre .....	295
East Hill Suite Sulfides .....	296
Overview .....	296
Nepheline Melasyenite.....	298
Type 1 Nepheline Leucosyenite.....	303
Types 2 & 3 Nepheline Leucosyenite .....	305
Eudialyte Syenite .....	308
Feldspar-Aegirine Dikes & Annite Lamprophyre .....	309
Titanosilicates .....	309
Kupletskite .....	309
Type 1 Nepheline Leucosyenite.....	309
Type 3 Nepheline Leucosyenite.....	309
Eudialyte Syenite .....	310
East Hill Suite Kupletskite.....	310
Titanite .....	311
Nepheline melasyenite .....	311
Zirconosilicates .....	313
Calciophilairite.....	313
Nepheline Melasyenite.....	313
Catapleiite .....	313
Eudialyte Syenite .....	313
Eudialyte Group .....	314
Eudialyte Syenite .....	314
Gaidonnayite .....	325
Eudialyte Syenite .....	325
Annite Lamprophyre .....	325
Hilairite .....	326
Annite Lamprophyre .....	326
Låvenite.....	327
Nepheline Melasyenite.....	327
Petarasite .....	328
Annite Lamprophyre .....	328
Zircon .....	329
Type 2 Nepheline Leucosyenite.....	329
Feldspar-Aegirine Dikes .....	330
East Hill Suite Zirconosilicates.....	330
Paragenesis.....	330
Zinc in Annite Lamprophyre Zirconosilicates .....	335
Other Silicates .....	336

Almandine.....	336
Type 2 Nepheline Leucosyenite.....	336
Annite.....	336
Nepheline Melasyenite.....	336
Feldspar-Aegirine Dikes .....	337
Annite Lamprophyre .....	340
East Hill Suite Annite .....	343
Pectolite-Sérandite Series .....	355
Type 1 Nepheline Leucosyenite.....	355
Type 3 Nepheline Leucosyenite.....	355
Eudialyte Syenite .....	355
Thorogummite.....	357
Type 2 Nepheline Leucosyenite.....	357
Eudialyte Syenite .....	357
Unidentified Phases .....	358
Ca-Zr Silicate .....	358
Ce-dominant Ca-REE Carbonate.....	358
Ce-dominant Ca-REE Phosphate #1 .....	359
Ce-dominant Ca-REE Phosphate #2.....	359
Na-Zr Silicate.....	360
Discussion.....	361
Variation in Magmatic Extensive Parameters.....	361
Oxygen Fugacity.....	361
Sulfur Fugacity.....	364
Alkalinity of the East Hill Suite.....	368
The Formal Concept of Alkalinity.....	368
Overview.....	368
Geochemical Alkalinity .....	368
Mineralogical Alkalinity.....	369
Geochemical Alkalinity of the East Hill Suite.....	371
Mineralogical Alkalinity of the East Hill Suite .....	373
Overview.....	373
Pyroxene Alkalinity .....	375
Evidence for & Behavior of Alkaline Fluids .....	377
Introduction.....	377
Nepheline Alteration Reactions .....	379
Nepheline → Sodalite .....	379
Nepheline → Cancrinite .....	381
Sodalite → Natrolite .....	381
Natrolite → Dawsonite & Late Carbonates .....	382
Zirconosilicate Mineralization .....	383
Melilite Alteration.....	383
Conclusions.....	384
References.....	386
Vita.....	413

## LIST OF TABLES

Table 1 – Primary igneous lithologies of the East Hill suite exposed in the Poudrette quarry. ...	23
Table 2 – Representative whole-rock XRF analyses and CIPW norms I – Major Elements .....	48
Table 3 – Representative whole-rock XRF analyses and CIPW norms II – Major Elements .....	49
Table 4 – Representative whole-rock XRF analyses and CIPW norms III – Major Elements .....	50
Table 5 – Representative whole-rock XRF analyses and CIPW norms IV – Major Elements ....	51
Table 6 – Estimated pre- & analyzed post-alteration whole-rock geochemistries and CIPW norms – Major Elements .....	67
Table 7 – Representative whole-rock XRF analyses – Trace Elements I .....	73
Table 8 – Representative whole-rock XRF analyses – Trace Elements II .....	74
Table 9 – Representative whole-rock XRF analyses – Trace Elements III .....	75
Table 10 – Representative whole-rock XRF analyses – Trace Elements IV .....	76
Table 11 – Geochemical differentiation trends – East Hill suite .....	101
Table 12 – Mineral survey catalogue – East Hill suite .....	121
Table 13 – Representative electron microprobe analyses of calcic amphiboles – Nepheline Melasyenite .....	128
Table 14 – Site-occupancies of calcic amphiboles from Table 13 – Nepheline Melasyenite ....	129
Table 15 – Representative electron microprobe analyses of sodic-calcic amphiboles – Nepheline Melasyenite .....	137
Table 16 – Site-occupancies of sodic-calcic amphiboles from Table 15 – Nepheline Melasyenite .....	138
Table 17 – Representative electron microprobe analysis of sodic amphibole – Eudialyte Syenite .....	142

Table 18 – Representative electron microprobe analyses of calcite – Type 2 Nepheline	
Leucosyenite .....	156
Table 19 – Representative electron microprobe analyses of calcite – Eudialyte Syenite.....	158
Table 20 – Representative electron microprobe analyses of calcite – Feldspar-Aegirine Dikes	161
Table 21 – Representative electron microprobe analyses of calcite – Annite Lamprophyre .....	163
Table 22 – Representative electron microprobe analysis of rhodochrosite – Annite Lamprophyre	
.....	169
Table 23 – Representative electron microprobe analyses of siderite – Type 2 Nepheline	
Leucosyenite .....	172
Table 24 – Representative electron microprobe analyses of alkali feldspar – Nepheline	
Melasyenite .....	181
Table 25 – Representative electron microprobe analyses of alkali feldspar – Type 1 Nepheline	
Leucosyenite .....	184
Table 26 – Representative electron microprobe analyses of alkali feldspar – Type 2 Nepheline	
Leucosyenite .....	187
Table 27 – Representative electron microprobe analyses of alkali feldspar – Type 3 Nepheline	
Leucosyenite .....	190
Table 28 – Representative electron microprobe analyses of alkali feldspar – Eudialyte Syenite	
.....	193
Table 29 – Representative electron microprobe analyses of alkali feldspar – Eudialyte Syenite	
(altered) .....	194
Table 30 – Representative electron microprobe analyses of alkali feldspar – Feldspar-Aegirine	
Dikes .....	198

Table 31 – Representative electron microprobe analyses of natrolite – East Hill suite .....	213
Table 32 – Representative electron microprobe analyses of nepheline – East Hill suite .....	216
Table 33 – Representative electron microprobe analyses of magnetite – Nepheline Melasyenite .....	231
Table 34 – Representative electron microprobe analyses of clinopyroxene – Nepheline Melasyenite .....	249
Table 35 – Representative electron microprobe analyses of titanaugite – Nepheline Melasyenite .....	251
Table 36 – Site-occupancies of titanaugite from Table 35 – Nepheline Melasyenite .....	252
Table 37 – Representative electron microprobe analyses of clinopyroxene – Type 1 Nepheline Leucosyenite .....	254
Table 38 – Representative electron microprobe analyses of clinopyroxene – Type 3 Nepheline Leucosyenite .....	256
Table 39 – Representative electron microprobe analyses of clinopyroxene – Eudialyte Syenite .....	259
Table 40 – Representative electron microprobe analyses of clinopyroxene – Altered Eudialyte Syenite.....	260
Table 41 – Representative electron microprobe analyses of clinopyroxene – Feldspar-Aegirine Dikes .....	263
Table 42 – Representative electron microprobe analyses of clinopyroxene – Annite Lamprophyre .....	265
Table 43 – Representative electron microprobe analyses of titanite – Nepheline Melasyenite .	312

Table 44 – Representative electron microprobe analyses of eudialyte group minerals – Eudialyte Syenite.....	316
Table 45 – Site-occupancies of eudialyte group minerals from Table 44, I – Eudialyte Syenite .....	317
Table 46 – Site-occupancies of eudialyte group mineral from Table 44, II – Eudialyte Syenite .....	318
Table 47 – Representative electron microprobe analyses of gaidonnayite – Annite Lamprophyre .....	326
Table 48 – Representative electron microprobe analysis of hilairite – Annite Lamprophyre ....	327
Table 49 – Representative electron microprobe analysis of låvenite – Nepheline Melasyenite	328
Table 50 – Representative electron microprobe analyses of petarasite – Annite Lamprophyre	329
Table 51 – Paragenesis of zirconsilicates – East Hill suite.....	330
Table 52 – Representative electron microprobe analyses of annite – Nepheline Melasyenite...	338
Table 53 – Representative electron microprobe analyses of annite – Feldspar-Aegirine Dikes	339
Table 54 – Representative electron microprobe analyses of annite – Annite Lamprophyre .....	341
Table 55 – Site-occupancies of annite from Table 54 – Annite Lamprophyre.....	342
Table 56 – Representative electron microprobe analysis of sérandite – Eudialyte Syenite .....	356
Table 57 – Mineralogical alkalinity & characteristic mineral assemblages .....	370
Table 58 – Characteristic mineral assemblages – East Hill suite .....	374



## LIST OF FIGURES

Figure 1 – Tectonostratigraphy of the western extreme of the Québec Appalachians. ....	6
Figure 2 – Extent of the New England-Québec igneous province.....	7
Figure 3 – Map of the Montereian Hills and the Eastern Townships of Québec.....	8
Figure 4 – The Saint Lawrence rift system. ....	9
Figure 5 – Mont Saint-Hilaire, viewed from the west. ....	11
Figure 6 – The northwest face of Mont Saint-Hilaire.....	11
Figure 7 – The northeast face of Mont Saint-Hilaire, showing the excavation of the Poudrette quarry as of July, 1995.....	12
Figure 8 – Geologic map of Mont Saint-Hilaire. The light-shaded polygonal area on the north- northeast side of the mountain indicates the extent of the excavation of the Poudrette quarry as of March, 2009. ....	13
Figure 9 – Feldspathoidal leucosyenite in the wall of the Poudrette quarry.....	23
Figure 10 – Leucosyenite in nepheline melasyenite, showing brecciation, as well as concordant and discordant enclosure.....	25
Figure 11 – Dikes crosscutting nepheline melasyenite in the Poudrette quarry. ....	25
Figure 12 – Feldspar-aegirine dikes cross-cutting nepheline melasyenite. ....	26
Figure 13 – Microcline crystals in wall zone of eudialyte-bearing pegmatite dike.....	26
Figure 14 – Panoramic view of the Poudrette quarry, July 1995.....	27
Figure 15 – Harker diagram for $\text{TiO}_2$ (post-alteration).....	55
Figure 16 – Harker diagram for $\text{Al}_2\text{O}_3$ (post-alteration). ....	56
Figure 17 – Harker diagram for total iron expressed as FeO (post-alteration). ....	57
Figure 18 – Harker diagram for MnO (post-alteration). ....	58

Figure 19 – Harker diagram for MgO (post-alteration). .....	59
Figure 20 – Harker diagram for FeO + MnO + MgO (post-alteration). .....	60
Figure 21 – Harker diagram for CaO (post-alteration). .....	61
Figure 22 – Harker diagram for Na <sub>2</sub> O (post-alteration). .....	62
Figure 23 – Harker diagram for K <sub>2</sub> O (post-alteration). .....	63
Figure 24 – Harker diagram for Na <sub>2</sub> O + K <sub>2</sub> O (post-alteration). .....	64
Figure 25 – Harker diagram for P <sub>2</sub> O <sub>5</sub> (post-alteration). .....	65
Figure 26 – Harker diagram for Na <sub>2</sub> O (including pre-alteration compositions). .....	68
Figure 27 – Harker diagram for K <sub>2</sub> O (including pre-alteration compositions). .....	69
Figure 28 – Harker diagram for Na <sub>2</sub> O + K <sub>2</sub> O (including pre-alteration compositions). .....	70
Figure 29 – Total alkalis <i>versus</i> silica diagram after Wilson (1989). .....	84
Figure 30 – Na <sub>2</sub> O <i>versus</i> SiO <sub>2</sub> , scaled as the total alkalis <i>versus</i> silica diagram of Wilson (1989). .....	85
Figure 31 – K <sub>2</sub> O <i>versus</i> SiO <sub>2</sub> , scaled as the total alkalis <i>versus</i> silica diagram of Wilson (1989). .....	86
Figure 32 – K <sub>2</sub> O <i>versus</i> Na <sub>2</sub> O, with the alkali basalt series of Middlemost (1975) superimposed. .....	87
Figure 33 – Aluminosity diagram after Shand (1943). Ratios calculated from a molar basis. .....	88
Figure 34 – Nb <i>versus</i> Ga/Al tectonic discrimination diagram after Whalen <i>et al.</i> (1987). .....	90
Figure 35 – Zr <i>versus</i> Ga/Al tectonic discrimination diagram after Whalen <i>et al.</i> (1987). .....	91
Figure 36 – Y <i>versus</i> Ga/Al tectonic discrimination diagram after Whalen <i>et al.</i> (1987). .....	92

Figure 37 – $\text{Na}_2\text{O} + \text{K}_2\text{O}$ versus Ga/Al tectonic discrimination diagram after Whalen <i>et al.</i> (1987).	93
Figure 38 – $(\text{Na}_2\text{O} + \text{K}_2\text{O})/\text{CaO}$ versus Ga/Al tectonic discrimination diagram after Whalen <i>et al.</i> (1987).	94
Figure 39 – $(\text{Na}_2\text{O} + \text{K}_2\text{O})/\text{CaO}$ versus HFSE tectonic discrimination diagram after Whalen <i>et al.</i> (1987).	95
Figure 40 – Nb-Y-Ce tectonic discrimination diagram after Eby (1992).	96
Figure 41 – Rb versus Y + Nb tectonic discrimination diagram after Pearce <i>et al.</i> (1984).	97
Figure 42 – Nb versus Y tectonic discrimination diagram after Pearce <i>et al.</i> (1984).	98
Figure 43 – Coryell-Masuda diagram for the East Hill suite, normalized to the primitive mantle (PM).	109
Figure 44 – Coryell-Masuda diagram for the East Hill suite, average OIB, E-MORB, and N-MORB, and the East Hill suite silicate xenolith, normalized to the primitive mantle (PM).	110
Figure 45 – Coryell-Masuda diagram comparing the East Hill suite with the Ilímaussaq intrusion, both normalized to the primitive mantle (PM).	113
Figure 46 – Coryell-Masuda diagram comparing the East Hill suite with the Kasungu and Chipala intrusions, North Nyasa alkaline province, both normalized to the primitive mantle (PM).	114
Figure 47 – Coryell-Masuda diagram comparing the East Hill suite with the Ilomba and Ulindi intrusions, North Nyasa alkaline province, both normalized to the primitive mantle (PM).	115

Figure 48 – Coryell-Masuda diagram comparing the East Hill suite with the Oslo alkaline province, both normalized to the primitive mantle (PM)..	116
Figure 49 – Coryell-Masuda diagram comparing the East Hill suite with the Khibina intrusion, both normalized to the primitive mantle (PM).	117
Figure 50 – Coryell-Masuda diagram comparing the East Hill suite with the Lovozero intrusion, both normalized to the primitive mantle (PM).	118
Figure 51 – Calcic amphibole compositions – Nepheline Melasyenite.....	130
Figure 52 – High-Ti calcic amphibole compositions – Nepheline Melasyenite.....	131
Figure 53 – Compositional variation of synthetic calcic amphiboles as a function of temperature.	132
Figure 54 – <sup>iv</sup> Al content of synthetic calcic amphiboles as a function of temperature.	133
Figure 55 – Al <sub>2</sub> O <sub>3</sub> (wt.%) content of synthetic calcic amphiboles as a function of pressure and temperature.	133
Figure 56 – TiO <sub>2</sub> (wt.%) content of synthetic calcic amphiboles as a function of pressure and temperature.	134
Figure 57 – Sodic-calcic amphibole compositions – Nepheline Melasyenite .....	139
Figure 58 – Ferro-eckermannite on microcline, associated with aegirine, eudialyte group, and sodalite pseudomorph after nepheline – Eudialyte Syenite .....	140
Figure 59 – Sodic amphibole composition – Eudialyte Syenite .....	143
Figure 60 – Variation in site-occupancy of <sup>[4]</sup> Na in sodic amphiboles as a function of pressure and temperature. System buffered by the reaction glaucophane = jadeite + talc. ....	144
Figure 61 – Oxygen fugacity isopleths for sodic amphiboles (blueschist facies p-T conditions).	144

Figure 62 – Relative oxygen fugacity <i>versus</i> estimated temperature for nepheline melasyenite amphiboles (calcic & sodic-calcic) .....	146
Figure 63 – $\text{Ca} + {}^{\text{iv}}\text{Al}$ <i>versus</i> $\text{Si} + \text{Na} + \text{K}$ in amphiboles – Nepheline Melasyenite .....	148
Figure 64 – Mn <i>versus</i> Zn in amphibole – Strange Lake granite.....	150
Figure 65 – Mn <i>versus</i> Zn in amphiboles – Nepheline Melasyenite .....	150
Figure 66 – Mn and ${}^{\text{vi}}\text{Ti}$ <i>versus</i> Zn in calcic amphiboles – Nepheline Melasyenite.....	151
Figure 67 – Mn and ${}^{\text{vi}}\text{Ti}$ <i>versus</i> Zn in sodic-calcic amphiboles – Nepheline Melasyenite.....	152
Figure 68 – Octahedral ferric iron <i>versus</i> octahedral aluminum in amphiboles – Nepheline Melasyenite .....	154
Figure 69 – Calcite compositions – Type 2 Nepheline Leucosyenite .....	157
Figure 70 – Calcite compositions – Eudialyte Syenite .....	159
Figure 71 – Calcite compositions – Feldspar-Aegirine Dikes .....	162
Figure 72 – Calcite compositions – Annite Lamprophyre.....	164
Figure 73 – Phase relations of dawsonite and associated phases in $\log a_{\text{Na}^+} / a_{\text{H}^+} - \log a_{\text{SiO}_2}$ space .....	165
Figure 74 – Phase relations of dawsonite and associated phases in $\log a_{\text{Na}^+} / a_{\text{H}^+} - \log f_{\text{CO}_2}$ space. ....	166
Figure 75 – Phase relations of natrolite and associated phases in $\log a_{\text{Na}^+} - \log a_{\text{SiO}_2}$ space. ..	168
Figure 76 – Rhodochrosite composition – Annite Lamprophyre .....	171
Figure 77 – Siderite compositions – Type 2 Nepheline Leucosyenite .....	173
Figure 78 – Stability fields in $f_{\text{O}_2}$ -T space of calcite, rhodochrosite, and siderite at 2 kbar .....	174
Figure 79 – Alkali feldspar compositions – Nepheline Melasyenite .....	182
Figure 80 – Alkali feldspar compositions – Type 1 Nepheline Leucosyenite .....	185

Figure 81 – Alkali feldspar compositions – Type 2 Nepheline Leucosyenite .....	188
Figure 82 – Alkali feldspar compositions – Type 3 Nepheline Leucosyenite .....	191
Figure 83 – Alkali feldspar compositions – Eudialyte Syenite.....	195
Figure 84 – Euhedral microcline in miarole, associated with aegirine and eudialyte group mineral – Eudialyte Syenite .....	196
Figure 85 – Alkali feldspar compositions – Feldspar-Aegirine Dikes .....	199
Figure 86 – Alkali feldspar structural states – East Hill suite.....	201
Figure 87 – Phase relations in the system $\text{NaAlSi}_3\text{O}_8$ – $\text{KAlSi}_3\text{O}_8$ for anhydrous conditions at 1 bar and for hydrous conditions at $p_{\text{H}_2\text{O}} = 0.2$ GPa and 0.5 GPa.....	204
Figure 88 – Ternary-feldspar compositions and calculated isotherms – East Hill suite.....	206
Figure 89 – Euhedral analcime in miarole, associated with alkali feldspar, aegirine, fluorite, and natrolite – Eudialyte Syenite .....	207
Figure 90 – Nepheline compositions and isotherms – East Hill suite. ....	217
Figure 91 – Fluorite, associated with aegirine and alkali feldspar – Eudialyte Syenite .....	225
Figure 92 – Fluorite in miarole, associated with aegirine, alkali feldspar, eudialyte group mineral, natrolite, and an unidentified yellow mineral. ....	226
Figure 93 – Estimated oxygen fugacity <i>versus</i> temperature based on coexisting magnetite- ulvöspinel and ilmenite-hematite solid solution pairs. ....	232
Figure 94 – Compositional relations in clinopyroxene.....	243
Figure 95 – Clinopyroxene compositions – Nepheline Melasyenite .....	250
Figure 96 – Clinopyroxene compositions – Nepheline Leucosyenite .....	257
Figure 97 – Clinopyroxene compositions – Eudialyte Syenite.....	261
Figure 98 – Clinopyroxene compositions – Feldspar-Aegirine Dikes.....	264

Figure 99 – Clinopyroxene compositions – Annite Lamprophyre .....	266
Figure 100 – Compositional evolution of clinopyroxene – East Hill suite.....	268
Figure 101 – Compositional trend in clinopyroxene in the East Hill suite from this study, compared to East Hill suite data from PIILONEN <i>ET AL.</i> (1998) and trends from other alkaline complexes. ....	270
Figure 102 – Variation of Ti with fractionation in clinopyroxene – East Hill suite .....	273
Figure 103 – Variation of ZrO <sub>2</sub> with fractionation in clinopyroxene – East Hill suite.....	274
Figure 104 – Variation of Ti with ferromagnesian elements in clinopyroxene – East Hill suite	278
Figure 105 – Variation of Zr with ferromagnesian elements in clinopyroxene – East Hill suite	279
Figure 106 – Ti <i>versus</i> Al in clinopyroxene – East Hill suite.....	280
Figure 107 – Zr <i>versus</i> Al in clinopyroxene – East Hill suite .....	281
Figure 108 – Variation of Al with fractionation in clinopyroxene – East Hill suite .....	284
Figure 109 – Variation of Fe <sup>3+</sup> with fractionation in clinopyroxene – East Hill suite.....	285
Figure 110 – Fe <sup>3+</sup> <i>versus</i> Na in clinopyroxene – East Hill suite.....	286
Figure 111 – Variation of Mn with fractionation in clinopyroxene – East Hill suite .....	287
Figure 112 – Measured wavelength peak shift for SK $\alpha$ <i>versus</i> experimental oxygen fugacity in $\Delta$ QFM log units. ....	297
Figure 113 – Corresponding $X(S^{6+})_{eq.}$ values for the curve from Figure 112 .....	298
Figure 114 – Isothermal sulfur fugacity <i>versus</i> oxygen fugacity spaces showing phase relations in the Fe-O <sub>2</sub> -S <sub>2</sub> -SiO <sub>2</sub> system. ....	299
Figure 115 – Oxygen fugacity <i>versus</i> temperature for Zn, Pb, and Ba sulfide-sulfate pairs.....	302
Figure 116 – Phase relations in $a_{S_2}$ –T space for the system Fe-As-S.....	305
Figure 117 – Phase relations in $f_{O_2}$ – $f_{S_2}$ space for Mo-W sulfide–calcium-oxyanion pairs. ....	307

Figure 118 – Euhedral eudialyte group mineral in miarole, associated with microcline, sodalite ps. nepheline, and aegirine – Eudialyte Syenite .....	315
Figure 119 – Site-occupancy of $M(3)$ in eudialyte group minerals – Eudialyte Syenite .....	320
Figure 120 – Relative site-occupancy of $M(3)$ by Si, Nb, and Ta in eudialyte group minerals with Si, Nb, or Ta dominant – Eudialyte Syenite .....	322
Figure 121 – Site-occupancy of $M(2)$ versus $M(3)$ and resulting speciation in eudialyte group minerals from the eudialyte and kentbrooksites series – Eudialyte Syenite .....	323
Figure 122 – Relative site-occupancy of $M(3)$ by Zr, Ti, and Hf in eudialyte group minerals with Zr, Ti, or Hf dominant – Eudialyte Syenite .....	324
Figure 123 – Schematic cooling paths in $[ZrO_2]$ –T space for three peralkaline magmas. ....	331
Figure 124 – Annite $X$ -indicatrix pleochroism – Annite Lamprophyre.....	344
Figure 125 – Annite $Y$ -indicatrix pleochroism – Annite Lamprophyre.....	345
Figure 126 – Annite $Z$ -indicatrix pleochroism – Annite Lamprophyre.....	346
Figure 127 – Annite compositions – East Hill suite. ....	348
Figure 128 – $^{iv}Fe^{3+}$ versus $^{iv}Al$ in annite – East Hill suite .....	349
Figure 129 – Ti versus $X_{Fe^{2+}}$ in annite – East Hill suite.....	351
Figure 130 – Annite enrichment trend in the East Hill suite, compared to enrichment trends from other nepheline syenite complexes. ....	352
Figure 131 – Total Al versus $X_{Fe^{2+}}$ in annite – East Hill suite.....	353
Figure 132 – $Mn^{2+}$ versus $X_{Fe^{2+}}$ in annite – East Hill suite.....	354
Figure 133 – Sérandite, associated with aegirine, alkali feldspar, and natrolite – Eudialyte Syenite.....	356



Figure 134 – Thorogummite (?) associated with alkali feldspar and natrolite – Eudialyte Syenite .....	357
Figure 135 – Estimated oxygen fugacity <i>versus</i> temperature path for the East Hill suite.....	363
Figure 136 – Estimated sulfur fugacity <i>versus</i> temperature path for the East Hill suite. ....	366
Figure 137 – Whole-rock agpaitic indices – East Hill suite .....	371
Figure 138 – Alkalinity moduli of pyroxene group minerals – East Hill suite.....	375
Figure 139 – Pyroxene alkalinity moduli compared with whole-rock agpaicity indices – East Hill suite .....	376

## ABSTRACT

The Mont Saint-Hilaire alkaline complex, Québec, is a Cretaceous rift-related intrusion comprising two gabbroic suites and the East Hill suite, an assemblage of several distinct nepheline syenites and evolved syenitic rocks. Whole-rock analysis of the East Hill suite reveals two fractionation trends, one which is described by the syenitic lithologies and one by the evolved syenites and syenoids. A lamprophyric unit stands on its own, geochemically, consistent with typical lamprophyre petrogenesis. Whole-rock geochemistry of the East Hill suite shows moderate silica content but highly alkaline rocks, enriched in Mn, Zn, Zr, Y, and Ce. Chlorine and sulfur are important and present in abundant secondary sodalite and pervasive microsulfides.

Mineral geochemistry indicates decreasing oxygen fugacity with cooling, and phases such as titanite (present) and aenigmatite (absent) defined boundaries in  $f_{\text{O}_2}$  – T space. Oxygen fugacity data combined with petrography and geothermometry defined an  $f_{\text{O}_2}$  – T curve for the East Hill suite magma, revealing that the oxygen fugacity ranged between approximately  $10^{-10}$  bar at intrusion down to  $10^{-25}$  bar subsolidus, and that, owing to non-linearity of oxygen buffers, the  $f_{\text{O}_2}$  – T path crossed below QFM early, went above QFM late in the crystallization history and then above HM with cooling. A similar procedure applied to sulfur fugacity generated a trend of initial increase from about  $10^{-4}$  to  $10^{-2}$  bar followed by decreasing sulfur fugacity with cooling down to approximately  $10^{-8}$  bar. The oxygen trend implies that earlier suggestions that oxidation of iron drove the evolution of pyroxenes towards aegirine are incorrect.

Textural evidence of abundant alteration and secondary mineralization suggests subsolidus action of alkaline fluids. Contrary to previous studies, most sodalite in the East Hill suite is not primary but is the product of reaction of nepheline with chloride-rich fluids after crystallization. Sodalite pseudomorphs continued to react with these fluids, whose chemistry

changed with time to silica- then carbonate-rich, resulting in further reactions that led to natrolite and dawsonite deposition, accompanied by late-stage rhodochrosite. It is hypothesized that the silica- and carbonate-rich phase of these fluids caused the decomposition of a melilite groundmass in the lamprophyre to a natrolite-calcite assemblage.

*Keywords:* Mont Saint-Hilaire, oxygen fugacity, sulfur fugacity, alkaline fluids, pyroxene trend

## INTRODUCTION

Alkaline plutonic complexes may be broadly defined as single or multiple-associated igneous intrusions characterized by an overall chemical enrichment in alkaline elements, especially sodium and potassium. More particularly, however, alkaline plutonic complexes exhibit one or more of a suite of distinctive attributes.

Firstly, in addition to their enrichment in alkali metals, the bulk chemistries of many of these complexes exhibit elevated levels of rare elements such as zirconium, cerium, yttrium, and niobium. As a result of their elaborate bulk chemistry, alkaline plutonic complexes typically host exceptional assemblages of minerals. Such assemblages may comprise a large number of mineral species, on the order of several hundred in a single locality,<sup>1</sup> perhaps including species peculiar to the locality. Also, individual species may have bizarre compositions or unusual trace-element chemistries.

Secondly, most, though not all, alkaline plutonic complexes are undersaturated in silica. Not only is free quartz uncommon as a primary mineral, but some lithologies within these complexes are so silica-poor as to be feldspar-free.

Thirdly, alkaline plutonic complexes tend to be composed of a wide range of petrologically distinct rock types, even when the complex is quite small in its areal extent (*e.g.* <10 km<sup>2</sup>).

Lastly, these complexes are found nearly exclusively in contemporary or ancient extensional tectonic settings, in particular those in which full-scale continental rifting is involved.

---

<sup>1</sup> The coeval Khibina and Lovozero massifs on the Kola peninsula in Russia collectively present over 550 species, for more than 100 of which the plutons are the type locality. (Arzamastsev *et al.* 2008) Mont Saint-Hilaire hosts over 370. (Back *et al.* 2006)

Attracted by these unusual and tantalizing properties, the mineralogical community has exhaustively studied alkaline plutonic complexes. The brilliance of this side of alkaline complexes, however, appears to blind science to the equally important aspects of petrology and paragenesis. Less research has been carried out in these areas save for petrological overviews that characterize the several lithologies of a site, either as a study in and of themselves or, more commonly, parenthetically to a mineralogical study.<sup>2</sup> Additionally, the more common rock-forming minerals such as the alkali feldspars and the pyroxenes tend to be overlooked. As a result, the lithologies of alkaline complexes remain some of the least-understood igneous rocks in terms of the specific aspects of their tectonic significance, petrogenesis, and mineralogy; Mont Saint-Hilaire is no exception.

As one of the world's premier sites for the collection of mineral specimens, the species mineralogy of Mont Saint-Hilaire has been extensively researched. Such efforts, however, have focused on rare or unusual minerals, some known from only a single crystal. Furthermore, the search for more mineral species led earlier studies to emphasize the mineralogy of microenvironments, such as pegmatites or miarolitic cavities. Consequently, common minerals are poorly characterized throughout the East Hill suite, the most alkaline suite of lithologies and the host of most of the exotic minerals, contributing to the lack of a formal petrologic description of the East Hill suite, not to mention a lesser understanding of the occurrence and characteristics of rock-forming minerals in alkaline igneous complexes.

This study set out to address this deficit in the knowledge of Mont Saint-Hilaire by examining the mineralogy and geochemistry of the rock-forming minerals of the East Hill suite,

---

<sup>2</sup> Of a comprehensive sampling of nearly 200 doctoral dissertations & journal articles on Mont Saint-Hilaire, dating back to 1860, only 31 have been concerned with the petrology or magmatic evolution of the intrusion. Over 80% of the sampled studies on Mont Saint-Hilaire strictly regard mineralogy. (Gault Nature Reserve 2007; *Canadian Mineralogist* 2009)

as part of a broader study into the petrology and magmatic evolution of the pluton. As work proceeded, it became apparent that understanding the role of volatiles was important to comprehending the evolution of the East Hill Suite and that their relative influence was both systematic and evolved systematically over time. In alkaline systems, volatiles play an important part throughout magmatic evolution—for examples, as components of fenitizing fluids or as participants in melt complexes.

The evolution of volatiles through the crystallization history of the East Hill Suite was described by applying mineral geochemistry to establish boundaries on oxygen and sulfur buffer diagrams and then using accompanying stability fields of relevant mineral species to trace magmatic evolution through crystallization. In addition to oxygen and sulfur, aqueous fluids were evidently not only an element in the petrogenesis of the East Hill suite magma but also a critical aspect of its subsolidus behavior. Numerous subsolidus reactions were combined with petrographic data to establish a geochemical evolutionary sequence for these fluids. Although this study does not fully address the petrogenesis of the East Hill suite magma or the origin of the aqueous fluids, it does lay the groundwork for further study and understanding of these issues.

## PREVIOUS WORK

Modern research projects concerning the petrology of Mont Saint-Hilaire commenced with POULIOT (1962), who traced the thermal history of the Montereian province using a comparative study of feldspars. GOLD (1963) examined the relationship between the intrusive nepheline syenites and the country rock limestone at Mont Oka and Mont Saint-Hilaire. RAJASEKARAN (1968) focused solely on Mont Saint-Hilaire, producing a petrologic study that characterized the mineralogy and whole-rock composition of the nepheline syenite.

In a special issue of *Canadian Mineralogist* devoted to the alkaline rocks of the Montereian Province, PHILPOTTS (1970) discussed the emplacement mechanism of the intrusions; KUMARAPALI (1970) related the time of intrusion to that of rifting, noting that they were contemporaneous; and CURRIE (1970) speculated about the genetic link between alkaline magmatism and continental rifting in the Montereian province.

A lull in research followed until the mid-eighties, at which time CURRIE (1983) and CURRIE *ET AL.* (1986) produced studies on the petrology of the Montereian Hills and the petrologic suites of Mont Saint-Hilaire, respectively. These studies went farthest towards understanding the evolution of the East Hill suite, recognizing the presence of a low-oxygen fugacity environment, but they did not adequately describe the numerous lithologies of the suite. BÉDARD (1985) investigated magma genesis and differentiation in intrusives across northeastern North America, and SCHUCKER & FOLAND (1992) elaborated on the subject using lead isotopes.

TICE (1995) and TICE & MARTIN (1996) examined the mineralogy and petrology of a nepheline-sodalite syenite pegmatite dike, modeled its cooling history, and presented a mechanism for the formation of banded aplite. Most recently, ZANGOUI (2003) studied magmatic evolution and alteration of annite.

## **GEOLOGIC SETTING**

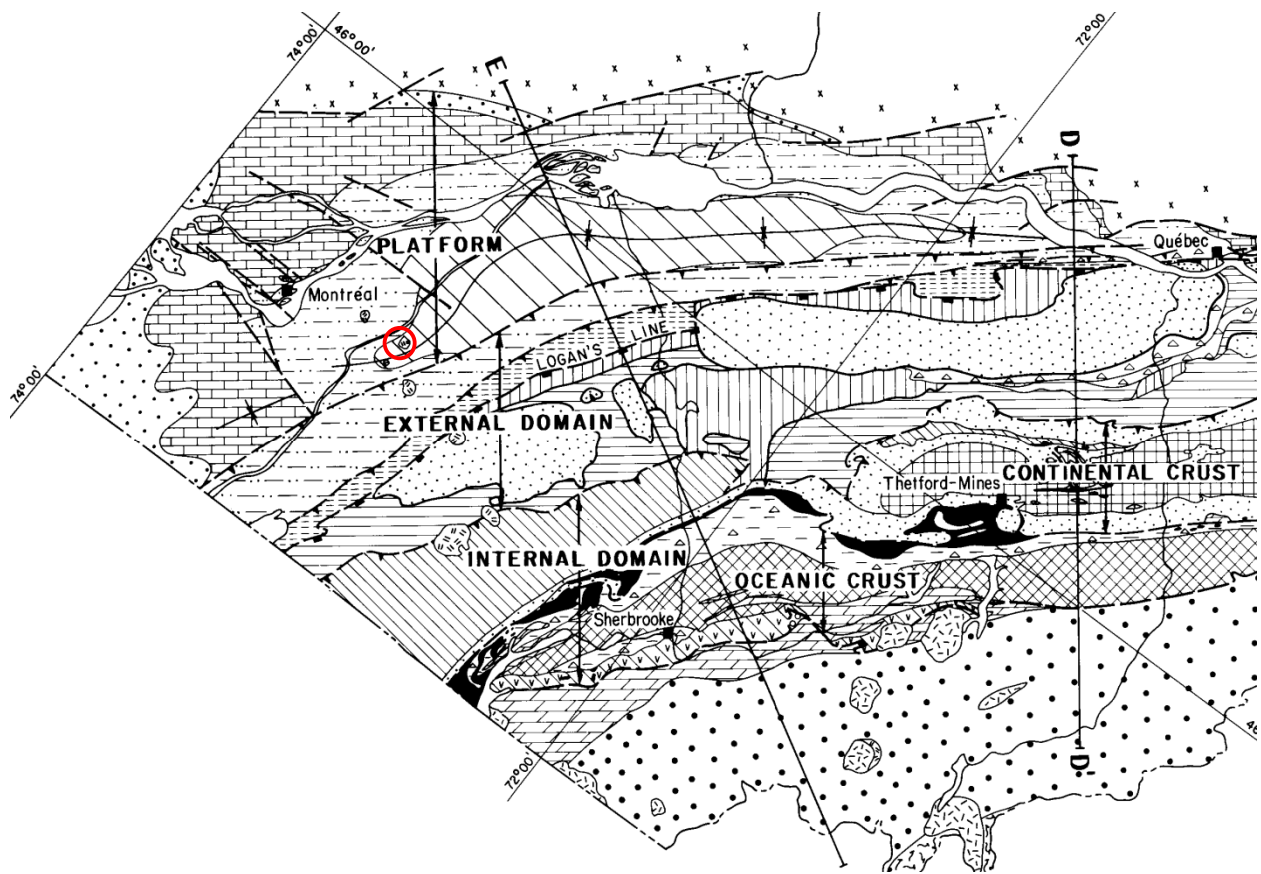
### **REGIONAL GEOLOGY**

#### **TECTONOSTRATIGRAPHY**

Mont Saint-Hilaire is located approximately 30 km east of Montréal, Québec (Figure 1) and intruded into the autochthonous platform immediately to the west of the Taconian orogenic belt. The autochthonous platform rocks comprise a thick succession of relatively undeformed Cambrian and Ordovician sedimentary formations that unconformably rest on crystalline Precambrian basement rocks. This Grenvillian basement consists of marble and quartzite with granite and gneiss. (Wilson 1964; St. Julien & Hubert 1975)

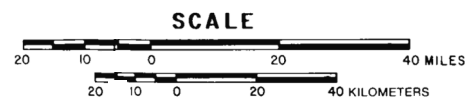
The autochthonous platform represents the Taconian transgressive continental shelf sequence. In the vicinity of Mont Saint-Hilaire, immediately overlying the Precambrian basement is the Upper Cambrian Potsdam sandstone, followed upwards by the Lower Ordovician Beekmantown dolomite, the Middle Ordovician Chazy, Black River, and Trenton limestones, the Middle and Upper Ordovician Utica shale, and the Upper Ordovician Lorraine flysch and Richmond shale. The Lorraine flysch consists primarily of shales, with sandstone in the earliest units and minor limestone and dolostone throughout (Wilson 1964; St. Julien & Hubert 1975) and, along with the Richmond shale, directly contacts the Mont Saint-Hilaire pluton at and near the present surface exposure. (Currie *et al.* 1986) The platform succession is itself unconformably overlain by Quaternary alluvium, varved clays and glacial till. (Wilson 1964; St. Julien & Hubert 1975)





### INTRUSIVE ROCKS

-  MONTEREGIAN INTRUSIVES.
-  DEVONIAN INTRUSIVES.



### CAMBRIAN AND ORDOVICIAN SHELF


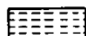
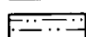
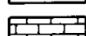
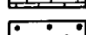
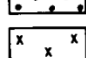
-  REGRESSIVE SEQUENCE. (U.O.).
-  ORDOVICIAN CARBONATES AND FLYSCH. (M.O.).
-  MIDDLE ORDOVICIAN FLYSCH. Canajoharie, Utica, Lorraine. (M.O., U.O.).
-  ORDOVICIAN CARBONATES. Beekmantown, Chazy, Black River, Trenton. (L.O., M.O.).
-  POTSDAM SANDSTONE. (U.E., L.O.).
-  PRECAMBRIAN BASEMENT.

FIGURE 1 – Tectonostratigraphy of the western extreme of the Québec Appalachians. Mont Saint-Hilaire is indicated by the red circle. (after St. Julien & Hubert 1975)

## MONTEREGIAN PROVINCE

During the Mesozoic, extensional tectonics in western New England and southern Québec resulted in the emplacement of several alkaline plutons and multitudes of dikes. This area of alkaline magmatism is collectively referred to as the New England-Québec igneous province (Figure 2). (McHone & Butler 1984)

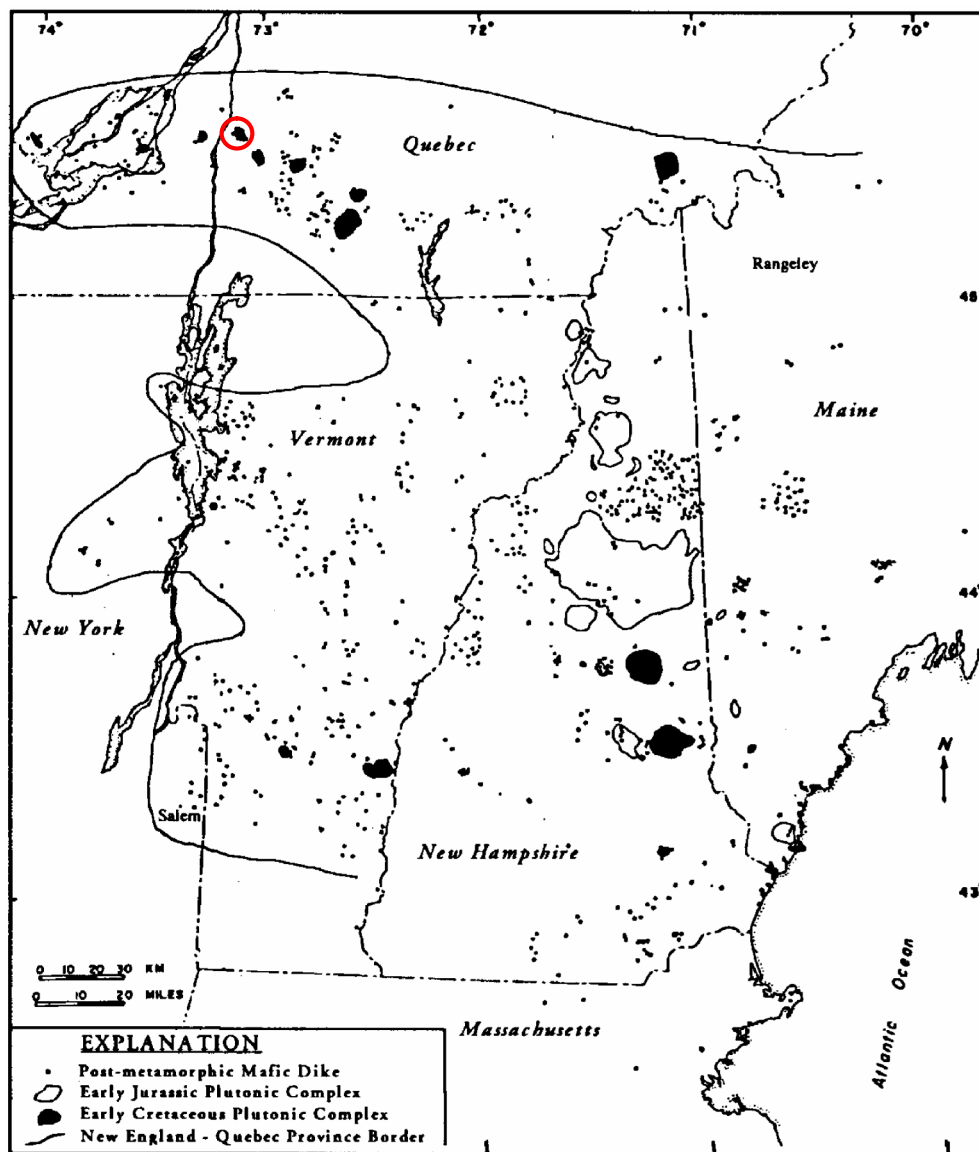


FIGURE 2 – Extent of the New England-Québec igneous province. Mont Saint-Hilaire is indicated by the red circle. (McHone & McHone 1993)

The boundaries of the Monteregian province, the Québec portion of the New England-Québec igneous province, are broadly defined by the Monteregian Hills, a series of about a dozen fault-controlled plutons (Figure 3), including Mont Saint-Hilaire, which intruded the autochthonous and allochthonous structures of the Taconian orogenic belt in the St. Lawrence lowlands during the Cretaceous. (Philpotts 1970)

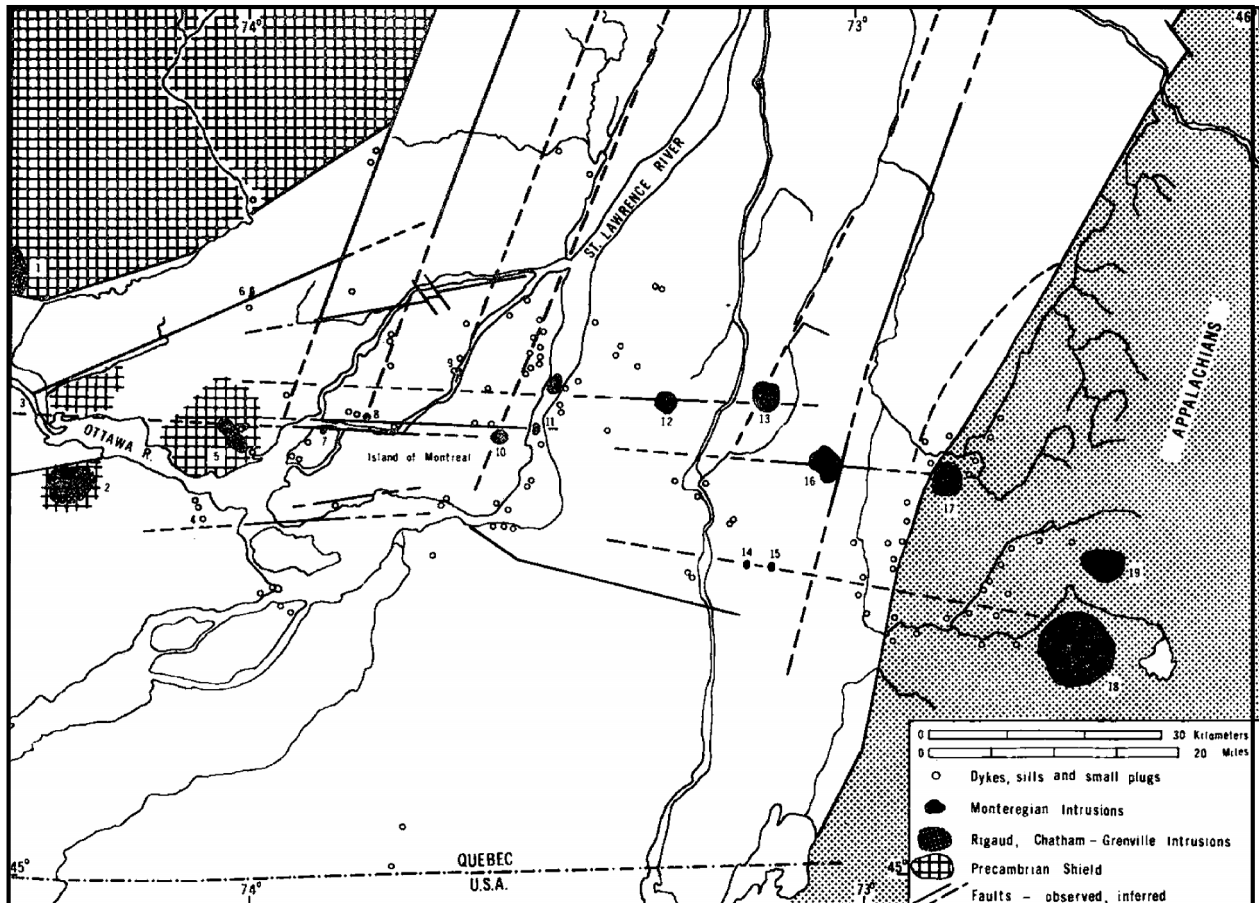


FIGURE 3 – Map of the Monteregian Hills and the Eastern Townships of Québec. Mont Saint-Hilaire is the intrusion labeled “13”. (after Philpotts 1970)

In addition to the regional extensional tectonics, the emplacement of the Monteregian Hills, in particular, was strongly influenced by the Saint Lawrence rift system (Figure 4), a massive network of failed rift arms that extends a total of nearly 2,500 km. (Currie 1970)

Although the intrusions are not coeval—magma has intruded the rift system periodically over the

past 600 Ma—they are interpreted to be broadly genetically related, having been formed through a combination of upper mantle and crustal partial melting and desilication, generated by the heat of upwelling mantle material and concomitant circulation of aqueous fluids, and varying degrees of crustal contamination. (Currie 1970; Eby 1984, 1985a, 1985b & 2006)

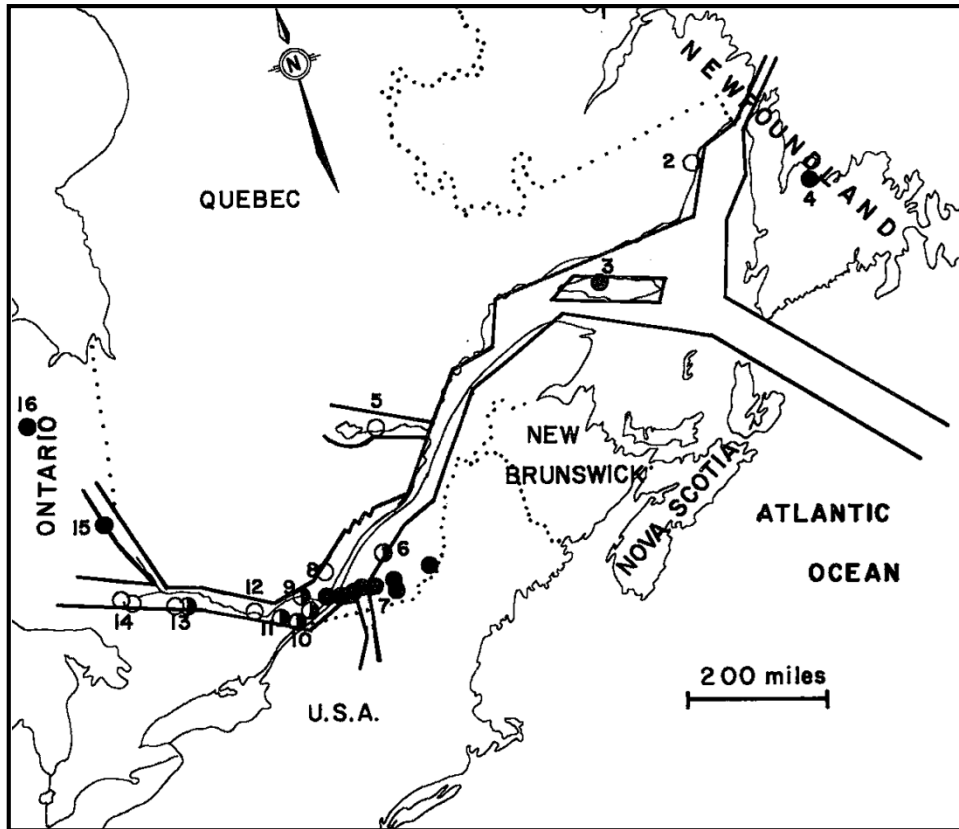


FIGURE 4 – The Saint Lawrence rift system. The Monteregian Hills are the linear trace of filled circles labeled “7”. (Currie 1970)

Despite their general genetic commonalities, rock types are highly varied—both across the province and within single intrusions—from tholeiitic to calc-alkaline to alkaline.

(Kumarapeli & Saull 1966; Doig & Barton 1968; Currie 1970; Bédard 1988) Silica saturation varies systematically with geography, increasing relatively continuously from west to east, from undersaturated at the western end of the province to oversaturated at the eastern end.

(Philpotts 1970)

Common intrusive rock types in the Monteregian Hills include sodalite and/or nepheline syenite, essexite, olivine gabbro, and monzonite. Additionally, several intrusions exhibit the unique lithologies and bulk chemistries associated with alkaline complexes, among them Mont Saint-Hilaire, Mont Yamaska, and Mont Oka, the last of which hosts carbonatite ring-dikes. (Clark 1955; Philpotts 1976; Currie *et al.* 1986; Gold *et al.* 1986)

### **MONT SAINT-HILAIRE – PHYSIOGRAPHY**

Differential erosion progressively exposed the Monteregian Hills until the present, at which time they stand as isolated hills, rising up to hundreds of meters above the flat surroundings of the Saint Lawrence and Richelieu river valleys (Figure 5). (Philpotts 1970) In plan view, Mont Saint-Hilaire is nearly circular and its exposure of intrusive rocks averages about 2.25 km in diameter; the mountain has a maximum elevation of roughly 420 m (375 m relief). (O'Neill 1914) Mont Saint-Hilaire has a rounded and smoothed profile, with a gentle slope at the top, becoming steeper towards the sides; in places, the walls are nearly vertical. Arboreal cover is nearly total where the slope is less than about 60°; even on many vertical walls, there is some vegetation (Figure 6).

The exception to this rule is on the northeast side of the mountain in the property of the Poudrette Quarry, which is largely devoid of vegetation. The quarry cuts the side of the pluton (Figure 7) to a maximum depth of approximately 150 m, offering a unique cross-sectional view of the lithologies therein. It is from this quarry that all samples were collected.





FIGURE 5 – Mont Saint-Hilaire, viewed from the west. As with most of the other Monteregian Hills, Mont Saint-Hilaire rises abruptly from level countryside. (photograph by the author)



FIGURE 6 – The northwest face of Mont Saint-Hilaire. Note the extensive forestation, even on steep, rocky slopes. (photograph by the author)



FIGURE 7 – The northeast face of Mont Saint-Hilaire, showing the excavation of the Poudrette quarry as of July, 1995. (photograph by the author)

### **MONT SAINT-HILAIRE – GENERAL GEOLOGY**

The exposed portion of Mont Saint-Hilaire itself is in direct contact with units of the Upper Ordovician Richmond and Lorraine Groups, which comprise red and grey shales with interbedded limestone and dolostone. (Wilson 1964; St. Julien & Hubert 1975) These shales were baked by the cooling Mont Saint-Hilaire magma to form a biotite-grade hornfels aureole that extends to roughly 150 m from the contact with the pluton. (Wilson 1964; Currie *et al.* 1986) No contact metamorphic effects whatsoever are detectable in the country rock further than 2 km from the contact. (Yang & Hesse 1991)

Interpretation of crystallization sequence-based pressure constraints by GREENWOOD & EDGAR (1984) suggests that the Mont Saint-Hilaire pluton emplaced at a depth of 3.5 to 8 km. The pluton is the result of a series of three intrusive events (Figure 8). Each batch of magma was of a distinct bulk composition, resulting in three main petrologic suites: 1) East Hill, 2) Pain de

Sucre, and 3) Sunrise. (Currie *et al.* 1986) The East Hill suite exhibits the greatest degree of chemical evolution and is the most alkaline of the three suites; it is the focus of this study.

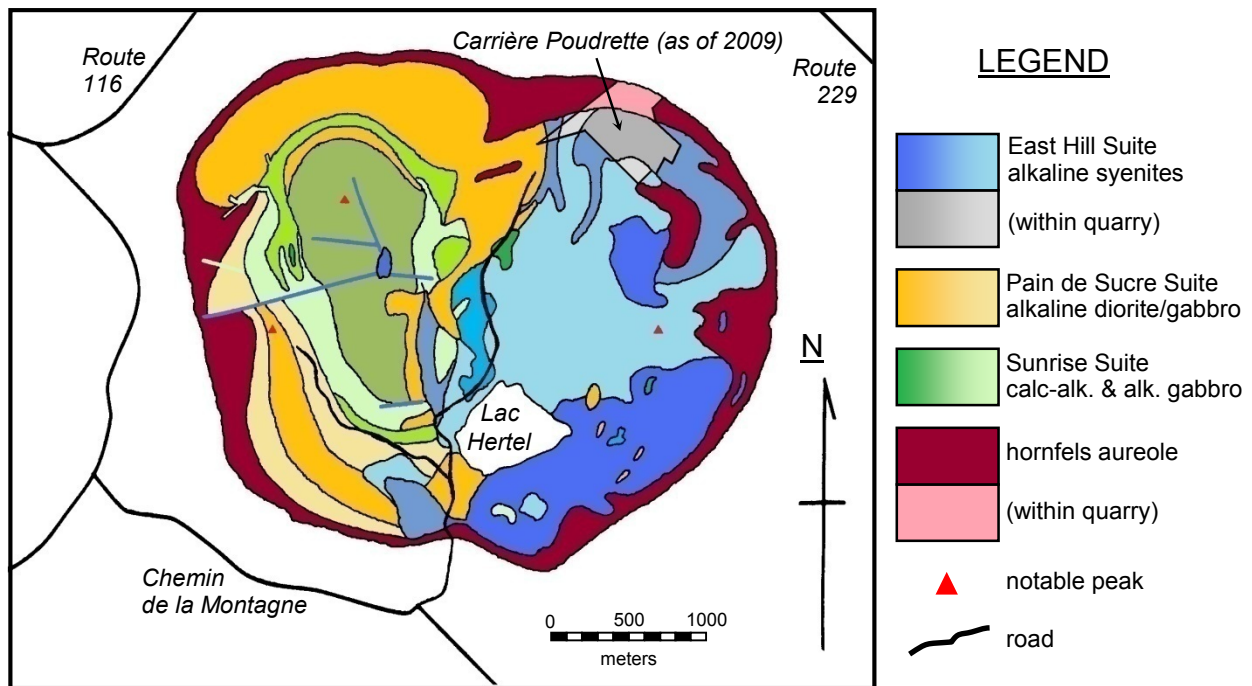


FIGURE 8 – Geologic map of Mont Saint-Hilaire. The light-shaded polygonal area on the north-northeast side of the mountain indicates the extent of the excavation of the Poudrette quarry as of March, 2009. (after Currie 1983)

### MONT SAINT-HILAIRE – AGE RELATIONSHIPS

The relative ages of the intrusive events are disputed. CURRIE *ET AL.* (1986) report  $134 \pm 6$  Ma for the Sunrise suite,  $120 \pm 3$  Ma for the Pain de Sucre suite, and  $123 \pm 12$  Ma for the East Hill suite, all by fission-track analysis performed on apatite and titanite. This relationship is supported by field observations, but overlap due to analytical uncertainty makes a definitive separation difficult.

In contrast, GILBERT & FOLAND (1986) suggest a much shorter (0.5 Ma) intrusion history, based on  $^{40}\text{Ar}/^{39}\text{Ar}$  dates from biotite. These dates span the range of  $124.1$  to  $124.6 \pm 1.3$  Ma,



which is at least partially consistent with the findings of CURRIE *ET AL.* (1986). Older ages determined from  $^{40}\text{Ar}/^{39}\text{Ar}$  dating on amphibole were found to be due to excess  $^{40}\text{Ar}$ .

It is difficult to come to a clear conclusion about the total elapsed time of intrusion. CURRIE (1983) suggested an intrusion history of 5-10 Ma. Considering the concordance, however, between  $^{40}\text{Ar}/^{39}\text{Ar}$  biotite dates and the overlap due to error in the fission track dates, the intrusion may have been complete in as little as 1 Ma. Based on the data of CURRIE *ET AL.* (1986), the intrusive sequence is Sunrise → East Hill/Pain de Sucre.

## ANALYTICAL METHODS

### SCANNING ELECTRON MICROSCOPY

#### BACKGROUND

The scanning electron microscope (SEM) was used for physical examination of microscopic crystals, preliminary phase identification (*via* energy-dispersive X-ray spectroscopy) prior to use of the microprobe, examination of microscopic phase relations, qualitative chemical analyses, and energy-dispersive X-ray mapping of polished sections. SEM analyses were carried out at the University of New Orleans using an AMRAY 1820 Scanning Electron Microscope.

#### SAMPLE PREPARATION

Samples for cursory or preliminary mineral identification were examined without substantial preparation. The material was chipped off of the master specimen using either needlepoint tweezers or a small screwdriver and hammer. The sample was then fixed to an aluminum SEM mount using graphite adhesive and coated with an aerosol mist of 2-butoxyethanol. This has proven to be a highly effective alternative to carbon and gold coating for short-term SEM work (Alexander U. Falster, pers. comm.).

Samples for X-ray map generation, for examination prior to electron microprobe analysis, or for imaging of zonation or similar features were prepared as polished mounts.

#### OPERATING CONDITIONS

For general specimen examination and imaging, acceleration potential was set at 15 kV, saturation voltage was varied automatically as needed, and a 300 or 400  $\mu\text{m}$  final aperture was in

place. Mineral identification was aided by the use of a Kevex Quantum EDS array. For such work, acceleration potential was set at 15 kV (25 kV to generate X-rays for Nb, Mo, Pb, Sr, Th, U, Y & Zr; 10 kV for Na), and a 400  $\mu\text{m}$  final aperture was in place. To maximize detector efficiency, samples were tilted at an angle of 30°. Patterns were resolved and peaks labeled using an enhanced, PC-resident software package.

## **X-RAY DIFFRACTOMETRY**

### **BACKGROUND**

X-ray diffractometry (XRD) was employed to confirm or determine the identity of various mineral phases; this technique was used on fragments and single crystals of individual minerals, as well as on fine-grained, polymineralic masses for which physical separation of phases was impractical. XRD analyses were carried out at the University of New Orleans using a Scintag XDS 2000 automated X-ray diffractometer.

### **OPERATING CONDITIONS**

An X-ray tube emitting  $\text{CuK}\alpha$  radiation was used at a potential of 40 kV and a current of 20 mA. The scan range was from 2 to 70 degrees- $2\theta$ , with a scan increment of 0.02 or 0.04 degrees- $2\theta$  and with a dwell time of 1 or 3 to 6 seconds, respectively. Diffraction patterns were processed through the resident software package, which includes a DMS algorithm for smoothing (three to five point smoothing being employed). Patterns were analyzed using the system-resident library and identification program for preliminary identification and were checked *versus* JCPDS standard reference manuals and cards for verification of results.

## UNIT CELL MEASUREMENT

Unit-cell dimensions of amphibole group minerals were measured using the XRD. For such examinations, the scan increment was set to 0.005 degrees-2 $\theta$  with a dwell time of 2 seconds. Output was processed using CELL refinement software.

## ANALYSIS OF FELDSPAR STRUCTURAL STATES

Structural states of alkali feldspar samples were determined using the method of WRIGHT (1968). Such measurements used a scan increment of 0.005 or 0.02 degrees-2 $\theta$  with a dwell time of 2 or 3 seconds, respectively.

## ELECTRON MICROPROBE ANALYSIS

### BACKGROUND

The electron microprobe (EMP) was used for obtaining quantitative chemical analyses of individual mineral phases and for wavelength-dispersive X-ray mapping. Analyses were done at the University of New Orleans using an ARL SEMQ automated electron microprobe. The microprobe is outfitted with nine wavelength-dispersive X-ray detectors, consisting of six fixed and three tunable detectors. An integral SEM permitted enhanced examination of specimens prior to analysis.

### OPERATING CONDITIONS & STANDARDS

Acceleration potential was set to 20 kV (25 kV for Ba, Hf, Mo, Nb, Sr, Ta, Th, W, Y, Zr & REE), with a sample current of 30 nA (measured on brass) and a 2  $\mu$ m spot size. The following materials [accompanied by the symbol(s) and X-ray line(s) for the relevant element(s)]

were used as standards: sodalite ( $\text{NaK}\alpha_{1,2}$ ), albite ( $\text{NaK}\alpha_{1,2}$ ;  $\text{AlK}\alpha_{1,2}$ ), adularia ( $\text{KK}\alpha_{1,2}$ ), clinopyroxene ( $\text{CaK}\alpha_{1,2}$ ;  $\text{FeK}\alpha_1$ ;  $\text{SiK}\alpha_{1,2}$ ), synthetic  $\text{SrSO}_4$  ( $\text{SrL}\alpha_1$ ), synthetic  $\text{BaSO}_4$  ( $\text{BaL}\alpha_1$ ), synthetic  $\text{YPO}_4$  ( $\text{YL}\alpha_1$ ), synthetic  $\text{TiO}_2$  ( $\text{TiK}\alpha_{1,2}$ ), synthetic  $\text{ZrO}_2$  ( $\text{ZrL}\alpha_1$ ), synthetic  $\text{HfO}_2$  ( $\text{HfL}\alpha_1$ ), synthetic  $\text{YNbO}_4$  ( $\text{NbL}\alpha_1$ ), microlite ( $\text{TaL}\alpha_1$ ), synthetic  $\text{CaMoO}_4$  ( $\text{MoL}\alpha_1$ ), synthetic  $\text{CaWO}_4$  ( $\text{WM}\alpha_1$ ), rhodonite ( $\text{MnK}\alpha_1$ ), fayalite ( $\text{FeK}\alpha_1$ ), synthetic  $\text{ZnO}$  ( $\text{ZnK}\alpha_1$ ), fluorite ( $\text{FK}\alpha_{1,2}$ ), apatite ( $\text{PK}\alpha_{1,2}$ ), labradorite ( $\text{An}_{50}$ ) ( $\text{CaK}\alpha_{1,2}$ ;  $\text{AlK}\alpha_{1,2}$ ), sillimanite ( $\text{AlK}\alpha_{1,2}$ ), synthetic  $\text{MgO}$  ( $\text{MgK}\alpha_{1,2}$ ), synthetic  $\text{V}_2\text{O}_5$  ( $\text{VK}\alpha_1$ ), synthetic  $\text{ThO}_2$  ( $\text{ThM}\alpha_1$ ), wollastonite ( $\text{CaK}\alpha_{1,2}$ ), hematite ( $\text{FeK}\alpha_1$ ), synthetic  $\text{Cr}_2\text{O}_3$  ( $\text{CrK}\alpha_1$ ), dolomite ( $\text{MgK}\alpha_{1,2}$ ), calcite ( $\text{CaK}\alpha_{1,2}$ ), rhodochrosite ( $\text{MnK}\alpha_1$ ), synthetic  $\text{LaPO}_4$  ( $\text{LaL}\alpha_1$ ), synthetic  $\text{CePO}_4$  ( $\text{CeL}\alpha_1$ ), synthetic  $\text{PrPO}_4$  ( $\text{PrL}\beta_1$ ), synthetic  $\text{NdPO}_4$  ( $\text{NdL}\beta_1$ ), synthetic  $\text{SmPO}_4$  ( $\text{SmL}\beta_1$ ), synthetic  $\text{GdPO}_4$  ( $\text{GdL}\alpha_1$ ), synthetic  $\text{DyPO}_4$  ( $\text{DyL}\beta_1$ ), synthetic  $\text{ErPO}_4$  ( $\text{ErL}\beta_1$ ), synthetic  $\text{YbPO}_4$  ( $\text{YbL}\alpha_1$ ), synthetic Gd-Sc-Y oxide ( $\text{ScK}\alpha_1$ ), quartz ( $\text{SiK}\alpha_{1,2}$ ), and willemite ( $\text{ZnK}\alpha_1$ ). Output was processed using an integral enhanced software package to effect ZAF corrections.

## FERRIC IRON ESTIMATION

Ferric iron content of amphibole and mica group minerals was estimated by the colorimetric method of WILSON (1960). In several of the lithologies, amphibole and mica are present as minuscule crystals or are intimately intergrown with other phases, complicating mineral separation. To mitigate the effects of possible contamination, the amphibole ferric/ferrous ratio was estimated for the entire East Hill suite from calcic and sodic-calcic amphibole extracted from the nepheline melasyenite, and the mica ratio was estimated for the suite from annite taken from the annite lamprophyre. This approach sacrificed lithology-specific ferric-ferrous ratios, but eliminated inaccuracies due to contamination.

Mineral separates were crushed, then dissolved in 50% HF/H<sub>2</sub>SO<sub>4</sub> solution. Ferric iron was determined by titration of mineral solutions with ammonium metavanadate, with 2,2'-dipyridyl as an indicator. Ferrous iron in solution participates in a redox reaction with pentavalent vanadium, oxidizing to ferric iron as the vanadium reduces to V<sup>4+</sup>. The titration end-point is observed by the disappearance of the violet color of the ferrous-dipyridyl complex. Ferrous-ferric ratios were taken as the average of analyses of three individual samples of mica and of each of the two amphibole groups.

## **X-RAY FLUORESCENCE**

### **BACKGROUND**

X-ray fluorescence (XRF) analysis was used for quantitative chemical analysis of whole rock samples. Analyses were conducted at the Inorganic Analysis Laboratory of the Coordinated Instrumentation Facility (CIF) at Tulane University using a Spectro X-lab automated energy-dispersive XRF (EDXRF) unit. The instrument is precalibrated from approximately 200 standards, but supplementary standards (*q.v.*) may be run as samples in order to improve analytical precision. Following sample loading, all aspects of instrument operation are computer-controlled. Based on the elements to be analyzed, the computer selects the best secondary or polarizing target(s) in order to optimize detector sensitivity. Available targets include Mo, B<sub>4</sub>C, Al<sub>2</sub>O<sub>3</sub>, Co, Cd, Pd & Sm. Based on target selection, tube potential is set between 25-60 kV. Current is automatically and continuously modulated from a starting value of 20 mA, in order to maximize sensitivity and to achieve dead time of approximately 50%. The system computer uses a suite of inter-element correction schemes to process instrument output.

## SAMPLE PREPARATION

Samples were prepared for analysis by fragmenting hand specimens into 0.5 cm pieces using a sledge hammer; whenever sample quantities permitted, at least 1 kg of bulk rock was used to provide a representative sampling. Hand specimens were wrapped in eight layers of 28  $\mu\text{m}$ -thick polyethylene sheet to minimize contamination. Sample fragments for both major- and trace-element samples were then reduced to a fine powder using a Spex shatterbox and tungsten-carbide-lined mill. The mill was precontaminated with a small quantity of sample for five minutes. Remaining fragments for each sample were processed in approximately 100 g batches for ten to twenty minutes; all batches were thoroughly mixed to homogenize the sample. Prior to final preparation for analysis, powders were dried at 110°C for twelve hours to remove adsorbed water.

The analytical samples were prepared by the author at the CIF, using 4.0000 g ( $\pm 0.0400$  g) of sample mixed with 0.9000 g ( $\pm 0.0300$  g) of Hoechst Micropowder Wax C as a binder. This mixture was weighed into a lidded polystyrene canister, blended with a spatula, and two acrylic agitator balls were placed in the canister. The canisters were then closed and run in a Retsch MM2000 mixer at 20 rpm for three minutes, in order to homogenize the mixture. Homogenized samples were transferred to polystyrene weighing boats, gently stirred, and then poured into a 32 mm-diameter stainless steel Graseby-Specac #3300 die assembly with tungsten carbide plates. Samples were compressed in a Graseby-Specac T-40 Autopress at 12 tons of force for fifteen seconds; the pellet was then ready for analysis.

## STANDARDS

A suite of international environmental reference materials was used for raw data correction. BHVO-1, JR-2, and SY-3 were used for major element correction. Trace element corrections were made with SY-3, except for Cs, which employed JR-2.

## OPTICAL MICROSCOPY

### BACKGROUND

Optical microscopes were used for detailed specimen examination and to confirm preliminary mineral identifications made in the SEM. All optical microscopy was done at the University of New Orleans. For hand specimen investigation, an Olympus SZ 60 binocular microscope was used. Examination of thin sections was done on an Olympus BX 60 petrographic microscope, outfitted with a reflected light module.

### PHOTOMICROSCOPY

Photomicrographs were taken as documentary evidence, as well as to illustrate mineralogical features in samples. Both digital and traditional photomicrographs were made. An Olympus SZ 60 binocular microscope was used for hand specimens, and an Olympus BX 60 petrographic microscope was used for thin sections. Digital photomicrographs were taken using a Sony CCD-IRIS color digital video camera and were processed using an ATI All-In-Wonder 128 digital video interface unit and Multimedia Center v.6.3 software. Traditional photomicrographs were taken with an Olympus PM 20 automatic photomicrographic system, using Kodak Gold 100 35 mm film.



## MONT SAINT-HILAIRE – PETROLOGY

### OVERVIEW

#### SUNRISE SUITE

The Sunrise suite is characterized by laminated, medium-grained melagabbro, pyroxenite, and perknite. CURRIE (1983) ascribes a cumulate origin to the suite. Amphibole, calcic plagioclase, and clinopyroxene are common phases. (Currie *et al.* 1986)

#### PAIN DE SUCRE SUITE

The Pain de Sucre suite intruded as a large ring dike. It is composed of nepheline-olivine gabbro, monzonite, and diorite, with occasional essexite. Glomerocrysts of mafic minerals are typically seen in this suite. These clots are usually composed of amphibole, pyroxene, and biotite; however, they can also contain magnetite, ilmenite, and olivine. (Currie *et al.* 1986)

#### EAST HILL SUITE

Observations in the Poudrette Quarry show that the East Hill suite is composed of at least eleven primary igneous lithologies (Table 1), belonging to three lithologic groups: 1) host rock, 2) feldspathoidal and rare-element syenites, and 3) dikes, pegmatites, and various syenoids. Trapped within members of these three groups are xenoliths of country rock, primarily limestones and shales. The host rock of the East Hill suite is a nepheline melasyenite that encloses numerous decimeter- to dekameter-scale leucosyenite masses (Figures 9 & 14). Most such masses are a nepheline leucosyenite but may consist of one or more of the four alkaline feldspathoidal and rare-element syenites of the second group and, consequently, may exhibit a variety of grain sizes, mineralogies, and textures. The nepheline melasyenite both concordantly

TABLE 1 – Primary igneous lithologies of the East Hill suite exposed in the Poudrette quarry.

Group 1: Host Rock	Group 2: Feldspathoidal & Rare-Element Syenites	Group 3: Dikes, Pegmatites & Various Syenoids
1) nepheline melasyenite ( <i>malignite</i> )	1) nepheline leucosyenite ( <i>litchfieldite</i> ) a) Type 1 b) Type 2 c) Type 3  2) eudialyte syenite ( <i>khibinite</i> )	1) feldspar-aegirine dikes 2) annite lamprophyre ( <i>alnøite</i> ) 3) pegmatites 4) various syenoids 5) perthite syenite ( <i>perthosite</i> ) 6) pyroxenite ( <i>aegirinite</i> )
The italicized names given in parentheses reflect earlier terms—more specific but currently out of favor—for each rock type.		



FIGURE 9 – Feldspathoidal leucosyenite in the wall of the Poudrette quarry. The leucosyenite mass is approximately 50 meters tall. (photograph by the author)

and discordantly encloses the leucosyenite masses (Figure 10) suggesting localized *in situ* differentiation accompanied by distal fracturing and injection; fractured nepheline melasyenite is characteristically brecciated. Nepheline melasyenite at discordant contacts exhibits a reaction rim; whereas concordant contacts do not.

The fine-grained host rock of the East Hill suite and its leucosyenite bodies are prominently crosscut by dozens of centimeter- to meter-scale dikes (Figure 11). These dikes are primarily of one of two types. Those of the first type are substantially more abundant and are nearly entirely composed of very coarse-grained (in some cases pegmatitic) alkali feldspar and aegirine (Figure 12); single crystals commonly span the width of the dike. Those of the second type are of a syenitic and an alkaline to peralkaline bulk composition. Several dikes of this type, especially those that are decimeter-scale, contain an aplitic core, and many of those that attain larger sizes develop pegmatitic textures (Figure 13).

Apart from the dike rocks of the East Hill suite, the dispositions of the members of the third group of lithologies cannot, by and large, be so neatly collectively described; as they are petrologically diverse, so, too, are their modes of occurrence. They either occur discordantly with respect to the host rock, clearly following fracture surfaces, as in the case of the feldspar-aegirine dikes, many of the pegmatites, and, presumably, the annite lamprophyre; or they are simply highly fractionated segregations or phases of a more ordinary lithology, as in the case of the various syenoids, the pyroxenite, the remainder of the pegmatites, and, perhaps, the perthite syenite.



FIGURE 10 – Leucosyenite in nepheline melasyenite, showing brecciation, as well as concordant and discordant enclosure. (photograph by the author)



FIGURE 11 – Dikes crosscutting nepheline melasyenite in the Poudrette quarry. (photograph by the author)





FIGURE 12 – Feldspar-aegirine dikes cross-cutting nepheline melasyenite. Note the range of modalities represented by the three dikes. (photograph by the author)



FIGURE 13 – Microcline crystals in wall zone of eudialyte-bearing pegmatite dike. (photograph by the author)



FIGURE 14 – Panoramic view of the Poudrette quarry, July 1995. The field of view represents approximately 800 m of continuous wall exposure, wrapping around an excavation approximately 500 m wide. The maximum depth pictured is approximately 150 m. The dark rock that constitutes the majority of the visible material is nepheline melasyenite. Note the presence of numerous leucosyenite masses of various sizes; the large mass from FIGURE 9 is visible on the quarry wall to the upper left of the drainage pond on the left side of the photograph. An especially large leucosyenite body is visible as a bench on the floor of the quarry at the center of the photograph. Also, note the numerous large-scale dikes crosscutting the melasyenite and the leucosyenite masses. (photograph by the author)



## EAST HILL SUITE – PETROGRAPHIC DESCRIPTIONS

### INTRODUCTION

The classification of alkaline igneous rocks presents unique challenges, not the least of which is the great variety of unusual constituent minerals and combinations in which they may occur. Crystallization in alkaline rocks is particularly sensitive to geochemical and thermal conditions, and alkaline magmas appear to exhibit high degrees of chemical heterogeneity, resulting in especially variable modalities within a single lithology and the abundant development of microenvironments that may deviate substantially in their bulk chemistry or modality from that of the lithology as a whole. As a result, the process of classifying an alkaline rock requires some flexibility and perspicacity. In many cases, a classification is made based on the grounds of sufficient similarity to a type specimen rather than fitting major mineral proportions (*e.g.* quartz *versus* feldspar) to hard mathematical boundaries, as in classifying calc-alkaline rocks. Such a technique may seem disorderly, if not downright sloppy, but this lack of hard boundaries allows for the inclusion of interesting and meaningful mineralogical variations while still maintaining the fundamental petrologic significance of the rock type.

A second problem, which can arise in any system, but that can be particularly noisome to alkaline petrologists is that of alteration and replacement mineralization. Such events can change a rock so that it appears, in its current state, to belong to a different formal classification than it would originally have represented (*cf.* Type 2 nepheline leucosyenite (*q.v.*) & sodalite syenite *sensu stricto*). Therefore, something should also be said regarding the state of being of the rock being classified: the pristine rock (if the mineralogy of which can be deduced) or the rock that results from the later action of heat and fluids. This work classifies each rock type based on the

original material (to the extent that it is possible to reconstruct the pristine mineralogy), due to the fact that this best preserves the fundamental petrologic meaning of each rock type.

One last consideration that seems particularly to have beset Mont Saint-Hilaire is a lack of general agreement on a systematic and formal petrologic nomenclature of the pluton, especially the East Hill suite. For example, HORVÁTH & GAULT (1990) refer to “nepheline syenite” to mean the melanocratic rock that hosts the other lithologies of the East Hill suite and to “sodalite syenite” to mean the leucocratic rock that hosts many of the pegmatites. CURRIE *ET AL.* (1986) catalogue mineral occurrences in the East Hill suite without referring them to a particular lithology; although, with familiarity thereof, the rock type may be deduced from the described associations. Presumably, their “coarse-grained nepheline-sodalite syenite” equals the “sodalite syenite” of HORVÁTH & GAULT (1990), and their “fine-grained nepheline syenite” equals “nepheline syenite”. GILBERT & FOLAND (1986) limit their lithologic descriptors for the entire suite to “nepheline syenite” and “nepheline syenite breccia”.

This review of nomenclature is not intended to impugn any of these studies, as each is rightly a classic of Mont Saint-Hilaire geology, and the petrologic descriptions put forward by each are not incorrect. A problem, however, is that, unlike the petrologic descriptions from, for example, Ilímaussaq, which are consistent from paper to paper (*e.g.* Ferguson 1964; Engell 1972; Marks & Markl 2001), at the East Hill suite, one person’s “nepheline syenite” may not be another’s. Also, even without falling victim to the temptation to play on subtle and interesting accessory mineral variations to classify alkaline rocks *ad infinitum*, there is more meaningful petrologic variety in the East Hill suite than is intimated by the aforementioned classifications. Perhaps it is presumptuous to take this to task, but this project endeavors to categorize formally the lithologies of the East Hill suite, based on the criteria discussed above. For the sake of



continuity, when possible, each of the following lithologies is referred to its presumed equivalent in HORVÁTH & GAULT (1990), as that paper is probably the most common reference for placing a mineral from Mont Saint-Hilaire into a petrologic context.

#### GROUP 1: HOST ROCK

##### *Nepheline Melasyenite*

Nepheline melasyenite is the most abundant rock type in the East Hill suite. Barring those dikes and pegmatites that crosscut it, the nepheline melasyenite concordantly encloses all of the other lithologies in the East Hill suite. This lithology is probably equivalent to the “nepheline syenite” from HORVÁTH & GAULT (1990).

The nepheline melasyenite is porphyritic, with mm-scale phenocrysts of light grey orthoclase and black hastingsite. Cryptoperthitic orthoclase phenocrysts are euhedral, overgrown by secondary albite, and constitute approximately 10% of the volume of the syenite; phenocrysts of hastingsite are subhedral, blocky prisms and also constitute about 10% of the modality.

The groundmass is hypidiomorphic with an average grain size of 0.1 to 2.0 mm. Crystals are randomly oriented and, aside from mafic stringers (*q.v.*), evenly distributed. Major<sup>3</sup> minerals in the groundmass include lightly albitized euhedral to subhedral cryptoperthitic orthoclase, anhedral interstitial albite, euhedral nepheline, and subhedral to euhedral augite and aegirine-augite, with minor corroded titanaugite, mantled or replaced by taramite or kaersutite, all together comprising approximately 70% of the modality of the rock. Winding through the groundmass are mm-scale mafic stringers consisting of ropy aggregates of aegirine-augite with trace to minor annite, fluorapatite, hastingsite, magnetite, pyrite, and titanite.

---

<sup>3</sup> Major minerals comprise 10.0% or more of the modality of a rock; minor minerals comprise between 1.0-10.0% of the modality of a rock; trace minerals comprise between 0.1-1.0% of the modality of a rock; and rare minerals comprise either less than 0.1% of the modality of a rock or were found as only one or two crystals.

Other minor minerals include natrolite and sodalite (mainly secondary but some primary). Other trace minerals include cancrinite, fluorite, ferro-edenite, ferrichterite, and katophorite. Calciophilite, galena, ilmenite, l  venite, sphalerite, and thorianite are present as rare minerals.

The nepheline melasyenite bears certain significant similarities to the leucogabbro and the kaersutite-biotite gabbro of the Pain de Sucre and the Sunrise suites. Like the nepheline melasyenite, the groundmass minerals of the leucogabbro are mostly randomly oriented, although towards the center of the suite the grain size of the leucogabbro increases, and it becomes foliated. The leucogabbro is the only nepheline-bearing gabbro at Mont Saint-Hilaire. Feldspars are primarily plagioclase (an<sub>45-55</sub>), with overgrowths of secondary orthoclase or cryptoperthite. Mafic minerals include olivine (fo<sub>25-55</sub>), clinopyroxene replaced and overgrown by kaersutite, magnetite, and biotite, which occurs as isolated crystals and as overgrowths on magnetite. Apatite is also present as an accessory phase. (Greenwood & Edgar 1984) The chief mineralogical differences between the leucogabbro and the nepheline melasyenite are the presence in the leucogabbro of olivine and calcic plagioclase, neither of which are present in the nepheline melasyenite. The leucogabbro also bears a higher modality of feldspar and a lower modality of clinopyroxene and amphibole. Apart from these distinctions, the nepheline melasyenite and the leucogabbro are mineralogically and modally quite similar.

The kaersutite-biotite gabbro displays foliation resulting from the disposition of its plagioclase and kaersutite phenocrysts. It is comparable to the leucogabbro in overall mineralogy, but it exhibits differences in modality. The kaersutite-biotite gabbro is nepheline-free and contains less feldspar, clinopyroxene, and magnetite than the leucogabbro; it is richer in kaersutite and biotite. Clinopyroxene is replaced and overgrown by kaersutite, but biotite has overgrown the remainder of the mafic phases. (Greenwood & Edgar 1984) Mineralogically, the

nepheline melasyenite contains nepheline, whereas the kaersutite-biotite gabbro does not. The kaersutite-biotite gabbro contains olivine and calcic plagioclase, but the nepheline melasyenite does not. Modally, the kaersutite-biotite gabbro contains more feldspar and less clinopyroxene than the nepheline melasyenite, but about the same amount of amphibole. Once again, these differences aside, the nepheline melasyenite and the kaersutite-biotite gabbro exhibit striking similarities.

Collection sites for the nepheline melasyenite were well within the boundaries of the East Hill suite (Figure 8), so nepheline melasyenite samples in this study are certainly neither leucogabbro nor kaersutite-biotite gabbro. Nevertheless, the remarkable textural and mineralogical similarity between the gabbros and the nepheline melasyenite suggests a certain degree of continuity between the Pain de Sucre and Sunrise suites and the East Hill suite.

The nepheline melasyenite is also comparable to mafic syenites from other alkaline complexes. The Coldwell alkaline complex, in Ontario, contains two series of augite syenite consisting primarily of alkali feldspar, fayalite ( $\text{fa}_{83-93}$ ), augite to aegirine-augite (depending on the series), titanomagnetite, and amphibole (again, depending on the series, ranging from hastingsite through edenite or from katophorite through ferrorichterite). Notably, aenigmatite, quartz, and zircon are present as late-stage phases. (Mitchell & Platt 1978)

Similar examples are augite syenites from Ilímaussaq and North Qôroq, which again represent some of the earliest magmatic activity in their complexes. These augite syenites comprise cryptoperthitic alkali feldspar,  $\pm$ fayalite, augite, hastingsite,  $\pm$ biotite, titanite, titanomagnetite, and apatite, with minor nepheline or quartz. Zircon, baddeleyite, pyrite, and pyrrhotite may be present as trace phases. (Marks & Markl 2001; Coulson 2003)

## GROUP 2: FELDSPATHOIDAL & RARE-ELEMENT SYENITES

### *Nepheline Leucosyenite*

Nepheline leucosyenite is the second most common lithology by volume in the East Hill suite. A cursory glance across the walls and benches of the quarry reveals numerous massive (dekameter-scale) leucosyenite bodies within the nepheline melasyenite host rock. The bulk of the material within these masses is nepheline leucosyenite. The nepheline leucosyenite occurs in three types. Each of the three types differs obviously from the others in terms of its appearance in hand specimen. All three, however, are very similar texturally and mineralogically, differing meaningfully only in terms of their minor and trace mineralogies and, strikingly, in terms of the color of the sodalite occurring in each. The nepheline leucosyenite is probably analogous to the “sodalite syenite” of HORVÁTH & GAULT (1990).

All three types of nepheline leucosyenite are coarse-grained nepheline syenites, which have an average of over 90%—in some samples, close to 100%—of their nepheline replaced by sodalite.<sup>4</sup> The sodalite pseudomorphs occur primarily as euhedral, hexagonal prismatic phenocrysts that occur in a nearly idiomorphic potassium feldspar and albite groundmass. Portions of all three nepheline leucosyenites exhibit a poikilitic texture, characterized by idiomorphic alkali feldspar and nepheline enclosed by clots of mafic minerals, for example aegirine or arfvedsonite; the reverse of their normal textural relationship.<sup>5</sup> These mafic clots may reach several centimeters in diameter and lend a striking appearance to the rock, both due to their size and contrast, as well as to the unexpected textural and paragenetic relationship that they

---

<sup>4</sup> Owing to the ubiquity in these rock types of sodalite pseudomorphs after nepheline, it is perhaps more proper to refer to these lithologies as pseudonepheline leucosyenites, in a similar vein as pseudoleucite syenite, in which phenocrystic leucite has been replaced by pseudomorphs consisting of an intergrowth of potassium feldspar and nepheline (Williams 1891; Larsen & Buie 1938); however, “nepheline leucosyenite” should suffice for the sake of simplicity without sacrificing too much accuracy.

<sup>5</sup> This is due to reversals in the order of melting temperatures that result both from shifts from calc-alkaline to alkaline compositions and from elevated pressure. (Yoder & Tilley 1962) Many examples of alkaline rocks that exhibit this poikilitic texture exhibit synneusis textures, as well.

exhibit. Mineralogically and texturally, the nepheline leucosyenites are very similar to naujaite, such as is found at Ilímaussaq (Nielsen & Steenfelt 1979), although in naujaite *sensu stricto*, alkali feldspar is one of the enclosing phases.

Type 1 nepheline leucosyenite is the most abundant variety. It is characterized by colorless to pale grey sodalite pseudomorphs after nepheline that represent approximately 65% of the modality. The groundmass consists of, in terms of modal percentages, about 25% cryptoperthitic microcline and 5% albite.

Aegirine and natrolite are present as minor minerals. Trace minerals include arfvedsonite, manganoan pectolite-sérandite, and pyrite. Rare minerals include alabandite, arsenopyrite, fluorapatite, fluorite, kupletskite, and sphalerite. In addition, an unidentified Na-zirconosilicate and two different Ca-Ce phosphates are also present as rare phases.

Type 2 nepheline leucosyenite is the second most abundant kind. It is characterized by mm-scale, pale bluish grey to deep ultramarine blue sodalite pseudomorphs after nepheline that represent about 65% of the volume of the rock. Regions of deep blue sodalite pseudomorphs suggest veins and patches, rather than a uniform or random distribution. All of the sodalite pseudomorphs are set in a groundmass of, in terms of modal percentages, approximately 10% cryptoperthitic microcline and 15% albite.

Minor minerals include calcite, dawsonite, natrolite, and siderite. Trace minerals include aegirine, almandine, nepheline (as the hearts of sodalite pseudomorphs that resisted alteration), pyrite, sphalerite, and zircon. Fluorapatite, galena, halite (in a ruptured fluid inclusion), molybdenite, pyrochlore, and rutile are present as rare minerals. In addition, an unidentified Ca-REE carbonate and possible synchysite-(Ce) and thorogummite are present as rare phases.

Type 3 nepheline leucosyenite has only been found as a few centimeter-scale hand specimens. It is characterized by the presence of the *hackmanite* variety of sodalite. *Hackmanite* exhibits tenebrescence or reversible photochromism, the ability of minerals to change color when exposed to sunlight.<sup>6</sup> The brilliant reddish-purple visible on freshly exposed surfaces fades within minutes to pale dove grey. After several days under fluorescent light or in darkness, the color returns as a dull purple. Due to the faded grey color of exposed sodalite in this type of nepheline syenite, specimens thereof may be mistaken in the field for Type 1 nepheline leucosyenite, unless they are broken to expose new surfaces that feature colored *hackmanite*.

The Type 3 nepheline leucosyenite should not be confused with “tawite” (Horváth & Gault 1990), which consists primarily of *hackmanite*, with small amounts of clinopyroxene, eudialyte, ussingite, and villiaumite, to name just a few of the more common accessory phases. “Tawite” occurs as centimeter-scale xenoliths that exhibit reaction textures with the nepheline melasyenite that hosts them. In contrast, the Type 3 nepheline leucosyenite displays the same smooth margin with the nepheline melasyenite as the other leucosyenites.

The Type 3 nepheline leucosyenite is the most mineralogically diverse of the three varieties in the East Hill suite. Sodalite pseudomorphs after nepheline make up about 45% of the volume of the rock. Unlike the sodalite pseudomorphs in the other two leucosyenites, those in the Type 3 leucosyenite vary in appearance based on their immediate accessory phases. Sodalite pseudomorphs associated with glomerocrysts of clinopyroxene are colorless, and appear to be

---

<sup>6</sup> LEE (1936), in his investigation of reversible photosensitivity in *hackmanite*, refers to VREDENBURG (1904), who, though writing nearly 100 years after the discovery of *hackmanite*, expressed its properties far more eloquently than the original authors, “Moreover, some of the sodalite exhibits an extraordinary phenomenon hitherto unrecorded in any mineral. While some of the specimens are of a bright blue color similar to that of the mineral from many other localities, others appear under ordinary conditions transparent and colourless. But some of these colourless fragments when kept in the dark for a fortnight or three weeks assume a pink color which disappears rapidly on exposure to bright daylight, and almost instantaneously in direct sunshine. The phenomenon is particularly brilliant when the rock is first broken in the field, and the large blocks of elæolite (some of which are over a yard wide) appear, on fracture, as if suffused with blood.”

sodalite *sensu stricto*; whereas those that occur in the absence of clinopyroxene exhibit a variety of colors typical of the *hackmanite* variety of sodalite: pink, magenta, fuchsia, and purple. Sodalite *sensu stricto* pseudomorphs in the Type 3 leucosyenite occur as mm-scale, euhedral hexagonal prisms. Some pseudomorphs of *hackmanite*, however, are also present as anhedral grains and colloform growths.

Glomerocrysts of dark green aegirine and aegirine-augite are prominent in the Type 3 leucosyenite, comprising about 30% of the modality. The groundmass consists of 15% albitized cryptoperthitic microcline and 5% albite. Natrolite is also present as a minor species replacing sodalite. Sérandite is present as a trace mineral. Rare minerals include barite, böhmite, calcioancylite-(Ce), calcite, cancrinite, fluorapatite, fluorite, kupletskite, molybdenite, pyrochlore, sphalerite, and thorianite. In addition, an unidentified Ca-zirconosilicate, a Ca-Ce carbonate, and a Ca-Ce phosphate are present as rare phases.

### ***Eudialyte Syenite***

The eudialyte syenite has the same mode of occurrence as the nepheline leucosyenites. It is a coarse-grained, idiomorphic leucosyenite characterized by the presence of abundant crystals of aegirine and less common, but visually striking, crystals of eudialyte group minerals. The eudialyte syenite contains about 45% microperthitic microcline by volume, with approximately equal proportions of blackish-green needles of aegirine and stubby, prismatic dark grey pseudomorphs of sodalite after nepheline, with interstitial euhedral beige natrolite that all together account for about 50% of the modality. No rock type resembling the eudialyte syenite is mentioned by HORVÁTH & GAULT (1990).

Anhedral, gemmy, yellowish- to reddish-brown eudialyte group minerals and anhedral pinkish-peach sérandite occur as minor minerals. Trace minerals include albite, catapleiite, fluorite, kupletskite, and, enclosed in aluminosilicate minerals, chalcopyrite, covellite, galena, pyrite, and sphalerite. Rare minerals include acanthite, analcime, ancylite-(Ce), apatite, calcioancylite-(Ce), calcite, fluorapatite, gaidonnayite, hochelagaite, pyrochlore, and thorogummite.

### GROUP 3: DIKES, PEGMATITES & VARIOUS SYENOIDS

#### ***Feldspar-Aegirine Dikes***

Feldspar-aegirine dikes are a prominent feature of the East Hill suite. They are cm-scale in thickness but extend for tens of meters, discordantly cross-cutting other lithologies in the suite. The feldspar-aegirine dikes are coarse-grained, nearly pegmatitic in many cases. They nearly entirely consist of approximately equal proportions of albitized cryptoperthitic microcline and aegirine, which together occupy about 95% of the volume of the rock. Crystals of both species occur as tapering, prismatic crystals, either singly or in tightly packed sheaves; some crystals of aegirine exhibit an intrafascicular texture. Crystals are oriented primarily perpendicular to the walls of the dike, although deformation due to shearing is visible in some dikes. Albite is present as a major mineral as irregular zones in albitized cryptoperthitic microcline; however, it also occurs as euhedral inclusions therein.

Trace minerals include ancylite-(Ce), annite, calcite, natrolite, pyrochlore, and pyrophanite. Rare minerals include aegirine-augite, galena, hematite, and zircon. Feldspar-aegirine dikes are not mentioned specifically by HORVÁTH & GAULT (1990), although they mention segments of pegmatite dikes, dominated by microcline and aegirine, that narrow to a



few centimeters in width. It seems likely that HORVÁTH & GAULT (1990) are simply referring to portions of larger pegmatites, as they correctly describe pegmatite dikes in the East Hill suite as not uncommonly changing width between cm- and m-scales, whereas the feldspar-aegirine dikes maintain their width over tens of meters of length.

### ***Annite Lamprophyre***

The annite lamprophyre is nearly the rarest rock type in the East Hill Suite. Its mode of occurrence is a matter of debate, as no samples from this study were found *in situ*. The small sizes of specimens that have been found (<15 cm in maximum dimension), smaller than those of any other rock type, implies that the original mass was of limited extent in one or, perhaps, two dimensions, thus suggesting occurrence as a dike or a pipe. This contention is supported by independent field observations of a similar annite- and petarasite-bearing rock—believed to be the same lithology—that occurred as a small (*ca.* 5 m diameter) sheet-like pod. (László Horváth, pers. comm.) The annite lamprophyre is not described by HORVÁTH & GAULT (1990).

In hand specimen, the annite lamprophyre has the general appearance of a glimmerite, but closer examination reveals that more fine distinctions may be made. It is an exceedingly melanocratic rock, with abundant dark brown-green to black annite phenocrysts set in a variously mauve, tan, and cream-colored groundmass. Equant books of annite to 5 mm diameter constitute about 65% of the modality of the rock. All of the annite crystals are euhedral, contributing (along with apatite, *q.v.*) to the idiomorphic texture of the rock.

The groundmass minerals are difficult to differentiate in hand specimen, as they are fine-grained and similar in color to one another. In thin section, a second phenocryst phase is revealed, as it is seen that fluorapatite, which makes up about 10% of the modality of the rock,

also occurs exclusively as euhedral crystals set into the groundmass. The groundmass itself makes up approximately 15% of the annite lamprophyre, and consists of fibrous natrolite embedded with subhedral to euhedral rhombs of calcite.

The balance of the annite lamprophyre consists of accessory minerals appearing interstitially to the annite and apatite but still texturally superior to the groundmass. Aegirine is present as a minor mineral. Trace minerals include gaidonnayite, hilairite, petarasite, pyrochlore, enclosed by annite and surrounded by pleochroic haloes, and sphalerite. Rare minerals include aegirine-augite, böhmite, calcioancylite-(Ce), galena, pyrite, rhodochrosite, riebeckite, sodalite, and possible baddeleyite, rhabdophane, and synchysite-(Ce).

The presumed mode of occurrence, combined with textural and mineralogical considerations (*q.v.*) leads to the general classification of this rock as a type of lamprophyre, in particular as alnøite. It should be said that based on the immediate evidence, it is only an alnøite inasmuch as it is a feldspar-free lamprophyre with annite as the dominant mafic mineral. It does not, in its present state, have the requisite melilite groundmass to be categorized as an alnøite *sensu stricto*. It does, however, have a natrolite/calcite groundmass, which may be theoretically achieved by the decomposition of melilite in the presence of sodium ions and carbon dioxide. This leads to two possibilities. First, this rock may represent a new type of lamprophyre, or second, this rock may have at one time been a true alnøite, only now having been altered to some different modality. In any case, specificity has been sacrificed for the sake of accuracy, and this rock is classified as an annite lamprophyre.

### *Pegmatites & Various Syenoids*

The pegmatites and various syenoids represent the multitude of microenvironments and extremities of magmatic evolution that pervade the East Hill suite. Within the context of this work, they cannot be categorically and practically described on an individual basis in terms of their mineralogy due to their great numbers, immense variety, and mineralogical complexity. Moreover, it would be contrary to the purpose of this study to discuss the minutiae of Mont Saint-Hilaire mineralogy. That having been said, owing to certain similarities between the two groups, some general observations may be made.

The pegmatites of the East Hill suite belong, in general, to two families: 1) those that are mineralogically similar to one of the major lithologies of the East Hill suite but whose magma evolved, or was influenced, chemically to the point that pegmatitic crystallization dynamics became dominant and 2) those that represent some highly-evolved, late-stage magma. Pegmatites of both varieties may be either discordant—typically occurring as dikes, up to meter-scale in thickness and tens of meters in extent, abruptly transitioning to the intruded lithology at their margins—or concordant—as cm- to dm-scale segregations or phases of their parental lithology that texturally grade gently into the latter. Discordant pegmatites appear to be more abundant than those that are concordant.

No pegmatites with the general composition or mineralogy of the nepheline melasyenite were observed nor have any been reported. Pegmatites with compositions that approximate the eudialyte syenite and some of the various syenoids are most abundant, although some that exhibit aspects of the nepheline leucosyenite have been observed. Although they do not boast the flamboyant zonation or mineralization of larger pegmatites, most of the feldspar-aegirine dikes are pegmatitic in texture.

The various syenoids exhibit distinctive textures and minerals that are much more abundant than in the major lithologies. Some typical features of the various syenoids are abundant mm- to cm-scale miaroles, felty masses of aegirine and astrophyllite group minerals, segregation of minerals into irregular, nearly-monomineralic, cm-scale domains, and euhedral miarolitic analcime and catapleiite. Also, numerous samples of syenoids exhibit one of two characteristic mineral associations: eudialyte-fluorite-astrophyllite or sodalite-aegirine-catapleiite.

### ***Perthite Syenite***

As with the annite lamprophyre, the perthite syenite is exceedingly uncommon, only a very few small samples were found, and no samples were found *in situ*. The perthite syenite is a very coarse-grained, perthitic leucosyenite. About 90% of the volume of the rock consists of heavily albitized perthite; unlike most of the other lithologies in the East Hill suite, the perthite syenite contains no nepheline. Titanian biotite is present as a minor mineral. Trace minerals include aegirine-augite and fluorapatite. Fluorite and wollastonite are present as rare minerals. The perthite syenite is not mentioned by HORVÁTH & GAULT (1990).

### ***Pyroxenite***

Only one example of pyroxenite was observed in the East Hill suite, and no samples were collected, due to the inaccessibility of the occurrence. The pyroxenite was found as an irregular ellipsoidal pod, measuring about 25 cm along its major axis and about 15 cm along its minor axis, enclosed by the nepheline melasyenite. It consisted almost entirely of tapering, prismatic, radially disposed crystals of aegirine, up to about 10 cm in length and 1 cm in width. HORVÁTH

& GAULT (1990) mention pyroxenite parenthetically in the context of xenoliths, but they do not describe pyroxenite as an evolutionary product of the East Hill suite magma.

### ***Xenoliths***

Xenoliths of country rock limestone and siltstone, as well as of brecciated fragments of the Sunrise and Pain de Sucre suites (Greenwood & Edgar 1984; Horváth & Gault 1990), are enclosed by the igneous rock of the East Hill suite. Samples of a limestone xenolith were collected in the course of this study. The xenolith is bright white, fine-grained, and chalky. It consists mainly of calcite with laths of tremolite. Samples of a silicate xenolith were also collected. The silicate xenolith is aphanitic and dark greenish grey, almost greenish black. It does not resemble any other rock type at Mont Saint-Hilaire, either from the East Hill suite or from the Pain de Sucre or Sunrise suites.

## **EAST HILL SUITE – WHOLE-ROCK GEOCHEMISTRY**

### **ALTERATION & WHOLE-ROCK GEOCHEMISTRY**

#### ***Introduction***

As was the case with petrographic descriptions, the condition of the rock in question is a serious consideration of whole-rock geochemical interpretation. Is the rock in its original, pristine state, or has it been subjected to alteration and secondary mineralization? Many of the lithologies of the East Hill suite exhibit such signs, most prominently and extensively in the forms of albitization and nepheline altering to sodalite.

Naturally, whole-rock geochemistry reveals a blend of pre- and post-alteration chemistry; some elements are mobilized, whereas others remain relatively immobile; some minerals resist alteration by a particular fluid but are easily altered by others. Both bulk chemistries are important. Post-alteration chemistry, by way of comparison with petrography and contrast with pre-alteration chemistry, reveals a great deal about the chemical and physical properties of the altering fluids. Similarly, the divination of pre-alteration chemistry is crucial to realistic interpretation of petrogenesis and parental magmas.

#### ***Estimation of Pre-Alteration Chemistry***

Pre-alteration chemistries were estimated for several lithologies in the East Hill suite by using electron microprobe mineral analyses and modal mineralogy derived from petrographic examination of a given lithology. Since many significant trace elements are either carried by trace or rare minerals or are simply not analyzed in certain major or minor minerals, estimates were strictly applied to major element geochemistry.

Petrography only adequately revealed the pre-alteration mineralogy for six lithologies: nepheline melasyenite, the three types of nepheline leucosyenite, eudialyte syenite, and perthite syenite. For each lithology, the major and most abundant minor minerals were selected, to total between 90 and 100% of the modality. Then, an average major element mineral composition was generated from electron microprobe analyses of unaltered specimens of each selected mineral. The average mineral compositions were combined with modal percentages from petrography to create a weighted average whole-rock composition. The estimates are not intended to portray precise pre-alteration geochemistries but are meant to indicate trends in geochemical changes during alteration.

### ***Trace Element Behavior***

Even though trace elements were excluded from the estimation process, their presence cannot be ignored. Not only are many trace elements significant in terms of establishing tectonic provenance, they are central to the reconstruction of parental magma compositions and magmatic differentiation paths. Therefore, the general behavior of trace elements, within the context of these interpretations, merits some discussion. Two factors govern the transport of trace elements: 1) the intrinsic mobility of the element & 2) local re-uptake of mobilized elements in secondary phases. The balance between these two factors determines the degree of retention of each element in the whole rock. Low mobility elements tend to stay in place, unless fluid flux is high and there are no suitable secondary phases to trap mobilized atoms. On the other hand, high mobility elements may be unable to exit the system if they are quickly incorporated into a secondary mineral.

In the most general sense, LILE tend to be relatively more mobile, while HFSE tend to be relatively less. All REE and U exhibit small-scale mobility, being mobilized easily but quickly redeposited in phases such as monazite and apatite. Rare-earth elements, however, exhibit variable mobility; LREE tend to be more mobile than HREE. (Floyd 1977; Lev *et al.* 1998; Ordóñez-Calderón *et al.* 2008; Zhao & Zheng 2008)

HUMPHRIS & THOMPSON (1978) examined hydrothermally altered greenschist facies pillow basalts to characterize trace element mobilities: Sr exhibited leaching without redeposition; Li, Ba, B, Cu, Fe, Mn, Ni, and Co were mobilized followed by local re-uptake; and Cr, V, Zr, and Y were not substantially mobilized.

STURCHIO *ET AL.* (1986) obtained similar results in hydrothermally altered rhyolite. Alkali and alkaline earth metals, Mn, and U exhibited redistributive mobility, with transport distances greater than 10-100 m; Al, Sc, Fe, Co, Zr, Hf, Ta, Y, REE, and Th were less mobile, with transport distances less than 10-100 m.

Differences in observed mobilities between HUMPHRIS & THOMPSON (1978) and STURCHIO *ET AL.* (1986) may be attributable to differences in absolute temperature and thermal gradients in the two systems. (Seewald & Seyfried 1990) Also, HUMPHRIS & THOMPSON (1978) were analyzing rock from an active mid-ocean ridge hydrothermal system, whereas STURCHIO *ET AL.* (1986) examined rock from a geyser field. Almost certainly, the basalts of HUMPHRIS & THOMPSON (1978) were subjected to high-flux, open-system mass transport, whereas there was likely less fluid flux and more recirculation in the rhyolites of STURCHIO *ET AL.* (1986). Redox conditions are another important factor in the variable mobility of polyvalent individual transition elements. Iron, notably, becomes less soluble with increasing oxidation. (Seyfried & Ding 1993; Aiuppa *et al.* 2000)



Observations in the East Hill suite are generally consistent with observations of element mobility in other localities and rock types. There is clear evidence of substantial mobility of certain LILE, in particular Na and K, in the form of albitization and other sodium metasomatism. On the other hand, although REE may have been mobilized, there is widespread secondary REE mineralization in microlites, indicating that if any such mobilization occurred, it likely resulted in local redistribution. Furthermore, REE-bearing and -essential minerals are present as matrix phases in several lithologies. HFSE-bearing minerals, when altered, exhibit *in situ* secondary HFSE mineralization, for example catapleiite pseudomorphs after eudialyte group minerals. Similarly, and including Fe and Mn, some aegirine-augite and titanite crystals are corroded but immediately mantled by amphibole group minerals of comparable composition.

Overall, then, it appears that only certain LILE exhibit large-scale mobility in the East Hill suite and that the whole-rock concentrations of most other elements should not differ substantially from those of the original, pristine lithology. Therefore, trace element concentrations should largely be unaffected, and the estimates of pre-alteration whole-rock geochemistry need only address major elements. Similarly, the estimates should reflect reasonable approximations of pristine whole-rock major- and trace element compositions for the purpose of interpreting tectonic setting and geochemical evolution.

### ***Post-Alteration***

Representative whole-rock major element analyses and corresponding CIPW norms are listed in TABLES 2 through 5. Low totals are due to the presence of hydrous and carbonate phases. Harker diagrams of major elements are shown in FIGURES 15 through 25. Most lithologies in the East Hill suite have basic silica contents, with some rock types edging into ultrabasic or intermediate ranges. Of equal importance to low silica content, rocks of the East Hill suite owe their nepheline-normative and otherwise alkaline mineralogy to their, in some cases absurdly, high alkali content.

In comparison with mineralogically similar lithologies (*i.e.* nepheline melasyenite *versus* augite syenite or lujavrite) from several other alkaline provinces and complexes, namely Gardar in Greenland (Jones & Larsen 1985; Upton 1985; Bailey *et al.* 2001; Khomyakov *et al.* 2001), Kola in Russia (Arzamastsev *et al.* 2001), North Nyasa in Malawi (Eby *et al.* 1998), and Oslo in Norway. (Neumann 1980; Andersen & Sørensen 1993), East Hill suite lithologies are comparable in silica and alumina, variably rich in alkalis, iron, and manganese, generally moderate in calcium content, and generally low in titanium and magnesium. The annite lamprophyre is exceptionally iron-rich but is low in sodium and phosphorus in comparison to alnøite from Damaraland in Namibia. (LeRoex & Lanyon 1998) Unless noted otherwise, subsequent comparisons to these complexes are based on the same references.

The Types 1 and 2 nepheline leucosyenite and the perthite syenite, in addition to being exceptionally alkali-rich, are enriched in Al, both in the context of the East Hill suite and that of the aforementioned alkaline suites. This enrichment in alumina partly depresses the relative silica content of these lithologies.

TABLE 2 – Representative whole-rock XRF analyses and CIPW norms I – Major Elements

Lithology:	<i>Nepheline Melasyenite</i>	<i>Type 1 Nepheline Leucosyenite</i>	<i>Type 2 Nepheline Leucosyenite</i>	<i>Type 3 Nepheline Leucosyenite</i>
Sample:	<i>MSH-B-8</i>	<i>MSH-B-12</i>	<i>MSH-B-4</i>	<i>MSH-B-10</i>
SiO <sub>2</sub> (wt.%)	54.41	47.84	44.52	53.59
TiO <sub>2</sub>	1.29	0.04	0.04	0.11
Al <sub>2</sub> O <sub>3</sub>	19.56	23.00	22.11	19.54
FeO*	5.94	1.30	2.93	3.73
MnO	0.27	0.13	0.20	0.56
MgO	0.97	nd	1.03	nd
CaO	4.50	0.44	0.30	1.87
Na <sub>2</sub> O	7.10	18.24	20.03	13.57
K <sub>2</sub> O	3.43	2.69	3.10	3.15
P <sub>2</sub> O <sub>5</sub>	0.71	0.08	0.10	0.26
SUM	98.17	93.76	94.36	96.37
<i>qtz</i> (wt.%)	–	–	–	–
<i>pl</i>	55.50	18.53	–	28.54
<i>or</i>	20.51	16.72	17.89	19.15
<i>ne</i>	8.73	48.75	54.46	30.83
<i>lct</i>	–	–	0.94	–
<i>kfs</i>	–	–	–	–
<i>crn</i>	–	–	–	–
<i>di</i>	5.38	0.50	0.71	2.92
<i>opx</i>	–	–	–	–
<i>wo</i>	–	0.52	–	1.95
<i>ol</i>	0.52	–	2.27	–
<i>aeg</i>	–	3.96	8.80	11.11
<i>ks</i>	–	–	–	–
<i>ns</i>	–	6.96	10.82	3.48
<i>rt</i>	–	–	–	–
<i>ilm</i>	2.49	0.08	0.08	0.21
<i>mag</i>	4.84	–	–	–
<i>hem</i>	–	–	–	–
<i>ap</i>	1.67	0.19	0.23	0.63
<i>zrn</i>	0.09	0.10	0.13	0.33
<i>ttn</i>	–	–	–	–
<i>py</i>	0.25	0.19	0.06	0.04
<i>hl</i>	0.21	2.44	2.49	0.66
nd = not detected * Total Fe reported as FeO Norm calculations based on JOHANNSEN (1931) Mineral abbreviations for CIPW norms from SIIVOLA & SCHMID (2009), except (ks) – potassium silicate & (ns) – sodium silicate				

TABLE 3 – Representative whole-rock XRF analyses and CIPW norms II – Major Elements

Lithology:	<i>Eudialyte Syenite</i>	<i>Eudialyte Syenite</i>	<i>Feldspar- Aegirine Dike</i>	<i>Annite Lamprophyre</i>
Sample:	<i>MSH-B-1</i>	<i>MSH-B-2</i>	<i>MSH-B-3</i>	<i>MSH-B-6</i>
SiO <sub>2</sub> (wt.%)	55.19	53.37	52.40	33.56
TiO <sub>2</sub>	0.17	0.12	0.33	0.83
Al <sub>2</sub> O <sub>3</sub>	16.94	17.75	12.44	9.60
FeO*	5.02	5.37	9.40	22.13
MnO	1.06	0.66	1.77	2.85
MgO	nd	nd	nd	6.50
CaO	2.10	2.13	1.84	2.20
Na <sub>2</sub> O	9.46	7.76	7.30	2.82
K <sub>2</sub> O	3.71	4.15	2.24	6.08
P <sub>2</sub> O <sub>5</sub>	0.21	0.10	0.17	0.48
SUM	93.85	91.41	87.89	87.03
<i>qtz</i> (wt.%)	–	–	0.97	–
<i>pl</i>	38.72	48.23	57.93	–
<i>or</i>	23.22	26.65	14.89	13.66
<i>ne</i>	17.13	13.24	–	9.66
<i>lct</i>	–	–	–	21.59
<i>kfs</i>	–	–	–	–
<i>crn</i>	–	–	–	–
<i>di</i>	3.16	–	–	6.98
<i>opx</i>	–	–	–	–
<i>wo</i>	2.64	3.88	3.81	–
<i>ol</i>	–	–	–	10.74
<i>aeg</i>	11.94	–	10.04	7.98
<i>ks</i>	–	–	–	–
<i>ns</i>	–	–	–	–
<i>rt</i>	–	–	–	–
<i>ilm</i>	0.34	0.25	0.70	1.80
<i>mag</i>	1.71	3.62	6.99	11.51
<i>hem</i>	–	3.34	2.87	13.41
<i>ap</i>	0.51	0.25	0.44	1.27
<i>zrn</i>	0.64	0.61	1.98	1.62
<i>ttn</i>	–	–	–	–
<i>py</i>	0.11	0.15	0.08	0.30
<i>hl</i>	0.11	0.04	0.02	0.06
nd = not detected * Total Fe reported as FeO Norm calculations based on JOHANNSEN (1931) Mineral abbreviations for CIPW norms from SIIVOLA & SCHMID (2009), except (ks) – potassium silicate & (ns) – sodium silicate				

TABLE 4 – Representative whole-rock XRF analyses and CIPW norms III – Major Elements

Lithology:	<i>Pegmatite</i>	<i>Pegmatite</i>	<i>Various Syenoid</i>	<i>Various Syenoid</i>	<i>Various Syenoid</i>
Sample:	<i>MSH-B-21</i>	<i>MSH-B-33</i>	<i>MSH-B-23</i>	<i>MSH-B-27</i>	<i>MSH-B-36</i>
SiO <sub>2</sub> (wt.%)	55.14	56.94	55.26	55.99	52.34
TiO <sub>2</sub>	0.19	0.25	0.29	0.68	0.34
Al <sub>2</sub> O <sub>3</sub>	17.90	16.61	10.86	19.46	7.20
FeO*	5.19	5.24	9.70	4.38	13.25
MnO	0.77	0.69	0.95	0.21	1.14
MgO	nd	nd	3.22	nd	nd
CaO	0.79	0.89	0.86	2.00	4.87
Na <sub>2</sub> O	7.01	6.72	13.31	7.11	5.94
K <sub>2</sub> O	5.32	5.49	1.25	3.92	3.86
P <sub>2</sub> O <sub>5</sub>	0.06	0.39	0.23	0.27	0.39
SUM	92.37	93.22	95.32	94.03	89.25
<i>qtz</i> (wt.%)	–	–	–	–	3.84
<i>pl</i>	47.96	51.70	34.80	64.79	21.46
<i>or</i>	33.80	34.57	7.56	24.47	25.00
<i>ne</i>	9.53	3.67	11.84	2.33	–
<i>lct</i>	–	–	–	–	–
<i>kfs</i>	–	–	–	–	–
<i>crn</i>	–	–	–	1.01	–
<i>di</i>	–	–	2.25	–	–
<i>opx</i>	–	–	–	–	–
<i>wo</i>	0.84	0.87	–	–	9.98
<i>ol</i>	–	–	5.20	–	–
<i>aeg</i>	–	0.82	31.30	–	29.20
<i>ks</i>	–	–	–	–	–
<i>ns</i>	–	–	4.75	–	–
<i>rt</i>	–	–	–	0.32	–
<i>ilm</i>	0.38	0.51	0.61	0.77	0.76
<i>mag</i>	2.92	2.16	–	–	5.11
<i>hem</i>	3.88	4.12	–	4.87	2.11
<i>ap</i>	0.14	0.97	0.58	0.65	1.04
<i>zrn</i>	0.73	0.48	0.34	0.13	1.95
<i>ttn</i>	–	–	–	–	–
<i>py</i>	0.06	0.11	0.19	0.17	0.19
<i>hl</i>	0.02	0.15	0.49	0.47	0.09
nd = not detected * Total Fe reported as FeO Norm calculations based on JOHANNSEN (1931) Mineral abbreviations for CIPW norms from SIIVOLA & SCHMID (2009), except (ks) – potassium silicate & (ns) – sodium silicate					

TABLE 5 – Representative whole-rock XRF analyses and CIPW norms IV – Major Elements

Lithology:	<i>Perthite Syenite</i>	<i>Limestone Xenolith</i>	<i>Silicate Xenolith</i>
Sample:	<i>MSH-B-9</i>	<i>MSH-B-16</i>	<i>MSH-B-51</i>
SiO <sub>2</sub> (wt.%)	44.00	17.38	52.50
TiO <sub>2</sub>	0.20	0.02	0.56
Al <sub>2</sub> O <sub>3</sub>	22.05	nd	11.01
FeO*	5.50	0.19	9.99
MnO	0.38	0.03	0.20
MgO	1.22	nd	10.29
CaO	0.68	49.96	9.18
Na <sub>2</sub> O	16.82	nd	3.06
K <sub>2</sub> O	3.01	nd	0.11
P <sub>2</sub> O <sub>5</sub>	0.20	0.18	0.11
TOTAL	94.07	67.75	97.01
<i>qtz</i> (wt.%)	–		–
<i>pl</i>	–		43.16
<i>or</i>	11.93		0.65
<i>ne</i>	54.65		–
<i>lct</i>	5.19		–
<i>kfs</i>	–		–
<i>crn</i>	–		–
<i>di</i>	1.72		24.29
<i>opx</i>	–		24.22
<i>wo</i>	–		–
<i>ol</i>	2.29		6.33
<i>aeg</i>	17.53		–
<i>ks</i>	–		–
<i>ns</i>	2.29		–
<i>rt</i>	–		–
<i>ilm</i>	0.40		1.10
<i>mag</i>	–		–
<i>hem</i>	–		–
<i>ap</i>	0.49		0.25
<i>zrn</i>	0.19		–
<i>ttn</i>	–		–
<i>py</i>	0.08		–
<i>hl</i>	2.27		–
nd = not detected * Total Fe reported as FeO Norm calculations based on JOHANNSEN (1931) Mineral abbreviations for CIPW norms from SIIVOLA & SCHMID (2009), except (ks) – potassium silicate & (ns) – sodium silicate			

Iron content is variably moderate to high; Fe/Mn ratios range from 4.74 to 22.36. Iron concentrations in the syenitic rocks of the East Hill suite are similar to those found in the Gardar province and in the Khibina-Lovozero complexes (Arzamastsev *et al.* 2001) but are somewhat lower than those in North Nyasa and notably higher than the range found in the Oslo graben. The annite lamprophyre and certain syenoids contain more iron than the more iron-rich lithologies in all four compared provinces, and the annite lamprophyre contains about double the iron of the Damaraland alnöites.

Manganese is elevated overall, running in line with Gardar, Khibina-Lovozero, North Nyasa and Oslo for the nepheline melasyenite and the Types 1 and 2 nepheline leucosyenite, but 2 to 5 times higher than those provinces in the more evolved syenites, pegmatites, and syenoids.

Magnesium is low to absent, consistent with Gardar, Khibina-Lovozero, and Oslo. The North Nyasa province rocks are enriched with 2 to 3 times the magnesium of the East Hill suite and the other three provinces.

Overall, calcium contents are comparable to or lower than those found in Gardar and Oslo and are comparable to those of the Khibina-Lovozero complexes, but they are 2 to 3 times lower than those of the North Nyasa complexes. Interestingly, though, calcium content runs somewhat high in some lithologies, contrary to the perception that sodium and calcium somewhat mutually exclude one another in alkaline systems; there is more to the story than aegirine-augite. The nepheline melasyenite runs particularly high in calcium, leaning towards a gabbroic affinity and higher than any reported rock type from Gardar, Khibina-Lovozero, or Oslo and higher than any syenitic rock from North Nyasa.

Potassium content is generally lower than that in Gardar, Khibina-Lovozero, and Oslo but on par with that of North Nyasa. Sodium content is comparable to that of Gardar, North Nyasa,

and Oslo but lower than that of Khibina-Lovozero in the nepheline melasyenite, eudialyte syenite, feldspar-aegirine dikes, and certain pegmatites and syenoids. In several other lithologies, however, it is high to tremendous, especially in the nepheline leucosyenites, the bulk of which run near 20 wt.% Na<sub>2</sub>O, and the perthite syenite. The annite lamprophyre is low in sodium, containing less than half the sodium of the Damaraland alnøites.

Phosphorus is present in similar concentrations to those found in Gardar, Khibina-Lovozero, North Nyasa, and Oslo, even in the nepheline melasyenite and the annite lamprophyre, which are P-rich lithologies in the East Hill suite. The annite lamprophyre, however, contains less than half the P found in the Damaraland alnøites.

The limestone xenolith is a strict calc-silicate rock, having picked up little to no major element content other than silica.

The silicate xenolith is wholly unlike the primary igneous lithologies of the East Hill suite. It is basaltic in composition, with more titanium, substantially more iron, magnesium, and calcium, and substantially less sodium and potassium than most of the East Hill suite lithologies.

CIPW norms generally point to an alkali-rich bulk composition for the East Hill suite, with a preponderance of silica-undersaturated lithologies and some exceptionally high sodium contents. Lithologies of the East Hill suite are generally nepheline-normative; however, the feldspar-aegirine dikes and one of the various syenoids are quartz normative, indicating positive fluctuations in silica availability late in the crystallization history. Another of the various syenoids, in addition to being nepheline-normative, contains normative corundum. The nepheline leucosyenites, one of the various syenoids, and the perthite syenite show normative sodium silicate. Several rock types calculate to normative olivine, although no olivine is present in the East Hill suite; this reflects the presence of iron-rich phases, unaccounted for by the



normative species. Similarly, the entire East Hill suite exhibits varying amounts of normative ilmenite, magnetite, hematite, and pyrite. Normative zircon is ubiquitous.

Plots of the major element whole-rock compositions of the East Hill suite lithologies reveal two prominent compositional trends, as well as a notable outlier or two. The syenitic lithologies (nepheline melasyenite, nepheline leucosyenites, and perthite syenite) largely follow horizontal to subhorizontal compositional trends that, with respect to the syenoid lithologies (eudialyte syenite, feldspar-aegirine dikes, pegmatites, and various syenoids), reflect generally lower contents of  $\text{TiO}_2$ ,  $\text{FeO}^*$ ,  $\text{MnO}$ ,  $\text{MgO}$ , and  $\text{CaO}$  and higher contents of  $\text{Al}_2\text{O}_3$  and  $\text{Na}_2\text{O}$ ; average  $\text{K}_2\text{O}$  and  $\text{P}_2\text{O}_5$  contents are roughly even between the two populations but are slightly lower in the syenitic lithologies.

The exception to the syenitic trend is the departure of the nepheline melasyenite in FIGURES 15, 21, and 25, in which the nepheline melasyenite plots substantially higher than the other syenitic lithologies, as well as the syenoid lithologies, in terms of its  $\text{TiO}_2$ ,  $\text{CaO}$ , and  $\text{P}_2\text{O}_5$  content. Apatite, titanite, titanian magnetite, and Ca-amphibole in the nepheline melasyenite account for its deviation in these three elements but its adherence in all other major elements and the crystallization of these phases in the nepheline melasyenite returns its bulk composition to the syenitic compositional trends for  $\text{TiO}_2$ ,  $\text{CaO}$ , and  $\text{P}_2\text{O}_5$  followed by the other syenitic lithologies.

In contrast, the syenoid lithologies follow a vertical to subvertical compositional trend, indicating that they not only did not participate in the same melt fractionation mechanism that yielded the syenitic lithologies but also that their compositions probably were more strongly governed by fluid-melt interactions and, more particularly, the later-stage input of elements released by destabilized complexes.

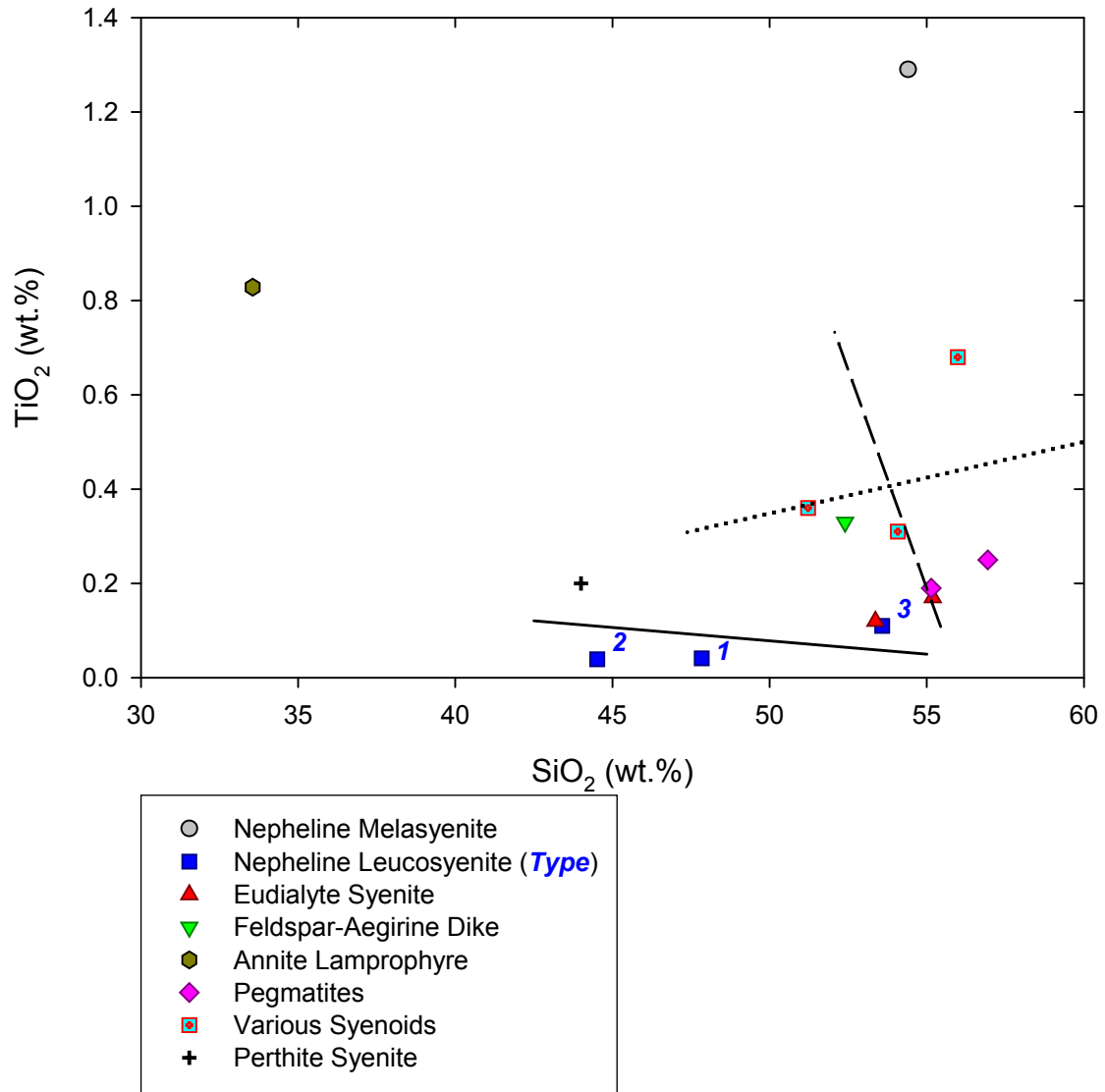


FIGURE 15 – Harker diagram for TiO<sub>2</sub> (post-alteration). The dotted line represents the compositional trend of East Hill suite syenites observed by CURRIE *ET AL.* (1986). The solid line represents the compositional trend of syenitic lithologies (nepheline leucosyenites & perthite syenite) from this study. The dashed line represents the compositional trend of syenoid lithologies (eudialyte syenite, feldspar-aegirine dikes, pegmatites & various syenoids) from this study.

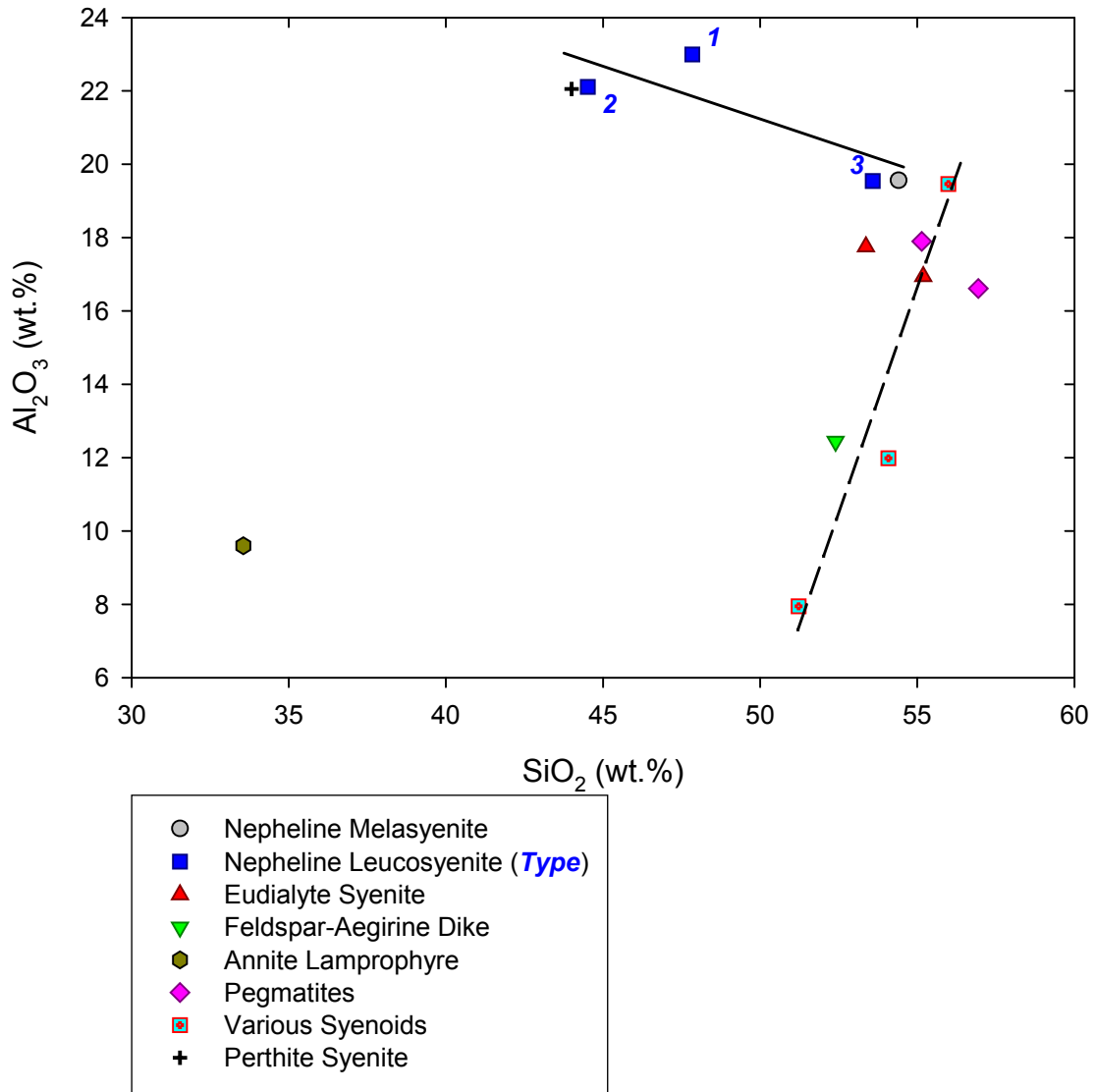


FIGURE 16 – Harker diagram for  $\text{Al}_2\text{O}_3$  (post-alteration). The solid line represents the compositional trend of syenitic lithologies (nepheline melasyenite, nepheline leucosyenites & perthite syenite) from this study. The dashed line represents the compositional trend of syenoid lithologies (eudialyte syenite, feldspar-aegirine dikes, pegmatites & various syenoids) from this study.

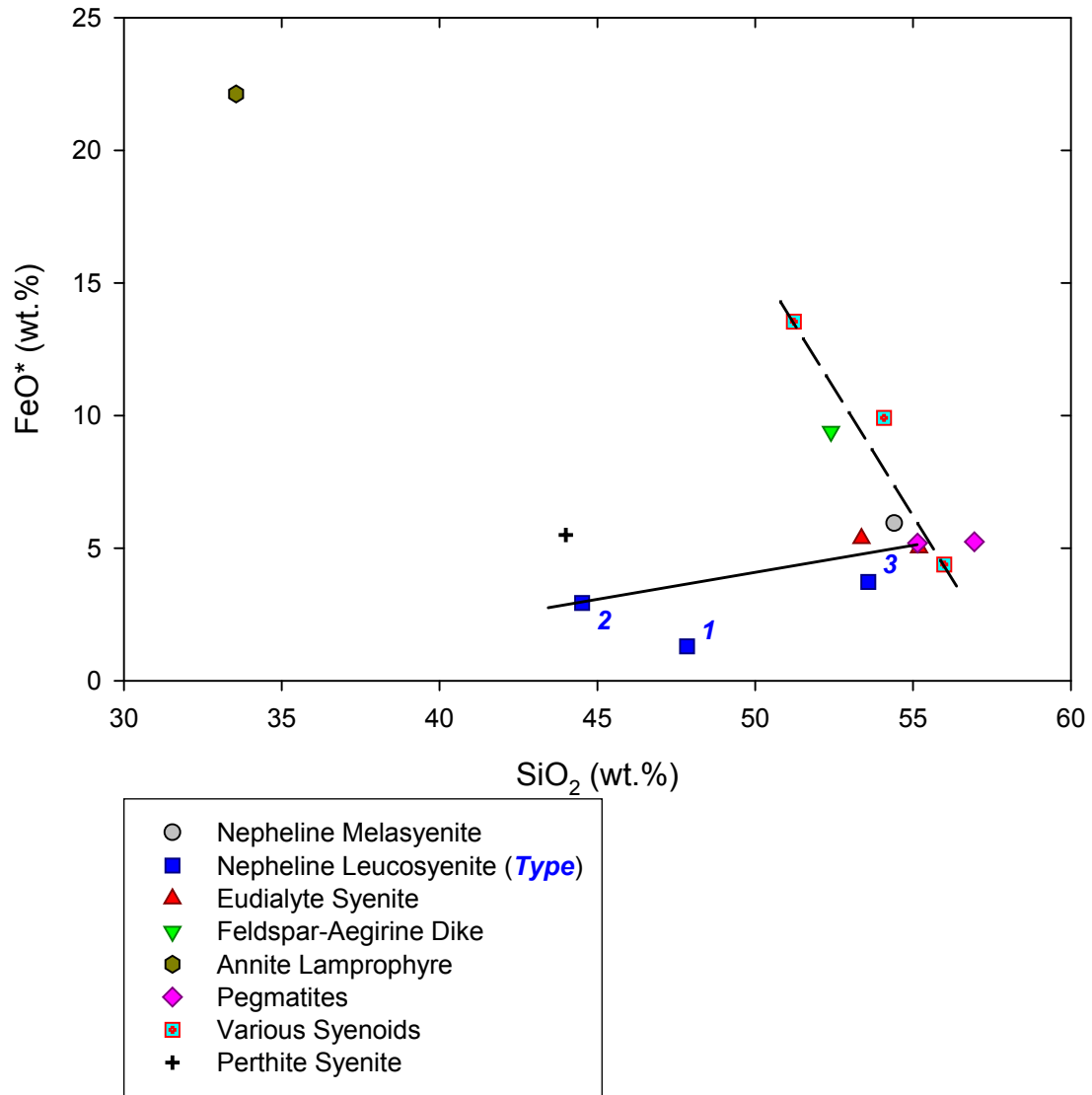


FIGURE 17 – Harker diagram for total iron expressed as FeO (post-alteration). The solid line represents the compositional trend of syenitic lithologies (nepheline melasyenite, nepheline leucosyenites & perthite syenite) from this study. The dashed line represents the compositional trend of syenoid lithologies (eudialyte syenite, feldspar-aegirine dikes, pegmatites & various syenoids) from this study.

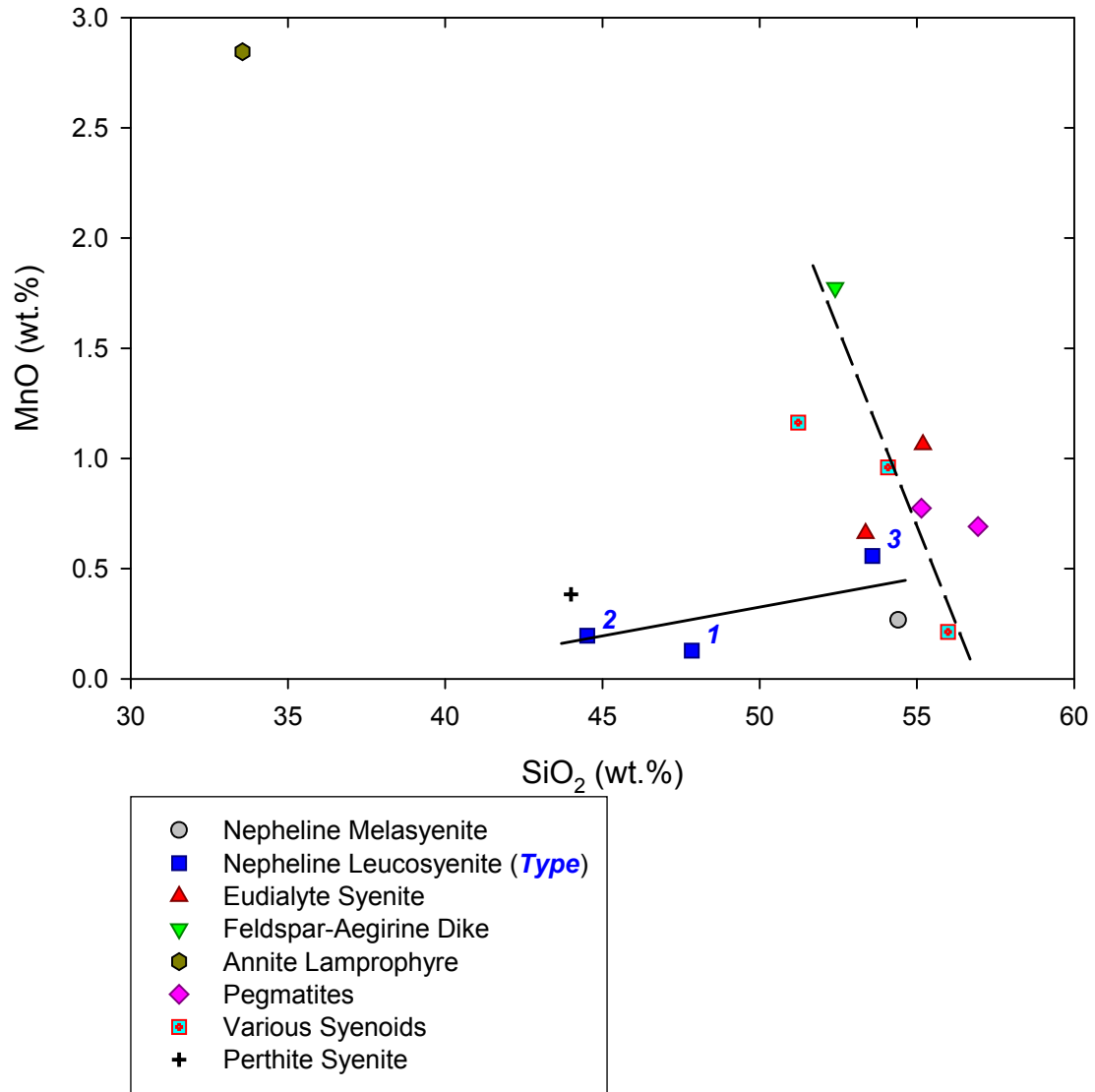


FIGURE 18 – Harker diagram for MnO (post-alteration). The solid line represents the compositional trend of syenitic lithologies (nepheline melasyenite, nepheline leucosyenites & perthite syenite) from this study. The dashed line represents the compositional trend of syenoid lithologies (eudialyte syenite, feldspar-aegirine dikes, pegmatites & various syenoids) from this study.

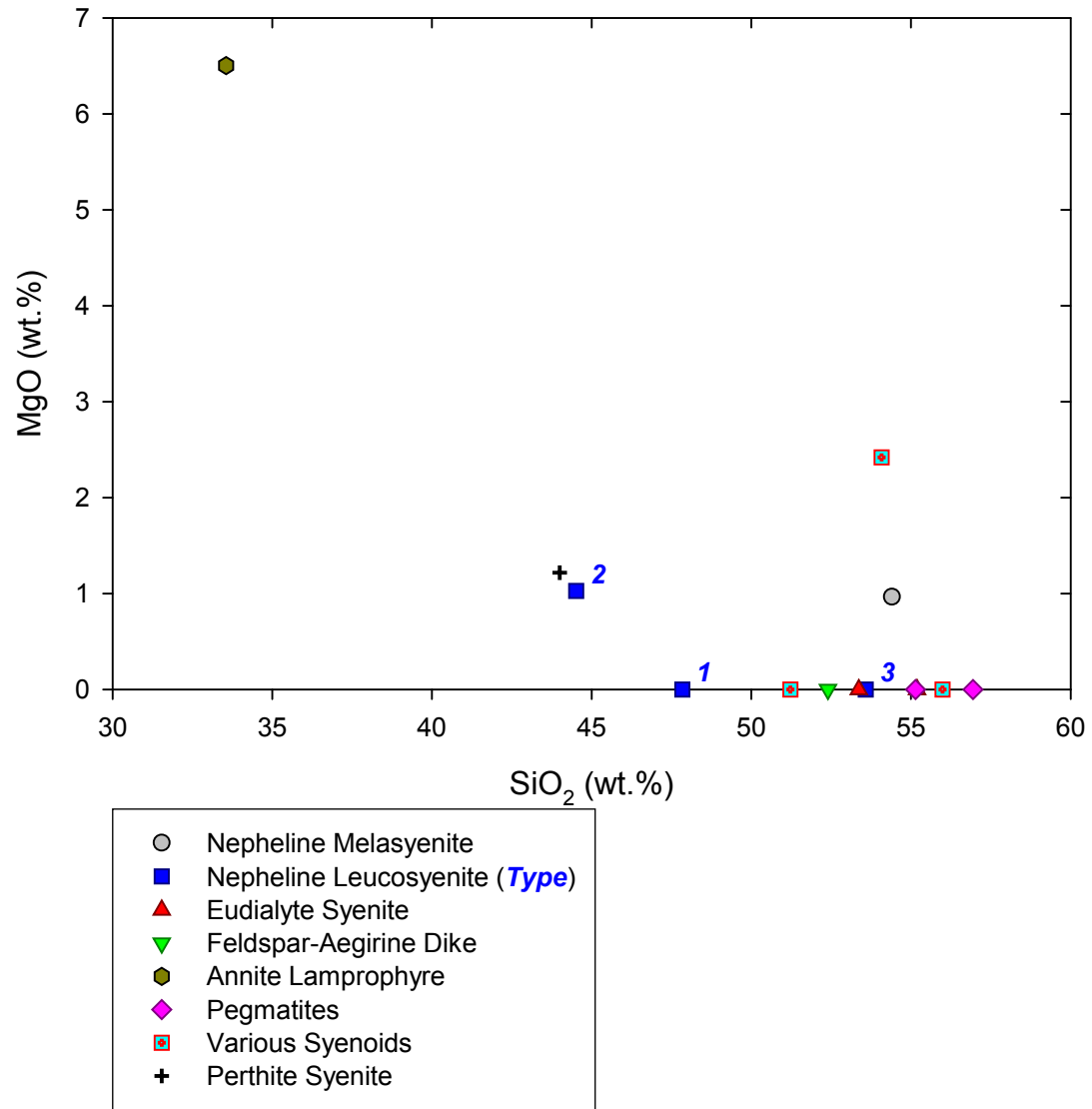


FIGURE 19 – Harker diagram for MgO (post-alteration).

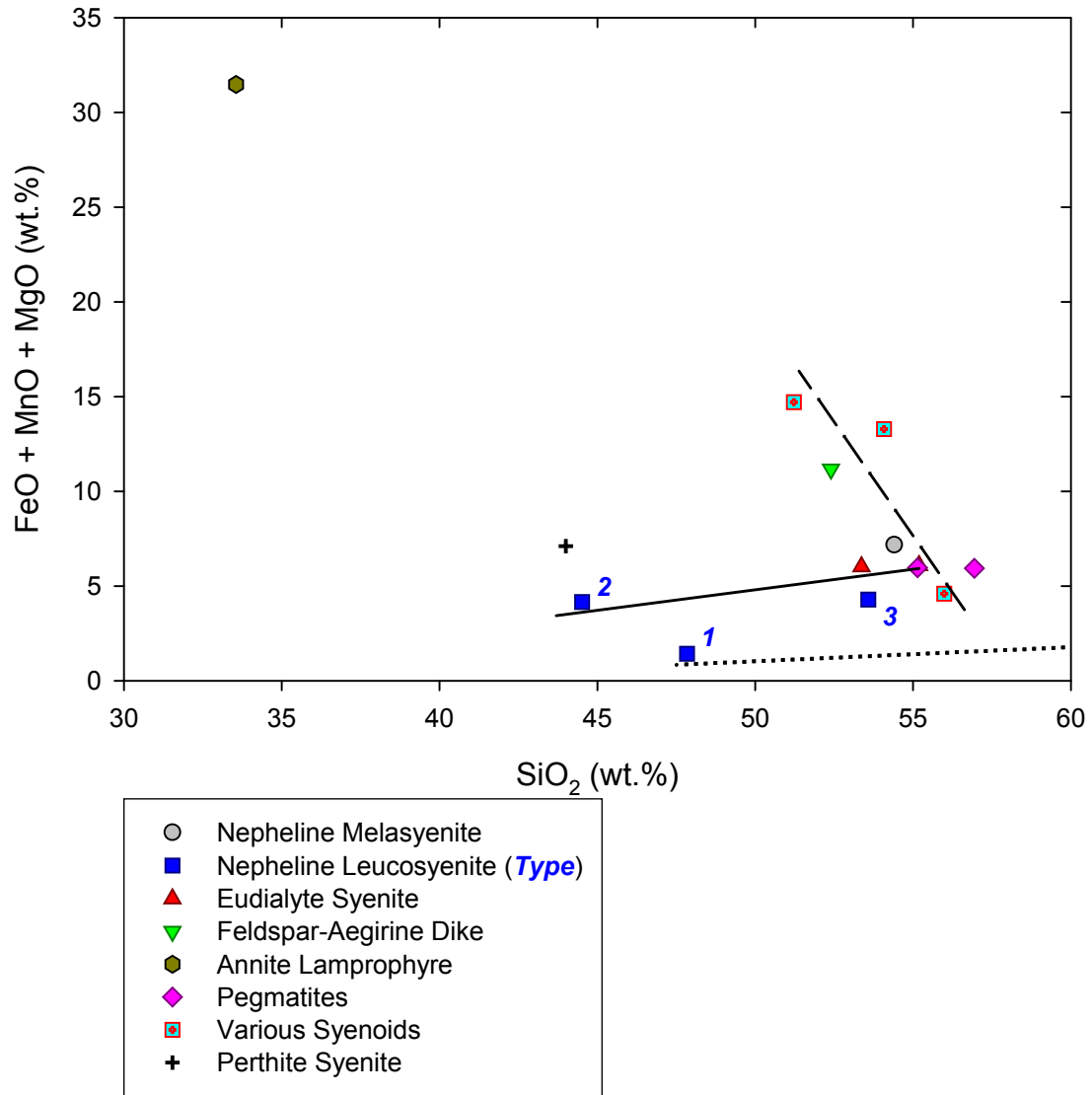


FIGURE 20 – Harker diagram for FeO + MnO + MgO (post-alteration). The dotted line represents the compositional trend of East Hill suite syenites observed by CURRIE *ET AL.* (1986). The solid line represents the compositional trend of syenitic lithologies (nepheline melasyenite, nepheline leucosyenites & perthite syenite) from this study. The dashed line represents the compositional trend of syenoid lithologies (eudialyte syenite, feldspar-aegirine dikes, pegmatites & various syenoids) from this study.

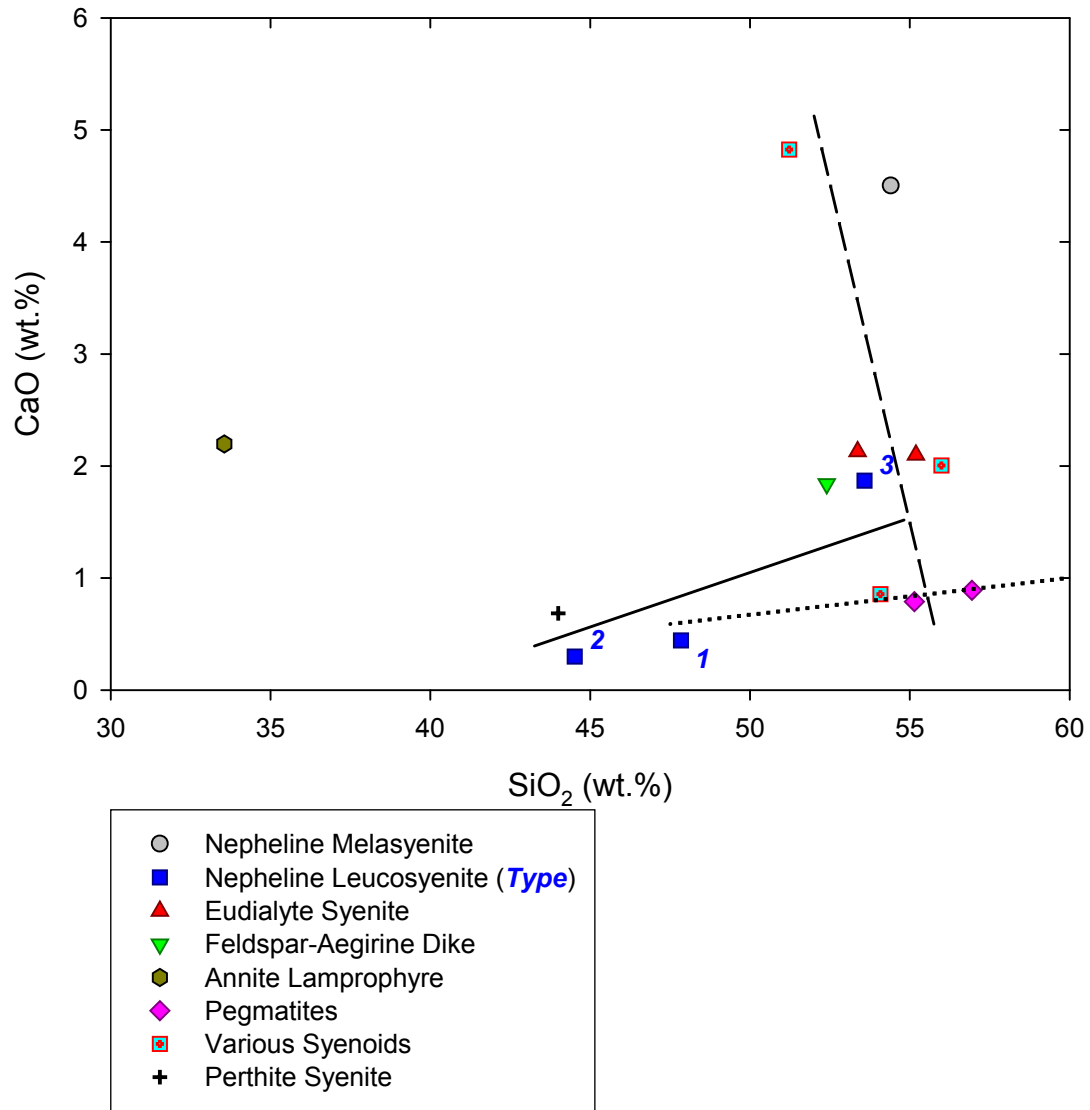


FIGURE 21 – Harker diagram for CaO (post-alteration). The dotted line represents the compositional trend of East Hill suite syenites observed by CURRIE *ET AL.* (1986). The solid line represents the compositional trend of syenitic lithologies (nepheline leucosyenites & perthite syenite) from this study. The dashed line represents the compositional trend of syenoid lithologies (eudialyte syenite, feldspar-aegirine dikes, pegmatites & various syenoids) from this study.



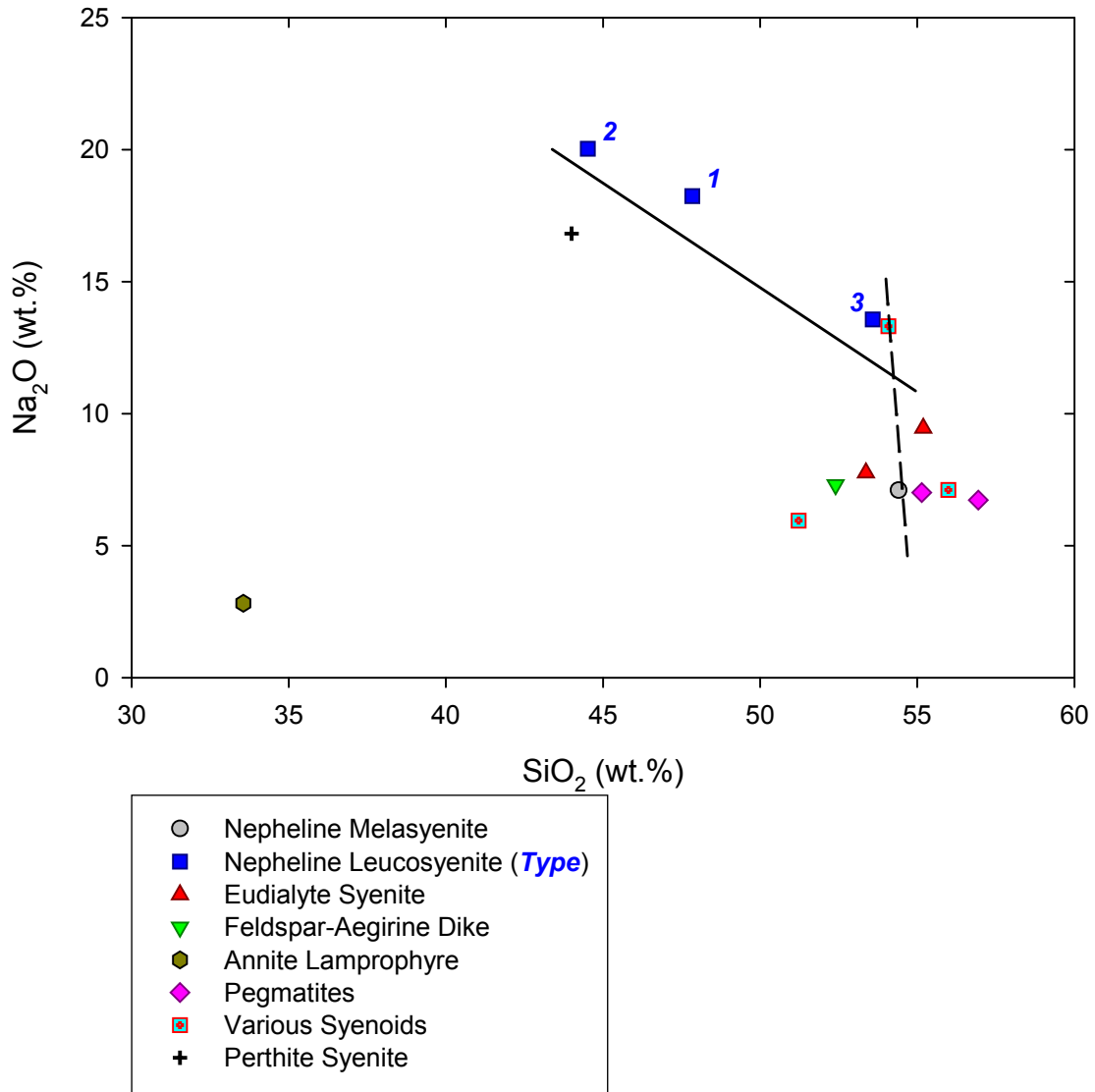


FIGURE 22 – Harker diagram for Na<sub>2</sub>O (post-alteration). The solid line represents the compositional trend of syenitic lithologies (nepheline melasyenite, nepheline leucosyenites & perthite syenite) from this study. The dashed line represents the compositional trend of syenoid lithologies (eudialyte syenite, feldspar-aegirine dikes, pegmatites & various syenoids) from this study.

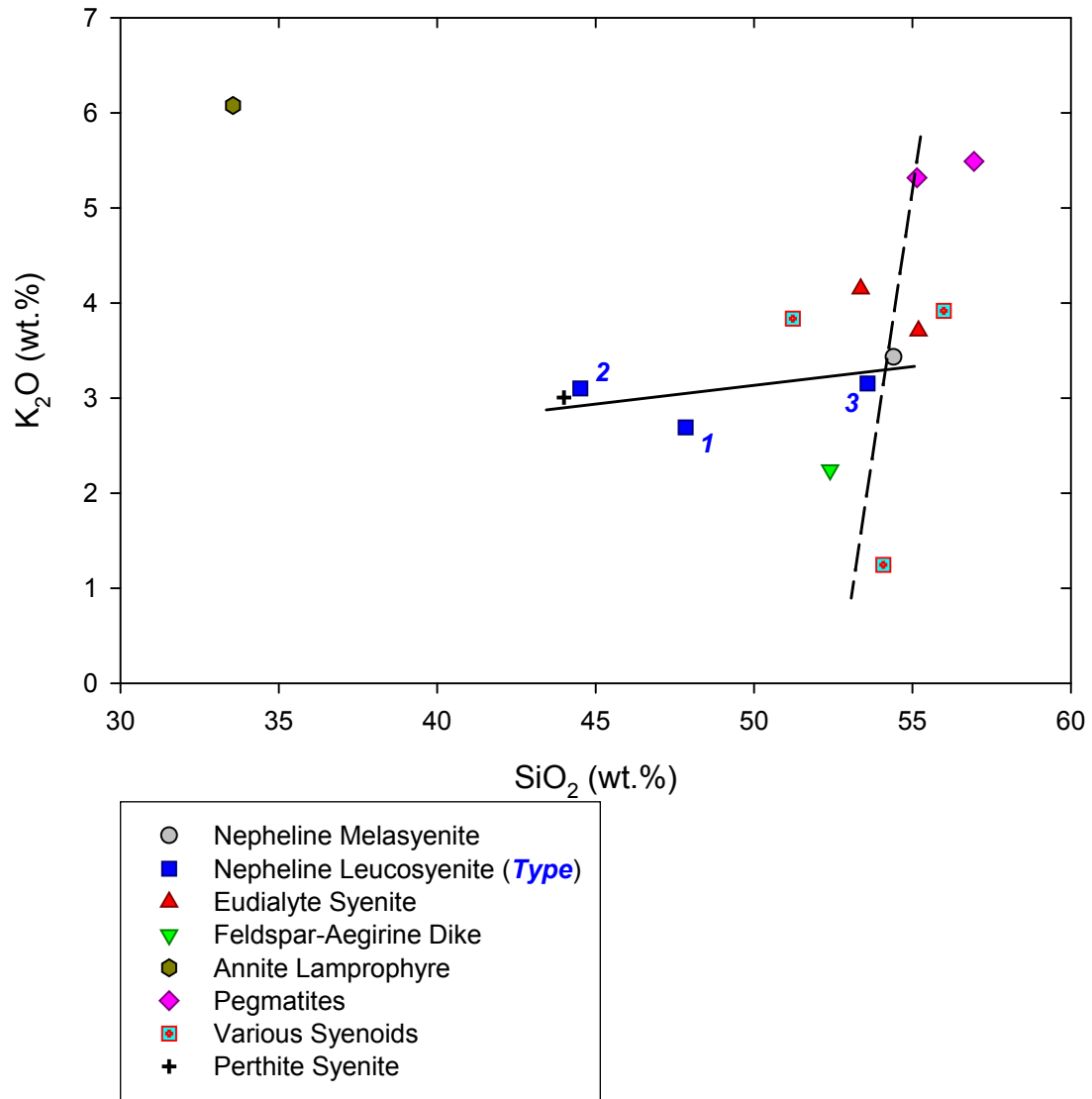


FIGURE 23 – Harker diagram for  $K_2O$  (post-alteration). The solid line represents the compositional trend of syenitic lithologies (nepheline melasyenite, nepheline leucosyenites & perthite syenite) from this study. The dashed line represents the compositional trend of syenoid lithologies (eudialyte syenite, feldspar-aegirine dikes, pegmatites & various syenoids) from this study.

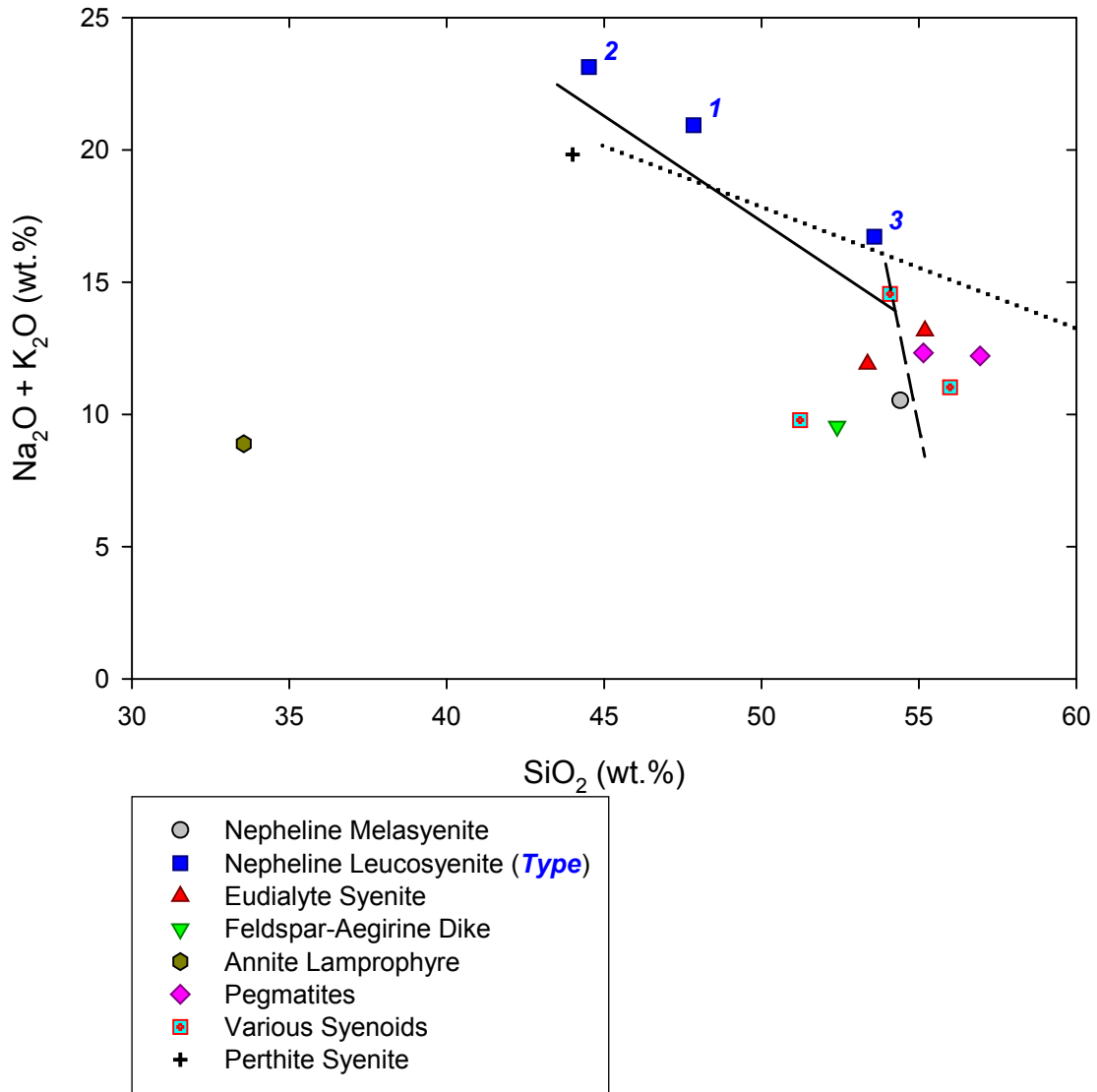


FIGURE 24 – Harker diagram for Na<sub>2</sub>O + K<sub>2</sub>O (post-alteration). The dotted line represents the compositional trend of East Hill suite syenites observed by CURRIE *ET AL.* (1986). The solid line represents the compositional trend of syenitic lithologies (nepheline melasyenite, nepheline leucosyenites & perthite syenite) from this study. The dashed line represents the compositional trend of syenoid lithologies (eudialyte syenite, feldspar-aegirine dikes, pegmatites & various syenoids) from this study.

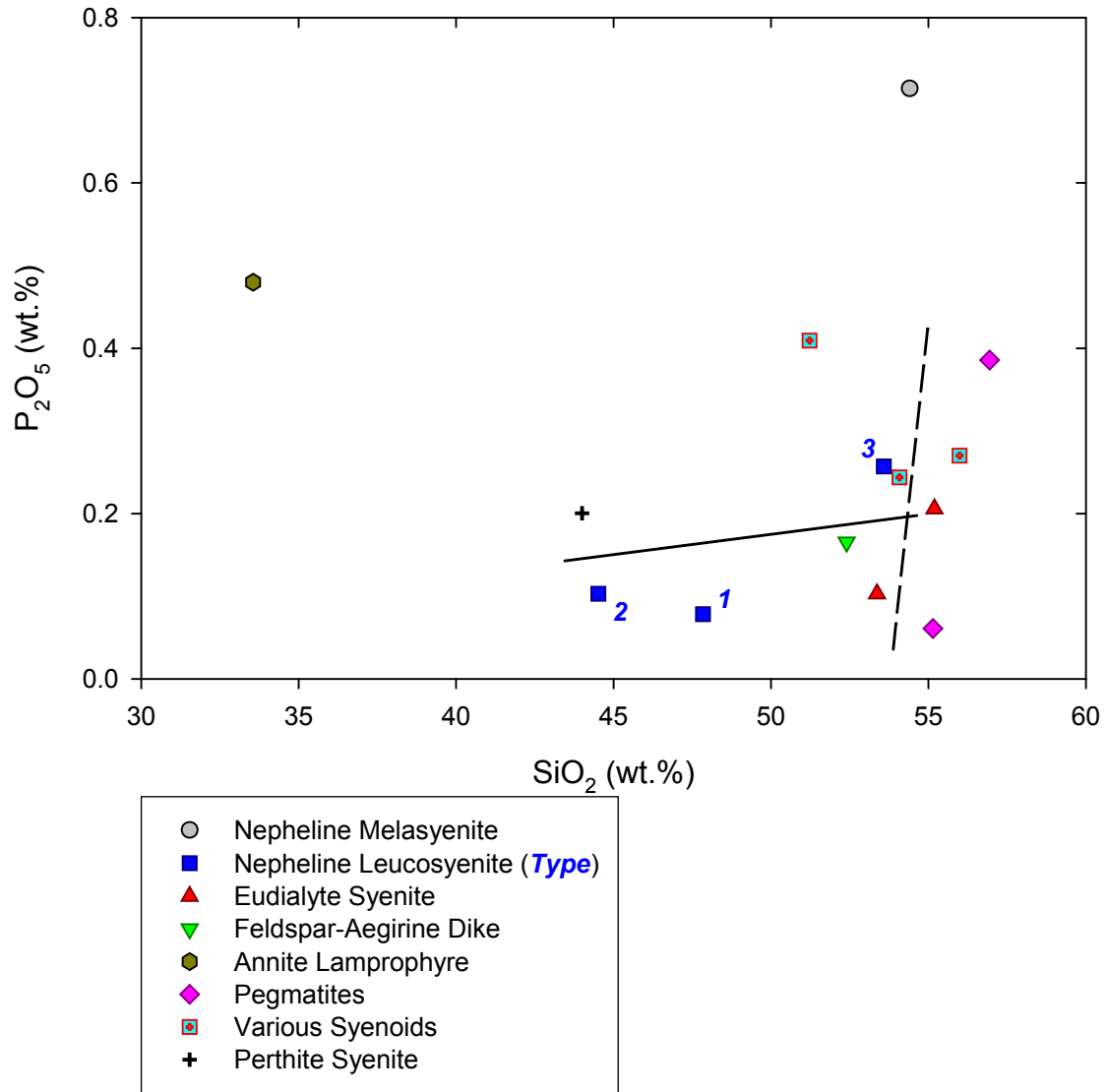


FIGURE 25 – Harker diagram for  $P_2O_5$  (post-alteration). The solid line represents the compositional trend of syenitic lithologies (nepheline leucosyenites & perthite syenite) from this study. The dashed line represents the compositional trend of syenoid lithologies (eudialyte syenite, feldspar-aegirine dikes, pegmatites & various syenoids) from this study.

The annite lamprophyre does not lie on either compositional trend, and its bulk composition lies so far off both that it likely indicates an independent magma.

The syenitic trends mirror those found in East Hill suite nepheline syenites by CURRIE *ET AL.* (1986) in terms of their geometry and approximate elemental concentrations. CURRIE *ET AL.* (1986), however, included neither the nepheline melasyenite nor the annite lamprophyre in their analyses, and they did not observe the compositional trend exhibited by the syenoid lithologies.

### ***Pre-Alteration & Comparison***

Estimates of pre-alteration whole-rock compositions for the nepheline melasyenite, all three types of nepheline leucosyenite, the eudialyte syenite, and the perthite syenite are given in TABLE 6, along with corresponding analyses of post-alteration compositions. Harker diagrams including estimates of pre-alteration alkali compositions are shown in FIGURES 26 through 28. Broad chemical trends mirror those post-alteration; alkalis, iron, and manganese are elevated, and calcium, titanium, and magnesium are moderate to low in tenor. Totals for estimated pre-alteration bulk compositions are generally higher than post-alteration bulk compositions, suggesting an increase in hydrous or carbonate phases during alteration.

With the exception of alkalis, the nepheline melasyenite, the nepheline leucosyenites, the eudialyte syenite, and the perthite syenite exhibit no significant differences in major element content. On alkali Harker diagrams, compositional trends for syenoid lithologies are essentially identical, post- and pre-alteration; those of syenitic lithologies are shifted but nearly parallel.

TABLE 6 – Estimated pre- &amp; analyzed post-alteration whole-rock geochemistries and CIPW norms – Major Elements

Lithology:	<i>Nepheline Melasyenite</i>		<i>Type 1 Nepheline Leucosyenite</i>		<i>Type 2 Nepheline Leucosyenite</i>		<i>Type 3 Nepheline Leucosyenite</i>		<i>Eudialyte Syenite</i>		<i>Perthite Syenite</i>	
Sample:	<i>MSH-B-8</i>		<i>MSH-B-12</i>		<i>MSH-B-4</i>		<i>MSH-B-10</i>		<i>MSH-B-1</i>		<i>MSH-B-9</i>	
(wt.%)	<i>Pre-</i>	<i>Post-</i>	<i>Pre-</i>	<i>Post-</i>	<i>Pre-</i>	<i>Post-</i>	<i>Pre-</i>	<i>Post-</i>	<i>Pre-</i>	<i>Post-</i>	<i>Pre-</i>	<i>Post-</i>
SiO <sub>2</sub>	53.00	<b>54.41</b>	46.05	<b>47.84</b>	45.66	<b>44.52</b>	46.74	<b>53.59</b>	54.81	<b>55.19</b>	60.60	<b>44.00</b>
TiO <sub>2</sub>	0.76	<b>1.29</b>	0.00	<b>0.04</b>	0.02	<b>0.04</b>	0.09	<b>0.11</b>	0.14	<b>0.17</b>	0.27	<b>0.20</b>
Al <sub>2</sub> O <sub>3</sub>	14.41	<b>19.56</b>	27.01	<b>23.00</b>	26.44	<b>22.11</b>	19.51	<b>19.54</b>	17.94	<b>16.94</b>	18.73	<b>22.05</b>
FeO*	10.16	<b>5.94</b>	0.53	<b>1.30</b>	1.51	<b>2.93</b>	7.53	<b>3.73</b>	4.51	<b>5.02</b>	2.86	<b>5.50</b>
MnO	0.75	<b>0.27</b>	0.02	<b>0.13</b>	0.08	<b>0.20</b>	0.49	<b>0.56</b>	1.17	<b>1.06</b>	0.15	<b>0.38</b>
MgO	2.91	<b>0.97</b>	0.01	nd	0.05	<b>1.03</b>	0.31	nd	0.19	nd	0.70	<b>1.22</b>
CaO	6.27	<b>4.50</b>	0.08	<b>0.44</b>	0.38	<b>0.30</b>	2.27	<b>1.87</b>	1.29	<b>2.10</b>	0.02	<b>0.68</b>
Na <sub>2</sub> O	5.62	<b>7.10</b>	13.38	<b>18.24</b>	15.14	<b>20.03</b>	12.69	<b>13.57</b>	6.76	<b>9.46</b>	1.86	<b>16.82</b>
K <sub>2</sub> O	4.64	<b>3.43</b>	9.38	<b>2.69</b>	6.97	<b>3.10</b>	6.49	<b>3.15</b>	8.32	<b>3.71</b>	14.20	<b>3.01</b>
P <sub>2</sub> O <sub>5</sub>	0.71	<b>0.71</b>	0.02	<b>0.08</b>	0.01	<b>0.10</b>	0.02	<b>0.26</b>	0.21	<b>0.21</b>	0.05	<b>0.20</b>
SUM	99.23	<b>98.17</b>	96.47	<b>93.76</b>	96.25	<b>94.36</b>	97.06	<b>96.13</b>	95.33	<b>93.85</b>	99.42	<b>94.07</b>
qtz (wt.%)	–	–	–	–	–	–	–	–	–	–	–	–
pl	27.57	<b>55.50</b>	–	<b>18.53</b>	–	–	–	<b>28.54</b>	12.31	<b>38.72</b>	4.42	–
or	27.42	<b>20.51</b>	–	<b>16.72</b>	–	<b>17.89</b>	27.02	<b>19.15</b>	51.24	<b>23.22</b>	84.09	<b>11.93</b>
ne	10.81	<b>8.73</b>	48.62	<b>48.75</b>	54.60	<b>54.46</b>	38.53	<b>30.83</b>	19.29	<b>17.13</b>	6.13	<b>54.65</b>
lct	–	–	39.35	–	33.35	<b>0.94</b>	12.13	–	–	–	–	<b>5.19</b>
kls	–	–	4.09	–	0.11	–	–	–	–	–	–	–
crn	–	–	–	–	–	–	–	–	–	–	0.31	–
di	21.83	<b>5.38</b>	–	<b>0.50</b>	–	<b>0.71</b>	3.91	<b>2.92</b>	2.98	<b>3.16</b>	–	<b>1.72</b>
opx	–	–	–	–	–	–	–	–	–	–	–	–
wo	–	–	–	<b>0.52</b>	–	–	3.27	<b>1.95</b>	0.83	<b>2.64</b>	–	–
ol	0.85	<b>0.52</b>	0.12 <sup>1</sup>	–	0.94 <sup>2</sup>	<b>2.27</b>	–	–	–	–	1.22	<b>2.29</b>
aeg	–	–	1.59	<b>3.96</b>	4.54	<b>8.80</b>	4.83	<b>11.11</b>	9.56	<b>11.94</b>	–	<b>17.53</b>
ks	–	–	–	–	–	–	–	–	–	–	–	–
ns	–	–	5.97	<b>6.96</b>	6.26	<b>10.82</b>	9.86	<b>3.48</b>	–	–	–	<b>2.29</b>
rt	–	–	–	–	–	–	–	–	–	–	–	–
ilm	1.44	<b>2.49</b>	–	<b>0.08</b>	0.04	<b>0.08</b>	0.19	<b>0.21</b>	0.28	<b>0.34</b>	0.51	<b>0.40</b>
mag	8.19	<b>4.84</b>	–	–	–	–	–	–	2.40	<b>1.71</b>	0.01	–
hem	–	–	–	–	–	–	–	–	–	–	3.02	–
ap	1.65	<b>1.67</b>	0.05	<b>0.19</b>	0.02	<b>0.23</b>	0.02	<b>0.63</b>	0.51	<b>0.51</b>	0.12	<b>0.49</b>
zrn	0.09	<b>0.09</b>	0.10	<b>0.10</b>	0.13	<b>0.13</b>	0.33	<b>0.33</b>	0.64	<b>0.64</b>	0.19	<b>0.19</b>
ttn	–	–	–	–	–	–	–	–	–	–	–	–
py	0.23	<b>0.25</b>	0.19	<b>0.19</b>	0.06	<b>0.06</b>	0.04	<b>0.04</b>	0.08	<b>0.11</b>	0.08	<b>0.08</b>
hl	0.11	<b>0.21</b>	–	<b>2.44</b>	–	<b>2.49</b>	–	<b>0.66</b>	0.11	<b>0.11</b>	–	<b>2.27</b>

nd = not detected      \* Total Fe reported as FeO      Norm calculations based on JOHANNSEN (1931)

Mineral abbreviations for CIPW norms from SIIVOLA &amp; SCHMID (2009),

except (ks) – potassium silicate &amp; (ns) – sodium silicate

<sup>1</sup> – includes 0.10 wt.% normative larnite, <sup>2</sup> – includes 0.58 wt.% normative larnite

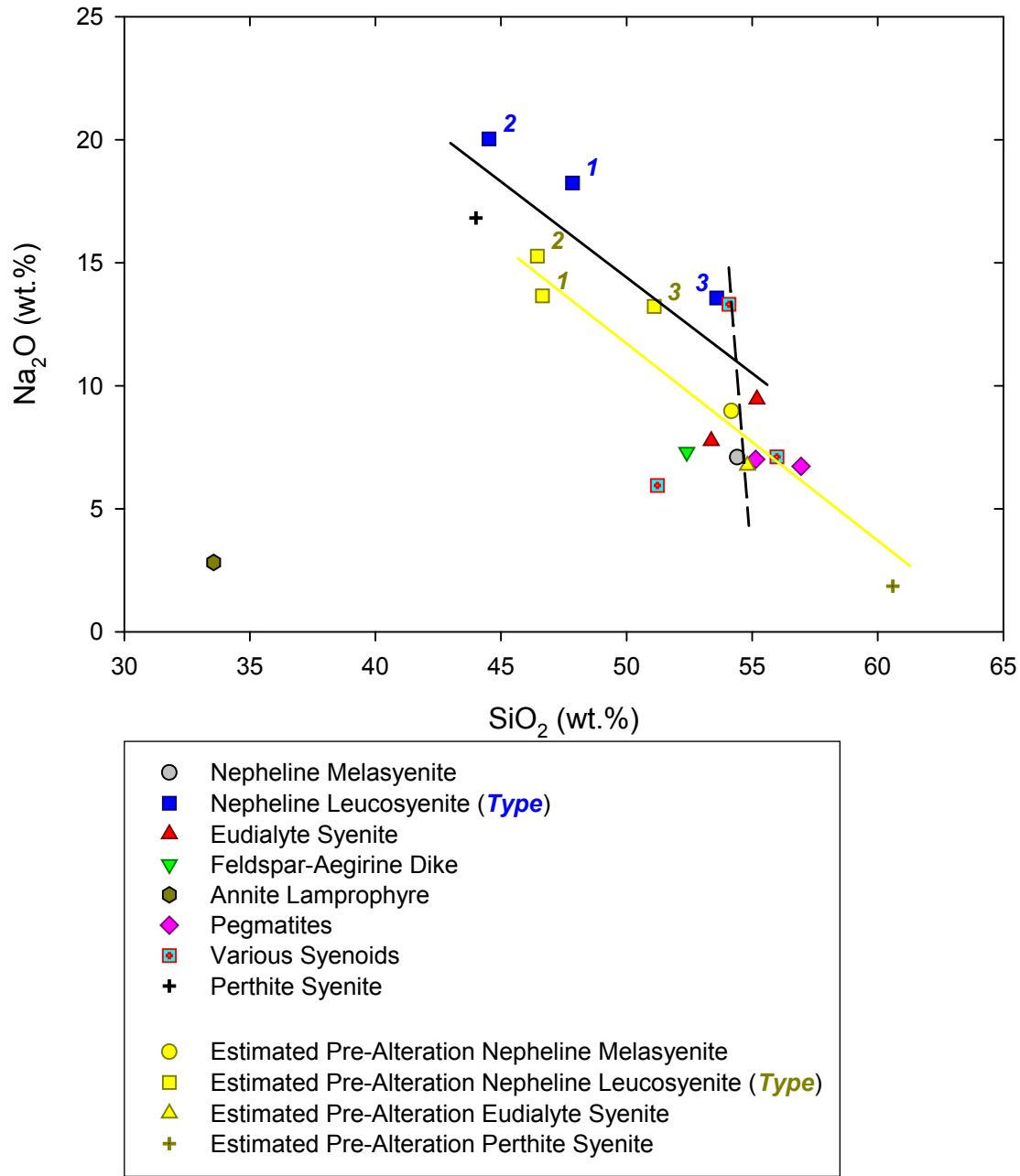


FIGURE 26 – Harker diagram for Na<sub>2</sub>O (including pre-alteration compositions). The solid black line represents the compositional trend of post-alteration syenitic lithologies (nepheline melasyenite, nepheline leucosyenites & perthite syenite) from this study. The solid yellow line represents the compositional trend of pre-alteration syenitic lithologies (nepheline melasyenite, nepheline leucosyenites & perthite syenite) from this study. The dashed line represents the compositional trend of post- and pre-alteration syenoid lithologies (eudialyte syenite, feldspar-aegirine dikes, pegmatites & various syenoids) from this study.

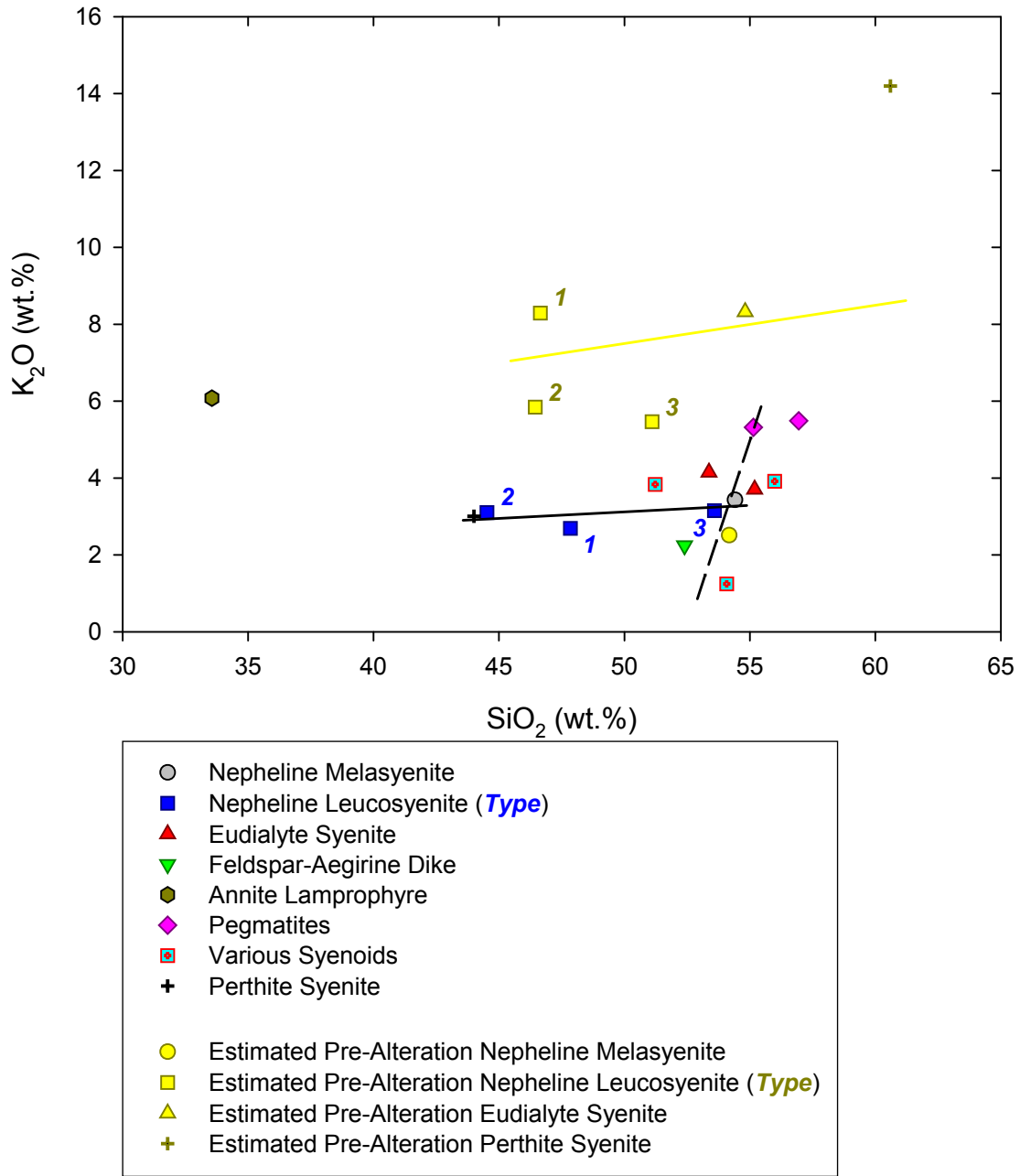


FIGURE 27 – Harker diagram for K<sub>2</sub>O (including pre-alteration compositions). The solid black line represents the compositional trend of post-alteration syenitic lithologies (nepheline melasyenite, nepheline leucosyenites & perthite syenite) from this study. The solid yellow line represents the compositional trend of pre-alteration syenitic lithologies (nepheline melasyenite, nepheline leucosyenites & perthite syenite) from this study. The dashed line represents the compositional trend of post- and pre-alteration syenoid lithologies (eudialyte syenite, feldspar-aegirine dikes, pegmatites & various syenoids) from this study.



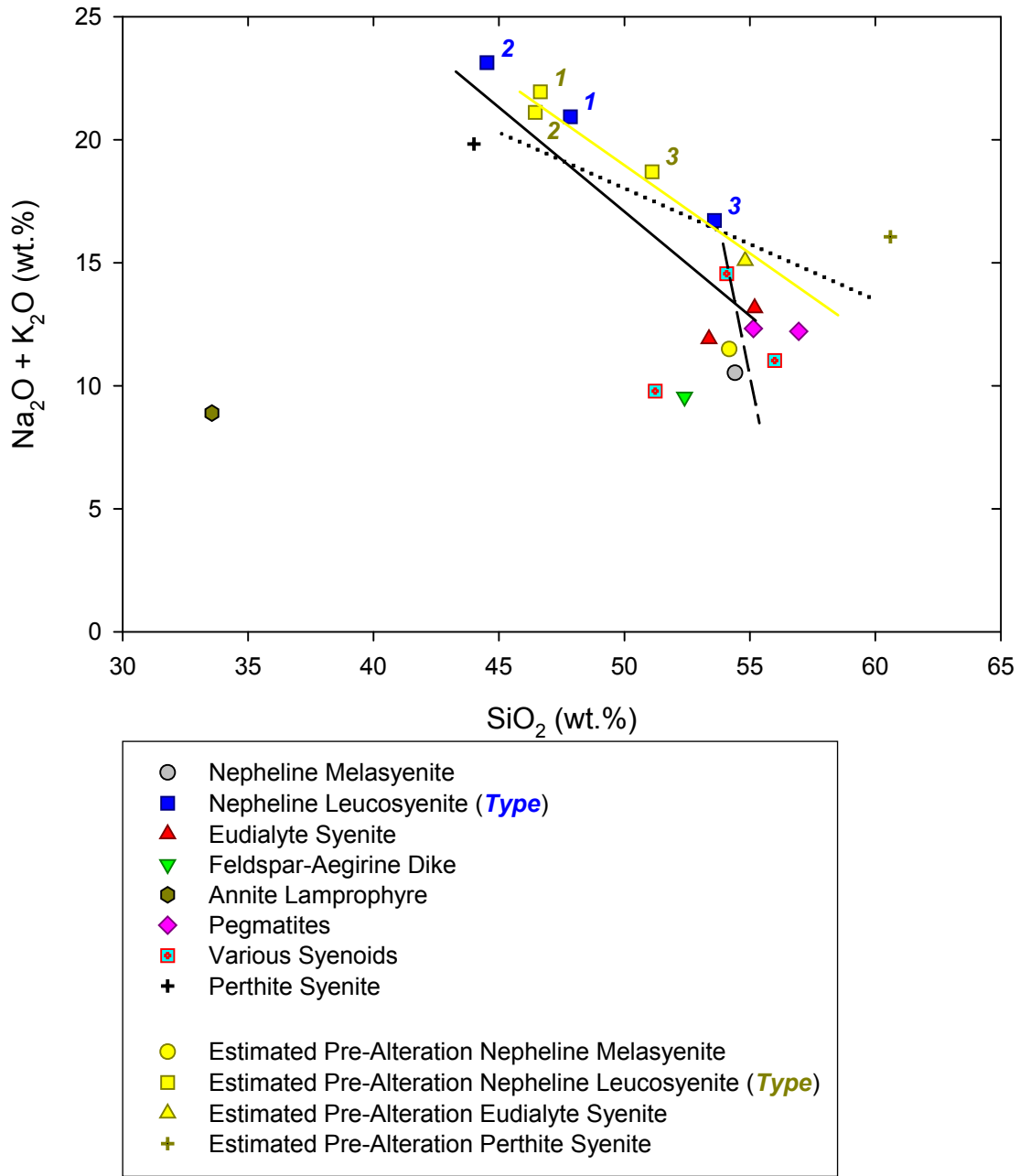


FIGURE 28 – Harker diagram for  $\text{Na}_2\text{O} + \text{K}_2\text{O}$  (including pre-alteration compositions). The dotted line represents the compositional trend of post-alteration East Hill suite syenites observed by CURRIE *ET AL.* (1986). The solid black line represents the compositional trend of post-alteration syenitic lithologies (nepheline melasyenite, nepheline leucosyenites & perthite syenite) from this study. The solid yellow line represents the compositional trend of pre-alteration syenitic lithologies (nepheline melasyenite, nepheline leucosyenites & perthite syenite) from this study. The dashed line represents the compositional trend of post- and pre-alteration syenoid lithologies (eudialyte syenite, feldspar-aegirine dikes, pegmatites & various syenoids) from this study.

The pre-alteration nepheline melasyenite exhibits higher  $\text{Na}_2\text{O}$  than post-alteration. The pre-alteration Types 1 & 2 nepheline leucosyenites and the eudialyte syenite, however, display lower  $\text{Na}_2\text{O}$ , and the pre-alteration perthite syenite much lower  $\text{Na}_2\text{O}$ , than post-alteration. The Type 3 nepheline leucosyenite exhibits almost identical  $\text{Na}_2\text{O}$ .

The pre-alteration nepheline melasyenite exhibits lower  $\text{K}_2\text{O}$  than post-alteration, but the pre-alteration Types 2 & 3 nepheline leucosyenites display higher, and the pre-alteration Type 1 nepheline leucosyenite, the eudialyte syenite, and the perthite syenite much higher  $\text{K}_2\text{O}$ , than post-alteration.

In spite of these substantial differences, total alkalis are much more consistent between post- and pre-alteration, in particular for the nepheline leucosyenites, which follow the same general trend of compositional variation.

Comparison of the post-alteration and pre-alteration whole-rock compositions, reveals two striking patterns: 1) the large-scale loss of potassium with concomitant gain of sodium and 2) dramatic similarities in the content of the remaining major elements. This indicates that the rocks of the East Hill suite interacted with a large quantity of sodium-rich fluid that remobilized alkalis without substantially affecting the bulk chemistry of other major elements.

**Overview**

Representative whole-rock trace element analyses are listed in TABLES 7 through 10. Rocks of the East Hill suite are volatile-rich, primarily in chlorine and, less so, in bromine and sulfur; iodine is almost non-existent. The bulk of the nepheline leucosyenite and the perthite syenite contain in excess of 1.0 wt.% Cl, on par with sodalite foyaite from Ilímaussaq (Ferguson 1970), sodalite-nepheline syenite from North Nyasa (Eby *et al.* 1998), and highly-evolved foyaite from Lovozero (Arzamastsev *et al.* 2001). Most other lithologies contain hundreds to thousands of ppm Cl, which is comparable to mineralogically-similar lithologies from Ilímaussaq (Ferguson 1970) and Lovozero (Arzamastsev *et al.* 2001) but generally higher than sodalite-absent syenitic rocks from North Nyasa. (Eby *et al.* 1998)

Br content is, on average, 2 or 3 orders of magnitude less than that of Cl. Both Br and Cl contents, however, are about 1 to 3 orders of magnitude higher than those of typical volcanic rocks and 2 to 4 orders of magnitude higher than those of typical plutonic rocks. (Sugiura 1968) Br/Cl ratios for all rock types range from  $6.7 \times 10^{-3}$  to  $36.9 \times 10^{-3}$ , with an average of  $12.2 \times 10^{-3}$ . These ratios are 2 to 3 times higher than observed range for calc-alkaline rocks, both volcanic and plutonic (Sugiura 1968) and about 10 times higher than the average ratio observed in the Lovozero alkaline complex. (Kogarko & Gulyayeva 1965) Sodalite, eudialyte group minerals, and amphiboles are the primary hosts of Cl in the East Hill suite.

Sulfur content is overall higher than would be expected for average granitoid magmas (~300 ppm), but is consistent with that of ore-bearing granitoids (~1,000 ppm). (Banks 1982; Poulson & Ohmoto 1990; Poulson *et al.* 1991) Also, sulfur contents are consistent with the

TABLE 7 – Representative whole-rock XRF analyses – Trace Elements I

Lithology:	<i>Nepheline Melasyenite</i>	<i>Type 1 Nepheline Leucosyenite</i>	<i>Type 2 Nepheline Leucosyenite</i>	<i>Type 3 Nepheline Leucosyenite</i>
Sample:	<i>MSH-B-8</i>	<i>MSH-B-12</i>	<i>MSH-B-4</i>	<i>MSH-B-10</i>
Br (ppm)	7.5	155.0	147.0	25.8
Cl	1068.0	12378.6	12743.1	3353.2
I	nd	2.3	nd	nd
S	1136.0	829.9	257.3	223.0
Co	59.6	22.1	nd	nd
Cr	nd	1.3	1.4	11.4
Ni	nd	nd	nd	6.4
V	38.7	7.6	nd	nd
Ag	nd	nd	nd	0.9
Cd	1.2	nd	nd	0.9
Cu	6.4	1.1	2.6	5.1
Hg	nd	nd	nd	nd
Pb	15.6	3.7	5.9	32.4
Zn	122.4	145.3	110.4	87.2
As	5.9	9.1	1.9	4.0
Bi	2.2	nd	nd	nd
Ga	21.6	33.9	28.0	40.4
Ge	13.9	4.7	3.8	4.8
In	0.7	nd	nd	0.6
Sb	nd	1.1	nd	1.2
Se	1.4	1.4	nd	nd
Te	nd	nd	nd	nd
Tl	nd	nd	nd	nd
Nb	124.3	85.5	136.8	246.2
Ta	nd	9.0	nd	10.7
Sn	2.3	4.0	4.5	11.5
Mo	nd	6.3	4.7	14.1
W	334.0	206.0	127.0	99.6
Zr	425.7	483.7	652.7	1659.5
Sr	2754.6	82.1	6.9	301.1
Ba	1417.8	95.1	19.5	129.6
Rb	70.4	110.0	122.0	174.8
Cs	nd	3.0	3.3	12.7
La	160.6	57.2	147.6	733.1
Ce	304.1	87.2	251.6	1288.9
Th	20.3	25.4	17.2	61.6
U	11.5	6.4	5.4	12.5
Y	41.9	26.0	49.7	139.3
nd = not detected				

TABLE 8 – Representative whole-rock XRF analyses – Trace Elements II

Lithology:	<i>Eudialyte Syenite</i>	<i>Eudialyte Syenite</i>	<i>Feldspar- Aegirine Dike</i>	<i>Annite Lamprophyre</i>
Sample:	<i>MSH-B-1</i>	<i>MSH-B-2</i>	<i>MSH-B-3</i>	<i>MSH-B-6</i>
Br (ppm)	3.6	nd	3.6	nd
Cl	541.3	138.5	97.6	268.9
I	nd	nd	nd	nd
S	425.5	606.7	380.3	1200.5
Co	87.6	86.6	nd	nd
Cr	19.5	5.1	4.7	nd
Ni	17.7	13.7	26.5	nd
V	42.5	nd	16.1	19.7
Ag	nd	nd	1.1	2.5
Cd	2.0	1.6	1.2	3.8
Cu	15.6	10.8	38.0	28.1
Hg	nd	nd	nd	nd
Pb	97.4	67.5	27.1	924.0
Zn	318.4	346.4	178.5	1216.1
As	6.2	6.4	18.4	nd
Bi	5.1	nd	15.4	15.1
Ga	36.7	38.2	66.6	54.9
Ge	0.8	1.0	27.8	0.7
In	nd	nd	nd	nd
Sb	1.9	nd	1.7	2.3
Se	nd	2.2	4.2	nd
Te	2.3	nd	nd	2.5
Tl	nd	nd	nd	nd
Nb	472.1	472.1	869.3	768.7
Ta	26.3	nd	nd	nd
Sn	16.6	16.5	49.9	14.5
Mo	nd	nd	4.5	4.5
W	171.0	156.0	206.0	41.0
Zr	3177.7	3028.8	9860.5	8089.3
Sr	661.8	435.1	211.4	172.0
Ba	370.6	197.2	58.6	29.9
Rb	176.6	183.5	136.2	1143.5
Cs	11.5	nd	nd	50.6
La	1408.0	581.6	830.6	643.4
Ce	2598.3	1043.4	1500.2	1267.0
Th	373.2	431.0	100.3	59.5
U	38.0	30.2	70.3	19.8
Y	371.6	231.3	311.6	87.6
nd = not detected				

TABLE 9 – Representative whole-rock XRF analyses – Trace Elements III

Lithology:	<i>Pegmatite</i>	<i>Pegmatite</i>	<i>Various Syenoid</i>	<i>Various Syenoid</i>	<i>Various Syenoid</i>
Sample:	<i>MSH-B-21</i>	<i>MSH-B-33</i>	<i>MSH-B-23</i>	<i>MSH-B-27</i>	<i>MSH-B-36</i>
Br (ppm)	nd	6.2	26.9	18.0	3.7
Cl	125.2	793.6	2495.1	2344.7	490.3
I	nd	nd	nd	nd	nd
S	258.0	449.1	894.3	756.5	837.9
Co	nd	67.4	nd	nd	nd
Cr	1.7	2.1	nd	nd	8.0
Ni	9.0	8.3	8.8	nd	34.5
V	nd	nd	nd	10.7	39.5
Ag	nd	nd	0.7	nd	1.6
Cd	3.6	nd	4.5	nd	9.9
Cu	10.9	11.2	6.6	3.7	58.0
Hg	nd	nd	nd	nd	nd
Pb	42.6	79.0	145.0	7.2	74.0
Zn	360.0	374.4	666.5	118.4	429.6
As	7.4	17.4	8.0	5.2	26.3
Bi	4.4	3.7	nd	nd	8.7
Ga	43.4	72.1	83.0	20.9	30.6
Ge	nd	nd	0.8	8.8	1.5
In	0.6	nd	nd	nd	1.0
Sb	1.6	1.9	1.7	nd	3.4
Se	1.7	2.5	nd	nd	3.6
Te	1.4	nd	nd	nd	nd
Tl	nd	nd	nd	nd	nd
Nb	383.7	827.7	1250.1	172.4	1343.5
Ta	16.6	nd	31.1	18.1	182.0
Sn	23.9	21.5	20.7	4.3	44.1
Mo	5.6	nd	nd	11.4	nd
W	88.4	156.0	80.9	235.0	210.0
Zr	3639.1	2374.0	1711.6	639.3	9674.4
Sr	208.4	176.2	85.6	1546.6	1198.8
Ba	164.3	314.9	37.3	1012.7	354.9
Rb	261.4	341.9	60.3	91.7	156.2
Cs	nd	nd	nd	nd	nd
La	459.3	581.6	135.0	145.4	1397.0
Ce	874.6	1043.4	254.4	220.0	2351.6
Th	118.2	352.8	20.6	21.6	143.7
U	21.6	76.8	8.5	10.7	40.5
Y	132.6	211.9	39.1	41.2	569.9
nd = not detected					

TABLE 10 – Representative whole-rock XRF analyses – Trace Elements IV

Lithology:	<i>Perthite Syenite</i>	<i>Limestone Xenolith</i>	<i>Silicate Xenolith</i>
Sample:	<i>MSH-B-9</i>	<i>MSH-B-16</i>	<i>MSH-B-51</i>
Br (ppm)	210.0	nd	nd
Cl	11621.4	46.3	133.5
I	7.1	nd	nd
S	357.7	121.8	224.0
Co	nd	nd	80.9
Cr	nd	nd	72.5
Ni	8.1	nd	79.3
V	nd	nd	259.7
Ag	0.6	nd	nd
Cd	1.1	1.9	nd
Cu	3.5	nd	47.1
Hg	nd	nd	nd
Pb	12.8	3.1	nd
Zn	172.9	10.5	55.1
As	6.1	5.4	1.0
Bi	1.9	nd	nd
Ga	29.5	nd	12.2
Ge	7.1	nd	3.1
In	nd	nd	nd
Sb	nd	nd	1.7
Se	nd	nd	nd
Te	1.2	nd	nd
Tl	nd	nd	nd
Nb	237.1	4.2	2.0
Ta	21.6	nd	nd
Sn	4.4	1.1	nd
Mo	10.2	18.9	nd
W	126.0	29.1	25.7
Zr	937.7	12.4	22.3
Sr	5.9	403.0	188.5
Ba	14.1	52.8	40.5
Rb	145.8	2.2	2.0
Cs	nd	nd	nd
La	268.0	nd	nd
Ce	482.5	nd	nd
Th	36.6	nd	nd
U	8.3	nd	nd
Y	53.6	10.0	18.3
nd = not detected			

range exhibited by agpaitic lithologies at Ilímaussaq (Ferguson 1970) and Lovozero (Arzamastsev *et al.* 2001)

Co, Cr, Ni, and V are generally scarce in East Hill suite lithologies, though there are some notably rich exceptions. Co and V are enriched in the nepheline melasyenite, the most apparently mafic of the East Hill suite lithologies. Interestingly, even higher concentrations of all four elements are present in the eudialyte syenite. Spikes of different elements occur in the pegmatites and various syenoids. Because of its mafic affinity, this element group is predictably depleted in many felsic East Hill suite lithologies; however, content of these elements is unexpectedly low in the annite lamprophyre, in which they range from one to two orders of magnitude lower than those in alnöite from the Namibian Damaraland alkaline igneous complexes. (LeRoex & Lanyon 1997) The silicate xenolith is enriched in Co, with a concentration between that of the primitive mantle and average N-MORB (Hofmann 1988), but its Ni content is disproportionately low, suggesting prior olivine fractionation.

Co content in the richest East Hill suite lithologies is comparable to or even greater than that of mafic alkaline lithologies from several other localities. Melteigite, ijolite, and urtite from Khibina contain approximately 60 ppm Co. (Arzamastsev *et al.* 1987) In the Fen alkaline complex, ijolite, damtjernite (nepheline/alkali feldspar ultramafic lamprophyre), rauhaugite (ankerite carbonatite), and vipetoite (titanaugite pyroxenite) exhibit Co contents ranging from 25 to 57 ppm. (Mitchell & Brunfelt 1974) Ijolite from the Magnet Cove alkaline complex contains between about 20 and 40 ppm Co. (Flohr & Ross 1989) Eudialyte group minerals seem to control Co content in felsic lithologies, in particular the eudialyte syenite and certain pegmatites; the same pattern of relatively high Co in eudialyte-bearing lithologies manifests itself in the



Lovozero complex. (Arzamastsev *et al.* 2001) In the nepheline melasyenite, Co is probably housed in magnetite.

Cr content is comparable to that of Lovozero nepheline syenites (Arzamastsev *et al.* 2001), but is lower than that of North Nyasa nepheline syenites (Eby *et al.* 1998) and foidolites from Khibina. (Arzamastsev *et al.* 1987) Magnet Cove ijolite, however, is less rich in Cr (Flohr & Ross 1989) than the Cr-rich felsic lithologies in the East Hill suite. Aegirine appears to govern Cr content throughout the East Hill suite.

Ni content of the eudialyte syenite, the feldspar-aegirine dikes, and certain syenoids is on the same order as that of Lovozero nepheline syenites (Arzamastsev *et al.* 2001) but is higher than that of the North Nyasa nepheline syenites. (Eby *et al.* 1998) In many samples, Ni and Co are decoupled, one or the other being below detection limits. When both elements are present, Ni/Co ratios are much less than unity, in contrast to those of alkali and tholeiitic basalts, in which ratios are greater than 2. (Taylor *et al.* 1969) The Ni/Co ratio for the silicate xenolith is close to 1, indicating some differentiation.

V loosely shadows Co in the East Hill suite, being most abundant in the nepheline melasyenite, the eudialyte syenite, and certain syenoids. Even at its most abundant, however, V content is rather low, being far less than in mafic foidolites from Khibina and Magnet Cove (Arzamastsev *et al.* 1987; Flohr & Ross 1989) and less even than in nepheline syenites from North Nyasa and Lovozero. (Eby *et al.* 1998; Arzamastsev *et al.* 2001)

Ag, Cd, and Hg are rare in the East Hill suite; the strongest chalcophile enrichments are in Zn, Pb, and Cu. The latter three elements are rather highly enriched throughout the suite but are especially so in the eudialyte syenite, the annite lamprophyre, and several syenoids and pegmatites. Zn exhibits its highest concentration in the annite lamprophyre, followed by certain

pegmatites and syenoids and the eudialyte syenite. Zn enrichment is not an uncommon feature amongst lamprophyres; ARMSTRONG & BARNETT (2003) reported lamprophyre-hosted zincian chromite containing up to 9.78 wt.% ZnO. Nevertheless, the Zn content of the annite lamprophyre in the East Hill suite is two orders of magnitude higher than that in Damaraland alnöites. (LeRoex & Lanyon 1997)

Pb follows the same enrichment pattern as Zn. Again, like Zn, the concentration of Pb in the East Hill suite annite lamprophyre is two orders of magnitude higher than that of Damaraland alnöites. (LeRoex & Lanyon 1997)

Cu exhibits a different pattern of enrichment than Zn and Pb. It is most concentrated in some more mafic syenoids, the feldspar-aegirine dikes, and the eudialyte syenite and least concentrated in the nepheline mela- and leucosyenites, as well as in the felsic pegmatites and syenoids. All three elements are concentrated in sulfides.

The East Hill suite contains unremarkable quantities of most analyzed main group elements, save for As, Ga, and Ge. Arsenic concentrations do not correlate well with the mafic or felsic character of the lithology. Concentrations are, in fact, highest in more mafic pegmatites and syenoids, the feldspar-aegirine dikes, and, less so, in the eudialyte syenite; however, the As content of the Type 1 nepheline leucosyenite, which has a highly felsic character, is similarly elevated and is higher than that of the nepheline melasyenite. Furthermore, As was not detected in the annite lamprophyre.

Ga content roughly correlates with the apparent order of crystallization derived from field relationships; lower in the nepheline mela- and leucosyenites and progressively higher in the eudialyte syenite, feldspar-aegirine dikes, annite lamprophyre, and the pegmatites and syenoids.

Ge is curiously distributed in the East Hill suite. Unlike Ga, its content appears to be

unrelated to degrees of magmatic evolution. Most analyses of Ge in the East Hill suite fall within a relatively narrow range. Concentrations at the lower end of this range are on par with typical Ge contents of both mafic and felsic calc-alkaline lithologies (Mielke 1979; Schroll 1999); most higher concentrations with the average Ge content of granitic pegmatites. (Schroll 1999) Two exceptionally rich analyses represent the nepheline melasyenite and the feldspar-aegirine dikes. The melasyenite contains slightly more Ge than an average granitic pegmatite; the dikes, nearly three times as much.

Although the absolute content of Ge of most of the East Hill suite lithologies is comparable to that of calc-alkaline suites, the molar Ge/Si ratios of the nepheline leucosyenites, certain syenoids, and the perthite syenite exhibit a strong Ge/Si enrichment. Molar ratios in these lithologies range from 7.06 to 13.35  $\mu\text{mol/mol}$ , about 3 to 5 times higher than that of calc-alkaline rocks; the nepheline melasyenite and the feldspar-aegirine dikes display ratios that are 10 to 20 times higher. (DeArgollo & Schilling 1978; Kurtz *et al.* 2002) Conversely, the eudialyte syenite, the annite lamprophyre, and certain pegmatites and syenoids are depleted in Ge with respect to calc-alkaline rocks. (Mielke 1979; Schroll 1999)

KURTZ *ET AL.* (2002) indicate that Ge concentrates in secondary aluminosilicates, while FRONDEL & ITO (1957) not only describe the remobilization of Ge during alteration but also point to carbonates as relatively strong Ge hosts. This suggests that Ge/Si ratios in the East Hill suite might correlate to the degree of subsolidus hydrothermal alteration. Other possible hosts for Ge are sulfides (Johan 1988; Melcher *et al.* 2006), in particular in the East Hill Suite, chalcopyrite, covellite, sphalerite, and galena, although the relatively low Ge content of the eudialyte syenite tends to diminish the potential role of sulfides as Ge hosts.

The East Hill suite is substantially enriched in Zr, less so in Nb and W; Ta, Sn, and Mo occur sporadically and in small concentrations. The most Zr-rich lithologies contain over 1 wt.% ZrO<sub>2</sub>. Even though these lithologies are the most Zr-rich, Zr is relatively abundant in most East Hill suite rock types. Zr is notably most concentrated in the feldspar-aegirine dikes, certain syenoids, and the annite lamprophyre, rather than the facial primary candidate, the eudialyte syenite; although the eudialyte syenite does contain a substantial quantity of Zr. Most of the Zr outside of the eudialyte syenite is contained by late-stage zirconosilicates, although aegirine in the feldspar-aegirine dikes is strongly enriched in Zr, accounting for the large Zr presence in a lithology almost devoid of Zr mineralization.

Nb is most concentrated, by an order of magnitude, in some of the various syenoids, followed by the feldspar-aegirine dikes and the annite lamprophyre. The eudialyte syenite also contains a substantial amount of Nb. Although eudialyte group minerals are variably enriched in Nb, most Nb mineralization in the East Hill suite is in the form of oxides, such as pyrochlore, or late-stage silicates, such as kupletskite.

Sr, Ba, and Rb concentrations each vary by several orders of magnitude between different lithologies in the East Hill suite; Cs is absent from much of the East Hill suite, never exceeding 50 ppm and showing its strongest presence in potassium feldspar and annite-rich lithologies. Sr and Ba tend to follow one another, but they are not strongly antipathetic with Rb. Sr and Ba are most concentrated in the nepheline melasyenite, certain syenoids, and the eudialyte syenite, in all of which they reside in Ca-rich phases such as calcic amphiboles, augite, eudialyte, or calcite. Rb contents are relatively steady through the whole East Hill suite, substituting as it does into potassium feldspar; however, it is enriched by an order of magnitude in the annite lamprophyre, due to the large quantity of annite.

La, Ce, and Y follow one another through the East Hill suite. The La/Ce ratio is remarkably constant, ranging from 0.51 to 0.66 with an average of 0.57. Similarly, the Ce/Y ratio ranges from 3.35 to 14.47 with an average of 6.59. The highest contents of REE and Y are in the later lithologies, the Type 3 nepheline leucosyenite, eudialyte syenite, and certain syenoids. Although REE carbonates host some of these elements, clinopyroxene and eudialyte group minerals are actually more important repositories in terms of their contribution to the total REE content of the bulk rock.

Th and U concentrations are generally rather low, although they are elevated in many of the same lithologies as the REE and Y. Thorianite and thorogummite are not generally important reservoirs of Th and U in the East Hill suite. Most substitution of these elements probably occurs in zirconosilicates.

### ***Geochemical Petrologic Classification***

A plot of total alkalis *versus* silica (Figure 29) defined more formal petrologic classifications for the East Hill suite lithologies. Syenitic rock types (nepheline melasyenite, nepheline leucosyenites, and perthite syenite) range from nepheline monzosyenite to nephelinolite pre- and post-alteration. Although field relationships suggest that they are more evolved, the syenoid rock types (eudialyte syenite, feldspar-aegirine dikes, pegmatites, and various syenoids) are generally lower in total alkalis, ranging from nepheline monzodiorite through nepheline monzosyenite (one syenoid bordering on monzonite) just into nepheline syenite, again pre- and post-alteration. Most lithologies exhibit at least small shifts in the plotted chemical parameters but retain close to their pre-alteration total alkali content.

The perthite syenite, however, not only displayed the largest shift in chemistry, it was the only rock type to undergo a substantial change in classification, going from a nepheline syenite composition to a nephelinolitic composition. The perthite syenite is only nepheline normative; in terms of modality, the perthite syenite is essentially nepheline-free. Its high alkali bulk chemistry is very likely the result of microcrystals of dawsonite or similar high-alkali, low-silica secondary phases.

The overall geochemical theme of alteration in the East Hill suite is that of sodium gain and potassium loss. Plots of sodium and potassium *versus* silica (Figures 30 & 31), using the same scaling as the total alkalis plot of FIGURE 29, show that for all six estimated lithologies, post-alteration sodium content is higher than pre-alteration; however, pre-alteration potassium content is higher than post-alteration.

These plots also reveal that for most lithologies, sodium is the dominant alkali; only the eudialyte syenite and the perthite syenite exhibit pre-alteration sodium content subordinate to potassium. Both sodium dominance and potassium loss are evident in FIGURE 32, which relates East Hill suite compositions to the alkali basalt series of MIDDLEMOST (1975).

The aluminosity diagram (Figure 33) of SHAND (1943) indicates that most East Hill suite lithologies are peralkaline, pre- and post-alteration. The pre-alteration nepheline melasyenite and one analysis each of post-alteration eudialyte syenite and pegmatite plot as metaluminous, and the post-alteration nepheline melasyenite, one of the various syenoids, and the pre-alteration perthite syenite plot as peraluminous.

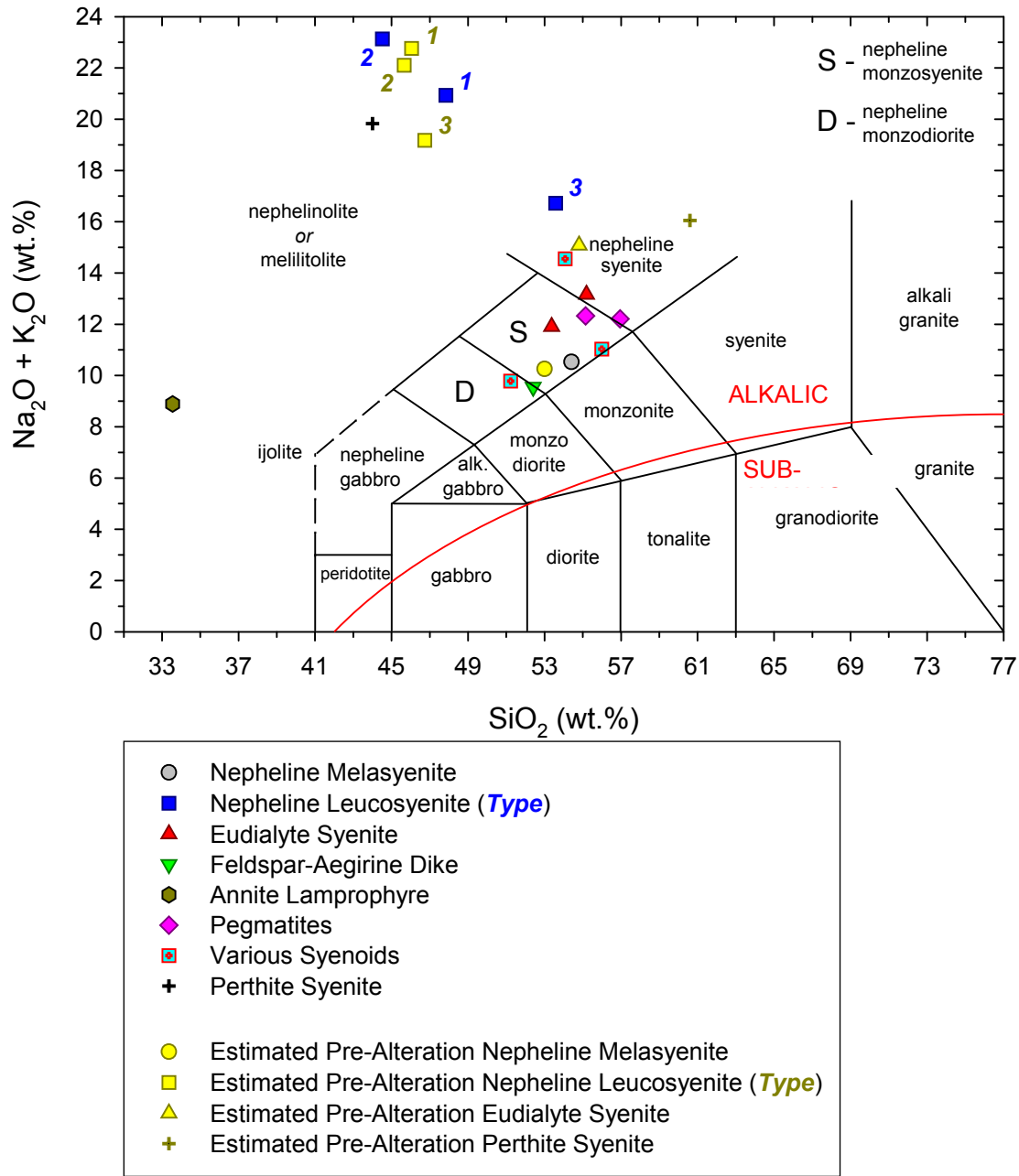


FIGURE 29 – Total alkalis *versus* silica diagram after WILSON (1989). Divisions after LE MAITRE (1989) and nomenclature after STRECKEISEN (1976). Alkalic/subalkalic border after MIYASHIRO (1978).

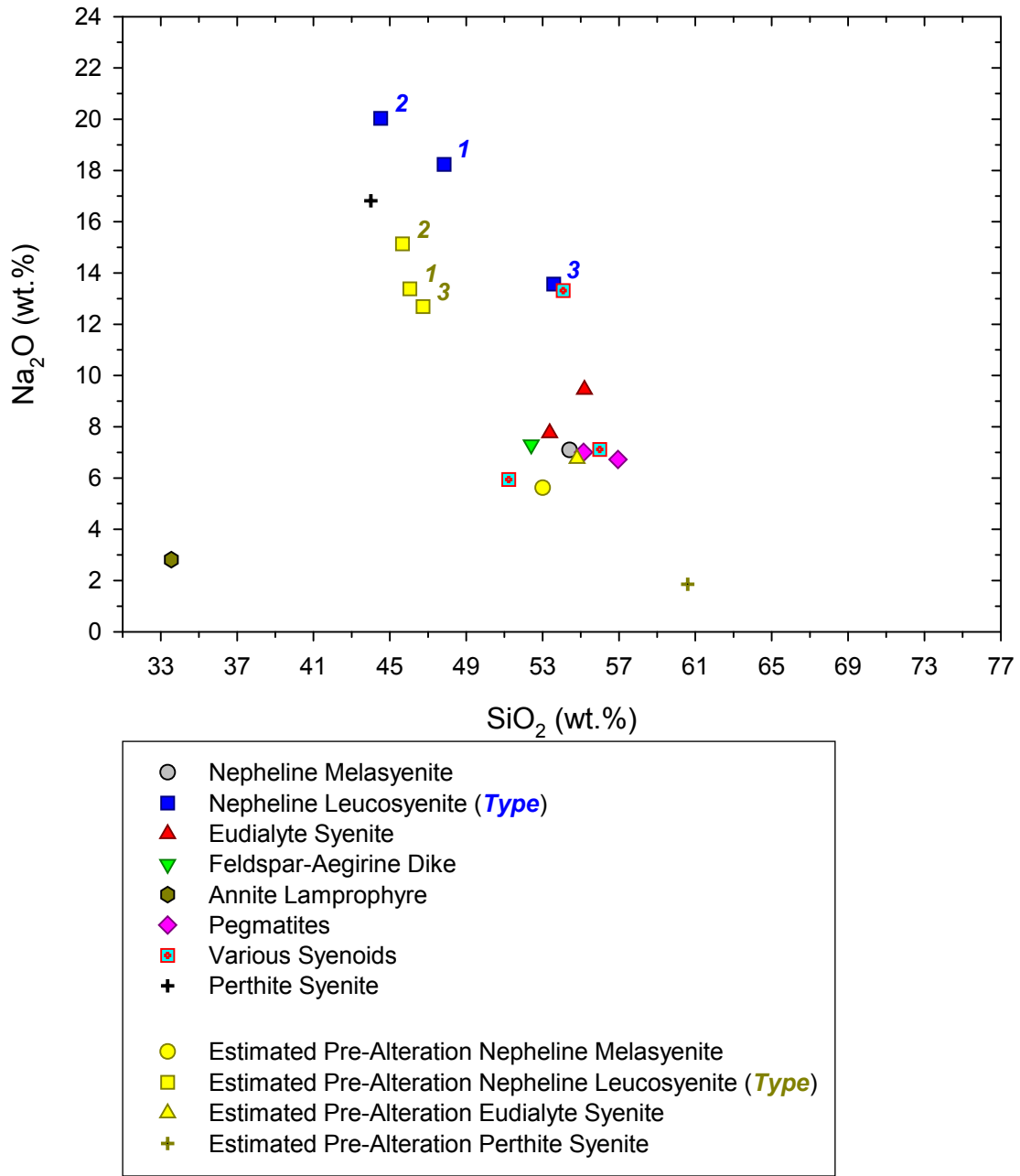


FIGURE 30 – Na<sub>2</sub>O versus SiO<sub>2</sub>, scaled as the total alkalis versus silica diagram of WILSON (1989).



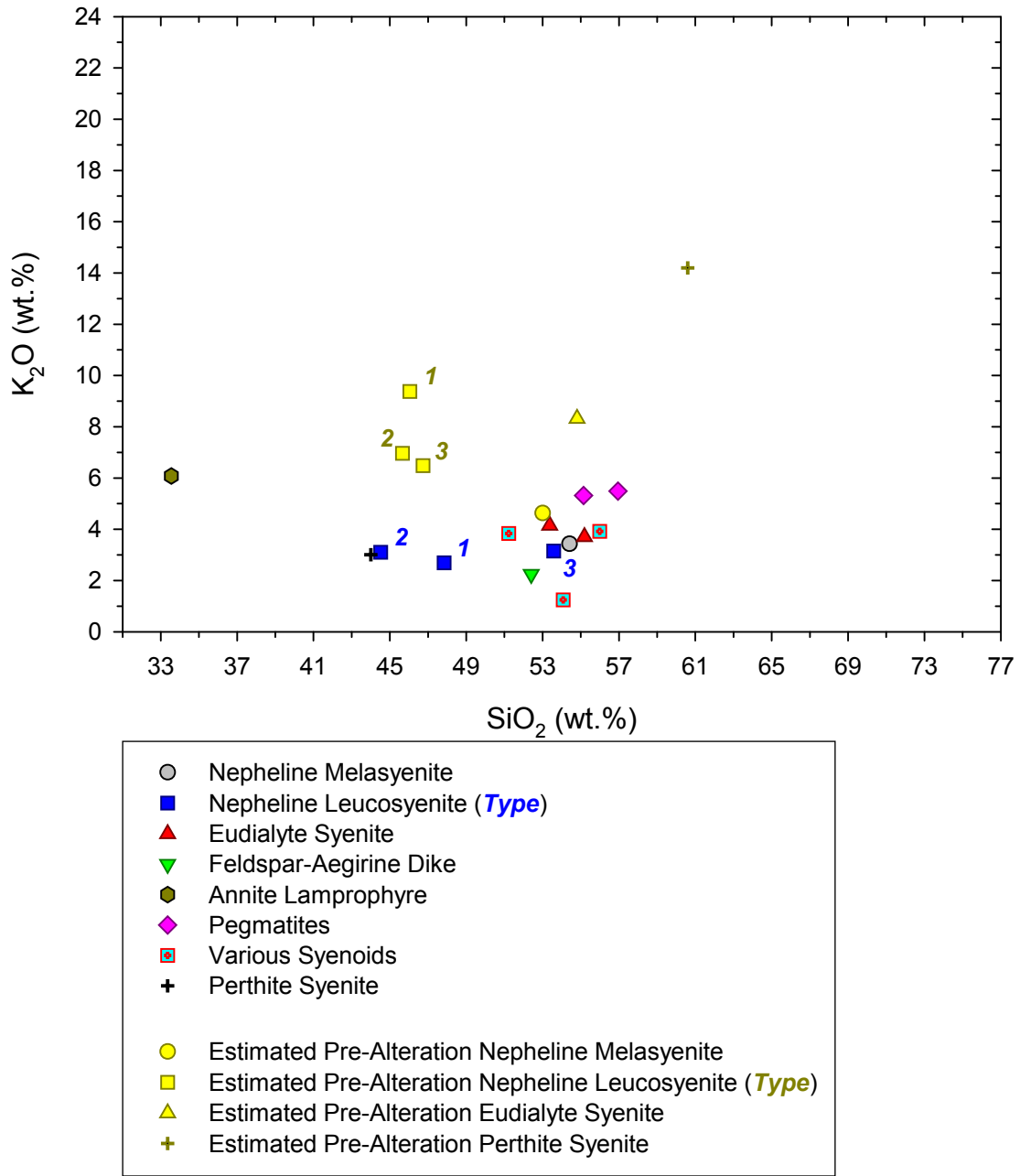


FIGURE 31 –  $K_2O$  versus  $SiO_2$ , scaled as the total alkalis versus silica diagram of WILSON (1989).

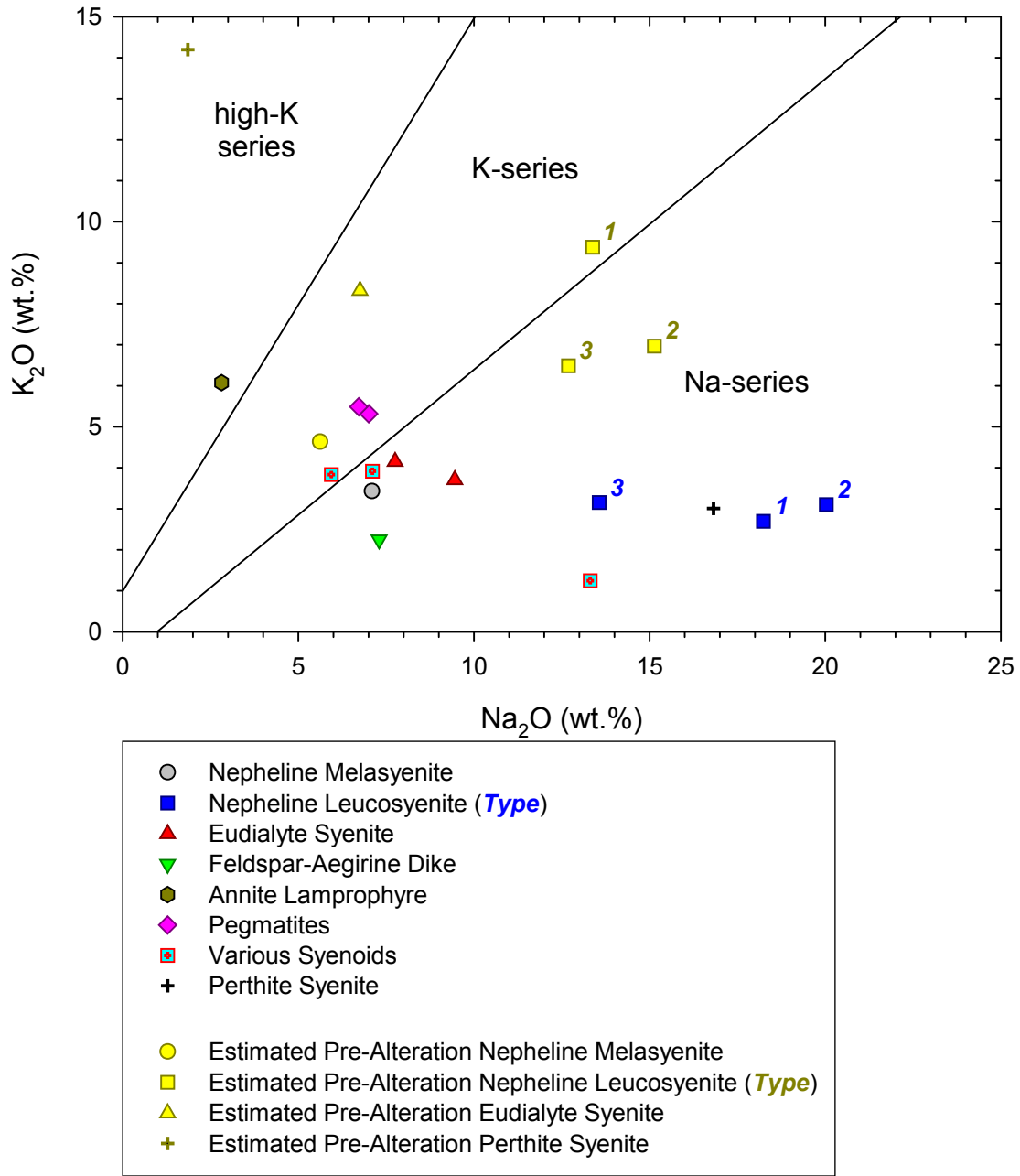


FIGURE 32 –  $K_2O$  versus  $Na_2O$ , with the alkali basalt series of MIDDLEMOST (1975) superimposed.

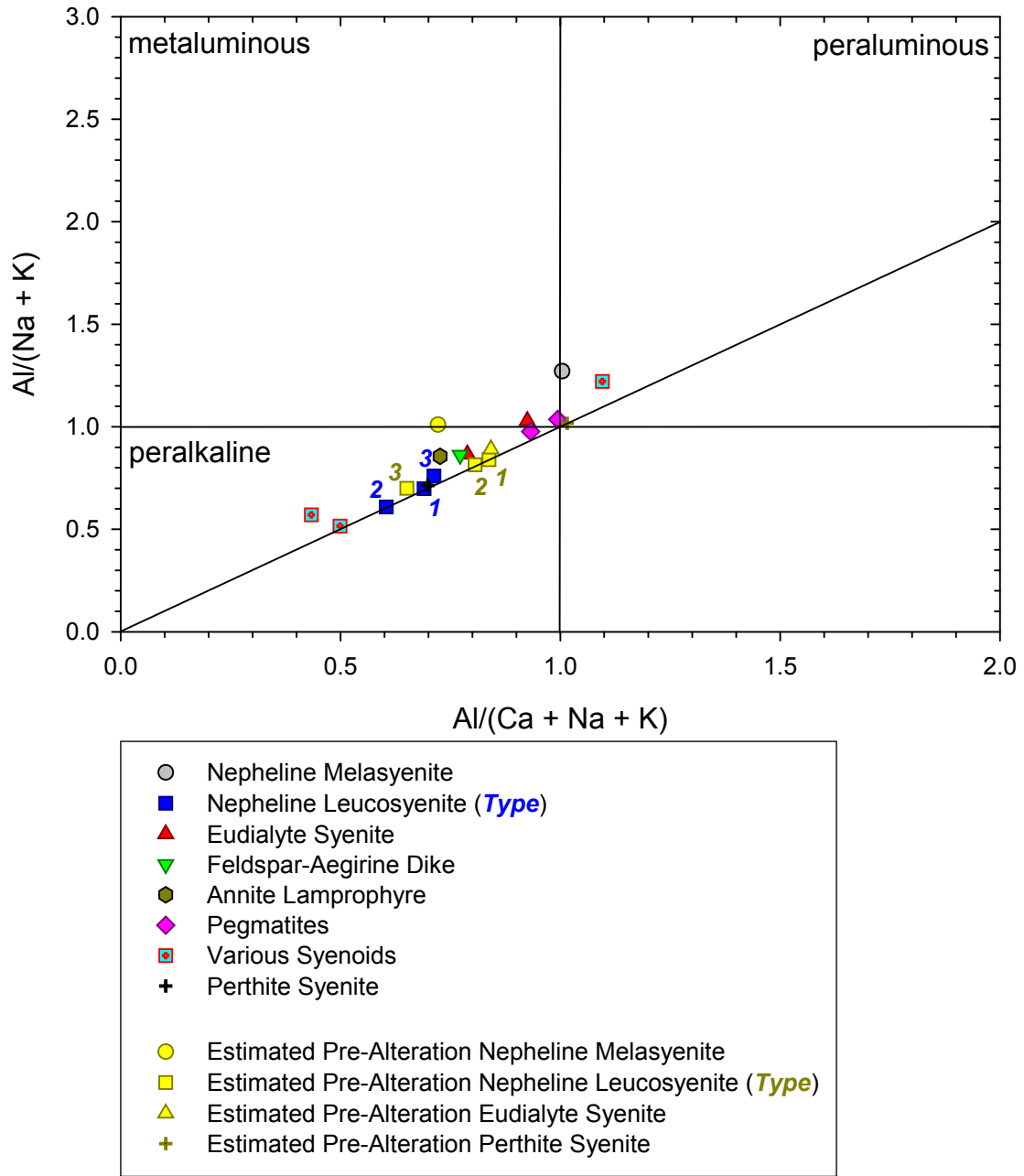


FIGURE 33 – Aluminosity diagram after SHAND (1943). Ratios calculated from a millication basis.

## ***Tectonic Setting***

### *Ga/Al Ratios*

Even though alumina contents were estimated for pre-alteration bulk compositions, analyzed post-alteration alumina contents were used for Ga/Al ratios in tectonic setting diagrams. No estimates could be made of pre-alteration Ga contents, so the analyzed post-alteration Ga contents had to be used. The alumina content can also be viewed as the available number of Al sites in the constituent minerals. Since Ga will primarily substitute for Al, as the number of available Al sites changes, the number of available Ga sites changes at the same rate. Moreover, changes in Ga/Al ratios are primarily driven by fractionation processes. (Whalen *et al.* 1987; Weaver *et al.* 1991; Kochhar 2000) Therefore, variance in the Ga/Al ratio is not related to the absolute concentration of alumina.

### *Tectonic Setting*

The lithologies of the East Hill suite primarily plot as A-type granitoids (Figures 34 to 39) according to the several schemes of WHALEN *ET AL.* (1987). Exceptions may be seen in plots of yttrium (Figure 36) and total alkalis over calcium (Figure 38). In the case of yttrium, the nepheline melasyenite, the Type 2 nepheline leucosyenite, one of the various syenoids, and the perthite syenite show an I- and S-type affinity; in that of total alkalis over calcium, the nepheline melasyenite and the same syenoid show the same affinity. On the zirconium plot (Figure 35), the nepheline melasyenite, the Types 1 and 2 nepheline leucosyenite, one of the various syenoids, and the perthite syenite are verging on an I- and S-type affinity.

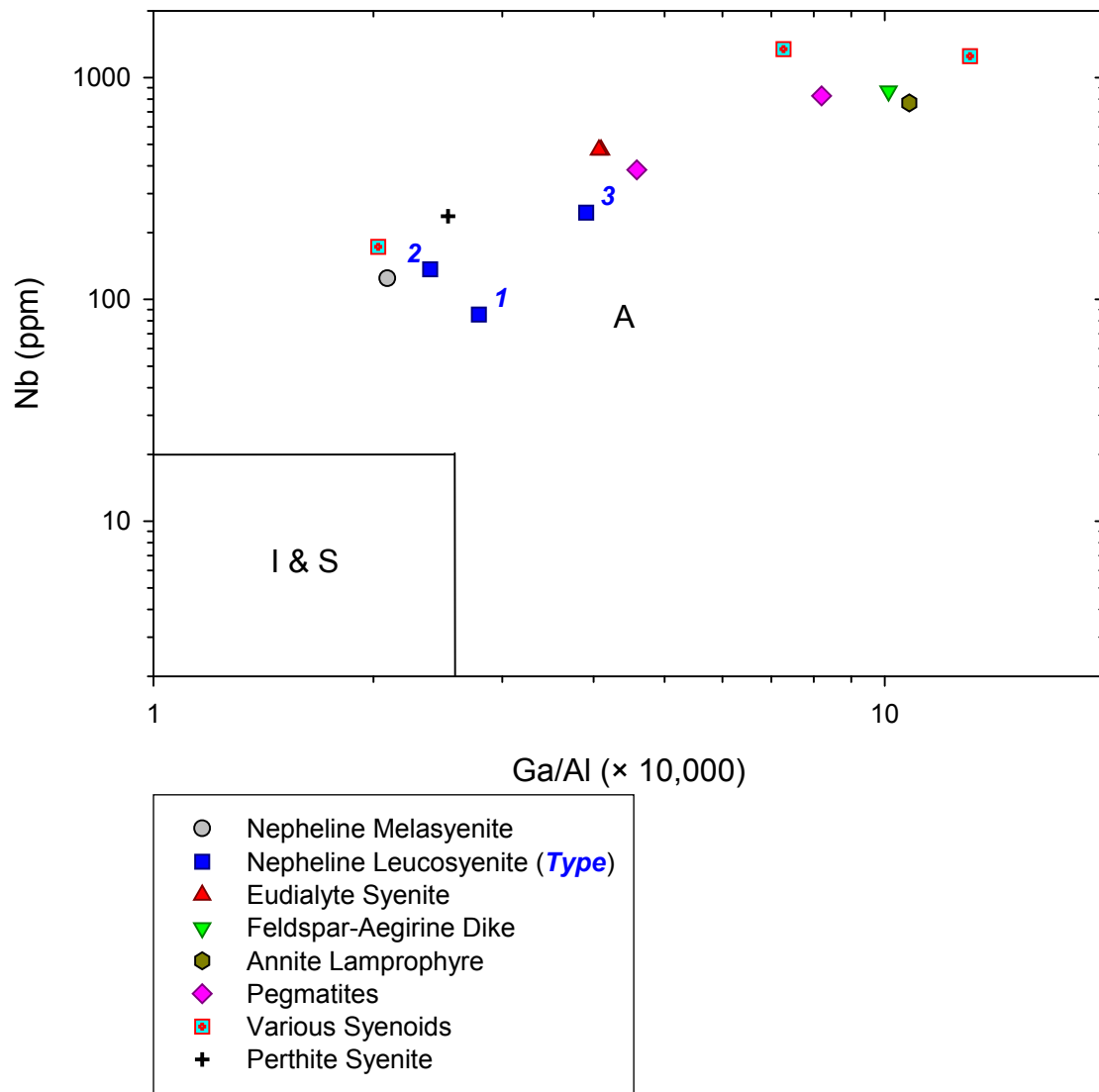


FIGURE 34 – Nb versus Ga/Al tectonic discrimination diagram after Whalen *et al.* (1987). Fields indicated by block letters are for A- and I- & S-type granitoids.

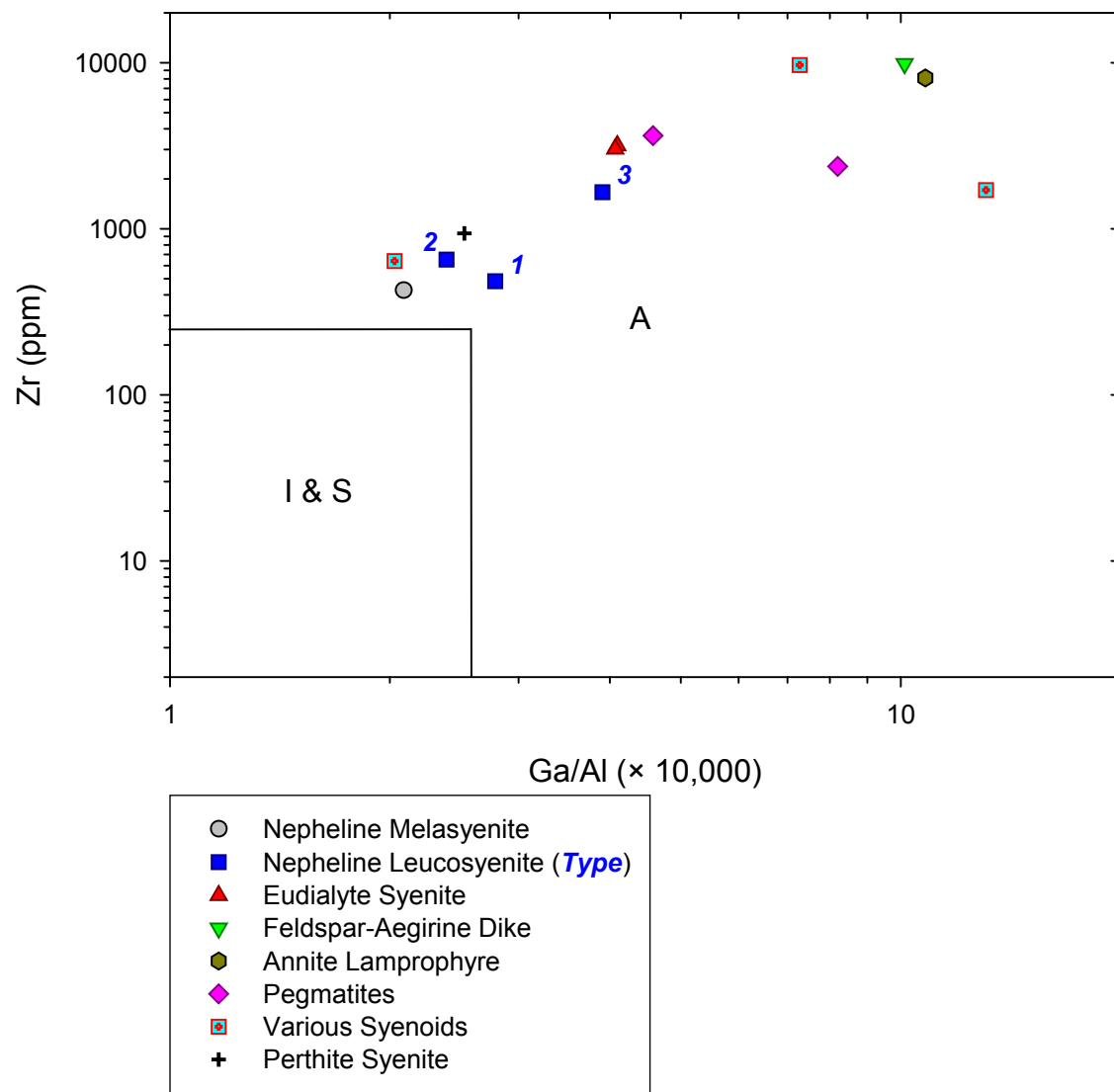


FIGURE 35 – Zr versus Ga/Al tectonic discrimination diagram after Whalen *et al.* (1987). Fields indicated by block letters are for A- and I- & S-type granitoids.

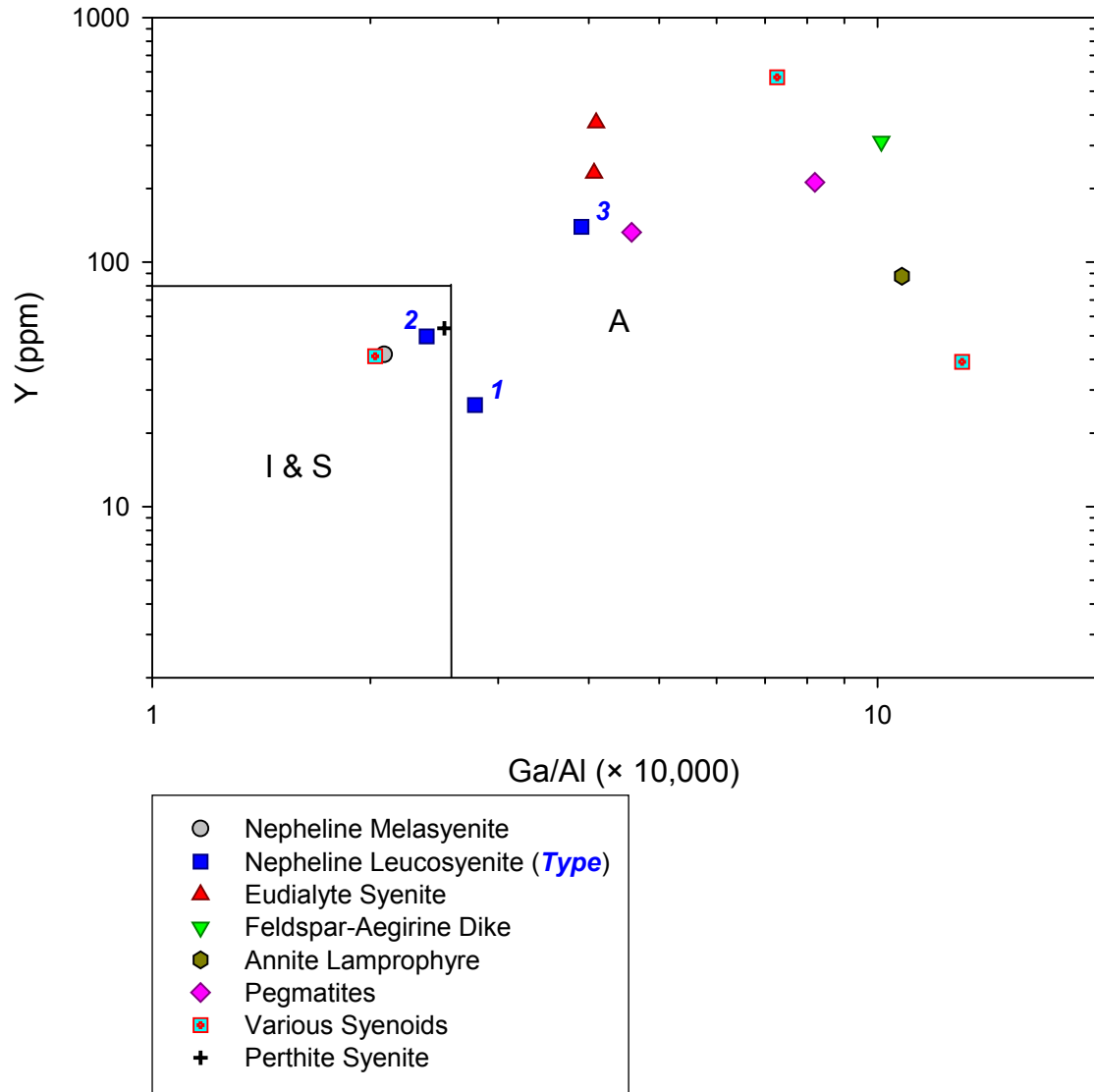


FIGURE 36 – Y versus Ga/Al tectonic discrimination diagram after Whalen *et al.* (1987). Fields indicated by block letters are for A- and I- & S-type granitoids.

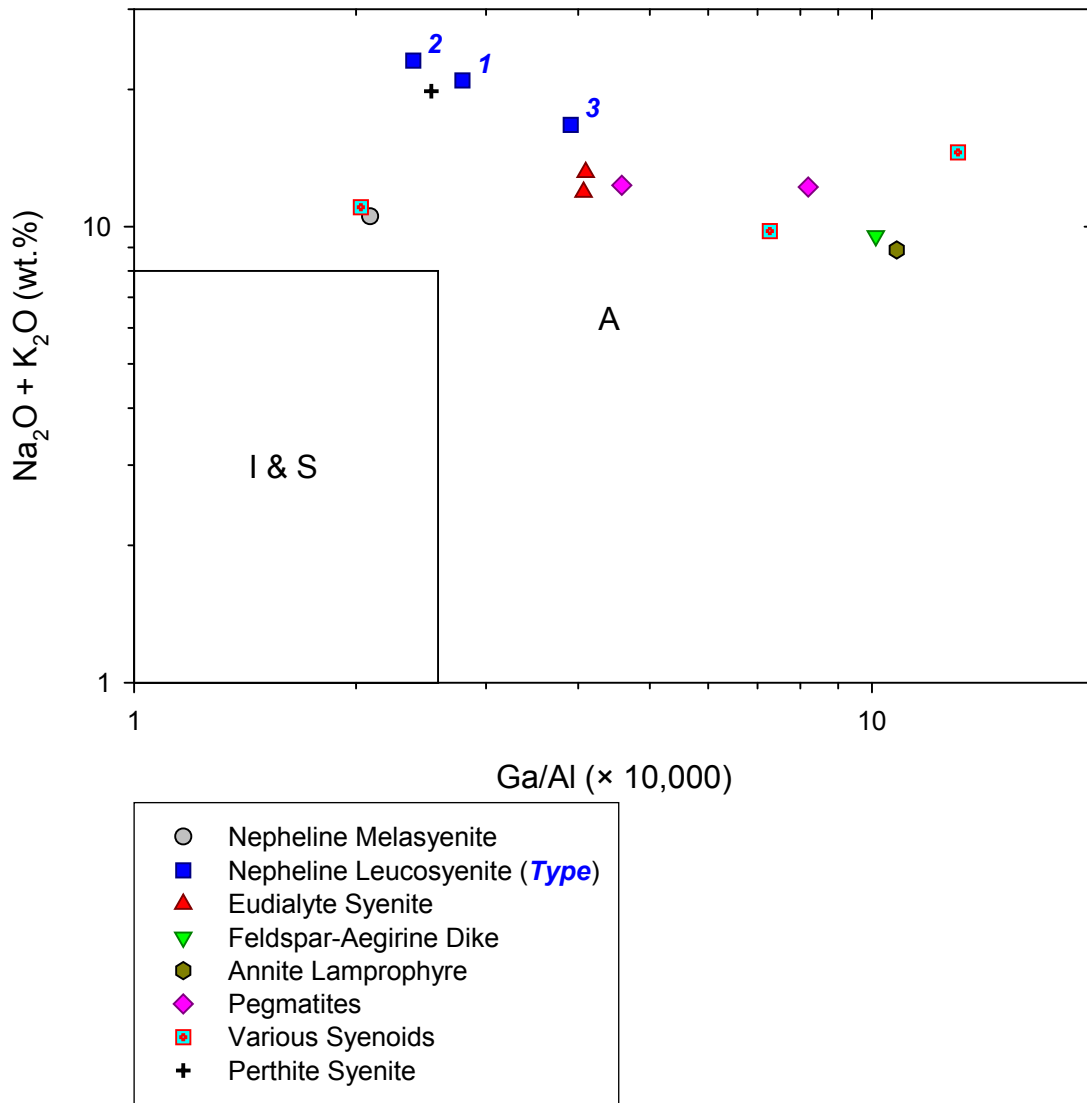


FIGURE 37 – Na<sub>2</sub>O + K<sub>2</sub>O versus Ga/Al tectonic discrimination diagram after Whalen *et al.* (1987). Fields indicated by block letters are for A- and I- & S-type granitoids.



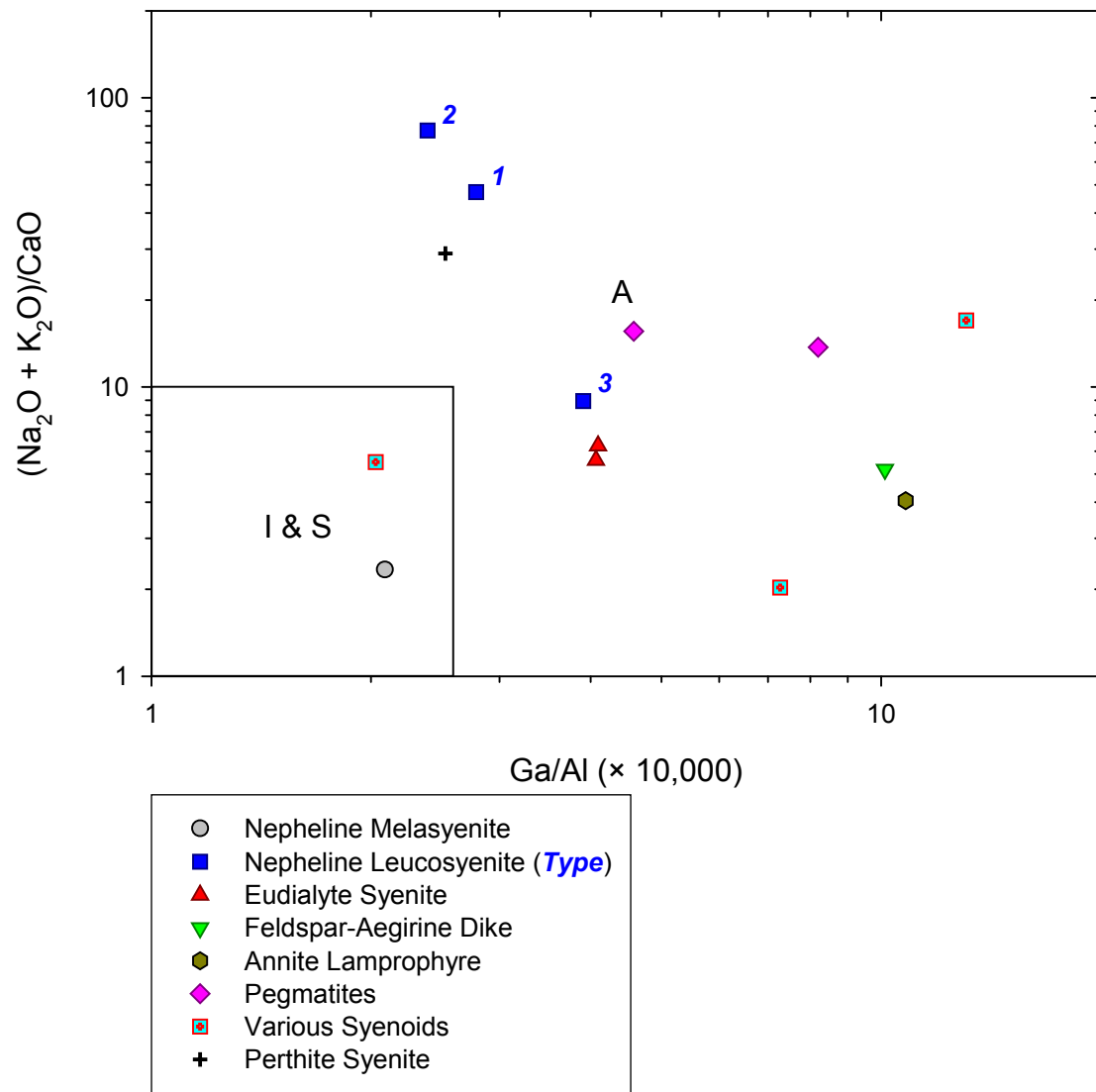


FIGURE 38 –  $(\text{Na}_2\text{O} + \text{K}_2\text{O})/\text{CaO}$  versus  $\text{Ga}/\text{Al}$  tectonic discrimination diagram after Whalen *et al.* (1987). Fields indicated by block letters are for A- and I- & S-type granitoids.

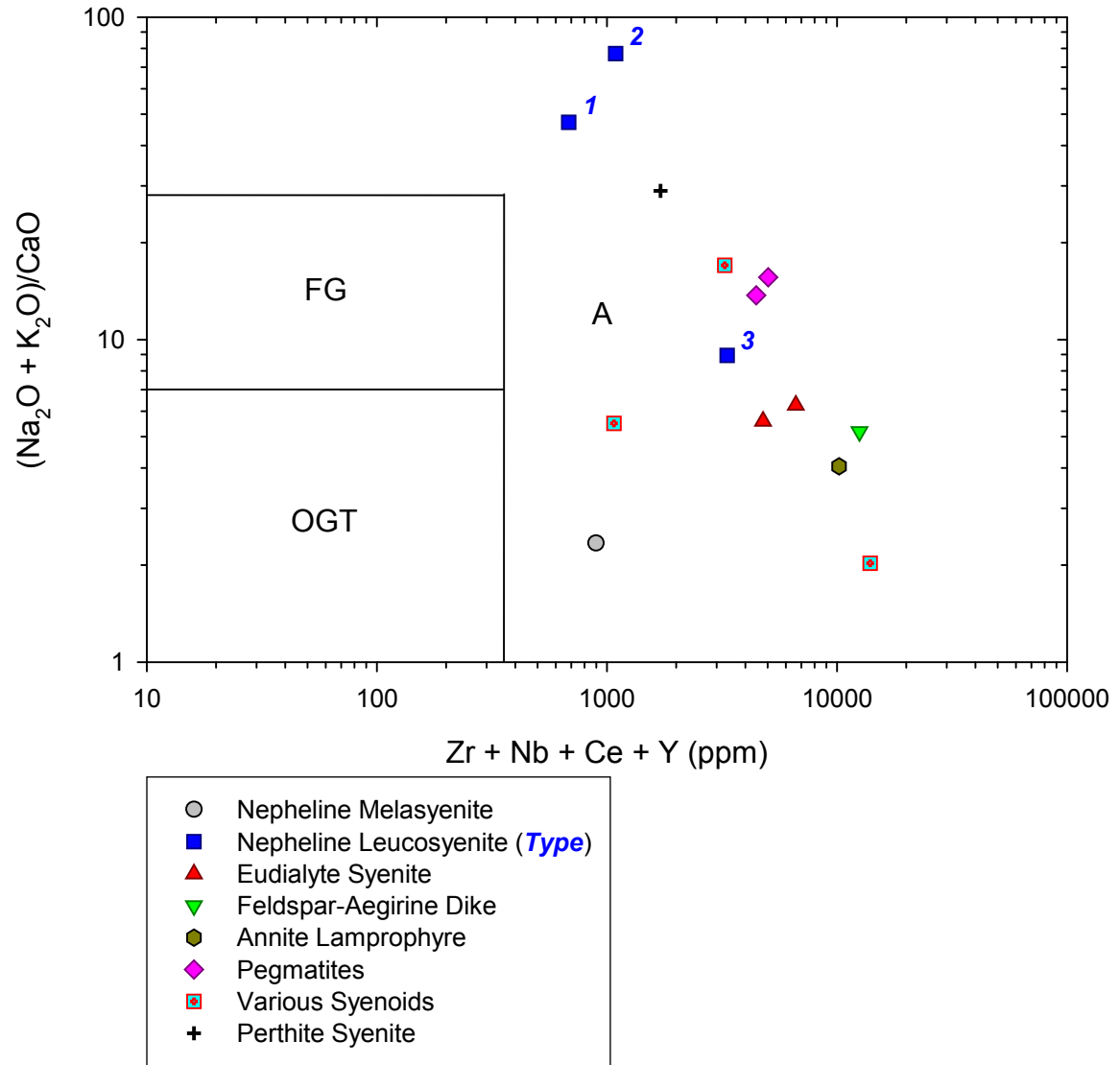


FIGURE 39 –  $(\text{Na}_2\text{O} + \text{K}_2\text{O})/\text{CaO}$  versus HFSE tectonic discrimination diagram after Whalen *et al.* (1987). Fields indicated by block letters are for A-type granitoids, fractionated granite (FG) & orogenic granite (OGT).

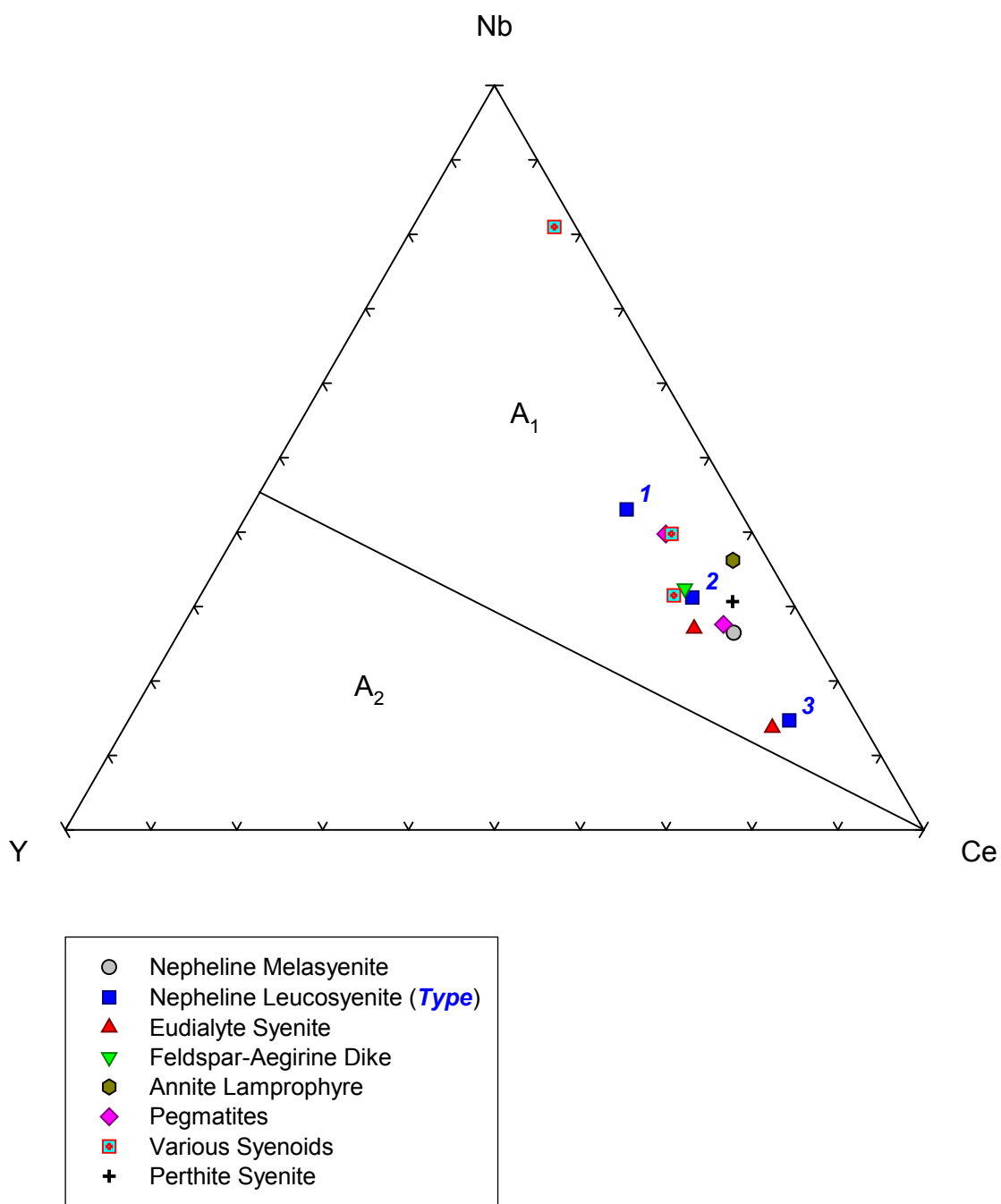


FIGURE 40 – Nb-Y-Ce tectonic discrimination diagram after Eby (1992). The two fields indicated by block letters represent differentiates from a basaltic source (A<sub>1</sub>) or from subcontinental lithosphere or lower crust (A<sub>2</sub>).

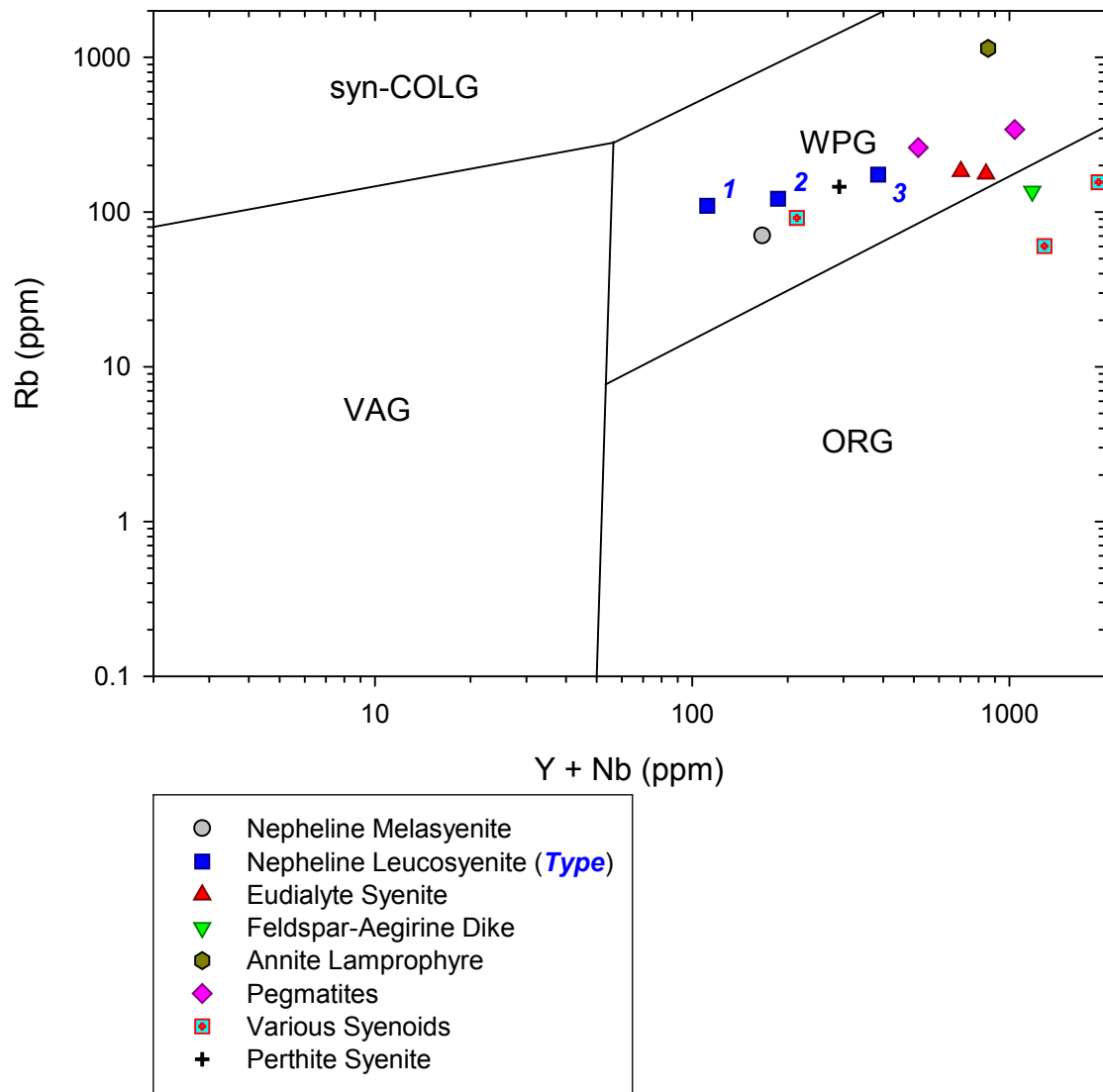


FIGURE 41 – Rb *versus* Y + Nb tectonic discrimination diagram after Pearce *et al.* (1984). Fields indicated by block letters are for syn-collisional granites (syn-COLG), volcanic arc granite (VAG), within plate granite (WPG) & orogenic granite (ORG).

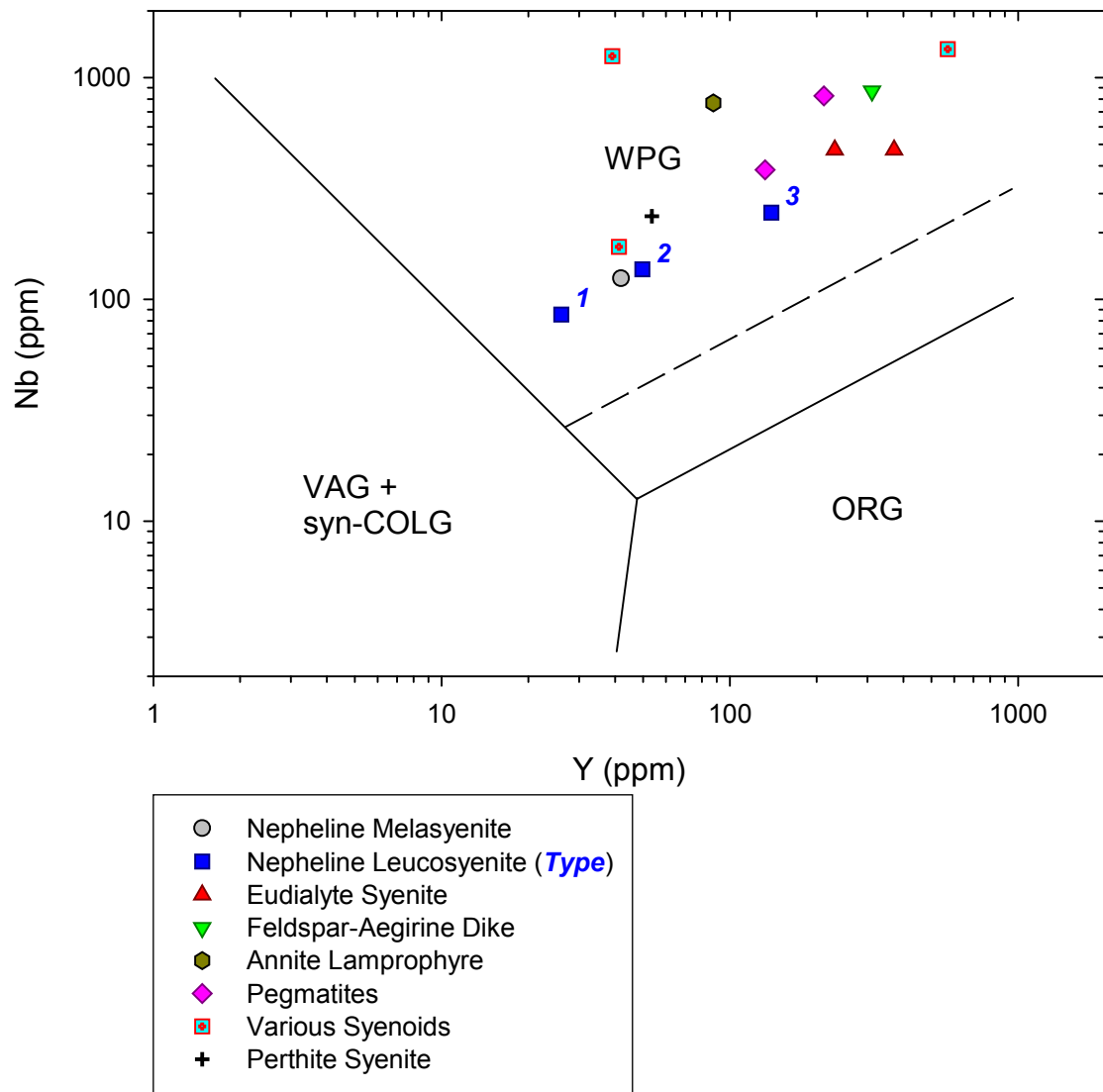


FIGURE 42 – Nb *versus* Y tectonic discrimination diagram after Pearce *et al.* (1984). Fields indicated by block letters are for syn-collisional granites (syn-COLG), volcanic arc granite (VAG), within plate granite (WPG) & orogenic granite (ORG).

All East Hill suite lithologies plot as A<sub>1</sub>-type granitoids (Figure 40) suggesting differentiation from a basaltic magma derived from an OIB-like source. This affinity also rather strictly suggests a within-plate intrusive environment, as opposed to a post-collisional or post-orogenic setting. (Eby 1992)

East Hill suite bulk compositions plotted onto the tectonic discrimination diagrams of PEARCE *ET AL.* (1984) indicate within-plate affinity, trending into an orogenic affinity, for the plot of Rb *versus* Y + Nb (Figure 41) and a strict within-plate affinity in the plot of Nb *versus* Y (Figure 42).

### ***Field Relationships Revisited & Differentiation Trends***

A rough differentiation and crystallization sequence was worked out based on field observations of enclosure and cross-cutting relationships: nepheline melasyenite → nepheline leucosyenite/perthite syenite → eudialyte syenite → pegmatites/syenoids → feldspar-aegirine dikes, followed separately by the annite lamprophyre.

The nepheline melasyenite is certainly the first lithology to be emplaced in the East Hill suite; it appears at the margins of the suite and encloses all other major lithologies. The nepheline leucosyenites probably crystallized next, as they are directly enclosed by the nepheline melasyenite. Exactly which type came first is unclear, although, texturally, the Type 3 leucosyenite appears to represent a transition to a syenoid, thus indicating later crystallization.

The perthite syenite held an uncertain position in the sequence from the outset, due partly to its peculiar mineralogy and partly to the lack of outcrop exposures, but its broad resemblance to the nepheline leucosyenites and its low content of rare-element minerals suggests that it holds a relatively early position in the differentiation sequence. As with the nepheline leucosyenites, it


is unclear from field relationships if the perthite syenite crystallized before, during, or after the leucosyenites.

The eudialyte syenite clearly followed the nepheline leucosyenites. In the field, it is texturally subordinate to the previous lithologies, and mineralogically, it represents a transition from leucosyenite to rare-element syenite. As a group, the pegmatites and syenoids crystallized next. In general, they either exist as apophyses of the nepheline mela- or leucosyenites or the eudialyte syenite, or they cross-cut one or more of the same. Nevertheless, some earlier episodes of pegmatitic or syenoid formation punctuate the crystallization sequence prior both to the complete solidification of the earlier lithologies, as well as to the main sequence of pegmatite/syenoid crystallization.

Essentially all of the lithologies are cross-cut by the feldspar-aegirine dikes, although very few pegmatites are cross-cut by them either due to contemporary emplacement or to the volumetric dominance of the syenitic lithologies. The emplacement path of the annite lamprophyre was not traced in the field, but the disposition of sample locations and the reported outcrop (László Horváth, pers. comm.) were in the center of the suite, suggesting that its magma came in last.

The differentiation and crystallization sequence from field relationships was refined using major and trace element geochemistry (Table 11). Values for Na, K, Ti, and Al were taken from the post-alteration whole-rock analyses. The Ga/Al ratios were used as the primary basis for ordering the lithologies in the crystallization sequence, as the order they suggested neither upset any known successions based on field observations nor did they clarify an incomplete succession in a nonsensical fashion. Ga/Al ratios are well-established as fractionation indicators in a magmatic system. (Whalen *et al.* 1987) Ga is primarily carried by aluminosilicates, and the

TABLE 11 – Geochemical differentiation trends – East Hill suite

	<i>Neph. Melsy.</i>	<i>Type 2 Leusy.</i>	<i>Perthite Syenite</i>	<i>Type 1 Leusy.</i>	<i>Type 3 Leusy.</i>	<i>Eudia. Syenite</i>	<i>Avg. Peg.</i>	<i>Avg. Synoid.</i>	<i>Fel-Aeg. Dikes</i>	<i>Annite Lamp.</i>
Na/K	1.85	5.77	5.00	6.06	3.85	1.98	1.14	4.19	2.91	0.41
K/Rb	405	211	171	203	150	181	151	243	137	44
Ba/K ( $\times 10^3$ )	49.8	0.8	0.6	4.3	5.0	8.9	5.3	15.3	3.1	0.6
Ba/Rb	20.15	0.16	0.10	0.86	0.74	1.59	0.77	4.65	0.43	0.03
Ba/Sr	0.51	2.84	2.41	1.16	0.43	0.51	1.29	0.46	0.28	0.17
Sr/Ca ( $\times 10^3$ )	85.6	3.2	1.2	25.9	22.5	36.3	32.3	52.2	16.1	11.0
Ti/Zr	18.16	0.36	1.28	0.51	0.40	0.28	0.47	2.56	0.20	0.61
Ti/Nb	62.2	1.7	5.1	2.9	2.7	1.8	2.4	8.9	2.3	6.5
Zr/Nb	3.4	4.8	4.0	5.7	6.7	6.6	6.2	4.1	11.3	10.5
Ga/Al ( $\times 10^4$ )	2.09	2.39	2.53	2.79	3.91	4.08	6.39	7.46	10.12	10.81
	<i>Increasing Differentiation</i> 									

tendency of these phases to preferentially incorporate Al concentrates residual Ga in the melt and fluids, thus increasing the Ga/Al ratio with increasing differentiation. In the context of the East Hill suite, annite may also take up Ga (Černý *et al.* 1985), contributing to the high Ga content of the feldspar-, but not zeolite-, free annite lamprophyre.

Ga/Al ratios for the East Hill suite range from  $2.09 \times 10^{-4}$  to  $13.08 \times 10^{-4}$ . The Ga/Al range in the East Hill suite partly overlaps the typical range of Ga/Al ratios for granites (approximately  $1.25 \times 10^{-4}$  to  $5.00 \times 10^{-4}$ ), which tend to have much more restricted ranges within a given differentiation sequence. (Kolbe & Taylor 1966; Černý *et al.* 1981; Černý *et al.* 1985) Higher values of the Ga/Al ratio and more extensive ranges within a single fractionation



sequence, as are found in the East Hill suite, are characteristic of alkaline suites. (Bowden 1964; Černý *et al.* 1985)

Besides magmatic fractionation, complexing is also a factor in late-stage Ga beneficiation, as its complexes remain stable to low temperature. Fluoride complexes are proposed by some investigators (Cotton & Wilkinson 1980; Manning *et al.* 1980) as important species in this process, and this is certainly true in systems in which F plays a more prominent role. In the East Hill suite, however, it is likely that chloride complexes are more prevalent, and CHURAKOV (2001) notes that, in the vapor phase, Ga prefers Cl complexes over F. Based on the thermal parameters of the study, this can probably be extended to include fluids and supercritical fluids, as well. Notably, as temperature decreases, the speciation of the Ga complexes changes from GaCl to GaCl<sub>2</sub> to GaCl<sub>3</sub>. This phenomenon holds true for certain other elements, as well, in which the molar proportion of halides in the complexes increases with decreasing temperature.

Metasomatic processes, in particular albitization, are also factors in increasing the Ga/Al ratio (Severov & Vershkovskaya 1960; Bowden 1964), and concordance of the Ga/Al trend with that of Zr/Nb, which probably also would show an increase with hydrothermal activity (Kosterin *et al.* 1964; Wang *et al.* 1982), at least supports the possibility that the increases in these trends are due in part to late-stage alteration, although it is difficult to divorce such increases from those resulting from fractionation processes.

The Na/K ratio proved to be essentially useless as an indicator of magmatic differentiation, as the value of the ratio did not correlate at all with fractionation. Na and K together behave too compatibly and are readily available throughout the crystallization sequence. Na and K frequently substitute into different minerals, so changes in modal mineralogy skew their ratio independently of fractionation trends. For example, sodium substitutes freely into

potassium feldspar but not annite; similarly, potassium tends to avoid clinopyroxene.

Furthermore, any possible meaning that could be gleaned from the data is swamped by the effects of sodium metasomatism. The best that can be said is that the Na/K values underscore the lithologies in which metasomatism had the strongest effects.

On the other hand, since K and Rb tend to follow one another in substitutions, a change in the total number of potassium sites does not change the proportion of K to Rb, and, in fact, the K/Rb ratio is remarkably constant across most rock types. (Ahrens *et al.* 1952) Besides its relative stability with respect to alteration, metasomatism, and mineral assemblage, the K/Rb ratio is also considered to be a useful parameter to trace magmatic differentiation. In rocks with significant plagioclase and hornblende content, K/Rb increases with fractionation, since K is favored slightly in these phases. (Hart & Aldrich 1967; Murthy & Griffin 1970) With potassium feldspar and biotite crystallization, as in the East Hill suite, it tends to decrease with increasing magmatic evolution. (Demin & Khitarov 1958; Siedner 1965)

The K/Rb ratio generally decreases with fractionation in the East Hill suite, ranging from 405 to 44, with small positive anomalies in the Type 1 nepheline leucosyenite, the eudialyte syenite, and the various syenoids. The K/Rb ratio for the nepheline melasyenite suggests a rather unevolved magma, whereas the value for the annite lamprophyre indicates extreme differentiation. (Ahrens *et al.* 1952; Taylor *et al.* 1956)

Including zeolite-rich samples from Ilímaussaq (Ferguson 1970) for K/Rb calculations on that complex introduced positive anomalies to the trend, whereas low-zeolite analyses yielded a relatively smooth and continuous decrease with fractionation. This suggests that the anomalies seen in the East Hill suite K/Rb fractionation trend are also due to the presence of zeolites, both primary and secondary.

The use of Ba as a fractionation indicator suffers from similar problems to those encountered in the application of the Na/K ratio. Ba concentrations notoriously display significant scatter, even at the scale of a single lithology. Furthermore, even though Ba rather rigidly follows K in substitution, it follows somewhat too rigidly and its content plummets after potassium feldspar crystallization begins in earnest. Consequently, in more evolved or in alkaline suites, in which potassium feldspar already plays a major role, Ba content either drops quickly or starts off low, making the problem of scatter even more pronounced. (Černý *et al.* 1985)

Even though Ba content is related to K mineralization, it is also geochemically allied with Ti, especially in titanian mica (Mansker *et al.* 1979; Bol *et al.* 1989; Shaw & Penczak 1996); therefore, fluctuations in Ti mineralization or substitution can lead to a mirror trend in Ba concentrations. As a result, changes in the modality, unrelated to fractionation, can lead to spurious shifts in Ba content and ratios.

For the East Hill suite as a whole, the Ba/K and Ba/Rb ratios exhibit scatter in their values, but, in general, decrease with increasing differentiation in the direction defined by the Ga/Al ratios. Ba/Rb ratios strongly correlate with Ba/K values. Ba/K ratios range from  $49.8 \times 10^{-3}$  to  $0.6 \times 10^{-3}$  and Ba/Rb ranges from 20.15 to 0.03. All three Ba ratios for the East Hill suite exhibit have their highest value (Ba/K and Ba/Rb) or a particularly low value (Ba/Sr) in the nepheline melasyenite. The Ba/K and Ba/Rb exhibit a precipitous drop following further differentiation; the Ba/Sr ratio increases, but not by as large a factor. Although scatter is prominent in the Ba ratios, scatter in all three is correlative, with anomalous values concentrated in the fractionation sequence between the Type 1 nepheline leucosyenite and the syenoids. This is likely related to increases in the modal proportion of aegirine-augite, as well as Ti-bearing

phases such as eudialyte group minerals and astrophyllite. North Nyasa, Oslo, and Khibina-Lovozero (Neumann 1980; Andersen & Sørensen 1993; Eby *et al.* 1998; Arzamastsev *et al.* 2001 & 2008) also have considerable scatter in their Ba/K values, with, as in the East Hill suite, positive anomalies in biotite- and eudialyte-bearing lithologies.

The high Ba/K and Ba/Rb ratios in the nepheline melasyenite are, in general, related to Ba concentrating in potassium feldspar. In terms of feldspar chemistry, this is the first significant departure in the East Hill suite from the plagioclase of the gabbroic rocks of the Pain de Sucre and Sunrise suites (Greenwood & Edgar 1984); this depleted the residual melt in Ba. The crystallization of titanian annite in the nepheline melasyenite probably had the same effect in terms of removing Ba from the system. An abundance of Ca minerals in the nepheline melasyenite elevated the Sr content of the nepheline melasyenite, lowered the Ba/Sr ratio, and depleted the residual melt in Sr.

Ba/Sr ratios in the East Hill suite range from 0.17 to 2.84 and are generally antipathetic to Ba/K and Ba/Rb ratios. In igneous suites, Sr whole rock geochemistry is governed by the interplay between several phases: apatite, augitic clinopyroxene, biotite, feldspar, and titanite. Apatite and titanite have a strong affinity for Sr (Morse 1982; Černý *et al.* 1985), so crystallization of these phases increases the Sr content of a lithology, lowers the Ba/Sr ratio, and depletes the melt in Sr. Biotite and pyroxene both tend to exclude Sr due to steric hindrances in substitution for K or Ca, so these phases drive Sr levels higher in the melt. (Brooks 1968; Černý *et al.* 1985) Plagioclase actually preferentially accepts Sr over Ca, but in terms of whole rock chemistry, this effect may be offset by pyroxene crystallization. (Brooks 1968) As a general rule, potassium feldspar has a similar affinity for Sr as plagioclase. (Heier 1962; Smith 1974) In the nepheline melasyenite, early crystallization of apatite and titanite depleted the residual melt

in Sr, leading to a relatively low Ba/Sr ratio for that lithology but generally elevating it in subsequent rock types. Scatter in the Ba/Sr ratio that is antipathetic and correlative to other Ba ratios is probably partly driven by uptake of Sr by feldspar, but is mainly caused by elevated Sr in eudialyte group minerals and carbonates. Without going too much further into mineralogical variation, it should be apparent that Ba ratios are, indeed, more reliable indicators of mineralogy than fractionation and, at the very least, both characteristics must be considered together.

As is to be expected from the preceding discussion of Sr behavior, the Sr/Ca ratio basically follows the opposite trend to that of Ba/Sr in the East Hill suite, ranging from  $85.6 \times 10^{-3}$  to  $1.2 \times 10^{-3}$ ; correlative deviations between the two trends are due to the greater exclusion of potassium mineralization from the Sr/Ca ratio.

The Ti/Zr, Ti/Nb, and Zr/Nb ratios are similarly valuable as Ga/Al ratios as differentiation indicators since these elements are not generally subject to remobilization by fluids, unless such fluids are rich in complexing agents. (Pearce & Norry 1979) Since this latter property is more typical of magmatic fluids than post-magmatic hydrothermal or meteoric fluids, these element ratios are more or less immune to the effects of alteration and secondary mineralization.

One consideration of Ti ratios in alkaline rocks, however, is that Ti tends to concentrate in miaskitic and early agpaitic assemblages. Consequently, the alkalinity of the melt, in particular the balance between Ca and Na + K can overprint the differentiation trend represented by the ratio, and similarly to Ba ratios, early crystallization of Ti phases means that steep negative gradients in Ti ratios are not uncommon early in the differentiation trend. Contrary to calc-alkaline systems, in which Zr is consumed early through zircon crystallization (Dietrich 1968; Watson 1979), Zr is present in alkaline melts as zirconium complexes (Vlasov 1966;

Dietrich 1968; Watson 1979), which concentrate Zr in the magma, elevating Zr content into later stages of fractionation. The behavior of Nb is also influenced by complexing, with the same effect that it concentrates into the melt. (Linnen 1998)

In the East Hill suite, both Ti/Zr and Ti/Nb exhibit the expected alkaline trend, decreasing suddenly at first and then gradually, with ranges of 18.16 to 0.20 and 62.2 to 1.5, respectively. Values show considerable scatter but with small variances due to fluctuations in mineralogy. Zr/Nb increases steadily with differentiation in the East Hill suite, from a value of 3.4 to 11.3. Neither Zr nor Nb is strongly subject to the influence of Ca in their mineralization, so they are freer to vary based on the behavior of their complexes in the melt. Zr concentrated more effectively in the East Hill suite magma, with a 20-fold increase in Zr concentration *versus* a seven-fold increase for Nb.

In the realm of alkaline complexes, the East Hill suite magma only underwent moderate differentiation. Based on a comparison of the same differentiation indicators, the East Hill suite overall experienced less fractionation than Ilímaussaq, more than the Kasungu and Chipala intrusions from North Nyasa, and about as much as the Ilomba and Ulindi intrusions from North Nyasa, the Oslo province, and Khibina-Lovozero. This is not to say that the degree of evolution correlates strictly with the ultimate mineralogy and lithologies observed in each complex. For example, the East Hill suite appears to be similarly differentiated to Khibina, and particularly, Lovozero; however, the late-stage mineral assemblages in the latter complexes suggest a substantially more evolved magma. Similarly, the Oslo province rocks do not exhibit the spectacular agpaitic mineralogy as Khibina-Lovozero, yet again, magmas in the Oslo province exhibit about as much differentiation as the East Hill suite. These differences are the result of interplay with other factors that are not directly addressed by differentiation trends, such as the

absolute contents of rare elements and alkalis in the parental magma, as well as the amount of differentiation that the magma had already experienced prior to emplacement.

The East Hill suite intruded as a relatively primitive alkaline magma, enriched in alkalis and rare-elements with respect to calc-alkaline magmas, but still containing high quantities of Ca, Ba, REE, Sr, Ti, and Zr. The earliest lithology at Ilímaussaq, the augite syenite, is strikingly similar to the nepheline melasyenite in the East Hill suite, yet the rare element content at Ilímaussaq is more uniformly high, resulting in more abundant rare-element lithologies in later stages of crystallization. Kasungu, Chipala, and Oslo started with relatively primitive magmas with generally high Ca and Ti contents, but the Oslo province underwent a greater degree of differentiation, resulting in more evolved, more typically-alkaline lithologies. Interestingly, the Ilomba and Ulindi intrusions, though less enriched in Ca and Ti and more enriched in alkalis, contain less Zr and La than Kasungu and Chipala. Khibina and Lovozero are rare element-rich and exceptionally alkali-rich, but their magmas did not evolve substantially more than that of the East Hill suite; yet owing to their bulk chemistry, they boast a greater number of minerals and contain proportionally more agpaitic phases. It is important, then, to consider numerous factors when analyzing the evolution of alkaline complexes, not only the degree of differentiation but also the geochemical starting point.

### ***Trace Element Variation***

Coryell-Masuda diagrams for the East Hill suite are shown in FIGURES 43 and 44. It is not uncommon practice, but HOFMANN (1997 & 2003) discourages the use of MORB- and OIB-normalized element variation diagrams due to the high variance intrinsic to these compositions. The preferred reservoir for mantle-normalization is the primitive mantle (PM) (Hofmann 1988),

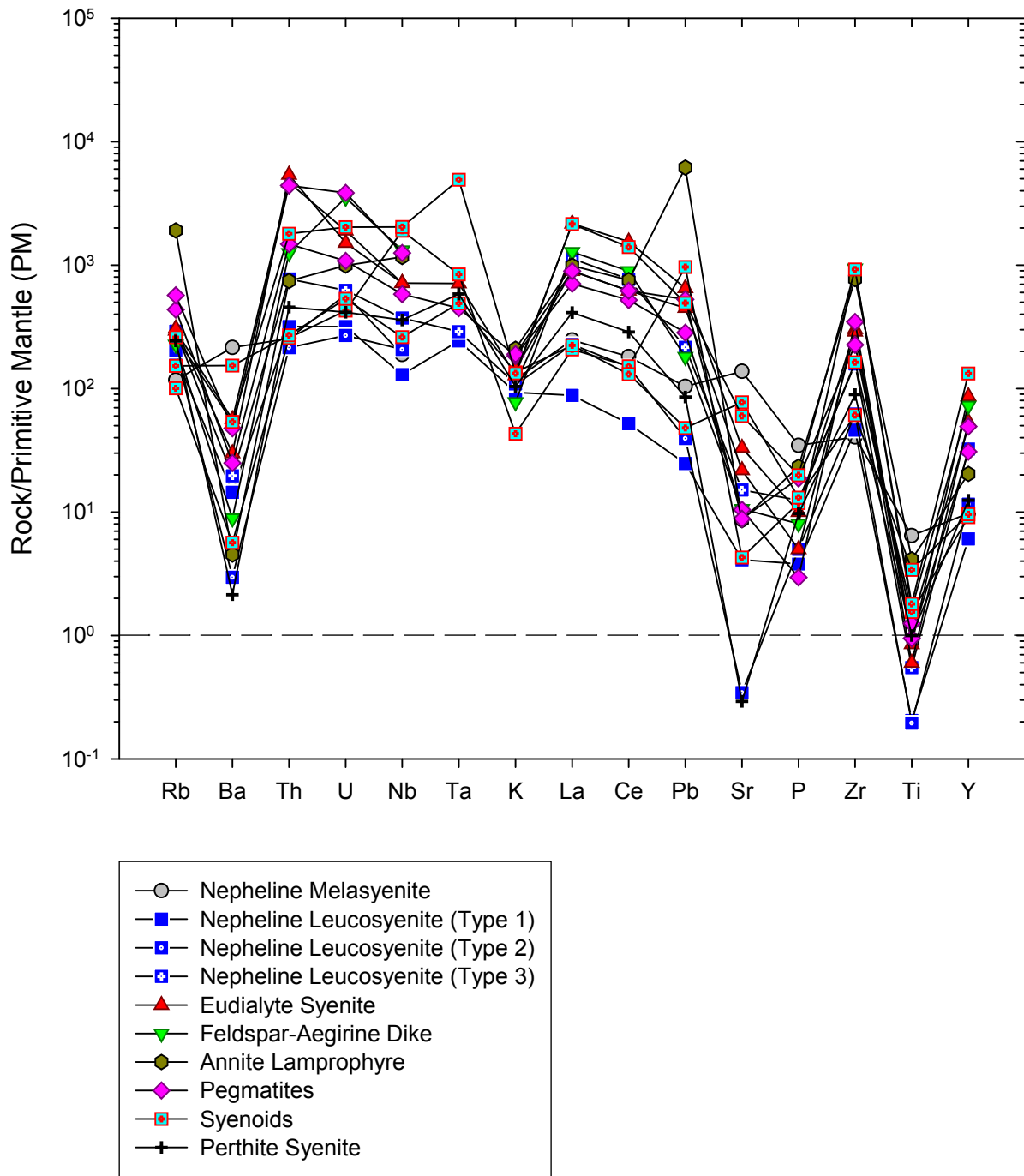


FIGURE 43 – Coryell-Masuda diagram for the East Hill suite, normalized to the primitive mantle (PM). PM data from McDONOUGH (2001).



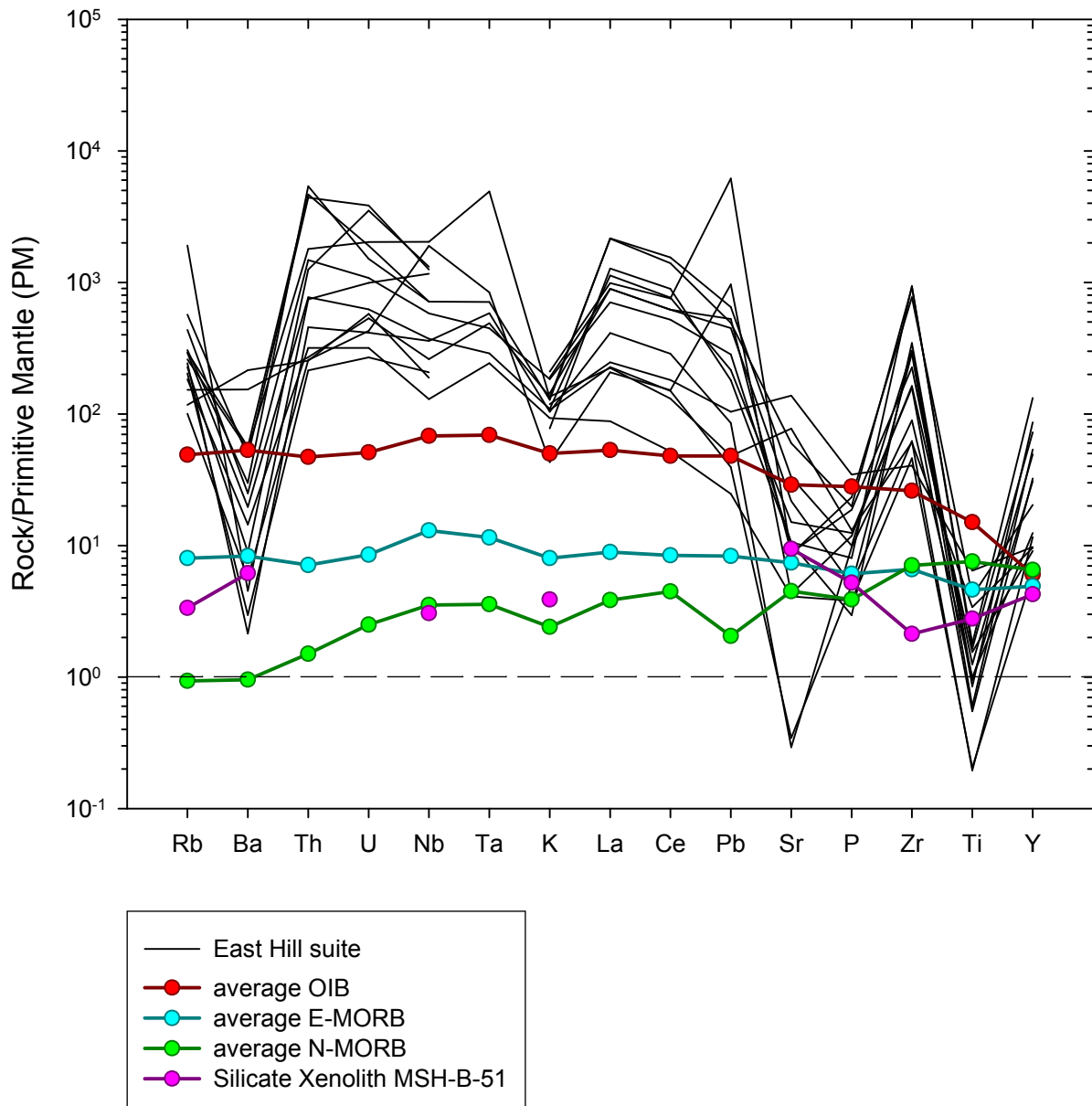


FIGURE 44 – Coryell-Masuda diagram for the East Hill suite, average OIB, E-MORB, and N-MORB, and the East Hill suite silicate xenolith, normalized to the primitive mantle (PM). OIB, E-MORB, and N-MORB data from SUN & McDONOUGH (1989), U, K, and Pb values for N-MORB corrected with data from HOFMANN (1988); PM data from McDONOUGH (2001).

and so trace element data from the East Hill suite and other alkaline complexes and provinces was normalized against this composition.

The East Hill suite exhibits prominent negative anomalies for Ba, K, Sr, and Ti, small negative anomalies for Nb, Sr, and P, and positive anomalies for Zr and Y, with a partial small positive Pb anomaly. The negative anomalies are indicative of fractionation of plagioclase, potassium feldspar, apatite, and rutile, ilmenite, or titanite prior to emplacement of the East Hill suite magma. Early crystallization of these phases is not only not unexpected in a general sense, but also these phases are abundant in the gabbroic suites that crystallized before the East Hill suite. (Greenwood & Edgar 1984) Relative to the mantle, the continental crust contains substantially higher concentrations of Pb (Miller *et al.* 1994), whereas Zr and Y contents are similar between the primitive mantle, MORBs, and the continental crust. (Hofmann 1988) The positive Pb anomaly is suggestive of crustal contamination of the East Hill suite magma, but such a process cannot explain the Zr and Y anomalies. Positive Zr and Y anomalies are indicative of enrichment *via* complexing and fractionation (Vlasov 1966; Bau 1996), a subject that will be revisited in the discussion of petrogenesis.

In general, the nepheline melasyenite contains moderately low concentrations of the examined elements, including the lowest of Zr and one of the lowest of Y, but it contains the highest quantities of four of the negatively anomalous elements, Ba, Sr, and Ti, as well as P. The syenitic lithologies (nepheline leucosyenites and perthite syenite) as well as some of the various syenoids are depleted in nearly all but the most compatible trace elements. Amongst the elements in which these lithologies are depleted, they generally contain lower concentrations of these elements than the nepheline melasyenite. Conversely, for the same elements, the syenoid

lithologies (eudialyte syenite, feldspar-aegirine dikes, pegmatites, and the remaining various syenoids) and the annite lamprophyre generally contain higher concentrations of these elements.

The trace element profile of the East Hill suite silicate xenolith is comparable to MORB profiles (Figure 44), but it shows enrichment and depletion anomalies that are largely opposite to those of the East Hill suite lithologies, enriched in Ba, K, Sr, P, and Ti, and depleted in Rb and Zr. In parallel with the East Hill suite, the xenolith is slightly depleted in Nb. Combined with the basaltic bulk composition of the xenolith, the negative correlation of the trace element profiles of the East Hill suite and the xenolith suggest that the xenolith may be a fragment of the direct source rock for the East Hill suite magma. The positive correlation of the Nb depletions suggest that this material may itself represent a fractionate of a more primitive composition.

Coryell-Masuda diagrams comparing the East Hill suite with the previously discussed alkaline complexes and provinces are shown in FIGURES 45 through 50. All of the compared intrusions have trace element profiles that are similar to that of the East Hill suite, at least in terms of the presence of positive and negative anomalies. With the added considerations of comparing relative abundances and the overall shape of the profiles, as well, the East Hill suite most resembles Ilímaussaq and Lovozero. In fact, Ilímaussaq is overall even more enriched in rare elements than the East Hill suite, in particular in Th, U, REE, and Y; however, Ilímaussaq contains substantially less Nb (and presumably Ta) than does the East Hill suite. Lovozero rather closely matches the East Hill suite in the abundances of highly incompatible elements, but it is actually less enriched in more compatible elements, and it displays a notable negative P anomaly. The trace element profile for Khibina is comparable to that of Lovozero, except that its tenor in incompatible elements is about an order of magnitude lower. In addition, Khibina and Lovozero do not display the negative Sr anomaly of the East Hill suite.

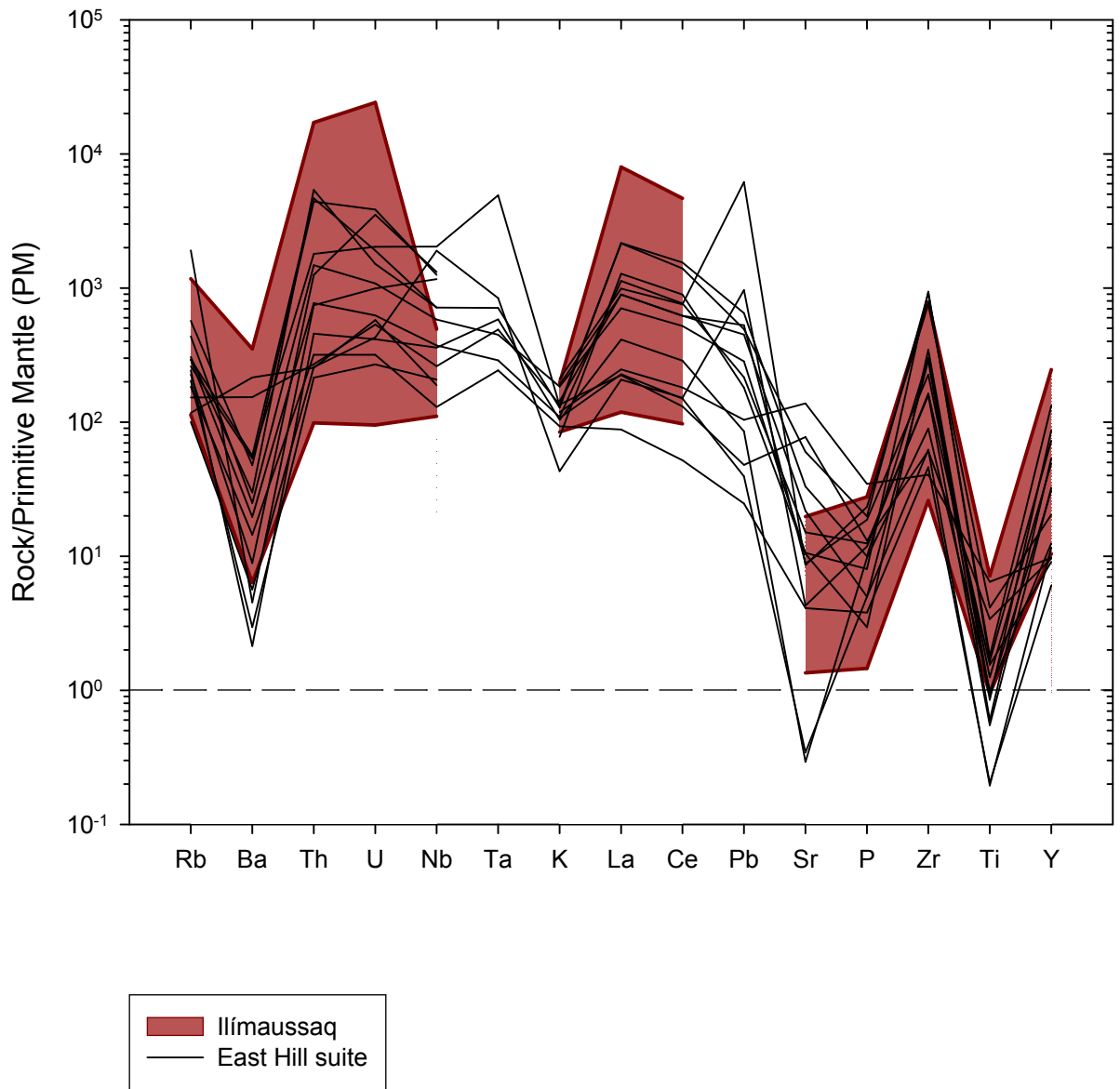


FIGURE 45 – Coryell-Masuda diagram comparing the East Hill suite with the Ilímaussaq intrusion (Ferguson 1970; Bailey *et al.* 2001; Khomyakov *et al.* 2001), both normalized to the primitive mantle (PM). PM data from McDONOUGH (2001).

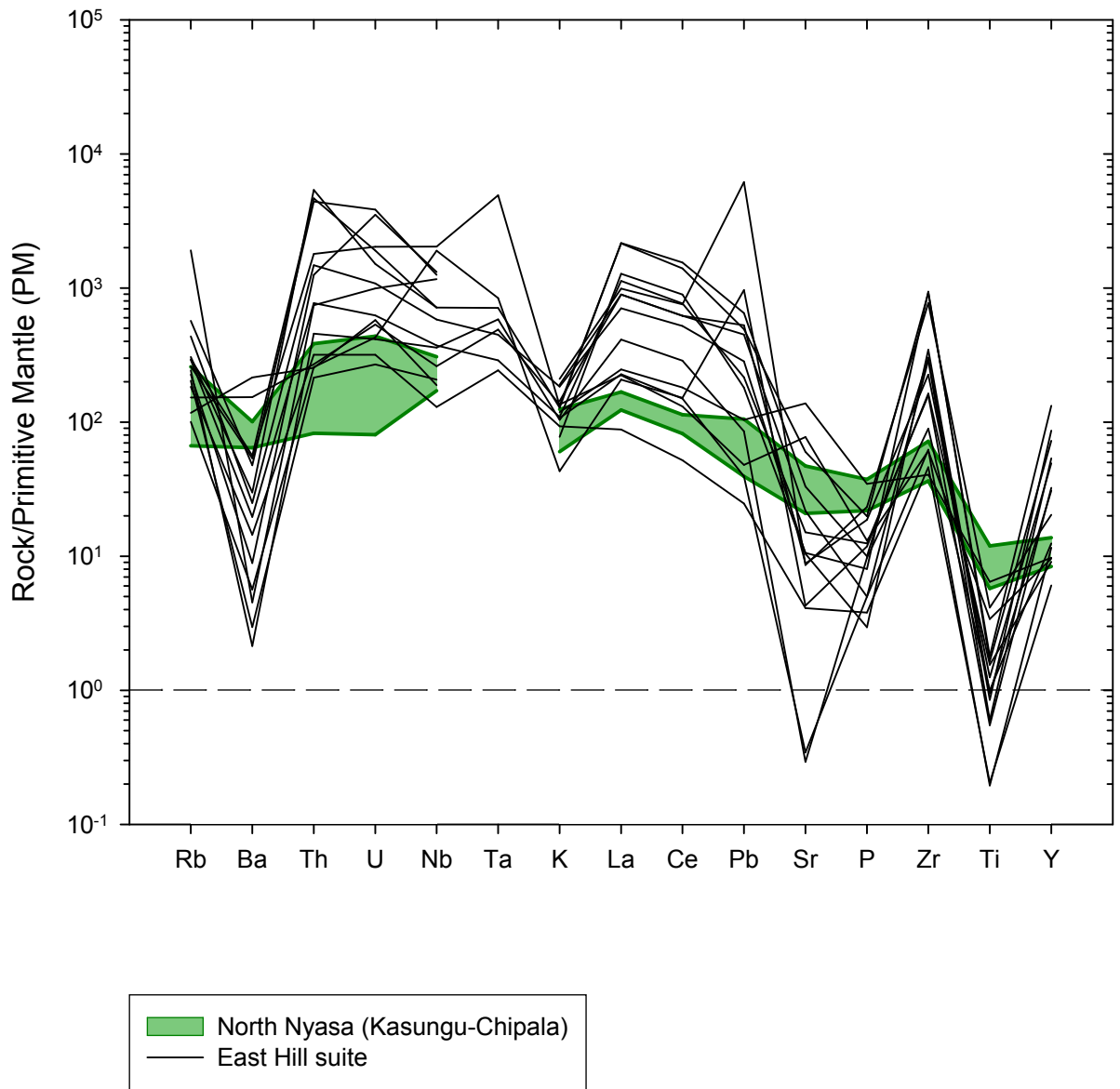


FIGURE 46 – Coryell-Masuda diagram comparing the East Hill suite with the Kasungu and Chipala intrusions, North Nyasa alkaline province (Eby *et al.* 1998), both normalized to the primitive mantle (PM). PM data from MCDONOUGH (2001).

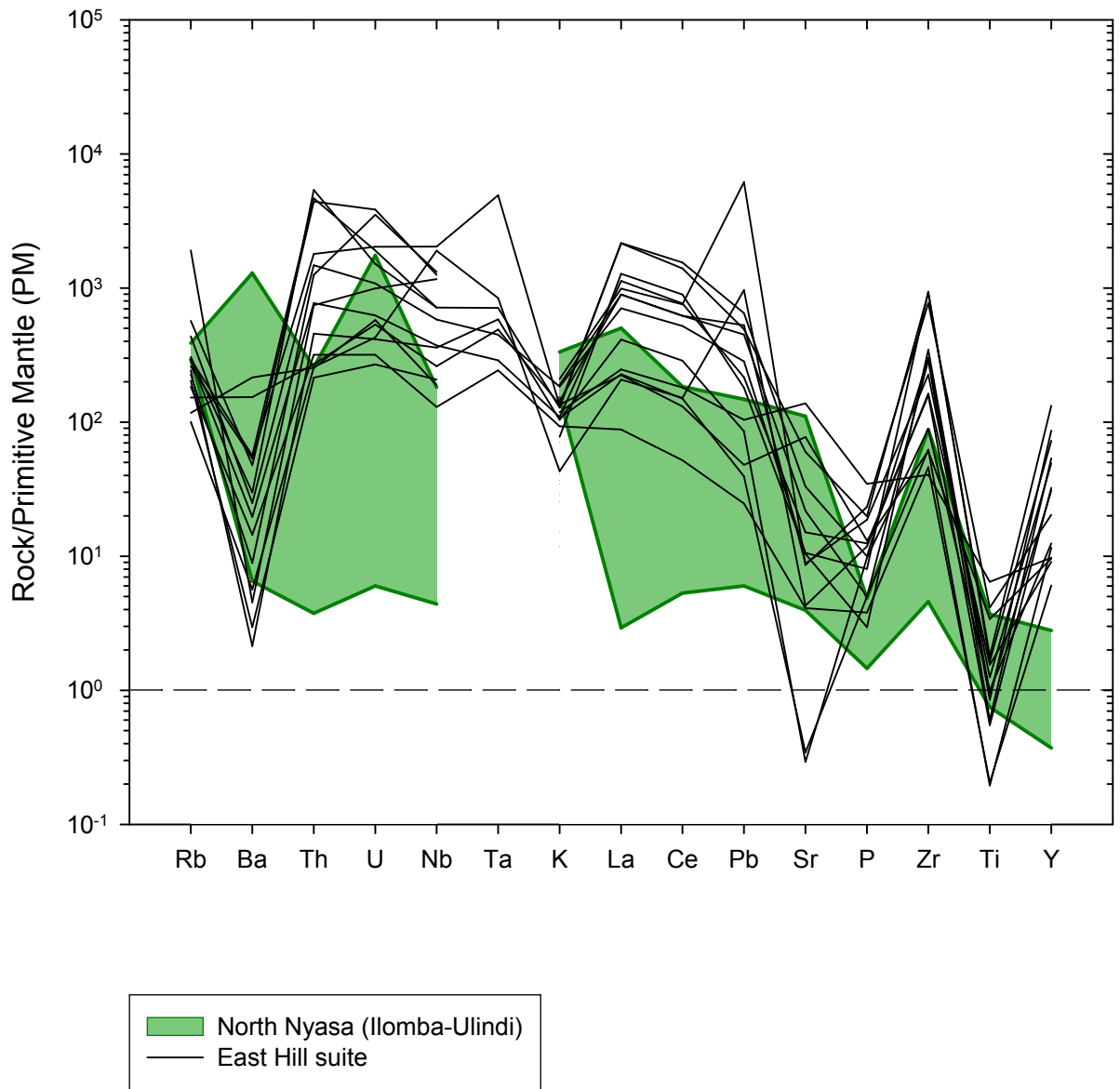


FIGURE 47 – Coryell-Masuda diagram comparing the East Hill suite with the Ilomba and Ulindi intrusions, North Nyasa alkaline province (Eby *et al.* 1998), both normalized to the primitive mantle (PM). PM data from McDONOUGH (2001).

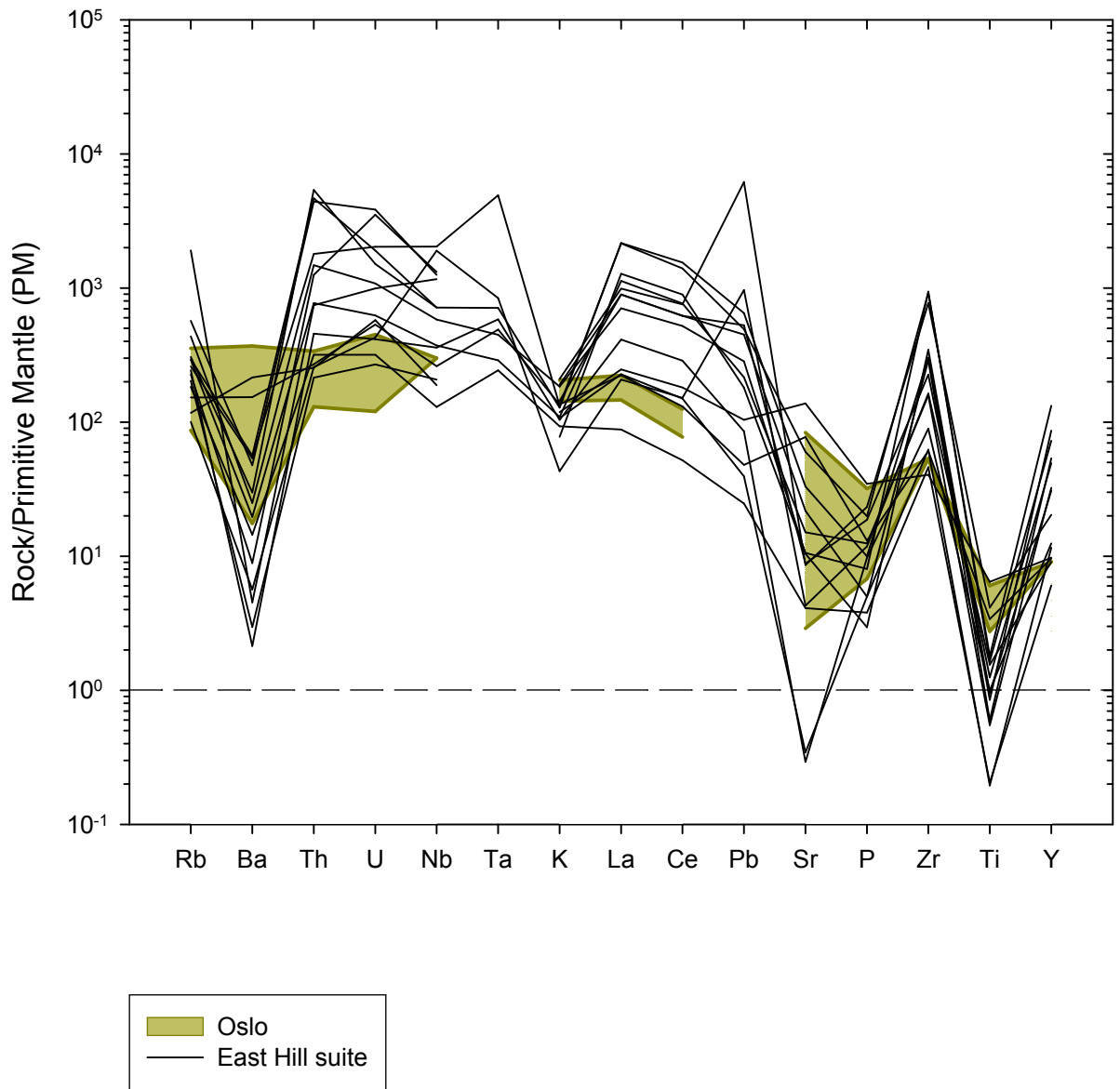


FIGURE 48 – Coryell-Masuda diagram comparing the East Hill suite with the Oslo alkaline province (Neumann 1980; Andersen & Sørensen 1993), both normalized to the primitive mantle (PM). PM data from McDONOUGH (2001).

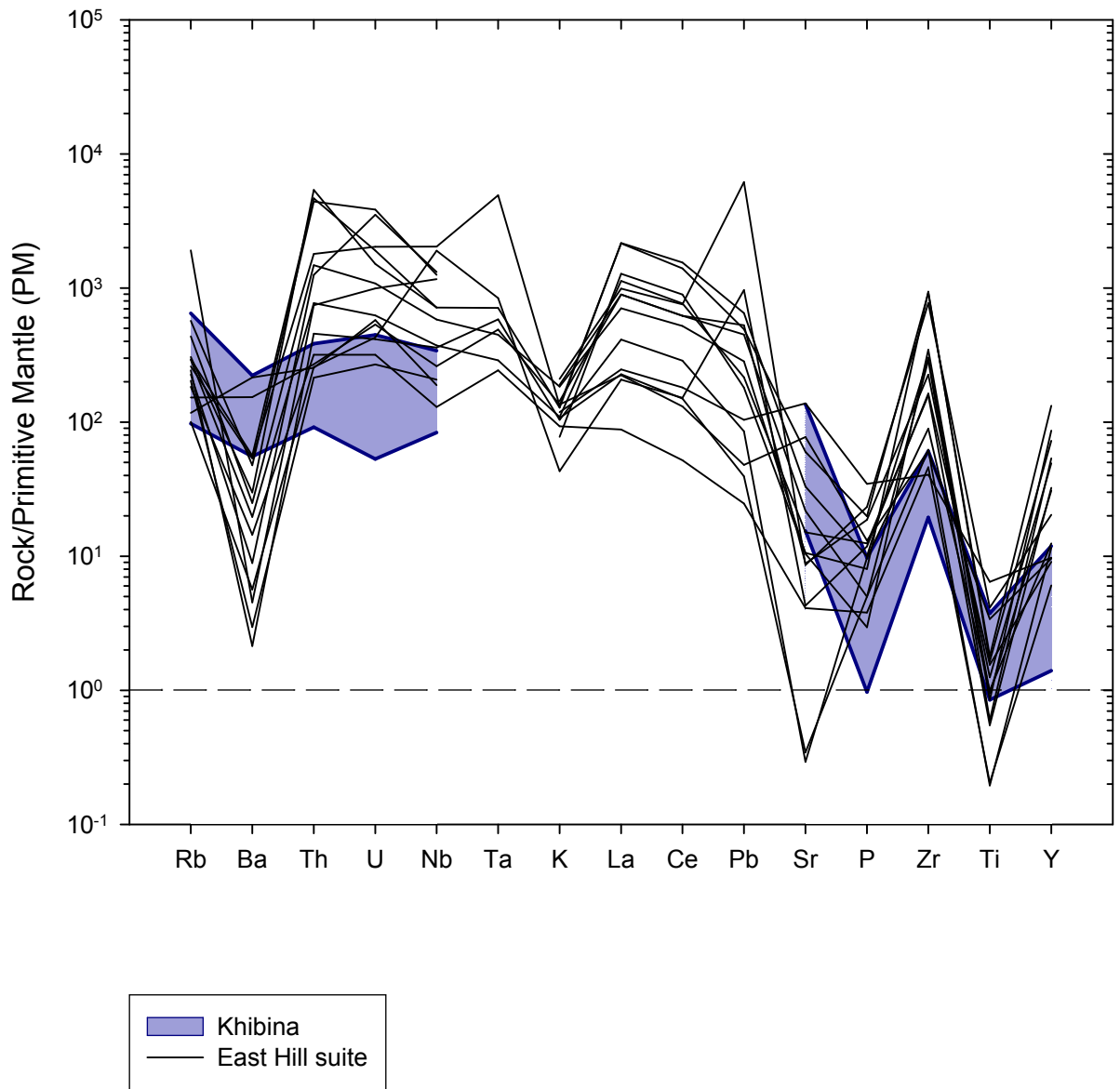


FIGURE 49 – Coryell-Masuda diagram comparing the East Hill suite with the Khibina intrusion (Arzamastsev *et al.* 2008), both normalized to the primitive mantle (PM). PM data from MCDONOUGH (2001).



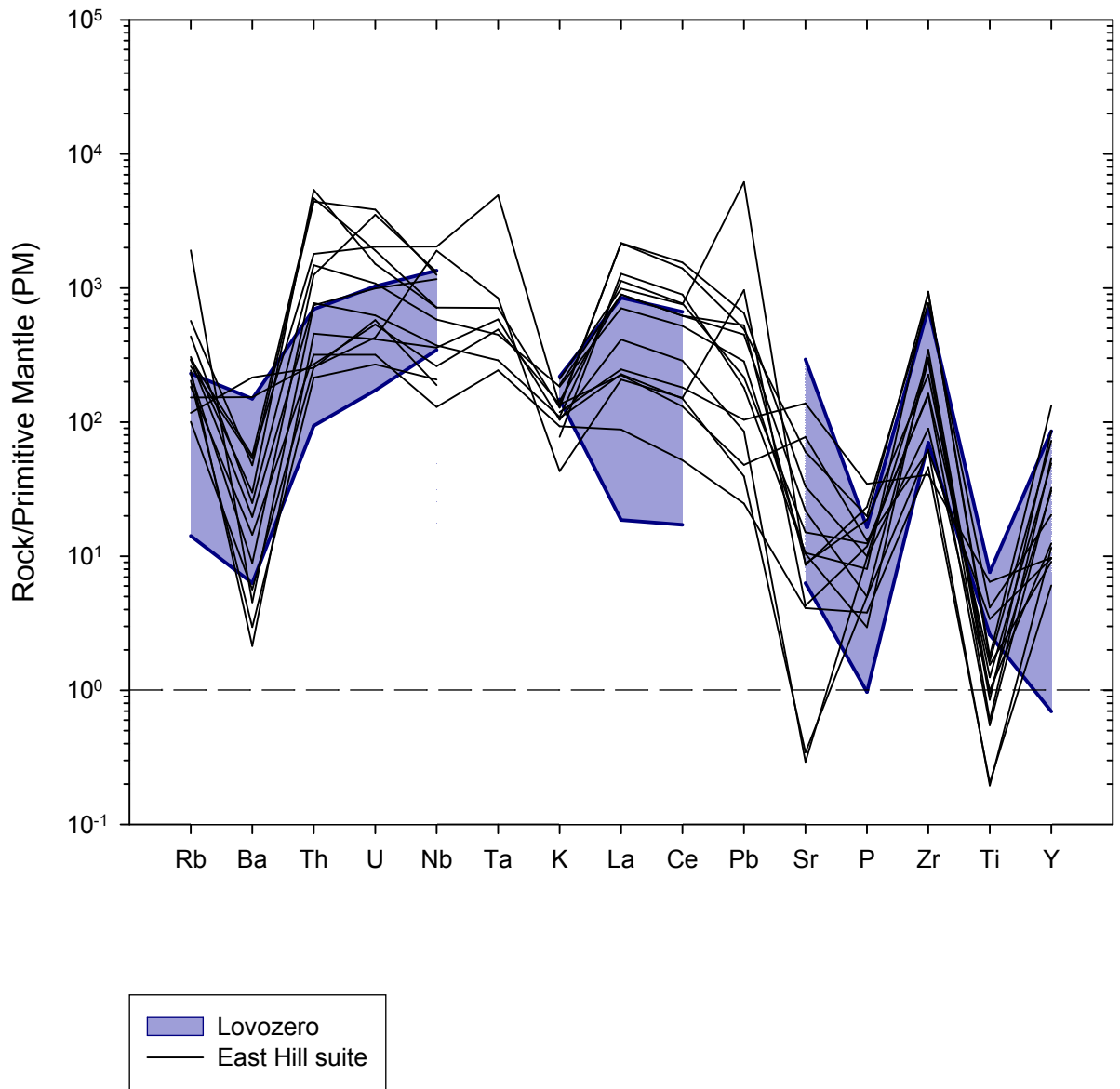


FIGURE 50 – Coryell-Masuda diagram comparing the East Hill suite with the Lovozero intrusion (Arzamastsev *et al.* 2001), both normalized to the primitive mantle (PM). PM data from MCDONOUGH (2001).

The Oslo and North Nyasa provinces are notably less enriched in trace elements than the East Hill suite and the intrusions already discussed. The trace element profiles of both the Oslo province and the Kasungu and Chipala intrusions are much flatter and, by individual elements, have narrower ranges of abundances than all of the other intrusions under consideration. The Ilomba and Ulindi intrusions show more of the anomalies of the other intrusions and exhibit a very broad range of abundances; also, these intrusions have a notable positive U anomaly. Even though they show other signs of greater magmatic evolution and trace element enrichment, the Ilomba and Ulindi intrusions are enriched in Ba and are, in fact, Y-depleted.

## MONT SAINT-HILAIRE, EAST HILL SUITE – MINERALOGY

### INTRODUCTION

The Mont Saint-Hilaire igneous complex is justifiably famous as a ripe hunting ground for mineral collectors and mineralogists alike. Several hundred mineral species have been documented, many of them new to science and most from alkaline environments. Perhaps owing to this sampling bias, and in spite of statements to the contrary (*e.g.* Currie *et al.* 1986), the general mineralogy of the East Hill suite commonly is perceived as peralkaline in nature, in line with that of Khibina, for example. On the contrary, the mineralogy of the nepheline melasyenite, which constitutes most of the volume of the East Hill suite, is geochemically borderline-alkaline, and a large proportion of the exotic minerals are restricted to peralkaline microenvironments in pegmatites and late-stage syenoids. (Currie *et al.* 1986; Mandarino & Anderson 1989)

The mineralogy of the East Hill suite (Table 12) is characterized by several geochemical shifts through the emplacement history of the suite: calcium- to sodium-dominant ferromagnesian minerals, calcium- to sodium-dominant titano- and zirconosilicates, oxide- to sulfide-dominant opaque minerals, and the late-stage emergence of carbonates, sulfates, and silica-enriched aluminosilicates as accessory phases. Numerous subsolidus reactions are evident, most prominently the wholesale replacement of nepheline by sodalite. Also, a subtle but geochemically important feature of the East Hill suite is the pervasive presence of microsulfides.

This study is not intended as an encyclopedic review of East Hill suite mineralogy; rather, it is a catalogue of such minerals as would be encountered by an informal survey of each lithology in hand-specimen and thin-section. Provisional identifications were refined with the SEM, XRD, and electron microprobe, but the thesis of the mineralogical study was to characterize the fundamental mineralogy and geochemistry of the East Hill suite.

TABLE 12 – Mineral survey catalogue – East Hill suite

<i>Mineral</i>	<i>Nepheline Melasyenite</i>	<i>Nepheline Leucosyenite</i>			<i>Eudialyte Syenite</i>	<i>Feldspar- Aegirine Dikes</i>	<i>Annite Lamprophyre</i>
		<i>Type 1</i>	<i>Type 2</i>	<i>Type 3</i>			
<b><i>amphiboles</i></b>							
<i>calcic amphibole group</i>	M	–	–	–	–	–	–
ferro-edenite	t	–	–	–	–	–	–
hastingsite	M	–	–	–	–	–	–
kaersutite (?)	t	–	–	–	–	–	–
magnesiohastingsite	◇	–	–	–	–	–	–
<i>sodic amphibole group</i>	–	t	–	–	m	–	◇
arfvedsonite	–	t	–	–	–	–	–
ferro-eckermannite	–	–	–	–	m	–	–
riebeckite	–	–	–	–	–	–	◇
<i>sodic-calcic amphibole group</i>	M	–	–	–	–	–	–
ferrichterite	t	–	–	–	–	–	–
katophorite	◇	–	–	–	–	–	–
magnesiotalamite	m	–	–	–	–	–	–
taramite	M	–	–	–	–	–	–
<b><i>carbonates</i></b>							
calcite	–	–	m	◇	◇	t	m
dawsonite	–	–	m	–	–	–	–
rhodochrosite	–	–	–	–	–	–	◇
siderite	–	–	m	–	–	–	–
<b><i>rare-earth carbonates</i></b>							
ancylite-(Ce)	–	–	–	–	◇	t	–
calcioancylite-(Ce)	–	–	–	◇	◇	–	◇
synchysite-(Ce)	–	–	◇	–	–	–	◇
<b><i>feldspars</i></b>							
<i>alkali feldspar group</i>	M	M	M	M	M	M	–
albite	M	m	M	m	t	M	–
microcline	–	M	M	M	M	M	–
orthoclase	M	–	–	–	–	–	–

TABLE 12 (CONT'D.)

<b>feldspathoids &amp; zeolites</b>	<i>Neph. Mel.</i>	<i>Leu. 1</i>	<i>Leu. 2</i>	<i>Leu. 3</i>	<i>Eud. Sy.</i>	<i>Feld.-Aeg.</i>	<i>Ann. Lamp.</i>
analcime	—	—	—	—	◇	—	—
cancrinite	t	—	—	◇	—	—	—
natrolite	m	m	m	M	M	t	M
nepheline	M	—	◇	◇	t	—	—
sodalite	t	—	—	—	—	—	◇
sodalite ps. nepheline	—	M	M	M	M	—	—
<b>halides</b>							
fluorite	t	◇	—	◇	t	—	—
halite	—	—	◇	—	—	—	—
<b>oxides &amp; hydroxides</b>							
baddeleyite	—	—	—	—	—	—	◇
böhmite	—	—	—	◇	—	—	◇
hematite	—	—	—	—	—	◇	—
hochelagaite	—	—	—	—	◇	—	—
ilmenite	◇	—	—	—	—	—	—
magnetite	m	—	—	—	—	—	—
pyrochlore	—	—	◇	◇	◇	t	t
pyrophanite	—	—	—	—	—	t	—
rutile	—	—	◇	—	—	—	—
thorianite (?)	◇	—	—	◇	—	—	—
<b>phosphates &amp; sulfates</b>							
barite	—	—	—	◇	—	—	—
fluorapatite	m	◇	◇	◇	◇	—	M
rhabdophane-(Ce)	—	—	—	—	—	—	◇
<b>pyroxenes</b>							
<i>pyroxene group</i>	M	m	t	M	M	M	m
aegirine	—	m	t	M	M	M	m
aegirine-augite	M	—	—	t	M	—	◇
augite	M	—	—	◇	—	—	—
titanaugite	m	—	—	—	—	—	—
<b>sulfides</b>							
acanthite (?)	—	—	—	—	◇	—	—
alabandite (?)	—	◇	—	—	—	—	—
arsenopyrite	—	◇	—	—	—	—	—
chalcopyrite	—	—	—	—	t	—	—
covellite	—	—	—	—	t	—	—
galena	◇	—	◇	—	t	◇	◇
molybdenite	—	—	◇	◇	—	—	—
pyrite	t	t	t	—	t	—	◇
sphalerite	◇	◇	t	◇	t	—	t

TABLE 12 (CONT'D.)

<b><i>titanosilicates</i></b>	<i>Neph. Mel.</i>	<i>Leu. 1</i>	<i>Leu. 2</i>	<i>Leu. 3</i>	<i>Eud. Sy.</i>	<i>Feld.-Aeg.</i>	<i>Ann. Lamp.</i>
kupletskite	–	◇	–	◇	t	–	–
titanite	m	–	–	–	–	–	–
<b><i>zirconosilicates</i></b>							
calciohilairite	◇	–	–	–	–	–	–
catapleiite	–	–	–	–	t	–	–
<i>eudialyte group</i>	–	–	–	–	m	–	–
eudialyte	–	–	–	–	m		–
ferrokentbrooksite	–	–	–	–	t	–	–
gaidonnayite	–	–	–	–	◇	–	t
hilairite	–	–	–	–	–	–	t
lâvenite	◇	–	–	–	–	–	–
petarasite	–	–	–	–	–	–	t
zircon	–	–	t	–	–	◇	–
<b><i>other silicates</i></b>							
almandine	–	–	t	–	–	–	–
annite	m	–	–	–	–	t	M
<i>pectolite-sérandite series</i>	–	t	–	t	m	–	–
pectolite	–	t	–	–	–	–	–
sérandite	–	t	–	t	m	–	–
thorogummite	–	–	◇	–	◇	–	–
(M) major mineral (>10.0 modal%), (m) minor mineral (1.0-10.0%), (t) trace mineral (0.1-1.0%), (◇) rare mineral (<0.1% or was only found as one or two crystals) & (–) not observed							

## IDENTIFIED MINERAL SPECIES

### AMPHIBOLE GROUP

#### *Calcic Amphibole Group*

Ferro-edenite,  $\text{NaCa}_2\text{Fe}_5^{2+}\text{Si}_7\text{AlO}_{22}(\text{OH})_2$

Hastingsite,  $\text{NaCa}_2(\text{Fe}_4^{2+}\text{Fe}^{3+})\text{Si}_6\text{Al}_2\text{O}_{22}(\text{OH})_2$

Kaersutite,  $\text{NaCa}_2(\text{Mg}_4\text{Ti})\text{Si}_6\text{Al}_2\text{O}_{23}(\text{OH})$

Magnesiohastingsite,  $\text{NaCa}_2(\text{Mg}_4\text{Fe}^{3+})\text{Si}_6\text{Al}_2\text{O}_{22}(\text{OH})_2$

#### *Sodic-Calcic Amphibole Group*

Ferrorichterite,  $\text{Na}(\text{CaNa})\text{Fe}_5^{2+}\text{Si}_8\text{O}_{22}(\text{OH})_2$

Katophorite,  $\text{Na}(\text{CaNa})\text{Fe}_4^{2+}(\text{Al}, \text{Fe}^{3+})\text{Si}_7\text{AlO}_{22}(\text{OH})_2$

Magnesiotaramite,  $\text{Na}(\text{CaNa})\text{Mg}_3\text{AlFe}^{3+}\text{Si}_6\text{Al}_2\text{O}_{22}(\text{OH})_2$

Taramite,  $\text{Na}(\text{CaNa})\text{Fe}_3^{2+}\text{AlFe}^{3+}\text{Si}_6\text{Al}_2\text{O}_{22}(\text{OH})_2$

#### *Sodic Amphibole Group*

Arfvedsonite,  $\text{NaNa}_2(\text{Fe}_4^{2+}\text{Fe}^{3+})\text{Si}_8\text{O}_{22}(\text{OH})_2$

Ferro-eckermannite,  $\text{NaNa}_2(\text{Fe}_4^{2+}\text{Al})\text{Si}_8\text{O}_{22}(\text{OH})_2$

Riebeckite,  $\square\text{Na}_2\text{Fe}_3^{2+}\text{Fe}_2^{3+}\text{Si}_8\text{O}_{22}(\text{OH})_2$

## *Overview of Speciation*

A variety of members of the amphibole group are found in the East Hill Suite. This report follows the nomenclature of the IMA CNMMN Amphibole Subcommittee reports on amphibole classification (IMA97 & IMA03) (Leake *et al.* 1997 & 2003). Under this scheme, amphiboles have been sorted into five groups: the Mg-Fe-Mn-Li Group, the Calcic Group, the Sodic-Calcic Group, the Sodic Group, and the Na-Ca-Mg-Fe-Mn-Li Group (officially alternately termed Group 5). The East Hill Suite hosts amphiboles from the Calcic Group (ferro-edenite, hastingsite, kaersutite & magnesiohastingsite), the Sodic-Calcic Group (ferrorichterite, magnesiotaramite & taramite), and the Sodic Group (arfvedsonite, ferro-eckermannite & riebeckite).

With regard to each of these groups, a selection of amphiboles from a single lithology, while being similar in physical properties, optics, and general chemistry, may plot, *sensu stricto*, as numerous amphibole species. As speciation is based on gradations of chemistry along a lengthy continuum, the numerous “end-member” compositions within amphibole groups are not necessarily so mutually different in chemical character nor in petrologic significance as, say, the end-members of the olivine group. It is prudent, therefore, to acknowledge the similarities between species common to a group rather than to focus strictly on their differences. In doing so, the nomenclature of the amphiboles may be a powerful tool for expressing chemical variation on a single theme, rather than a noisome maze, fraught with niggling distinctions. In terms of the IMA scheme, then, one should recognize amphiboles by their groups first, then look to the subtle differences within. In keeping with this philosophy, amphiboles from the East Hill Suite are listed in this section by their IMA97/IMA03 group.



### *Nepheline Melasyenite*

Minerals of the calcic amphibole group collectively occur as a major mineral group in this syenite. Ferro-edenite is a rare mineral in the nepheline melasyenite, occurring as a 250  $\mu\text{m}$  subhedral crystal, enclosed by orthoclase. As it is the only positively identified specimen of ferro-edenite, it was not possible to fully characterize its pleochroism, but as it is oriented with its crystallographic axes oblique to the plane of the thin section, it was possible to approximate the colors associated with two indicatrix axes:  $Y = \text{tan}$  and  $Z = \text{grass green}$ . Identification was by examination in the petrographic microscope (habit and pleochroism) and electron microprobe analysis.

Hastingsite is a major mineral in this syenite, in which it occurs as black, subhedral prismatic crystals, usually to 1 mm in length, but up to 1 cm. The smallest and the largest crystals are anhedral and tend to be free of inclusions. Crystals close to 1 mm in size are subhedral but are poikilitic, enclosing nepheline and orthoclase, and are interstitial along their margins to the same. Hastingsite is strongly pleochroic:  $X = \text{greenish tan}$ ;  $Y = \text{amber}$ ;  $Z = \text{olive green to teal blue}$ . Hastingsite is associated with nepheline, orthoclase, magnetite, titanite, aegirine-augite, and annite; it is not associated with titanaugite, in contrast to taramite, with which it may be easily confused. Initial identification as an amphibole was based on examination in the petrographic microscope, but speciation ultimately relied on electron microprobe data.

Kaersutite is tentatively identified as a trace mineral in the nepheline melasyenite. It is present as a portion of a crystal of taramite that mantles a titanaugite individual. It does not present any substantially different appearance in thin section, as compared to the taramite and was only detected by electron microprobe analysis. It is possible that the kaersutite composition

of the analysis is the result of simultaneous electron beam interaction with the taramite and the titanaugite. Kaersutite is a calcium- and magnesium-rich amphibole with essential titanium. Taramite, on the other hand, is a sodium- and iron-rich amphibole. As the zone of kaersutite is so close to the titanaugite crystal, if the electron-beam interaction volume penetrated the titanaugite and the taramite at the same time, calcium, magnesium, and titanium from the titanaugite could spuriously drift the taramite analysis towards kaersutite.

Magnesiohastingsite is a rare mineral in this syenite, occurring in two crystals. It is found as an overgrowth on augite, and it occurs as a distal portion of a prominently zoned amphibole crystal that is an overgrowth on and near-total replacement of a titanaugite crystal. This is the only instance seen in which an amphibole of hastingsitic composition is found near titanaugite, but it is preceded in paragenesis by magnesiotaramite, as is to be expected. Magnesiohastingsite cannot be visually distinguished from hastingsite.

Representative analyses of calcic amphibole minerals are listed in TABLES 13 & 14. The ferrous/ferric ratio was determined colorimetrically using the metavanadate technique of WILSON (1960). Most calcic amphiboles from the nepheline melasyenite have hastingsitic compositions (Figure 51); several high-Ti calcic amphiboles plot as kaersutite (Figure 52). Calcic amphibole compositions in the nepheline melasyenite are enriched in  $\text{Fe}^{3+}$ , K, Mn, and Ti, less so in Zr. Hastingsite specimens exhibit the same K, Mn, and Ti enrichment, though to a greater extent and are also enriched in Ce and Zn. About 50% of the calcic amphibole analyses contain sufficient K to be termed potassian; about 25% of the analyses, excluding kaersutitic compositions, contain sufficient Ti to be termed titanian; and a further 25% of the analyses are kaersutite. Nearly all calcic amphibole analyses, excluding kaersutitic compositions, recalculate to the ferri- analogue of the particular species. Fluorine tends to exceed chlorine in all species, and although in no

TABLE 13 – Representative electron microprobe analyses of calcic amphiboles – Nepheline Melasyenite

Lithology:	<i>Nepheline Melasyenite</i>					
Sample:	<i>MSH-B-8</i>					
Target:	<i>5n</i>	<i>7a</i>	<i>7c</i>	<i>23e</i>	<i>11r</i>	<i>12h</i>
SiO <sub>2</sub> (wt. %)	44.07	41.45	38.67	40.40	38.52	42.78
TiO <sub>2</sub>	0.57	1.97	2.02	2.34	11.79	1.75
ZrO <sub>2</sub>	0.14	0.06	0.39	0.18	0.28	0.04
Al <sub>2</sub> O <sub>3</sub>	6.84	9.41	9.36	9.64	7.81	10.55
REE <sub>2</sub> O <sub>3</sub>	0.00	0.84	0.51	0.84	0.00	0.00
Ce <sub>2</sub> O <sub>3</sub>	0.00	0.84	0.51	0.84	0.00	0.00
FeO <sub>tot</sub>	22.60	25.65	22.75	23.71	17.07	18.16
MnO	1.48	1.91	1.71	1.82	1.21	1.40
MgO	4.98	4.79	4.89	5.63	5.61	7.29
ZnO	0.00	0.64	0.54	0.84	0.00	0.00
CaO	9.60	9.47	9.40	9.25	11.90	9.52
Na <sub>2</sub> O	3.41	3.45	3.25	3.80	2.84	4.88
K <sub>2</sub> O	0.84	1.74	1.68	1.68	1.05	1.92
Cl	0.38	0.10	0.49	0.29	na	0.36
F	0.80	0.38	0.41	0.65	na	2.00
O≡Cl	-0.09	-0.02	-0.11	-0.07	na	-0.08
O≡F	-0.34	-0.16	-0.17	-0.27	na	-0.84
SUM	95.28	101.67	95.79	100.74	98.09	99.71
Species:	<i>fluorian ferri-ferro- edenite</i>	<i>potassian ferrihastingsite</i>	<i>potassian ferrihastingsite</i>	<i>fluorian potassian titanian ferrihastingsite</i>	<i>ferri kaersutite</i>	<i>fluorian ferrimagnesio hastingsite</i>
FeO/FeO <sub>tot</sub>	0.51	0.51	0.51	0.51	0.51	0.51
Fe <sub>2</sub> O <sub>3</sub>	12.31	13.97	12.39	12.91	9.30	9.89
FeO	11.52	13.08	11.60	12.09	8.71	9.26
NEW SUM	96.51	103.90	97.53	102.87	99.02	100.70
$\frac{\text{Mg}}{(\text{Mg}+\text{Fe}^{2+})}$	0.43	0.39	0.43	0.45	0.53	0.58
$\frac{\text{Mg}}{(\text{Mg}+\text{Fe}^{2+}+\text{Mn}^{2+})}$	0.41	0.36	0.40	0.42	0.50	0.55
Recalculated according to the scheme of LEAKE <i>ET AL.</i> (1997 & 2003) Normalized to 23 oxygen <i>apfu</i> na = not analyzed OH site-occupancy calculated by difference Fe <sup>3+</sup> estimated by wet-chemical analysis (Wilson 1960)						

TABLE 14 – Site-occupancies of calcic amphiboles from TABLE 13 – Nepheline Melasyenite

Lithology:	<i>Nepheline Melasyenite</i>					
Sample:	<i>MSH-B-8</i>					
Target:	<i>5n</i>	<i>7a</i>	<i>7c</i>	<i>23e</i>	<i>11r</i>	<i>12h</i>
<i>T-site</i>						
Si	6.870	6.209	6.147	6.117	5.822	6.390
<sup>iv</sup> Al	1.130	1.661	1.754	1.720	1.392	1.610
<sup>iv</sup> Ti	0.000	0.130	0.099	0.163	0.787	0.000
Σ[T]	<i>8.000</i>	<i>8.000</i>	<i>8.000</i>	<i>8.000</i>	<i>8.000</i>	<i>8.000</i>
<i>C-site</i>						
<sup>vi</sup> Al	0.127	0.000	0.000	0.000	0.000	0.247
<sup>vi</sup> Ti	0.067	0.092	0.142	0.104	0.553	0.196
Zr	0.010	0.004	0.030	0.013	0.021	0.003
Fe <sup>3+</sup>	1.443	1.575	1.482	1.471	1.057	1.111
Fe <sup>2+</sup>	1.502	1.639	1.542	1.531	1.100	1.157
Mn <sup>2+</sup>	0.195	0.242	0.230	0.233	0.155	0.177
Mg	1.156	1.070	1.158	1.271	1.264	1.622
Zn	0.000	0.070	0.064	0.094	0.000	0.000
Σ[C]	<i>4.501</i>	<i>4.692</i>	<i>4.648</i>	<i>4.718</i>	<i>4.150</i>	<i>4.513</i>
<i>B-site</i>						
Fe <sup>2+</sup>	0.000	0.000	0.000	0.000	0.000	0.000
Mn <sup>2+</sup>	0.000	0.000	0.000	0.000	0.000	0.000
Mg	0.000	0.000	0.000	0.000	0.000	0.000
Ca	1.603	1.519	1.601	1.500	1.927	1.524
Na	0.397	0.481	0.399	0.500	0.073	0.476
Σ[B]	<i>2.000</i>	<i>2.000</i>	<i>2.000</i>	<i>2.000</i>	<i>2.000</i>	<i>2.000</i>
<i>A-site</i>						
Na	0.632	0.522	0.604	0.616	0.759	0.937
K	0.168	0.332	0.340	0.325	0.201	0.366
Σ[A]	<i>0.800</i>	<i>0.855</i>	<i>0.944</i>	<i>0.941</i>	<i>0.961</i>	<i>1.303</i>
<i>OH-Site</i>						
Cl	0.100	0.025	0.132	0.074	na	0.091
F	0.394	0.180	0.206	0.311	na	0.945
OH	1.505	1.795	1.662	1.614	2.000*	0.964
Σ[OH]	<i>2.000</i>	<i>2.000</i>	<i>2.000</i>	<i>2.000</i>	<i>2.000*</i>	<i>2.000</i>
Recalculated according to the scheme of LEAKE <i>ET AL.</i> (1997 & 2003) Normalized to 23 oxygen <i>apfu</i> na = not analyzed OH site-occupancy calculated by difference (* - by default) Fe <sup>3+</sup> estimated by wet-chemical analysis (Wilson 1960)						

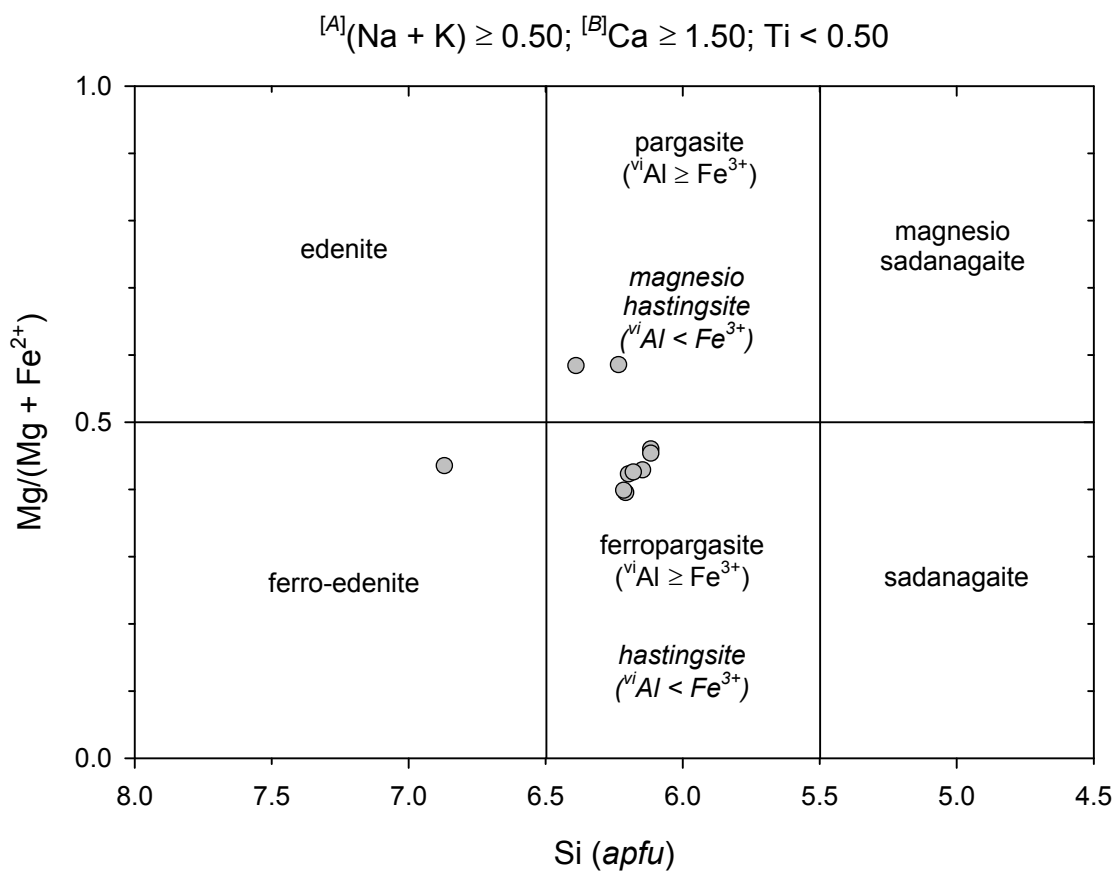


FIGURE 51 – Calcic amphibole compositions – Nepheline Melasyenite

$$^{[A]}(\text{Na} + \text{K}) \geq 0.50; ^{[B]}\text{Ca} \geq 1.50; \text{Ti} \geq 0.50$$

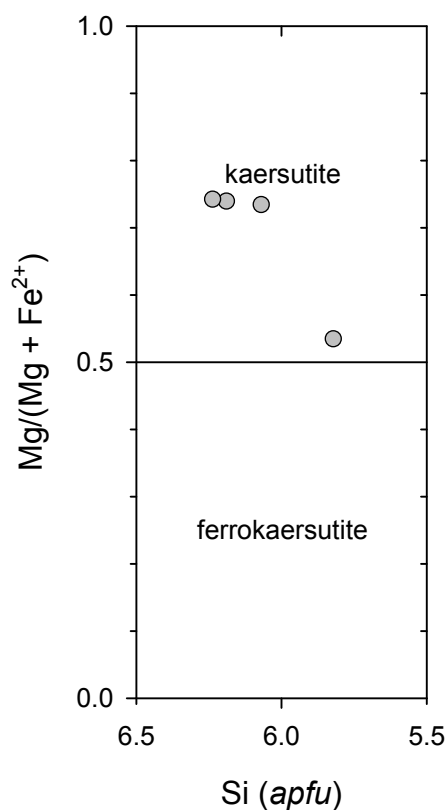


FIGURE 52 – High-Ti calcic amphibole compositions – Nepheline Melasyenite

analysis was F the dominant *OH*-site anion, about 30% of calcic amphibole analyses are fluorian amphiboles.

Application of the calcic amphibole geothermobarometer of ERNST & LIU (1998) to compositions from the nepheline melasyenite indicates the approximate temperature and pressure of crystallization of these phases. As a general rule, ERNST & LIU (1998) conclude that calcic amphibole equilibrium temperature is directly related to *apfu* Si; therefore, for example, a transition from edenitic to hastingsitic to sadanagaïtic compositions represents decreasing temperature (Figure 53). For the likely pressure range of the East Hill suite suggested by

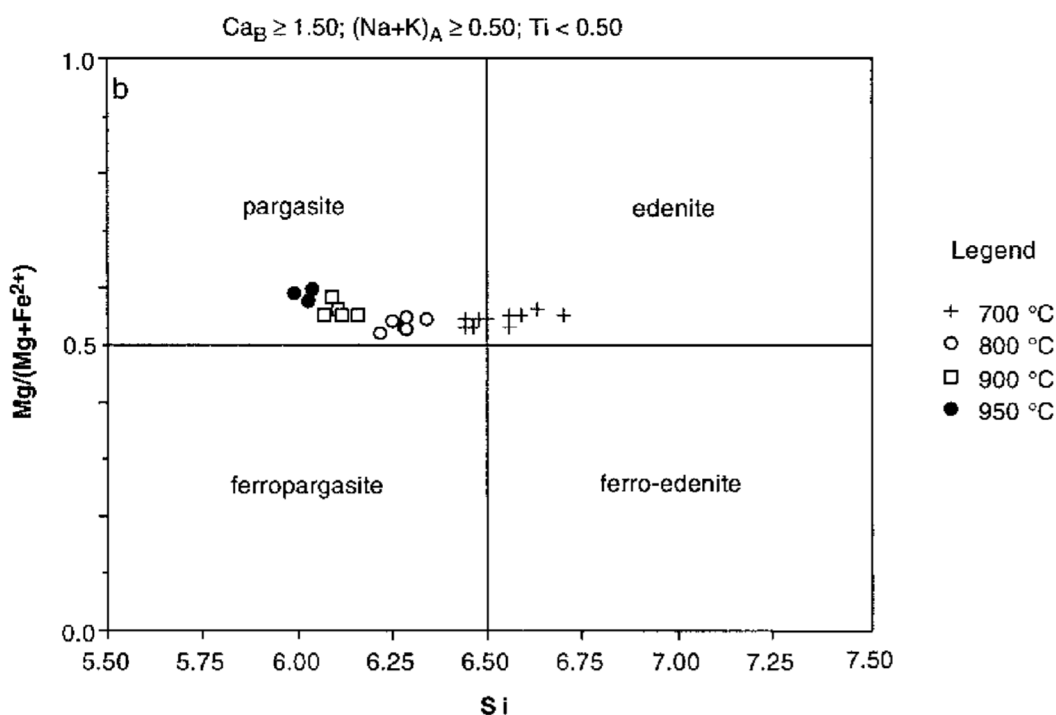


FIGURE 53 – Compositional variation of synthetic calcic amphiboles as a function of temperature. Data from LIU (1997). (Ernst & Liu 1998)

GREENWOOD & EDGAR (1984), 1 to 2.5 kbar, the dominance of hastingsitic compositions indicates maximum amphibole temperatures in the 800-900°C range.

According to experimental results from ERNST & LIU (1998), site-occupancy of <sup>iv</sup>Al in nepheline melasyenite calcic amphiboles (Figure 54) indicates a crystallization temperature range of ~650-875°C, with most analyses in the 775-825°C range. Content of Al<sub>2</sub>O<sub>3</sub> and TiO<sub>2</sub> (Figures 55 & 56) both yield similar temperatures and a pressure range of 1 to 2.5 kbar, the pressure range consistent with that of GREENWOOD & EDGAR (1984).

Minerals of the sodic-calcic amphibole group collectively occur as a major mineral group in the nepheline melasyenite. Ferrichterite is a trace mineral in the nepheline melasyenite. It occurs as a 50 µm anhedral crystal, associated with taramite overgrowing a titanaugite crystal. It

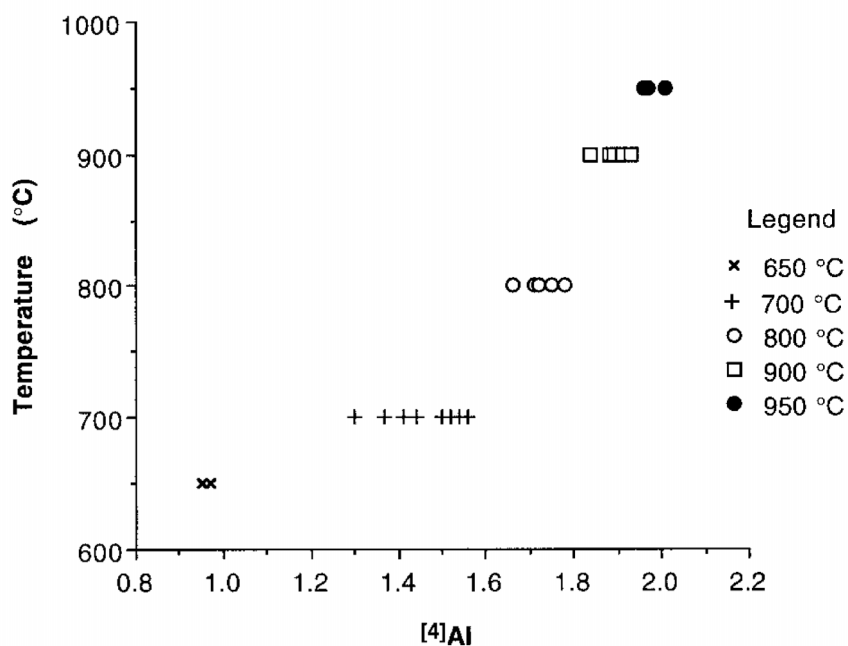


FIGURE 54 – <sup>iv</sup>Al content of synthetic calcic amphiboles as a function of temperature. Data from LIU (1997). (Ernst & Liu 1998)

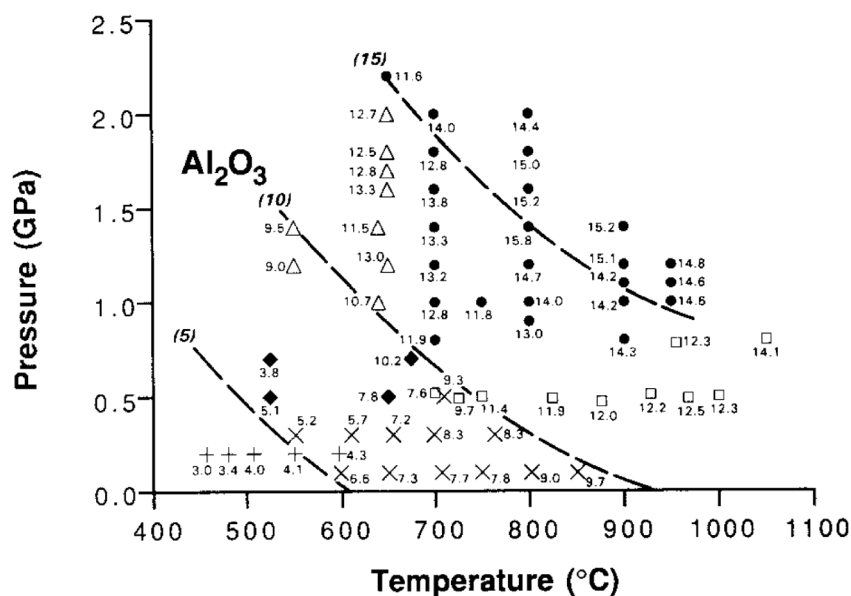


FIGURE 55 –  $\text{Al}_2\text{O}_3$  (wt.%) content of synthetic calcic amphiboles as a function of pressure and temperature. Data from: (□) – HELZ (1973 & 1979), (+) – LIU *ET AL.* (1974), (x) – SPEAR (1981), (◆) – APTED & LIU (1983), (△) – POLI (1993), (●) – ERNST & LIU (1998). (Ernst & Liu 1998)



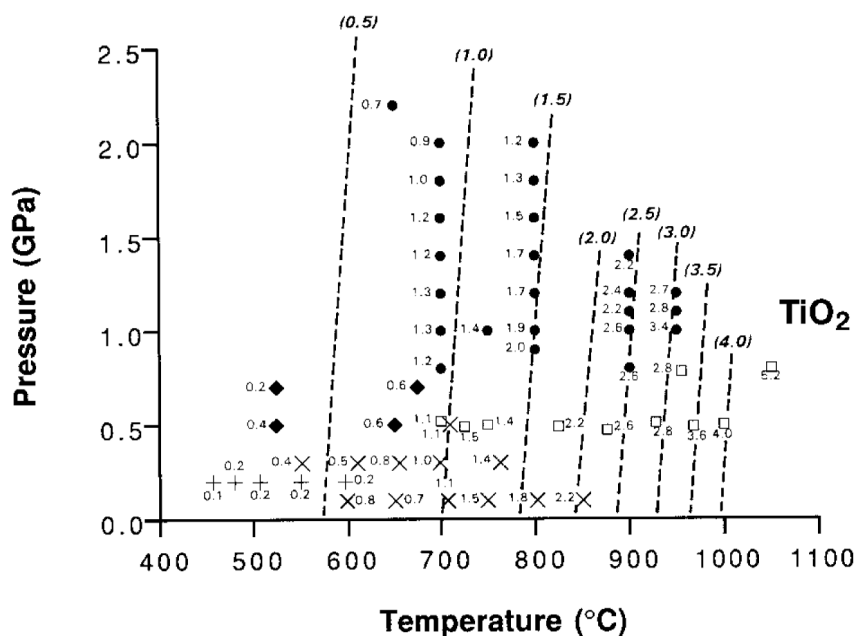


FIGURE 56 – TiO<sub>2</sub> (wt.%) content of synthetic calcic amphiboles as a function of pressure and temperature. Data from: (□) – HELZ (1973 & 1979), (+) – LIOU *ET AL.* (1974), (x) – SPEAR (1981), (◆) – AP TED & LIOU (1983), (●) – ERNST & LIU (1998). (Ernst & Liu 1998)

is strongly pleochroic between straw yellow and a grayish blue-green, but it was not possible to associate either color with a particular indicatrix axis. Identification was primarily on the basis of electron microprobe analysis, but the more distinctive pleochroic colors (with respect to other amphibole group minerals) of ferrichterite lent supporting evidence.

Katophorite is a rare mineral in this syenite, occurring as a narrow overgrowth on a taramite crystal. Katophorite cannot be visually distinguished from taramite, and identification was strictly by electron microprobe analysis.

Magnesiotaramite is a minor mineral in this syenite. It occurs as regions of transitional chemistry in zoned amphibole crystals that overgrow and replace titanaugite crystals. One noteworthy occurrence is as the primary, and proximal, portion of an overgrowth on a nearly completely replaced titanaugite crystal. The amphibole overgrowth is prominently zoned and grades from magnesiotaramite to magnesiohastingsite. Viewed with crossed polars, the

amphibole exhibits splendid symmetrical sweeping extinction parallel to the prism faces of the relic titanaugite crystal. Similarly, its pleochroism varies axially and systematically from the centerline to the margin, most notably from the *Z*=olive green of taramite to the *Z*=teal blue of hastingsite. In all respects but its composition, magnesiotaramite resembles taramite, and the two minerals cannot be visually distinguished. Identification was based on electron microprobe analysis.

Taramite is a major mineral in the nepheline melasyenite. Similarly to hastingsite, it is present as black, subhedral prismatic crystals, usually to 1 mm in length, but up to 1 cm. The smallest and the largest crystals are anhedral and tend to be free of inclusions. Crystals close to 1 mm in size are subhedral but are poikilitic, enclosing nepheline and orthoclase, and are interstitial along their margins to the same. Taramite is pleochroic: *X*=amber green, *Y*=amber olive green, *Z*=olive green. Taramite is closely associated with titanaugite. It is found as overgrowths on titanaugite, either directly in contact or as an overgrowth to an aegirine-augite mantle around titanaugite, to 0.5 mm in thickness. When found as an overgrowth on titanaugite, it may include small crystals of magnetite; if the titanaugite is completely replaced by taramite, the taramite will carry a cluster of magnetite crystals in the shape of the original titanaugite. Taramite also occurs as isolated crystals, always situated within 1 mm of a titanaugite crystal.

Representative analyses of sodic-calcic amphibole minerals are listed in TABLES 15 & 16. The ferrous/ferric ratio was determined colorimetrically using the metavanadate technique of WILSON (1960). Most sodic-calcic amphiboles from the nepheline melasyenite have taramitic compositions (Figure 57). Sodic-calcic amphibole compositions in the nepheline melasyenite are enriched in Ce, Fe<sup>3+</sup>, K, Mn, Ti, and Zn, with sporadic Zr. Nearly all of the sodic-calcic

amphibole analyses contain sufficient K to be termed potassian; about 10% contain sufficient K to be termed potassic. Overall, the sodic-calcic amphiboles are more K rich than the calcic amphiboles, with average  $^{[4]}\text{K}$  site-occupancies of 0.218 and 0.353 for the calcic and sodic-calcic amphiboles, respectively. Approximately 20% of the analyses contain sufficient Mn to be termed manganoan. About 20% of the analyses contain sufficient Ti to be termed titanian, and about 5% recalculate as titano-amphiboles. Although Zr enrichment is variable, one sample exhibits 1.38 wt.%  $\text{ZrO}_2$ , an exceptional tenor even in peralkaline complexes, exceeding maximum concentrations from Ilímaussaq and Motzfeldt (Larsen 1976; Jones 1980) and perhaps second only to Igaliko. (Pearce 1989) Nearly all sodic-calcic amphibole analyses recalculate to the ferri- analogue of the particular species. Fluorine tends to exceed chlorine in all species, and although in no analysis was F the dominant *OH*-site anion, about 20% of sodic-calcic amphibole analyses are fluorian amphiboles.

Using the experimental data of ERNST & LIU (1998), extrapolation of the  $^{\text{iv}}\text{Al}$  content of the ferrichterite yields a crystallization temperature of approximately 600°C. CHARLES (1975 & 1977) examined the thermal stability of the richterite–ferrichterite series up to 7 kbar and found that the richterite series gradually decomposes to pyroxene + olivine ± magnetite + melt + vapor as either isothermal oxygen fugacity or isobaric temperature rises too high. The absolute upper limit of thermal stability for near end-member ferrichterite is  $730 \pm 10^\circ\text{C}$  at the QFM buffer, dropping to  $550 \pm 20^\circ\text{C}$  at the HM buffer; but these values represent the temperatures at which the decomposition reaction goes to completion. The ferrichterite in the nepheline melasyenite shows no signs of decomposition, therefore  $f_{\text{O}_2}$  must have been below the minimum decomposition fugacity. For the estimated crystallization temperature, this corresponds to  $f_{\text{O}_2} = 10^{-22}$  bar, below the QFM buffer at 600°C.

TABLE 15 – Representative electron microprobe analyses of sodic-calcic amphiboles – Nepheline Melasyenite

Lithology:	<i>Nepheline Melasyenite</i>					
Sample:	<i>MSH-B-8</i>					
Target:	<i>12f</i>	<i>8h</i>	<i>11j</i>	<i>14f</i>	<i>15e</i>	<i>16e</i>
SiO <sub>2</sub> (wt. %)	43.94	40.96	41.68	41.76	42.26	41.84
TiO <sub>2</sub>	1.79	1.71	2.52	1.56	1.40	2.21
ZrO <sub>2</sub>	0.00	0.23	0.09	0.00	0.00	0.00
Al <sub>2</sub> O <sub>3</sub>	10.67	8.70	10.01	8.07	9.03	9.65
REE <sub>2</sub> O <sub>3</sub>	0.53	0.74	0.74	0.54	0.55	0.55
Ce <sub>2</sub> O <sub>3</sub>	0.53	0.74	0.74	0.54	0.55	0.55
FeO <sub>tot</sub>	18.51	25.07	23.17	24.91	27.72	26.85
MnO	1.42	1.92	1.80	1.85	1.91	1.93
MgO	7.27	4.54	5.79	5.37	4.35	4.93
ZnO	0.85	0.69	0.11	0.26	0.68	0.72
CaO	9.58	8.66	9.26	7.31	6.89	8.31
Na <sub>2</sub> O	5.08	3.46	3.45	4.28	5.05	4.00
K <sub>2</sub> O	1.98	1.63	1.84	1.74	1.79	1.50
Cl	0.26	0.32	0.30	0.27	0.26	0.00
F	0.49	0.48	1.80	0.37	0.78	0.00
O≡Cl	-0.06	-0.07	-0.07	-0.06	-0.06	0.00
O≡F	-0.21	-0.20	-0.76	-0.16	-0.33	0.00
SUM	102.08	98.83	101.72	98.05	102.28	102.49
Species:	<i>potassian ferrimagnesio- taramite</i>	<i>manganoan potassian ferritaramite</i>	<i>fluorian potassian titanian ferritaramite</i>	<i>potassian ferritaramite</i>	<i>fluorian potassian ferritaramite</i>	<i>potassian ferritaramite</i>
FeO/FeO <sub>tot</sub>	0.50	0.50	0.50	0.50	0.50	0.50
Fe <sub>2</sub> O <sub>3</sub>	10.28	13.93	12.88	13.84	15.40	14.92
FeO	9.25	12.54	11.59	12.45	13.86	13.42
NEW SUM	103.64	100.96	103.75	99.98	104.37	104.54
$\frac{\text{Mg}}{(\text{Mg}+\text{Fe}^{2+})}$	0.58	0.39	0.47	0.43	0.36	0.40
$\frac{\text{Mg}}{(\text{Mg}+\text{Fe}^{2+}+\text{Mn}^{2+})}$	0.55	0.36	0.44	0.40	0.33	0.36

Recalculated according to the scheme of LEAKE *ET AL.* (1997 & 2003)Normalized to 23 oxygen *apfu*

na = not analyzed

OH site-occupancy calculated by difference

Fe<sup>3+</sup> estimated by wet-chemical analysis (Wilson 1960)

TABLE 16 – Site-occupancies of sodic-calcic amphiboles from TABLE 15 – Nepheline Melasyenite

Lithology:	<i>Nepheline Melasyenite</i>					
Sample:	<i>MSH-B-8</i>					
Target:	<i>12f</i>	<i>8h</i>	<i>11j</i>	<i>14f</i>	<i>15e</i>	<i>16e</i>
<i>T-site</i>						
Si	6.389	6.311	6.216	6.433	6.316	6.181
<sup>iv</sup> Al	1.611	1.580	1.759	1.465	1.591	1.681
<sup>iv</sup> Ti	0.000	0.109	0.025	0.102	0.093	0.138
Σ[T]	<i>8.000</i>	<i>8.000</i>	<i>8.000</i>	<i>8.000</i>	<i>8.000</i>	<i>8.000</i>
<i>C-site</i>						
<sup>vi</sup> Al	0.218	0.000	0.000	0.000	0.000	0.000
<sup>vi</sup> Ti	0.195	0.090	0.257	0.078	0.064	0.107
Zr	0.000	0.018	0.006	0.000	0.000	0.000
Fe <sup>3+</sup>	1.125	1.615	1.445	1.604	1.732	1.659
Fe <sup>2+</sup>	1.125	1.615	1.445	1.604	1.732	1.659
Mn <sup>2+</sup>	0.175	0.251	0.227	0.241	0.242	0.242
Mg	1.575	1.041	1.288	1.232	0.969	1.084
Zn	0.091	0.078	0.012	0.030	0.075	0.079
Σ[C]	<i>4.505</i>	<i>4.708</i>	<i>4.680</i>	<i>4.790</i>	<i>4.815</i>	<i>4.829</i>
<i>B-site</i>						
Fe <sup>2+</sup>	0.000	0.000	0.000	0.000	0.000	0.000
Mn <sup>2+</sup>	0.000	0.000	0.000	0.000	0.000	0.000
Mg	0.000	0.000	0.000	0.000	0.000	0.000
Ca	1.492	1.429	1.479	1.207	1.103	1.316
Na	0.508	0.571	0.521	0.793	0.897	0.684
Σ[B]	<i>2.000</i>	<i>2.000</i>	<i>2.000</i>	<i>2.000</i>	<i>2.000</i>	<i>2.000</i>
<i>A-site</i>						
Na	0.924	0.462	0.477	0.486	0.565	0.461
K	0.366	0.319	0.350	0.341	0.342	0.283
Σ[A]	<i>1.291</i>	<i>0.781</i>	<i>0.827</i>	<i>0.827</i>	<i>0.907</i>	<i>0.744</i>
<i>OH-Site</i>						
Cl	0.064	0.084	0.076	0.070	0.066	0.000
F	0.225	0.234	0.849	0.180	0.369	0.000
OH	1.711	1.683	1.075	1.749	1.565	2.000
Σ[OH]	<i>2.000</i>	<i>2.000</i>	<i>2.000</i>	<i>2.000</i>	<i>2.000</i>	<i>2.000</i>
Recalculated according to the scheme of LEAKE <i>ET AL.</i> (1997 & 2003) Normalized to 23 oxygen <i>apfu</i> na = not analyzed OH site-occupancy calculated by difference Fe <sup>3+</sup> estimated by wet-chemical analysis (Wilson 1960)						

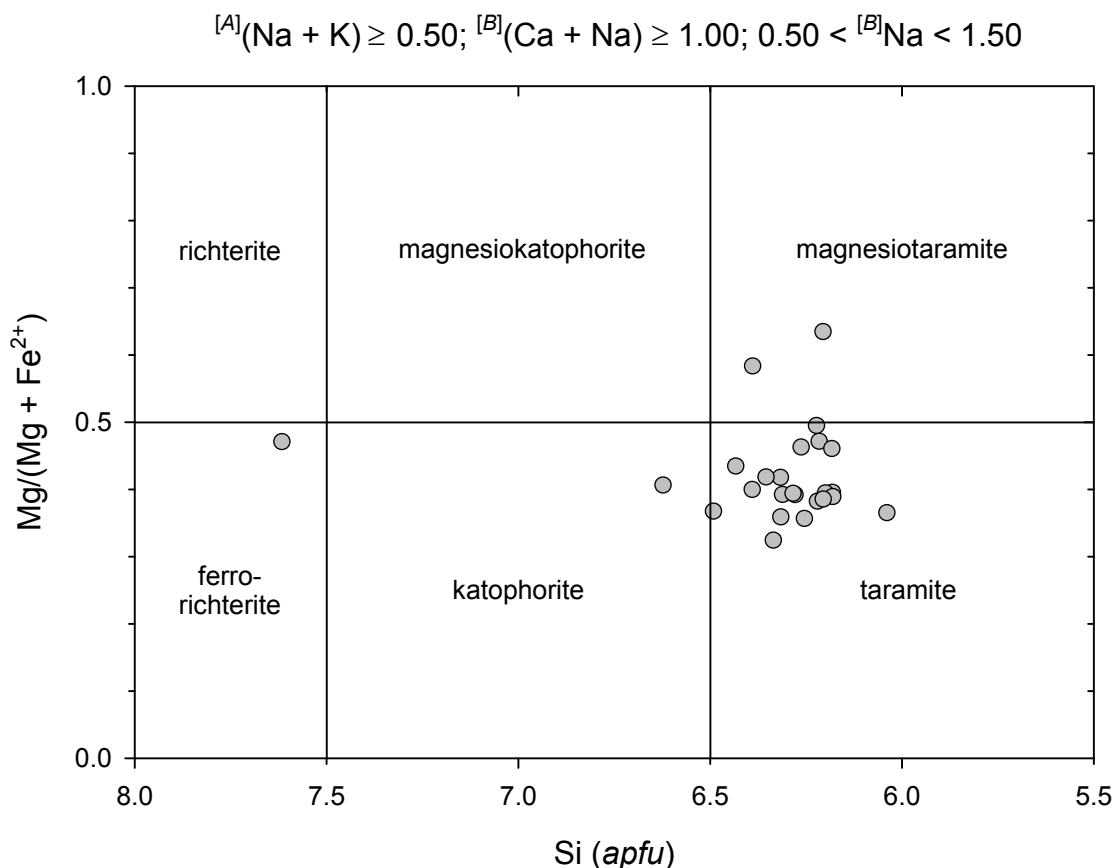


FIGURE 57 – Sodic-calcic amphibole compositions – Nepheline Melasyenite

### *Type 1 nepheline leucosyenite*

Arfvedsonite occurs as a trace mineral in the Type 1 nepheline leucosyenite. It is found as greenish blue (unpolarized light), subhedral, prismatic crystals to 35  $\mu\text{m}$  in length. They vary in habit from acicular to bladed. The arfvedsonite is pleochroic according to the scheme:  $X =$  blue green,  $Z =$  yellow green; no crystals were oriented suitably to measure the pleochroism associated with  $Y$ . Arfvedsonite is included by microcline in an albitized zone and by sodalite near a natrolite reaction rim.

Identification was based on optical properties ( $\delta \approx 0.007$ ,  $2V_x \approx 45^\circ$ , biaxial negative, pleochroism). In thin section, arfvedsonite is superficially similar to eckermannite and

riebeckite, but eckermannite and riebeckite both tend to have higher birefringences and riebeckite exhibits distinctly different pleochroism. Identification was supported by EDS analysis, which indicates a low-aluminum, iron-dominant composition, thus pointing to arfvedsonite over eckermannite.

### *Eudialyte Syenite*

Ferro-eckermannite, one of three representatives of the sodic amphibole group in the East Hill Suite, occurs as a minor mineral in the eudialyte syenite. It is found as Prussian blue, subhedral, equant masses to 6 mm in diameter. It also occurs as subhedral, acicular individuals to 2 mm in length on the surface of microcline crystals (Figure 58). Such ferro-eckermannite crystals tend to be gemmier and lighter in color than those occurring in aggregates.

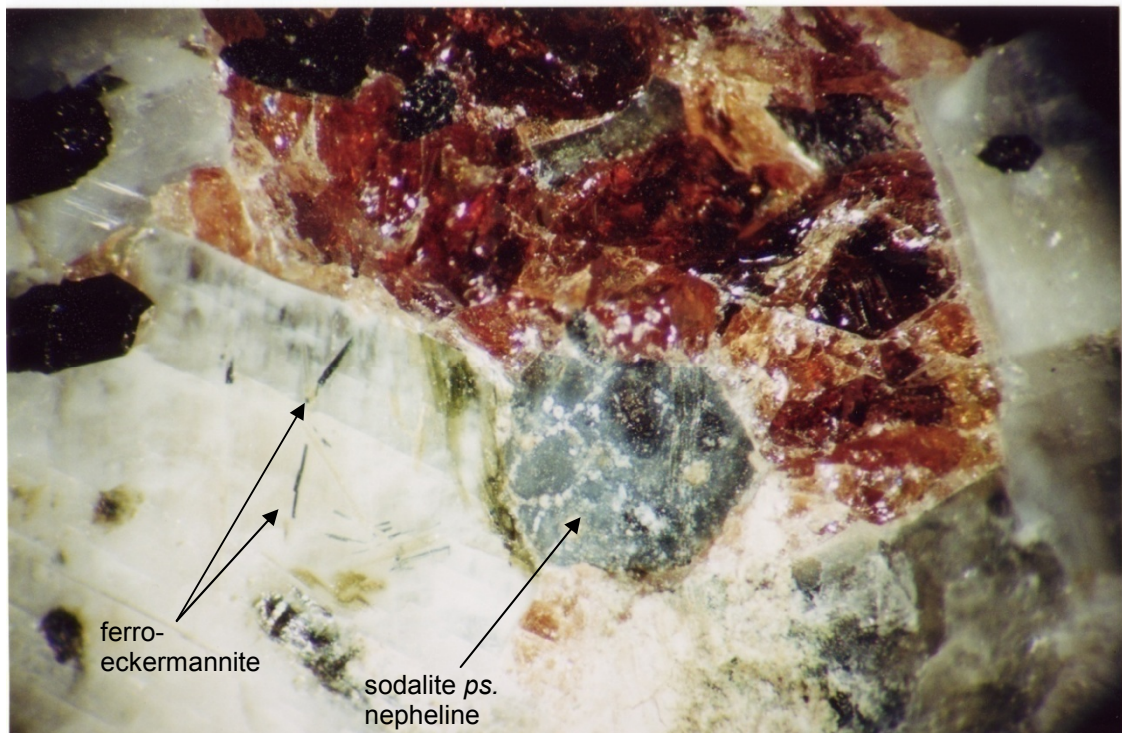


FIGURE 58 – Ferro-eckermannite on microcline, associated with aegirine (green), eudialyte group (red), and sodalite pseudomorph after nepheline (grey-blue) – Eudialyte Syenite (20x)

A representative analysis of ferro-eckermannite is in TABLE 17. A compositional diagram is shown as FIGURE 59. Ferro-eckermannite in the eudialyte syenite is enriched in Ti, Zr, Mn, and K, with potassium enrichment sufficient to term the sample potassian, nearly sufficient to be termed potassic.

TROPPER *ET AL.* (2000) propose a geothermobarometer for sodic amphiboles, based on investigation of natural and synthetic specimens, notably those representing a solid solution series between glaucophane and nyböite. Ferro-eckermannite is sufficiently similar to these species to warrant applying their geothermobarometer, which is based on site-occupancy of <sup>iv</sup>Al; however, the isopleths in p-T space have a nearly vertical slope below about 20 kbar, making the pressure data not interpretable for the East Hill suite. Temperature data, however, may be distantly extrapolated, yielding an estimated temperature range of 700-750°C.

Fortunately, the sodium geothermometer (Figure 60) of TROPPER *ET AL.* (2000) is more useful, as the slopes of the <sup>[4]</sup>Na isopleths permit straightforward extrapolation to the 1 to 2.5 kbar range of the East Hill suite. Application of the geothermometer indicates an approximate crystallization temperature of 725°C for the eudialyte syenite ferro-eckermannite. Relative oxygen fugacities of ferro- and magnesio-sodic amphiboles (Figure 61) suggest that ferro-eckermannite crystallized below the HM buffer. (Okay 1980)



TABLE 17 – Representative electron microprobe analysis of sodic amphibole – Eudialyte Syenite

Lithology:	<i>Eudialyte Syenite</i>		
Sample:	<i>MSH-B-2</i>		
Target:	<i>9a</i>	Target:	<i>9a</i>
SiO <sub>2</sub> (wt.%)	51.74	<i>T-site</i>	
TiO <sub>2</sub>	1.01	Si	8.061
ZrO <sub>2</sub>	1.05	<sup>iv</sup> Al	0.000
Al <sub>2</sub> O <sub>3</sub>	4.12	<sup>iv</sup> Ti	0.000
REE <sub>2</sub> O <sub>3</sub>	0.00	Σ[T]	<i>8.061</i>
Ce <sub>2</sub> O <sub>3</sub>	0.00	<i>C-site</i>	
FeO <sub>tot</sub>	23.35	<sup>vi</sup> Al	0.756
MnO	0.73	<sup>vi</sup> Ti	0.118
MgO	0.01	Zr	0.080
ZnO	0.00	Fe <sup>3+</sup>	0.461
CaO	0.64	Fe <sup>2+</sup>	2.582
Na <sub>2</sub> O	9.43	Mn <sup>2+</sup>	0.097
K <sub>2</sub> O	4.47	Mg	0.003
Cl	0.00	Zn	0.000
F	0.00	Σ[C]	<i>4.096</i>
O≡Cl	0.00	<i>B-site</i>	
O≡F	0.00	Fe <sup>2+</sup>	0.000
SUM	96.54	Mn <sup>2+</sup>	0.000
Species:	<i>potassian</i> <b><i>ferro-eckermannite</i></b>	Mg	0.000
FeO/FeO <sub>tot</sub>	0.84	Ca	0.106
Fe <sub>2</sub> O <sub>3</sub>	4.15	Na	1.894
FeO	19.62	Σ[B]	<i>2.000</i>
NEW SUM	96.96	<i>A-site</i>	
$\frac{\text{Mg}}{(\text{Mg}+\text{Fe}^{2+})}$	>0.00	Na	0.954
$\frac{\text{Mg}}{(\text{Mg}+\text{Fe}^{2+}+\text{Mn}^{2+})}$	>0.00	K	0.888
		Σ[A]	<i>1.842</i>
		<i>OH-Site</i>	
		Cl	0.000
		F	0.000
		OH	2.000
		Σ[OH]	<i>2.000</i>
Recalculated according to the scheme of LEAKE <i>ET AL.</i> (1997 & 2003) – Minimum Fe <sup>3+</sup> Normalized to 23 oxygen <i>apfu</i> OH site-occupancy calculated by difference Fe <sup>3+</sup> determined by site-occupancy according to the scheme of LEAKE <i>ET AL.</i> (1997)			

$^{[B]}Na \geq 1.50$ ;  $(Mg + Fe^{2+} + Mn^{2+}) > 2.50$ ;  $(^{vi}Al \text{ or } Fe^{3+}) > Mn^{3+}$ ;  
 $Li < 0.5$ ;  $(Mg \text{ or } Fe^{2+}) > Mn^{2+}$ ;  $^{[A]}(Na + K) \geq 0.50$

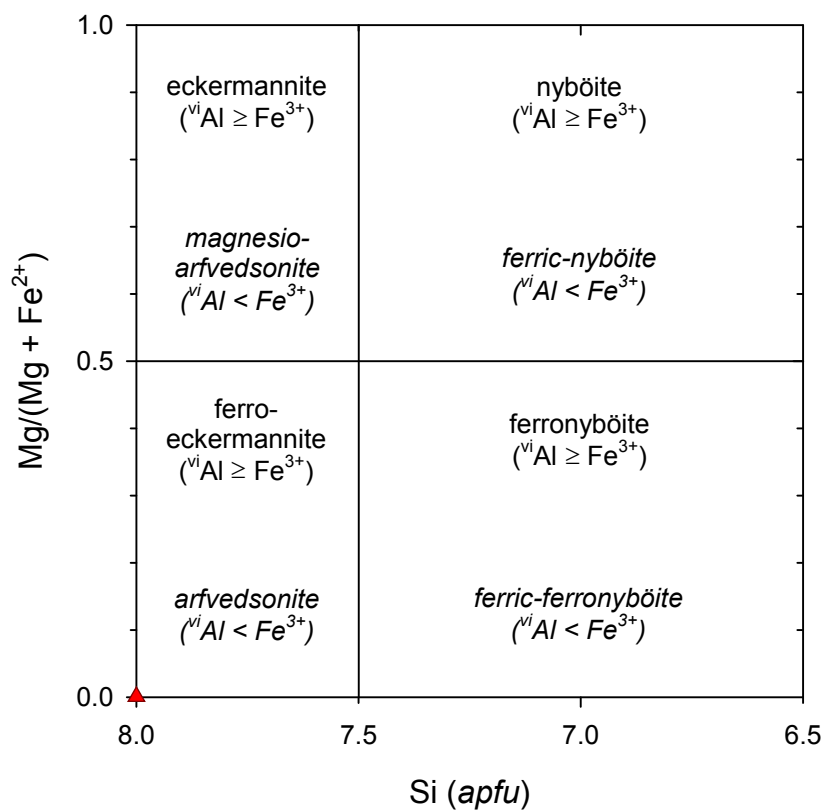


FIGURE 59 – Sodic amphibole composition – Eudialyte Syenite

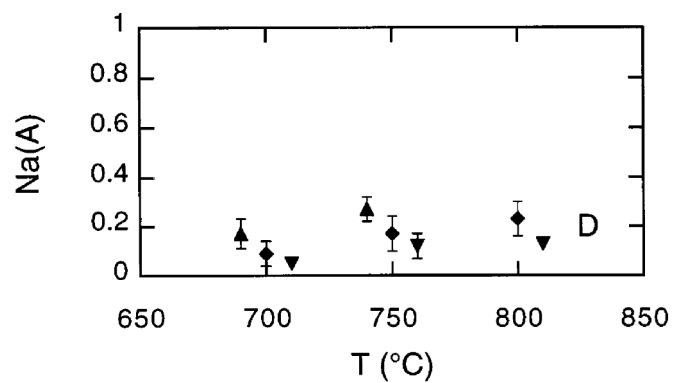


FIGURE 60 – Variation in site-occupancy of  $^{[4]}\text{Na}$  in sodic amphiboles as a function of pressure and temperature. (▼) – 30 kbar, (◆) – 25 kbar, (▲) – 20 kbar. System buffered by the reaction glaucophane = jadeite + talc. (Tropper *et al.* 2000)

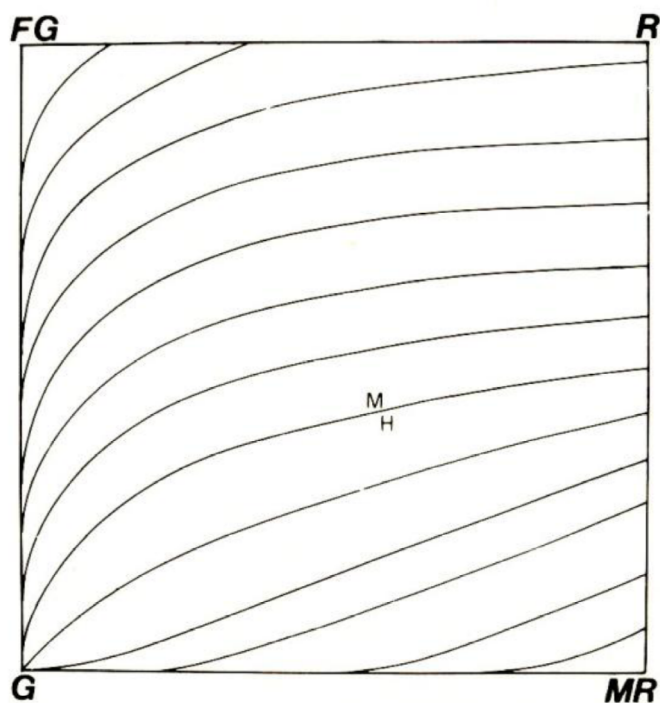


FIGURE 61 – Oxygen fugacity isopleths for sodic amphiboles (blueschist facies p-T conditions). Note that oxygen fugacity increases downward in this diagram. (FG) – ferroglaucophane, (G) – glaucophane, (R) – riebeckite, (MR) – magnesioriebeckite. (Okay 1980)

### *Annite Lamprophyre*

Riebeckite is found as a rare mineral in the annite lamprophyre as euhedral, blocky, prismatic crystals to 250  $\mu\text{m}$  in length. They are found associated with annite and aegirine. Identification was based initially on EDS analysis and observation in the petrographic microscope. Final identification was based on optical properties (length fast and pleochroism:  $X$  = blue,  $Y$  = grey blue,  $Z$  = pale brown).

PLATT & WOOLLEY (1986) suggest a hydrothermal origin for riebeckite in the Mulanje peralkaline syenite-granite complex. Riebeckite coexists with annite and aegirine, the prominent mafic assemblage in the annite lamprophyre, up to a maximum temperature of about 570°C. (Ernst 1962; Eugster & Wones 1962; Platt & Woolley 1986) An examination of the oxygen fugacities during the formation of sodic amphiboles by OKAY (1980) (Figure 61) indicates that riebeckite would have crystallized well below the HM buffer, a result that is consistent with the findings of PLATT & WOOLLEY (1986).

### *East Hill Suite Amphiboles*

PE-PIPER (1988) and MITCHELL (1990) highlight the positive correlation between Mg content in amphiboles and magmatic oxygen fugacity. Although absolute oxygen fugacity cannot be directly determined using this method, magnesium content may be used as a proxy for the relative oxygen fugacity at the time of crystallization. Considering both calcic and sodic-calcic amphiboles from the nepheline melasyenite, estimated crystallization temperatures (Figure 54), based on  $^{iv}\text{Al}$  content (Ernst & Liu 1998), decrease from calcic to sodic-calcic compositions. Calcic cores generally represent higher temperatures than sodic-calcic cores; small, late-stage crystals and the rims of large crystals tend to be sodic-calcic and represent lower temperatures.

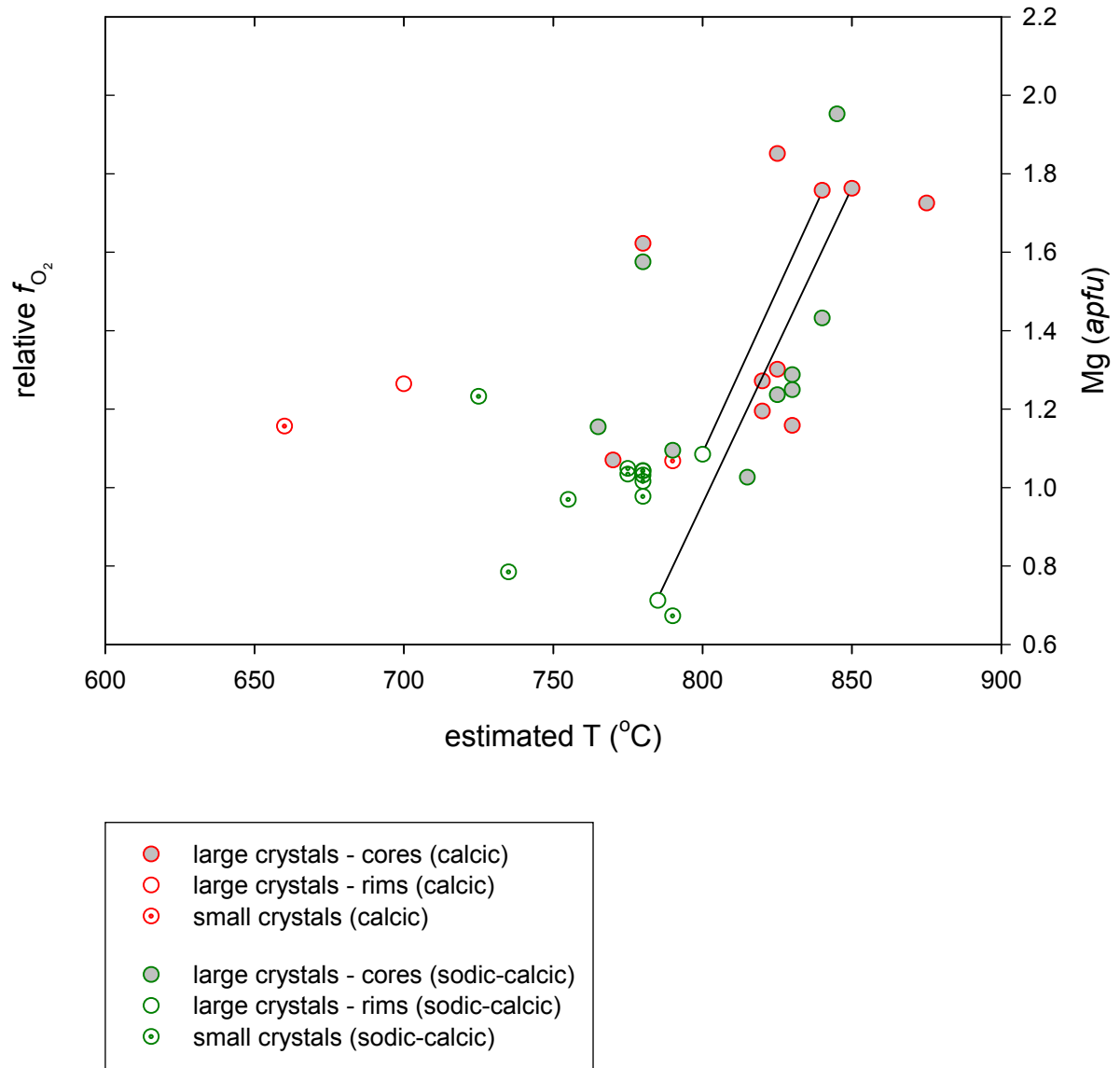


FIGURE 62 – Relative oxygen fugacity *versus* estimated temperature for nepheline melasyenite amphiboles (calcic & sodic-calcic). MgO content serves as a proxy for oxygen fugacity (Pe-Piper 1988); no scale is implied. Temperature estimates are from  $^{iv}\text{Al}$  site-occupancy. (Ernst & Liu 1998) Tie lines link cores and rims common to individual crystals.

Relative  $f_{O_2}$  (Figure 62), based on Mg content, decreases with temperature. The average Mg-number of nepheline melasyenite amphiboles decreases from 54 for calcic amphiboles to 41 for sodic-calcic amphiboles. This indicates that the magma oxygen fugacity decreased during the crystallization of amphiboles in the nepheline melasyenite. Tie lines connecting cores and rims common to individual crystals have roughly the same slope, which supports the concept that the apparent decrease in  $f_{O_2}$  is magmatic rather than a crystal chemical effect confined to particular crystals.

The compositional trend on a plot of  $Ca + {}^{iv}Al$  versus  $Si + Na + K$  (Figure 63) points to several substitution mechanisms that effect this transition: 1)  $\square Ti \leftrightarrow NaAl$ , 2)  $Ti + O^{2-} \leftrightarrow Fe^{3+} + OH^-$ , 3)  $CaAl \leftrightarrow NaSi$ , and 4)  $\square Fe^{3+} \leftrightarrow NaFe^{2+}$ . (Giret *et al.* 1980) Altogether, these data point to an increase in magma alkalinity simultaneous with cooling and decreasing  $f_{O_2}$ .

Similarly, potassium content of East Hill suite amphiboles increases with magmatic evolution and lower crystallization temperature. This is consistent with the observations of DYULGEROV & PLATEVOET (2006) in the Buhovo-Seslavytzi complex, a potassic peralkaline pluton, prominently distinct from Mont Saint-Hilaire in being oversaturated with respect to silica. Buhovo-Seslavytzi presents sodic-calcic and sodic amphiboles ranging from ferrowinchite in the least evolved rocks to potassic magnesio-arfvedsonite in the most evolved. The potassic magnesio-arfvedsonite contains up to 4.67 wt.%  $K_2O$ , comparable to the K content of the ferro-eckermannite in the East Hill suite eudialyte syenite.

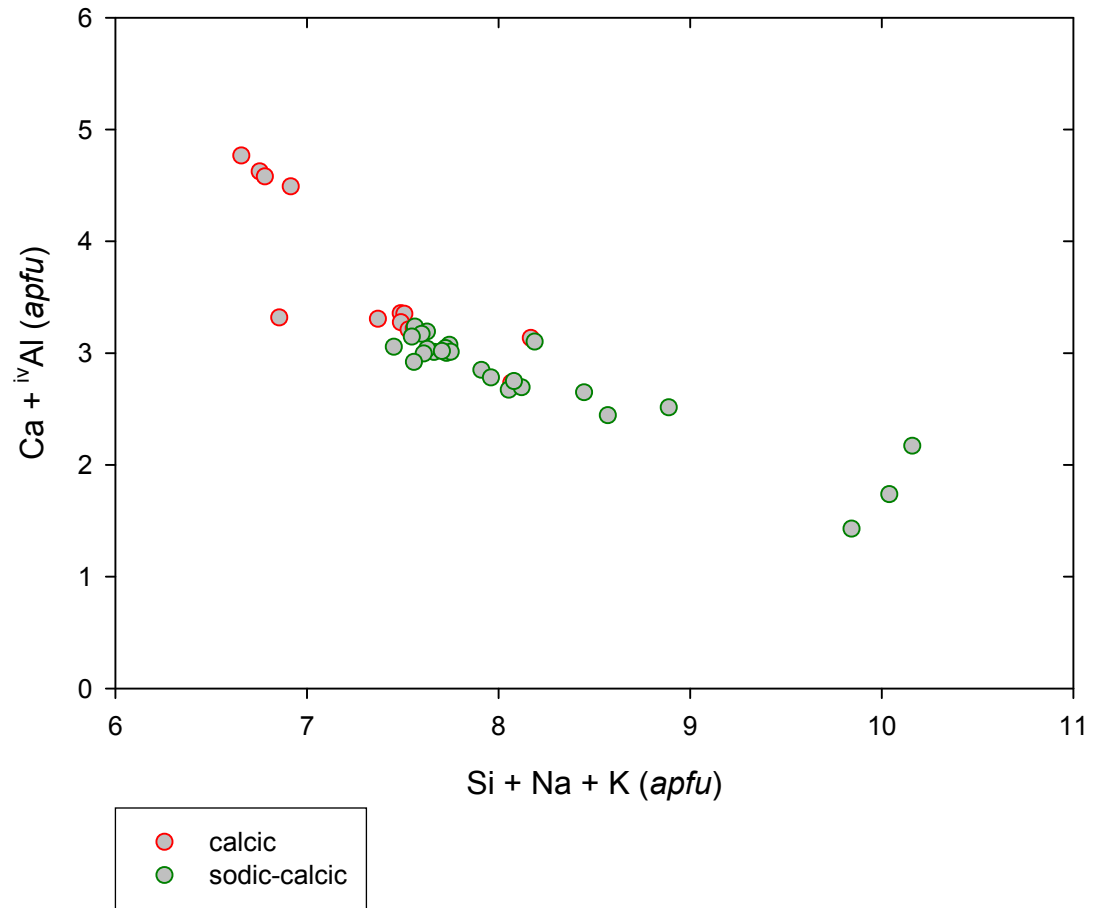


FIGURE 63 –  $\text{Ca} + {}^{\text{iv}}\text{Al}$  versus  $\text{Si} + \text{Na} + \text{K}$  in amphiboles – Nepheline Melasyenite

Calcic and sodic-calcic amphiboles in the nepheline melasyenite exhibit, in part, a similar trend in Mn and Zn enrichment to that found in Li-arfvedsonite from Strange Lake, Québec (Hawthorne *et al.* 2001), in which Mn and Zn display a prominent positive correlation. Amphiboles from both the East Hill suite nepheline melasyenite and the Strange Lake granite are enriched in Zn and Mn over precisely the same range: up to 0.25 *apfu* Mn and up to 0.12 *apfu* Zn (Figures 64 & 65). Melasyenite amphiboles with Mn  $\lesssim$  0.25 *apfu* show the same positive correlation between Mn and Zn, but the nepheline melasyenite contains a population of amphiboles with Mn  $\approx$  0.25 *apfu* that do not correlate at all with Zn content, corresponding rather to the entire range of Zn content from 0.00 to 0.12 *apfu* Zn. Both calcic and sodic-calcic amphiboles are present in both trends. For amphiboles in the correlative trend, sodic-calcic amphiboles contain higher concentrations of both Mn and Zn than calcic amphiboles.

HAWTHORNE *ET AL.* (2001) ascribe the correlation to magmatic rather than crystal chemical influences, and the same could perhaps be said of the East Hill suite amphiboles, as well; however, the non-systematic Zn content of the Mn  $\approx$  0.25 *apfu* amphiboles merits exploration. Some insight into the relationship comes from examination of the  $^{vi}\text{Ti}$  content of the nepheline melasyenite amphiboles. Six-coöordinated titanium is the only other element that varies systematically with Zn, and it varies in a fascinating way.

In both the calcic (Figure 66) and sodic-calcic (Figure 67) amphiboles,  $^{vi}\text{Ti}$  exhibits an antipathetic variation with Mn. Calcic amphiboles on the correlative trend exhibit high  $^{vi}\text{Ti}$  content, whereas calcic amphiboles on the Mn  $\approx$  0.25 *apfu* trend exhibit low  $^{vi}\text{Ti}$  content; furthermore, Mn and  $^{vi}\text{Ti}$  are highly negatively correlated. The trends are not as striking in the sodic-calcic amphiboles, in which most samples exhibit low  $^{vi}\text{Ti}$  content. The single sodic-calcic analysis that shows high  $^{vi}\text{Ti}$  contains no Mn, reflecting the pattern of the calcic amphiboles.



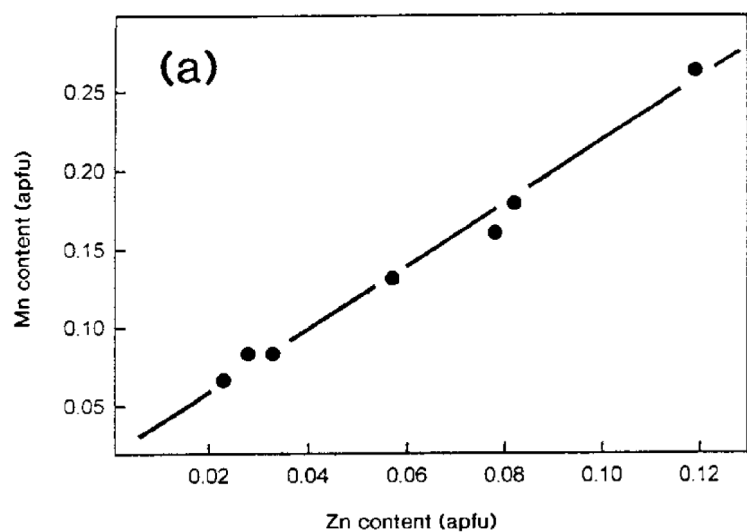


FIGURE 64 – Mn versus Zn in amphibole – Strange Lake granite (Hawthorne *et al.* 2001)

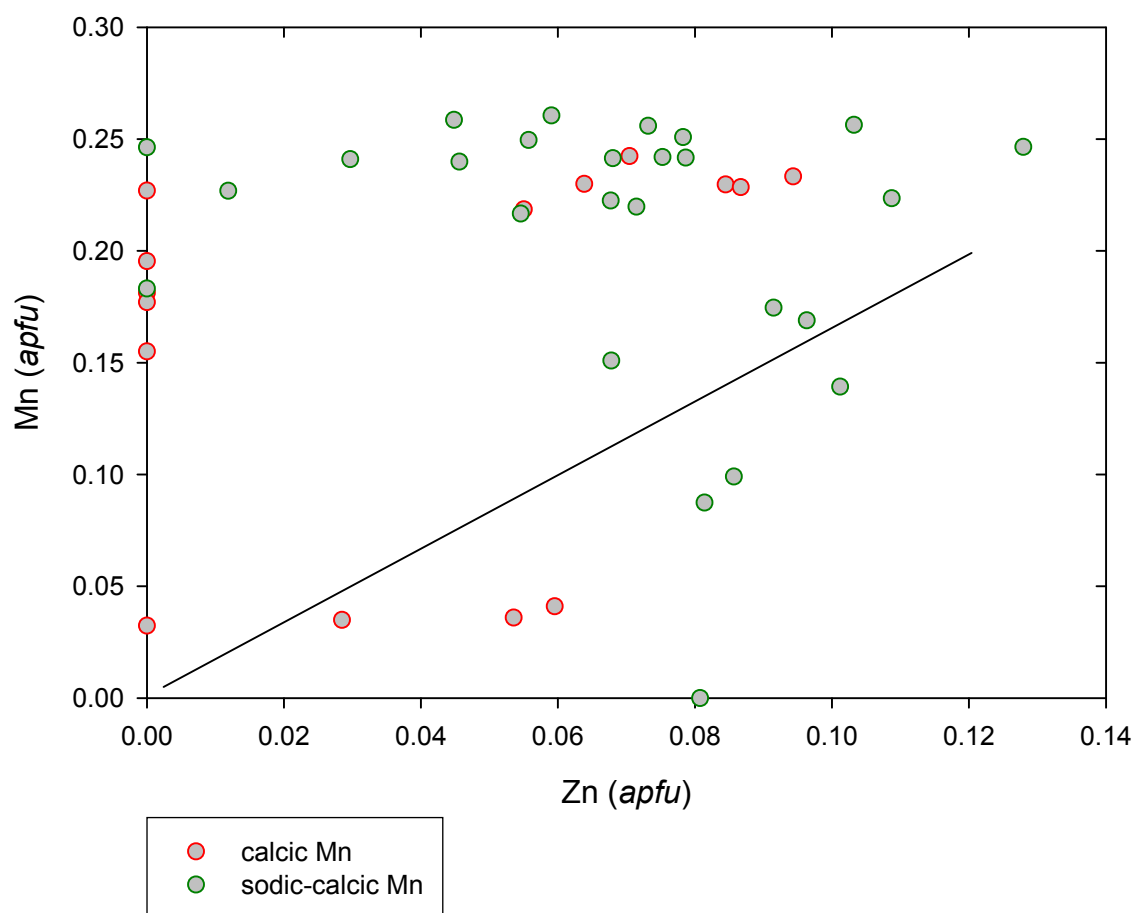


FIGURE 65 – Mn versus Zn in amphiboles – Nepheline Melasyenite

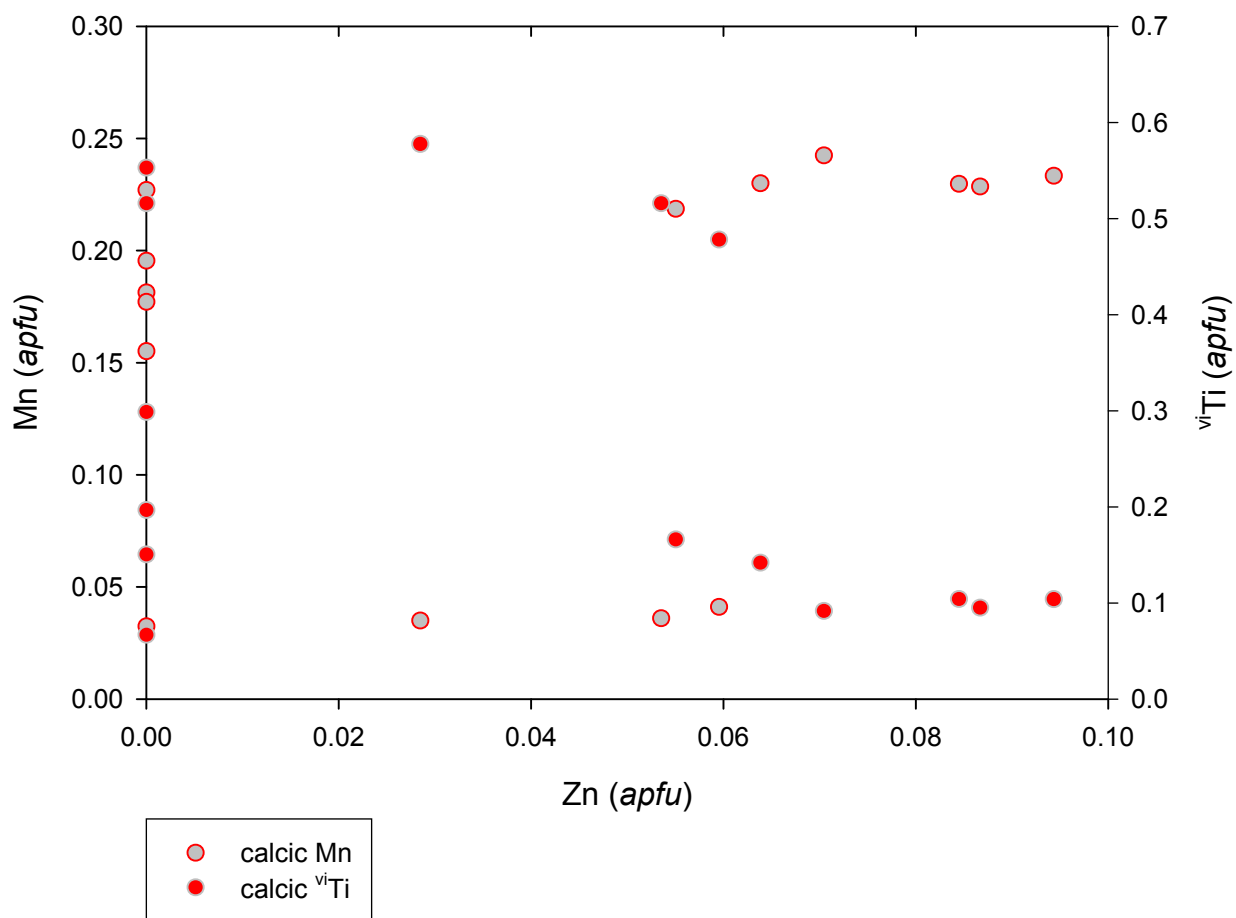


FIGURE 66 – Mn and  $^{vi}\text{Ti}$  *versus* Zn in calcic amphiboles – Nepheline Melasyenite

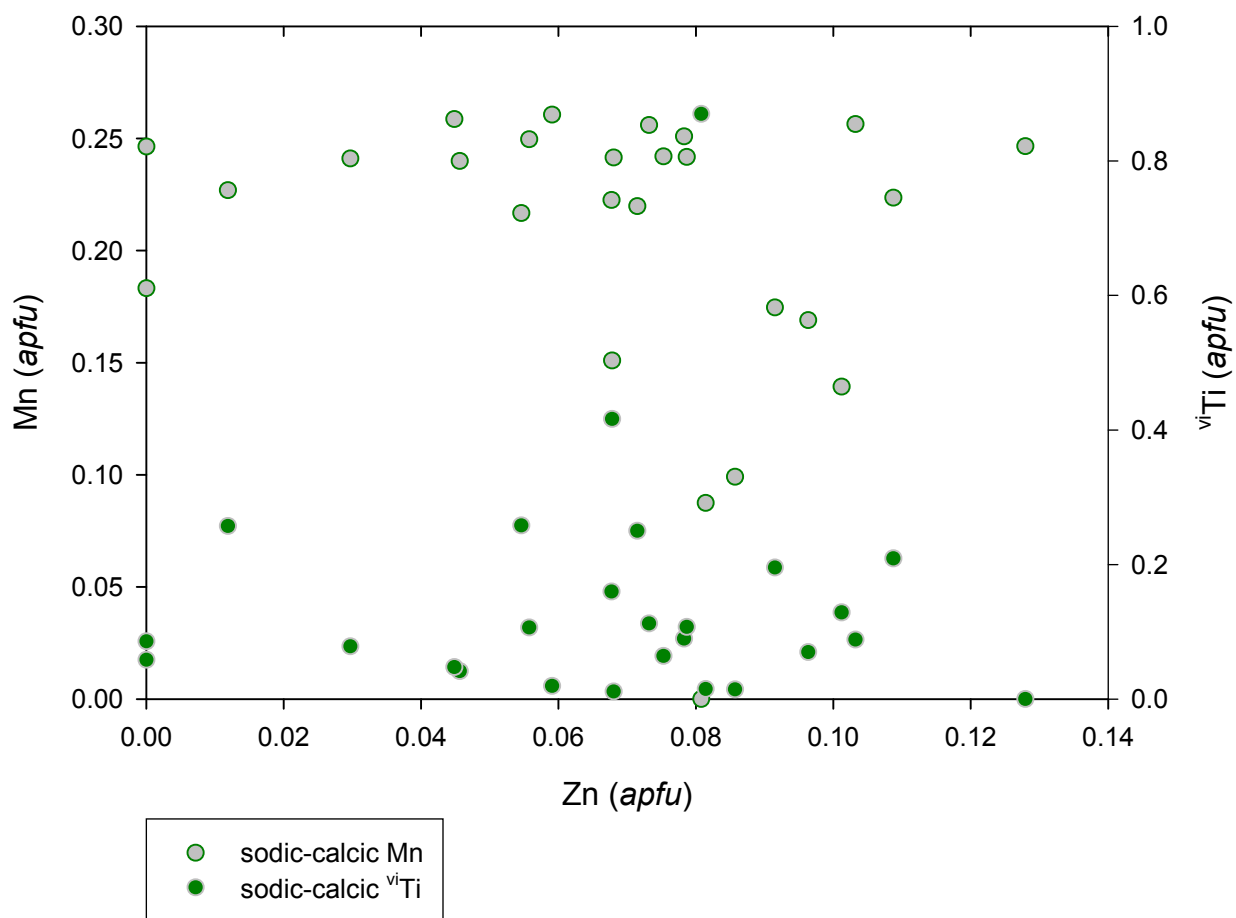


FIGURE 67 – Mn and  $^{vi}\text{Ti}$  *versus* Zn in sodic-calcic amphiboles – Nepheline Melasyenite

Notably, at the concentration of Zn found in this analysis, the <sup>vi</sup>Ti content of the calcic amphiboles had already dropped to low levels.

All together, this suggests that a combination of magmatic and crystal chemical influences is involved. There is a clear trend of Mn and Zn enrichment and Ti depletion in the overall chemistry of the nepheline melasyenite amphiboles, reflecting changes in the bulk chemistry of the magma. The close negative correlation, however, of Mn and <sup>vi</sup>Ti in the calcic amphiboles suggests that, while <sup>vi</sup>Ti is present in any great quantity, it acts as a crystal chemical barrier to Mn enrichment in the amphibole structure. Furthermore, the manganese “ceiling” encountered at Mn  $\approx$  0.25 *apfu*, and the same trend geometry of Zn enrichment in two unrelated magmatic systems implies a crystal chemical mechanism.

Most amphiboles in the nepheline melasyenite contain sufficient ferric iron to be named as a ferri- species. Ferric iron enters the amphibole structure *via* one of two mechanisms, either a dehydrogenation reaction:



or substitution of octahedral ferric iron for aluminum. (Clowe *et al.* 1988) A plot of <sup>vi</sup>Fe<sup>3+</sup> *versus* <sup>vi</sup>Al (Figure 68) reveals a lack of correlation for calcic amphiboles but a rather strong correlation for sodic-calcic amphiboles, implying that ferric iron in the nepheline melasyenite amphiboles entered the structure *via* both mechanisms at different stages of crystallization.

Crystallization temperature and oxygen fugacity estimates indicated that the calcic amphiboles crystallized earlier and at higher oxygen fugacities than the sodic-calcic amphiboles. The trends of ferric iron incorporation reflect these data, in that the calcic trend shows that the amount of <sup>vi</sup>Fe<sup>3+</sup> in the structure did not rely substantially on the amount of <sup>vi</sup>Al, meaning that the dehydrogenation mechanism was dominant, relying on the uptake of oxygen from the system.

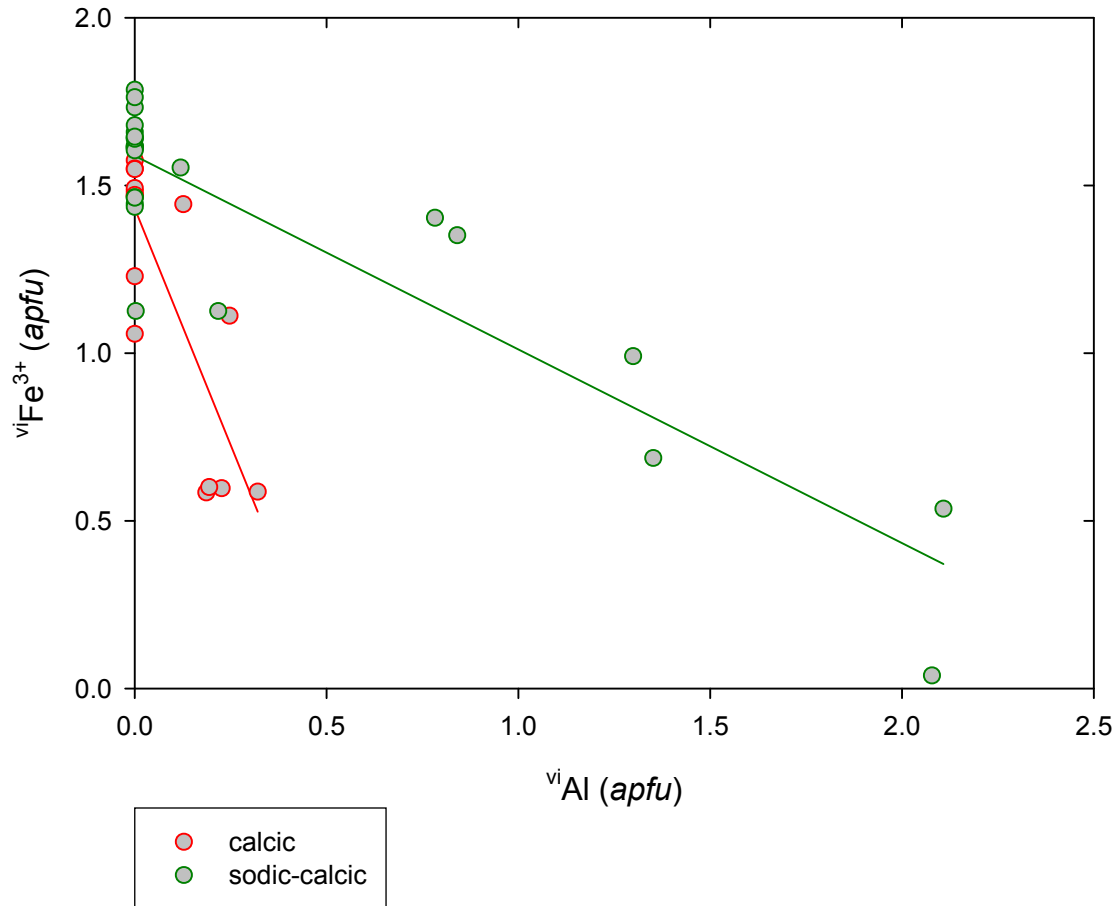


FIGURE 68 – Octahedral ferric iron *versus* octahedral aluminum in amphiboles – Nepheline Melasyenite

This is consistent with the relatively higher oxygen fugacity early in the crystallization of the nepheline melasyenite. On the other hand, the sodic-calcic trend shows a rough balance between ferric iron input and aluminum output, meaning that the substitution mechanism had taken over later in the crystallization sequence. This is not causatively related to the relatively lower oxygen fugacity late in the crystallization of the nepheline melasyenite, but neither is it unexpected in such a chemical environment.

## CARBONATES

### *Calcite*



#### *Type 2 Nepheline Leucosyenite*

Calcite occurs as a minor mineral in the Type 2 nepheline leucosyenite. It is found as colorless, resinous, euhedral to subhedral rhombohedral and scalenohedral crystals to 4 mm in their maximum dimension. These crystals are generally isolated in matrix, but examination in thin section reveals that some occurrences are as irregular veinlets running through sodalite-natrolite-dawsonite associations. Identification was on the basis of EDS analysis, as well as optical properties ( $\delta \approx 0.16$ ).

Representative analyses of calcite from the Type 2 nepheline leucosyenite are listed in TABLE 18. Most calcite from the Type 2 nepheline leucosyenite plots near end-member calcite (Figure 69) but contains up to 7 mol% rhodochrosite and 3 mol% siderite. Calcite compositions from the Type 2 nepheline leucosyenite are enriched in Zn but are nearly all Mg-free.

#### *Type 3 Nepheline Leucosyenite*

Calcite is a rare mineral in the Type 3 nepheline leucosyenite. It occurs as a skeletal, poikilitic, euhedral hexagonal crystal 2 mm in diameter. The crystal is formed as a mosaic of subhedral scalenohedral crystals of calcite. The calcite contains oikocrysts of sodalite pseudomorphs after nepheline, some exhibiting incipient alteration to natrolite. The calcite also hosts some inclusions of fluorite and sérandite. Identification was on the basis of examination under the petrographic microscope (habit, variable relief, uniaxial, and  $\delta \approx 0.15$ ).

TABLE 18 – Representative electron microprobe analyses of calcite – Type 2 Nepheline Leucosyenite

Lithology:	<i>Type 2 Nepheline Leucosyenite</i>		
Sample:	<i>MSH-B-4</i>		
Target:	<i>6c</i>	<i>6d</i>	<i>7d</i>
SiO <sub>2</sub> (wt. %)	0.00	0.00	0.01
P <sub>2</sub> O <sub>5</sub>	0.04	0.04	0.00
Al <sub>2</sub> O <sub>3</sub>	0.00	0.00	0.00
Sc <sub>2</sub> O <sub>3</sub>	na	na	na
FeO	1.89	1.80	1.86
MnO	4.42	4.16	3.73
MgO	0.00	0.00	0.00
ZnO	0.29	0.47	0.63
CaO	46.62	46.07	46.08
BaO	0.00	0.04	0.00
Na <sub>2</sub> O	0.00	0.00	0.00
K <sub>2</sub> O	0.00	0.00	0.02
CO <sub>2</sub> *	40.71	40.17	39.99
SUM	93.98	92.76	92.32
Cations			
Si	0.000	0.000	0.000
P	0.001	0.001	0.000
Al	0.000	0.000	0.000
Sc	na	na	na
Fe <sup>2+</sup>	0.028	0.027	0.028
Mn <sup>2+</sup>	0.067	0.064	0.058
Mg	0.000	0.000	0.000
Zn	0.004	0.006	0.009
Ca	0.899	0.900	0.904
Ba	0.000	0.000	0.000
K	0.000	0.000	0.001
Na	0.000	0.000	0.000
CO <sub>3</sub> <sup>2-</sup>	1.000	1.000	1.000
Normalized to 3 oxygen <i>apfu</i> na = not analyzed *CO <sub>2</sub> calculated to make 1 CO <sub>3</sub> <sup>2-</sup> <i>pfu</i>			

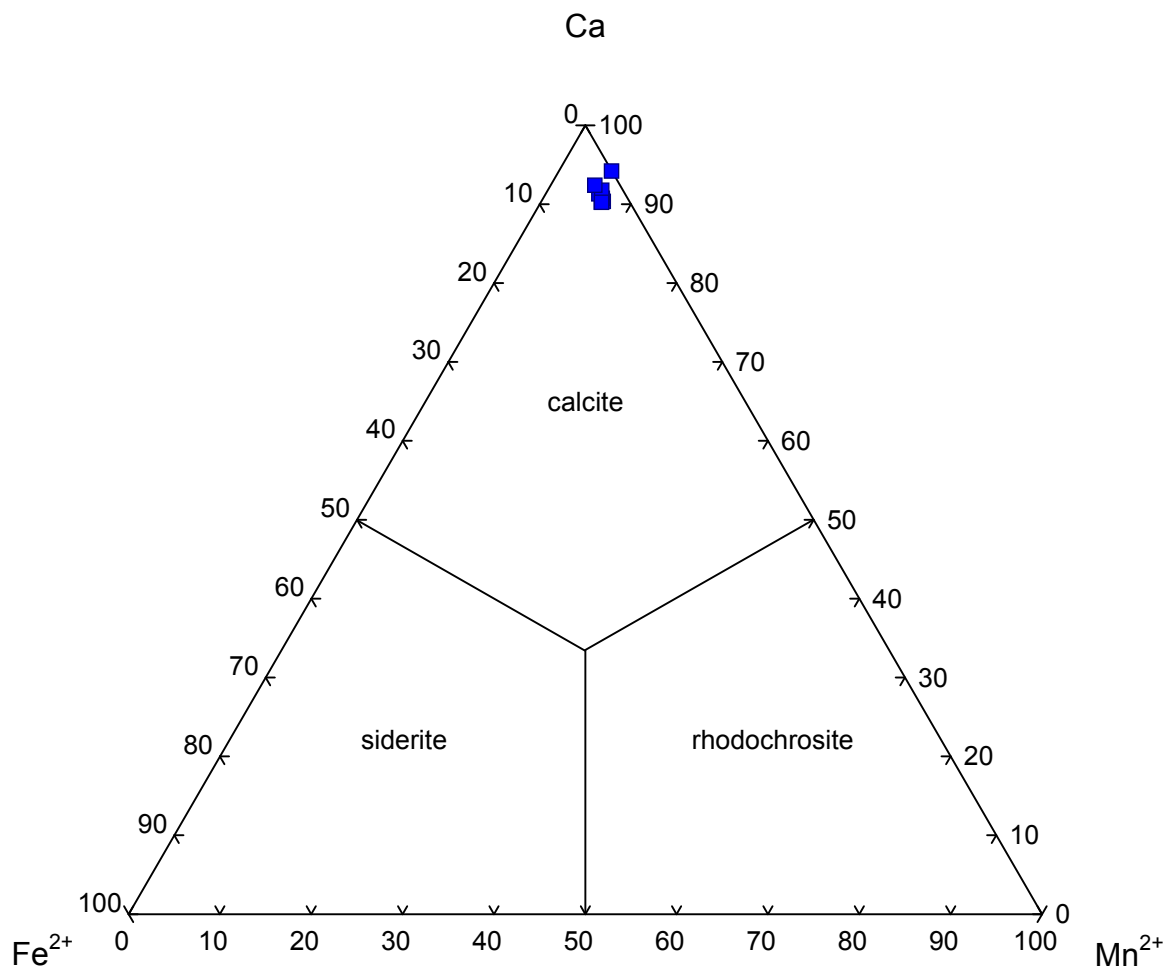


FIGURE 69 – Calcite compositions – Type 2 Nepheline Leucosyenite

### *Eudialyte Syenite*

Calcite is found as a rare mineral in the eudialyte syenite. It is seen both in matrix and in vugs. In matrix, it occurs as subhedral, rhombohedral crystals to 40  $\mu\text{m}$  in their maximum dimension. In vugs, it occurs as euhedral, rhombohedral crystals to 4 mm along edge. Such crystals are translucent and pale grey in color. Identification of calcite in matrix was on the basis of EDS analysis, supported by examination in the petrographic microscope (uniaxial and  $\delta \approx 0.16$ ). Calcite from vugs was positively identified by XRD analysis.



TABLE 19 – Representative electron microprobe analyses of calcite – Eudialyte Syenite

Lithology:	<i>Eudialyte Syenite</i>		
Sample:	<i>MSH-B-2</i>		
Target:	<i>6b</i>	<i>10d</i>	<i>13e</i>
SiO <sub>2</sub> (wt. %)	0.28	0.19	0.51
P <sub>2</sub> O <sub>5</sub>	0.20	0.05	0.41
Al <sub>2</sub> O <sub>3</sub>	0.19	0.16	0.24
Sc <sub>2</sub> O <sub>3</sub>	0.08	0.00	0.28
FeO	0.62	0.51	0.87
MnO	9.01	2.63	6.91
MgO	0.22	0.00	0.24
ZnO	0.00	0.00	0.00
CaO	38.23	44.37	37.95
BaO	0.17	0.09	0.14
Na <sub>2</sub> O	0.00	0.00	0.00
K <sub>2</sub> O	0.00	0.00	0.11
CO <sub>2</sub> *	37.30	37.34	36.91
SUM	86.30	85.33	84.57
Cations			
Si	0.005	0.004	0.010
P	0.003	0.001	0.007
Al	0.004	0.004	0.006
Sc	0.001	0.000	0.005
Fe <sup>2+</sup>	0.010	0.008	0.014
Mn <sup>2+</sup>	0.150	0.044	0.116
Mg	0.006	0.000	0.007
Zn	0.000	0.000	0.000
Ca	0.804	0.932	0.807
Ba	0.001	0.001	0.001
K	0.000	0.000	0.003
Na	0.000	0.000	0.000
CO <sub>3</sub> <sup>2-</sup>	1.000	1.000	1.000
Normalized to 3 oxygen <i>apfu</i> na = not analyzed *CO <sub>2</sub> calculated to make 1 CO <sub>3</sub> <sup>2-</sup> <i>pfu</i>			

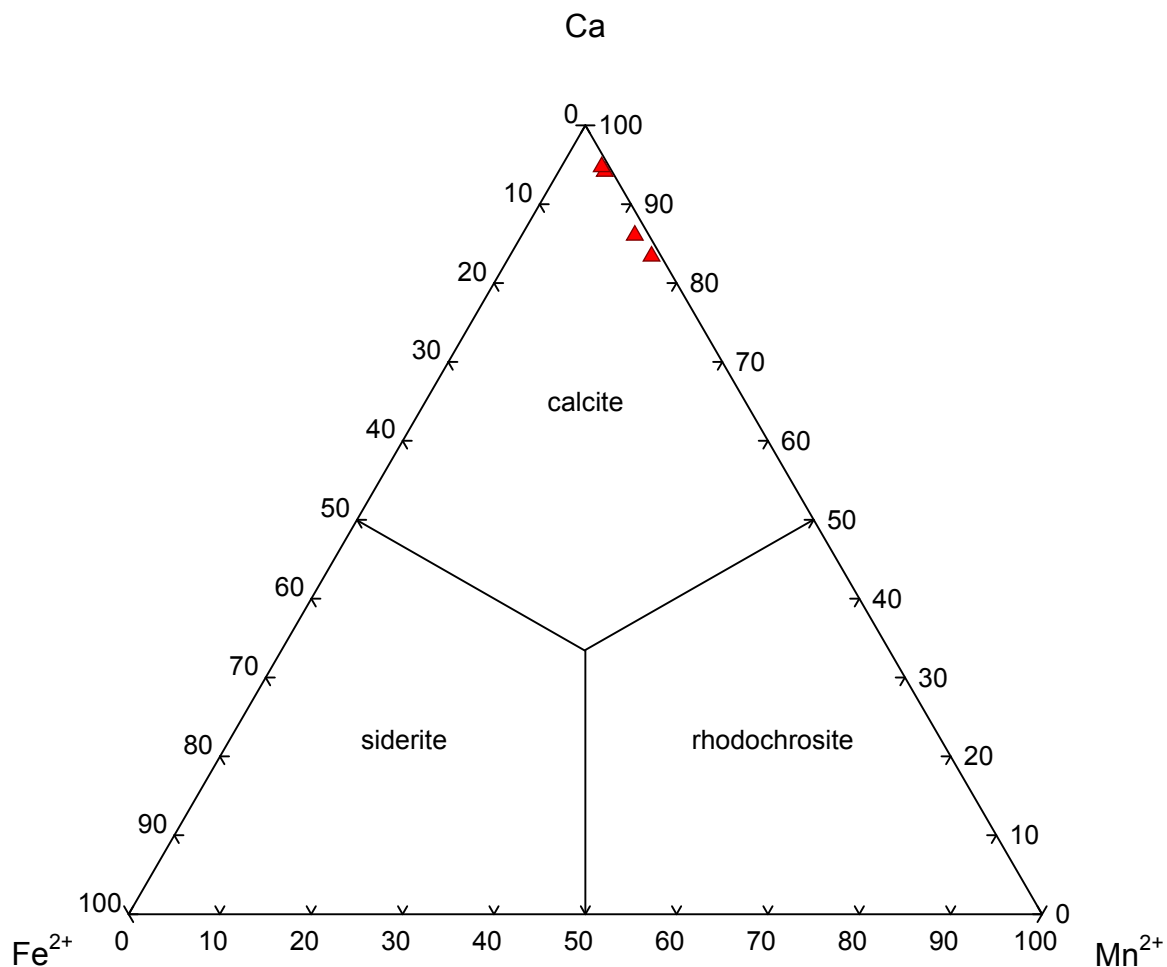


FIGURE 70 – Calcite compositions – Eudialyte Syenite

Representative analyses of calcite from the eudialyte syenite are listed in TABLE 19.

Calcite from the eudialyte syenite (Figure 70) contains up to 15 mol% rhodochrosite and 1 mol% siderite. Calcite from the eudialyte syenite contains up to 0.17 wt.% BaO, 0.47 wt.% MgO, and 0.28 wt.%  $\text{Sc}_2\text{O}_3$ , but it is Zn-free.

### *Feldspar-Aegirine Dikes*

Calcite is found as a trace mineral in the feldspar-aegirine dikes as interstitial masses composed of a mosaic of hexagonal prismatic crystals. Individual crystals measure up to 250  $\mu\text{m}$  in diameter and 3 mm in length. Overall, the crystals form masses up to about 5 mm in length, intergrown with ancylite-(Ce) and associated with microcline and pyrophanite. Identification was on the basis of EDS analysis and optical properties (habit, variable relief, and  $\delta \approx 0.15$ ).

Representative analyses of calcite from the feldspar-aegirine dikes are listed in TABLE 20. Most calcite from the feldspar-aegirine dikes plots near end-member calcite (Figure 71) but contains up to 7 mol% rhodochrosite. Calcite from the feldspar-aegirine dikes contains up to 0.22 wt.% BaO and 0.36 wt.%  $\text{Sc}_2\text{O}_3$ , but it is Mg- and Zn-free.

### *Annite Lamprophyre*

Calcite is found as a minor mineral in the annite lamprophyre. It is the subordinate member of the pair of groundmass minerals, the major member being natrolite, and occurs as subhedral to euhedral, equant rhombohedral crystals, individually to 0.5 mm and in clusters to 4 mm in their maximum dimension. The primary association involving calcite in the annite lamprophyre is that with natrolite; it is also commonly seen with apatite. Calcite also uncommonly occurs, infilling cavities in annite. Identification was on the basis of EDS and EMP analyses, as well as on optical properties (habit, variable relief, uniaxial, and  $\delta \approx 0.15$ ).

Representative analyses of calcite from the annite lamprophyre are listed in TABLE 21. Calcite from the annite lamprophyre (Figure 72) contains up to 12 mol% rhodochrosite and 1 mol% siderite. Calcite from the annite lamprophyre is variably-enriched in Zn up to 1.24 wt.% ZnO.

TABLE 20 – Representative electron microprobe analyses of calcite – Feldspar-Aegirine Dikes

Lithology:	<i>Feldspar-Aegirine Dikes</i>	
Sample:	<i>MSH-B-3</i>	
Target:	<i>7b</i>	<i>8d</i>
SiO <sub>2</sub> (wt. %)	0.11	0.29
P <sub>2</sub> O <sub>5</sub>	0.70	0.09
Al <sub>2</sub> O <sub>3</sub>	0.54	0.76
Sc <sub>2</sub> O <sub>3</sub>	0.36	0.00
FeO	0.01	0.00
MnO	4.13	0.24
MgO	0.00	0.00
ZnO	0.00	0.00
CaO	42.56	44.20
BaO	0.22	0.00
Na <sub>2</sub> O	0.00	0.00
K <sub>2</sub> O	0.00	0.00
CO <sub>2</sub> *	38.32	36.39
SUM	86.95	81.98
Cations		
Si	0.002	0.006
P	0.011	0.002
Al	0.012	0.018
Sc	0.006	0.000
Fe <sup>2+</sup>	0.000	0.000
Mn <sup>2+</sup>	0.067	0.004
Mg	0.000	0.000
Zn	0.000	0.000
Ca	0.872	0.953
Ba	0.002	0.000
K	0.000	0.000
Na	0.000	0.000
CO <sub>3</sub> <sup>2-</sup>	1.000	1.000
Normalized to 3 oxygen <i>apfu</i> na = not analyzed *CO <sub>2</sub> calculated to make 1 CO <sub>3</sub> <sup>2-</sup> <i>pfu</i>		

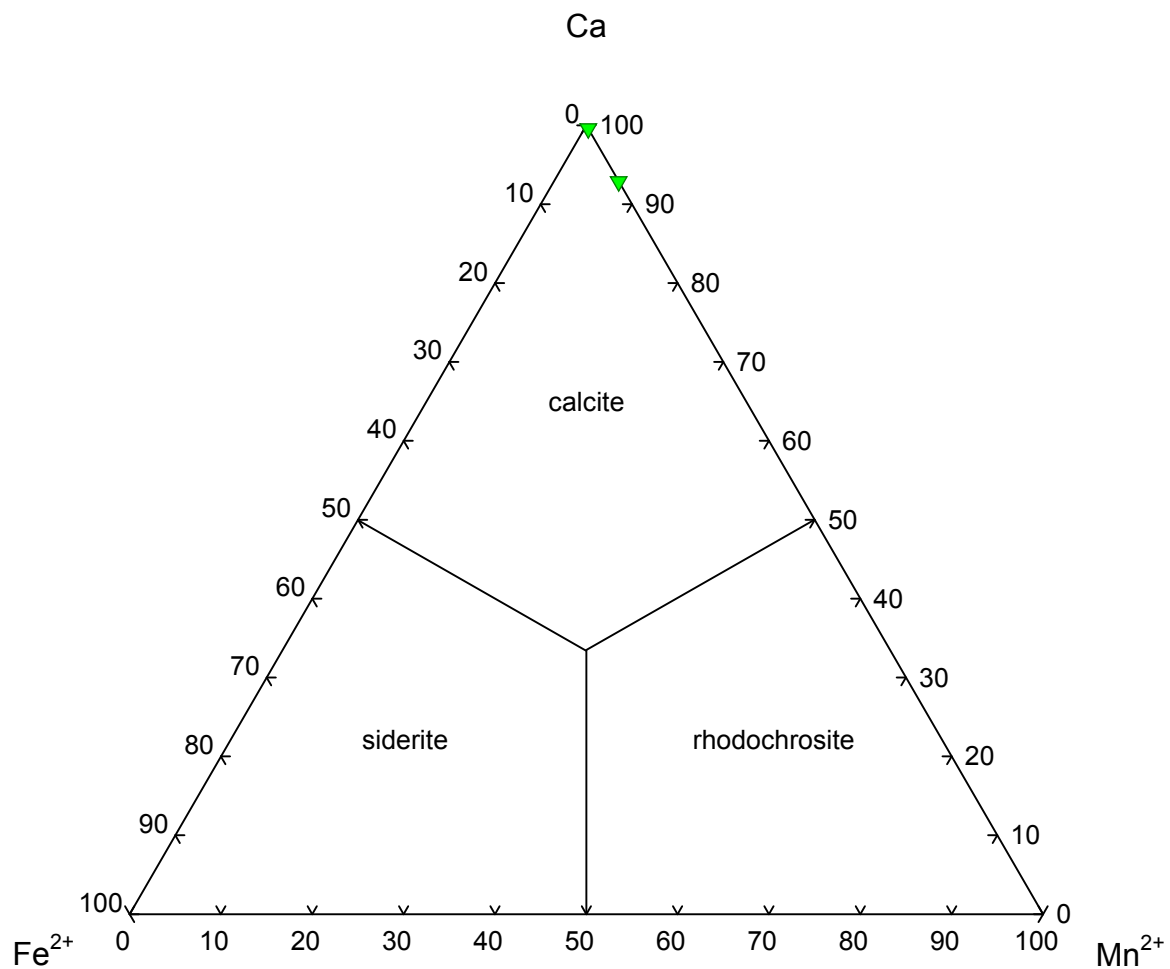


FIGURE 71 – Calcite compositions – Feldspar-Aegirine Dikes

TABLE 21 – Representative electron microprobe analyses of calcite – Annite Lamprophyre

Lithology:	<i>Annite Lamprophyre</i>		
Sample:	<i>MSH-B-6</i>		
Target:	<i>3f</i>	<i>7g2</i>	<i>12b</i>
SiO <sub>2</sub> (wt. %)	0.01	0.00	0.00
P <sub>2</sub> O <sub>5</sub>	na	na	0.00
Al <sub>2</sub> O <sub>3</sub>	0.00	0.00	0.00
Sc <sub>2</sub> O <sub>3</sub>	na	na	na
FeO	1.00	0.07	0.83
MnO	3.45	8.36	2.56
MgO	0.00	0.18	0.00
ZnO	0.00	na	1.24
CaO	50.18	47.44	51.58
BaO	na	na	na
Na <sub>2</sub> O	0.00	0.00	0.00
K <sub>2</sub> O	0.03	0.00	0.00
CO <sub>2</sub> *	42.16	42.65	43.24
SUM	96.83	98.69	99.44
Cations			
Si	0.000	0.000	0.000
P	na	na	0.000
Al	0.000	0.000	0.000
Sc	na	na	na
Fe <sup>2+</sup>	0.015	0.001	0.012
Mn <sup>2+</sup>	0.051	0.122	0.037
Mg	0.000	0.005	0.000
Zn	0.000	na	0.015
Ca	0.934	0.873	0.936
Ba	na	na	na
K	0.001	0.000	0.000
Na	0.000	0.000	0.000
CO <sub>3</sub> <sup>2-</sup>	1.000	1.000	1.000
Normalized to 3 oxygen <i>apfu</i> na = not analyzed *CO <sub>2</sub> calculated to make 1 CO <sub>3</sub> <sup>2-</sup> <i>pfu</i>			

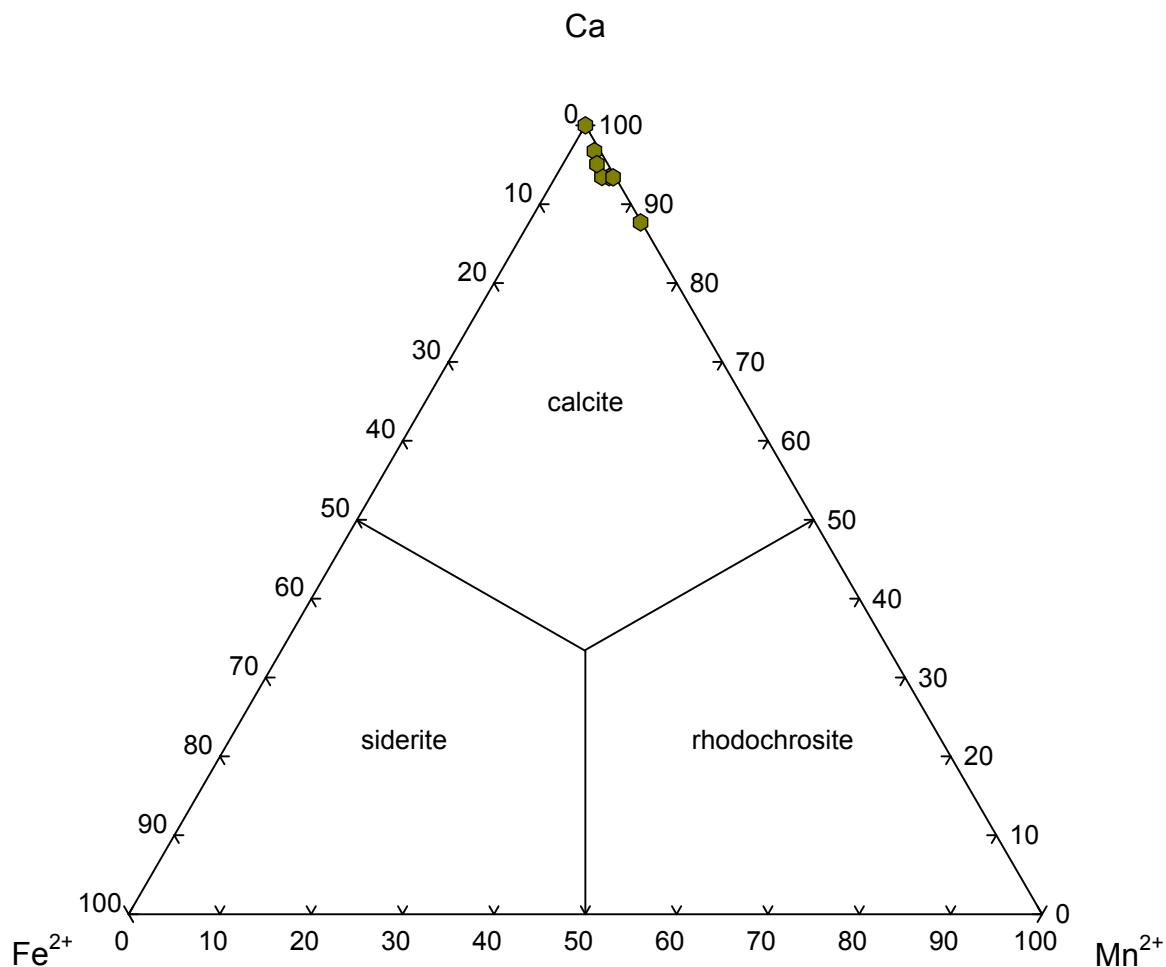
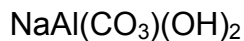


FIGURE 72 – Calcite compositions – Annite Lamprophyre

### ***Dawsonite***



#### *Type 2 Nepheline Leucosyenite*

Dawsonite occurs as a minor mineral in the Type 2 nepheline leucosyenite. It is found as masses of granular to fibrous anhedral crystals forming irregular patches and rims on or stringers through natrolite, itself formed through alteration of sodalite pseudomorphs after nepheline.

Dawsonite also occurs in the form of rinds surrounding natrolite masses. Several such occurrences of dawsonite contain or are adjacent to a void, indicating the presence of a cavity or

a fissure. Identification was made primarily on the basis of EDS analysis, as the strictly Na-Al signature is quite distinctive. Identification was supported by the association, as well as by optical properties (habit and  $\delta \approx 0.11$ ). Electron microprobe analyses of dawsonite were problematic, owing to the beam-sensitive nature of the mineral. Sodium loss was immediately evident upon recalculation, with Na site-occupancy averaging only about 28% of ideal.

Texturally, dawsonite is clearly one of the last phases to crystallize in the East Hill suite. The stability of dawsonite is influenced not only by temperature but also by pH,  $a_{\text{SiO}_2}$ ,  $f_{\text{CO}_2}$  and the ratio of  $a_{\text{Na}^+}$  to  $a_{\text{H}^+}$ . The stability fields of albite and kaolinite expand at the expense of dawsonite with increasing temperature (Figure 73) and silica activity, with the most favorable

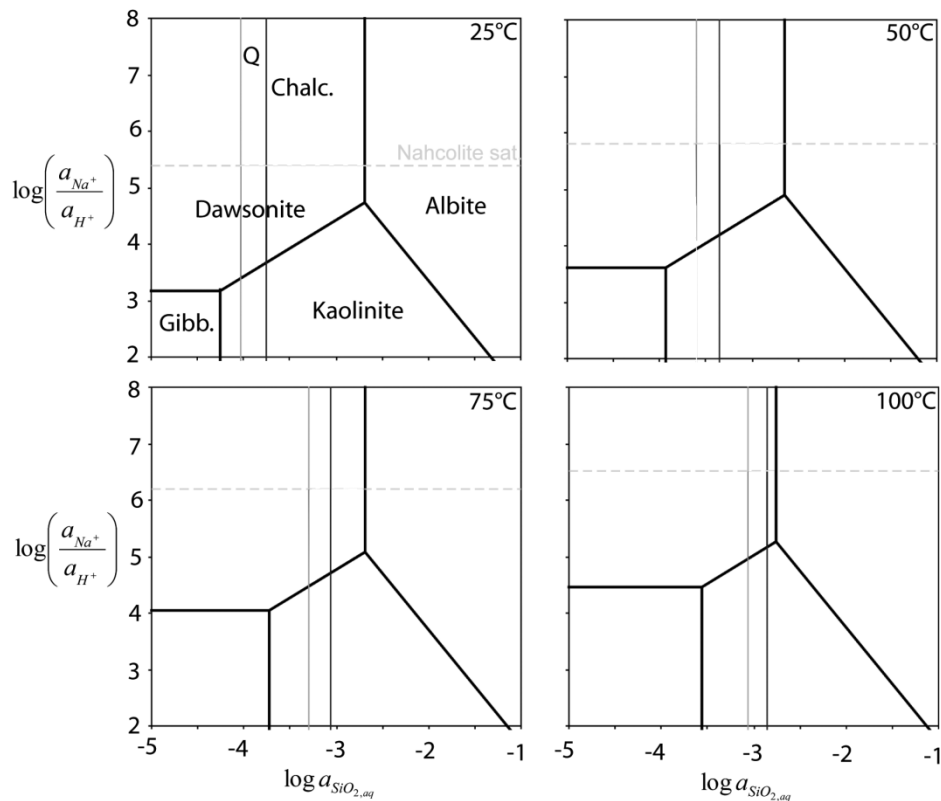


FIGURE 73 – Phase relations of dawsonite and associated phases in  $\log a_{\text{Na}^+} / a_{\text{H}^+} - \log a_{\text{SiO}_2}$  space. (Hellevang *et al.* 2009)



temperature range for dawsonite formation between 75-110°C. Although it is clear from the phase diagrams in FIGURE 73 that silica activity does not strongly shift the phase boundaries for dawsonite at different temperatures, silica competes with dawsonite as temperature increases by removing sodium and aluminum from the system to form albite or kaolinite. Dawsonite crystallization is also favored by a higher  $a_{\text{Na}^+}/a_{\text{H}^+}$  ratio and increased  $f_{\text{CO}_2}$ , the effect of which on the phase boundaries of dawsonite (Figure 74) is substantially stronger than that of  $a_{\text{SiO}_2}$ . (Hellevang *et al.* 2004 & 2009)

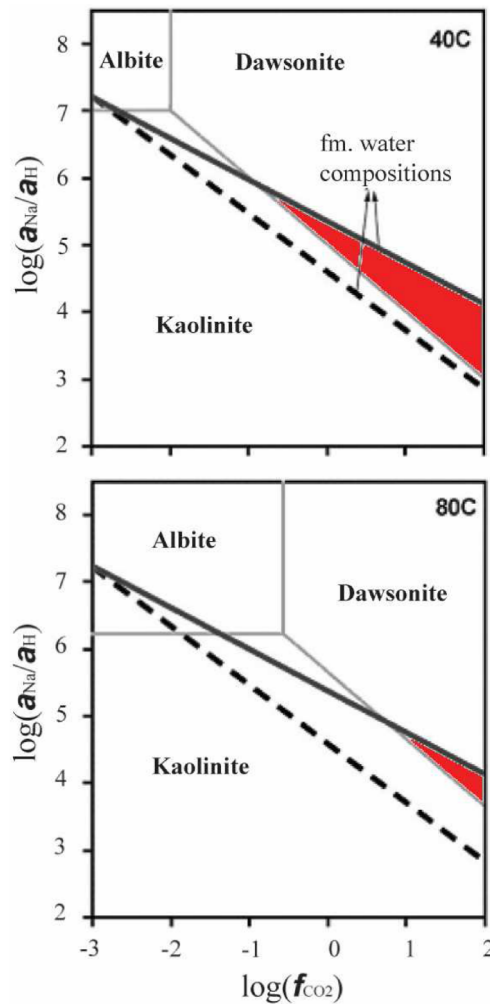


FIGURE 74 – Phase relations of dawsonite and associated phases in  $\log a_{\text{Na}^+}/a_{\text{H}^+} - \log f_{\text{CO}_2}$  space. Diagonal lines represent formation water compositions. (Hellevang 2006)

No geochemical data exists for the stability boundaries of dawsonite with respect to natrolite, but for a solution with a pH of 4.8 at 100°C with  $a_{\text{Na}^+} = 1$ ,  $f_{\text{CO}_2}$  must be at least 52 bar to form dawsonite at the expense of kaolinite; with  $a_{\text{Na}^+} = 0.158$ ,  $f_{\text{CO}_2}$  must be at least 330 bar. Formation of dawsonite at the expense of albite is independent of the  $a_{\text{Na}^+} / a_{\text{H}^+}$  ratio; for a solution with a pH of 4.8 at 100°C,  $f_{\text{CO}_2}$  must be at least 4 bar to form dawsonite at the expense of albite. (Marini 2007) Thus, for dawsonite-producing reactions that depend on  $a_{\text{Na}^+} / a_{\text{H}^+}$ , a higher  $a_{\text{Na}^+}$  results in a lower minimum  $f_{\text{CO}_2}$ ; nevertheless, the  $f_{\text{CO}_2}$  must remain relatively high to stabilize dawsonite.

Not only does dawsonite require a relatively high  $f_{\text{CO}_2}$ , the presence of carbon dioxide in the system must not diminish in systems with high aqueous flux or the dawsonite will quickly destabilize in favor of kaolinite. (Hellevang *et al.* 2005) Although the East Hill suite was open to fluid flow during crystallization, there is no evidence that a high  $f_{\text{CO}_2}$  was maintained following crystallization, indicating that the system closed once cooling was complete.

Besides these factors, the crystallization of dawsonite relies on the presence of dissolved aluminum, the paucity of which in neutral hydrothermal fluids forces dawsonite to rely on dissolution of aluminosilicates, such as natrolite, indicating that dawsonite crystallization can only effectively occur within a narrow pH range. (Hellevang 2006) Furthermore, the availability of dissolved aluminosilicate components governs the total amount of dawsonite formed in a system, not the rate of formation of dawsonite. (Xu *et al.* 2005) Therefore, the crystallization conditions of dawsonite in the East Hill suite will be closely related to the stability field of natrolite, its chief source of material.

DECLERCQ *ET AL.* (2009) show that dawsonite stability is favored by an alkaline environment. Solubility increases rapidly as pH decreases from pH = 4 but is essentially independent of pH for  $4 < \text{pH} < 7$ ; solubility decreases as pH increases from pH = 8. Natrolite stability is favored by an acidic environment (Sinkankas 1961; Eitel 1964), and it destabilizes in an alkaline environment; absent any other changes in fluid chemistry, the fluid shifts into the stability field of analcime. (Eitel 1964) This indicates that the pH of the fluids that altered natrolite to dawsonite would have had a pH close to 7 to have inhibited analcime crystallization.

For natrolite to have remained stable, the  $a_{\text{SiO}_2}$  of the fluids must have remained below  $10^{-3.5}$  to  $10^{-3}$  (Figure 75) over the presumed dawsonite crystallization temperature range. This is

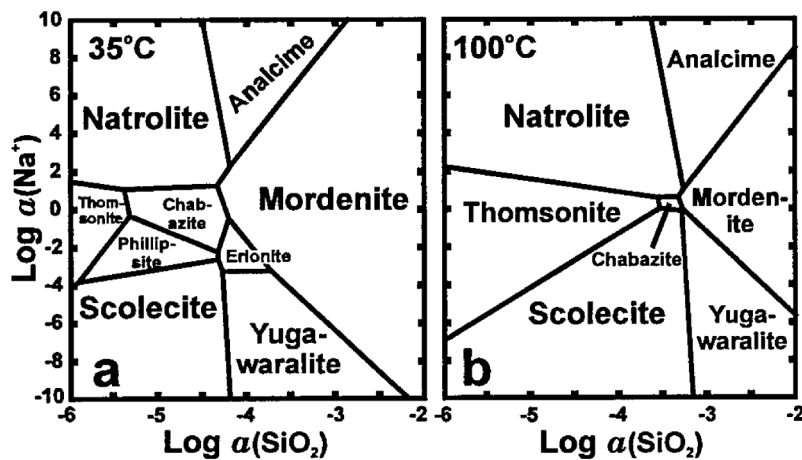


FIGURE 75 – Phase relations of natrolite and associated phases in  $\log a_{\text{Na}^+} - \log a_{\text{SiO}_2}$  space. (Chipera & Bish 1997)

coincident with the upper  $a_{\text{SiO}_2}$  stability field limit of dawsonite for the same temperature range. Assuming that the stability field of natrolite more resembles that of albite than that of kaolinite,  $f_{\text{CO}_2}$  would have been at least  $10^0$  for the dawsonite temperature range. For natrolite to have remained stable, the  $a_{\text{Na}^+}$  of the fluids must not have been far below  $10^0$  (Figure 75), considering a minor thomsonite component in the East Hill suite natrolite (*q.v.*), over the presumed

dawsonite crystallization temperature range. Nahcolite is not present in the mineral assemblage of the East Hill suite; therefore, the  $a_{\text{Na}^+} / a_{\text{H}^+}$  ratio of the dawsonite-forming fluids (Figure 73) must have been below  $10^{6.5}$ . The minimum  $a_{\text{Na}^+} / a_{\text{H}^+}$  ratio for dawsonite stability is  $10^{4.5}$ . The previous pH estimate corresponds to an  $a_{\text{H}^+} \approx 10^{-7}$ , meaning that  $a_{\text{Na}^+}$  must have been close to  $10^0$  to satisfy both the  $a_{\text{Na}^+}$  limit of the natrolite stability field and the  $a_{\text{Na}^+} / a_{\text{H}^+}$  ratio.

### ***Rhodochrosite***



#### *Annite Lamprophyre*

Rhodochrosite occurs as a rare mineral in the annite lamprophyre. It is found as granular masses of subhedral, skeletal (corroded?) crystals, individually to 20  $\mu\text{m}$ . These are associated with calcite, apatite, petarasite, and natrolite. Identification was on the basis of EDS and EMP analyses, as well as on optical properties ( $\delta \approx 0.20$ ).

A representative analysis of rhodochrosite from the annite lamprophyre is listed in TABLE 22. Rhodochrosite from the annite lamprophyre (Figure 76) contains up to 11 mol% siderite, 7 mol% calcite, and 3 mol% magnesite. Rhodochrosite from the annite lamprophyre contains up to 1.06 wt.% MgO.

For the presumed  $f_{\text{O}_2}$  conditions of the East Hill suite, below the HM buffer, the upper thermal stability limit (Figure 78) of rhodochrosite at 2 kbar pressure is approximately 400-800°C. (Huebner 1969) Rhodochrosite from the annite lamprophyre shows no signs of alteration to manganese oxides, so crystallization occurred within or below this temperature range.

TABLE 22 – Representative electron microprobe analysis of rhodochrosite – Annite Lamprophyre

Lithology:	<i>Annite Lamprophyre</i>
------------	---------------------------

Sample:	MSH-B-6
Target:	4mo
SiO <sub>2</sub> (wt. %)	0.16
P <sub>2</sub> O <sub>5</sub>	na
Al <sub>2</sub> O <sub>3</sub>	0.12
Sc <sub>2</sub> O <sub>3</sub>	na
FeO	6.66
MnO	46.39
MgO	1.06
ZnO	0.00
CaO	3.08
BaO	na
Na <sub>2</sub> O	0.36
K <sub>2</sub> O	0.00
CO <sub>2</sub> *	37.08
SUM	94.91
Cations	
Si	0.003
P	na
Al	0.003
Sc	na
Fe <sup>2+</sup>	0.110
Mn <sup>2+</sup>	0.776
Mg	0.031
Zn	0.000
Ca	0.065
Ba	na
K	0.000
Na	0.014
CO <sub>3</sub> <sup>2-</sup>	1.000
Normalized to 3 oxygen <i>apfu</i> na = not analyzed *CO <sub>2</sub> calculated to make 1 CO <sub>3</sub> <sup>2-</sup> <i>pfu</i>	

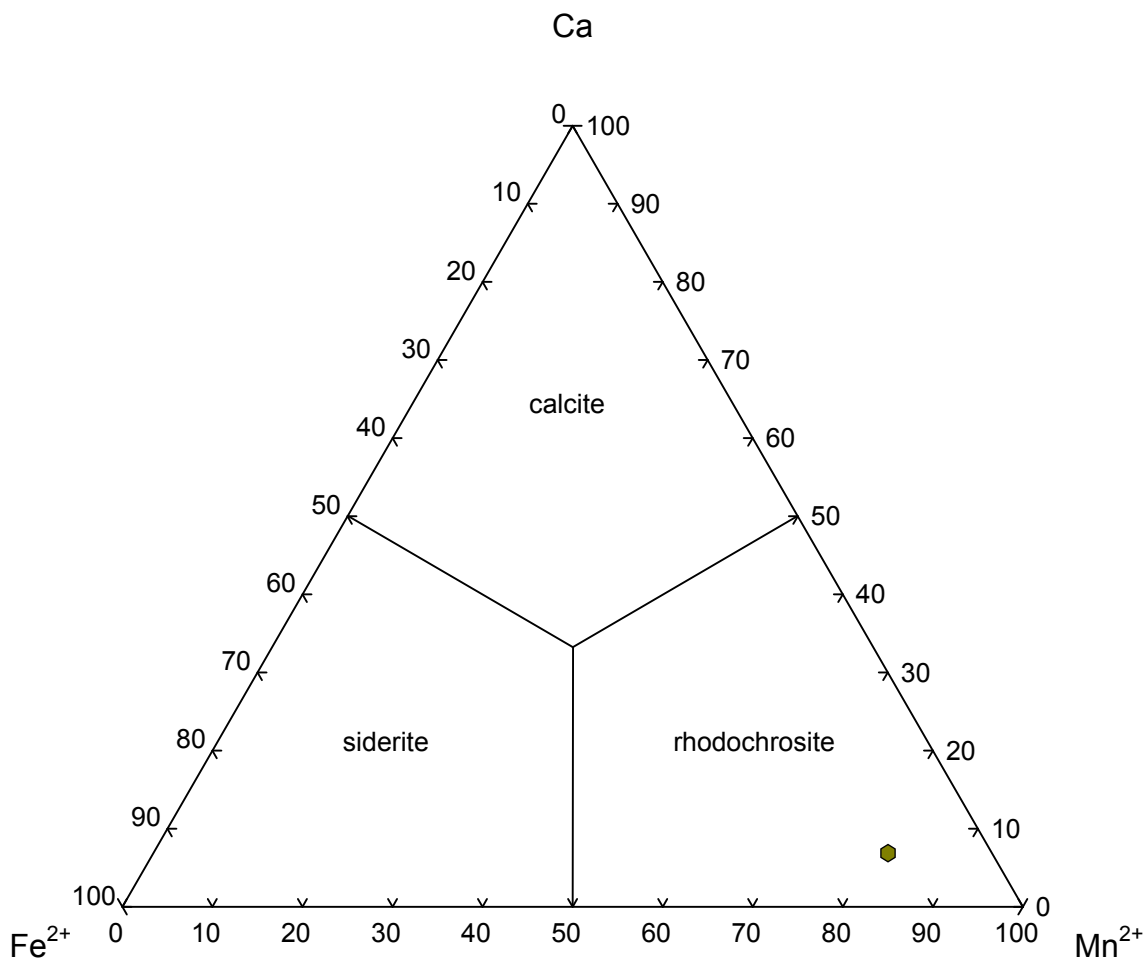


FIGURE 76 – Rhodochrosite composition – Annite Lamprophyre

### *Siderite*



#### *Type 2 nepheline leucosyenite*

Siderite is present as a minor mineral in the Type 2 nepheline leucosyenite as yellow-tan, resinous, euhedral to subhedral rhombohedral crystals to 5 mm in their maximum dimension. They are generally found randomly in matrix, but are also found associated in particular with sodalite-natrolite-dawsonite associations. Siderite is also seen as an intergrowth/overgrowth

TABLE 23 – Representative electron microprobe analyses of siderite – Type 2 Nepheline Leucosyenite

Lithology:	<i>Type 2 Nepheline Leucosyenite</i>		
Sample:	<i>MSH-B-4</i>		
Target:	<i>7m</i>	<i>10d</i>	<i>11g</i>
SiO <sub>2</sub> (wt. %)	0.03	0.26	0.07
P <sub>2</sub> O <sub>5</sub>	0.04	0.18	0.02
Al <sub>2</sub> O <sub>3</sub>	0.00	0.32	0.09
Sc <sub>2</sub> O <sub>3</sub>	na	na	na
FeO	30.65	44.56	40.10
MnO	9.35	11.87	18.88
MgO	0.20	0.27	0.44
ZnO	0.48	0.37	0.35
CaO	15.35	0.25	0.44
BaO	0.00	0.00	0.00
Na <sub>2</sub> O	0.02	0.00	0.11
K <sub>2</sub> O	0.00	0.00	0.00
CO <sub>2</sub> *	37.22	36.44	37.61
SUM	93.34	94.53	98.10
Cations			
Si	0.001	0.005	0.001
P	0.001	0.003	0.000
Al	0.000	0.008	0.002
Sc	na	na	na
Fe <sup>2+</sup>	0.504	0.749	0.653
Mn <sup>2+</sup>	0.156	0.202	0.312
Mg	0.006	0.008	0.013
Zn	0.007	0.005	0.005
Ca	0.324	0.005	0.009
Ba	0.000	0.000	0.000
K	0.000	0.000	0.000
Na	0.001	0.000	0.004
CO <sub>3</sub> <sup>2-</sup>	1.000	1.000	1.000
Normalized to 3 oxygen <i>apfu</i> na = not analyzed *CO <sub>2</sub> calculated to make 1 CO <sub>3</sub> <sup>2-</sup> <i>pfu</i>			

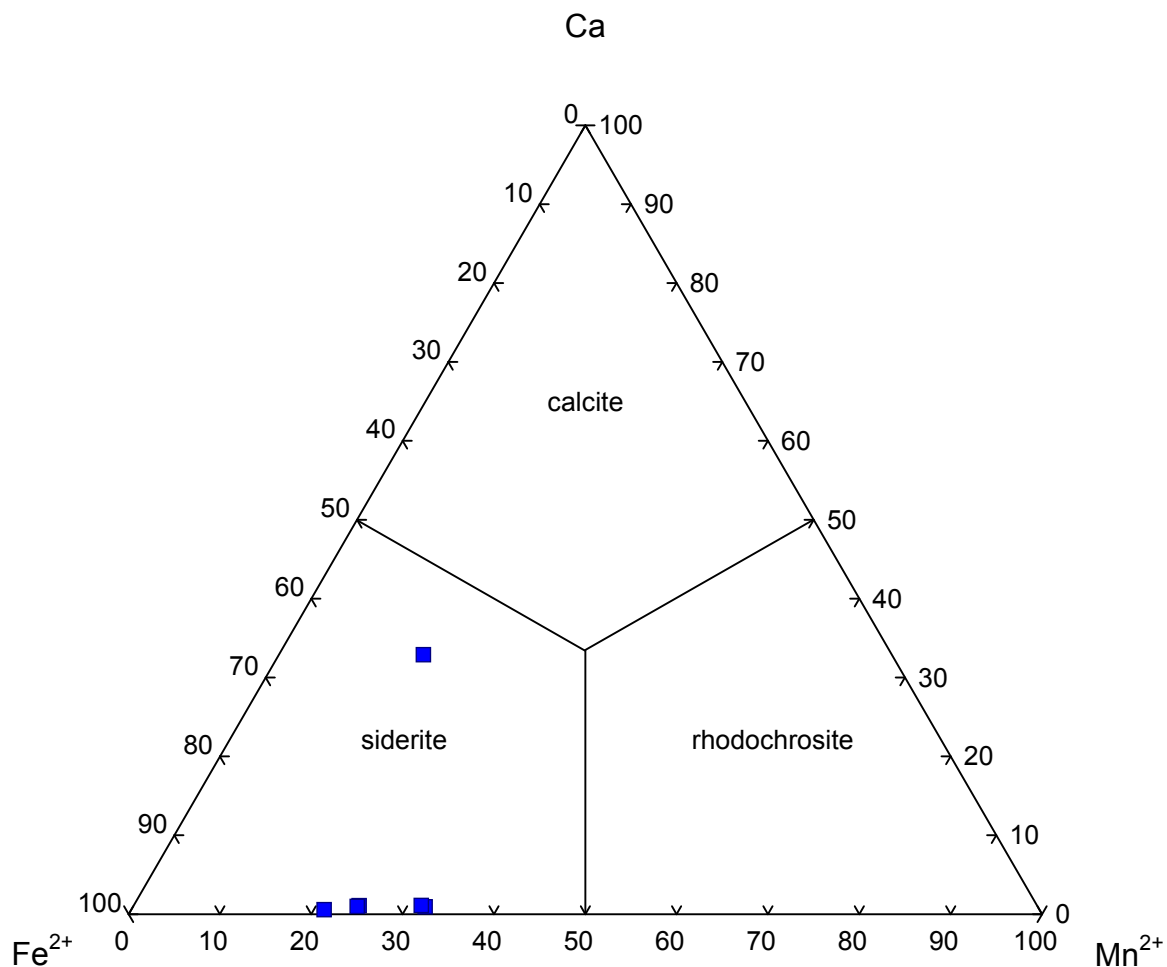


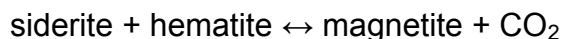
FIGURE 77 – Siderite compositions – Type 2 Nepheline Leucosyenite

with calcite, associated with natrolite and sodalite. Besides macroscopic physical properties, identification was supported by EDS and EMP analyses and optical properties (uniaxial and  $\delta \approx 0.23$ ).

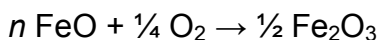
Representative analyses of siderite from the Type 2 nepheline leucosyenite are listed in TABLE 23. Siderite from the Type 2 nepheline leucosyenite (Figure 77) contains up to 32 mol% calcite and 16 mol% rhodochrosite. Siderite from the Type 2 nepheline leucosyenite is enriched in Mn and Zn up to 18.88 wt.% MnO and 0.50 wt.% ZnO.



The upper stability limits of siderite in p-T space under low  $f_{O_2}$  conditions are defined by the reaction (Chai & Navrotsky 1994),



The initial assemblage need not contain hematite, as it may be formed *via* decomposition of siderite (Chang & Ahmad 1982),



As should be readily apparent, the yield of FeO from the first step of decomposition is non-stoichiometric. (Chai & Navrotsky 1994) For the pressure range of the East Hill suite, 1 to 2.5 kbar, the ideal upper thermal stability limit (Figure 78) of siderite is approximately 425-450°C.

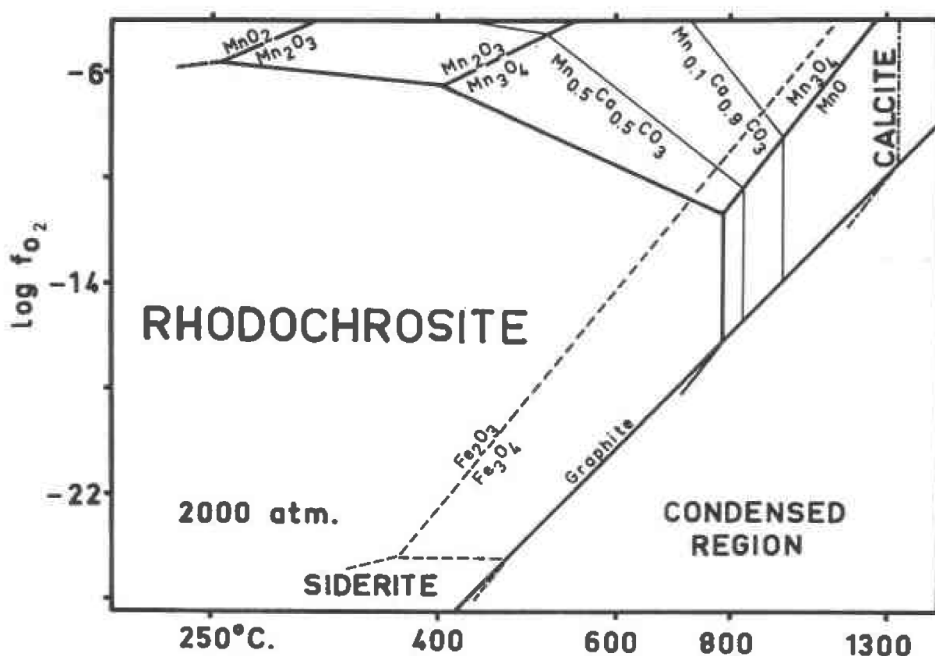


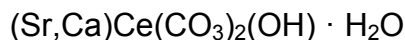
FIGURE 78 – Stability fields in  $f_{O_2}$  -T space of calcite, rhodochrosite, and siderite at 2 kbar. (Huebner 1969)

Since the siderite in the Type 2 nepheline leucosyenite contains such a large proportion of MnO, however, the actual upper thermal stability limit is probably higher because substitution of divalent manganese expands the siderite stability field. (Huebner 1969) Siderite compositions contain up to about 25 mol% rhodochrosite, which, by extrapolation (Figure 78), suggests that the upper thermal limit could be as high as approximately 500°C.

The siderite in the Type 2 nepheline leucosyenite shows no sign of alteration to hematite or magnetite, indicating that it crystallized below that temperature range. This also points to the oxygen fugacity at the time of crystallization, less than  $10^{-22}$  bar.

#### RARE-EARTH CARBONATES

##### *Ancylite-(Ce)*



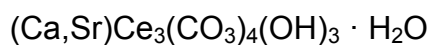
##### *Eudialyte Syenite*

Ancylite-(Ce) occurs in the eudialyte syenite as a rare mineral. It is present as subhedral, equant to anhedral grains to 60  $\mu\text{m}$  in their maximum dimension. They are typically found in association with microcline, fluorite, gaidonnayite, and a eudialyte group mineral. Identification was made primarily on the basis of EDS analysis. Ancylite-(Ce) is distinctive in EDS analyses with respect to other rare-earth carbonates in that its spectrum reveals the presence of Sr. Therefore, the presence of Sr and La or Ce, with or without Ca, in an EDS spectrum is strong evidence that the sample is ancylite. Supporting evidence was derived from examination in the petrographic microscope (biaxial and  $\delta \approx 0.12$ ).

### *Feldspar-Aegirine Dikes*

Ancylite-(Ce) occurs in the feldspar-aegirine dikes as a trace mineral. It is seen as anhedral grains to 10 µm and as irregular polycrystalline veins and stringers that may reach 1.5 mm in length and 0.5 mm in width. It is found intergrown with calcite and associated with pyrophanite. Identification was on the basis of EDS analysis, as in the case of ancylite-(Ce) from the eudialyte syenite.

### ***Calcioancylite-(Ce)***



### *Type 3 Nepheline Leucosyenite*

Calcioancylite-(Ce) is a rare mineral in the Type 3 nepheline leucosyenite. It was found as an anhedral, elongate crystal 10 µm wide by 30 µm long. It is enclosed by a sodalite pseudomorph after nepheline. Identification was based on EDS analysis. Calcioancylite-(Ce) is distinguishable from other rare-earth carbonates in EDS by the presence of Sr (confirmed at 25 kV) in the spectrum. The specimen is too small to determine reliable optical properties.

### *Eudialyte Syenite*

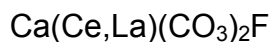
Calcioancylite-(Ce) is found as a rare mineral in the eudialyte syenite. It occurs as anhedral, equant crystals to 10 µm in maximum dimension. They are found in association with albite, microcline, natrolite, and gaidonnayite. Identification was based on EDS analysis. Calcioancylite-(Ce) is distinguishable from other rare-earth carbonates in EDS by the presence of Sr (confirmed at 25 kV) in the spectrum. The specimen is too small to determine reliable optical properties.

### *Annite Lamprophyre*

Calcioancylite-(Ce) occurs as a rare mineral in the annite lamprophyre. It is present as aggregates to 1 mm of anhedral to subhedral individuals, associated with calcite, aegirine, natrolite, and a zirconosilicate believed to be hilairite. Identification was based primarily on EDS analysis. Calcioancylite-(Ce) is distinguishable from other rare-earth carbonates in EDS by the presence of Sr (confirmed at 25 kV) in the spectrum. This tentative conclusion was supported by examination in the petrographic microscope (biaxial,  $\delta \approx 0.10$ ).

One electron microprobe analysis of calcioancylite-(Ce) from the annite lamprophyre exhibited a good total but was problematic in recalculation. This specimen contains 30.12 wt.%  $\text{Ce}_2\text{O}_3$  but also 10.16 wt.%  $\text{La}_2\text{O}_3$ .

### *Synchysite-(Ce)*



#### *Type 2 nepheline leucosyenite*

Synchysite-(Ce) has been tentatively identified as a rare mineral in the Type 2 nepheline leucosyenite. It occurs as a granular mass of anhedral crystals, measuring about 150  $\mu\text{m}$ , occupying a void space with dawsonite. A second specimen of possible synchysite-(Ce) occurs as delicate, tuft-like needles to 5  $\mu\text{m}$ , penetrating natrolite, associated with sodalite pseudomorphs after nepheline and dawsonite, and, possibly thorogummite. Several other minuscule grains occur randomly through the body of the rock, embedded in sodalite or microcline. These have a maximum dimension of 5-10  $\mu\text{m}$ . Identification was primarily based on EDS analysis, in which solely Ca and Ce are present in the spectrum. The absence of Sr indicates that the specimen is not likely calcioancylite-(Ce), and the absence of Ba indicates that

the specimen is not likely cordylite-(Ce). Parisite-(Ce),  $\text{Ca}(\text{Ce},\text{La})_2(\text{CO}_3)_3\text{F}_2$ , would have the same spectrum, in terms of chemistry, but has a Ca:Ce ratio of 1:2. The EDS spectrum for this sample showed a Ca:Ce ratio of about 1:1, matching that of synchysite-(Ce). Identification was supported by examination with the petrographic microscope ( $\delta \approx 0.09$ ).

### *Annite Lamprophyre*

Synchysite-(Ce) has been tentatively identified in the annite lamprophyre. It occurs as ragged patches and stringers to 50  $\mu\text{m}$  in their maximum dimension. These masses are enclosed by calcite and gaidonnayite. It is also found as an irregular mass to 15  $\mu\text{m}$ , associated with rhabdophane-(Ce), rhodochrosite, and possibly gaidonnayite. Identification was on the same basis as above.

### *East Hill Suite Rare-Earth Carbonates*

In a general sense, ancylite-(Ce) is decidedly more common than calcioancylite-(Ce), the latter only being reported from a handful of localities and typically associated with sulfide mineralization. (Zaitsev & Chakhmouradian 2002)

Rare-earth carbonates typically occur as late-stage or hydrothermal phases. (Chakhmouradian & Zaitsev 2002; Zaitsev & Chakhmouradian 2002; Chakhmouradian 2004) ZAITSEV & CHAKHMOURADIAN (2002) estimate a crystallization temperature range of 200-250°C for ancylite-(Ce) and calcioancylite-(Ce) in the Khibina complex. ZAITSEV (1996) reports an equilibration temperature range of  $285\text{--}330 \pm 15^\circ\text{C}$  for synchysite-(Ce) in the Khibina complex. Electron microprobe analyses of rare-earth carbonates were problematic, with almost universally low totals (< 35 wt.%) due to excessive beam sensitivity.

## FELDSPAR GROUP

### ***Alkali Feldspar Group***

Albite,  $\text{NaAlSi}_3\text{O}_8$

Microcline & Orthoclase,  $\text{KAlSi}_3\text{O}_8$

*Nepheline Melasyenite*

Albite is a major mineral in the nepheline melasyenite, in which it is found in three forms. The first type is seen as colorless (when transparent) to light grey (when opaque), irregular patches in cryptoperthitic orthoclase. Well-defined albite twinning is visible, and compositional estimates *via* the Michel-Lévy method put the composition between  $\text{ab}_{90}\text{an}_{10}$  and  $\text{ab}_{95}\text{an}_5$ , based on maximum extinction angles between 10 and 15°, with a biaxial positive optic sign. These measurements are consistent with electron microprobe data for the same areas.

The second form of albite in the nepheline melasyenite is as pale grey overgrowths on orthoclase. These overgrowths are up to 0.5 mm thick on orthoclase laths up to 3.0 mm in width. The overgrowths have a patchy appearance in thin section, but have locally well-defined albite twinning.

The third type of albite in the nepheline melasyenite is seen as colorless (when transparent) to light grey or white (when opaque), anhedral crystals, interstitial to orthoclase, nepheline, titanite, and amphibole. Some such crystals exhibit albite twinning that is continuous across the crystal; although the twin lamellae are low in contrast to one another and are diffuse.

Representative analyses of albite are listed in TABLE 24. Primary albite from the nepheline melasyenite plots near end member albite (Figure 79); compositions run from about  $\text{ab}_{94}\text{or}_{1}\text{an}_5$ , leaning towards the plagioclase series, to  $\text{ab}_{99}\text{or}_1$ . Numerous analyses of alkali feldspar from the nepheline melasyenite plot in intermediate compositions, from approximately

ab<sub>30</sub>or<sub>70</sub> to ab<sub>90</sub>or<sub>10</sub>, with multiple compositions plotting near ab<sub>65</sub>or<sub>35</sub> to ab<sub>85</sub>or<sub>15</sub>. These are interpreted to be analyses of cryptoperthite that has experienced little to no unmixing. Iron is present as a minor trace element, strictly by analysis up to 1.05 wt.% FeO with three other analyses at 0.41, 0.47, and 0.62 wt.% FeO. These analyses, however, stand out considerably from most, which range between 0.00 and 0.19 wt.% FeO. This distribution suggests that FeO substitutes reliably up to about 0.20 wt.% and that significantly higher quantities are probably the result of mechanical contamination by secondary iron oxide/oxyhydroxides.

Orthoclase is a major mineral in the nepheline melasyenite. It is present as light grey, translucent and vitreous to opaque and porcelaneous, prismatic, euhedral to subhedral perthitic crystals to 10 mm in length by 6 mm in width; many individuals are phenocrysts. No twinning is visible, but most crystals are cryptoperthitic. Many crystals are overgrown by albite. Individuals of orthoclase in this syenite are generally free of inclusions, but some crystals poikilitically enclose magnetite, aegirine-augite, fluorapatite, l  venite, fluorite, and titanite.

Much of the orthoclase from the nepheline melasyenite has experienced exsolution of albite and at least partial albitization. Therefore, it is more meaningful to describe compositions of crystals or portions of crystals that have not been affected by those processes. Representative analyses of orthoclase are listed in TABLE 24. Unaltered orthoclase plots near end-member K-feldspar, between ab<sub>6</sub>or<sub>94</sub> and or<sub>100</sub> (Figure 79). Such orthoclase exhibits virtually no deviation towards anorthite. As was noted in the discussion of albite in the nepheline melasyenite, intermediate compositions past about 10 mol% albite are interpreted as analyses of incompletely unmixed cryptoperthite. Orthoclase in the nepheline melasyenite contains iron as a trace element, reliably up to about 0.15 wt.% FeO.

TABLE 24 – Representative electron microprobe analyses of alkali feldspar – Nepheline Melasyenite

Lithology:	<i>Nepheline Melasyenite</i>					
Sample:	<i>MSH-B-8</i>					
Target:	<i>5c</i>	<i>12n</i>	<i>11c</i>	<i>11e</i>	<i>4c</i>	<i>3j</i>
SiO <sub>2</sub> (wt.%)	66.67	67.46	64.76	64.03	67.59	64.67
P <sub>2</sub> O <sub>5</sub>	na	na	na	na	na	na
Al <sub>2</sub> O <sub>3</sub>	20.88	20.46	19.30	19.08	20.62	19.17
Sc <sub>2</sub> O <sub>3</sub>	na	na	na	na	na	na
FeO	0.19	0.13	0.02	0.00	0.07	0.17
CaO	0.31	0.24	0.01	0.00	0.03	0.00
BaO	na	na	na	na	na	na
Na <sub>2</sub> O	11.33	11.93	0.14	0.00	8.90	3.23
K <sub>2</sub> O	0.19	0.17	16.34	16.24	4.49	11.17
SUM	99.57	100.39	100.58	99.34	101.70	98.41
<i>Cations</i>						
Si	2.933	2.947	2.974	2.976	2.951	2.980
P	na	na	na	na	na	na
Al	1.083	1.054	1.044	1.045	1.061	1.041
Sc	na	na	na	na	na	na
Fe <sup>2+</sup>	0.007	0.005	0.001	0.000	0.003	0.007
Ca	0.014	0.011	0.001	0.000	0.001	0.000
Ba	na	na	na	na	na	na
K	0.010	0.009	0.957	0.962	0.250	0.657
Na	0.966	1.010	0.013	0.000	0.753	0.288
<i>or</i>	1.06	0.92	98.62	100.00	24.88	69.50
<i>ab</i>	97.49	97.98	1.32	0.00	74.98	30.50
<i>an</i>	1.45	1.10	0.06	0.00	0.15	0.00
<i>cn</i>	na	na	na	na	na	na
Normalized to 8 oxygen <i>apfu</i> na = not analyzed						



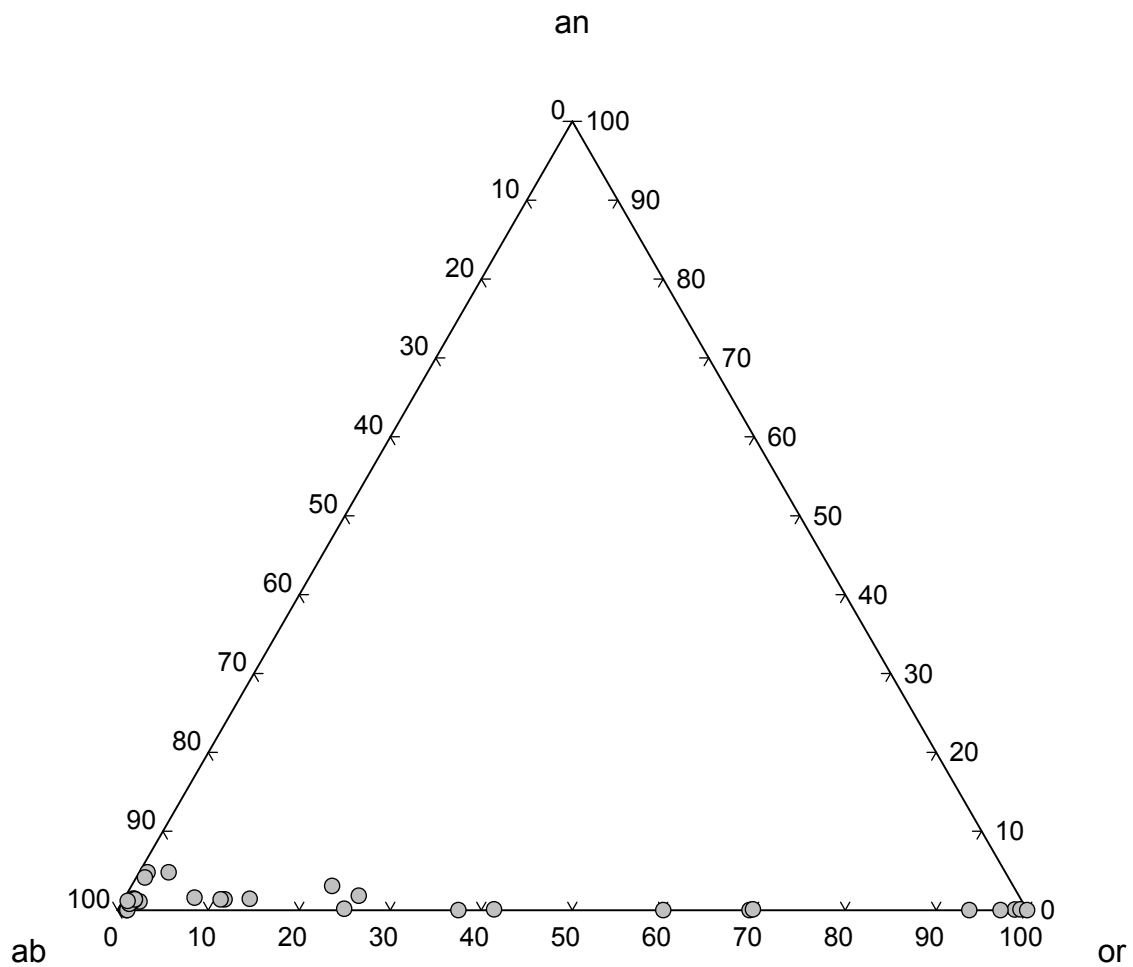


FIGURE 79 – Alkali feldspar compositions – Nepheline Melasyenite

### *Type 1 Nepheline Leucosyenite*

Albite is a minor mineral in the Type 1 nepheline leucosyenite. It is found as irregular exsolution zones within and ragged alteration rims on microcline cryptoperthite. The albite appears white in hand specimen and is colorless and transparent in thin section. Exsolution zones may be up to about 200  $\mu\text{m}$  in maximum dimension, and alteration rims are generally about 100  $\mu\text{m}$  thick. Zones exhibit sharp to diffuse albite twinning, but rims are untwinned.

Representative analyses of albite are listed in TABLE 25. Albite from the Type 1 nepheline leucosyenite ranges in composition from  $\text{ab}_{94}\text{or}_6$  to  $\text{ab}_{98}\text{or}_2$  (Figure 80). Intermediate compositions, near  $\text{ab}_{60}\text{or}_{40}$ , are analyses of incompletely unmixed cryptoperthite. Barium occurs as a trace element up to 0.20 wt.% BaO, and iron up to 0.23 wt.% FeO.

Microcline is a major mineral in the Type 1 nepheline leucosyenite. It occurs as porcelainous, white to pale grey, euhedral to subhedral prismatic crystals to 4 mm width by 10 mm length. Laths are opaque with a dull vitreous luster. In thin section, microcline exhibits slight albitization (about 10%) along crystal margins and is cryptoperthitic. The microcline appears clouded and moth-eaten, especially directly adjacent to albite reaction rims; the centers of microcline crystals are generally less turbid. No coherent twinning is visible, save for a few crystals that exhibit what might be degraded M-twinning. Microcline in the Type 1 nepheline leucosyenite is nearly devoid of inclusions, except for minuscule crystals of aegirine and of trace and rare minerals, such as sérandite or pyrochlore.

Representative analyses of microcline are listed in TABLE 25. Microcline from the Type 1 nepheline leucosyenite ranges in composition from  $\text{ab}_4\text{or}_{96}$  to  $\text{ab}_2\text{or}_{98}$  (Figure 80). Barium is present as a trace element up to 0.10 wt.% BaO, and iron substitutes up to 0.16 wt.% FeO.

TABLE 25 – Representative electron microprobe analyses of alkali feldspar – Type 1 Nepheline Leucosyenite

Lithology:	<i>Type 1 Nepheline Leucosyenite</i>					
Sample:	<i>MSH-B-14</i>					
Target:	<i>2a</i>	<i>2e</i>	<i>3a</i>	<i>7d</i>	<i>1b</i>	<i>1c</i>
SiO <sub>2</sub> (wt.%)	68.02	64.96	63.03	61.78	62.69	61.90
P <sub>2</sub> O <sub>5</sub>	0.00	0.00	0.09	na	0.00	0.00
Al <sub>2</sub> O <sub>3</sub>	19.60	18.86	19.49	17.90	18.42	18.21
Sc <sub>2</sub> O <sub>3</sub>	na	na	na	na	na	na
FeO	0.23	0.11	0.03	0.16	0.11	0.17
CaO	0.00	0.00	0.00	0.00	0.00	0.00
BaO	0.17	0.00	0.00	na	0.20	0.04
Na <sub>2</sub> O	13.66	12.49	0.27	0.23	7.89	7.80
K <sub>2</sub> O	0.31	1.15	17.72	19.66	7.62	7.47
SUM	102.00	97.57	100.62	99.73	96.94	95.59
<i>Cations</i>						
Si	2.951	2.949	2.927	2.940	2.939	2.939
P	0.000	0.000	0.004	na	0.000	0.000
Al	1.002	1.009	1.066	1.004	1.018	1.019
Sc	na	na	na	na	na	na
Fe <sup>2+</sup>	0.008	0.004	0.001	0.006	0.004	0.007
Ca	0.000	0.000	0.000	0.000	0.000	0.000
Ba	0.003	0.000	0.000	na	0.004	0.001
K	0.017	0.067	1.049	1.194	0.455	0.453
Na	1.149	1.099	0.024	0.022	0.717	0.718
<i>or</i>	1.47	5.71	97.74	98.22	38.73	38.63
<i>ab</i>	98.28	94.29	2.26	1.78	60.95	61.31
<i>an</i>	0.00	0.00	0.00	0.00	0.00	0.00
<i>cn</i>	0.25	0.00	0.00	na	0.32	0.07
Normalized to 8 oxygen <i>apfu</i> na = not analyzed						

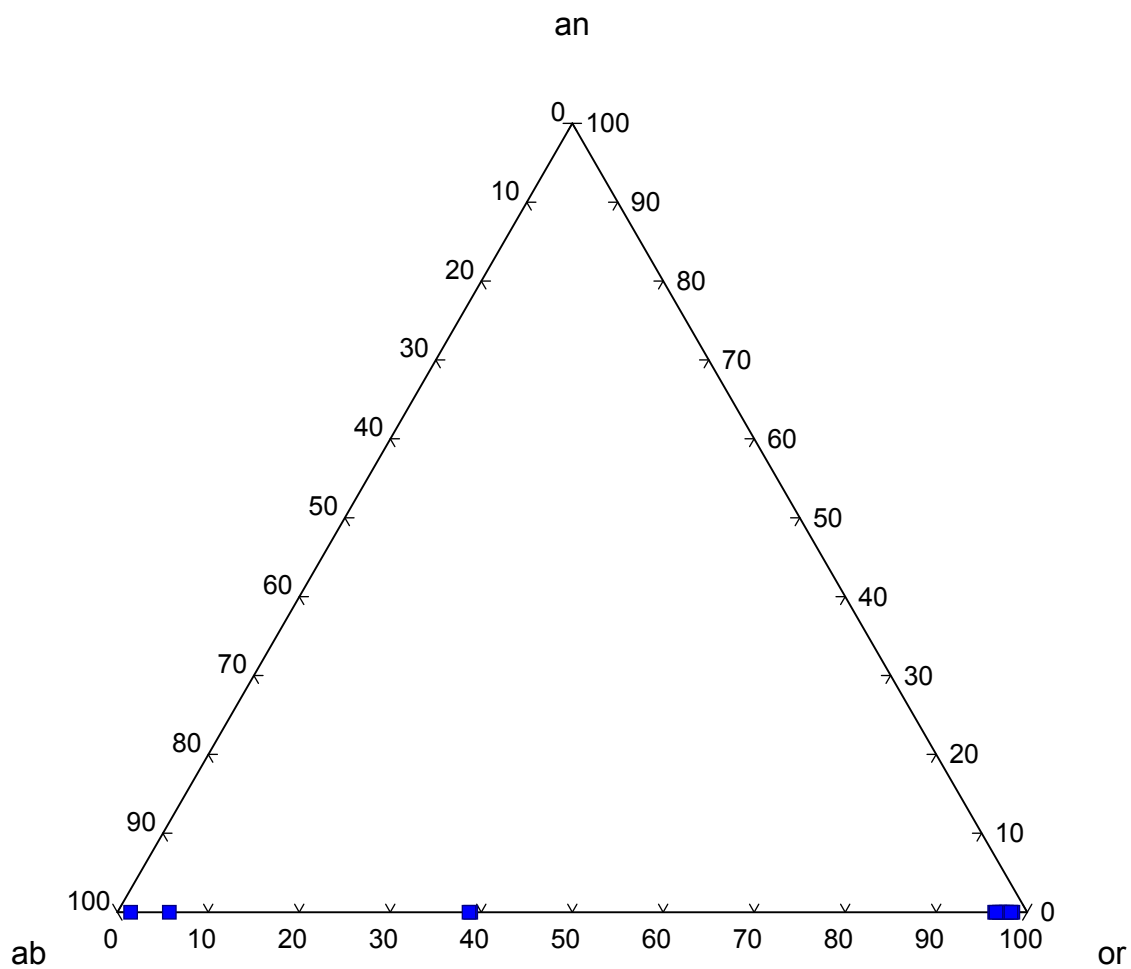


FIGURE 80 – Alkali feldspar compositions – Type 1 Nepheline Leucosyenite

### *Type 2 Nepheline Leucosyenite*

Albite is a major mineral in the Type 2 nepheline leucosyenite. It occurs primarily as white, translucent, euhedral mm-scale laths. Such crystals generally have a fresh surface appearance. They are found as subhedral to euhedral single crystals, intergrown in random orientations with microcline, as well as in the form of aggregates with no particular association. Albite also occurs in this syenite as irregular zones in microcline cryptoperthite.

Representative analyses of albite are listed in TABLE 26. Most albite from the Type 2 nepheline leucosyenite plots near end member albite (Figure 81), running from about  $ab_{94}or_6$  to  $ab_{100}$ . Some analyses of alkali feldspar from the nepheline syenite plot in intermediate compositions, in contrast to the bulk of analyses, which are near-end-member albite or microcline. These are interpreted to be analyses of partially unmixed cryptoperthite. Barium, iron, and phosphorus act as trace elements up to 0.02 wt.% BaO, 0.27 wt.% FeO, and 0.29 wt.%  $P_2O_5$ , respectively.

Microcline occurs as a major mineral in the Type 2 nepheline leucosyenite. It is present as dull, white euhedral to subhedral laths to 4 mm in length. Many crystals have a chalky appearance and are opaque. Examination in thin-section and with the SEM reveals that this is due to cryptoperthitic exsolution and slight albitization. The microcline commonly encloses randomly oriented laths of primary albite.

Representative analyses of microcline are listed in TABLE 26. Most microcline from the Type 2 nepheline leucosyenite is near end-member in composition (Figure 81), ranging from about  $ab_3or_{97}$  to  $or_{100}$ . As was the case with albite, some analyses plot to intermediate compositions. These are similarly interpreted as partially unmixed cryptoperthite. Barium is present up to 0.01 wt.% BaO, iron up to 0.12 wt.% FeO, and phosphorus up to 0.24 wt.%  $P_2O_5$ .

TABLE 26 – Representative electron microprobe analyses of alkali feldspar – Type 2 Nepheline Leucosyenite

Lithology:	<i>Type 2 Nepheline Leucosyenite</i>					
Sample:	<i>MSH-B-4</i>					
Target:	<i>2b</i>	<i>9b</i>	<i>4a</i>	<i>21a</i>	<i>1a</i>	<i>2a</i>
SiO <sub>2</sub> (wt.%)	68.04	67.64	62.30	62.99	58.86	68.15
P <sub>2</sub> O <sub>5</sub>	0.03	0.00	0.24	0.04	0.00	0.00
Al <sub>2</sub> O <sub>3</sub>	19.75	19.53	18.51	19.89	22.32	19.70
Sc <sub>2</sub> O <sub>3</sub>	na	na	na	na	na	na
FeO	0.06	0.08	0.01	0.00	0.12	0.06
CaO	0.00	0.00	0.00	0.00	0.03	0.00
BaO	0.00	0.00	0.00	0.00	0.00	0.01
Na <sub>2</sub> O	12.57	12.36	0.08	0.27	3.67	10.75
K <sub>2</sub> O	0.17	0.11	17.88	16.18	10.40	2.50
SUM	100.62	99.71	99.01	99.37	95.40	101.17
<i>Cations</i>						
Si	2.968	2.974	2.944	2.933	2.811	2.976
P	0.001	0.000	0.009	0.002	0.000	0.000
Al	1.016	1.012	1.031	1.091	1.256	1.014
Sc	na	na	na	na	na	na
Fe <sup>2+</sup>	0.002	0.003	0.000	0.000	0.005	0.002
Ca	0.000	0.000	0.000	0.000	0.001	0.000
Ba	0.000	0.000	0.000	0.000	0.000	0.000
K	0.010	0.006	1.078	0.961	0.634	0.139
Na	1.063	1.054	0.007	0.024	0.340	0.910
<i>or</i>	0.89	0.56	99.34	97.52	64.98	13.26
<i>ab</i>	99.11	99.44	0.66	2.48	34.87	86.73
<i>an</i>	0.00	0.00	0.00	0.00	0.15	0.00
<i>cn</i>	0.00	0.00	0.00	0.00	0.00	0.01
Normalized to 8 oxygen <i>apfu</i> na = not analyzed						

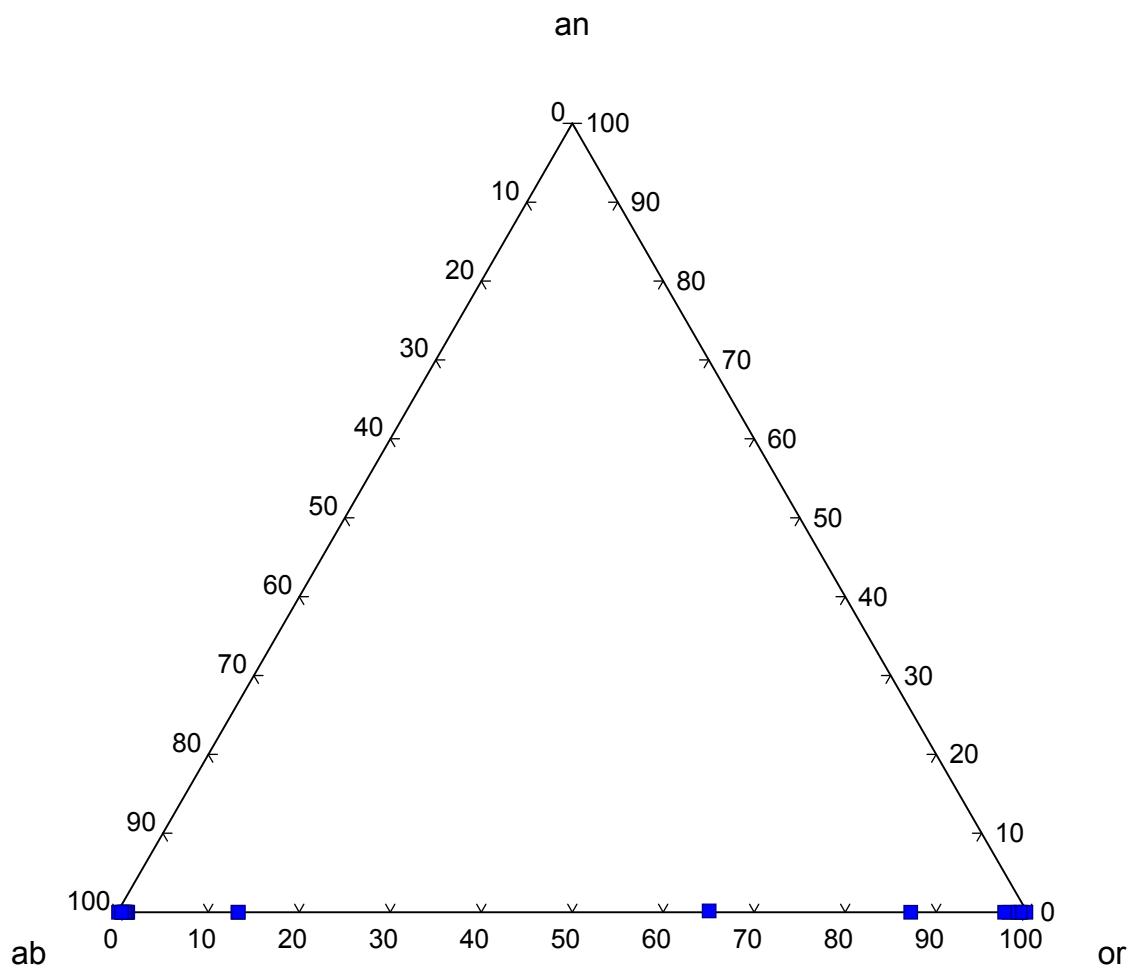


FIGURE 81 – Alkali feldspar compositions – Type 2 Nepheline Leucosyenite

### *Type 3 Nepheline Leucosyenite*

Albite is found as a minor mineral in the Type 3 nepheline leucosyenite. It occurs as irregular zones in cryptoperthitic microcline, which is itself partially albitized. Exsolution zones and albitization are evident in backscattered electron images in the SEM and from electron microprobe analyses, but they are, by and large, not obvious from examination with the petrographic microscope. Although albitized areas appear corroded, microcline in the Type 3 nepheline leucosyenite is generally corroded whether it is albitized or not, so making a visual distinction between albitization and simple corrosion is unreliable. Exsolution zones exhibit diffuse albite twinning.

No reliable electron microprobe analyses were collected of albite from the Type 3 nepheline leucosyenite. Albitized portions of microcline were too altered to yield good totals.

Microcline is a major mineral in the Type 3 nepheline leucosyenite. It is found as white, euhedral, prismatic cryptoperthitic crystals to 0.5 mm wide by 2 mm long. In thin section, they appear clouded and corroded. No twinning is visible in microcline in the Type 3 nepheline leucosyenite.

This mode of occurrence of microcline grades into macroscopic, weakly banded, colloform intergrowths with sodalite pseudomorphs after nepheline. Examination in thin section reveals that the crystals of microcline are smaller than those that occur outside of colloform regions, averaging about 150  $\mu\text{m}$  wide by 250  $\mu\text{m}$  long.

Representative analyses of microcline are listed in TABLE 27. Microcline from the Type 3 nepheline leucosyenite plots near end-member microcline, with compositions from  $\text{ab}_{20}\text{or}_{98}$  to  $\text{ab}_{10}\text{or}_{99}$  (Figure 82). Barium is present as a trace element up to 0.10 wt.% BaO.



TABLE 27 – Representative electron microprobe analyses of alkali feldspar – Type 3 Nepheline Leucosyenite

Lithology:	<i>Type 3 Nepheline Leucosyenite</i>		
Sample:	<i>MSH-B-10</i>		
Target:	<i>1b</i>	<i>1e</i>	<i>2a</i>
SiO <sub>2</sub> (wt. %)	60.78	60.38	63.26
P <sub>2</sub> O <sub>5</sub>	0.00	0.00	0.00
Al <sub>2</sub> O <sub>3</sub>	17.39	17.68	18.08
Sc <sub>2</sub> O <sub>3</sub>	na	na	na
FeO	0.00	0.00	0.01
CaO	0.00	0.00	0.00
BaO	0.10	0.00	0.00
Na <sub>2</sub> O	0.15	0.09	0.18
K <sub>2</sub> O	17.50	16.99	17.67
SUM	95.91	95.14	99.21
<i>Cations</i>			
Si	2.971	2.965	2.978
P	0.000	0.000	0.000
Al	1.002	1.023	1.003
Sc	na	na	na
Fe <sup>2+</sup>	0.000	0.000	0.001
Ca	0.000	0.000	0.000
Ba	0.002	0.000	0.000
K	1.091	1.064	1.061
Na	0.014	0.009	0.017
<i>or</i>	98.57	99.17	98.46
<i>ab</i>	1.27	0.83	1.54
<i>an</i>	0.00	0.00	0.00
<i>cn</i>	0.16	0.00	0.00
Normalized to 8 oxygen <i>apfu</i> na = not analyzed			

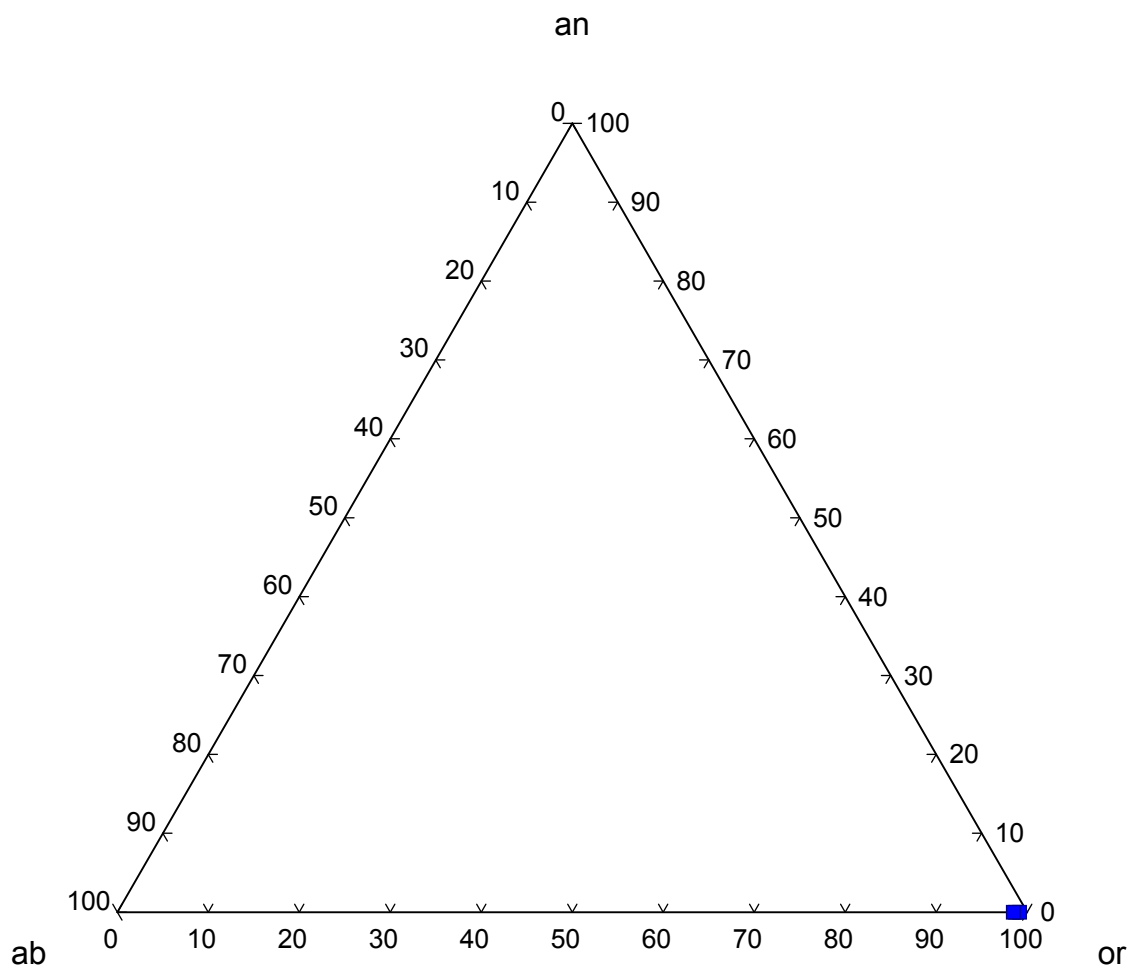


FIGURE 82 – Alkali feldspar compositions – Type 3 Nepheline Leucosyenite

### *Eudialyte Syenite*

Albite occurs as a trace mineral in the eudialyte syenite in two habits and occurrences. In both cases, it is only readily visible in thin-section. Firstly, it is present as isolated subhedral laths to 0.5 mm in length, randomly oriented in and enclosed by microcline. Secondly, it occurs as stellate or plumose clusters, interstitial to other phases.

Representative analyses of albite are listed in TABLES 28 & 29. Albite from the eudialyte syenite is entirely end-member albite (Figure 83), from about  $\text{ab}_{96}\text{or}_4$  to  $\text{ab}_{100}$ . One analysis shows a small (approximately 1 mol%) deviation towards anorthite. Albite from the eudialyte syenite contains scandium in remarkable quantity, up to 0.35 wt%  $\text{Sc}_2\text{O}_3$ . Barium is present up to 0.16 wt.% BaO, iron up to 0.21 wt.% FeO, and phosphorus up to 0.10 wt.%  $\text{P}_2\text{O}_5$ .

Microcline is present as a major mineral in the eudialyte syenite. It occurs as dull to vitreous, white to pale grey subhedral to euhedral laths to 10 mm in length (Figure 84). Most crystals are opaque, but some are translucent to transparent; some of the more diaphanous individuals reveal the presence of microperthite. Opacity is related to the degree of albitization, as seen by examination in thin-section and with EDS analysis. Opaque portions of translucent crystals are concentrated near rims and along fractures and cleavage planes.

Representative analyses of microcline are listed in TABLES 28 & 29. Microcline analyses from the eudialyte syenite spread over a larger range than those from other lithologies (Figure 83), probably due to straddling of microperthite lamellae by the electron beam. Compositions range from about  $\text{ab}_{13}\text{or}_{87}$  to  $\text{or}_{100}$ . Microcline from the eudialyte syenite contains a large amount of scandium, with up to 0.35 wt.%  $\text{Sc}_2\text{O}_3$ . Other trace elements include barium up to 0.22 wt.% BaO, iron up to 0.17 wt.% FeO, and phosphorus up to 0.38 wt.%  $\text{P}_2\text{O}_5$ .

TABLE 28 – Representative electron microprobe analyses of alkali feldspar – Eudialyte Syenite

Lithology:	<i>Eudialyte Syenite</i>					
Sample:	<i>MSH-B-1</i>					
Target:	<i>2a3</i>	<i>16h</i>	<i>1(1)c</i>	<i>11a</i>	<i>1b</i>	<i>3i</i>
SiO <sub>2</sub> (wt.%)	66.94	66.83	63.41	64.05	64.92	62.73
P <sub>2</sub> O <sub>5</sub>	na	na	na	na	na	na
Al <sub>2</sub> O <sub>3</sub>	19.91	18.98	18.82	18.78	19.63	18.68
Sc <sub>2</sub> O <sub>3</sub>	na	na	na	na	na	na
FeO	0.00	0.12	0.02	0.00	0.01	0.00
CaO	0.00	0.00	0.00	0.00	0.00	0.00
BaO	na	na	na	na	na	na
Na <sub>2</sub> O	11.49	11.69	0.38	0.33	1.07	1.46
K <sub>2</sub> O	0.14	0.10	16.89	17.39	15.93	14.37
SUM	98.48	97.71	99.52	100.54	101.55	97.24
<i>Cations</i>						
Si	2.970	2.992	2.962	2.967	2.955	2.968
P	na	na	na	na	na	na
Al	1.041	1.001	1.036	1.025	1.053	1.042
Sc	na	na	na	na	na	na
Fe <sup>2+</sup>	0.000	0.004	0.001	0.000	0.001	0.000
Ca	0.000	0.000	0.000	0.000	0.000	0.000
Ba	na	na	na	na	na	na
K	0.008	0.005	1.007	1.027	0.925	0.867
Na	0.989	1.015	0.034	0.030	0.094	0.134
<i>or</i>	0.78	0.53	96.69	97.20	90.77	86.60
<i>ab</i>	99.22	99.47	3.31	2.80	9.23	13.40
<i>an</i>	0.00	0.00	0.00	0.00	0.00	0.00
<i>cn</i>	na	na	na	na	na	na
Normalized to 8 oxygen <i>apfu</i> na = not analyzed						

TABLE 29 – Representative electron microprobe analyses of alkali feldspar – Eudialyte Syenite (altered)

Lithology:	<i>Eudialyte Syenite (altered)</i>					
Sample:	<i>MSH-B-2</i>					
Target:	<i>2c</i>	<i>6f</i>	<i>3b</i>	<i>4e</i>	<i>6a</i>	<i>14a</i>
SiO <sub>2</sub> (wt.%)	68.60	68.68	68.26	61.54	62.74	63.29
P <sub>2</sub> O <sub>5</sub>	0.01	0.00	0.00	0.00	0.04	0.10
Al <sub>2</sub> O <sub>3</sub>	20.05	20.01	19.31	18.01	18.51	18.53
Sc <sub>2</sub> O <sub>3</sub>	0.33	0.00	0.15	0.28	0.00	0.21
FeO	0.19	0.18	0.17	1.70	0.04	0.16
CaO	0.01	0.00	0.00	0.08	0.01	0.00
BaO	0.09	0.02	0.01	0.09	0.15	0.13
Na <sub>2</sub> O	10.65	11.09	10.54	0.00	0.08	0.00
K <sub>2</sub> O	0.51	0.57	0.54	19.19	18.98	18.18
SUM	100.44	100.56	98.98	100.89	100.56	100.60
<i>Cations</i>						
Si	2.983	2.986	3.008	2.912	2.942	2.951
P	0.000	0.000	0.000	0.000	0.002	0.004
Al	1.028	1.025	1.003	1.004	1.023	1.018
Sc	0.013	0.000	0.006	0.012	0.000	0.009
Fe <sup>2+</sup>	0.007	0.007	0.006	0.067	0.002	0.006
Ca	0.001	0.000	0.000	0.004	0.001	0.000
Ba	0.001	0.000	0.000	0.002	0.003	0.002
K	0.028	0.032	0.031	1.159	1.135	1.081
Na	0.898	0.935	0.900	0.000	0.008	0.000
<i>or</i>	3.03	3.28	3.28	99.50	99.04	99.77
<i>ab</i>	96.75	96.68	96.70	0.00	0.66	0.00
<i>an</i>	0.06	0.00	0.00	0.35	0.06	0.00
<i>cn</i>	0.16	0.04	0.02	0.14	0.24	0.23
Normalized to 8 oxygen <i>apfu</i> na = not analyzed						

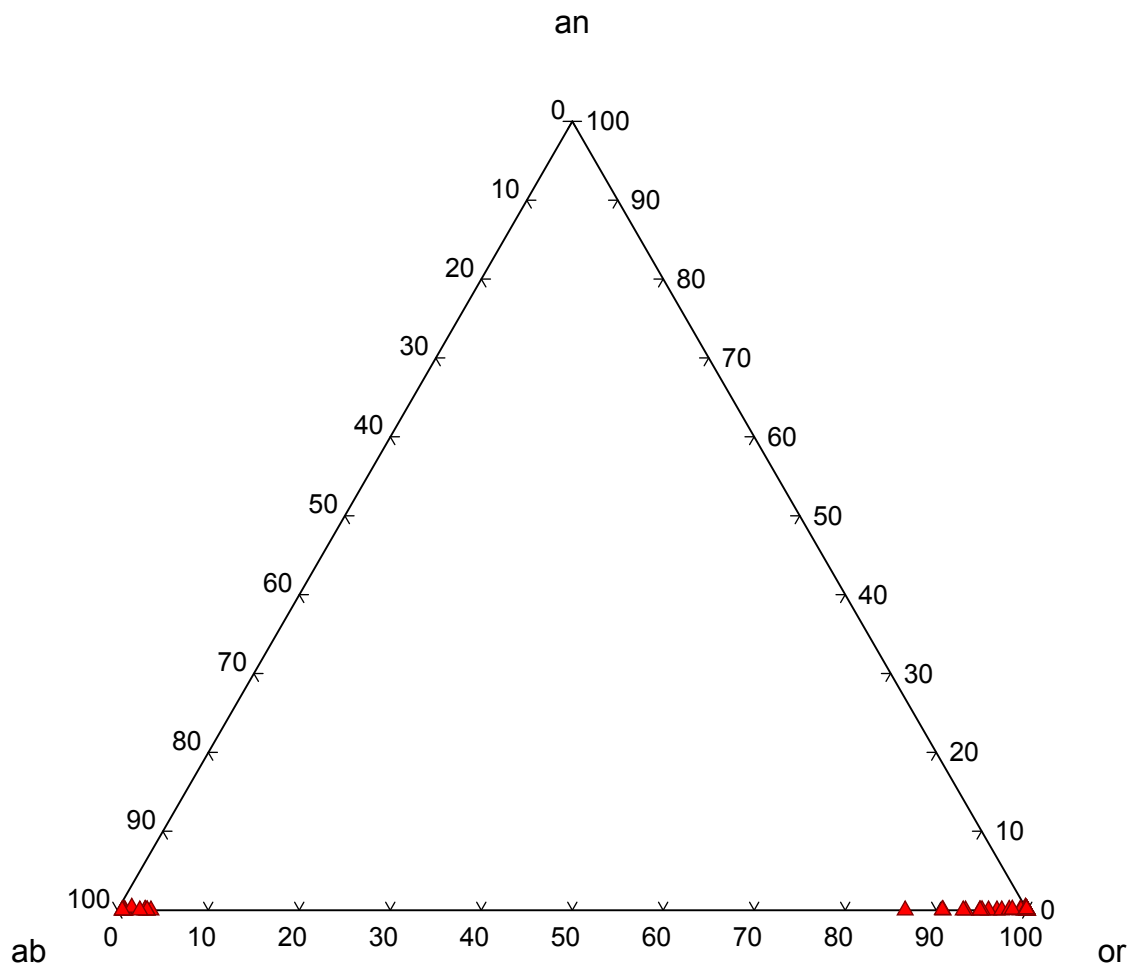


FIGURE 83 – Alkali feldspar compositions – Eudialyte Syenite

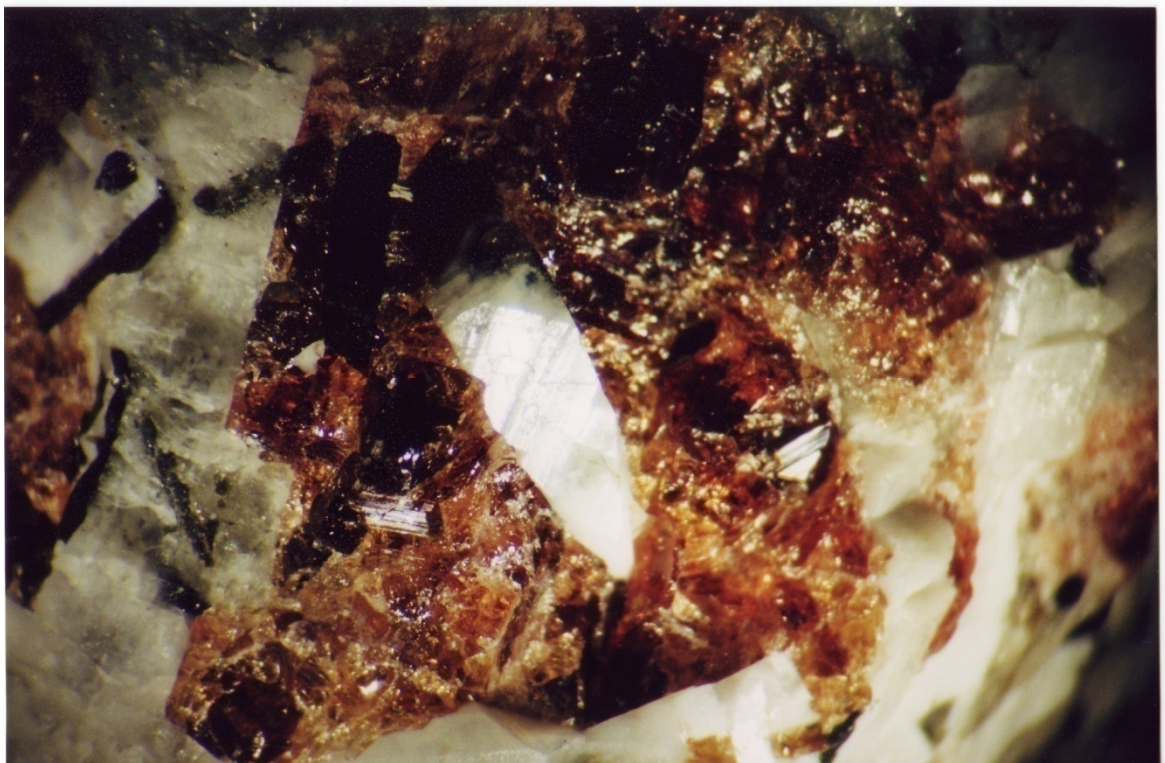


FIGURE 84 – Euhedral microcline in miarole, associated with aegirine (black) and eudialyte group mineral (red) – Eudialyte Syenite (12x)

### *Feldspar-Aegirine Dikes*

Albite is a major mineral in the feldspar-aegirine dikes. It occurs in two modes. The first is as opaque, white, irregular exsolution zones in cryptoperthitic microcline to 5 mm in maximum dimension. These zones are, for the most part, clouded and corroded in appearance in thin section, but portions are translucent and exhibit albite twinning.

The second form of albite is present as euhedral laths to 20  $\mu\text{m}$  wide by 350  $\mu\text{m}$  long, with one individual 2 mm wide by 3 mm long. The smaller crystals occur as randomly oriented inclusions in microcline. They display sharp albite twinning. The larger crystal is interstitial to microcline laths, altering in places to natrolite, and includes small crystals of annite and hematite.

A representative analysis of albite is listed in TABLE 30. Albite from the feldspar-aegirine dikes is near end-member albite (Figure 85), with one analysis plotting at  $ab_{97}or_3$ . Phosphorus is present in an unusually high concentration, 0.71 wt.%  $P_2O_5$ ; the analysis has a low total (96.76 %), but no other phases are visible nearby in backscattered electron mode. Other trace elements include barium and iron, each with 0.18 wt.% BaO and FeO, respectively.

Microcline is a major mineral in the feldspar-aegirine dikes. It occurs as pale grey to white, euhedral, tapering laths to 1 cm in width and 5 cm in length; these crystals are narrower near the margins of a dike and become wider towards the center. The microcline is cryptoperthitic and exhibits signs of corrosion and albitization, being turbid in places in thin section with a whitish, earthy appearance in hand specimen. No twinning is visible. Numerous, randomly oriented laths of albite are included in all portions of the microcline.

Representative analyses of microcline are listed in TABLE 30. Microcline from the feldspar-aegirine dikes is nearly end-member microcline (Figure 85), ranging from  $ab_3or_{97}$  to  $or_{100}$ . Barium substitutes up to 0.15 wt.% BaO, iron to 0.18 wt.% FeO, and phosphorus to 0.09 wt.%  $P_2O_5$ .



TABLE 30 – Representative electron microprobe analyses of alkali feldspar – Feldspar-Aegirine Dikes

Lithology:	<i>Feldspar-Aegirine Dikes</i>					
Sample:	<i>MSH-B-3</i>					
Target:	<i>14b</i>	<i>1a</i>	<i>5c</i>	<i>8e</i>	<i>10b</i>	<i>18b</i>
SiO <sub>2</sub> (wt.%)	65.22	64.09	61.89	62.15	62.01	63.62
P <sub>2</sub> O <sub>5</sub>	0.71	0.09	0.00	0.07	0.04	0.00
Al <sub>2</sub> O <sub>3</sub>	19.00	19.01	18.10	18.79	18.11	18.35
Sc <sub>2</sub> O <sub>3</sub>	0.00	0.00	0.00	0.00	0.04	0.00
FeO	0.18	0.16	0.03	0.03	0.16	0.18
CaO	0.00	0.00	0.00	0.01	0.00	0.00
BaO	0.18	0.00	0.00	0.03	0.06	0.04
Na <sub>2</sub> O	11.02	0.00	0.00	0.00	0.00	0.35
K <sub>2</sub> O	0.45	17.11	18.86	17.49	17.18	17.67
SUM	96.76	100.46	98.89	98.57	97.60	100.21
<i>Cations</i>						
Si	2.953	2.963	2.950	2.944	2.965	2.968
P	0.027	0.004	0.000	0.003	0.002	0.000
Al	1.014	1.036	1.017	1.049	1.021	1.009
Sc	0.000	0.000	0.000	0.000	0.002	0.000
Fe <sup>2+</sup>	0.007	0.006	0.001	0.001	0.006	0.007
Ca	0.000	0.000	0.000	0.001	0.000	0.000
Ba	0.003	0.000	0.000	0.001	0.001	0.001
K	0.026	1.009	1.147	1.057	1.048	1.052
Na	0.967	0.000	0.000	0.000	0.000	0.032
<i>or</i>	2.61	100.00	100.00	99.89	99.89	97.02
<i>ab</i>	97.07	0.00	0.00	0.00	0.00	2.91
<i>an</i>	0.00	0.00	0.00	0.06	0.00	0.00
<i>cn</i>	0.32	0.00	0.00	0.05	0.11	0.06
Normalized to 8 oxygen <i>apfu</i> na = not analyzed						

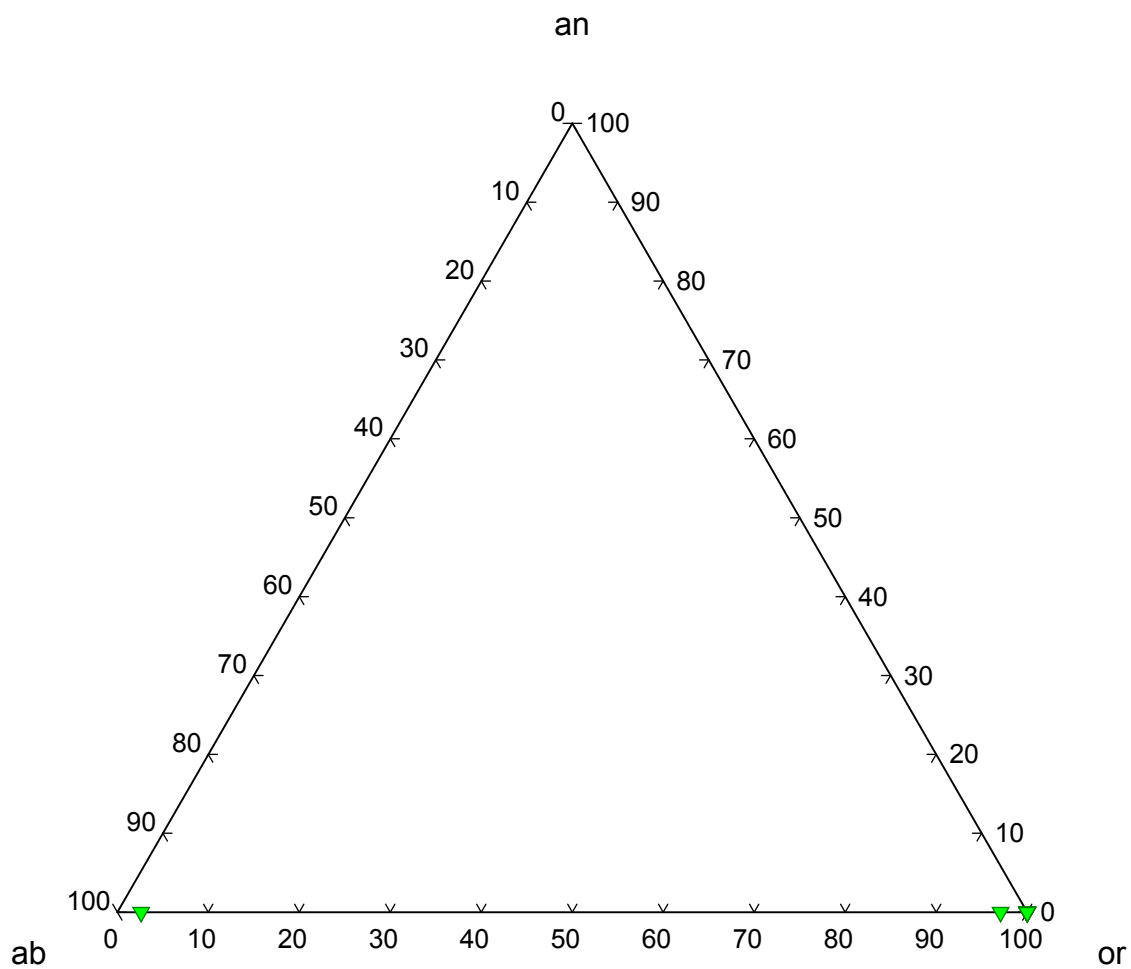


FIGURE 85 – Alkali feldspar compositions – Feldspar-Aegirine Dikes

### *East Hill Suite Alkali Feldspars*

The structural states of alkali feldspar from the East Hill suite were examined using the technique of WRIGHT (1968) (Figure 86). Many analyses lie outside the ideal geometric limits of the plot. This variance is attributed to trace-element substitution. All lithologies for which there are analyses of both unaltered and altered alkali feldspar exhibit an increase in ordering in the altered specimens with respect to unaltered specimens, reflecting the influence of fluids on the structure.

In the nepheline melasyenite, unaltered albite crystals plot near intermediate albite, with a slight deviation towards K-feldspar; altered crystals plot near low albite. No useful structural state analyses of potassium feldspar were obtained from the nepheline melasyenite. Although further analyses from the cores of large, relatively pristine alkali feldspar crystals would be needed for a definitive identification, the albite from unaltered alkali feldspar plots near intermediate albite, suggesting that the K-feldspar is likely orthoclase.

Analyses of unaltered alkali feldspar from the Type 1 nepheline leucosyenite clearly plot in the region of maximum microcline, but atomic plane reflection angles deviate below ideal permissible limits by  $-0.06^\circ 2\theta$  for  $\bar{2}04$  and by  $-0.04^\circ 2\theta$  for 060.

Analyses of unaltered alkali feldspar from the Type 3 nepheline leucosyenite clearly plot in the region of maximum microcline, but atomic plane reflection angles deviate below ideal permissible limits by  $-0.06^\circ 2\theta$  for  $\bar{2}04$ .

Analyses of unaltered alkali feldspar from the eudialyte syenite clearly plot in the region of maximum microcline, but atomic plane reflection angles deviate below ideal permissible limits, in 3 out of 5 analyses, by up to  $-0.05^\circ 2\theta$  for  $\bar{2}04$  and, in 4 out of 5 analyses, by up to  $-0.09^\circ 2\theta$  for 060.

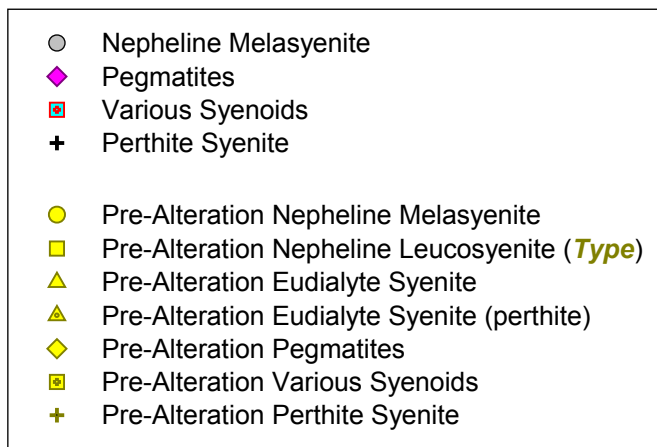
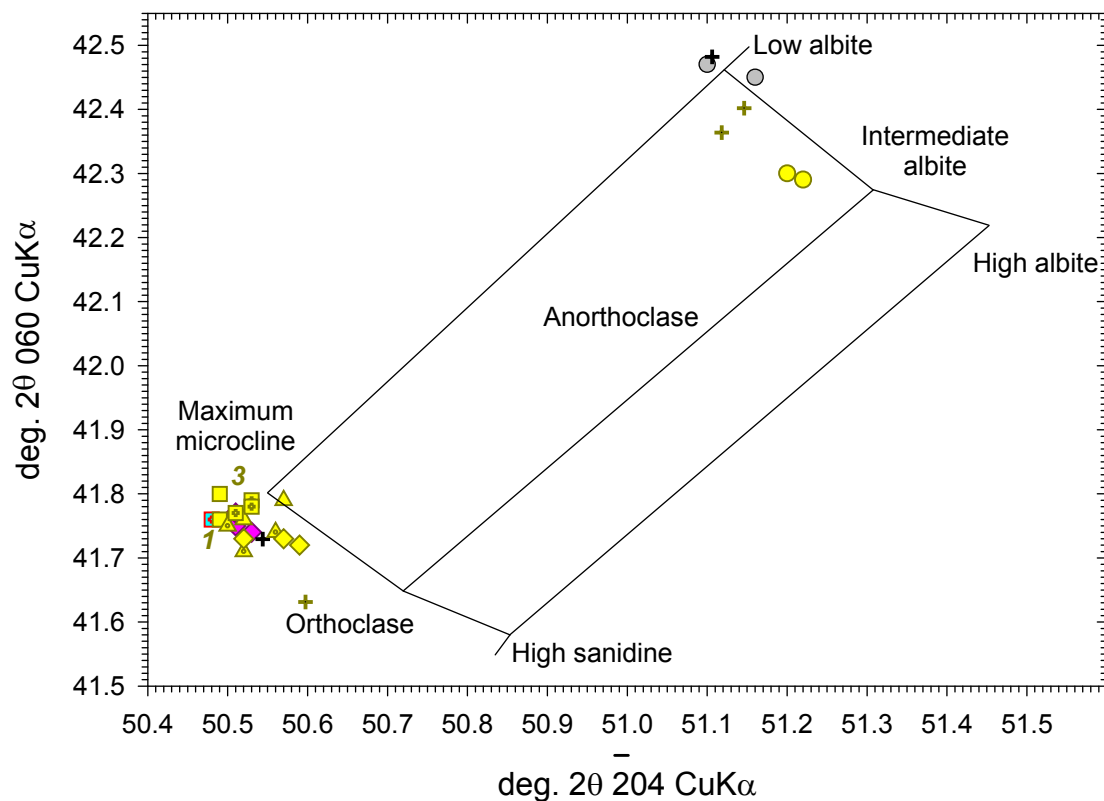


FIGURE 86 – Alkali feldspar structural states – East Hill suite

Analyses of unaltered and altered alkali feldspar from pegmatites clearly plot in the region of maximum microcline, but atomic plane reflection angles deviate from ideal permissible limits by up to  $-0.05^\circ 2\theta$  for  $\bar{2}04$  and by  $-0.05^\circ 2\theta$  for 060.

Analyses of unaltered and altered alkali feldspar from various syenoids clearly plot in the region of maximum microcline, but atomic plane reflection angles deviate below ideal permissible limits by up to  $-0.07^\circ 2\theta$  for  $\bar{2}04$  and by up to  $-0.04^\circ 2\theta$  for 060.

In the perthite syenite, unaltered Na-feldspar crystals plot between low and intermediate albite, with a slight deviation towards K-feldspar. Altered Na-feldspar crystals plot near low albite. Unaltered K-feldspar crystals plot near orthoclase. Altered K-feldspar crystals plot near maximum microcline. Atomic plane reflection angles for unaltered Na-feldspar are within ideal permissible limits; those for altered Na-feldspar deviate from ideal permissible limits by up to  $-0.02^\circ 2\theta$  for  $\bar{2}04$  and by up to  $+0.02^\circ 2\theta$  for 060. Atomic plane reflection angles for unaltered K-feldspar deviate below ideal permissible limits by up to  $-0.12^\circ 2\theta$  for  $\bar{2}04$  and by up to  $-0.02^\circ 2\theta$  for 060; those for altered Na-feldspar deviate below ideal permissible limits by up to  $-0.01^\circ 2\theta$  for  $\bar{2}04$  and by up to  $-0.05^\circ 2\theta$  for 060.

The dominance of cryptoperthitic and microperthitic alkali feldspar phenocrysts in the East Hill suite indicates the prevalence of low  $f_{\text{H}_2\text{O}}$  hypersolvus conditions through early and middle stages of crystallization. This is supported by alkali feldspar compositions in the nepheline melasyenite and the Type 1 nepheline leucosyenite, in which partially unmixed alkali feldspar compositions are restricted to a range of compositions that exclude the ends of the  $\text{NaAlSi}_3\text{O}_8$ – $\text{KAlSi}_3\text{O}_8$  join. (Parsons 1978) The dominance of near end-member compositions in the remaining lithologies indicates that slower cooling allowed for more complete unmixing.

Late-stage albitization and interstitial albite suggests that  $f_{\text{H}_2\text{O}}$  only increased to saturated, subsolvus conditions near the end of the crystallization history of the major lithologies. Subsolvus crystallization either indicates that the solvus was elevated by the presence of anorthite solid solution or by the presence of  $\text{H}_2\text{O}$ , which lowers the solidus. (Parsons 1978; Brown & Parsons 1989) None of the alkali feldspar in the East Hill suite exhibits substantial substitution by anorthite, so the subsolvus conditions are the result of dissolved  $\text{H}_2\text{O}$  in the magma.

In the nepheline melasyenite cryptoperthite, unmixed potassium feldspar domains generally contain less than 10 mol% albite. The perthite is present as large, euhedral phenocrysts indicating that it was one of the first phases to crystallize, and, as discussed above, orthoclase is presumed to be the initial structural state of the potassium feldspar.

Albite inclusions in perthite are absent in the nepheline melasyenite and the Types 1 and 3 nepheline leucosyenite but are present in the Type 2 nepheline leucosyenite, the eudialyte syenite, and the feldspar-aegirine dikes. Referring to FIGURE 87, compositions of unmixed perthite from the nepheline melasyenite and the Type 1 nepheline leucosyenite closely correspond to the binary eutectic between albite and orthoclase. Cooling a composition near this minimum would generate intermediate-composition alkali feldspar phenocrysts with no accessory alkali feldspars. A shift in bulk composition towards albite would result in albite crystallization at the liquidus, followed by descent to the eutectic and crystallization of one intermediate-composition alkali feldspar. Texturally, this would appear as albite phenocrysts enclosed by perthite. This indicates that  $a_{\text{Na}}$  increased during crystallization of the East Hill suite following crystallization of the nepheline melasyenite and the Type 1 nepheline leucosyenite.

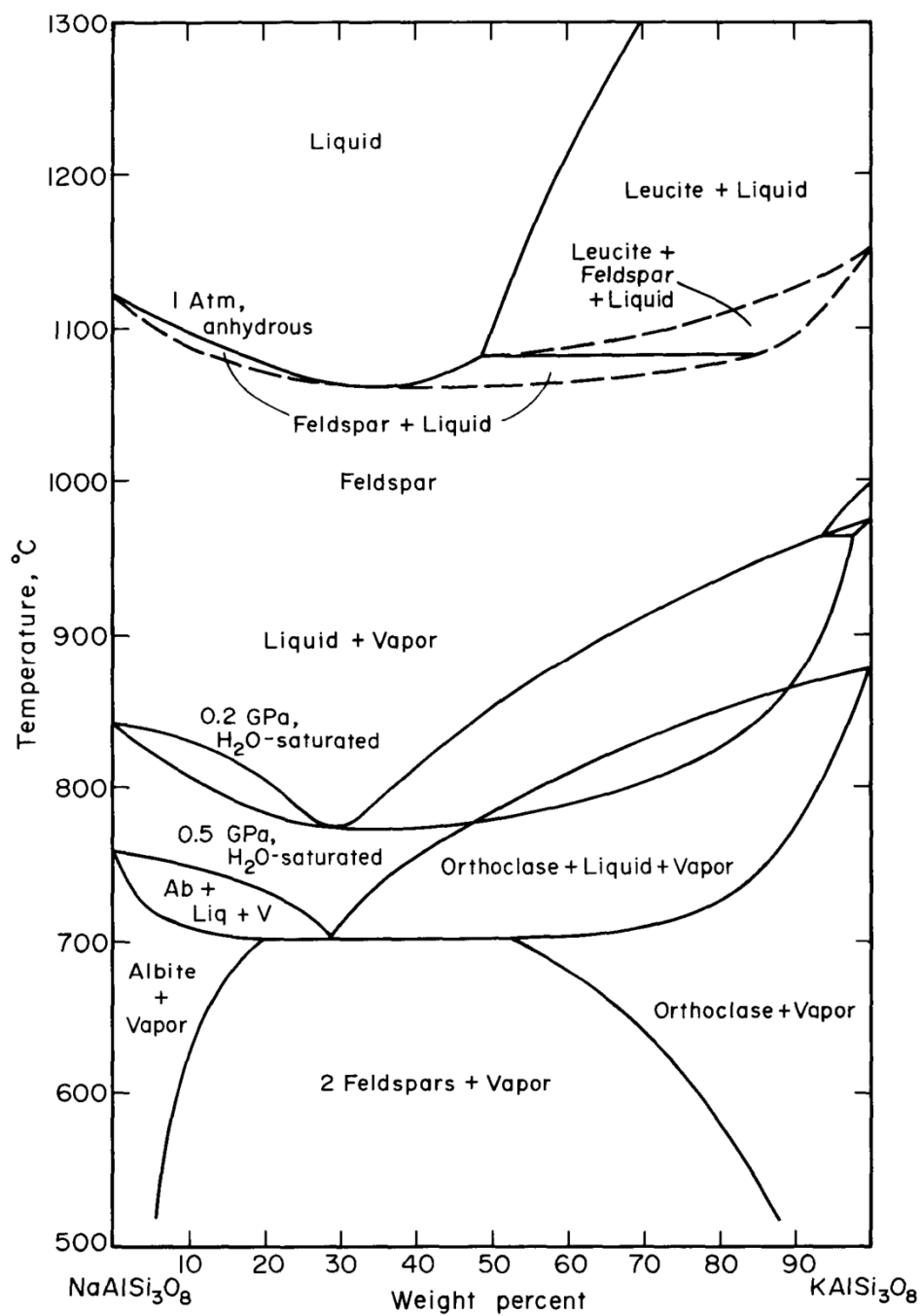


FIGURE 87 – Phase relations in the system NaAlSi<sub>3</sub>O<sub>8</sub> – KAlSi<sub>3</sub>O<sub>8</sub> for anhydrous conditions at 1 bar (Schairer 1950) and for hydrous conditions at  $p_{\text{H}_2\text{O}} = 0.2$  GPa (Bowen & Tuttle 1950) and 0.5 GPa (Yoder *et al.* 1957; Morse 1970). (Presnall 1995)

Continued cooling would cause the composition to depart the solidus until intersecting the solvus. Normally, this would result in unmixing, creating perthite. The presence of cryptoperthite, however, indicates fluid-mediated exsolution, probably at or below 500°C. (Parsons & Brown 1988) The presence and ubiquity of cryptoperthite suggest that the East Hill suite cooled too quickly for solid-state exsolution, although only the nepheline melasyenite cooled too quickly for solid-state ordering. In the nepheline melasyenite, unaltered albite is structurally frozen as intermediate albite and so, too, presumably, are unaltered potassium feldspars frozen as orthoclase; altered albite has ordered to low albite. In the rest of the suite, unaltered potassium feldspar is already maximum microcline, indicating solid-state ordering.

Ternary feldspar isotherms (Figure 88) calculated by FUHRMAN & LINDSLEY (1988) show that alkali feldspars in the nepheline melasyenite commenced crystallization at or below 750°C. Comparison with FIGURE 87 shows that the alkali feldspar eutectic for  $p_{H_2O} = 2$  kbar is at about 775°C. Evidence suggests, however, that the alkali feldspar in the nepheline melasyenite crystallized under hypersolvus conditions. This would elevate the eutectic well above the crystallization temperatures indicated by the ternary-feldspar isotherms. The CIPW norm for the unaltered nepheline melasyenite indicates that it is silica-undersaturated. Although it does not point to excess sodium silicate, it appears that fluxing by alkalis depressed the eutectic to the vicinity of 750°C.

Isotherms further show that alkali feldspar in the remaining lithologies crystallized well below 750°C; however, they are certainly magmatic in spite of their compositions suggesting crystallization temperatures below the alkali feldspar solidus. The most important piece of textural evidence in this regard is the presence of randomly oriented inclusions of albite and other silicate phases in perthite. (Wintsch & Aleinikoff 2005)



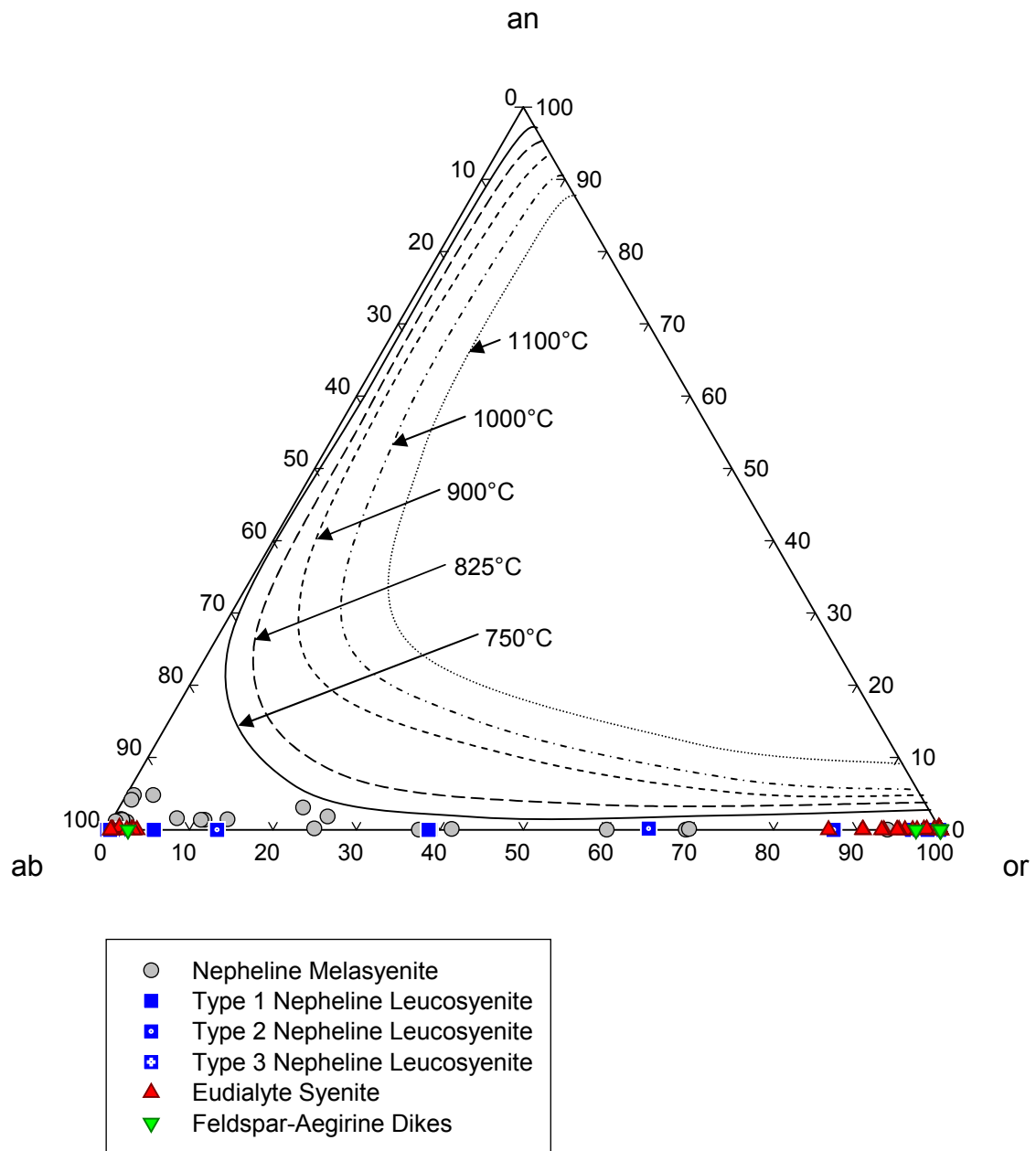
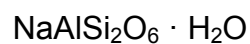


FIGURE 88 – Ternary-feldspar compositions and calculated isotherms – East Hill suite. Isotherms are valid for 1 kbar (0.5 kbar at 900°C), but pressure effects are minimal on the position of the isotherms between 1 and 5 kbar. (after Fuhrman & Lindsley 1988)

*Analcime*



*Eudialyte Syenite*

Analcime has been tentatively identified as a rare mineral in the eudialyte syenite. It occurs in a miarole as a cluster of white, opaque euhedral crystals (Figure 89), individually about 125  $\mu\text{m}$  in maximum dimension, associated with alkali feldspar, natrolite, aegirine, and fluorite. Identification was based on EDS analysis and physical properties (form). The presence of analcime either represents a shift in fluid chemistry to a higher pH or higher  $a_{\text{SiO}_2}$  and  $a_{\text{Na}^+}$ . (Eitel 1964; Chipera & Bish 1997)

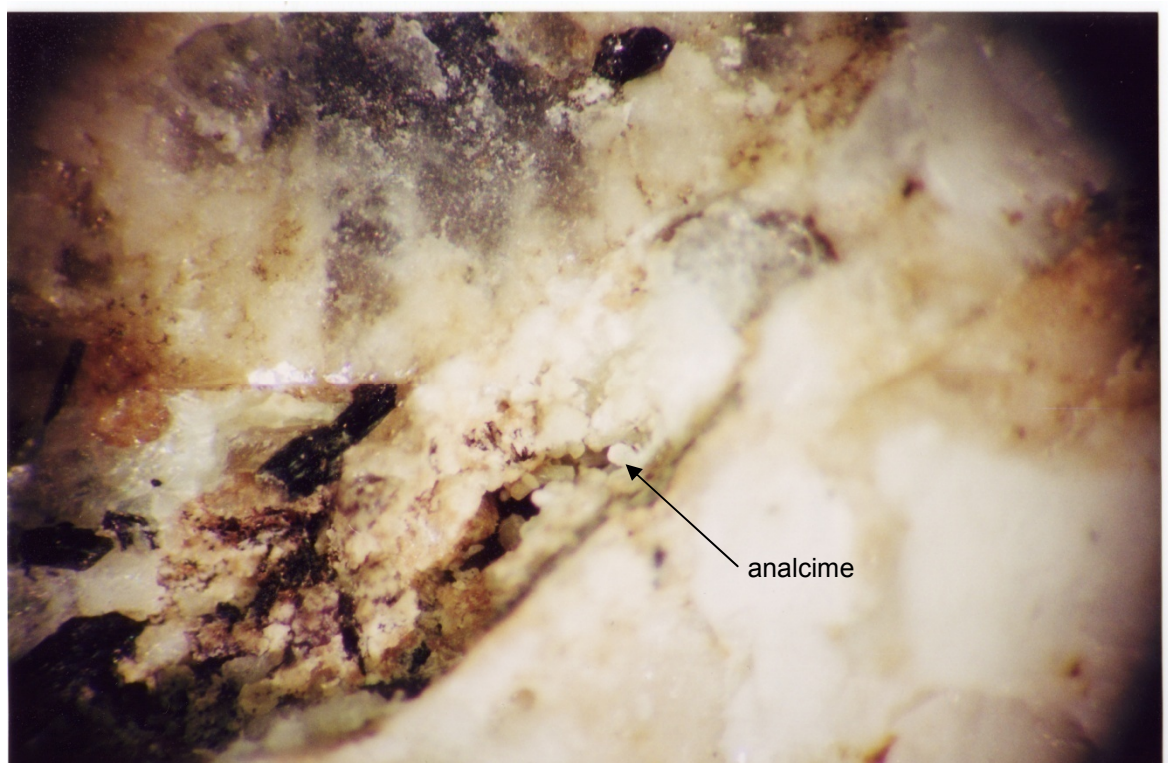


FIGURE 89 – Euhedral analcime in miarole, associated with alkali feldspar, aegirine (black), fluorite (purple), and natrolite – Eudialyte Syenite (25x)

### *Cancrinite*



### *Nepheline Melasyenite*

Cancrinite is a trace mineral in the nepheline melasyenite. It occurs as anhedral, interstitial crystals to 1 mm in maximum dimension. Cancrinite may, however, embay crystals of nepheline, with which it is almost always associated. In this type of occurrence, it likely represents an alteration product of nepheline. Identification was on the basis of EDS analysis and optical properties (uniaxial negative,  $\delta = 0.020$ ).

Electron microprobe analyses of cancrinite exhibited beam sensitivity with low totals (approximately 90 wt.%). This compromised recalculations, and whereas application of a correction factor restored stoichiometry for both Na and Ca, it increased error for Al and Si. Corrections aside, if Na and Ca proportions in the recalculation are correct, then cancrinite in the nepheline melasyenite contains about 0.6 *apfu* surplus Na with a concomitant reduction in Ca.

### *Type 3 Nepheline Leucosyenite*

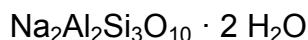
Cancrinite is a rare mineral in the Type 3 nepheline leucosyenite. It is found as subhedral to euhedral prismatic crystals to 500  $\mu\text{m}$  wide by 700  $\mu\text{m}$  long; most crystals of cancrinite in this syenite are approximately 100  $\mu\text{m}$  wide by 200  $\mu\text{m}$  long. Forms present include the hexagonal prism,  $\{10\bar{1}0\}$ , and the hexagonal dipyrmaid,  $\{hk\bar{l}\}$ . Cancrinite is included by sodalite pseudomorphs after nepheline, peripheral to an aegirine clot. The cancrinite crystals may represent an early stage of alteration of the original nepheline crystal; subsequent changes in fluid chemistry may have caused a reaction to sodalite to become more favorable. Identification

was on the basis of EDS analysis, morphology, association with sodalite and nepheline, and optical properties ( $\delta = 0.021$ ).

#### *East Hill Suite Cancrinite*

Cancrinite generally forms either by reaction of nepheline with calcite or by reaction of nepheline with CO<sub>2</sub>-rich fluids. (Sirbescu & Jenkins 1999) For a pressure range of 1 to 1.5 kbar, equilibrium temperatures have been determined ranging from 630°C (Sobolev *et al.* 1974) to 750-900°C (Henderson & Ezepue 1989). For either mechanism, SIRBESCU & JENKINS (1999) propose that water-saturated conditions are a prerequisite for cancrinite formation. Cancrinite growing at the expense of nepheline indicates an increase in  $a_{\text{Ca}^{2+}}$  and  $f_{\text{CO}_2}$  in subsolidus hydrothermal fluids.

#### *Natrolite*



#### *Nepheline Melasyenite*

Natrolite is found as a minor mineral in the nepheline melasyenite, in which it occurs as irregular patches to 20  $\mu\text{m}$  in alkali feldspar or nepheline. It may also be seen as alteration rinds on or complete pseudomorphs after the same. Natrolite occurs as an incipient alteration product of some sodalite crystals. It is further found associated with calcic amphibole and titanite. Identification was on the basis of EDS analysis and optical properties ( $\delta = 0.015$ ). A representative analysis of natrolite is listed in TABLE 31.

### *Type 1 Nepheline Leucosyenite*

Natrolite is a minor mineral in the Type 1 nepheline leucosyenite. It occurs as an alteration product after sodalite, as aggregates of  $\mu\text{m}$ -scale anhedral crystals that form reaction rims along sodalite pseudomorph crystal margins and fractures to about 50  $\mu\text{m}$  thickness. The natrolite is colorless in thin section, but under high magnification (400x), the rims appear to contain a finely-disseminated opaque phase that probably is the cause of the black rind visible on sodalite pseudomorphs in hand specimen. Although the opaque mineral crystals are too small (approximately 1  $\mu\text{m}$ ) and dispersed for EDS analysis or for meaningful optical examination, previous work by TICE (1995) identified pyrite (*q.v.*) as the sole opaque mineral in black rinds on sodalite pseudomorphs after nepheline in the East Hill suite. Identification was on the basis of EDS and EMP analysis, as well as optical properties ( $\delta = 0.013$ ). A representative analysis of natrolite is listed in TABLE 31. Natrolite from the Type 1 nepheline leucosyenite is enriched in Ba up to 0.11 wt.% BaO.

### *Type 2 Nepheline Leucosyenite*

Natrolite occurs as a minor mineral in the Type 2 nepheline leucosyenite in two habits. Firstly, it is found as dull, off-white granular to fibrous masses of anhedral crystals. In thin section, such natrolite is generally seen to occur as a rind on and as patches and veins through sodalite pseudomorphs after nepheline. The distribution pattern of the natrolite suggests a network of fractures or veinlets in the sodalite, although they are not visible in hand specimen. Some specimens, however, exhibit macroscopic voids and fractures lined with natrolite. This observable relationship lends support to the aforementioned concept of microscopic veins. Some natrolite rinds and veinlets are also associated with dawsonite, which is seen as a further

overgrowth on the natrolite. Secondly, natrolite may occur as euhedral prismatic crystals to 1 mm in length, associated with microcline. Identification was on the basis of EDS and EMP analyses. A representative analysis of natrolite is listed in TABLE 31.

### *Type 3 Nepheline Leucosyenite*

Natrolite is a minor mineral in the Type 3 nepheline leucosyenite. It occurs as an alteration product of sodalite as white irregular patches and craggy stringers along fractures in sodalite pseudomorphs after nepheline. The sodalite pseudomorphs are associated with clots of aegirine and vary in distance from these clots. The degree of alteration to natrolite is roughly proportional to the distance of a given sodalite pseudomorph from the center of an aegirine clot; sodalite pseudomorphs contained by aegirine exhibit little to no alteration, and those that are further from aegirine exhibit more alteration. Identification was on the basis of EDS and EMP analyses and was supported by optical properties ( $\delta \approx 0.012$ ). A representative analysis of natrolite is listed in TABLE 31. Natrolite from the Type 3 nepheline leucosyenite is enriched in Ba up to 0.13 wt.% BaO.

### *Eudialyte Syenite*

Natrolite is a major mineral in the eudialyte syenite, in which it occurs as subhedral to euhedral prismatic crystals to 5 mm in maximum dimension. Their color ranges from beige to buff to pale yellow, and they exhibit a dull to vitreous luster. The natrolite occurs generally interstitially to other minerals, although it is also seen, using the SEM, as irregular patches associated with—perhaps overgrowing—albitized microcline. Peak positions in most XRD analyses match well with natrolite, but some appear to either be slightly shifted towards

gonnardite,  $\text{Na}_2\text{CaAl}_4\text{Si}_6\text{O}_{20} \cdot 7 \text{H}_2\text{O}$ . One XRD analysis points to the presence of small quantities of thomsonite,  $\text{NaCa}_2\text{Al}_5\text{Si}_5\text{O}_{20} \cdot 6 \text{H}_2\text{O}$ . Electron microprobe analyses of natrolite from the eudialyte syenite do contain more Ca than those from other lithologies; however no analysis exceeds 0.1 *apfu* Ca, meaning that the specimens are dominated by natrolite. Identification was on the basis of EDS, XRD, and EMP analyses and was supported by optical properties ( $\delta \approx 0.012$ ). A representative analysis of natrolite is listed in TABLE 31. Natrolite from the eudialyte syenite is enriched in Sc and Ba up to 0.29 wt.%  $\text{Sc}_2\text{O}_3$  and 0.15 wt.% BaO.

#### *Feldspar-Aegirine Dikes*

Natrolite occurs in the feldspar-aegirine dikes as an interstitial trace mineral, appearing as subhedral to euhedral crystals averaging approximately 150  $\mu\text{m}$ , but up to 0.7 mm, intergrown and filling void space. It is associated with microcline and aegirine. It is also found as irregular patches in microcline and albite to 300  $\mu\text{m}$  in maximum dimension. Identification was based on EDS and EMP analyses, supported by the occurrence and optical properties ( $\delta \approx 0.013$ ). Natrolite from the feldspar-aegirine dikes is enriched in Sc and Ba up to 0.14 wt.%  $\text{Sc}_2\text{O}_3$  and 0.12 wt.% BaO.

#### *Annite Lamprophyre*

Natrolite is a major mineral in the annite lamprophyre, occurring as the dominant member of the pair of groundmass minerals, the other being calcite. It is present as fibrous masses of anhedral to subhedral acicular crystals to 0.5 mm in maximum dimension. As a groundmass mineral, the importance of associations with natrolite is somewhat diminished; however, it is commonly seen in intimate association with apatite and/or petarasite. In hand

specimen, crystals have a dull to dull-vitreous luster and are pale grey in color. Examination in the SEM reveals in some masses of natrolite, patches of what appears to be böhmite (*q.v.*), perhaps present as an alteration product. Identification was by EDS and EMP analyses, as well as by examination of optical properties ( $\delta \approx 0.012$ ). A representative analysis of natrolite is listed in TABLE 31.

TABLE 31 – Representative electron microprobe analyses of natrolite – East Hill suite

Lithology:	<i>Nepheline Melasyenite</i>	<i>Type 1 Nepheline Leucosyenite</i>	<i>Type 2 Nepheline Leucosyenite</i>	<i>Type 3 Nepheline Leucosyenite</i>	<i>Eudialyte Syenite</i>	<i>Annite Lamprophyre</i>
Sample:	<i>MSH-B-8</i>	<i>MSH-B-14</i>	<i>MSH-B-4</i>	<i>MSH-B-10</i>	<i>MSH-B-2</i>	<i>MSH-B-6</i>
Target:	<i>19b</i>	<i>6a77</i>	<i>5b</i>	<i>4j</i>	<i>3c</i>	<i>14a</i>
SiO <sub>2</sub> (wt. %)	46.64	45.41	53.34	45.90	48.42	49.33
Al <sub>2</sub> O <sub>3</sub>	26.33	25.68	22.92	25.61	27.11	27.22
Sc <sub>2</sub> O <sub>3</sub>	na	na	na	na	0.09	na
FeO	0.06	0.00	0.00	0.00	0.04	3.29
CaO	0.00	0.00	0.00	0.02	0.32	0.15
BaO	na	na	0.00	0.03	0.04	na
Na <sub>2</sub> O	15.50	15.38	13.69	16.87	10.35	7.66
K <sub>2</sub> O	0.00	0.00	0.01	0.00	0.09	0.00
H <sub>2</sub> O*	9.28	9.06	9.62	9.20	9.31	9.42
SUM	97.81	95.53	99.57	97.62	95.76	97.08
<i>Cations</i>						
Si	3.011	3.005	3.324	2.991	3.117	3.140
Al	2.004	2.003	1.683	1.967	2.057	2.042
Sc	na	na	na	na	0.005	na
Fe <sup>2+</sup>	0.003	0.000	0.000	0.000	0.002	0.175
Ca	0.000	0.000	0.000	0.001	0.022	0.010
Ba	na	na	0.000	0.001	0.001	na
K	0.000	0.000	0.000	0.000	0.007	0.000
Na	1.940	1.974	1.654	2.132	1.291	0.946
OH	3.997	3.999	3.999	3.999	3.998	3.999
Normalized to 12 oxygen <i>apfu</i> , including that of water of hydration						
na = not analyzed						
*H <sub>2</sub> O calculated to yield best combination of charge-balance and 4 OH <i>pfu</i>						



## *Nepheline*



### *Nepheline Melasyenite*

Nepheline is a major mineral in the nepheline melasyenite. It occurs as transparent, euhedral, equant hexagonal prisms to 0.2 mm in length and diameter. They occur distributed through the syenite, associated with orthoclase, albite, and amphibole; some occur as oikocrysts in amphibole, but never in titanaugite, even when the amphibole is intimately associated with the titanaugite. Some individuals exhibit incipient alteration to sodalite or natrolite. Identification was on the basis of EDS analysis, crystal habit, and optical properties (uniaxial negative,  $\delta = 0.005$ ). Representative analyses of nepheline are listed in TABLE 32. Nepheline from the nepheline melasyenite is enriched in Fe up to 0.65 wt.% FeO.

### *Type 2 Nepheline Leucosyenite*

Nepheline occurs as a rare mineral in the Type 2 nepheline leucosyenite as irregular remnants in the cores of sodalite pseudomorphs after nepheline. Such remnants are pale dove grey in color, with a dull to dull-greasy luster. EDS analysis reveals the presence of Cl in the nepheline, indicating that the even the remnant nepheline was in the process of being converted to sodalite. Further inspection in the SEM shows that the nepheline is altered progressively to sodalite, then natrolite, then, in some specimens, dawsonite. Identification was primarily on the basis of EDS analysis, physical properties, and morphology.

### *Type 3 Nepheline Leucosyenite*

Nepheline occurs as a rare mineral in the Type 3 nepheline leucosyenite as irregular remnants in the cores of sodalite pseudomorphs after nepheline. These remnant patches are colorless and transparent with a dull-greasy to greasy luster. Examination in the SEM reveals that some of the sodalite has itself been replaced by natrolite along fractures and rims. Identification was primarily on the basis of EDS and EMP analysis, physical properties, and morphology. A representative analysis of nepheline is listed in TABLE 32. Nepheline from the Type 3 nepheline leucosyenite is enriched in Fe up to 0.39 wt.% FeO.

### *Eudialyte Syenite*

Nepheline occurs as a trace mineral in the eudialyte syenite. It is found as irregular remnants in the cores of sodalite pseudomorphs after nepheline. Unaltered nepheline is grey, nearly transparent, and has a greasy luster. Representative analyses of nepheline are listed in TABLE 32. Nepheline from the nepheline melasyenite is enriched in Fe up to 0.22 wt.% FeO.

### *East Hill Suite Nepheline*

Nepheline compositions from the East Hill suite, plotted into the nepheline-kalsilite-silica system (Figure 90), generally follow the Barth compositional join. Nepheline from the nepheline melasyenite comprises two populations, unaltered and partially altered; that from the Type 3 nepheline leucosyenite and the eudialyte syenite is strictly unaltered. Unaltered nepheline plots towards the  $K_2Na_6Al_8Si_8O_{32}$  end of the Barth compositional join, as does nepheline from the eudialyte syenite and the Type 3 nepheline leucosyenite, which furthermore plots close to the Morozewicz-Buerger convergence field. (Tilley 1954; Platt 1996) Partially altered nepheline

TABLE 32 – Representative electron microprobe analyses of nepheline – East Hill suite

Lithology:	<i>Nepheline Melasyenite</i>			<i>Type 3</i> <i>Nepheline</i> <i>Eudialyte Syenite</i> <i>Leucosyenite</i>		
Sample:	<i>MSH-B-8</i>			<i>MSH-B-10</i>	<i>MSH-B-1</i>	
Target:	<i>12b</i>	<i>10e</i>	<i>14l</i>	<i>3b</i>	<i>1f</i>	<i>9d</i>
SiO <sub>2</sub> (wt.%)	44.25	44.36	49.09	38.57	42.17	41.25
Al <sub>2</sub> O <sub>3</sub>	32.80	34.01	31.99	30.72	34.61	34.78
FeO	0.60	0.60	0.30	0.39	0.07	0.01
CaO	0.13	0.09	0.08	0.00	0.00	0.00
BaO	na	na	na	0.17	na	na
Na <sub>2</sub> O	16.95	14.94	15.04	18.99	16.01	15.62
K <sub>2</sub> O	5.85	5.15	3.60	6.31	7.67	8.21
SUM	100.58	99.15	100.09	95.16	100.52	99.87
<i>Cations</i>						
Si	8.465	8.490	9.136	8.000	8.129	8.030
Al	7.394	7.670	7.017	7.510	7.863	7.980
Fe <sup>2+</sup>	0.096	0.096	0.046	0.068	0.012	0.002
Ca	0.026	0.019	0.016	0.000	0.000	0.000
Ba	na	na	na	0.014	na	na
K	1.428	1.256	0.854	1.670	1.886	2.039
Na	6.287	5.543	5.429	7.638	5.983	5.896
<i>qtz</i>	0.09	0.20	0.31	0.00	0.03	0.01
<i>ne</i>	0.74	0.65	0.59	0.82	0.74	0.73
<i>kfs</i>	0.17	0.15	0.09	0.18	0.23	0.25
Normalized to 32 oxygen <i>apfu</i> na = not analyzed						

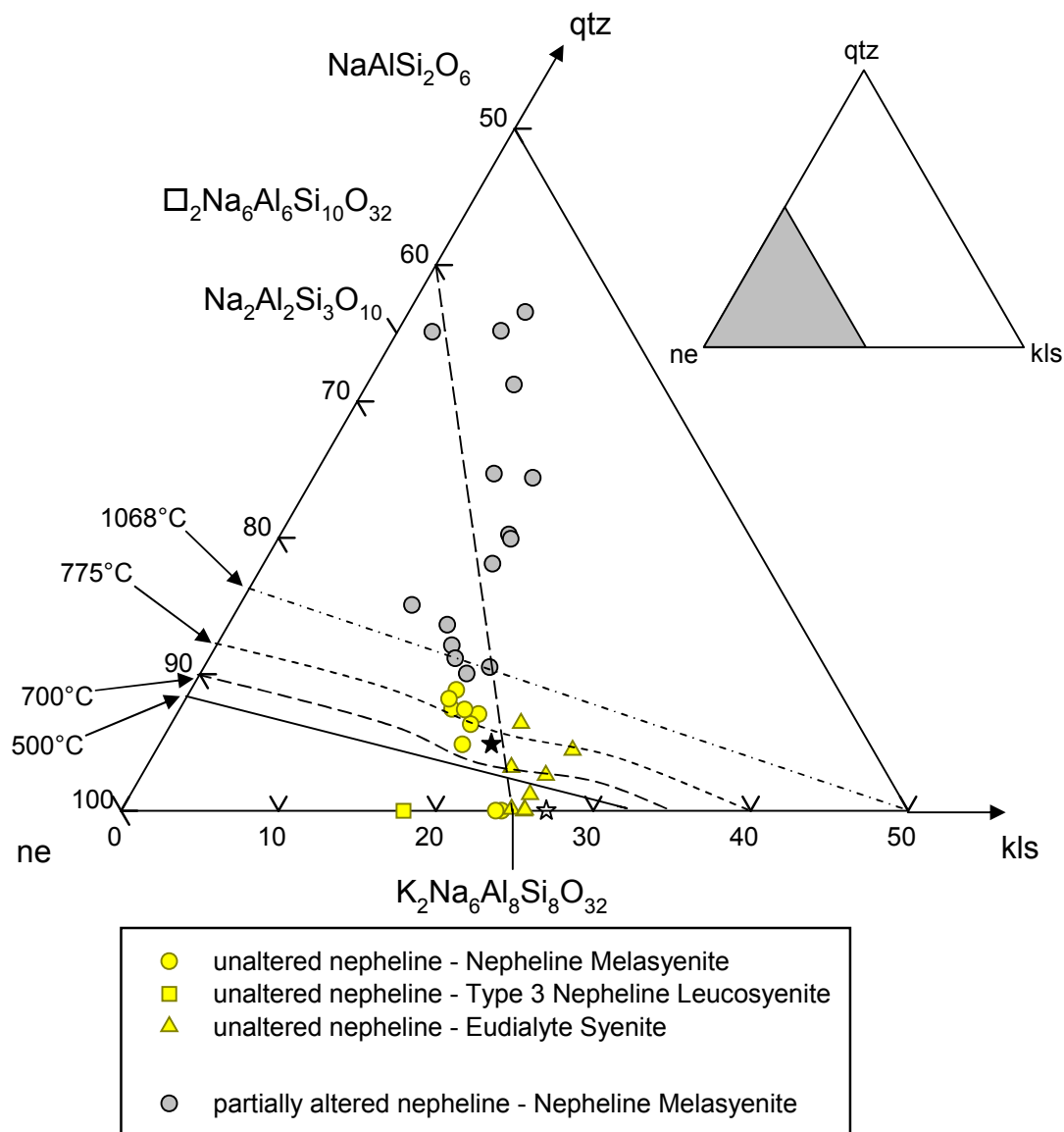


FIGURE 90 – Nepheline compositions and isotherms – East Hill suite. Isotherms are after HAMILTON (1961) and are valid at 1 kbar. Morozewicz (★) and Buerger (☆) ideal nepheline compositions. (Tilley 1954; Platt 1996) (after Wilkinson & Hensel 1994)

from the nepheline melasyenite plots towards the  $\square_2\text{Na}_6\text{Al}_6\text{Si}_{10}\text{O}_{32}$  end of the Barth compositional join and represents incipient alteration, mostly to natrolite but also, in some specimens, to sodalite.

Application of crystallization temperature isotherms (Figure 90) would suggest that nepheline in the nepheline melasyenite may have commenced crystallization at temperatures as high as 1,000-1,100°C. Indeed, nepheline in the nepheline melasyenite is present as euhedral phenocrysts, indicating early crystallization. Nevertheless, such high temperatures are inconsistent with estimates of alkali feldspar crystallization temperatures (Figure 88), with which those of nepheline should be comparable. Also, SOOD (1981) proposes, based on experimental evidence, that the liquidus for typical miaskitic magmas should be no higher than about 820°C at 1 kbar. Therefore, the indication of high-temperature crystallization is likely the result of metasomatic alteration that caused compositions to drift towards natrolite. Similarly, it is more likely that the well-clustered group of analyses near the 775°C isotherm is representative of the initiation of nepheline crystallization. In any case, due to the steep gradient of isotherms at high temperatures, application of nepheline composition to geothermometry is not as precise as other techniques and should not be viewed as the basis for interpretation of magmatic evolution, only as supporting evidence.

Although most analyses are above the 700°C isotherm, a few are clustered well below the 500°C isotherm. Miaskitic magmas such as the nepheline melasyenite generally reach their solidus by approximately 620°C at 1 kbar (Sood 1981), so these very low-temperature nepheline analyses could either represent subsolidus equilibration with alkali feldspar and other alkali aluminosilicates (Powell & Powell 1977), or they could be indicative of late-stage hydrothermal crystallization. (Tait *et al.* 2003) Texturally, most nepheline specimens in the nepheline

melasyenite point to a magmatic origin, although some ambiguous textures suggest that it is possible that a few crystallized from hydrothermal fluid through the alteration of alkali feldspar.

Nepheline compositions indicate that nepheline crystallization also began in the eudialyte syenite at about 775°C. Some compositions suggest crystallization temperatures below 500°C; however, due to this magma being so enriched in alkalis, the eudialyte syenite melt may not have reached its solidus until it had cooled to about 400°C at 1 kbar. (Sood 1981) Again, the resolution of nepheline geothermometry is inadequate to independently and categorically define such low crystallization temperatures. No high-temperature nepheline from the Type 3 nepheline leucosyenite survived metasomatism for analysis, but comparison of alkali feldspar crystallization temperatures from the Type 3 nepheline leucosyenite and the eudialyte syenite (Figure 88) suggests that the crystallization temperature range for both lithologies should be similar. Furthermore, the likelihood of an exceptionally cool solidus for the nepheline leucosyenite melt seems comparably high to that of the eudialyte syenite.

Nepheline that crystallized between about 500-700°C plots near the Morozewicz-Buerger convergence field; this includes the lower-temperature nepheline from the nepheline melasyenite (excluding subsolidus compositions), and all nepheline from the eudialyte syenite and the nepheline leucosyenite. Nepheline compositions in this field are indicative of slow cooling rates. (Tilley 1954; Platt 1996)

### ***Sodalite***



#### ***Nepheline melasyenite***

Sodalite is a trace mineral in the nepheline melasyenite. It is present as subhedral, equant crystals to 3 mm in maximum dimension. They are transparent and largely free of inclusions, but sodalite crystals may include small individuals of nepheline, aegirine-augite, orthoclase, cancrinite, and pyrite. Minor, incipient alteration to natrolite is visible in some sodalite. Accessory minerals, such as aegirine-augite, are concentrated at the interface between sodalite crystals and the groundmass. Positive identification, however, relied on EDS analysis (Cl in sodalite spectrum) or the petrographic microscope (isotropic).

#### ***Annite Lamprophyre***

Sodalite occurs in the annite lamprophyre as a rare mineral. It is found as subhedral crystals to 20 µm, embedded in annite. Identification was based on EDS analysis and on optical properties (isotropic).

### ***Sodalite ps. Nepheline***



#### ***Type 1 nepheline leucosyenite***

Sodalite is a major mineral in the Type 1 nepheline leucosyenite. It is found as colorless to light grey pseudomorphs after euhedral, prismatic nepheline crystals. These pseudomorphs are up to 5 mm in diameter and 10 mm in length. Their turbidity varies with distance from their cores, ranging from transparent at the core to translucent at their margins. Many crystals are at

least partly rimmed by a thin black rind. In thin section, it is evident that all of the sodalite pseudomorphs are mantled by a reaction rim of natrolite containing microcrystals of pyrite; natrolite also crosscuts some sodalite crystals along natural fractures. A very few crystals include small laths of microcline or aegirine-augite, but there are otherwise very few inclusions. Identification was on the basis of EDS and EMP analysis and optical properties (isotropic).

#### *Type 2 nepheline leucosyenite*

Sodalite is a major mineral in the Type 2 nepheline leucosyenite, occurring as pseudomorphs after nepheline. It is found as euhedral prismatic crystals to 7 mm in length and 5 mm in width, with an average size of 4 mm by 3 mm. These pseudomorphs have a dull to vitreous luster, are translucent to transparent, and are pale blue-grey to deep ultramarine blue in color. In thin section and in the SEM, the sodalite is seen to be rimmed by and shot through with veins and patches of natrolite, many of which are themselves rimmed by and shot through with dawsonite (*q.v.*). These veins and patches follow an irregular distribution pattern, typically exhibiting elongate structures, suggesting fractures or veins through the sodalite. In some cases, macroscopic cavities are, in fact, visible, these cavities being lined first by natrolite, then, in some instances, by dawsonite. This concentric or progressive relationship, nepheline → sodalite → natrolite → dawsonite is characteristic and is, for whichever members of the series that are present, invariant in its sequence. Identification was on the basis of EDS and EMP analysis and optical properties (isotropic).



### *Type 3 nepheline leucosyenite*

Sodalite is present as the dominant major mineral in the Type 3 nepheline leucosyenite, occurring in three modes. The first is as colorless, transparent pseudomorphs after euhedral, hexagonal prismatic crystals of nepheline to 4 mm width and 10 mm length. Forms present include the hexagonal prism,  $\{10\bar{1}0\}$ , the hexagonal dipyrmaid,  $\{hk\bar{l}\}$ , and the pinacoid,  $\{0001\}$ , although the pinacoid is not as prominent in the original nepheline crystals as in those from the Type 1 and Type 2 nepheline leucosyenites. These crystals are found as phenocrysts enclosed by aegirine, the extent of the aegirine defining clots up to 5 cm in diameter; some sodalite of this type is also associated with calcite. Sodalite in this mode of occurrence is visibly fractured in thin section. Crystals that occur near the centers of aegirine clots are free to nearly free of alteration, but as the boundaries of such clots are approached, alteration of sodalite along fractures and margins becomes more prevalent.

The second mode of occurrence is as small (250  $\mu\text{m}$ ) anhedral pseudomorphs after nepheline that occur with microcline in weakly-banded, colloform growths that are present outside of aegirine clots. Sodalite in these bands is altered to natrolite in the same pattern as in the first mode.

The third mode of occurrence of sodalite in the Type 3 nepheline leucosyenite is as the *hackmanite* variety of sodalite, and it is really a variant of each of the first two modes.

*Hackmanite* is photosensitive; on older exposures, it is colorless to grey, taking the appearance of nepheline or colorless sodalite; however, on freshly broken surfaces, *hackmanite* presents a dazzling fuchsia color. This color will fade upon exposure to light, the time required to render the sample colorless being in proportion to the intensity of the light. The color may be restored quickly by exposing the *hackmanite* to ultraviolet radiation for a few seconds or slowly by letting

it rest in the dark or under fluorescent lamps for several days. Interestingly, although the color will return, it never achieves its original brilliance, displaying, rather, a bruised purple cast.

*Hackmanite* occurs as pink, magenta, fuchsia, or purple zones in euhedral sodalite pseudomorphs of the first mode and in colloform growths of the second mode. Notably, regardless of the mode of occurrence, *hackmanite* is almost strictly excluded from aegirine clots, and, in fact, most *hackmanite* in the Type 3 nepheline leucosyenite has an antipathetic relationship with aegirine and aegirine-augite. Colorless sodalite strongly dominates where aegirine or aegirine-augite is abundant, and *hackmanite* appears in varying quantities where aegirine or aegirine-augite is scarce to absent. Identification of all three modes was on the basis of EDS and EMP analysis and optical properties (isotropic).

#### *Eudialyte Syenite*

Sodalite occurs as a major mineral in the eudialyte syenite as pseudomorphs after nepheline. Individuals occur as subhedral to euhedral, stubby prismatic crystals which are light to dark grey in color, with some tending towards a slight Prussian blue tint (Figure 58). As such, they are visually very similar to those nepheline crystals that remain unaltered. They may be distinguished visually with a moderate degree of confidence based on differences in luster, nepheline having a greasy luster and sodalite (in this case) having a dull luster, and in diaphaneity, nepheline being translucent to transparent and sodalite being more nearly opaque. Identification was on the basis of EDS analysis and optical properties (isotropic).

## HALIDES

### ***Fluorite***



#### *Nepheline Melasyenite*

Fluorite is found as a trace mineral in the nepheline melasyenite. It occurs as subhedral to euhedral cubic and octahedral crystals to 200  $\mu\text{m}$  in their maximum dimension. It is included in alkali feldspar. Identification was on the basis of EDS analysis and optical properties (isotropic). Fluorite from the nepheline melasyenite exhibited a green fluorescence in the electron beam. Although electron microprobe analyses gave poor totals, fluorite compositions contained up to 1.01 wt.%  $\text{Ce}_2\text{O}_3$  and 1.04 wt.%  $\text{ZnO}$ .

#### *Type 1 Nepheline Leucosyenite*

Fluorite is found in the Type 1 nepheline leucosyenite as a rare mineral. It is present as a 15  $\mu\text{m}$  wide by 100  $\mu\text{m}$  -long stringer in natrolite after sodalite after nepheline. It is associated with aegirine-augite. Identification was based on EDS analysis and optical properties (isotropic).

#### *Type 3 Nepheline Leucosyenite*

Fluorite occurs as a rare mineral in the Type 3 nepheline leucosyenite. It is found as subhedral, cuboctahedral crystals to 90  $\mu\text{m}$  in diameter. They are associated with oikocrysts in calcite of sodalite pseudomorphs after nepheline, along with sérandite. Identification was made on the basis of EDS analysis, combined with examination in the petrographic microscope (isotropic).

### *Eudialyte Syenite*

Fluorite occurs as a trace mineral in the eudialyte syenite. It occurs as yellow interstitial masses to 2.5 mm in their maximum dimension (Figure 91), associated with aegirine, sodalite pseudomorphs after nepheline, and potassium feldspar. Fluorite also occurs in the eudialyte syenite in vugs, as colorless to deep violet, transparent, subhedral to euhedral, equant crystals to 1.5 mm in diameter (Figure 92). Subhedral crystals may display {111}, although this is not well defined, whereas euhedral crystals are cuboctahedral in form. Furthermore, there appears to be evidence of graphic intergrowth with microcline. Identification was made on the basis of EDS analysis, combined with examination in the petrographic microscope (isotropic).



FIGURE 91 – Fluorite (yellow), associated with aegirine (black) and alkali feldspar – Eudialyte Syenite (20x)

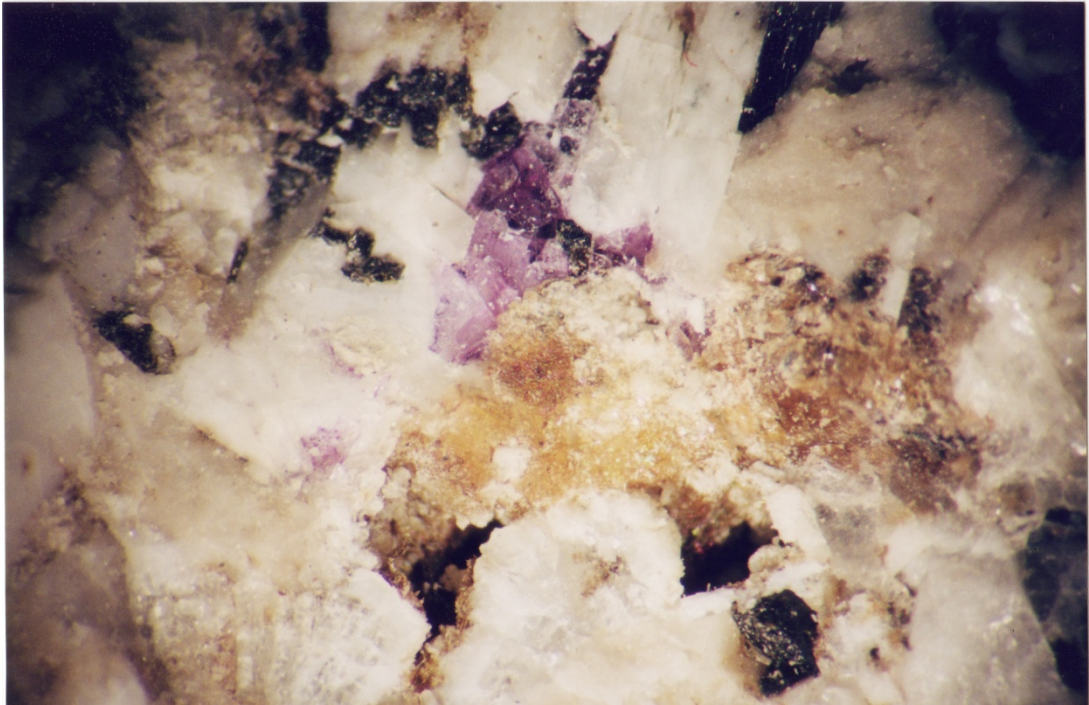


FIGURE 92 – Fluorite (purple) in miarole, associated with aegirine (black), alkali feldspar, eudialyte group mineral, natrolite, and an unidentified yellow mineral. (15x)

### ***Halite***

NaCl

#### *Type 2 Nepheline Leucosyenite*

Halite is a rare mineral in the Type 2 nepheline leucosyenite. One crystal group was found in a vug, which was presumably the remains of a ruptured fluid inclusion. It occurs as euhedral to skeletal cubic crystals to 10  $\mu\text{m}$  in their maximum dimension. Identification was based on EDS analysis and was supported by the apparent mode of occurrence, as well as by the morphology.

## OXIDES & HYDROXIDES

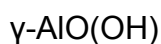
### ***Baddeleyite***



#### *Annite Lamprophyre*

Baddeleyite has been tentatively identified as a rare mineral in the annite lamprophyre. It occurs as irregular masses of fibrous crystals to 10  $\mu\text{m}$  in length. These masses are found within interstices between petarasite, apatite, and annite crystals. The baddeleyite is virtually never seen more than 20  $\mu\text{m}$  from a petarasite crystal, and it, in fact, typically occurs as an intimate overgrowth or as veining. Identification is primarily based on EDS analysis, which yields solely a Zr signature. Examination with the petrographic microscope is inconclusive due to the small size and fibrous habit of the crystals, although the fibrous habit itself lends some support to the identification.

### ***Böhmite***



#### *Type 3 Nepheline Leucosyenite*

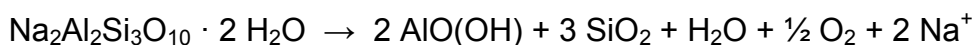
Böhmite has been tentatively identified as a rare mineral in the Type 3 nepheline leucosyenite. It occurs as anhedral grains to 50  $\mu\text{m}$  in diameter, which are present in a cavity in decomposing natrolite that occurs as an alteration product of a sodalite pseudomorph after nepheline. Identification was on the basis of EDS analysis and optical properties ( $\delta \approx 0.011$ ).

### *Annite Lamprophyre*

Böhmite has been tentatively identified in the annite lamprophyre, in which it occurs as a rare mineral. It is present as irregular masses to 0.1 mm of fibrous crystals, embedded within natrolite. Identification is based on EDS analysis, which reveals solely an Al signature, on the association with natrolite, and on examination in the petrographic microscope (habit and  $\delta \approx 0.011$ ).

### *East Hill Suite Böhmite*

Böhmite formed by low-temperature alteration of aluminosilicates. Unlike most alteration reactions in the East Hill suite, böhmite formation is favored by lower  $a_{\text{H}_2\text{O}}$ , and in fact, the decomposition reaction of natrolite to böhmite is a dehydration reaction:



Notice that the reaction also results in the release of free silica and an increase in  $f_{\text{O}_2}$ . At higher  $a_{\text{H}_2\text{O}}$ , gibbsite formation is favored. (Tardy & Nahon 1985) Under ideal conditions, böhmite is stable up to about 450-550°C; larger crystals are stable to higher temperatures, and crystals in the 10-30  $\mu\text{m}$  represent the 450-500°C limit. (Tsukada *et al.* 1999) The upper thermal stability limit of böhmite is not strongly pressure-dependent, varying by only approximately 50°C between 0.1 and 1.0 kbar, and increasing with pressure. (Al'myasheva *et al.* 2005) Its stability field expands with decreasing temperature, with optimum crystallization temperatures between 125-300°C. (Castet *et al.* 1993; Al'myasheva *et al.* 2005) The böhmite in the Type 3 nepheline leucosyenite and the annite lamprophyre is crystalline, rather than amorphous. This habit of böhmite indicates that mildly alkaline, rather than acidic, fluids were involved. (Okada *et al.* 2002)

### ***Hematite***



#### *Feldspar-Aegirine Dikes*

Hematite occurs as a rare mineral in the feldspar-aegirine dikes. It was found as a dark red-brown, euhedral, hexagonal platy crystal 20  $\mu\text{m}$  in diameter. It is included by albite and associated with annite (directly) and natrolite. Identification was on the basis of EDS analysis, morphology, and optical properties (color). The morphology of the hematite and the absence of apparent alteration of iron-bearing phases in its immediate vicinity suggest that it is a primary phase. Therefore, at some time during the crystallization of the feldspar-aegirine dikes, oxygen fugacity reached the HM buffer.

### ***Hochelagaite***



#### *Eudialyte Syenite*

Hochelagaite has been tentatively identified in the eudialyte syenite as a rare mineral. It occurs as anhedral blebs to 10  $\mu\text{m}$ , which form a 0.3 mm seam in alkali feldspar. Identification was based primarily on EDS analysis, and the anisotropic nature of the mineral under crossed polars in the petrographic microscope discounts the possibility of pyrochlore (hochelagaite is biaxial, pyrochlore is isotropic). The mode of occurrence also supports the identification of hochelagaite, which typically is found as a late-stage mineral in vugs or fractures. The occurrence also indicates that the conditions of formation are comparable to those of dawsonite.



### ***Ilmenite***



#### *Nepheline Melasyenite*

Ilmenite is found as a rare mineral in the nepheline melasyenite. It occurs as a metallic black, anhedral mass to 150  $\mu\text{m}$  in its maximum dimension. It is enclosed by a large magnetite grain that also contains pyrite at its margin. The assemblage is associated with annite and aegirine-augite. Identification was by EDS analysis and optical properties (color, birefractance).

### ***Magnetite***



#### *Nepheline Melasyenite*

Magnetite is found as a minor mineral in the nepheline melasyenite. It occurs as euhedral to subhedral octahedral crystals to 250  $\mu\text{m}$  in diameter, although most individuals are smaller than 50  $\mu\text{m}$ . It may also be seen as aggregates of small crystals to 1 mm in maximum dimension. It is generally intimately associated with aegirine-augite and titanite, the group being associated with alkali feldspar and nepheline. It also occurs in simple association with alkali feldspar. A distinctive occurrence of magnetite is as a group of minuscule crystals disposed in the outline of a relic titanaugite crystal, enclosed by taramite; similarly, some magnetite crystals are present near the embayed and replaced fringes of titanaugite crystals. Identification was based on EDS analysis and was supported by examination in the petrographic microscope (morphology and color). Representative analyses of magnetite are listed in TABLE 33. Magnetite from the nepheline melasyenite is enriched in Ti up to 13.56 wt.%  $\text{TiO}_2$ , in Al, reliably up to 2.89 wt.%  $\text{Al}_2\text{O}_3$ , in Mn up to 4.27 wt.% MnO and in Zn up to 1.00 wt.% ZnO.

TABLE 33 – Representative electron microprobe analyses of magnetite – Nepheline Melasyenite

Lithology:	<i>Nepheline Melasyenite</i>		
Sample:	<i>MSH-B-8</i>		
Target:	<i>3a</i>	<i>8c</i>	<i>23a</i>
TiO <sub>2</sub> (wt. %)	6.15	4.89	0.95
ZrO <sub>2</sub>	0.00	0.00	0.06
Al <sub>2</sub> O <sub>3</sub>	0.26	0.22	0.11
REE <sub>2</sub> O <sub>3</sub>	0.71	0.00	0.79
Ce <sub>2</sub> O <sub>3</sub>	0.71	0.00	0.79
FeO <sub>tot</sub>	83.29	85.34	90.81
MnO	4.27	2.72	0.74
MgO	0.00	0.01	0.00
ZnO	0.68	0.00	0.78
SUM	95.36	93.20	94.25
Fe <sub>2</sub> O <sub>3</sub>	56.91	58.65	66.84
FeO	32.08	32.56	30.67
NEW SUM	101.77	99.06	101.74
<i>Cations</i>			
Ti	0.176	0.142	0.027
Zr	0.000	0.000	0.001
Al	0.012	0.010	0.005
REE	0.010	0.000	0.011
Fe <sup>3+</sup>	1.627	1.706	1.927
Fe <sup>2+</sup>	1.019	1.052	0.982
Mn <sup>2+</sup>	0.137	0.089	0.024
Mg	0.000	0.001	0.000
Zn	0.019	0.000	0.022
<i>usp</i>	0.16	0.13	0.03
Recalculated according to the scheme of STORMER (1983) Normalized to 3 cations Fe <sup>3+</sup> calculated to yield 8 cationic charges			

Compositions of coexisting magnetite and ilmenite may be used to estimate  $f_{O_2}$  and crystallization temperature. (Spencer & Lindsley 1981) Insufficient ilmenite was found during this study to obtain electron microprobe analyses, but CURRIE *ET AL.* (1986) give an average of East Hill suite ilmenite and magnetite analyses. Although strict oxygen fugacity and temperature

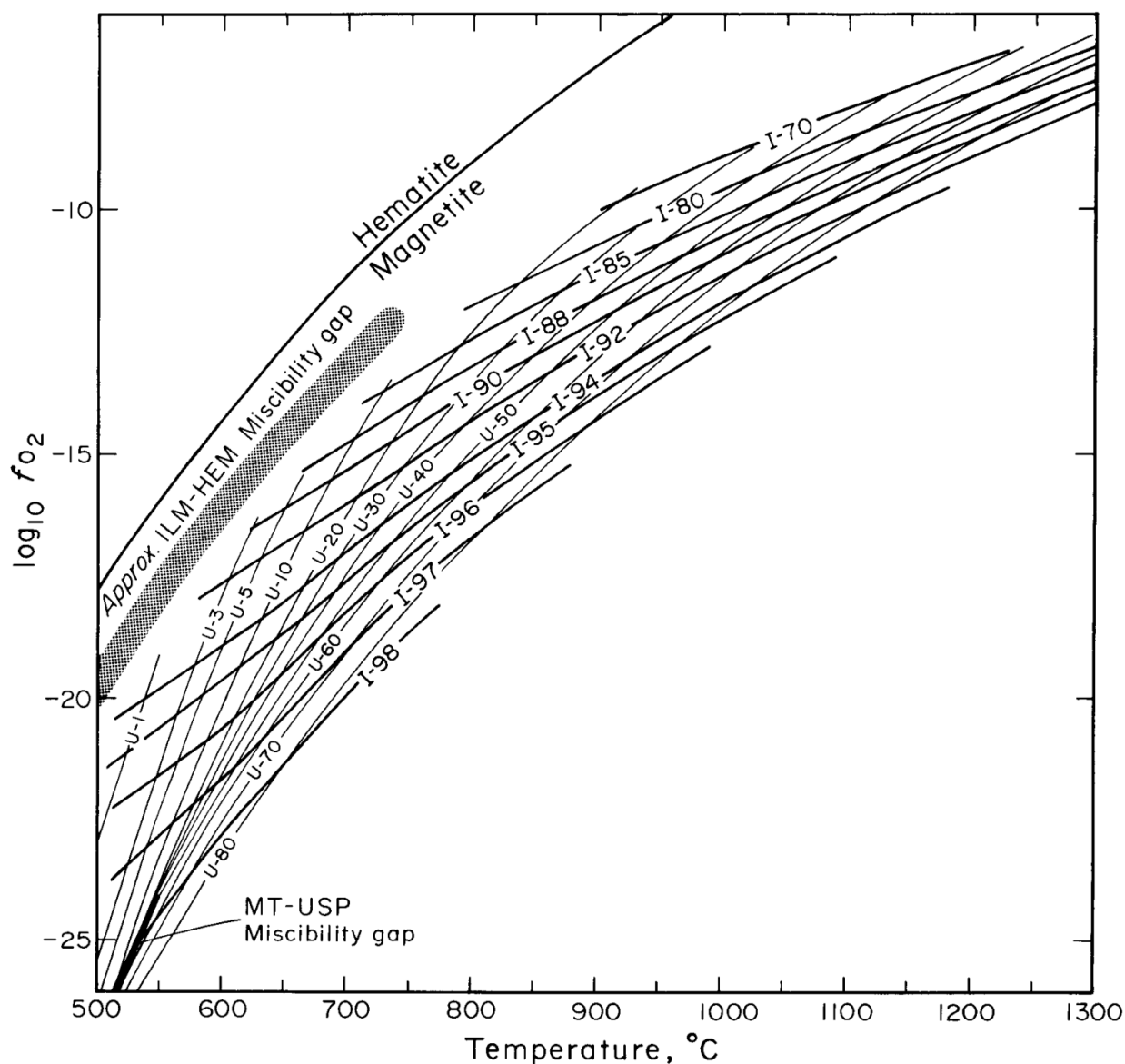


FIGURE 93 – Estimated oxygen fugacity *versus* temperature based on coexisting magnetite-ulvöspinel and ilmenite-hematite solid solution pairs. (Spencer & Lindsley 1981) I- labeled isopleths indicate mole fraction ilmenite component; U-labeled isopleths indicate mole fraction ulvöspinel component.

determinations should be based on immediately coexisting magnetite-ilmenite pairs, such analyses are unavailable here. The average magnetite analysis given by CURRIE *ET AL.* (1986) falls within the range of magnetite analyses from this study. By the method of STORMER (1983), their average ilmenite analysis recalculates to  $X_{ilm} = 0.97$ ; since this value is so close to end-member ilmenite, the range of individual analyses must be relatively narrow. Since the range of ilmenite analyses from CURRIE *ET AL.* (1986) is restricted in range, the average  $X_{ilm}$  must be close to that of any individual analysis, which means that the average may be a reasonable proxy for an ilmenite analysis. Since the coexisting magnetite analyses from CURRIE *ET AL.* (1986) are similar to those from this study, it is a reasonable approximation to say that the magnetite analyses from both studies may be treated as coexisting compositions with ilmenite in order to estimate a reasonable range of  $f_{O_2}$  values and temperatures.

Referring to FIGURE 93, the ilmenite composition is represented by the I-97 isopleth. East Hill suite magnetite analyses from this study recalculate to a  $X_{ulv}$  range of 0.03 to 0.37, which corresponds to the U-3 to near the U-40 isopleths. The intersection of the I- and U-isopleths suggests an approximate range of  $f_{O_2}$  from  $10^{-22}$  to  $10^{-23.5}$  bar, decreasing with temperature, and an approximate temperature range of 600 to 525°C. Over this temperature range, the estimated oxygen fugacities are slightly below the QFM buffer; however, in systems absent of free silica, the  $f_{O_2}$ -T space stability field of magnetite extends down to the MW buffer, nearly 3 log units lower in oxygen fugacity. (Eugster & Wones 1962)

The highest  $f_{O_2}$  values and temperatures are found in numerous small magnetite crystals occurring as relic haloes in amphibole around decomposed titanite crystals. A similar texture is described from the Montagnes Vertes ring complex, Kerguelen Island, where magnetite occurs as reaction haloes in clinopyroxene around amphibole. (Giret *et al.* 1980) Clearly, these two

reactions represent contrary  $p_{\text{H}_2\text{O}}$  trends, but they are both interpreted to occur with oxygen fugacity elevated with respect to the rest of each suite. Similarly, relatively high  $f_{\text{O}_2}$  magnetite crystals are early-crystallizing, as inclusions in clinopyroxene. Magnetite analyses that recalculate to the lowest  $f_{\text{O}_2}$  and temperatures are small, late-stage crystals, interstitial to other phases or found in mafic stringers.

### ***Pyrochlore***



#### *Type 2 Nepheline Leucosyenite*

Pyrochlore occurs in the Type 2 nepheline leucosyenite as a rare mineral. Although its population does not constitute any significant volume of the rock, it is, in fact, widespread, and its individuals are small, but numerous. It is seen as euhedral octahedral crystals to 100  $\mu\text{m}$  in diameter (most to 30  $\mu\text{m}$ ). In hand specimen, they have a brilliant lemon yellow color, and, in thin section, a similar but subdued color. The pyrochlore is associated with calcite, siderite, and sodalite-natrolite with dawsonite. Pyrochlore is also seen with the same association, but as irregular, micron-scale stringers through calcite. Identification was on the basis of EDS analysis, morphology, and examination in the petrographic microscope (isotropic).

#### *Type 3 Nepheline Leucosyenite*

Pyrochlore is a rare mineral in the Type 3 nepheline leucosyenite. It occurs as euhedral, cuboctahedral crystals to 10  $\mu\text{m}$  diameter. They are included by microcline and associated with aegirine-augite.

### *Eudialyte Syenite*

Pyrochlore was found as two euhedral octahedral crystals in the eudialyte syenite, associated with potassium feldspar. They are each approximately 10  $\mu\text{m}$  in diameter and appear bright yellow in thin section. Identification was on the basis of EDS analysis, morphology, and examination in the petrographic microscope (isotropic).

### *Feldspar-Aegirine Dikes*

Pyrochlore is seen as a trace mineral in the feldspar-aegirine dikes as subhedral octahedral crystals to 30  $\mu\text{m}$  in diameter and as irregular stringers to 20  $\mu\text{m}$  in thickness and 1.5 mm in length. It also occurs filling micron-scale seams in microcline. It is associated with aegirine, zircon, and natrolite. Identification was on the basis of EDS analysis, morphology, and examination in the petrographic microscope (isotropic).

### *Annite Lamprophyre*

Pyrochlore occurs as a trace mineral in the annite lamprophyre as euhedral octahedral crystals to 50  $\mu\text{m}$ , although some individuals occur as a thin plate, perhaps flattened on (111), infilling seams, especially in annite. In thin section, the pyrochlore crystals appear a light forest green to greenish-yellow color. In this rock, pyrochlore is typically associated with apatite or annite. Pyrochlore crystals embedded in annite are surrounded by pleochroic haloes. Pyrochlore also occurs as sparse inclusions in gaidonnayite crystals. Identification was on the basis of EDS analysis, morphology, and examination in the petrographic microscope (isotropic).

### ***Pyrophanite***



#### *Feldspar-Aegirine Dikes*

Pyrophanite occurs as a trace mineral in the feldspar-aegirine dikes. It is found as subhedral, tabular crystals to 250  $\mu\text{m}$  in diameter by 30  $\mu\text{m}$  in thickness. Crystals are opaque at their thickest portions; thinner areas are translucent and range (with increasing thickness) from amber to deep blood-red in color. Pyrophanite is associated with microcline, calcite, and ancylite-(Ce). Identification was on the basis of EDS analysis and optical properties (color). Pyrophanite is generally a postmagmatic phase (Ferguson 1978; Mitchell & Liferovich 2004), and crystallization temperatures in the vicinity of 300°C are not unreasonable. (Zaccarini *et al.* 2004)

### ***Rutile***



#### *Type 2 Nepheline Leucosyenite*

Rutile has been tentatively identified in the Type 2 nepheline leucosyenite as a rare mineral. It occurs as subhedral, stubby prismatic crystals to 50  $\mu\text{m}$  in their maximum dimension. These crystals are associated with sodalite pseudomorphs after nepheline, natrolite, and dawsonite. Identification was primarily on the basis of EDS analysis. Due to the small size of the crystals, it is impossible to extract a sample for XRD analysis, so as to identify the particular  $\text{TiO}_2$  polymorph; however, the morphology is consistent with that of rutile. Further support for this identification came from examination in the petrographic microscope (uniaxial and very high birefringence), as well as previous descriptions of rutile from Mont Saint-Hilaire (Mandarino &

Anderson 1989). The absence of ilmenite in the Type 2 nepheline leucosyenite obviates the use of the ilmenite–rutile oxygen barometer to estimate  $f_{\text{O}_2}$ . (Carmichael & Nicholls 1967; Zhao *et al.* 1999)

### ***Thorianite***

ThO<sub>2</sub>

#### *Nepheline Melasyenite*

Thorianite has been tentatively identified in the nepheline melasyenite. The specimen in question is a subhedral crystal, 10 µm wide by 20 µm long, grown in a minuscule interstice in an intergrowth of annite and aegirine-augite. It is associated with lāvenite and fluorapatite. Identification is primarily on the basis of EDS analysis, which gives only a thorium signal.

#### *Type 3 Nepheline Leucosyenite*

Thorianite has been tentatively identified in the Type 3 nepheline leucosyenite as a rare mineral. It is present as a group of subhedral, blocky crystals, individually to 10 µm and collectively to 50 µm, occurring in a fracture in a sodalite pseudomorph after nepheline. The sodalite surrounding the supposed thorianite grouping is altered to natrolite. Identification is primarily on the basis of EDS analysis, which gives only a thorium signal.



## PHOSPHATES & SULFATES

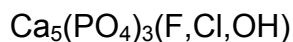
### ***Barite***



#### *Type 3 Nepheline Leucosyenite*

Barite occurs as a rare mineral in the Type 3 nepheline leucosyenite. It is found as euhedral, stout, prismatic crystals 10  $\mu\text{m}$  long in a parallel growth of 3  $\mu\text{m}$  crystals that are collectively 10  $\mu\text{m}$  wide. These crystals appear to be elongated along [100] and display {001}, {100}, {011}, and {201}. Barite is associated with fluorapatite and with natrolite after a sodalite pseudomorph after nepheline. Barite also occurs as anhedral grains to 5  $\mu\text{m}$  diameter in natrolite. Identification was on the basis of EDS analysis, morphology, and optical properties ( $\delta \approx 0.009$ ).

### ***Fluorapatite***



#### *Nepheline Melasyenite*

Fluorapatite is found as a minor mineral in the nepheline melasyenite. It occurs as euhedral, stubby prismatic crystals to 250  $\mu\text{m}$  in diameter and 500  $\mu\text{m}$  in length. The crystals are slightly rounded at their edges and vertices, similar to an incipient fire-polish, and are heavily-fractured. Forms present include the hexagonal prism,  $\{10\bar{1}0\}$ , and the pinacoid, {0001}. Larger crystals are associated with titanaugite and taramite; smaller crystals are associated with alkali feldspar, nepheline, and aegirine-augite but are still near concentrations of mafic minerals. Identification was on the basis of EDS analysis, as well as on examination in the petrographic microscope (uniaxial negative and  $\delta = 0.007$ ). Fluorapatite from the nepheline melasyenite is enriched in Ce up to 1.23 wt.%  $\text{Ce}_2\text{O}_3$  and in Zn, generally about 0.5 wt.% but up to 12.12 wt.%

ZnO. This highest Zn content approximately represents the theoretical substitution limit of Zn in apatite (Miyaji *et al.* 2005) and is probably a real composition, as there are no Zn-bearing phases near the crystal.

#### *Type 1 Nepheline Leucosyenite*

Fluorapatite has been tentatively identified as a rare mineral in the Type 1 nepheline leucosyenite. It is found as colorless, euhedral, hexagonal prismatic crystals to 20  $\mu\text{m}$  in diameter by 60  $\mu\text{m}$  in length. Forms present include the hexagonal prism,  $\{10\bar{1}0\}$ , and the pinacoid,  $\{0001\}$ . Fluorapatite is included by sodalite pseudomorphs after nepheline, microcline, and manganoan pectolite. Common associated minerals are pyrochlore, aegirine-augite, sphalerite, pyrite, arsenopyrite, arfvedsonite, and an unidentified Na-Zr silicate. Although the crystals of apatite in the Type 1 nepheline leucosyenite were too small for microprobe analysis or physical separation for unit-cell measurement by X-ray diffractometry, the strong trend in apatite chemistry in the East Hill Suite is towards fluorapatite; therefore, it is presumed that that is the case for those in this syenite, as well. Identification was based on EDS analysis, morphology, and optical properties ( $\delta \approx 0.006$ ).

#### *Type 2 Nepheline Leucosyenite*

Fluorapatite occurs as a rare mineral in the Type 2 nepheline leucosyenite. It is found as euhedral, stubby prismatic crystals to 30  $\mu\text{m}$  in length. Forms present include the hexagonal prism,  $\{10\bar{1}0\}$ , the hexagonal dipyrmaid,  $\{hk\bar{l}\}$ , and the pinacoid,  $\{0001\}$ . The fluorapatite is found in association with sodalite pseudomorphs after nepheline, albite, aegirine-augite, and almandine. Identification was based on EDS analysis and optical properties ( $\delta \approx 0.007$ ).

### *Type 3 Nepheline Leucosyenite*

Fluorapatite is a rare mineral in the Type 3 nepheline leucosyenite. It was found as a euhedral, hexagonal prismatic crystal 200  $\mu\text{m}$  in diameter. Owing to the orientation of the crystal, with  $[0001]$  vertical, the only form visible is  $\{10\bar{1}0\}$ . It is associated with natrolite after a sodalite pseudomorph after nepheline, barite, and microcline. It also occurs as anhedral grains to about 5  $\mu\text{m}$  in diameter, included by aegirine-augite. Although the crystals of apatite in the Type 3 nepheline leucosyenite were too small for microprobe analysis or physical separation for unit-cell measurement by X-ray diffractometry, the strong trend in apatite chemistry in the East Hill Suite is towards fluorapatite; therefore, it is presumed that that is the case for those in this syenite, as well. Identification was based on EDS analysis, morphology, and optical properties ( $\delta \approx 0.007$ ).

### *Eudialyte Syenite*

Fluorapatite has been tentatively identified as a rare mineral in the eudialyte syenite. It was found as two colorless, subhedral crystals to 25  $\mu\text{m}$  in maximum dimension. One crystal of fluorapatite is associated with thorogummite. The other is included by albite. Although the crystals of apatite in the eudialyte syenite were too small for microprobe analysis or physical separation for unit-cell measurement by X-ray diffractometry, the strong trend in apatite chemistry in the East Hill Suite is towards fluorapatite; therefore, it is presumed that that is the case for those in this syenite, as well. Identification was based on EDS analysis, morphology, and optical properties ( $\delta \approx 0.006$ ).

### *Annite Lamprophyre*

Fluorapatite occurs as a major mineral in the annite lamprophyre, as pale grey to pale tan, vitreous, euhedral prismatic crystals to 0.6 mm in length and 200  $\mu\text{m}$  in diameter. Forms are dominated by the hexagonal prism,  $\{10\bar{1}0\}$ , and the pinacoid,  $\{0001\}$ . Backscattered-electron imaging in the SEM reveals subtle concentric REE-rich zonation in the core with a prominent low-REE overgrowth. Under the EMP electron beam, fluorapatite exhibits a bluish-lilac luminescence, perhaps due to REE but also possibly to the presence of  $\text{Mn}^{5+}$ . (Hughes *et al.* 2004) Fluorapatite is generally found between annite crystals, with natrolite, petarasite, pyrochlore, and calcite. Identification was based on EDS analysis and optical properties (uniaxial negative and  $\delta \approx 0.007$ ). Fluorapatite from the annite lamprophyre is enriched in La and Ce up to 1.13 wt.%  $\text{La}_2\text{O}_3$  and 3.94 wt.%  $\text{Ce}_2\text{O}_3$ , Mn up to 3.70 wt.%  $\text{MnO}$ , and Zn up to 2.28 wt.%  $\text{ZnO}$ . The Mn content is high for the East Hill suite, about half of the theoretical substitution limit of Mn in apatite. (Suitch *et al.* 1985; Hughes *et al.* 2004)

### ***Rhabdophane-(Ce)***



### *Annite Lamprophyre*

Rhabdophane-(Ce) has been tentatively identified as a rare mineral in the annite lamprophyre based on EDS analysis and morphology. Individuals are too small to determine reliable optical properties, although the birefringence appears to be close to an appropriate value ( $\delta_{\text{meas}} \approx 0.030$ ,  $\delta_{\text{ideal}} = 0.027\text{-}0.049$ ). One small natrolite-filled seam in aegirine contains rhabdophane-(Ce) as subhedral to euhedral hexagonal prismatic, equant crystals to 5  $\mu\text{m}$  in their maximum dimension.

## PYROXENE GROUP

Aegirine,  $\text{NaFe}^{3+}\text{Si}_2\text{O}_6$

Aegirine-Augite,  $(\text{Ca}, \text{Na})(\text{Mg}, \text{Fe}^{2+}, \text{Fe}^{3+}, \text{Al}, \text{Ti})\text{Si}_2\text{O}_6$

Augite,  $\text{Ca}(\text{Mg}, \text{Fe}^{2+}, \text{Al})_2(\text{Si}, \text{Al})_2\text{O}_6$

Augite, *var.* Titanaugite,  $(\text{Ca}, \text{Mn}^{2+}, \text{REE})(\text{Mg}, \text{Fe}^{2+}, \text{Fe}^{3+}, \text{Ti}, \text{Al})(\text{Si}, \text{Al})_2\text{O}_6$

### *Crystal Chemistry*

The pyroxene group has the general formula  $[M(2)][M(1)]T_2\text{O}_6$ . In clinopyroxenes, the  $M(2)$  site primarily hosts Ca and Na; the  $M(1)$  site primarily hosts  $\text{Fe}^{2+}$ ,  $\text{Fe}^{3+}$ , Mg, and  $\text{Mn}^{2+}$ ; and the  $T$  site primarily hosts Si; although substitutions of other atoms are possible, and sometimes prevalent. Furthermore, in most clinopyroxenes, divalent cations, such as  $\text{Fe}^{2+}$ , in the  $M(1)$  site are charge-balanced by the presence of Ca in the  $M(2)$  site, and trivalent cations, such as  $\text{Fe}^{3+}$ , in the  $M(1)$  site, as in aegirine, are charge-balanced by the presence of Na in the  $M(2)$  site.

The pyroxene group is represented in the East Hill Suite by sodic-calcic clinopyroxenes of the aegirine-augite series and titanaugite (Figure 94). True aegirine is defined as a clinopyroxene containing more than 80 mol% of the aegirine molecule,  $\text{NaFe}^{3+}\text{Si}_2\text{O}_6$  (Morimoto 1989). Augite comprises a solid-solution series between diopside,  $\text{CaMgSi}_2\text{O}_6$ , and hedenbergite,  $\text{CaFe}^{2+}\text{Si}_2\text{O}_6$ . Aegirine-augite is intermediate between these two fields. Titanaugite is a titanium- and aluminum-rich variety of augite. It exhibits limited solid-solution with aegirine, but lies more properly on a join between augite and a hypothetical end member, “ $\text{CaFe}^{2+}_{0.5}\text{Ti}^{4+}_{0.5}\text{AlSiO}_6$ ”. (Tracy & Robinson 1977)

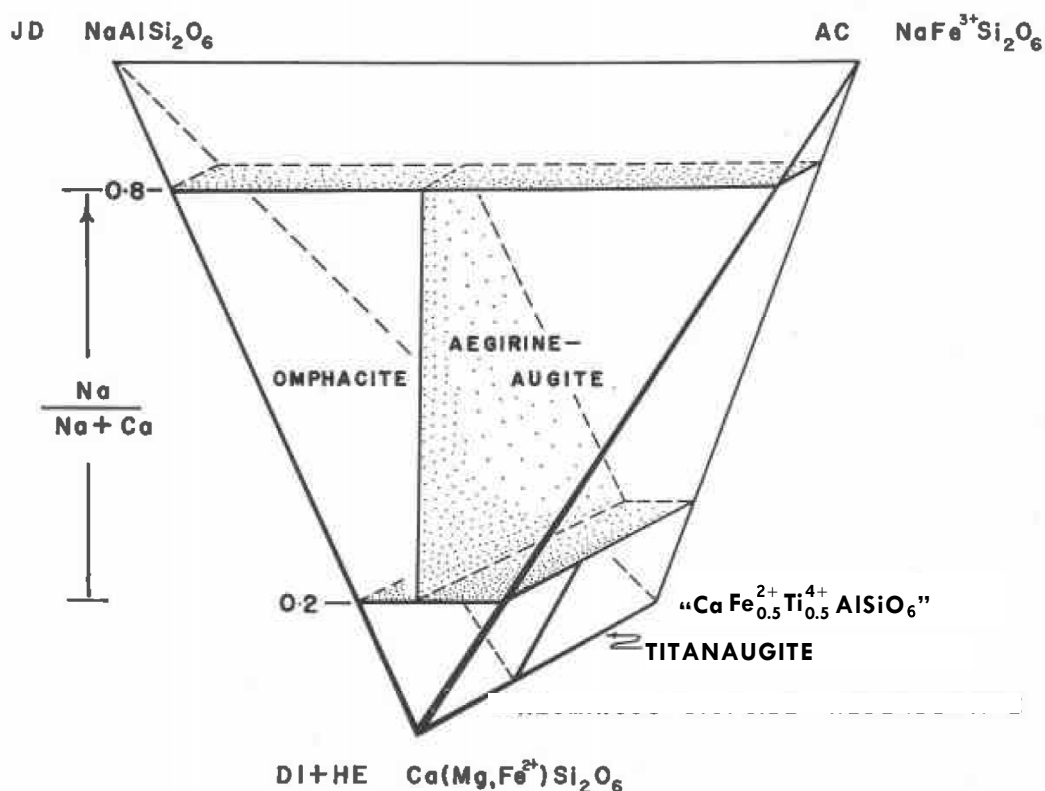


FIGURE 94 – Compositional relations in clinopyroxene. (modified after Clark & Papike 1968; Tracy & Robinson 1977)

Although the crystal chemistry of the pyroxene group is more or less straightforward, compared to that of groups with more complex structures such as the amphibole and eudialyte groups, some complications in recalculations arose.

The first and most pressing issue was the partitioning of iron between the ferric and ferrous states. Electron microprobe analyses do not differentiate between the two oxidation states of iron. Output is reported as “total iron” and is usually expressed as FeO. In the East Hill Suite, however, clinopyroxene with a large aegirine ( $\text{NaFe}^{3+}\text{Si}_2\text{O}_6$ ) component is a common, rock-forming mineral; therefore, it is essential to have a scheme estimating ferric iron in such analyses.

### *Aegirine-Augite Recalculation Scheme*

In a recalculation of an analysis of a clinopyroxene that is free of high-valence cations ( $\text{Al}^{3+}$ ,  $\text{Ti}^{4+}$ ,  $\text{Zr}^{4+}$ , *etc.*), ferric iron is estimated stoichiometrically, by converting total iron (as FeO) to  $\text{Fe}_2\text{O}_3$  until the number of  $\text{Fe}^{3+}$  cations is equal to the number of Na cations. The balance of the iron remains as FeO and gives the estimated FeO analysis for the mineral.

Clinopyroxene from alkaline rock, however, is characterized by containing elevated quantities of Al and Ti. (Donaldson 1977) In accounting for these cations, Na must first be allocated to charge-balance with  $\text{Al}^{3+}$  and  $\text{Ti}^{4+}$ . The remaining Na is then used to estimate  $\text{Fe}^{3+}$ , as described above. This modified scheme is that used for most recalculations in this work, and it provides reasonable results for nearly all the analyses. The exceptions led to the second issue in clinopyroxene recalculations, involving titanaugite analyses.

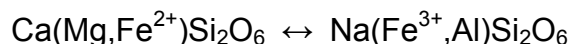
### *Titanaugite Recalculation Scheme*

Several clinopyroxene analyses, especially amongst those from the nepheline melasyenite, reported high amounts of  $\text{Al}_2\text{O}_3$  (up to 7.98 wt.%) and  $\text{TiO}_2$  (up to 2.49 wt.%). These analyses were of titanaugite crystals, as could easily be inferred from the chemistry, but which was confirmed by examination in the petrographic microscope. The contents of Al and Ti were so high in certain analyses as to yield negative  $\text{Fe}^{3+}$  contents and  $\text{Fe}^{2+}$  contents in excess of the analyzed iron. Clearly, there was a problem with the recalculation scheme. Furthermore, the analyses were oxygen-deficient; that is, they indicated a surplus of cations (up to 4.1 cations amongst the three cationic sites, *versus* an ideal content of 4.0). In contrast with that of the negative ferric iron, this phenomenon was found to be consistent with titanaugite analyses from the literature. (Yagi & Onuma 1967; Tracy & Robinson 1977) An examination of the

recalculation scheme used by TRACY & ROBINSON (1977) shed some light on a possible solution to the problem.

The approach is based on important differences between the crystal chemistry of titanaugite and that of other clinopyroxenes. TRACY & ROBINSON (1977) found that certain systematic chemical trends existed in titanaugite crystals from Tahiti. Aluminum content is positively correlated with that of titanium; magnesium and silicon are negatively correlated with titanium. Calcium content is not affected by variation in titanium. These data are consistent with experimental work by YAGI & ONUMA (1967) and are not believed to be unique to titanaugite from a particular locality.

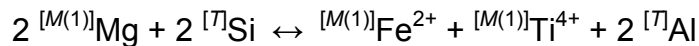
Perhaps more striking is the fact that sodium does not vary systematically with increasing titanium. (Tracy & Robinson 1977) This is in contrast to the usual sodium substitution mechanism (hereafter referred to as the aegirine substitution) in clinopyroxenes (represented simplistically):



in which sodium in the  $M(2)$  site is the primary actor in charge balance with substituted higher-valence cations in the  $M(1)$  site. It is important to make the distinction that TRACY & ROBINSON (1977) *do not* contend that there is no substitution by the aegirine component but rather that sodium is nearly exclusively devoted to charge balance with ferric iron and that its content in titanaugite is generally insufficient to substantially play a role in charge balance with other high-valence cations. This sodium-deficiency, so to speak, also exists in titanaugite samples from the East Hill Suite.



TRACY & ROBINSON (1977) found that the *T* site is the main actor in charge balance with high-valence cations in the *M*(1) site. Plots of their site-occupancy data indicated that high-valence cations were incorporated *via* the scheme:



This amounts to a solid solution series between diopside and a hypothetical titanium- and aluminum-rich end-member:



This scheme accounts for the incorporation of Ti and Al into the structure without invoking the presence of Na. Note that as Ti is incorporated into the *M*(1) site, charge balance arises from substitution of Al in the *T* site. The aegirine substitution may then account for substitution of ferric iron. Indeed, there is excellent agreement with calculated ferric iron and sodium content for East Hill Suite titanaugite samples; and while that may seem like faint praise, as the ferric iron is still determined by charge balance with sodium, the fact that the estimated ferric iron results in near-ideal site occupancies provides independent conceptual support.

The recalculation and site-assignment scheme for this work was based, with one modification, on that used by TRACY & ROBINSON (1977), as it accounts for both *T*-site charge balance of high-valence cations and oxygen deficiency (cationic surplus). The recalculation proceeds in the usual fashion, normalizing to 6 oxygen atoms, up to the point of calculating the number of cations. The number of cations is summed, and a correction factor is imposed to normalize the number of cations to 4.0. The normalized cations are then distributed amongst the three sites.

All of the Si is given to the *T* site, and the balance of the site is filled with Al. Note that this is in contrast to the aegirine substitution, and more specifically to that found in jadeite, in

which Al enters the  $M(1)$  site. This is a result of the observation that  $Ti^{4+}$  is preferentially excluded from the  $T$  site by Al, in high-Ti clinopyroxene, provided that sufficient Al and/or  $Fe^{3+}$  is available to fill the  $T$  site. (Dowty & Clark 1973) Any remaining Al is given to  $M(1)$ , which then receives Sc, Ti, Zr, P, Mg, and Zn. Distribution of iron between the ferrous and ferric states in  $M(1)$  is held off until  $M(2)$  is filled.

The  $M(2)$  site is filled with Na, K, Ca, Ba, and  $Mn^{2+}$ . (Tracy & Robinson 1977) The scheme deviates from that of TRACY & ROBINSON (1977) in the disposition of REE. Any REE content is also partitioned to  $M(2)$ , *via* substitution for Ca, according to the findings of FLEET & PAN (1995). The specific substitution in diopside of REE for Ca was documented by PAN & FLEET (1996), who examined the stereochemical environment of and performed bond-valence calculations on Ca atoms in a variety of calc-silicate minerals. The  $M(2)$  site is then filled to 1.0 cations with  $Fe^{2+}$ .

Following renormalization of the formulæ to 4.0 cations, TRACY & ROBINSON (1977) add oxygen atoms to restore the oxygen total to 6; ferric iron content is calculated from added oxygen.

### *Nepheline Melasyenite*

Augite and aegirine-augite occur as major minerals in the nepheline melasyenite. There appear to be two general populations of crystals. The first population consists of blackish green, subhedral to euhedral prismatic crystals to 2 mm in length by 1 mm in width. In thin section, these crystals are zoned, with pale green to tan cores and deep green rims. This same disposition of color is present in augite and aegirine-augite overgrowths on titanaugite. The second group comprises smaller crystals (50-100  $\mu\text{m}$  in maximum dimension) that are usually deeper green than the first group. Both populations are pleochroic:  $X$  = emerald green,  $Y$  = greenish yellow,  $Z$  = yellow green. Augite and aegirine-augite are associated with titanite, magnetite, and annite and may include or be included by the latter. Representative analyses of clinopyroxene are listed in TABLE 34. Clinopyroxene from the nepheline melasyenite plots from augite to aegirine-augite (Figure 95), with compositions ranging from  $\text{ae}_2\text{di}_{60}\text{hd}_{38}$  to  $\text{ae}_{53}\text{di}_{24}\text{hd}_{22}$ . Clinopyroxene in the nepheline melasyenite is enriched in Ti up to 1.33 wt%  $\text{TiO}_2$ , Zr, in general, about 0.33 wt.% but, in the extreme, up to 5.22 wt.%  $\text{ZrO}_2$ , Al up to 2.91 wt.%  $\text{Al}_2\text{O}_3$ , Ce up to 0.99 wt.%  $\text{Ce}_2\text{O}_3$ , Mn up to 1.85 wt.% MnO, and Zn up to 1.18 wt.% ZnO.

Titanaugite is present as a minor mineral in the nepheline melasyenite as dark, red-tinged, blackish brown, euhedral to subhedral, prismatic crystals to 2 mm in length and width. In thin section, the titanaugite exhibits distinctive pleochroism, according to the scheme:  $X$  = reddish tan,  $Y$  = light tan,  $Z$  = pale violet tan. Some crystals are twinned on  $\{100\}$ . Titanaugite is the central species in a noteworthy mineral association in the nepheline melasyenite. Titanaugite crystals are overgrown with a thin rind of aegirine-augite; the suite of clinopyroxenes is then corroded and embayed, replaced and overgrown by kaersutite, as rare thin veneers directly overlying the titanaugite, or, more generally, taramite. Annite may or may not be present along

TABLE 34 – Representative electron microprobe analyses of clinopyroxene – Nepheline Melasyenite

Lithology:	<i>Nepheline Melasyenite</i>		
Sample:	<i>MSH-B-8</i>		
Target:	<i>9(6)</i>	<i>17c</i>	<i>15f</i>
SiO <sub>2</sub> (wt.%)	52.20	50.30	53.20
TiO <sub>2</sub>	0.79	0.37	0.15
ZrO <sub>2</sub>	0.14	1.38	0.00
Al <sub>2</sub> O <sub>3</sub>	1.94	1.23	1.08
Sc <sub>2</sub> O <sub>3</sub>	na	na	na
REE <sub>2</sub> O <sub>3</sub>	0.60	0.00	0.82
La <sub>2</sub> O <sub>3</sub>	na	na	na
Ce <sub>2</sub> O <sub>3</sub>	0.60	0.00	0.82
FeO <sub>tot</sub>	12.42	20.70	21.52
MnO	1.18	1.67	1.70
MgO	10.40	3.75	3.83
ZnO	0.24	0.00	0.54
CaO	20.64	13.95	12.51
BaO	na	na	na
Na <sub>2</sub> O	1.48	5.00	7.04
K <sub>2</sub> O	0.01	0.00	0.00
SUM	102.05	98.36	102.38
Fe <sub>2</sub> O <sub>3</sub>	0.77	10.96	16.44
FeO	11.73	10.84	6.73
NEW SUM	102.12	99.45	104.03
$\frac{\text{Mg}}{(\text{Mg}+\text{Fe}^{2+})}$	0.61	0.38	0.50
$\frac{\text{Mg}}{(\text{Mg}+\text{Fe}^{2+}+\text{Mn}^{2+})}$	0.59	0.35	0.45

Target:	<i>9(6)</i>	<i>17c</i>	<i>15f</i>
<i>Cations</i>			
Si	1.953	1.974	1.984
Ti	0.022	0.011	0.004
Zr	0.003	0.026	0.000
Al	0.086	0.057	0.047
Sc	na	na	na
REE	0.008	0.000	0.011
Fe <sup>3+</sup>	0.022	0.324	0.461
Fe <sup>2+</sup>	0.367	0.356	0.210
Mn <sup>2+</sup>	0.037	0.056	0.054
Mg	0.580	0.219	0.213
Zn	0.007	0.000	0.015
Ca	0.827	0.587	0.500
Ba	na	na	na
Na	0.107	0.380	0.509
K	0.001	0.000	0.000
<i>ae</i>	0.02	0.36	0.52
<i>di</i>	0.60	0.24	0.24
<i>hd</i>	0.38	0.40	0.24
Normalized to 6 oxygen <i>apfu</i> na = not analyzed			

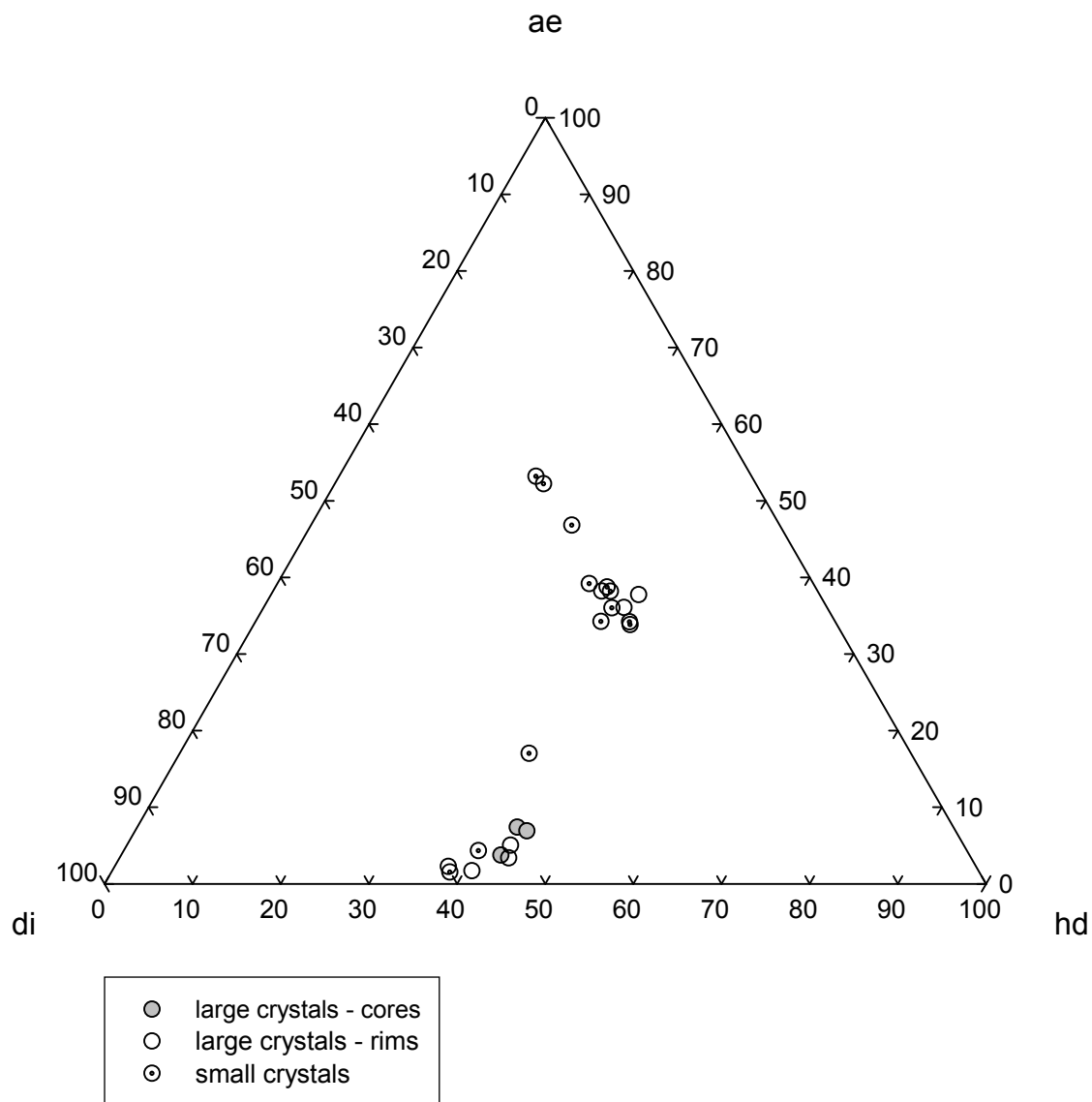


FIGURE 95 – Clinopyroxene compositions – Nepheline Melasyenite

TABLE 35 – Representative electron microprobe analyses of titanaugite – Nepheline Melasyenite

Lithology:	<i>Nepheline Melasyenite</i>			
Sample:	<i>MSH-B-8</i>			
Target:	<i>8e</i>	<i>8g</i>	<i>11q</i>	<i>11s</i>
SiO <sub>2</sub> (wt. %)	47.13	45.95	40.61	40.16
TiO <sub>2</sub>	2.49	2.27	3.62	2.40
ZrO <sub>2</sub>	0.00	0.13	0.02	0.27
Al <sub>2</sub> O <sub>3</sub>	7.07	6.28	9.98	9.61
Sc <sub>2</sub> O <sub>3</sub>	na	na	na	na
REE <sub>2</sub> O <sub>3</sub>	0.57	0.62	0.61	0.54
La <sub>2</sub> O <sub>3</sub>	na	na	na	na
Ce <sub>2</sub> O <sub>3</sub>	0.57	0.62	0.61	0.54
FeO <sub>tot</sub>	9.77	9.15	17.61	22.58
MnO	0.54	0.54	1.17	1.65
MgO	10.41	10.40	8.57	6.20
ZnO	0.58	0.86	0.60	0.48
CaO	18.61	18.57	8.26	7.83
BaO	na	na	na	na
Na <sub>2</sub> O	1.73	1.64	3.68	3.22
K <sub>2</sub> O	0.00	0.00	1.29	1.33
SUM	98.89	96.41	96.02	96.27
Fe <sub>2</sub> O <sub>3</sub>	0.97	3.10	7.36	7.59
FeO	8.90	11.41	16.51	21.82
NEW SUM	98.99	101.77	102.28	103.10
$\frac{\text{Mg}}{(\text{Mg}+\text{Fe}^{2+})}$	0.68	0.62	0.48	0.34
$\frac{\text{Mg}}{(\text{Mg}+\text{Fe}^{2+}+\text{Mn}^{2+})}$	0.66	0.61	0.46	0.32
Normalized to 4 cations <i>apfu</i> na = not analyzed				

TABLE 36 – Site-occupancies of titanaugite from TABLE 35 – Nepheline Melasyenite

Lithology:	<i>Nepheline Melasyenite</i>			
Sample:	<i>MSH-B-8</i>			
Target:	<i>8e</i>	<i>8g</i>	<i>11q</i>	<i>11s</i>
<i>T-site</i>				
Si	1.785	1.716	1.522	1.529
<sup>iv</sup> Al	0.215	0.277	0.441	0.431
Σ[T]	2.000	1.992	1.963	1.960
<i>M(1)-site</i>				
<sup>vi</sup> Ti	0.071	0.066	0.102	0.069
Zr	0.000	0.002	0.000	0.005
<sup>vi</sup> Al	0.101	0.000	0.000	0.000
Sc	na	na	na	na
Fe <sup>3+</sup>	0.028	0.087	0.208	0.217
Fe <sup>2+</sup>	0.189	0.243	0.223	0.377
Mg	0.588	0.579	0.479	0.352
Zn	0.016	0.024	0.017	0.013
Σ[M(1)]	0.992	0.999	1.029	1.033
<i>M(2)-site</i>				
REE	0.008	0.008	0.008	0.007
Fe <sup>2+</sup>	0.093	0.113	0.294	0.318
Mn <sup>2+</sup>	0.017	0.017	0.037	0.053
Mg	0.000	0.000	0.000	0.000
Ca	0.755	0.743	0.332	0.319
Ba	na	na	na	na
Na	0.127	0.119	0.268	0.238
K	0.000	0.000	0.061	0.064
Σ[M(2)]	1.000	1.000	1.000	1.000
Normalized to 4 cations <i>apfu</i> na = not analyzed				

the fringes of the association. Magnetite occurs sparingly near the margins of the titanaugite crystals, though in instances wherein the titanaugite appears to have been completely replaced by amphibole, a relic outline of magnetite is present within the pseudomorph. Representative analyses of titanaugite are listed in TABLES 35 & 36. Titanaugite from the nepheline melasyenite is enriched in Ti up to 5.19 wt% TiO<sub>2</sub>, Zr up to 0.28 wt.% ZrO<sub>2</sub>, Al up to 12.19 wt.% Al<sub>2</sub>O<sub>3</sub>, Ce up to 1.01 wt.% Ce<sub>2</sub>O<sub>3</sub>, Mn up to 1.65 wt.% MnO, and Zn up to 0.87 wt.% ZnO. In addition, titanaugite analyses average 0.33 wt.% K<sub>2</sub>O, well above the average for other clinopyroxenes from the nepheline melasyenite, 0.01 wt.% K<sub>2</sub>O. Examination in the petrographic microscope and SEM did not reveal any potassic inclusions near the target spots, so this may be real potassium content.

#### *Type 1 Nepheline Leucosyenite*

Aegirine is a minor mineral in the Type 1 nepheline leucosyenite. It occurs as black, euhedral, acicular prismatic crystals to 3 mm length with aspect ratios ranging from 1:3 to 1:10 and as black, euhedral, blocky prismatic crystals to 3 mm in width by 4 mm in length. Aegirine is pleochroic, following the scheme: *X* = grass green, *Y* = yellow green, *Z* = greenish tan. Representative analyses of clinopyroxene are listed in TABLE 37. Clinopyroxene from the Type 1 nepheline leucosyenite has a narrow range of compositions, plotting nearly exclusively as aegirine (Figure 96), with compositions ranging from ae<sub>79</sub>di<sub>5</sub>hd<sub>16</sub> to ae<sub>86</sub>di<sub>10</sub>hd<sub>4</sub>. Clinopyroxene in the Type 1 nepheline leucosyenite is enriched in Ti up to 1.03 wt% TiO<sub>2</sub>, Al up to 1.61 wt.% Al<sub>2</sub>O<sub>3</sub>, and Mn up to 2.10 wt.% MnO. Zn and K are minor substituents with up to 0.06 wt.% ZnO and 0.14 wt.% K<sub>2</sub>O.



TABLE 37 – Representative electron microprobe analyses of clinopyroxene – Type 1 Nepheline Leucosyenite

Lithology:	<i>Type 1 Nepheline Leucosyenite</i>			
Sample:	<i>MSH-B-14</i>			
Target:	<i>5d</i>	<i>6d</i>	Target:	<i>5d</i> <i>6d</i>
SiO <sub>2</sub> (wt. %)	49.04	49.25	<i>Cations</i>	
TiO <sub>2</sub>	1.03	1.03	Si	1.947      1.944
ZrO <sub>2</sub>	na	na	Ti	0.031      0.030
Al <sub>2</sub> O <sub>3</sub>	0.57	1.61	Zr	na      na
Sc <sub>2</sub> O <sub>3</sub>	na	na	Al	0.026      0.075
REE <sub>2</sub> O <sub>3</sub>	0.00	0.00	Sc	na      na
La <sub>2</sub> O <sub>3</sub>	na	na	REE	0.000      0.000
Ce <sub>2</sub> O <sub>3</sub>	0.00	0.00	Fe <sup>3+</sup>	0.782      0.731
FeO <sub>tot</sub>	24.61	24.14	Fe <sup>2+</sup>	0.035      0.066
MnO	2.39	2.10	Mn <sup>2+</sup>	0.080      0.070
MgO	1.51	1.39	Mg	0.090      0.082
ZnO	0.06	0.03	Zn	0.002      0.001
CaO	5.20	5.15	Ca	0.221      0.218
BaO	0.03	0.00	Ba	0.000      0.000
Na <sub>2</sub> O	10.50	10.53	Na	0.808      0.806
K <sub>2</sub> O	0.00	0.14	K	0.000      0.007
SUM	94.93	95.37	<i>ae</i>	0.86      0.83
Fe <sub>2</sub> O <sub>3</sub>	26.17	24.61	<i>di</i>	0.10      0.09
FeO	1.06	2.00	<i>hd</i>	0.04      0.07
NEW SUM	97.55	97.83	Normalized to 6 oxygen <i>apfu</i> na = not analyzed	
$\frac{\text{Mg}}{(\text{Mg}+\text{Fe}^{2+})}$	0.72	0.55		
$\frac{\text{Mg}}{(\text{Mg}+\text{Fe}^{2+}+\text{Mn}^{2+})}$	0.44	0.38		

### *Type 2 Nepheline Leucosyenite*

Aegirine is a trace mineral in Type 2 nepheline leucosyenite, in which it occurs as dark green, subhedral to euhedral prismatic crystals to 6 mm in length. Aegirine is pleochroic, following the scheme:  $X$  = emerald green,  $Y$  = yellow green,  $Z$  = brown. Clinopyroxene in the Type 1 nepheline leucosyenite is enriched in Al up to 4.88 wt.%  $\text{Al}_2\text{O}_3$  and Mn up to 2.39 wt.% MnO. Zn is a minor constituent, with up to 0.45 wt.% ZnO.

### *Type 3 Nepheline Leucosyenite*

Aegirine occurs as a major mineral, and aegirine-augite occurs as a trace mineral, in the Type 3 nepheline leucosyenite. Aegirine has two modes of occurrence. The first is as dark forest green, euhedral, prismatic, idiomorphic and interstitial crystals to 3 mm width by 7 mm length. These have a vitreous luster and exhibit crimson red internal reflections at some fractures. These crystals occur in clots up to 5 cm in diameter, in which the aegirine crystals are interstitial to the felsic minerals in the assemblage, primarily, colorless sodalite pseudomorphs after nepheline. Aegirine is pleochroic, according to the scheme:  $X$  = deep emerald green,  $Y$  = yellow green,  $Z$  = greenish amber. The pleochroism is undulose in some crystals with concomitant undulose extinction.

The second mode of aegirine in the Type 3 nepheline leucosyenite is as the rims of euhedral prismatic to interstitial crystals of sodic-calcic clinopyroxene. These crystals are up to 4 mm in width and 10 mm in length and have augite or aegirine-augite cores. The aegirine rims are dark green to black, with a splendid vitreous luster; the aegirine-augite cores are dark olive green, felty in appearance in hand specimen, and exhibit incipient alteration to hematite and goethite. These zoned crystals of clinopyroxene occur at or near the margins of aegirine clots.

TABLE 38 – Representative electron microprobe analyses of clinopyroxene – Type 3 Nepheline Leucosyenite

Lithology:	<i>Type 3 Nepheline Leucosyenite</i>		
Sample:	<i>MSH-B-10</i>		
Target:	<i>4d</i>	<i>6d</i>	<i>7c</i>
SiO <sub>2</sub> (wt. %)	50.65	48.60	50.41
TiO <sub>2</sub>	0.27	0.16	0.32
ZrO <sub>2</sub>	na	na	na
Al <sub>2</sub> O <sub>3</sub>	0.65	0.66	0.96
Sc <sub>2</sub> O <sub>3</sub>	na	na	na
REE <sub>2</sub> O <sub>3</sub>	0.00	0.00	na
La <sub>2</sub> O <sub>3</sub>	na	na	na
Ce <sub>2</sub> O <sub>3</sub>	0.00	0.00	na
FeO <sub>tot</sub>	26.32	25.52	25.65
MnO	2.01	3.01	2.01
MgO	1.00	0.93	1.14
ZnO	0.08	0.00	0.16
CaO	5.65	14.62	7.73
BaO	0.11	0.00	0.05
Na <sub>2</sub> O	11.90	4.77	10.20
K <sub>2</sub> O	0.00	0.00	0.30
SUM	98.62	98.31	98.92
Fe <sub>2</sub> O <sub>3</sub>	29.25	11.26	24.78
FeO	0.00	15.39	3.35
NEW SUM	101.55	99.43	101.40
$\frac{\text{Mg}}{(\text{Mg}+\text{Fe}^{2+})}$	1.00	0.10	0.38
$\frac{\text{Mg}}{(\text{Mg}+\text{Fe}^{2+}+\text{Mn}^{2+})}$	0.47	0.08	0.27

Target:	<i>4d</i>	<i>6d</i>	<i>7c</i>
<i>Cations</i>			
Si	1.939	1.964	1.943
Ti	0.008	0.005	0.009
Zr	na	na	na
Al	0.029	0.031	0.043
Sc	na	na	na
REE	0.000	0.000	na
Fe <sup>3+</sup>	0.843	0.342	0.719
Fe <sup>2+</sup>	0.000	0.520	0.108
Mn <sup>2+</sup>	0.065	0.103	0.066
Mg	0.057	0.056	0.065
Zn	0.002	0.000	0.005
Ca	0.232	0.633	0.319
Ba	0.002	0.000	0.001
Na	0.883	0.374	0.762
K	0.000	0.000	0.015
<i>ae</i>	0.94	0.37	0.81
<i>di</i>	0.06	0.06	0.07
<i>hd</i>	0.00	0.57	0.12
Normalized to 6 oxygen <i>apfu</i> na = not analyzed			

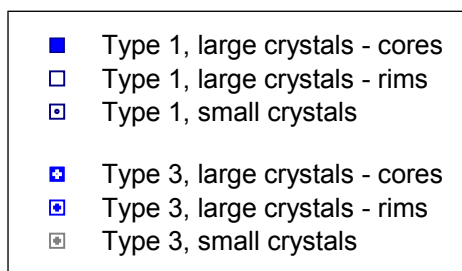
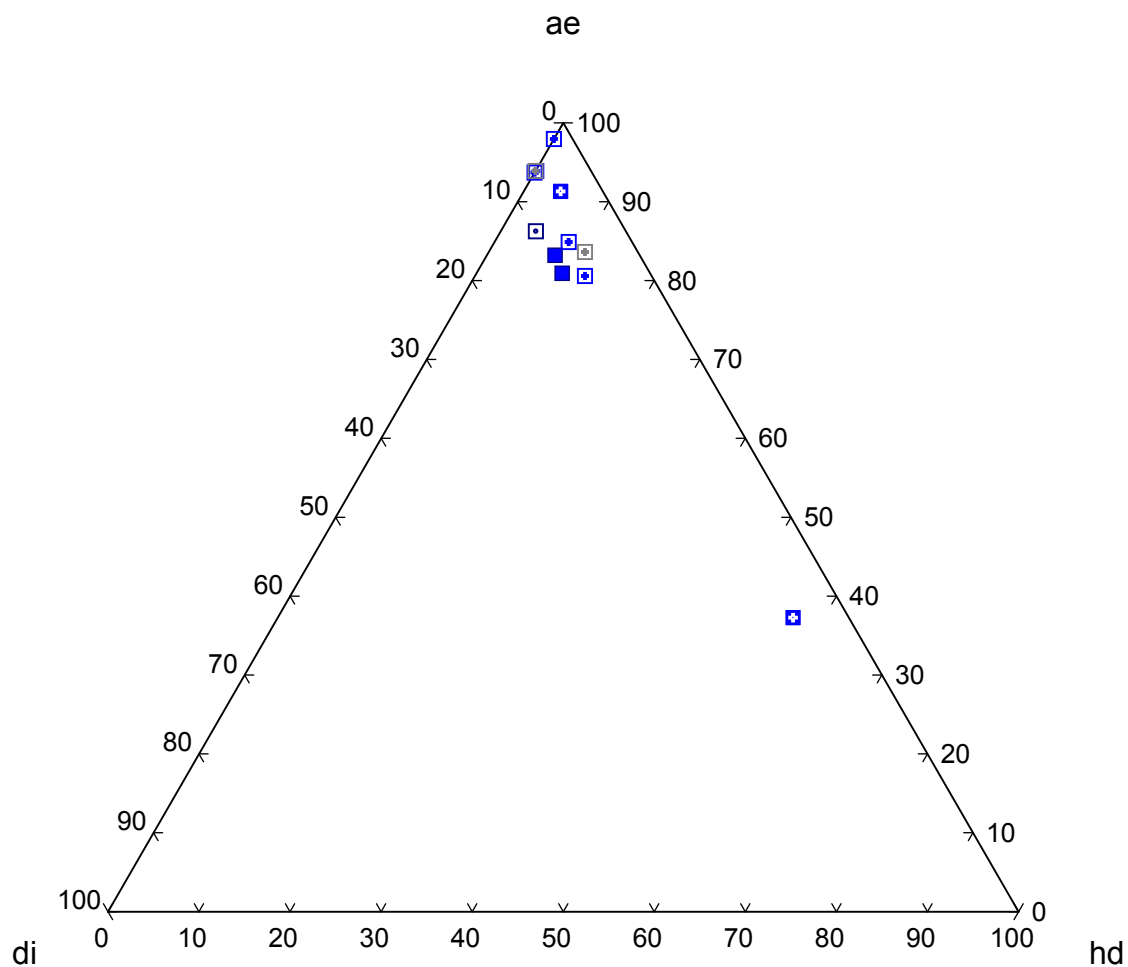


FIGURE 96 – Clinopyroxene compositions – Nepheline Leucosyenite

Representative analyses of clinopyroxene are listed in TABLE 38. Clinopyroxene from the Type 3 nepheline leucosyenite has a wide range of compositions, with extremes near the end-members of both augite and aegirine (Figure 96). Cores tend to be more augitic than rims, although some core compositions are more aegirine-rich than some rim compositions, indicating an extended clinopyroxene crystallization window. Compositions range from  $ae_6di_6hd_{88}$  to  $ae_{98}di_2hd_0$ . Clinopyroxene in the Type 3 nepheline leucosyenite is enriched in Al up to 3.13 wt.%  $Al_2O_3$ , and Mn up to 3.01 wt.% MnO. Ti, Zn, Ba, and K are minor substituents with up to 1.03 wt.%  $TiO_2$ , 0.17 wt.% ZnO, 0.12 wt.% BaO, and 0.61 wt.%  $K_2O$ .

#### *Eudialyte Syenite*

Aegirine and aegirine-augite are major minerals in the eudialyte syenite, occurring as euhedral, acicular crystals to 11 mm in length and 1 mm in width. Some crystals that occur in small vugs exhibit pyramidal terminations. Aegirine and aegirine-augite in this syenite are dark forest green in color, although gemmy crystals may appear lighter in color with yellow or red tones to the green. In thin section, the crystals are pleochroic, following the scheme:  $X$  = emerald green,  $Y$  = yellow green,  $Z$  = greenish amber. Representative analyses of clinopyroxene are listed in TABLES 39 & 40. Clinopyroxene from the eudialyte syenite varies from aegirine-augite to aegirine (Figure 97); cores are markedly more augitic than rims. Compositions range from  $ae_{31}di_{25}hd_{43}$  to  $ae_{100}di_0hd_0$ . Clinopyroxene in the eudialyte syenite is enriched in Ti up to 2.12 wt.%  $TiO_2$ , Zr up to 2.54 wt.%  $ZrO_2$ , Al, in general, about 1.00-1.50 wt.% but, in the extreme, up to 6.62 wt.%  $Al_2O_3$ , Mn, in general, about 1.00-2.00 wt.% but, in the extreme, up to 5.06 wt.% MnO. Sc and Ba are minor elements with up to 0.16 wt.%  $Sc_2O_3$  and 0.13 wt.% BaO. Clinopyroxene is slightly lower in Ti content in the altered eudialyte syenite than in the fresh.

TABLE 39 – Representative electron microprobe analyses of clinopyroxene – Eudialyte Syenite

Lithology:	<i>Eudialyte Syenite</i>		
Sample:	<i>MSH-B-1</i>		
Target:	<i>1c</i>	<i>11h</i>	<i>12a</i>
SiO <sub>2</sub> (wt.%)	53.60	51.31	50.61
TiO <sub>2</sub>	2.12	0.20	0.31
ZrO <sub>2</sub>	na	na	na
Al <sub>2</sub> O <sub>3</sub>	0.89	6.62	1.89
Sc <sub>2</sub> O <sub>3</sub>	na	na	na
REE <sub>2</sub> O <sub>3</sub>	na	na	na
La <sub>2</sub> O <sub>3</sub>	na	na	na
Ce <sub>2</sub> O <sub>3</sub>	na	na	na
FeO <sub>tot</sub>	27.89	24.56	23.95
MnO	1.68	0.43	1.47
MgO	0.61	0.09	2.27
ZnO	na	na	na
CaO	1.70	0.43	9.41
BaO	na	na	na
Na <sub>2</sub> O	12.94	14.47	7.34
K <sub>2</sub> O	0.03	0.00	0.00
SUM	101.45	98.76	97.24
Fe <sub>2</sub> O <sub>3</sub>	30.99	26.92	15.94
FeO	0.00	0.33	9.61
NEW SUM	104.55	101.45	98.83
$\frac{\text{Mg}}{(\text{Mg}+\text{Fe}^{2+})}$	1.00	0.33	0.30
$\frac{\text{Mg}}{(\text{Mg}+\text{Fe}^{2+}+\text{Mn}^{2+})}$	0.39	0.18	0.27

Target:	<i>1c</i>	<i>11h</i>	<i>12a</i>
<i>Cations</i>			
Si	1.965	1.909	1.986
Ti	0.058	0.024	0.009
Zr	na	na	na
Al	0.038	0.290	0.088
Sc	na	na	na
REE	na	na	na
Fe <sup>3+</sup>	0.855	0.754	0.471
Fe <sup>2+</sup>	0.000	0.010	0.316
Mn <sup>2+</sup>	0.052	0.014	0.049
Mg	0.033	0.005	0.133
Zn	na	na	na
Ca	0.067	0.017	0.396
Ba	na	na	na
Na	0.920	1.044	0.558
K	0.001	0.000	0.000
<i>ae</i>	0.96	0.98	0.51
<i>di</i>	0.04	0.01	0.14
<i>hd</i>	0.00	0.01	0.34
Normalized to 6 oxygen <i>apfu</i> na = not analyzed			

TABLE 40 – Representative electron microprobe analyses of clinopyroxene – Altered Eudialyte Syenite

Lithology:	<i>Altered Eudialyte Syenite</i>		
Sample:	<i>MSH-B-2</i>		
Target:	<i>Aa</i>	<i>7a2</i>	<i>9d</i>
SiO <sub>2</sub> (wt.%)	52.45	50.10	50.11
TiO <sub>2</sub>	0.28	0.29	0.27
ZrO <sub>2</sub>	0.84	1.41	0.81
Al <sub>2</sub> O <sub>3</sub>	1.19	0.92	0.89
Sc <sub>2</sub> O <sub>3</sub>	0.16	0.00	0.00
REE <sub>2</sub> O <sub>3</sub>	0.00	0.00	0.00
La <sub>2</sub> O <sub>3</sub>	na	na	na
Ce <sub>2</sub> O <sub>3</sub>	0.00	0.00	0.00
FeO <sub>tot</sub>	25.76	24.61	23.85
MnO	0.82	1.80	1.86
MgO	0.58	1.03	1.51
ZnO	0.00	0.00	0.00
CaO	2.99	9.84	11.88
BaO	0.00	0.13	0.03
Na <sub>2</sub> O	11.25	6.71	4.10
K <sub>2</sub> O	0.00	0.02	0.02
SUM	96.31	96.86	95.31
Fe <sub>2</sub> O <sub>3</sub>	27.12	15.83	9.16
FeO	1.36	10.37	15.60
NEW SUM	99.03	98.44	96.23
$\frac{\text{Mg}}{(\text{Mg}+\text{Fe}^{2+})}$	0.43	0.15	0.15
$\frac{\text{Mg}}{(\text{Mg}+\text{Fe}^{2+}+\text{Mn}^{2+})}$	0.32	0.13	0.13

Target:	<i>Aa</i>	<i>7a2</i>	<i>9d</i>
<i>Cations</i>			
Si	2.017	1.997	2.046
Ti	0.008	0.009	0.008
Zr	0.016	0.027	0.016
Al	0.054	0.043	0.043
Sc	0.005	0.000	0.000
REE	0.000	0.000	0.000
Fe <sup>3+</sup>	0.785	0.475	0.281
Fe <sup>2+</sup>	0.044	0.346	0.533
Mn <sup>2+</sup>	0.027	0.061	0.064
Mg	0.033	0.061	0.092
Zn	0.000	0.000	0.000
Ca	0.123	0.420	0.520
Ba	0.000	0.002	0.000
Na	0.839	0.518	0.324
K	0.000	0.001	0.001
<i>ae</i>	0.91	0.54	0.31
<i>di</i>	0.04	0.07	0.10
<i>hd</i>	0.05	0.39	0.59
Normalized to 6 oxygen <i>apfu</i> na = not analyzed			

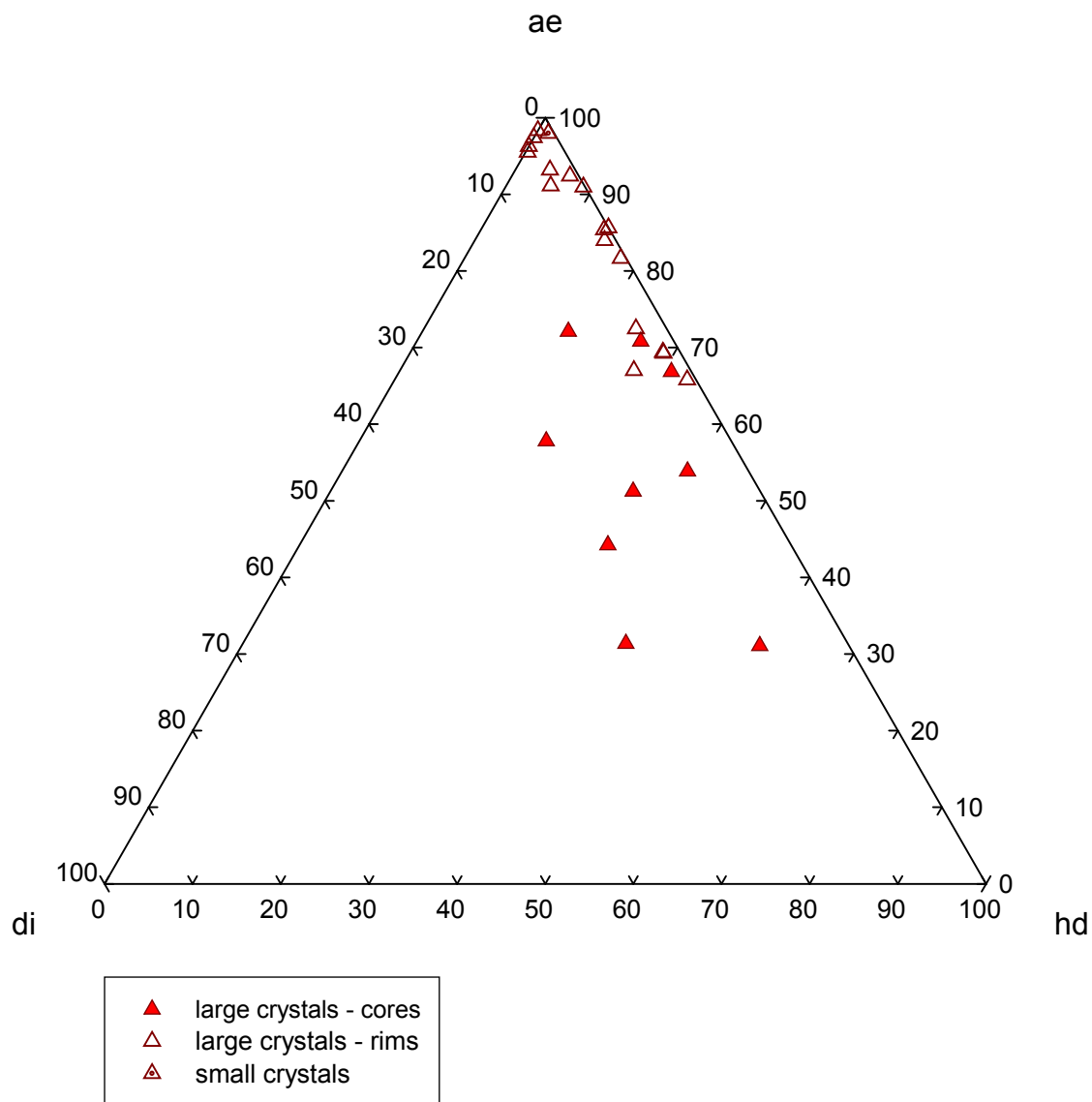


FIGURE 97 – Clinopyroxene compositions – Eudialyte Syenite



### *Feldspar-Aegirine Dikes*

Aegirine is a major mineral in the feldspar-aegirine dikes. It occurs as dark green, charcoal grey, and black, euhedral, tapering crystals to 1.5 cm in width by 5 cm in length. Ranks of crystals in some dikes are curved along their length, indicating shear during crystallization. All crystals are wider at their terminations than at their bases. In thin section, aegirine exhibits possible twinning on {100}. Crystals that have [001] parallel to the stage display prominent color zoning in an hourglass or concentric pattern. Aegirine is pleochroic with the scheme:  $X$  = emerald to grass green,  $Y$  = yellow green,  $Z$  = amber. Representative analyses of clinopyroxene are listed in TABLE 41. Clinopyroxene from the feldspar-aegirine dikes is strictly aegirine (Figure 98). Compositions range from  $ae_{80}di_1hd_{19}$  to  $ae_{100}di_0hd_0$ . Clinopyroxene in the feldspar-aegirine dikes is enriched in Ti up to 1.35 wt%  $TiO_2$ , Zr up to 3.06 wt.%  $ZrO_2$ , Al up to 1.66 wt.%  $Al_2O_3$ , and Mn up to 1.50 wt.% MnO. Ba is a minor constituent with up to 0.17 wt.% BaO.

### *Annite Lamprophyre*

Aegirine occurs as a minor mineral in the annite lamprophyre. Aegirine-augite is a rare phase, found only in the core of one analyzed pyroxene crystal. Aegirine is present as dark green to black, subhedral, prismatic crystals to 1.5 mm in length. They are pleochroic according to the scheme:  $X$  = grass green,  $Y$  = yellow green,  $Z$  = amber. Chemical zonation that is evident from electron microprobe analyses is invisible in thin section. Representative analyses of clinopyroxene are listed in TABLE 42. Compositions range from  $ae_{91}di_1hd_8$  to  $ae_{99}di_1hd_0$  (Figure 99). Clinopyroxene in the annite lamprophyre is enriched in Ti up to 1.57 wt%  $TiO_2$  but with most analyses below 0.50 wt.%, Zr up to 1.76 wt.%  $ZrO_2$ , Al up to 1.13 wt.%  $Al_2O_3$ , Mn up to 1.26 wt.% MnO but with most analyses below 0.25 wt.%, and Zn up to 3.23 wt.% ZnO.

TABLE 41 – Representative electron microprobe analyses of clinopyroxene – Feldspar-Aegirine Dikes

Lithology:	<i>Feldspar-Aegirine Dikes</i>		
Sample:	<i>MSH-B-3</i>		
Target:	<i>9d</i>	<i>14d</i>	<i>15b</i>
SiO <sub>2</sub> (wt.%)	49.46	50.88	50.63
TiO <sub>2</sub>	1.30	0.71	1.18
ZrO <sub>2</sub>	3.06	0.00	1.41
Al <sub>2</sub> O <sub>3</sub>	0.98	1.53	1.06
Sc <sub>2</sub> O <sub>3</sub>	0.00	0.00	0.00
REE <sub>2</sub> O <sub>3</sub>	0.00	0.00	0.00
La <sub>2</sub> O <sub>3</sub>	na	na	na
Ce <sub>2</sub> O <sub>3</sub>	0.00	0.00	0.00
FeO <sub>tot</sub>	25.98	26.30	26.41
MnO	0.79	0.62	0.88
MgO	0.15	0.14	0.09
ZnO	0.00	0.00	0.00
CaO	1.83	1.16	1.62
BaO	0.09	0.09	0.13
Na <sub>2</sub> O	11.00	12.72	13.00
K <sub>2</sub> O	0.02	0.01	0.01
SUM	94.66	94.17	96.41
Fe <sub>2</sub> O <sub>3</sub>	26.80	29.23	29.35
FeO	1.86	0.00	0.00
NEW SUM	97.34	97.10	99.35
$\frac{\text{Mg}}{(\text{Mg}+\text{Fe}^{2+})}$	0.12	1.00	1.00
$\frac{\text{Mg}}{(\text{Mg}+\text{Fe}^{2+}+\text{Mn}^{2+})}$	0.09	0.29	0.15

Target:	<i>9d</i>	<i>14d</i>	<i>15b</i>
<i>Cations</i>			
Si	1.949	1.980	1.958
Ti	0.038	0.021	0.034
Zr	0.059	0.000	0.027
Al	0.046	0.070	0.048
Sc	0.000	0.000	0.000
REE	0.000	0.000	0.000
Fe <sup>3+</sup>	0.795	0.856	0.854
Fe <sup>2+</sup>	0.061	0.000	0.000
Mn <sup>2+</sup>	0.026	0.020	0.029
Mg	0.009	0.008	0.005
Zn	0.000	0.000	0.000
Ca	0.077	0.048	0.067
Ba	0.001	0.001	0.002
Na	0.841	0.959	0.975
K	0.001	0.001	0.000
<i>ae</i>	0.92	0.99	0.99
<i>di</i>	0.01	0.01	0.01
<i>hd</i>	0.07	0.00	0.00
Normalized to 6 oxygen <i>apfu</i> na = not analyzed			

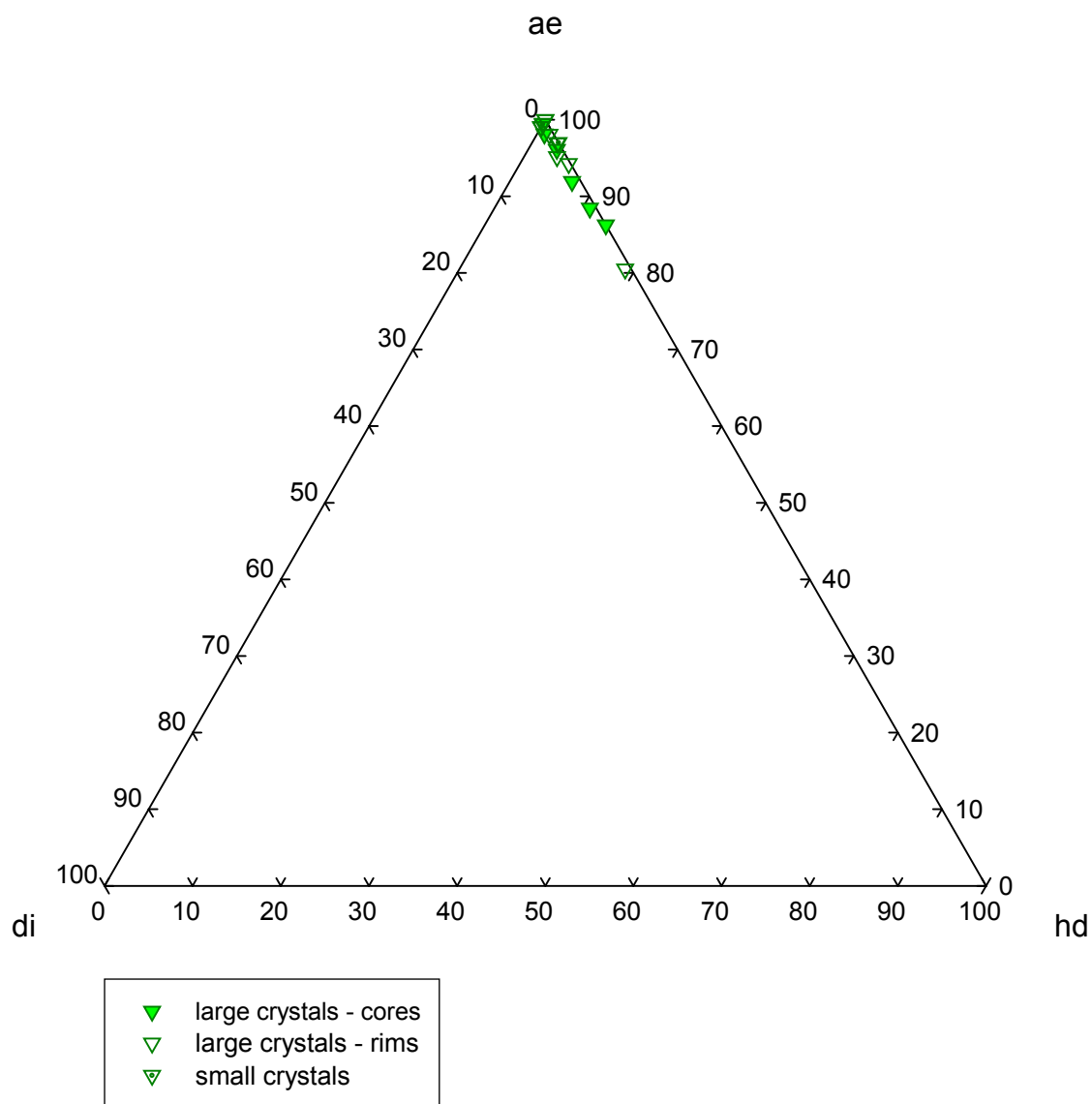


FIGURE 98 – Clinopyroxene compositions – Feldspar-Aegirine Dikes

TABLE 42 – Representative electron microprobe analyses of clinopyroxene – Annite Lamprophyre

Lithology:	<i>Annite Lamprophyre</i>		
Sample:	<i>MSH-B-6</i>		
Target:	<i>12d</i>	<i>13b</i>	<i>13g</i>
SiO <sub>2</sub> (wt.%)	51.95	53.45	53.83
TiO <sub>2</sub>	1.57	0.41	0.43
ZrO <sub>2</sub>	1.76	0.45	0.24
Al <sub>2</sub> O <sub>3</sub>	1.13	0.89	0.85
Sc <sub>2</sub> O <sub>3</sub>	na	na	na
REE <sub>2</sub> O <sub>3</sub>	0.11	0.06	0.08
La <sub>2</sub> O <sub>3</sub>	0.11	0.06	0.08
Ce <sub>2</sub> O <sub>3</sub>	0.00	0.00	0.00
FeO <sub>tot</sub>	28.52	29.52	29.45
MnO	0.18	0.17	0.25
MgO	0.19	0.25	0.21
ZnO	2.17	1.63	1.42
CaO	0.17	0.70	0.68
BaO	na	na	na
Na <sub>2</sub> O	13.23	12.82	12.70
K <sub>2</sub> O	0.00	0.00	0.00
SUM	100.99	100.33	100.13
Fe <sub>2</sub> O <sub>3</sub>	31.70	31.64	31.38
FeO	0.00	1.05	1.21
NEW SUM	104.16	103.50	103.27
$\frac{\text{Mg}}{(\text{Mg}+\text{Fe}^{2+})}$	1.00	0.30	0.23
$\frac{\text{Mg}}{(\text{Mg}+\text{Fe}^{2+}+\text{Mn}^{2+})}$	0.66	0.27	0.20

Target:	<i>12d</i>	<i>13b</i>	<i>13g</i>
<i>Cations</i>			
Si	1.938	1.991	2.004
Ti	0.044	0.012	0.012
Zr	0.032	0.008	0.004
Al	0.050	0.037	0.037
Sc	na	na	na
REE	0.002	0.001	0.001
Fe <sup>3+</sup>	0.890	0.887	0.879
Fe <sup>2+</sup>	0.000	0.033	0.038
Mn <sup>2+</sup>	0.006	0.005	0.008
Mg	0.011	0.014	0.011
Zn	0.060	0.045	0.039
Ca	0.007	0.028	0.027
Ba	na	na	na
Na	0.956	0.926	0.917
K	0.000	0.000	0.000
<i>ae</i>	0.99	0.95	0.95
<i>di</i>	0.01	0.01	0.01
<i>hd</i>	0.00	0.04	0.04
Normalized to 6 oxygen <i>apfu</i> na = not analyzed			

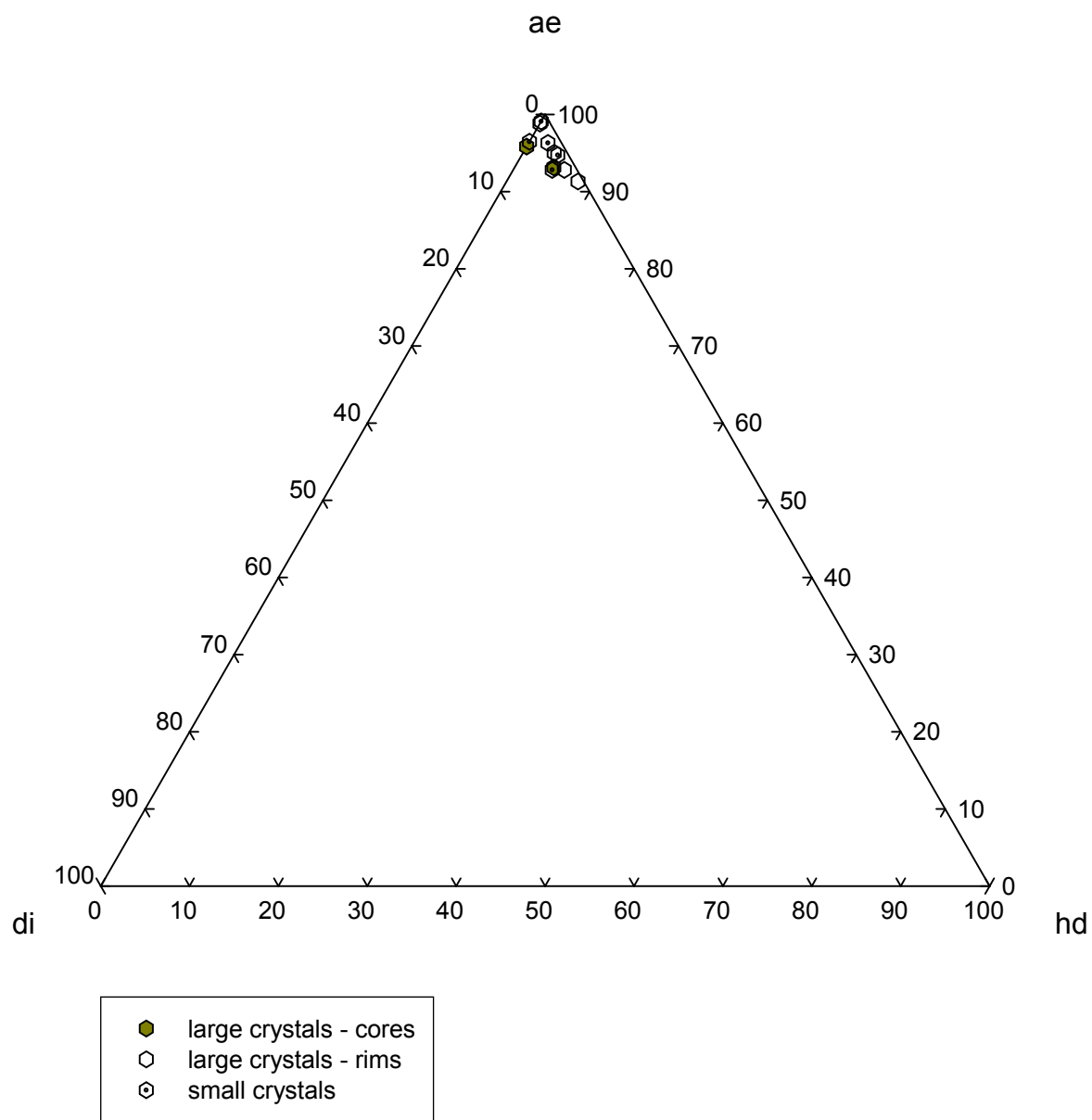


FIGURE 99 – Clinopyroxene compositions – Annite Lamprophyre

### *East Hill Suite Clinopyroxene*

Minerals of the pyroxene group exhibit a consistent increase in aegirine component through the sequence of lithologies in the East Hill Suite (Figure 100). Augite and aegirine-augite are prominent, along with minor titanaugite, in the nepheline melasyenite. They are quickly supplanted by aegirine-augite in diminishing proportion and aegirine in increasing proportion through the remaining syenites. The average proportion of aegirine component in clinopyroxene, however, more or less reaches a plateau in the nepheline syenites and the eudialyte syenite. There is a slight decrease in the average aegirine content of clinopyroxene in the eudialyte syenite, owing to crystal cores enriched in aegirine-augite relative to those of the nepheline syenites.

An earlier study from the East Hill suite suggested a much shorter and less varied evolutionary history for clinopyroxene (Figure 101). (Piilonen *et al.* 1998) However, that study focused on clinopyroxene from microenvironments in the East Hill Suite (*viz.* aplites, igneous breccias, miaroles, pegmatites, and syenite xenoliths). In doing so, they excluded major clinopyroxene-bearing rock types that constitute a larger volumetric fraction of the East Hill suite and that represent a more significant assemblage with respect to magmatic evolution. Interestingly, the compositional trend described by PIILONEN *ET AL.* (1998) follows a somewhat different path than that seen in this study; their trend notably lacks hedenbergite enrichment prior to trending towards aegirine. Although the path described by PIILONEN *ET AL.* (1998) deviates from the mean clinopyroxene compositional trend from this study, it overlaps numerous individual analyses. Rather than a separate evolutionary trend, their limited sample set simply may represent a portion of the complete range of East Hill suite clinopyroxene compositions.

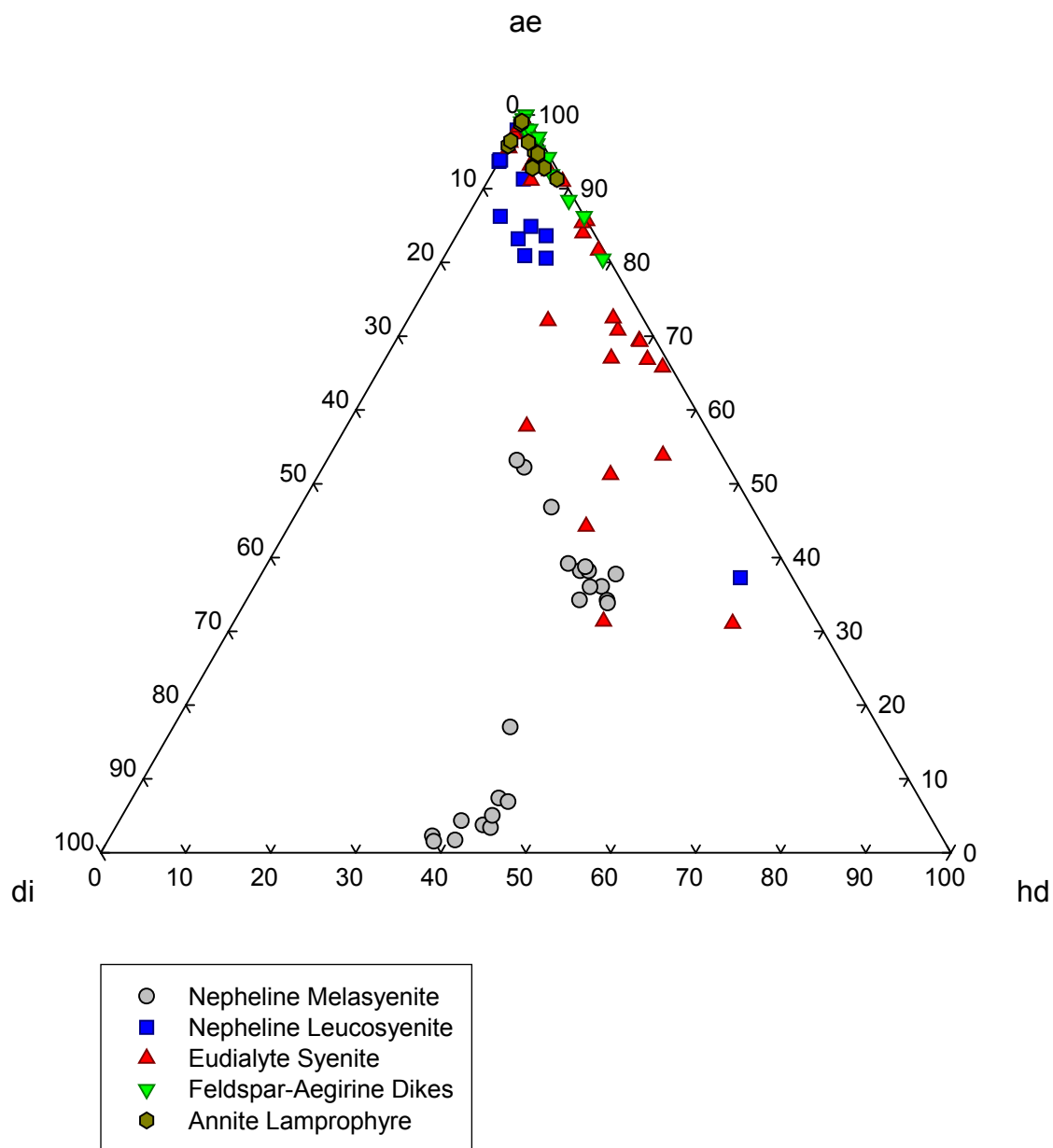


FIGURE 100 – Compositional evolution of clinopyroxene – East Hill suite

Investigators ascribe the compositional evolution of clinopyroxene towards aegirine to numerous mechanisms. One of the more popular and intuitive explanations is that increasing  $f_{O_2}$  increases the  $Fe^{3+}/Fe^{2+}$  ratio in the melt and, consequently, in ferromagnesian phases. (Aoki 1964; Yagi 1966; Nash & Wilkinson 1970; Larsen 1976; Mitchell & Platt 1978; Stephenson & Upton 1982) PLATT & WOOLLEY (1986) state that while clinopyroxene compositions may evolve towards aegirine under low  $f_{O_2}$  conditions, oxygen fugacities above QFM invariably result in enrichment in the aegirine molecule. It is important to recognize, however, that the causes of compositional evolution in clinopyroxene are circumstantial and that aegirine enrichment can occur even under low  $f_{O_2}$  conditions *via* increased alkalinity of the melt. (Anderson 1974; Mitchell & Platt 1978; Stephenson & Upton 1982; Platt & Woolley 1986)

These latter conditions appear to be precisely the case in the East Hill suite. Oxygen fugacity estimates from amphibole, magnetite, and mica compositions portray a trend of early, substantial decrease in oxygen fugacity with temperature followed by a leveling off of oxygen fugacity while temperature continues to decrease. As oxygen fugacity is decreasing while the aegirine component of clinopyroxene is increasing, the elevated  $Fe^{3+}$  in East Hill suite clinopyroxene must be the result of increasing alkalinity in the melt. This is also evident from a reëxamination of FIGURE 100. The early compositional trend in East Hill suite clinopyroxene is one of hedenbergite enrichment. About halfway through the evolution of clinopyroxene in the nepheline melasyenite, the trend turns abruptly towards aegirine, and trends of all subsequent lithologies parallel this path. This turning point represents the paragenetic moment when amphibole crystallization switched from calcic to sodic-calcic compositions and, not to put too



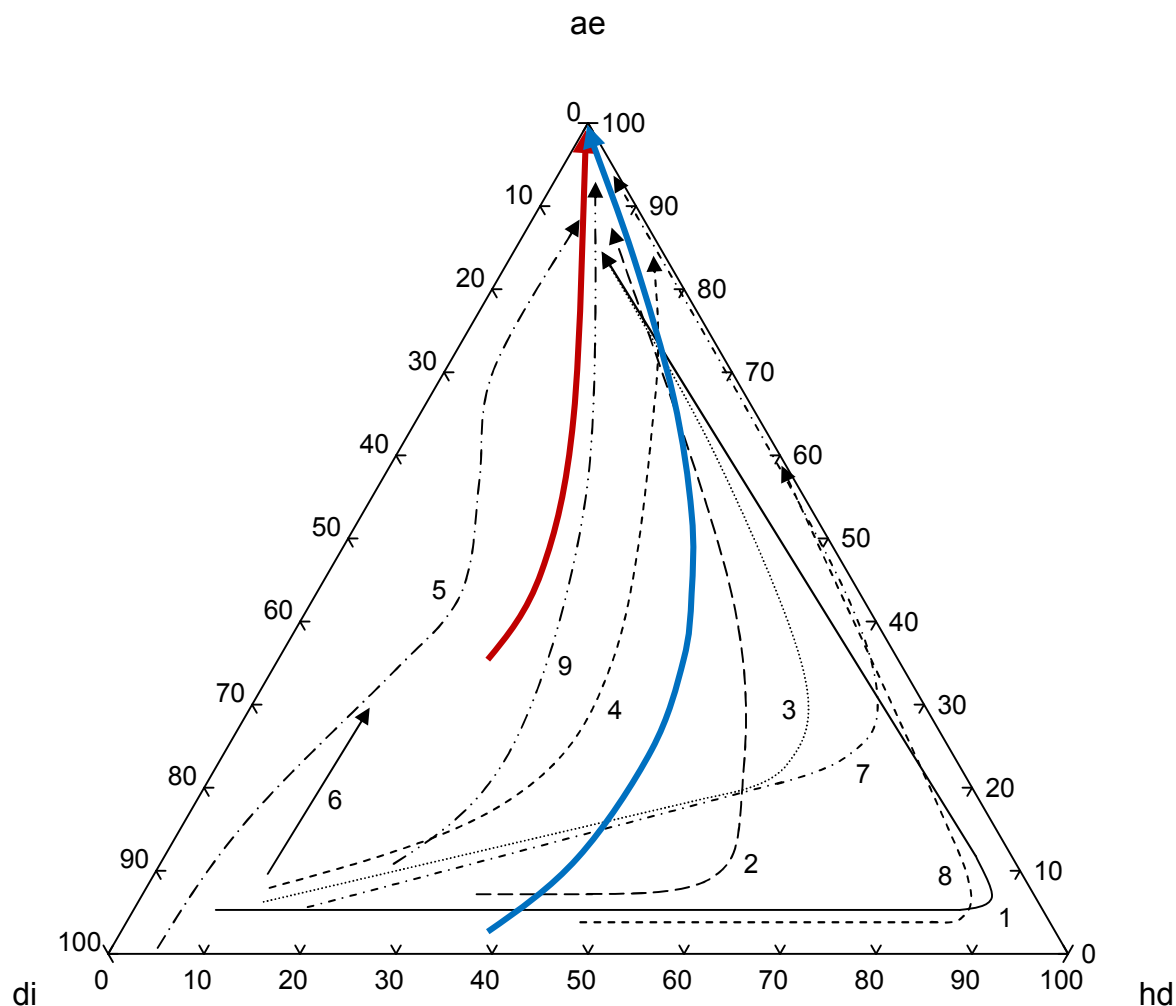


FIGURE 101 – Compositional trend in clinopyroxene in the East Hill suite from this study (blue), compared to East Hill suite data from PHILONEN *ET AL.* (1998) (red) and trends from other alkaline complexes. (1) Ilimaussaq, Greenland (Larsen 1976), (2) Morutu, Japan (Yagi 1966), (3) South Qôroq, Greenland (Stephenson 1972), (4) Auvergne, France (Varet 1969), (5) Little Murun, Russia (Mitchell & Vladykin 1996), (6) Fen, Norway (Mitchell 1980), (7) Magnet Cove, Arkansas (Flohr & Ross 1990), (8) Coldwell, Ontario (Mitchell & Platt 1982), (9) North Nyasa, Malawi (Eby *et al.* 1998).

find a point on it, the moment at which oxygen fugacity became sufficiently low as to cease influencing  $\text{Fe}^{3+}$  in silicates.

PIILONEN *ET AL.* (1998) also propose that the high aegirine content of East Hill suite clinopyroxene was a consequence of elevated oxygen fugacity in the East Hill suite magma. They did not, however, address independent mineralogical estimates of oxygen fugacity, which clearly point to decreasing oxygen fugacity with the evolution of the East Hill suite magma.

The shift towards high-aegirine compositions in the middle of the nepheline melasyenite indicates that the East Hill suite magma became peralkaline early in its evolution, despite having started by crystallizing the nepheline melasyenite, a rather miaskitic lithology. The clinopyroxene trend of the East Hill suite is, indeed, comparable to that of several peralkaline intrusive complexes (Figure 101), most notably those of Morutu, Auvergne, South Qôroq, and North Nyasa (Yagi 1966; Varet 1969; Stephenson 1972; Eby *et al.* 1998), the trends of all of which show hedenbergite enrichment followed by a relatively early onset of peralkalinity. Auvergne and North Nyasa exhibit particularly similar trends to that of the East Hill suite, with a more or less continuous aegirine enrichment gradient, though becoming peralkaline even earlier in their evolutionary history. Morutu and South Qôroq became peralkaline relatively later in their history and their clinopyroxene compositions more suddenly turned towards aegirine. At the outset, clinopyroxene from Auvergne and South Qôroq show more diopsidic compositions than the trend for the East Hill suite, though not for Mont Saint-Hilaire as a whole. (Greenwood & Edgar 1984)

In spite of numerous petrological and mineralogical similarities to the East Hill suite, on the scale of the whole complex, clinopyroxene from Ilímaussaq, Coldwell, and Magnet Cove most certainly follow a distinct trend with a strong enrichment in hedenbergite prior to

crystallization of aegirine, indicating a later onset of peralkalinity. (Larsen 1976; Mitchell & Platt 1982; Flohr & Ross 1990) In contrast to the East Hill suite and, in particular, to the immediately preceding complexes, Fen and Little Murun exhibit peralkaline trends in their clinopyroxene, with essentially no hedenbergite enrichment, right from the beginning of crystallization. (Mitchell 1980; Mitchell & Vladykin 1996) The compared trends are for entire complexes, however, and early high-diopside compositions are also the case for Mont Saint-Hilaire as a whole. (Greenwood & Edgar 1984) Therefore, the East Hill suite became peralkaline relatively early, but on the scale of the entire complex, the timing of the onset of peralkalinity for the Mont Saint-Hilaire magma is intermediate between early-peralkaline complexes such as Fen and late-peralkaline complexes such as Ilímaussaq.

Trace element variation with the fractionation index (Na – Mg) overall suggests a single fractionation trend for clinopyroxene in the studied lithologies. Compositional trends are generally well defined with excursions that are unrelated to separate fractionation events. Ti content was elevated early on (Figure 102), though it declined sharply as fractionation proceeded out of the nepheline melasyenite due to the depletion of the melt in Ti by titanaugite, kaersutite, titanite, and magnetite; also, there is a curious slight elevation in Ti in the most evolved lithologies. In contrast, Zr content began near zero and steadily rose through the fractionation sequence (Figure 103).

Systematic zoning of Ti and Zr in clinopyroxene, with high-Zr cores and high-Ti rims, is not uncommon in alkaline complexes, due to the so-called “peralkaline effect”. (Farges *et al.* 1994) The action of the “peralkaline effect” is in two parts. In the first, elevated alkalis depolymerize the melt, promoting the formation of <sup>vi</sup>Ti and <sup>vi</sup>Zr and allowing their incorporation into clinopyroxene. In the second, increasing oxygen fugacity during crystallization drives the

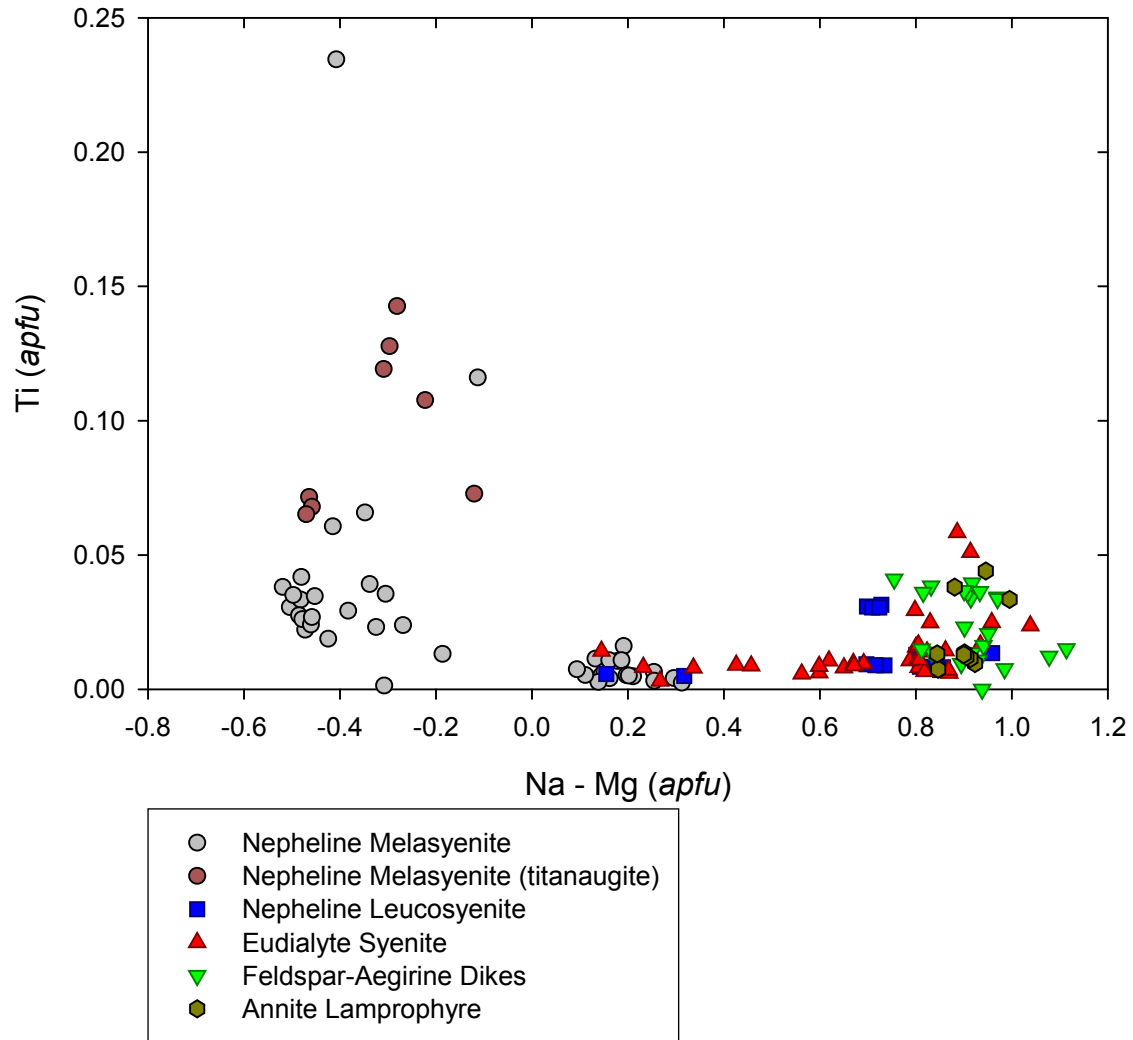


FIGURE 102 – Variation of Ti with fractionation in clinopyroxene – East Hill suite

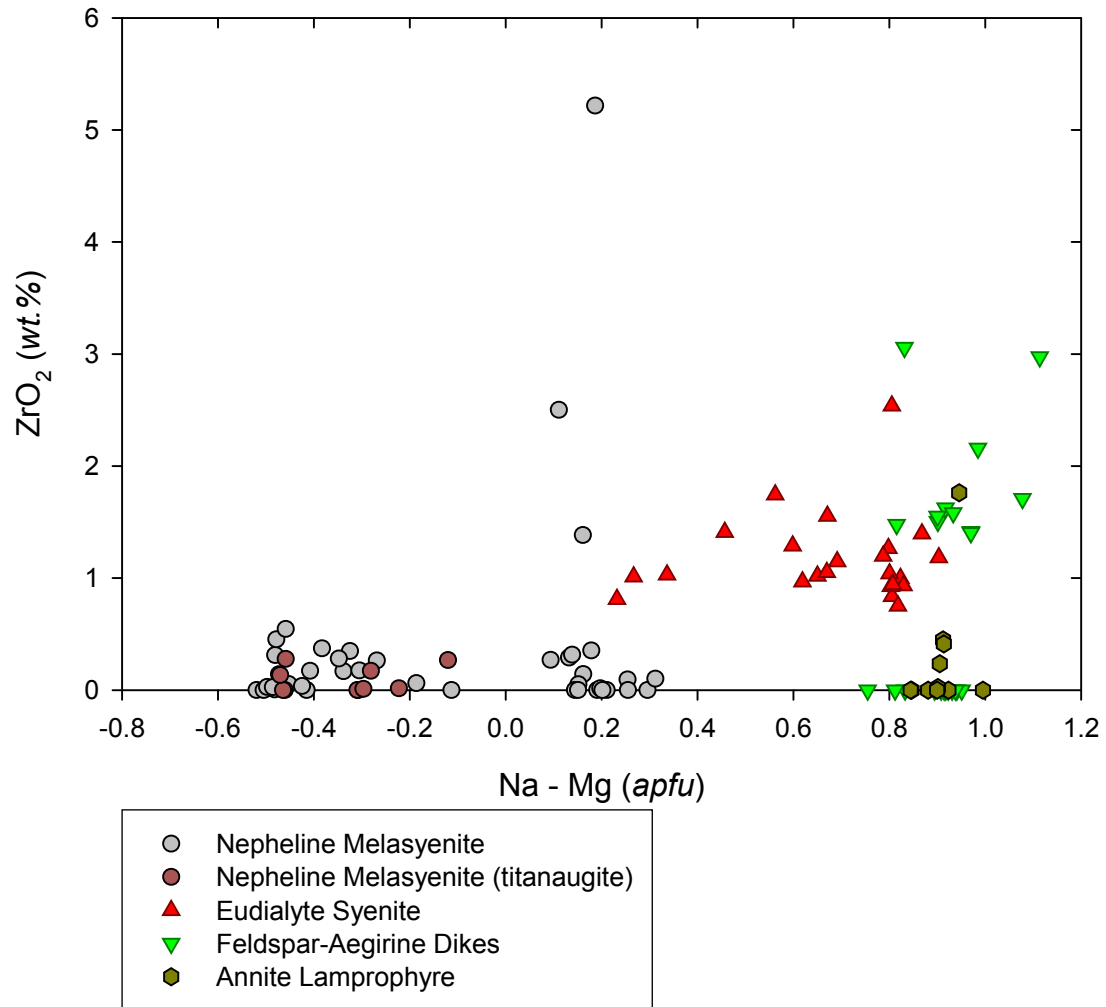


FIGURE 103 – Variation of  $\text{ZrO}_2$  with fractionation in clinopyroxene – East Hill suite

formation of  ${}^{\text{vi}}\text{Zr-O}-(\text{Si,Na})$  complexes that sequester Zr in the melt and create a local coordination environment more suitable to inclusion in alkali zirconosilicates. Increased oxygen fugacity does not affect the behavior of  ${}^{\text{vi}}\text{Ti}$ , so it remains available for incorporation into clinopyroxene. Consequently, under both of these conditions, earlier-formed clinopyroxene would be enriched in Zr and later-formed clinopyroxene would be enriched in Ti. Since the Zr-rich clinopyroxene forms under less evolved conditions, it is relatively rich in Ca; likewise, the later Ti-rich clinopyroxene is relatively high in Na. (Gomes *et al.* 1970; Watson 1979; Jones & Peckett 1980; Farges *et al.* 1994; Piilonen *et al.* 1998) Zoned clinopyroxene that follows this pattern is observed in the East Hill suite. (Piilonen *et al.* 1998)

Yet, the geochemical consequences of the “peralkaline effect” are not observed in clinopyroxene in the East Hill suite, as a whole. Ti content of clinopyroxene does increase slightly towards the end of fractionation, but Zr content increases continuously, in spite of coexisting alkali zirconosilicates. Also, the late-stage increase in Ti is a general geochemical feature of the East Hill suite. Whole rock Ti content increases progressively from the nepheline leucosyenites through the eudialyte syenite, pegmatites, various syenoids, and feldspar-aegirine dikes. Astrophyllite becomes relatively common in the highly evolved syenoids, and there is extensive evidence of Ti exhalation into the hornfels aureole in the presence of anatase, brookite, and rutile, as well as astrophyllite and narsarsukite,  $\text{Na}_2(\text{Ti,Fe}^{3+})\text{Si}_4(\text{O,F})_{11}$ . (Horváth & Gault 1990) Ti exhalation is not unique to the East Hill suite; brookite is abundant in the novaculite surrounding the Magnet Cove complex. (Fryklund & Holbrook 1950; Flohr 1994) Empirically, the late-stage increase in Ti in the melt is not uncommon in alkaline systems as a result of fractionation. (Wm. B. Simmons, Jr., pers. comm.)

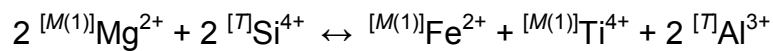
The only substantial evidence for a relative shift towards an oxidative environment is from the presence of hematite in the feldspar-aegirine dikes and hydrothermal natrolite in several lithologies, both of which would be either terminal magmatic or post-magmatic parageneses. Field and geochemical evidence indicates that the feldspar-aegirine dikes were essentially emplaced at the end of the East Hill suite magmatic phase. Intrafascicular textures and strongly tapered crystals in these dikes are indicative of rapid crystallization, and alkali feldspar geothermometry suggests emplacement temperatures near the solidus. At such temperatures, at or below 500°C, the slope of the HM buffer steepens to the point that simply cooling the melt can drive it across the buffer into the hematite stability field. Natrolite formation is promoted by a decrease in pH (Eitel 1964), and arguably this could positively influence oxidizing conditions. Both of these minerals, however, reflect circumstances that would have developed too late to affect the geochemical environment surrounding clinopyroxene crystallization. Independent geochemical evidence uniformly points to generally decreasing oxygen fugacity through the magmatic crystallization sequence of the East Hill suite, and the persistent increase in Zr in clinopyroxene is consistent with these conditions, as lower oxygen fugacity creates a geochemical environment in the melt that is favorable to the incorporation of Zr in clinopyroxene.

Therefore, the increase in Ti in clinopyroxene in the more evolved lithologies is probably not related to the “peralkaline effect” *sensu stricto*, although the peralkaline character of the melt almost certainly played a major role in the clinopyroxene crystal chemistry. The fundamental question with respect to Ti and Zr is which molecule governs their incorporation into clinopyroxene. Are they present as a Ca molecule, such as  $\text{Ca}(\text{Ti,Zr})\text{Al}_2\text{O}_6$  (Jones & Peckett 1980; Farges *et al.* 1994; Coulson 2003), or as a Na molecule, either *via* aegirine-neptunite,

$\text{Na}_2\text{Fe}^{2+}_2\text{TiSi}_4\text{O}_{12}$ , solid solution (Ferguson 1977) or as strict clinopyroxene solid solution,  $\text{Na}(\text{Fe}^{2+}, \text{Mg})_{0.5}(\text{Ti}, \text{Zr})_{0.5}\text{Si}_2\text{O}_6$  (Grapes *et al.* 1979; Nielsen 1979; Jones & Peckett 1980; Ramløv & Dymek 1991)? An examination of the relationships between Na and  $M(1)$  cations may shed some light on the basis of the compositional trends.  $^{[M(2)]}\text{Na} - ^{[M(1)]}(\text{Ti} + \text{Zr} + \text{Al} + \text{Fe}^{3+})$  calculates to within an average of 0.024 *apfu* of zero, suggesting that both Ti and Zr are balanced against Na, rather than discrete Ca-Zr and Na-Ti couplings.

A plot of Ti *versus* FMM ( $\text{Fe}^{2+} + \text{Mn} + \text{Mg}$ ) (Figure 104) shows a slight general negative correlation between Ti and FMM. Titanaugite analyses stand off the main trend at high FMM values and themselves do not exhibit a strong trend. A comparable plot for Zr (Figure 105) reveals a more consistent negative correlation. This shows that the clinopyroxene solid solution mechanism,  $^{[M(1)]}(\text{Fe}^{2+}, \text{Mn}, \text{Mg})_{0.5} + ^{[M(1)]}(\text{Ti}, \text{Zr})_{0.5} \leftrightarrow ^{[M(1)]}\text{Fe}^{3+}$  is dominant, meaning that, for compositions other than titanaugite, the  $\text{Na}(\text{Fe}^{2+}, \text{Mg})_{0.5}(\text{Ti}, \text{Zr})_{0.5}\text{Si}_2\text{O}_6$  molecule (Grapes *et al.* 1979; Nielsen 1979; Jones & Peckett 1980; Ramløv & Dymek 1991) is responsible for Ti and Zr incorporation and that Ca and Zr, though negatively autocorrelated, are largely decoupled in clinopyroxene in the East Hill suite.

Similarly, Ti shows no correlation with Al (Figure 106) except for augite and titanaugite compositions from the nepheline melasyenite, in which they are strongly positively correlated. This positive correlation is to be expected due to the titanaugite substitution mechanism:



The lack of correlation for clinopyroxene from other lithologies shows that molecules such as  $\text{CaTiAl}_2\text{O}_6$  are of little to no importance in the East Hill suite clinopyroxene. Essentially the same result is seen for Zr (Figure 107) except that Zr content does not correlate with Al content, showing that  $\text{CaZrAl}_2\text{O}_6$  is not significant, either.



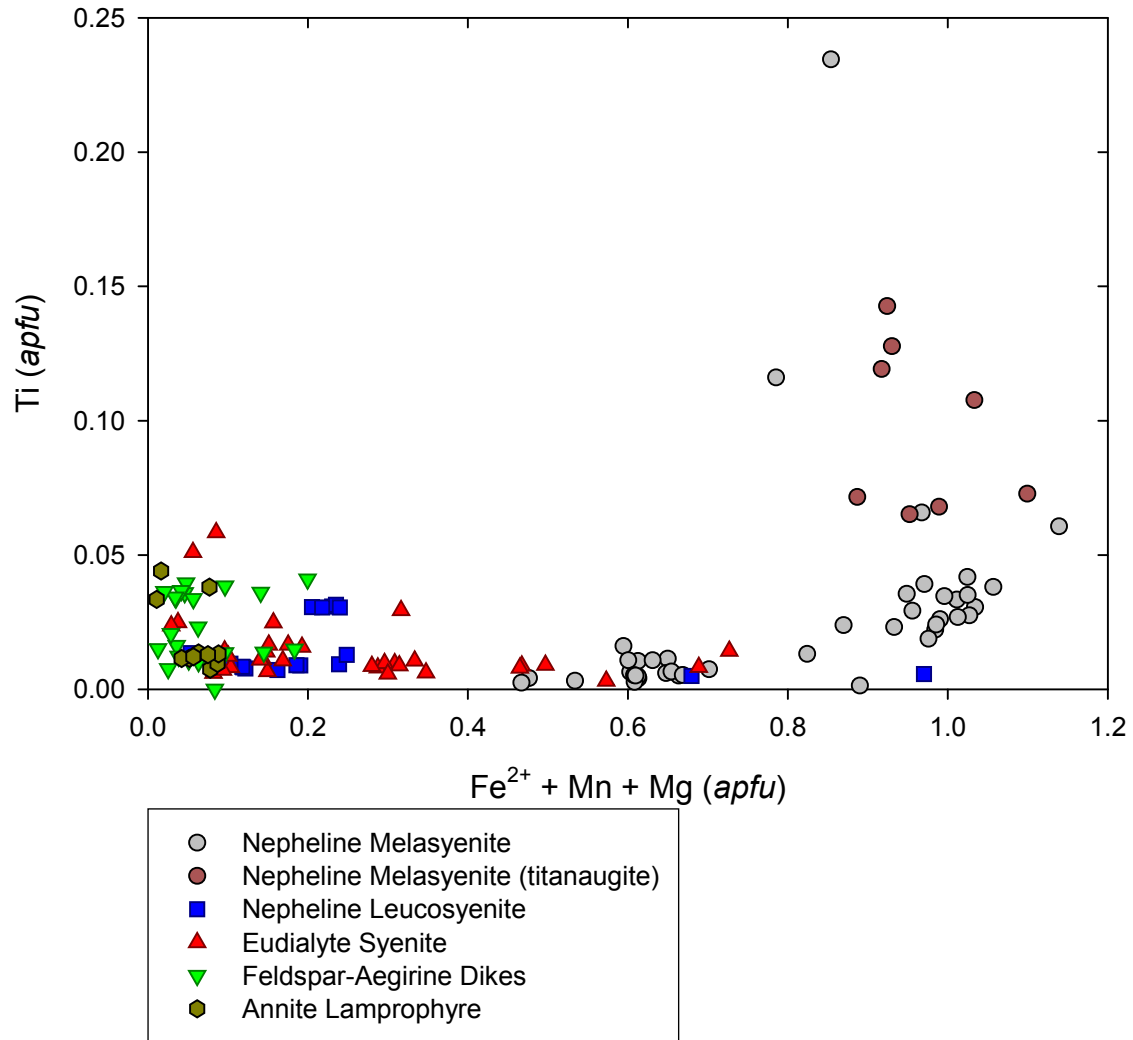


FIGURE 104 – Variation of Ti with ferromagnesian elements in clinopyroxene – East Hill suite

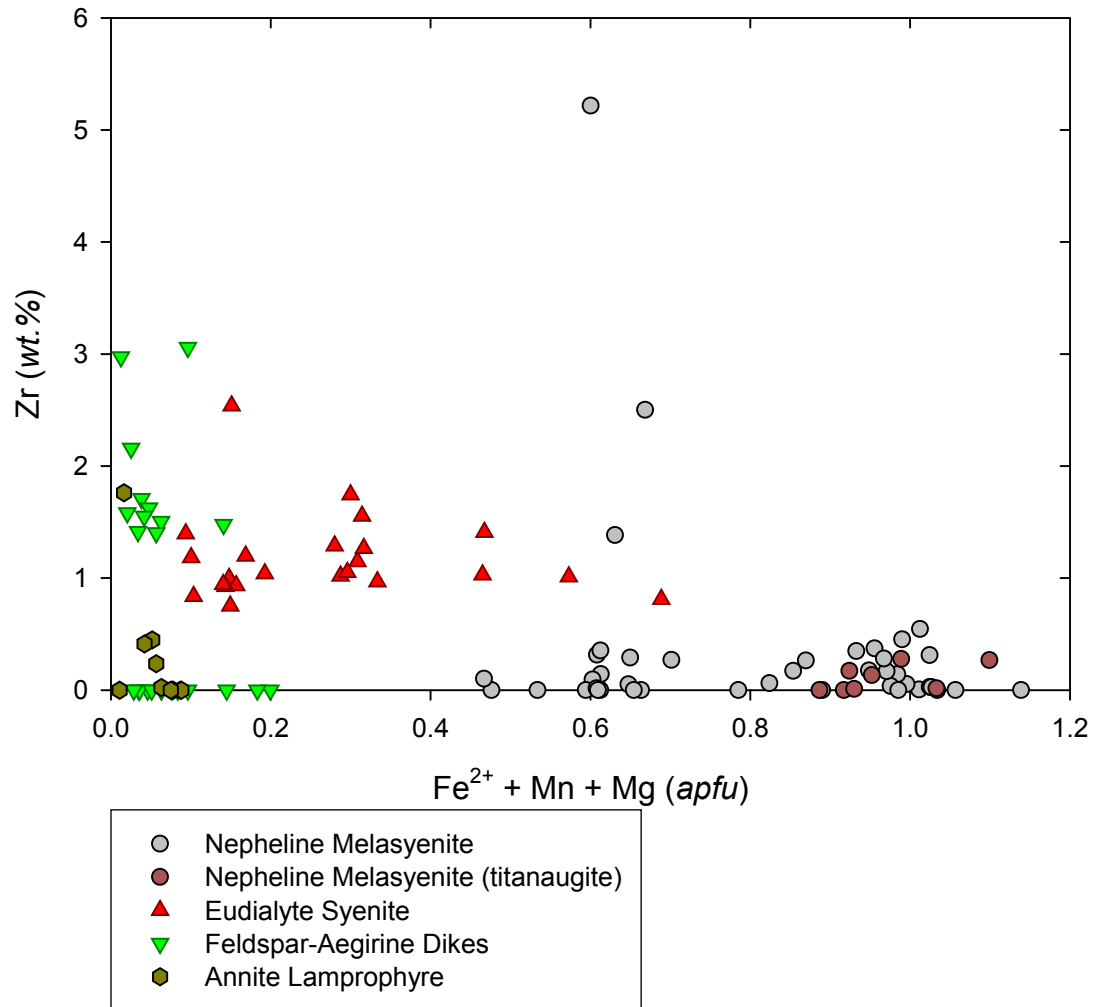


FIGURE 105 – Variation of Zr with ferromagnesian elements in clinopyroxene – East Hill suite

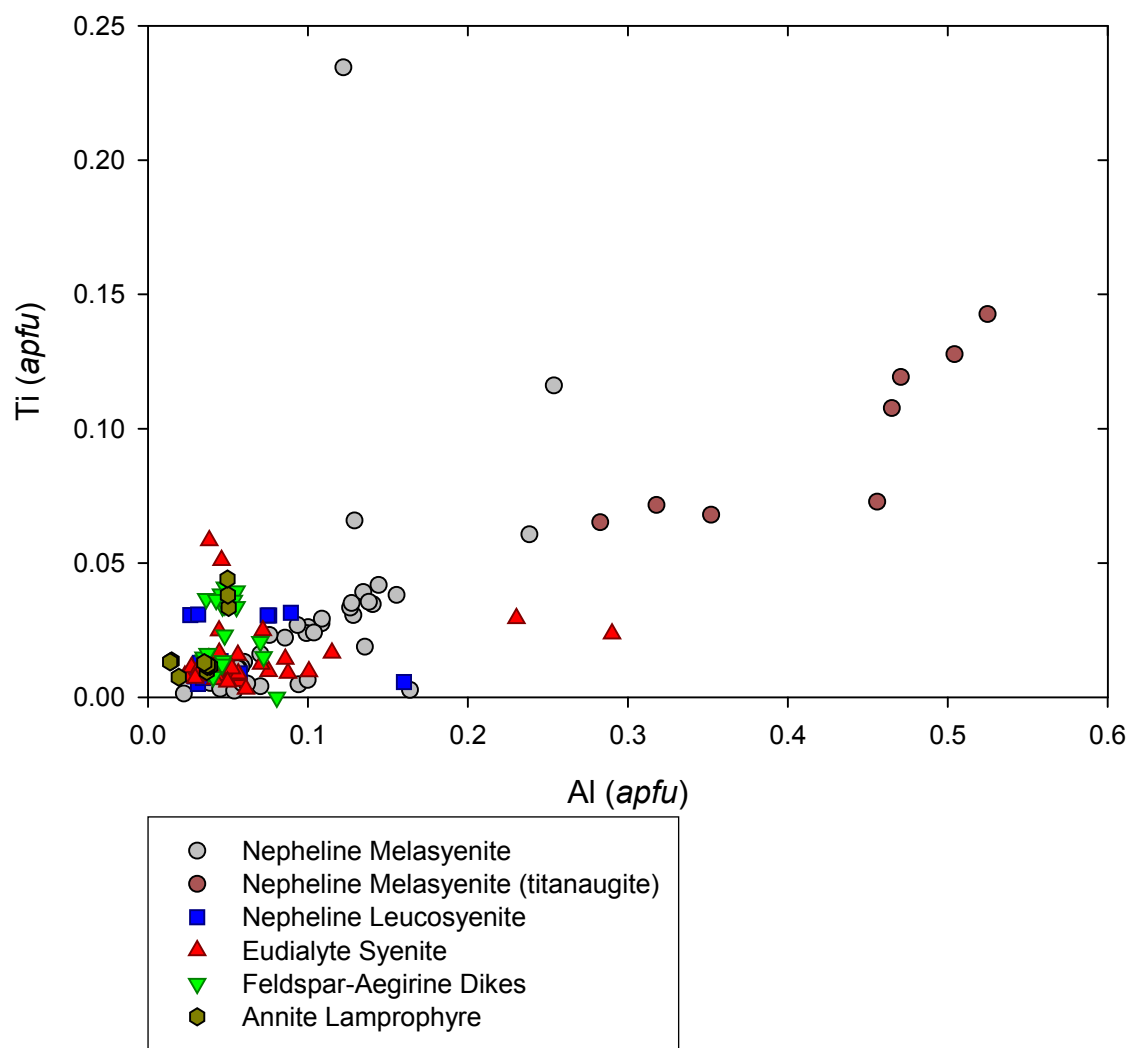


FIGURE 106 – Ti *versus* Al in clinopyroxene – East Hill suite

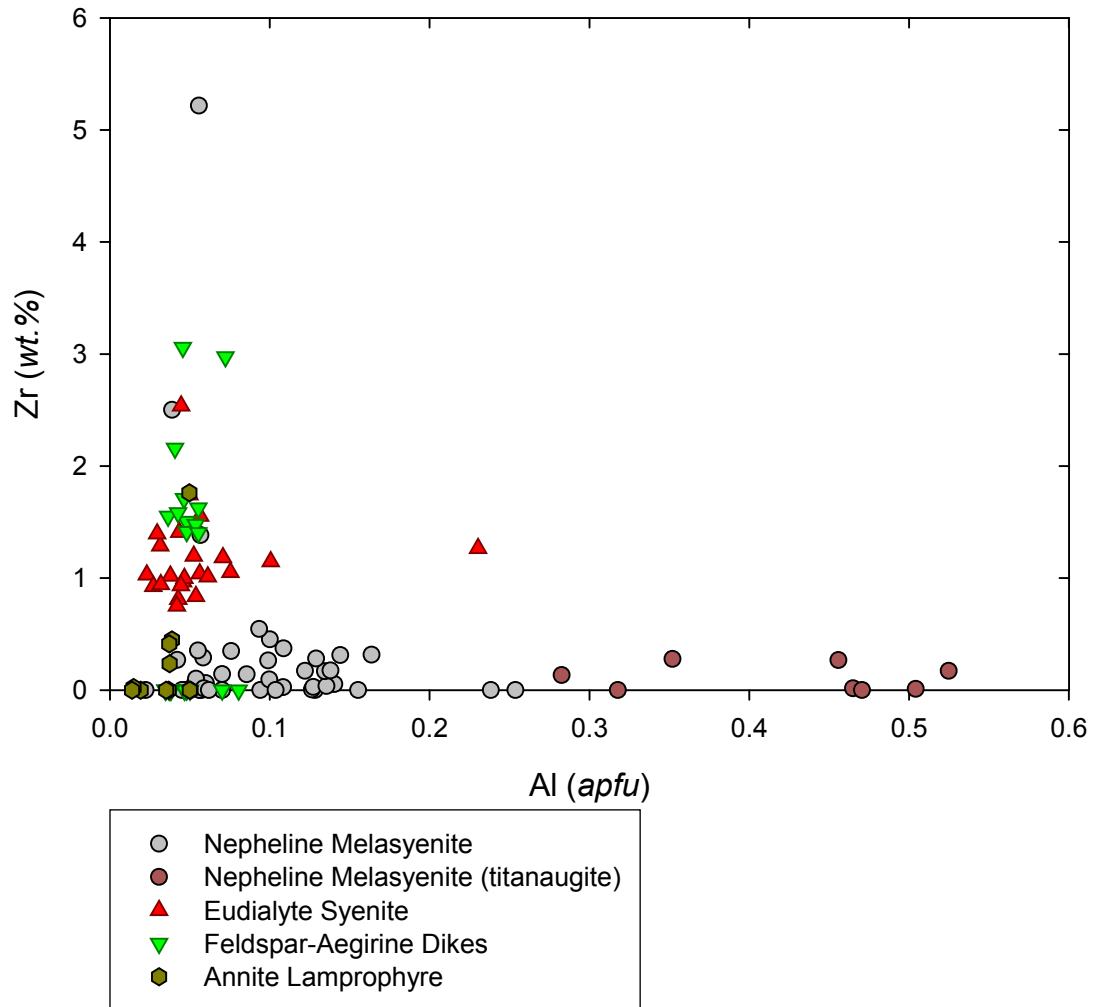


FIGURE 107 – Zr versus Al in clinopyroxene – East Hill suite

Aegirine-augite from the peralkaline potassic Buhovo-Seslavitzi complex, Bulgaria, is enriched in both Ti and Zr. At Buhovo-Seslavitzi, Zr enrichment is associated with mildly peralkaline conditions and Ti enrichment with strongly peralkaline conditions. Buhovo-Seslavitzi, however, crystallized under highly oxidizing conditions, between the HM and NNO buffers (Dyulgerov & Platevoet 2006), thus allowing the “peralkaline effect” to be in force. Similar high-Ti aegirine is found in teschenite sills in the Sydney Basin, Australia, again under high  $f_{O_2}$  conditions. (Martin 1984)

Conversely, exceedingly Zr-rich, up to 7.0 wt.%  $ZrO_2$ , aegirine occurs in the Motzfeldt Centre, Greenland, having crystallized under peralkaline, low  $f_{O_2}$  conditions. (Jones & Peckett 1980) Even more spectacular Zr enrichment, up to 14.5 wt.%  $ZrO_2$ , is seen in aegirine from Warrumbungle volcano, Australia, at which particularly low  $f_{O_2}$ , probably below the QFM buffer, prevailed. (Duggan 1988)

It would seem that the partitioning of Zr between clinopyroxene and alkali zirconosilicates is the result of a dual balance between peralkalinity and oxygen fugacity. High peralkalinity tends to favor assimilation of Zr by alkali zirconosilicates; low peralkalinity favors clinopyroxene. Similarly, high oxygen fugacity favors the exclusion of Zr from clinopyroxene, and low oxygen fugacity favors Zr-rich clinopyroxene. Obviously, however, these parameters are free to vary independently, so the relative abundances of these phases, as well as the degree of Zr enrichment in clinopyroxene, may be highly variable depending on local conditions. The simultaneous occurrence of late-stage, Zr-rich (up to about 3.0 wt.%  $ZrO_2$ ) aegirine and alkali zirconosilicates in the East Hill suite points to and supports the external evidence for both a high level of peralkalinity and low oxygen fugacity.

Variation of Al with fractionation (Figure 108) initially would appear to suggest two fractionation trends; however, early Al enrichment is common in alkaline complexes (Stephenson & Upton 1982; Platt & Woolley 1986), probably owing to early crystallization of titanite. Ferric iron clearly exhibits a single fractionation trend (Figure 109) but its variation follows two different slopes. In the nepheline melasyenite, the Na-Zr and, in particular, the jadeite molecules are more important, as shown by the more rapid increase in Na content than  $\text{Fe}^{3+}$ , the slight Zr content, and the elevated Al contents of nepheline melasyenite clinopyroxene. Ferric iron is more closely correlated with Na in more evolved lithologies, but a plot of  $\text{Fe}^{3+}$  versus Na (Figure 110) still shows a faster increase in Na than  $\text{Fe}^{3+}$ . Arguably, the excess sodium could be consumed by Ti and Zr, but  $\text{Na} - (\text{Ti} + \text{Zr} + \text{Fe}^{3+})$  is not only positive but close to the content of Al for nearly all analyses, suggesting that jadeite is of some importance throughout the crystallization sequence of the East Hill suite.

Mn content follows an interesting arc through fractionation (Figure 111), increasing early and decreasing in the most evolved lithologies. This pattern is seen in other alkaline complexes, such as North Qôroq, Greenland. At North Qôroq, the highest Mn contents occur in clinopyroxene that crystallized at about the same time the compositions began to turn away from hedenbergite (Coulson 2003), and the same concurrence is found in the East Hill suite. COULSON (2003) speculates that  $\text{Mn}^{3+}$  may play a role in clinopyroxene crystal chemistry in high-Mn alkaline pyroxenes. This would either require an especially oxidizing environment or some similar chemical extreme such as excessive peralkalinity. In the East Hill suite clinopyroxenes,  $^{[M(2)]}\text{Na} - ^{[M(1)]}(\text{Ti} + \text{Zr} + \text{Al} + \text{Fe}^{3+})$  leaves residual Na that could balance  $\text{Mn}^{3+}$  in less than 10% of analyses, and none of them are in the high-Mn portion of the trend.  $\text{Mn}^{3+}$  in East Hill suite clinopyroxenes cannot be excluded, but the evidence in favor is not strong.

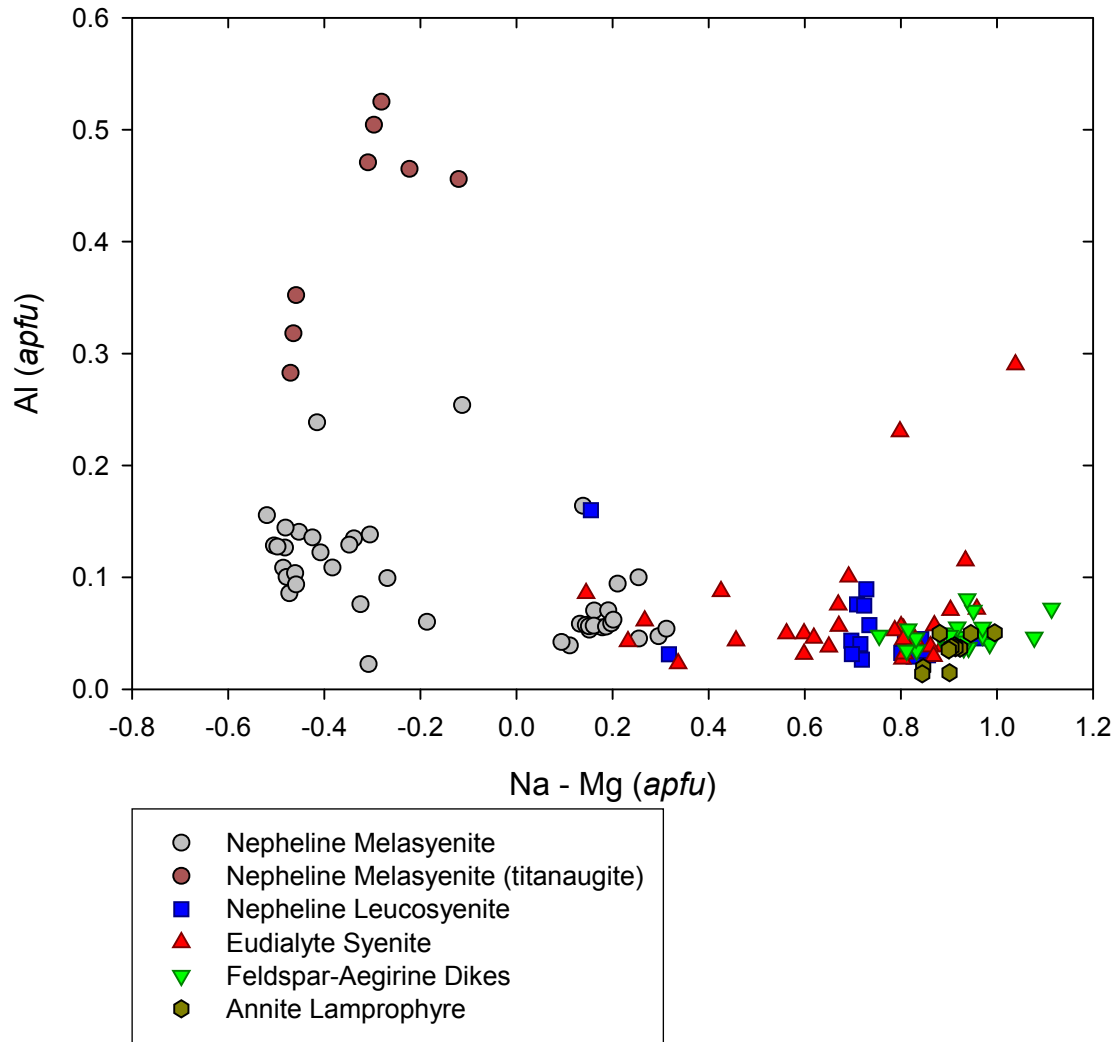


FIGURE 108 – Variation of Al with fractionation in clinopyroxene – East Hill suite

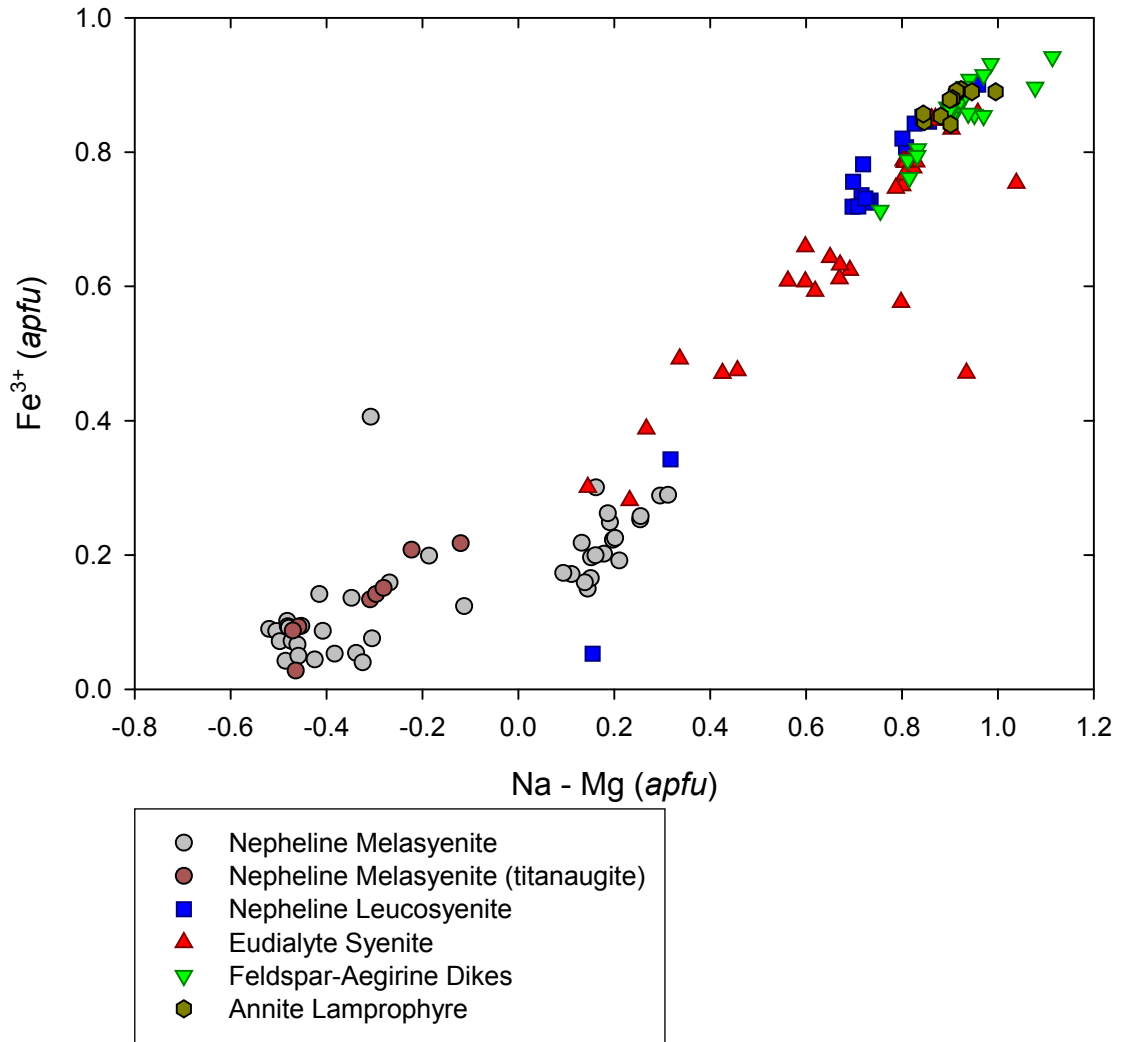


FIGURE 109 – Variation of  $\text{Fe}^{3+}$  with fractionation in clinopyroxene – East Hill suite



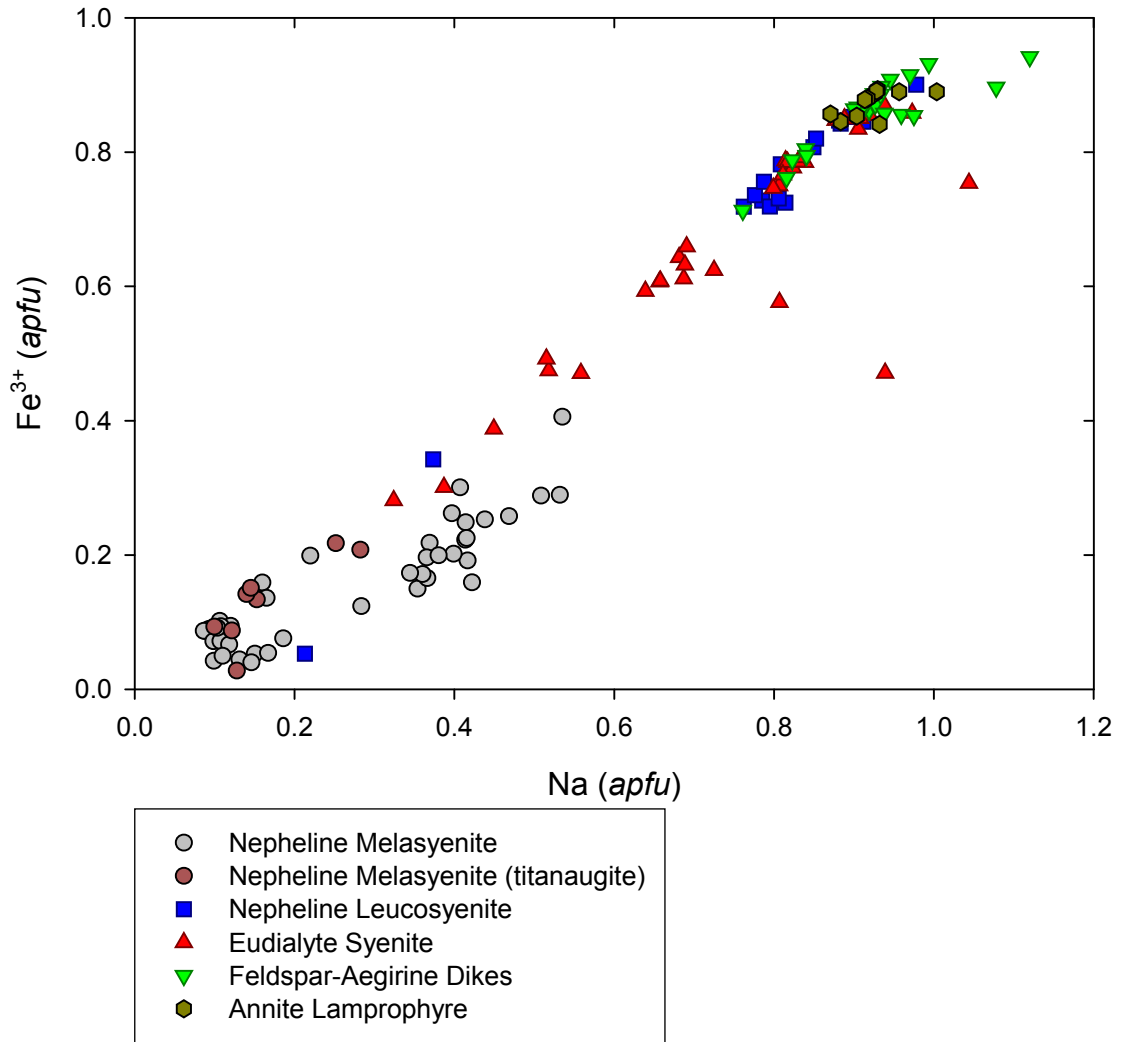


FIGURE 110 –  $\text{Fe}^{3+}$  versus Na in clinopyroxene – East Hill suite

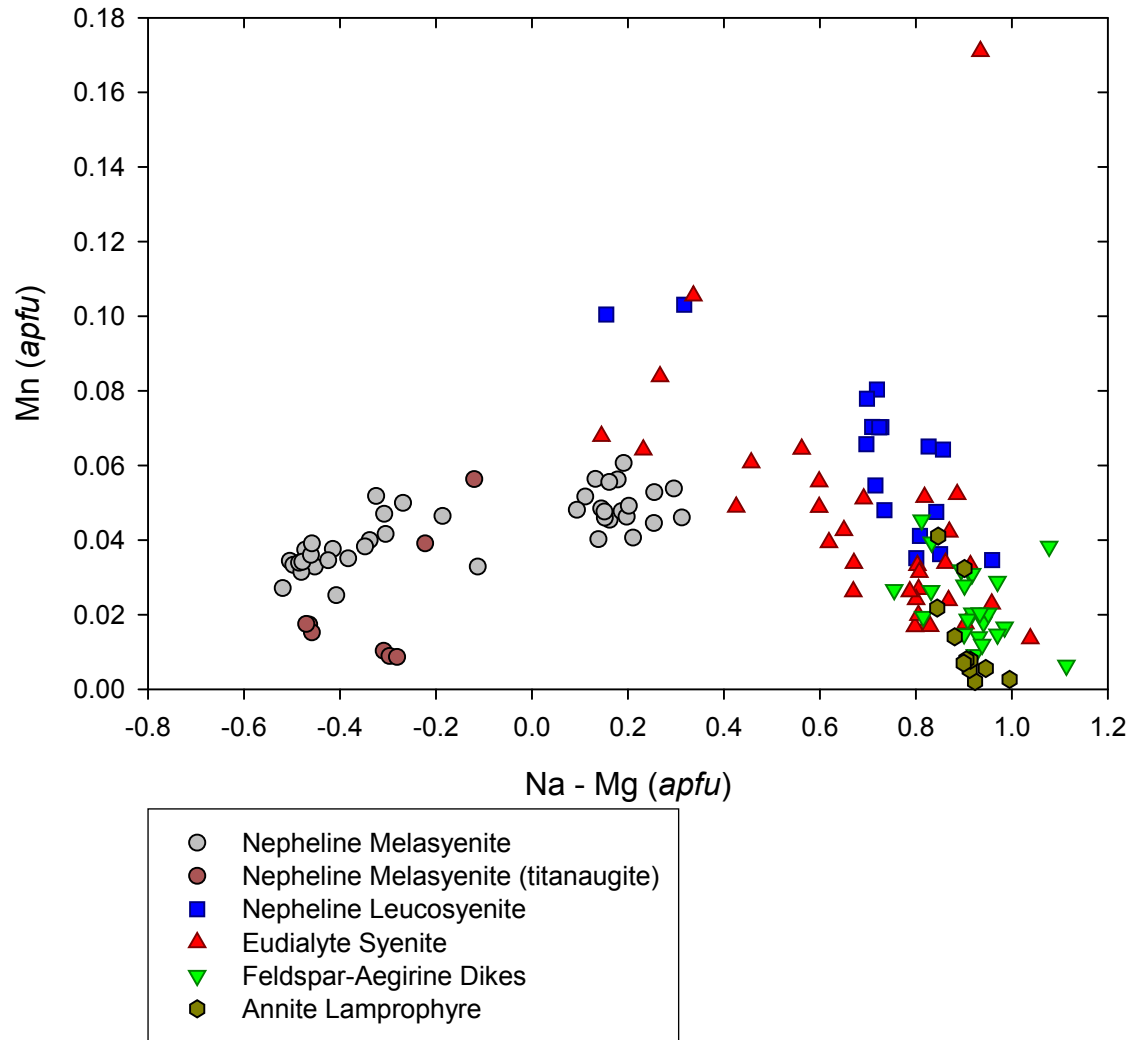


FIGURE 111 – Variation of Mn with fractionation in clinopyroxene – East Hill suite

## SULFIDES

### *Acanthite*



#### *Eudialyte Syenite*

Acanthite has been tentatively identified as a rare mineral in the eudialyte syenite. One anhedral crystal, about 0.3 mm in maximum dimension, was found associated with alkali feldspar and natrolite. The specimen is charcoal grey with brassy overtones and a dull metallic luster. Identification was based on EDS analysis and physical properties (color and luster).

### *Alabandite*



#### *Type 1 Nepheline Leucosyenite*

Alabandite has been tentatively identified as a rare mineral in the Type 1 nepheline leucosyenite. It occurs as a skeletal, anhedral crystal 3  $\mu\text{m}$  wide by 10  $\mu\text{m}$  long, directly associated with sérandite and an unidentifiable mass of similar size that yields a Ba, Th, and Si signature with EDS analysis. The lot is associated with aegirine-augite and is collectively included by an albitized microcline crystal.

Identification of the mineral began with EDS analysis, which yielded a clean Mn and S signature; this indicates either a manganese sulfide or a manganese sulfate. Manganese sulfates, such as jokokuite ( $\text{MnSO}_4 \cdot 5 \text{H}_2\text{O}$ ), mallardite ( $\text{MnSO}_4 \cdot 7 \text{H}_2\text{O}$ ), or szmikite ( $\text{MnSO}_4 \cdot \text{H}_2\text{O}$ ) typically form under surface p-T conditions in subaerial or aqueous environments. (Anthony *et al.* 2003) Considering the association and texture of the specimen and its environment of formation, it seemed a fair assumption to eliminate manganese sulfates and their allies, leaving

manganese sulfides for consideration. There are two manganese sulfide minerals: alabandite, MnS, and hauerite, MnS<sub>2</sub>. There was no good basis for comparison to try to estimate stoichiometry from relative EDS peak heights; so, an alternative discriminator was needed.

Alabandite is typically found in epithermal vein deposits, associated with galena, pyrite, and sphalerite. Hauerite is typically found as a precipitate from high-sulfur hydrothermal fluids, in association with gypsum and native sulfur (Palache *et al.* 1966). The former assemblage is representative of the sulfur-bearing species in the Type 1 nepheline leucosyenite. Therefore, alabandite seems a likely identity for this specimen. Alabandite is  $\alpha$ -MnS (Tappero *et al.* 1997), but it is interesting to note that sodium silicate gels have been used to synthesize  $\gamma$ -MnS (Schwartz *et al.* 1967), suggesting some commonality in chemical environments favorable to the formation of the various MnS polymorphs.

### ***Arsenopyrite***

#### **FeAsS**

#### ***Type 1 Nepheline Leucosyenite***

Arsenopyrite is found as a rare mineral in the Type 1 nepheline leucosyenite. It occurs as a subhedral crystal 5  $\mu$ m in maximum dimension. The shape of the crystal appears to be a combination of {210} and {101}, although it is impossible to determine the dominant form, owing to the small size of the specimen. It is directly associated with sphalerite, and it occurs at the interface between a crystal of manganoan pectolite and one of an unidentified Na-Zr silicate. Identification was on the basis of EDS analysis.

### ***Chalcopyrite***



#### *Eudialyte Syenite*

Chalcopyrite was tentatively identified as a trace mineral in the eudialyte syenite as anhedral, blebby grains to 10  $\mu\text{m}$ , embedded in natrolite. Identification is on the basis of EDS analysis. Differentiation from cubanite  $[\text{CuFe}_2\text{S}_3]$  was primarily on the basis of the observed Cu:Fe ratio.

### ***Covellite***



#### *Eudialyte Syenite*

Covellite was tentatively identified as a trace mineral in the eudialyte syenite. It is present as blebby crystals to 10  $\mu\text{m}$  in natrolite. Identification was on the basis of EDS analysis. Differentiation from chalcocite  $[\text{Cu}_2\text{S}]$  was on the basis of Cu:S ratio.

### ***Galena***



#### *Nepheline Melasyenite*

Galena has been found as a rare mineral in the nepheline melasyenite. It occurs as a colloform to dendritic aggregate of subhedral to euhedral cubic crystals, individually to 5  $\mu\text{m}$  and collectively to 40  $\mu\text{m}$ . This mass occurs within a crystal of aegirine-augite. Identification was on the basis of EDS analysis and on examination in the petrographic microscope (opaque).

### *Type 2 Nepheline Leucosyenite*

Galena is a rare mineral in the Type 2 nepheline leucosyenite. It occurs as an elongate cubic crystal to 5  $\mu\text{m}$  in length. It is found associated with pyrite and aegirine-augite.

Identification was on the basis of EDS analysis and optical properties (opaque).

### *Eudialyte Syenite*

Galena occurs in the eudialyte syenite as a trace mineral. It is present as anhedral, blebby grains to 10  $\mu\text{m}$ , embedded in natrolite. Identification was on the basis of EDS analysis and optical properties (opaque).

### *Annite Lamprophyre*

Galena was found as a single crystal in a specimen of annite lamprophyre. This individual is a euhedral elongate cube, 1.5 mm in its maximum dimension. It is found associated with natrolite, sphalerite, and annite. Identification was based on EDS analysis, visual hand specimen examination, and examination in the petrographic microscope under reflected light (isotropic, bright white color, cubic cleavage, triangular pits along cleavage).

### *Feldspar-Aegirine Dikes*

Galena occurs as a rare mineral in the feldspar-aegirine dikes. It is found as anhedral grains to 15  $\mu\text{m}$ , embedded in microcline, and associated with aegirine. It is also seen as an anhedral grain, 20  $\mu\text{m}$  in diameter, included by natrolite. Identification was on the basis of EDS analysis.

### ***Molybdenite***



#### *Type 2 Nepheline Leucosyenite*

Molybdenite is present as a rare mineral in the Type 2 nepheline leucosyenite. It occurs as subhedral to euhedral platy crystals to 40  $\mu\text{m}$  in diameter. They occur in association with sodalite pseudomorphs after nepheline, natrolite, and pyrochlore. Identification was based on EDS analysis and morphology in the SEM.

#### *Type 3 Nepheline Leucosyenite*

Molybdenite occurs as a rare mineral in the Type 3 nepheline leucosyenite as an opaque, subhedral, idiomorphic, hexagonal tabular crystal 90  $\mu\text{m}$  in diameter. It is associated with aegirine-augite and kupletskite.

### ***Pyrite***



#### *Nepheline Melasyenite*

Pyrite occurs as a trace mineral in the nepheline melasyenite, in which it is found as subhedral to euhedral cubic and cuboctahedral crystals to 0.7 mm in diameter. When freshly broken, they are brassy yellow in color, but may appear purplish red on tarnished surfaces and may be partly oxidized to hematite, giving a rusty stain to the surrounding rock. It is associated with aegirine-augite, magnetite, titanite, and alkali feldspar. Also, it is found as inclusions in titanaugite, taramite, and hastingsite. Identification was based on EDS analysis. Differentiation was made from other iron sulfide species based on the Fe:S ratio.

### *Type 1 Nepheline Leucosyenite*

Pyrite occurs as a trace mineral in the Type 1 nepheline leucosyenite. It is found as subhedral to euhedral cubic crystals to 20 µm on edge. They are included by natrolite reaction rims on sodalite pseudomorphs after nepheline. This association, and the fact that pyrite is the only opaque mineral found in these reaction rims, suggests that the minuscule crystals described in natrolite in the Type 1 nepheline leucosyenite are also pyrite. Finely disseminated pyrite would tint the natrolite reaction rim black, as is observed. This broader association of sodalite pseudomorphs after nepheline, rimmed by pyrite-included natrolite, was also described by TICE (1995) in a sodalite-nepheline syenite pegmatite in the East Hill Suite. Identification was on the basis of EDS analysis and morphology.

### *Type 2 Nepheline Leucosyenite*

Pyrite is found as a trace mineral in the Type 2 nepheline leucosyenite as anhedral crystals to 35 µm, associated with sodalite pseudomorphs after nepheline, aegirine-augite, galena, and siderite. Identification was on the basis of EDS analysis.

### *Eudialyte Syenite*

Pyrite occurs in the eudialyte syenite as anhedral grains to 10 µm. It is found associated with manganoan calcite, as well as embedded in natrolite. Identification followed the same scheme as above.



### *Annite Lamprophyre*

Pyrite is a rare mineral in the annite lamprophyre, in which it occurs as anhedral, blebby crystals to 10  $\mu\text{m}$  in diameter. Identification followed the same scheme as above.

### ***Sphalerite***

ZnS

### *Nepheline Melasyenite*

Sphalerite has been tentatively identified in the nepheline melasyenite as a rare mineral. It occurs as an anhedral bleb, approximately 10  $\mu\text{m}$  in diameter, associated with magnetite. Identification was primarily on the basis of EDS analysis.

### *Type 1 Nepheline Leucosyenite*

Sphalerite has been tentatively identified as a rare mineral in the Type 1 nepheline leucosyenite. It occurs as a subhedral, modified tetrahedral crystal 5  $\mu\text{m}$  in diameter. The shape of the crystal appears to be a combination of  $\{001\}$  and  $\{111\}$ , although it is impossible to determine the dominant form, owing to the small size of the specimen. The sphalerite is in direct association with arsenopyrite, and it occurs at the interface between a crystal of manganoan pectolite and one of an unidentified Na-Zr silicate. Identification was on the basis of EDS analysis and morphology.

### *Type 2 Nepheline Leucosyenite*

Sphalerite occurs in the Type 2 nepheline leucosyenite as a trace mineral. It is found as resinous brown, subhedral to euhedral crystals to 2.5 mm in maximum dimension. These

crystals are associated with albite, sodalite pseudomorphs after nepheline, and natrolite.

Identification was on the basis of EDS analysis. Differentiation from wurtzite [ZnS] is not possible with high confidence, but this occurrence is thought to be more consistent with known occurrences of sphalerite rather than wurtzite. Furthermore, individuals exhibiting better development of habit appear more consistent with sphalerite than with wurtzite (Alexander U. Falster, pers. comm.).

### *Type 3 Nepheline Leucosyenite*

Sphalerite is a rare mineral in the Type 3 nepheline leucosyenite. It occurs as subhedral to euhedral crystals to 75  $\mu\text{m}$  in maximum dimension that appear amber in thin section. The forms {001} and {111} are combined in various proportions in different crystals. Sphalerite is associated with microcline and sodalite pseudomorphs after nepheline. Identification was on the basis of EDS analysis, morphology, and optical properties (isotropic).

### *Eudialyte Syenite*

Sphalerite has been tentatively identified in the eudialyte syenite, in which it occurs as a trace mineral. It is found as anhedral to subhedral grains to 30  $\mu\text{m}$ , embedded in natrolite. Identification was made on the basis of EDS analysis, with supporting evidence as above.

### *Annite Lamprophyre*

Sphalerite has been tentatively identified as a trace mineral in the annite lamprophyre. It occurs as subhedral crystals to 60  $\mu\text{m}$ , associated with annite and galena. It is also found as a skeletal, subhedral individual to 0.6 mm maximum dimension, associated with aegirine and

annite. In thin-section, the sphalerite has an amber-brown color. Identification was made on the basis of EDS analysis, with supporting evidence as above.

## ***East Hill Suite Sulfides***

### *Overview*

Sulfide minerals vary in abundance in the East Hill suite, appearing late in the nepheline melasyenite, increasing in the nepheline leucosyenite, and peaking in the eudialyte syenite, followed by a more sudden decline into the feldspar-aegirine dikes and the annite lamprophyre. Unfortunately, most sulfide specimens are too small to determine reliable compositions *via* electron microprobe analysis. Consequently, the lack of such analyses precludes the use of the arsenopyrite geothermometer (Sharp *et al.* 1985) or the sphalerite geothermobarometer (Scott & Barnes 1971). Nevertheless, the application of known phase relations to observed sulfide assemblages allowed the development of plausible ranges of temperature and oxygen and sulfur fugacities.

An important factor in the study of sulfur-bearing melts is the partitioning of sulfur between sulfide,  $S^{2-}$ , and sulfate,  $S^{6+}$ . This speaks to oxygen fugacity and helps at least to define boundary conditions, if not precise measures. The shift in the wavelength of the  $SK\alpha$  peak, as measured in the electron microprobe, may be used to estimate sulfur speciation and, by extension, oxygen fugacity. (Carroll & Rutherford 1988; Jugo *et al.* 2005) The proportion of  $S^{6+}$  with respect to total sulfur is related to oxygen fugacity by the following relationship:

$$X(S^{6+})_{eq.} = \frac{0.86}{(1 + e^{(2.89 - 2.23 \Delta QFM)})}$$

in which  $X(S^{6+})_{eq.}$  is the mole fraction equivalents of sulfur as sulfate and  $\Delta QFM$  is oxygen fugacity, expressed as the number of log units from the QFM buffer. (Jugo *et al.* 2005)

As is evident from its equation, this function has a complex exponential form (Figure 112). It exhibits a steep slope and inflection point near  $\Delta\text{QFM} = +1$ , and calculated values of  $X(\text{S}^{6+})_{\text{eq.}}$  change rapidly with  $\Delta\text{QFM}$  on either side of this inflection point. At  $\Delta\text{QFM} = +1$ ,  $X(\text{S}^{6+})_{\text{eq.}} = 0.293$ , but by  $\Delta\text{QFM} = +2$ ,  $X(\text{S}^{6+})_{\text{eq.}}$  has already increased to 0.712. Similarly, at  $\Delta\text{QFM} = 0$ ,  $X(\text{S}^{6+})_{\text{eq.}} = 0.045$ , and at  $\Delta\text{QFM} = -1$ ,  $X(\text{S}^{6+})_{\text{eq.}}$  has diminished to 0.005. Outside of this range, approximately  $-1 \leq \Delta\text{QFM} \leq +2$ , changes in oxygen fugacity have little effect on the speciation of sulfur. Above  $\Delta\text{QFM} = +2$ , sulfur is dominantly present as sulfate, and below  $\Delta\text{QFM} = 0$ , sulfur is dominantly present as sulfide (Figure 113).

Sulfate minerals are only present in any quantity as rare barite in the Type 3 nepheline leucosyenite. Interpolation suggests that the oxygen fugacity must have been at or slightly below the QFM buffer, to allow sulfide dominance through much of the crystallization history of the East Hill suite; although it climbed above QFM late, allowing barite to stabilize.

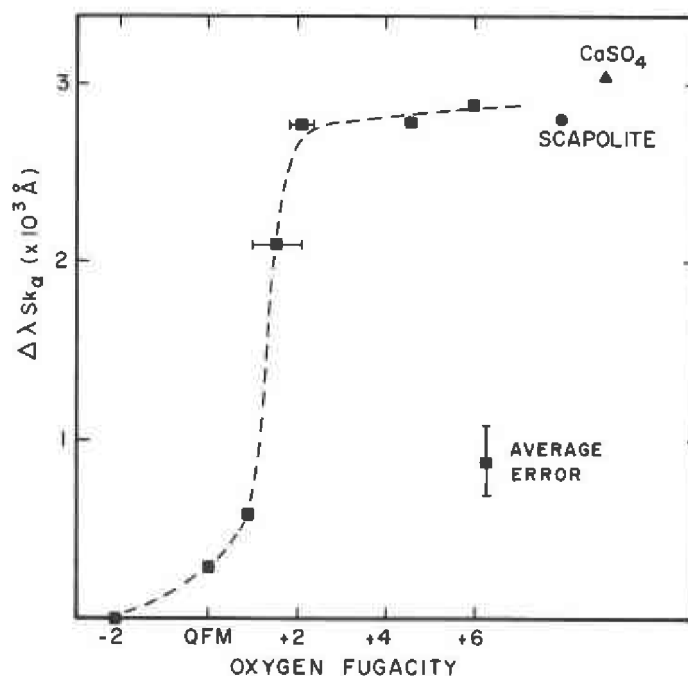


FIGURE 112 – Measured wavelength peak shift for  $\text{SK}\alpha$  versus experimental oxygen fugacity in  $\Delta\text{QFM}$  log units. (Carroll & Rutherford 1988)

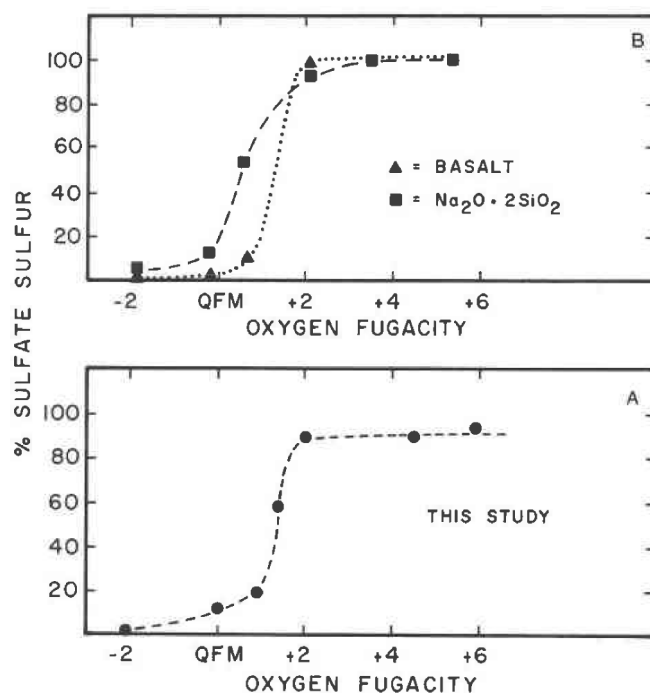


FIGURE 113 – A) Corresponding  $X(S^{6+})_{eq}$  values for the curve from FIGURE 112; data from CARROLL & RUTHERFORD (1988). B) Experimental results from NAGASHIMA & KATSURA (1973) (dotted line) and KATSURA & NAGASHIMA (1974) (dashed line). Both at 1 atm and 1250°C. (Carroll & Rutherford 1988)

### *Nepheline Melasyenite*

The nepheline melasyenite contains the assemblage galena-pyrite-sphalerite, with pyrite dominating the sulfide mineralogy, as well as magnetite and clinopyroxene. Magnetite and pyrite are both found as inclusions in clinopyroxene and amphibole, but only magnetite is found as inclusions in alkali feldspar and sodalite pseudomorphs after nepheline. Petrography indicates that alkali feldspar and nepheline crystallized before the ferromagnesian phases. Therefore, the presence of magnetite, exclusive of pyrite, as inclusions in the aluminosilicates indicates that magnetite crystallization commenced prior to that of pyrite. Furthermore, in some specimens, pyrite and magnetite coexist in apparent equilibrium.

Above approximately 750°C, the pyrite stability field in  $f_{S_2} - f_{O_2}$  space is excluded by that of pyrrhotite (Figure 114). As the system cools below 750°C, the pyrite field expands down

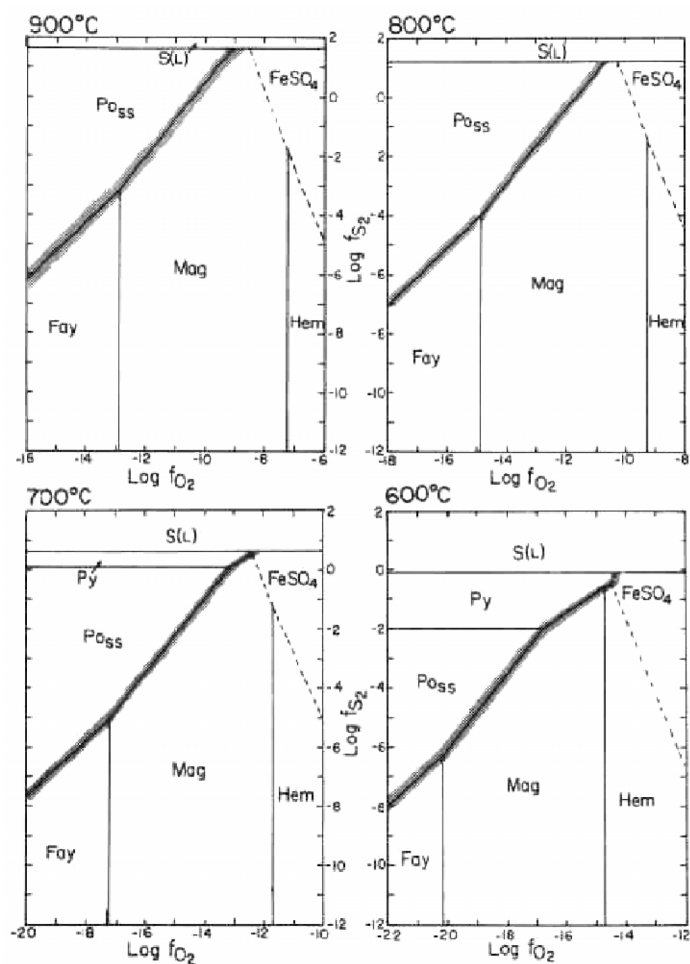


FIGURE 114 – Isothermal sulfur fugacity *versus* oxygen fugacity spaces showing phase relations in the Fe-O<sub>2</sub>-S<sub>2</sub>-SiO<sub>2</sub> system. (Whitney 1984)

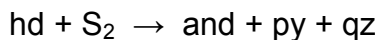
$f_{S_2}$ , at the expense of pyrrhotite, and the magnetite field shifts to lower  $f_{O_2}$ . (Whitney 1984)

Evidence from amphibole chemistry indicates decreasing  $f_{O_2}$  during the crystallization of the nepheline melasyenite, and pyrrhotite is essentially absent from the major syenites in the East Hill suite. (Horváth & Gault 1990) A shift in  $f_{S_2}$ – $f_{O_2}$  space from the magnetite to the pyrite stability field was accomplished either by passing directly into the pyrite field or by traversing the pyrrhotite field. Since the pyrite field expands with cooling, it is not immediately clear whether sulfur fugacity increased, decreased, or stayed constant during the transition.

Even though pyrrhotite is absent from the major lithologies in the East Hill suite, it is still conceivable that the melt passed through the pyrrhotite field in  $f_{S_2} - f_{O_2}$  space. Pyrrhotite is metastable (Sweeney & Kaplan 1973), and the higher sulfur activity in the pyrite field would have driven the conversion of pyrrhotite into pyrite. Furthermore, it may be that the East Hill suite magma necessarily passed through the pyrrhotite field, due to possible mismatch between the thermal stability of primary pyrite and the liquidus temperature of the melt. (Kullerud & Yoder 1959) Further study, including more precise characterization of the sulfur fugacity at emplacement, is necessary to fully address this issue.

Below about 800°C, magnetite may coexist with pyrite in the pyrite stability field. (Oyarzun *et al.* 2001) Therefore, the position of the melt in  $f_{S_2} - f_{O_2}$  space (Figure 114) need not have hugged the pyrite-magnetite boundary and must have fully entered the pyrite field in order to conform to the estimated oxygen fugacities for magnetite, which are far lower than those traced by the pyrite-magnetite boundary.

Hedenbergite has a composition-dependent stability relationship with pyrite in  $f_{S_2} - T$  space. (Burt 1972) At 2 kbar, pyroxene of composition  $hd_{100}$  may only coexist with pyrite below approximately 300°C and  $f_{S_2} < 10^{-10}$  bar, but  $hd_{85}jo_{15}$  is stable with pyrite below about 500°C and  $f_{S_2} < 10^{-4}$  bar. Above these  $f_{S_2} - T$  ranges, hedenbergite undergoes the sulfidation reaction (Barton *et al.* 1982):



The nepheline melasyenite is andradite- and quartz-absent; therefore the sulfidation reaction did not take place, and the pyrite that is present is primary and in equilibrium with the pyroxene. Since the susceptible element in hedenbergite is ferrous iron, presumably it should not make a

substantial difference to the  $f_{S_2}$  – T stability boundaries whether hedenbergite is substituted by johannsenite, diopside, aegirine, or any other Fe<sup>2+</sup>-absent molecule. Clinopyroxene in the nepheline melasyenite contains up to 50 mol% hedenbergite. For an estimated pyrite crystallization temperature of 500°C from magnetite-ilmenite geothermometry and petrographic relationships, the  $f_{S_2}$  ceilings for hd<sub>100</sub> and hd<sub>85</sub>jo<sub>15</sub>, are 10<sup>-5.6</sup> bar and 10<sup>-4.1</sup> bar, respectively. Evidence suggests that the stability relationship between hedenbergite composition and sulfur fugacity is linear (Barton *et al.* 1982), so extrapolating to hd<sub>50</sub> returns a maximum  $f_{S_2}$  of 10<sup>-0.6</sup> bar, consistent with the estimated  $f_{S_2}$  range from pyrite-magnetite stability relations.

Galena is present as an inclusion in aegirine-augite. Because the exact temperature of crystallization of the galena is not known, the galena-anglesite buffer cannot be used to give a precise oxygen fugacity. Even though the galena is included by aegirine-augite, its colloform habit suggests that it may be a low-temperature precipitate or colloidal deposit from late-stage fluids rather than a primary magmatic phase. (Koroleva *et al.* 1970; Chen 1978) This proposition is reasonable considering the proximity of the inclusion to fractures in the clinopyroxene. If the galena were primary magmatic, an estimate of the oxygen fugacity during its formation, based on a temperature estimate of 700°C for the aegirine-augite, would be less than 10<sup>-14</sup> bar, consistent with the oxygen fugacity indicated by magnetite. If the galena is, in fact, a late-stage precipitate, in the 100-250°C range, this points to an approximate oxygen fugacity range of 10<sup>-48</sup> to 10<sup>-32</sup> bar. (Kajiwara 1971; Kajiwara & Date 1971; Sato 1977; Simon *et al.* 1997)

Sphalerite is certainly indicative of sulfide-dominant oxygen fugacity, that is, near the QFM buffer. (Jugo *et al.* 2005) Sphalerite is present in the nepheline melasyenite as an inclusion in magnetite, and is probably equilibrated to the same oxygen fugacity as the magnetite itself.



Indeed, projection of a presumed crystallization temperature of the magnetite, 500°C, onto the sphalerite-ZnSO<sub>4</sub> buffer (Figure 115) yields  $f_{\text{O}_2} \approx 10^{-22}$ , which is in excellent agreement with the estimated crystallization  $f_{\text{O}_2}$  of the magnetite itself.

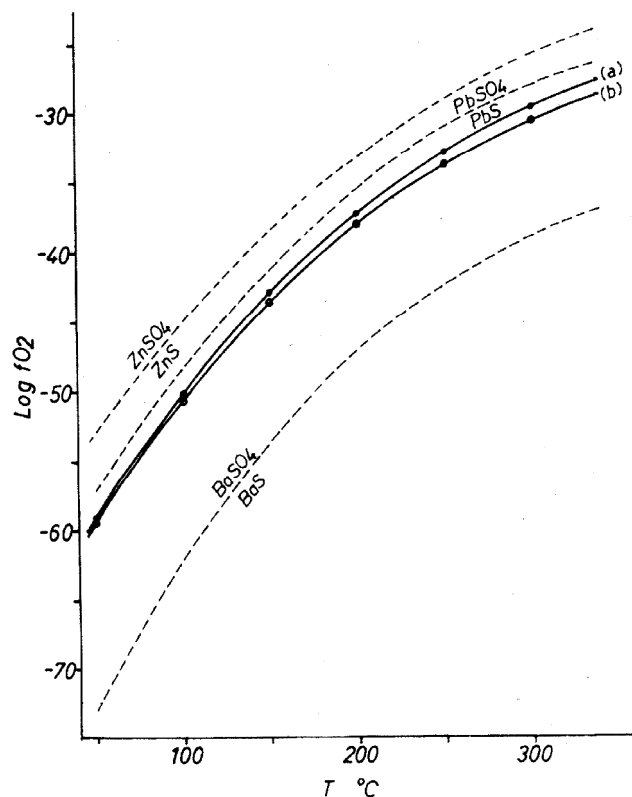


FIGURE 115 – Oxygen fugacity *versus* temperature for Zn, Pb, and Ba sulfide-sulfate pairs. Curve (a) represents coprecipitation of barite and galena; curve (b) of barite and sphalerite. (Kajiwara 1973)

Sulfur fugacity estimates using sphalerite require not only reliable temperature and compositional data, in terms of Fe content, but also adherence to specific buffer assemblages. (Barton & Toulmin 1966; Czamanske 1974) Sphalerite seems to be particularly sensitive to control of the boundary conditions; in using the sphalerite geobarometer, a 0.5 mole percent error in compositional analysis results in a pressure error of 0.5 kbar. (Scott 1976) None of this supporting evidence was available for sphalerite in the nepheline melasyenite.

### *Type 1 Nepheline Leucosyenite*

A comparison of amphibole, alkali feldspar, and nepheline geothermometry indicates that the nepheline leucosyenites began to crystallize during the intermediate stages of crystallization of the nepheline melasyenite, around 750-800°C. Since amphibole and annite geochemistry indicate generally decreasing  $f_{O_2}$ , the oxygen fugacity during the crystallization of the Type 1 nepheline leucosyenite should be equal to or less than approximately  $10^{-22}$  to  $10^{-24}$  bar, the  $f_{O_2}$  range indicated by magnetite-ilmenite geochemistry from the nepheline melasyenite.

The Type 1 nepheline leucosyenite contains the assemblage alabandite-arsenopyrite-pyrite-sphalerite; pyrite is the most abundant of these. Hauerite is stable at higher sulfur fugacity, but at lower  $f_{S_2}$ , alabandite becomes the dominant phase. If  $f_{CO_2}$  rises high enough relative to  $f_{S_2}$ , then alabandite destabilizes in favor of rhodochrosite (Olivo & Gibbs 2003). The more evolved rocks in the East Hill Suite contain rhodochrosite; therefore,  $f_{CO_2}$  and  $f_{S_2}$  in the East Hill Suite are probably, by and large, close to the alabandite-rhodochrosite reaction line. Furthermore, alabandite and rhodochrosite are both stable in assemblages that include arsenopyrite, pyrite, and sphalerite (Olivo & Gibbs 2003).

The Oka carbonatite complex exhibits the assemblage calcite-dolomite-periclase-apatite-forsterite-magnesioferrite-pyrrhotite-alabandite, which buffers oxygen and sulfur fugacity near the QFM buffer. In particular,  $f_{S_2}$  is held near the QFM-pyrrhotite boundary, corresponding to a sulfur fugacity of approximately  $10^{-6}$  bar at the estimated eutectic conditions, similar to p-T conditions in the East Hill suite, 640°C at 1 kbar. (Treiman & Essene 1984)

The presence of pyrite, rather than pyrrhotite, in the Type 1 nepheline leucosyenite shows that the sulfur fugacity was higher than in the Oka complex. Nepheline and alkali feldspar

geothermometry suggest crystallization temperatures extending below 500°C for the nepheline leucosyenite. The minimum sulfur fugacity to stabilize pyrite varies with temperature, from  $10^0$  bar at 700°C, decreasing by about 2 log units for every 100°C drop in temperature, down to approximately  $10^{-6}$  bar at 400°C. Recall that 400°C is not an unrealistic solidus temperature for an agpaitic magma. (Sood 1981)

Phase relations of arsenopyrite are only weakly dependent on pressure (Kretschmar & Scott 1976), so the most important parameters are composition,  $f_{S_2}$ , and temperature. The arsenopyrite specimen was too small for a useful electron microprobe analysis, but an initial estimated range of  $f_{S_2}$  and temperature can be taken from phase relations in the Fe-As-S system. Even though the arsenopyrite was in direct contact with sphalerite, pyrite is another important accessory phase in the Type 1 nepheline leucosyenite. The assemblage arsenopyrite-pyrite suggests arsenopyrite crystallization temperatures less than about 500°C and  $f_{S_2}$  less than about  $10^{-5}$  (Figure 116). Unfortunately, the lack of compositional data on the arsenopyrite precludes a strong, direct refinement of the temperature and, subsequently, the sulfur fugacity, but the association with low-Fe sphalerite points to relatively high sulfur fugacity, perhaps near the upper stability limit.

Sphalerite coexisting with pyrrhotite, at low  $f_{S_2}$  is Fe-rich, whereas that coexisting with pyrite, at higher  $f_{S_2}$  is Fe-poor. (Hannington & Scott 1989) EDS and electron microprobe analyses point to minimal Fe content in sphalerite in the nepheline leucosyenite. This is consistent with the high sulfur fugacity associated with primary pyrite.

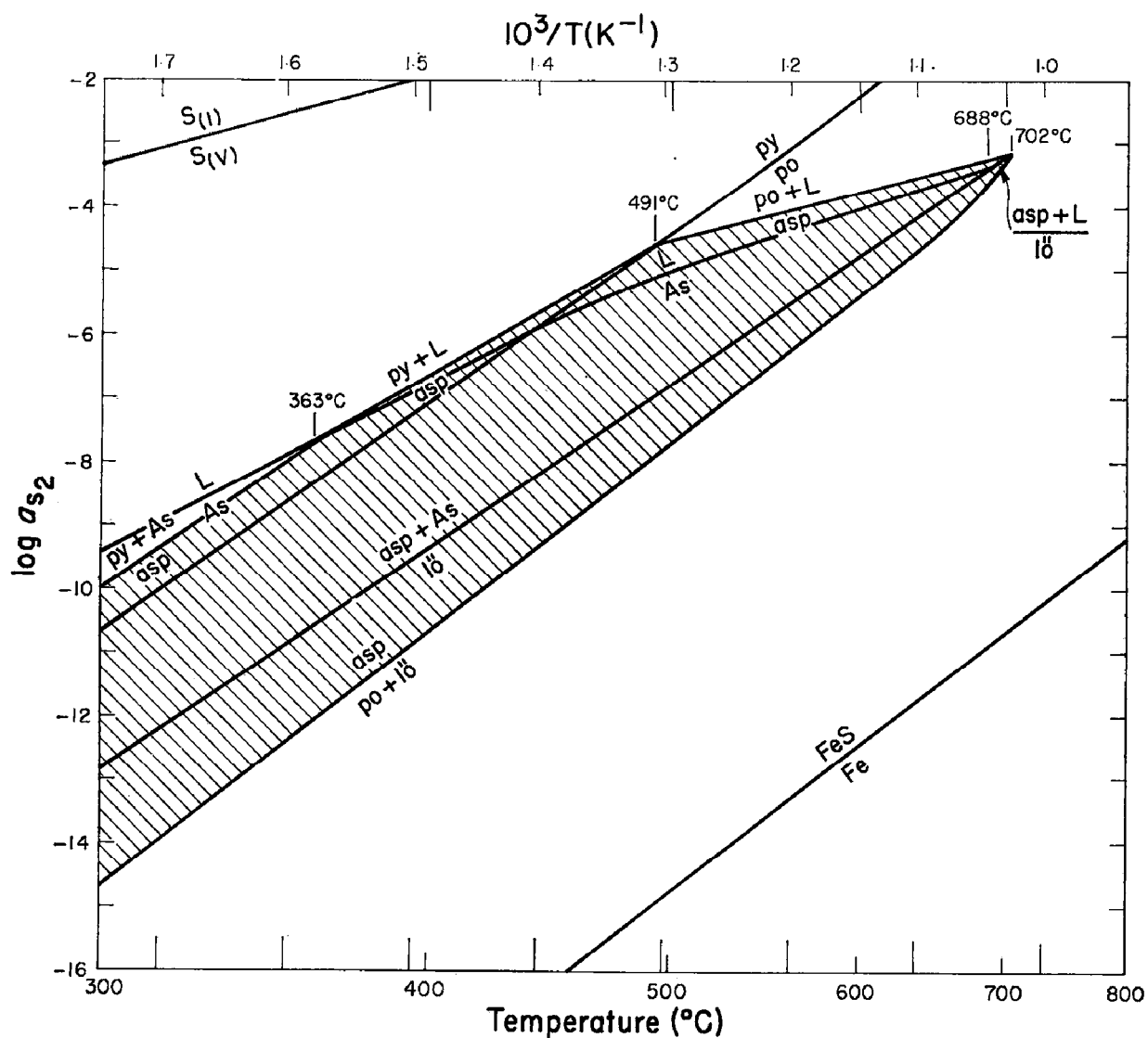


FIGURE 116 – Phase relations in  $a_{S_2}$ – $T$  space for the system Fe-As-S. The hashed region represents the stability field of arsenopyrite. (Kretschmar & Scott 1976)

### *Types 2 & 3 Nepheline Leucosyenite*

In addition to galena, pyrite, and sphalerite, molybdenite appears in the Type 2 nepheline leucosyenite; only molybdenite and sphalerite are present in the Type 3 nepheline leucosyenite. The crystallization temperatures of the Types 2 and 3 nepheline leucosyenite are almost certainly comparable to that of the Type 1 nepheline leucosyenite, with maximum temperatures certainly

below 700°C and minimum temperatures likely below 500°C before complete crystallization.

Also, the estimated oxygen fugacity range for these lithologies should be similar to that of the Type 1 nepheline leucosyenite, equal to or less than approximately  $10^{-22}$  to  $10^{-24}$  bar.

The assemblage galena-pyrite-sphalerite, crystallizing in a similar temperature interval to the Type 1 nepheline leucosyenite, points to a comparable range of sulfur fugacity,  $10^0$  to  $10^{-6}$  bar.

Although the absence of arsenopyrite in the Type 2 and 3 nepheline leucosyenites prevents narrowing this range to  $10^{-5}$  to  $10^{-6}$  bar, as in the Type 1 leucosyenite, it is unlikely that the sulfur fugacity drifted substantially from this latter range.

The introduction of molybdenite (Figure 117), however, allows for a partial refinement of  $f_{S_2}$ . The oxygen fugacity of the East Hill suite magma, through the latter part of the nepheline melasyenite and through all of the nepheline leucosyenites, was, at emplacement temperatures, below the QFM but always above the MW buffer. At the temperature represented in FIGURE 117, 577°C, this is an  $f_{O_2}$  range of about  $10^{-21}$  to  $10^{-25}$  bar, which fits with earlier estimates of  $f_{O_2}$ . However, stabilizing pyrite at this temperature requires an  $f_{S_2}$  higher than about  $10^{-3}$  bar, which is inconsistent with sulfur fugacity parameters dictated by arsenopyrite crystallization. Moreover, a temperature below approximately 500°C is also required by arsenopyrite in a pyrite-bearing assemblage. Such a temperature would be consistent with the solubility behavior of molybdenite in alkaline magmas. At 1 kbar, molybdenite achieves its maximum solubility in vapor-saturated alkaline melts at approximately 650°C, decreasing quickly with temperature until it becomes insoluble below about 375°C. (Isuk & Carman 1981) Consequently, cooling below 500°C would promote rapid molybdenite crystallization.

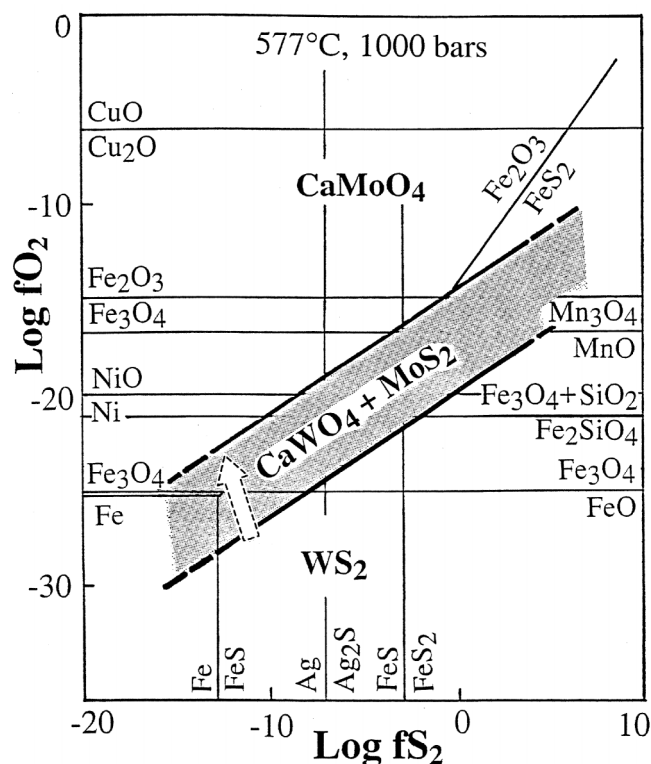


FIGURE 117 – Phase relations in  $f_{O_2} - f_{S_2}$  space for Mo-W sulfide–calcium-oxyanion pairs. The shaded region represents the joint stability field of scheelite and molybdenite. (Barkov *et al.* 2000)

Recasting the phase boundaries in FIGURE 117 to about 475°C shifts the QFM buffer to an  $f_{O_2}$  of  $10^{-26}$  bar, the MW buffer to an  $f_{O_2}$  of  $10^{-29}$  bar (Eugster & Wones 1962), and the pyrrhotite-pyrite boundary to an  $f_{S_2}$  of about  $10^{-5}$  to  $10^{-6}$  bar (Whitney 1984). There is no evidence of a large drop in magmatic oxygen fugacity that would keep  $f_{O_2}$  below the QFM buffer with cooling; in fact, the evidence suggests the opposite. So, as the leucosyenite magma approached its solidus, it probably reëmerged above the QFM buffer. The recast sulfur fugacity is appropriate to the predicted sulfur fugacity of the leucosyenites.

The position of the molybdenite stability field at this lower temperature is not well-established. (Hsu 1976 & 1977) It is a safe assumption, based on the behavior of other species, that a decrease in temperature would be accompanied by a molybdenite stability field boundary

shift to lower  $f_{\text{O}_2}$  and  $f_{\text{S}_2}$ ; the question, then, is, what is the magnitude of the shift?

Molybdenite is stable to relatively high temperatures, up to approximately 1350°C. (Morimoto & Kullerud 1962) Therefore,  $df_{\text{S}_2}/dT$  must be relatively small, lest the presence of molybdenite in a high-T environment demand absurdly high sulfur fugacities; the same argument may be presented for oxygen fugacity. A shift down  $f_{\text{O}_2}$  and  $f_{\text{S}_2}$ , on the order of 1 or 2 log units, would keep the  $\text{MoS}_2$ – $\text{CaMoO}_4$  boundary at about the same position in  $f_{\text{O}_2}$ – $f_{\text{S}_2}$  space, which would correspond to the earlier oxygen fugacity range of  $10^{-21}$  to  $10^{-25}$  bar and a minimum sulfur fugacity of approximately  $10^{-10}$  bar.

#### *Eudialyte Syenite*

The eudialyte syenite exhibits the assemblage acanthite-chalcopyrite-covellite-galena-pyrite-sphalerite. Phase relations in the Cu-Fe-Pb-Zn-S system suggest that chalcopyrite crystallization temperatures were no higher than about 500°C. Between 400-500°C, in the Cu-Fe-Zn-S system, there are two stable sulfide assemblages that are mineralogically possible in the East Hill suite: chalcopyrite + iss (intermediate solid solution) + pyrite + sphalerite and iss + pyrite + pyrrhotite + sphalerite. (Kojima & Sugaki 1985) Other stable assemblages include either bornite or nukundamite,  $(\text{Cu,Fe})_4\text{S}_4$ , neither of which is found in the East Hill suite. (Horváth & Gault 1990) At these temperatures, acanthite requires an approximate sulfur fugacity of at least  $10^{-9}$  bar (Hsu 1977), which has already shown to be the case for the evolving East Hill suite magma. Along these same lines, covellite stabilizes at temperatures below 500°C. (Yund & Kullerud 1966) The galena-pyrite-sphalerite assemblage further indicates that oxygen and sulfur fugacity conditions did not change substantially from the leucosyenites into the eudialyte syenite.

### *Feldspar-Aegirine Dikes & Annite Lamprophyre*

By the end of crystallization in the East Hill suite, sulfide mineralization had declined in abundance and variety. The feldspar-aegirine dikes only contain rare galena, and the annite lamprophyre has the assemblage galena-pyrite-sphalerite, with sphalerite dominant. As in the eudialyte syenite, the persistence of the galena-pyrite-sphalerite assemblage reflects stabilized oxygen and sulfur fugacities, in contrast to the rather rapid evolution of these parameters early in the crystallization of the East Hill suite.

### TITANOSILICATES

#### ***Kupletskite***



#### *Type 1 Nepheline Leucosyenite*

Kupletskite is a rare mineral in the Type 1 nepheline leucosyenite. It occurs as a dark amber twin of two euhedral, bladed crystals 5 µm wide by 15 µm long. The two crystals are twinned along their length, on an indeterminate pinacoidal face that is oblique to the elongation, yielding a symmetrical twin somewhat in the form of a butterfly, akin to the appearance of a Japan-law twin in quartz. The kupletskite occurs in an albitized patch of microcline. Identification was on the basis of EDS analysis, morphology, and color.

#### *Type 3 Nepheline Leucosyenite*

Kupletskite is a rare mineral in the Type 3 nepheline leucosyenite. It occurs as amber, euhedral, equant, bladed crystals to 90 µm in length. It is associated with aegirine-augite and molybdenite.

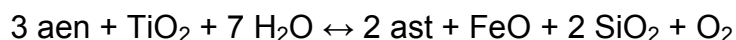


### *Eudialyte Syenite*

Kupletskite is a trace mineral in the eudialyte syenite. It is present as subhedral books of dark amber to dark brown platy crystals. Entire books measure up to 7 mm in length and 4 mm in thickness. The edges of these books are earthy and granular, whereas the faces have a vitreous luster; individual plates are transparent. Fundamental identification of samples as members of the astrophyllite group was on the basis of XRD analysis. Differentiation from other astrophyllite group minerals was on the basis of EDS analysis.

### *East Hill Suite Kupletskite*

The astrophyllite group is represented, to date, by three members in the East Hill suite: astrophyllite, kupletskite, and niobokupletskite (Mandarino & Anderson 1989; Piilonen *et al.* 2000); however, only kupletskite was found in the major lithologies. Astrophyllite group minerals are strong indicators of minimum oxygen fugacity due to their buffer reaction relationship with aenigmatite,  $\text{Na}_2\text{Fe}_5^{2+}\text{TiSi}_6\text{O}_{20}$ :



Aenigmatite is only stable below the QFM buffer (Marsh 1975); therefore, its absence in the East Hill suite indicates that by the time alkali titanosilicates had stabilized, oxygen fugacity was above the QFM buffer.

## ***Titanite***



### *Nepheline melasyenite*

Titanite is found as a minor mineral in the nepheline melasyenite. It occurs as resinous yellow to amber, euhedral tabular crystals to 3 mm in maximum dimension. Most titanite crystals in this syenite, however, measure 50-100  $\mu\text{m}$  in maximum dimension. Titanite crystals exhibit a diamond shaped cross-section in thin-section. Titanite is typically closely associated with aegirine-augite and magnetite, which all together are associated with alkali feldspar and nepheline. It may also be found in association with calcic amphibole. Identification was on the basis of color and morphology, EDS analysis, and optical properties (biaxial positive, high positive relief,  $\delta \approx 0.150$ ).

Representative analyses of titanite are listed in TABLE 43. Significant trace elements in titanite from the nepheline melasyenite include Zr, up to 2.41 wt.%  $\text{ZrO}_2$ , Al, up to 5.45 wt.%  $\text{Al}_2\text{O}_3$ , and Ce, up to 2.44 wt.%  $\text{Ce}_2\text{O}_3$ . Other notable substituent elements are Fe, up to 2.55 wt.%  $\text{FeO}$ , Zn, up to 9.18 wt.%  $\text{ZnO}$ , and Na, up to 1.31 wt.%  $\text{Na}_2\text{O}$ . Zirconium is a natural substitution in titanite for Ti (Prowatke & Klemme 2005), as is Ce (Tiepolo *et al.* 2002), but aluminum substitution is particularly important because it reflects the influence of aluminous melts on trace element partition coefficients in titanite. (Prowatke & Klemme 2005) Aluminum may substitute for up to half the Ti on an *apfu* basis (Oberti *et al.* 1991), and high-Al melts promote the incorporation of REE and HFSE *via* the coupled substitutions,  $\text{Ca}^{2+} + \text{Ti}^{4+} \leftrightarrow \text{REE}^{3+} + \text{Al}^{3+}$  and, possibly,  $2 \text{Ti}^{4+} \leftrightarrow (\text{Nb,Ta})^{5+} + \text{Al}^{3+}$ . (Horng & Hess 2000; Tiepolo *et al.* 2002; Prowatke & Klemme 2005) Sodium may play a similar role, though subdued in the nepheline melasyenite, through the substitution,  $2 \text{Ca}^{2+} \leftrightarrow \text{Na}^+ + \text{REE}^{3+}$ . (Tiepolo *et al.* 2002) As would

TABLE 43 – Representative electron microprobe analyses of titanite – Nepheline Melasyenite

Lithology:	<i>Nepheline Melasyenite</i>						
Sample:	<i>MSH-B-8</i>						
Target:	<i>6b</i>	<i>11l</i>	<i>12j</i>	Target:	<i>6b</i>	<i>11l</i>	<i>12j</i>
SiO <sub>2</sub> (wt.%)	29.79	31.09	31.15	<i>Cations</i>			
TiO <sub>2</sub>	34.86	40.42	40.36	Si	1.024	0.974	1.016
ZrO <sub>2</sub>	1.49	0.14	0.05	Ti	0.901	0.952	0.990
Al <sub>2</sub> O <sub>3</sub>	1.51	3.38	1.32	Zr	0.025	0.002	0.001
Sc <sub>2</sub> O <sub>3</sub>	na	na	na	Al	0.061	0.125	0.051
REE <sub>2</sub> O <sub>3</sub>	0.00	1.87	0.42	Sc	na	na	na
La <sub>2</sub> O <sub>3</sub>	na	na	na	REE	0.000	0.021	0.005
Ce <sub>2</sub> O <sub>3</sub>	0.00	1.87	0.42	Fe <sup>2+</sup>	0.073	0.028	0.035
FeO <sub>tot</sub>	2.55	1.08	1.27	Mn <sup>2+</sup>	0.001	0.004	0.003
MnO	0.03	0.13	0.12	Mg	0.000	0.003	0.001
MgO	0.00	0.07	0.03	Zn	0.000	0.014	0.022
ZnO	0.00	0.60	0.93	Ca	0.931	0.839	0.830
CaO	25.26	24.99	23.76	Ba	na	na	na
BaO	na	na	na	Na	0.004	0.006	0.010
Na <sub>2</sub> O	0.06	0.10	0.16	K	0.000	0.001	0.001
K <sub>2</sub> O	0.00	0.02	0.02	Normalized to 5 oxygen <i>apfu</i>			
SUM	95.54	103.88	99.57	na = not analyzed			

be expected, the borderline peraluminous bulk chemistry of the nepheline melasyenite resulted in both elevated Al and REE content in titanite. Although Nb and Ta were not analyzed, titanite certainly played a role in increasing the Nb/Ta ratio in later fractionates, due to the higher partition coefficient of Ta into titanite than that of Nb. (Prowatke & Klemme 2005)

Titanite also lends some insight into the oxidation conditions at the moment of emplacement of the East Hill suite. Titanite was an early-crystallizing phase in the nepheline melasyenite, and the presence of titanite indicates that oxygen fugacity was above the QFM buffer (Carmichael & Nicholls 1967). Therefore, the oxygen fugacity in the nepheline melasyenite, and by extension, in the early East Hill suite magma, fell from above the QFM buffer.

## ZIRCONOSILICATES

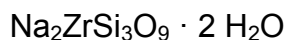
### ***Calciohilairite***



#### *Nepheline Melasyenite*

Calciohilairite was tentatively identified as a rare mineral in the nepheline melasyenite. Two specimens were found: a euhedral, prismatic crystal, 25  $\mu\text{m}$  wide by 75  $\mu\text{m}$  long, included by potassium feldspar, and a euhedral, prismatic crystal, 50  $\mu\text{m}$  wide by 100  $\mu\text{m}$  long, included by nepheline. The latter individual itself includes titanite and is associated with annite, fluorapatite, aegirine-augite, and possible thorianite. Calciohilairite is a more direct identification compared to a sodium zirconosilicate, in that the Ca-Zr association is less common at Mont Saint-Hilaire. Identification was based on an EDS analysis, supported by examination in the petrographic microscope (uniaxial,  $\delta = 0.007$ ).

### ***Catapleiite***



#### *Eudialyte Syenite*

Catapleiite occurs as a trace mineral in the eudialyte syenite as a secondary mineral after eudialyte group minerals. It is present as subhedral platy crystals to 0.1 mm in intimate contact with a eudialyte group mineral and in association with manganoan pectolite. As with the other alkali zirconosilicates at Mont Saint-Hilaire, only a very preliminary identification can be made with an EDS spectrum. Final identification was on the basis of examination in the petrographic microscope (hexagonal habit, biaxial).

### ***Eudialyte Group***

Eudialyte,  $\text{Na}_{15}\text{Ca}_6\text{Fe}_3^{2+}\text{Zr}_3\text{Si}(\text{Si}_{25}\text{O}_{73})(\text{O},\text{OH},\text{H}_2\text{O})_3(\text{Cl},\text{OH})_2$

Ferrokentbrooksit,  $\text{Na}_{15}\text{Ca}_6\text{Fe}_3^{2+}\text{Zr}_3\text{Nb}(\text{Si}_{25}\text{O}_{73})(\text{O},\text{OH},\text{H}_2\text{O})_3(\text{Cl},\text{F},\text{OH})_2$

### ***Eudialyte Syenite***

Members of the eudialyte group occur singly and in solid-solution with one another, as minor and trace minerals in the eudialyte syenite; allies of eudialyte *sensu stricto* are more abundant than those of kentbrooksit or other compositions. The eudialyte group minerals are found as yellowish to reddish brown, anhedral to subhedral grains from 0.5 to 5 mm in diameter (Figure 118). They may also occur in vugs as euhedral crystals of the same general description. Some such crystals display striations on some faces; this is probably an exhibition of growth hillocks, rather than an expression of a structural feature in the sense of kink-banding in orthopyroxene. Eudialyte group minerals have a splendid vitreous luster, though this may be diminished somewhat by rare alteration. Catapleite appears to be the dominant alteration product of eudialyte group minerals. Identification was based initially on physical properties, supported by EDS and EMP analyses and examination in the petrographic microscope (pseudouniaxial,  $\delta \approx 0.012$ ).

The crystal chemistry of the eudialyte group in the East Hill suite was studied by TICE (2009). The several species of the eudialyte group are not systematically distinguishable from one another based solely on visual observation, so differentiation ultimately relied on electron microprobe analyses. The eudialyte group is ripe with opportunity for chemical substitution, and this was reflected in these previous findings. Out of 51 total analyses, only 13 represented IMA-approved species, and these recalculated to a mere two of the seven such species known to occur in the East Hill suite. (Mandarino & Anderson 1989; Johnsen *et al.* 1999a; Johnsen *et al.* 1999b;



FIGURE 118 – Euhedral eudialyte group mineral in miarole, associated with microcline, sodalite *ps.* nepheline (grey), and aegirine (black) – Eudialyte Syenite (10x)

Johnsen *et al.* 2003a; Johnsen *et al.* 2003b; Grice & Gault 2006; Tice 2009) The remaining 38 analyses represented 13 previously undescribed compositions. Eudialyte group speciation primarily turns on the site-occupancy of  $M(2)$ , which holds Fe and Mn, and of  $M(3)$ , which holds Si and HFSE. In addition to eudialyte *sensu stricto*, which is  $^{[M(2)]}\text{Fe-}$  and  $^{[M(3)]}\text{Si-}$  dominant, and ferrokentbrooksite, which is  $^{[M(2)]}\text{Fe-}$  and  $^{[M(3)]}\text{Nb-}$  dominant, these remaining analyses included  $^{[M(2)]}\text{Mn-}$  dominant compositions, as well as those dominant in Hf, W, and Zr in  $M(3)$ . In addition, in terms of anion content, these undescribed compositions comprised Cl-, F-, OH-, and S-dominant chemistries, as well. (Tice 2009)

Representative analyses of eudialyte group minerals are listed in TABLES 44 through 46. Substitutions are numerous and remarkable in variety and magnitude. Among tetra-, penta-, and

TABLE 44 – Representative electron microprobe analyses of eudialyte group minerals – Eudialyte Syenite (Tice 2009)

Target:	6-5	16-4	17-5	16-3	21-5	10-2
SiO <sub>2</sub> (wt. %)	45.66	44.20	39.11	45.14	47.92	45.09
TiO <sub>2</sub>	0.07	0.12	0.15	0.09	0.05	0.10
ZrO <sub>2</sub>	11.97	13.67	10.85	10.73	15.54	13.80
HfO <sub>2</sub>	0.33	0.00	0.00	4.47	0.00	0.00
Nb <sub>2</sub> O <sub>5</sub>	0.96	1.87	0.73	0.64	0.90	0.82
Ta <sub>2</sub> O <sub>5</sub>	0.09	1.95	1.06	0.00	0.43	0.00
MoO <sub>3</sub>	0.00	0.00	0.00	0.00	0.07	0.00
WO <sub>3</sub>	0.23	0.00	3.58	0.71	0.00	0.00
Al <sub>2</sub> O <sub>3</sub>	0.22	0.08	0.00	0.00	0.09	0.13
Sc <sub>2</sub> O <sub>3</sub>	0.00	0.00	0.00	0.08	0.00	0.06
REE <sub>2</sub> O <sub>3</sub>	6.17	4.64	6.67	2.40	3.32	4.95
La <sub>2</sub> O <sub>3</sub>	1.71	0.93	1.55	0.96	0.79	1.06
Ce <sub>2</sub> O <sub>3</sub>	3.96	2.17	3.56	0.70	1.46	2.48
Pr <sub>2</sub> O <sub>3</sub>	0.00	0.00	0.00	0.00	0.00	0.00
Nd <sub>2</sub> O <sub>3</sub>	0.00	1.19	1.01	0.45	0.76	0.71
Sm <sub>2</sub> O <sub>3</sub>	0.00	0.00	0.00	0.00	0.00	0.00
Gd <sub>2</sub> O <sub>3</sub>	0.49	0.35	0.55	0.29	0.32	0.70
Dy <sub>2</sub> O <sub>3</sub>	0.00	0.00	0.00	0.00	0.00	0.00
Er <sub>2</sub> O <sub>3</sub>	0.00	0.00	0.00	0.00	0.00	0.00
Yb <sub>2</sub> O <sub>3</sub>	0.00	0.00	0.00	0.00	0.00	0.00
Y <sub>2</sub> O <sub>3</sub>	0.94	0.00	3.19	0.69	0.00	1.32
FeO	4.78	5.17	5.15	5.26	4.38	4.45
MnO	6.51	4.48	7.45	4.85	6.79	7.19
ZnO	0.00	0.00	0.00	0.00	0.04	0.00
CaO	7.25	8.56	4.99	8.91	8.67	6.62
SrO	na	na	na	na	na	na
BaO	0.00	0.00	0.49	0.00	0.03	0.51
MgO	0.02	0.00	0.02	0.02	0.04	0.00
Na <sub>2</sub> O	13.35	12.60	14.33	12.96	11.38	14.50
K <sub>2</sub> O	0.51	0.42	0.38	0.48	0.49	0.47
Cl	0.93	0.70	0.87	0.87	1.01	0.33
F	0.01	0.74	0.00	0.00	0.00	0.24
SO <sub>3</sub>	0.03	0.17	0.03	0.56	0.00	1.94
H <sub>2</sub> O*	0.15	0.45	0.15	0.13	0.16	0.11
O≡Cl	-0.21	-0.16	-0.20	-0.20	-0.23	-0.07
O≡F	-0.01	-0.31	0.00	0.00	0.00	-0.10
TOTAL	99.94	99.34	98.99	98.78	101.08	102.46
Species:	<i>eudialyte</i>	<i>ferro-kentbrooksite</i>	"Cl-Mn- [M(3)]W-dom."	"[M(3)]Hf-dom."	"[M(3)]Zr-dom."	"S- [M(3)]Zr-dom."

Recalculated after TICE (2009)  
Normalized to 29 cations (Σ Si + Al + Zr + Ti + Hf + Nb + W + Ta) *apfu*  
na = not analyzed  
\*H<sub>2</sub>O calculated based on charge-balance, assuming presence as OH

TABLE 45 – Site-occupancies of eudialyte group minerals from TABLE 44, I – Eudialyte Syenite

	6-5	16-4	17-5			6-5	16-4	17-5
<i>N(φ)</i>				<i>Z</i>				
Na	8.090	7.779	9.687	W	0.000	0.000	0.000	
□	0.910	1.221	0.000	Nb	0.000	0.000	0.000	
				Ta	0.000	0.000	0.000	
<i>N(4)</i>				Zr	3.000	3.000	3.000	
<i>REE</i>	1.242	0.929	0.791	Hf	0.000	0.000	0.000	
Ca	0.000	0.000	0.000	Ti	0.000	0.000	0.000	
Sr	na	na	na	□	0.000	0.000	0.000	
Ba	0.000	0.000	0.121					
K	0.356	0.299	0.308	<i>M(3)</i>				
Na	4.353	4.503	4.780	W	0.033	0.000	0.584	
□	0.049	0.269	0.000	Nb	0.241	0.467	0.208	
				Ta	0.013	0.293	0.181	
<i>M(1)</i>				Zr	0.228	0.188	0.000	
<i>REE</i>	0.000	0.000	0.730	Hf	0.052	0.000	0.000	
Y	0.276	0.000	1.070	Ti	0.031	0.052	0.027	
Fe <sup>2+</sup>	0.000	0.000	0.000	Si	0.401	0.000	0.000	
Mn <sup>2+</sup>	1.430	0.929	0.832	□	0.001	0.000	0.000	
Ca	4.294	5.071	3.368					
□	0.000	0.000	0.000	<i>M(4) + Si</i>				
				Si	24.854	24.453	24.624	
<i>M(2)</i>				Al	0.146	0.049	0.000	
Zr	0.000	0.499	0.330	□	0.000	0.498	0.376	
Hf	0.000	0.000	0.000					
Ti	0.000	0.000	0.045	X				
Fe <sup>2+</sup>	2.210	2.392	2.710	Cl	0.871	0.659	0.928	
Mn <sup>2+</sup>	1.619	1.169	3.140	F	0.021	1.298	0.000	
Mg	0.014	0.000	0.015	S	0.012	0.070	0.012	
□	0.000	0.000	0.000	OH	0.536	0.000	0.621	
				□	0.560	0.000	0.439	
Recalculated after TICE (2009)								
Normalized to 29 cations (Σ Si + Al + Zr + Ti + Hf + Nb + W + Ta) <i>apfu</i>								
na = not analyzed								
*H <sub>2</sub> O calculated based on charge-balance, assuming presence as OH								



TABLE 46 – Site-occupancies of eudialyte group mineral from TABLE 44, II – Eudialyte Syenite

	16-3	21-5	10-2			16-3	21-5	10-2
<i>N(ϕ)</i>				<i>Z</i>				
Na	8.107	6.583	8.849	W	0.000	0.000	0.000	
□	0.893	2.417	0.151	Nb	0.000	0.000	0.000	
				Ta	0.000	0.000	0.000	
<i>N(4)</i>				Zr	3.000	3.000	3.000	
<i>REE</i>	0.481	0.619	0.670	Hf	0.000	0.000	0.000	
Ca	0.000	0.000	0.000	Ti	0.000	0.000	0.000	
Sr	na	na	na	□	0.000	0.000	0.000	
Ba	0.000	0.006	0.111					
K	0.338	0.322	0.330	<i>M(3)</i>				
Na	4.837	3.863	4.889	W	0.584	0.000	0.000	
□	0.344	1.190	0.000	Nb	0.208	0.210	0.205	
				Ta	0.181	0.060	0.000	
<i>M(1)</i>				Zr	0.000	0.713	0.724	
<i>REE</i>	0.000	0.000	0.318	Hf	0.000	0.000	0.000	
Y	0.204	0.000	0.390	Ti	0.027	0.017	0.040	
Fe <sup>2+</sup>	0.000	0.000	0.000	Si	0.000	0.000	0.030	
Mn <sup>2+</sup>	0.489	1.206	1.369	□	0.000	0.000	0.001	
Ca	5.307	4.794	3.923					
□	0.000	0.000	0.000	<i>M(4) + Si</i>				
				Si	24.624	24.743	24.917	
<i>M(2)</i>				Al	0.000	0.057	0.083	
Zr	0.000	0.200	0.000	□	0.376	0.200	0.000	
Hf	0.000	0.000	0.000					
Ti	0.000	0.000	0.000	<i>X</i>				
Fe <sup>2+</sup>	2.444	1.891	2.059	Cl	0.928	0.880	0.311	
Mn <sup>2+</sup>	1.791	1.764	2.003	F	0.000	0.000	0.420	
Mg	0.019	0.031	0.000	S	0.012	0.000	0.806	
□	0.000	0.000	0.000	OH	0.621	0.558	0.401	
				□	0.439	0.561	0.062	
Recalculated after TICE (2009)								
Normalized to 29 cations (Σ Si + Al + Zr + Ti + Hf + Nb + W + Ta) <i>apfu</i>								
na = not analyzed								
*H <sub>2</sub> O calculated based on charge-balance, assuming presence as OH								

hexavalent elements, titanium is present up to 0.47 wt.%  $\text{TiO}_2$ , Hf, up to 4.47 wt.%  $\text{HfO}_2$ , Nb, up to 3.13 wt.%  $\text{Nb}_2\text{O}_5$ , Ta, up to 1.95 wt.%  $\text{Ta}_2\text{O}_5$ , Mo, up to 0.46 wt.%  $\text{MoO}_3$ , and W, up to 3.58 wt.%  $\text{WO}_3$ . Al substitutes up to 0.35 wt.%  $\text{Al}_2\text{O}_3$ , and Sc, up to 0.18 wt.%  $\text{Sc}_2\text{O}_3$ . (Tice 2009)

The REE collectively presented up to a content of 7.50 wt.%  $\text{REE}_2\text{O}_3$ ; notable individual enrichments include up to 2.27 wt.%  $\text{La}_2\text{O}_3$ , 4.50 wt.%  $\text{Ce}_2\text{O}_3$ , 1.19 wt.%  $\text{Nd}_2\text{O}_3$ , and 1.90 wt.%  $\text{Gd}_2\text{O}_3$ . Eudialyte group minerals from the East Hill suite exhibit a negative Nd anomaly in their chondrite-normalized REE abundances, regardless of other chemical affinities in the composition. Yttrium exhibits similarly large enrichments to the REE, with up to 5.68 wt.%  $\text{Y}_2\text{O}_3$ . (Tice 2009)

A minimal amount of Mg and Zn is taken up by eudialyte group minerals, only up to 0.12 wt.%  $\text{MgO}$  and 0.08 wt.%  $\text{ZnO}$ . Barium, however, is variably abundant, up to 1.81 wt.%  $\text{BaO}$ . Potassium substitutes for Na up to 0.57 wt.%  $\text{K}_2\text{O}$ . (Tice 2009)

Chlorine is typically more prevalent than fluorine, although fluorine has a higher maximum of 1.38 wt.% F against 1.31 wt.% Cl. Sulfur has a highly variable abundance, up to 1.94 wt.%  $\text{SO}_3$ . Water and hydroxyl were not distinguished in the previous study, but the eudialyte group minerals assimilated up to 0.74 wt.%  $\text{H}_2\text{O}$ , calculated by difference and all expressed as the oxide. (Tice 2009)

Speciation-related compositional variation is shown in FIGURES 119 to 122. The first decision gate for eudialyte group speciation is the occupancy of  $M(3)$ . Analyses were plotted in ternary space (Figure 119) based on the dominant cation in  $M(3)$  between Si, the sum of all pentavalent cations, Nb + Ta, and the sum of the remaining tetravalent cations, Zr + Hf + Ti. Although it is not illustrated due to its rarity in the sample set, W-dominance, accompanied by Sr substitution, puts the sample in the khomyakovite series. (Johnsen *et al.* 2003a)  $^{[M(3)]}\text{Si}$ -dominant

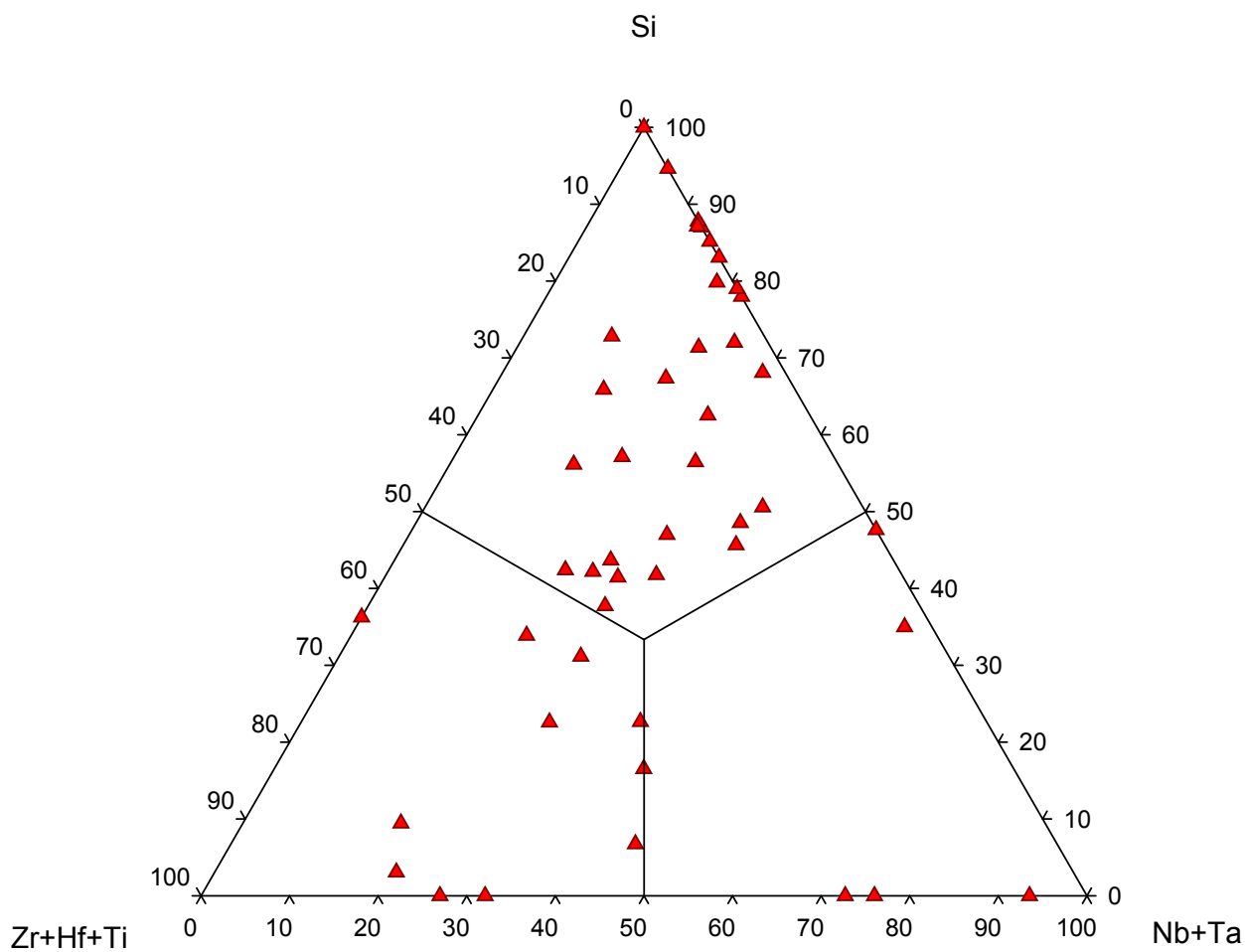


FIGURE 119 – Site-occupancy of  $M(3)$  in eudialyte group minerals – Eudialyte Syenite (Tice 2009)

analyses were most abundant, followed by  $^{[M(3)]}(\text{Zr} + \text{Hf} + \text{Ti})$  and  $^{[M(3)]}(\text{Nb} + \text{Ta})$ . Compositions define a rough trend sweeping out of the Si field into the tetravalent field. Scatter and a lack of analyses prevent the definition of any trend into the pentavalent field; a number of analyses in the Si field show essentially no tetravalent substitution and trend towards the pentavalent field, although they only show substitution of (Nb + Ta) up to 20 mol%. (Tice 2009)

Si-dominance places the sample in the eudialyte series and Nb in the kentbrooksite series; Ta-dominant compositions are undescribed from any source and are undefined in speciation. (Johnsen *et al.* 2003a) Compositions from FIGURE 119 were recast into Si-Nb-Ta space (Figure 120) to illustrate relative populations. Eudialyte series analyses outnumbered kentbrooksite series compositions by about 6-to-1. Although all kentbrooksite series analyses were Nb-dominant, some showed relatively high Ta substitution, coming within about 3 mol% of Ta dominance. Projection of the eudialyte and kentbrooksite series analyses onto a  $X_{\text{Mn}} - X_{\text{Nb}}$  plane (Figure 121) shows the prevalence of  $^{[M(2)]}$ Mn-dominant compositions, although most analyses are clustered in the range  $0.4 \leq X_{\text{Mn}} \leq 0.65$ . (Tice 2009) Even though two analyses plotted into the kentbrooksite field on this diagram, they may not be identified as kentbrooksite *sensu stricto*, due to Cl-dominance in the anionic site.

There are, as yet, no IMA-approved Zr-, Hf-, and Ti-dominant eudialyte group minerals (Johnsen *et al.* 2003a), although compositions fitting the first two descriptions were observed (Figure 122). Zr-dominant compositions outnumbered Hf-dominant by 4-to-1. Both sets showed only limited relative substitution by Ti. (Tice 2009)

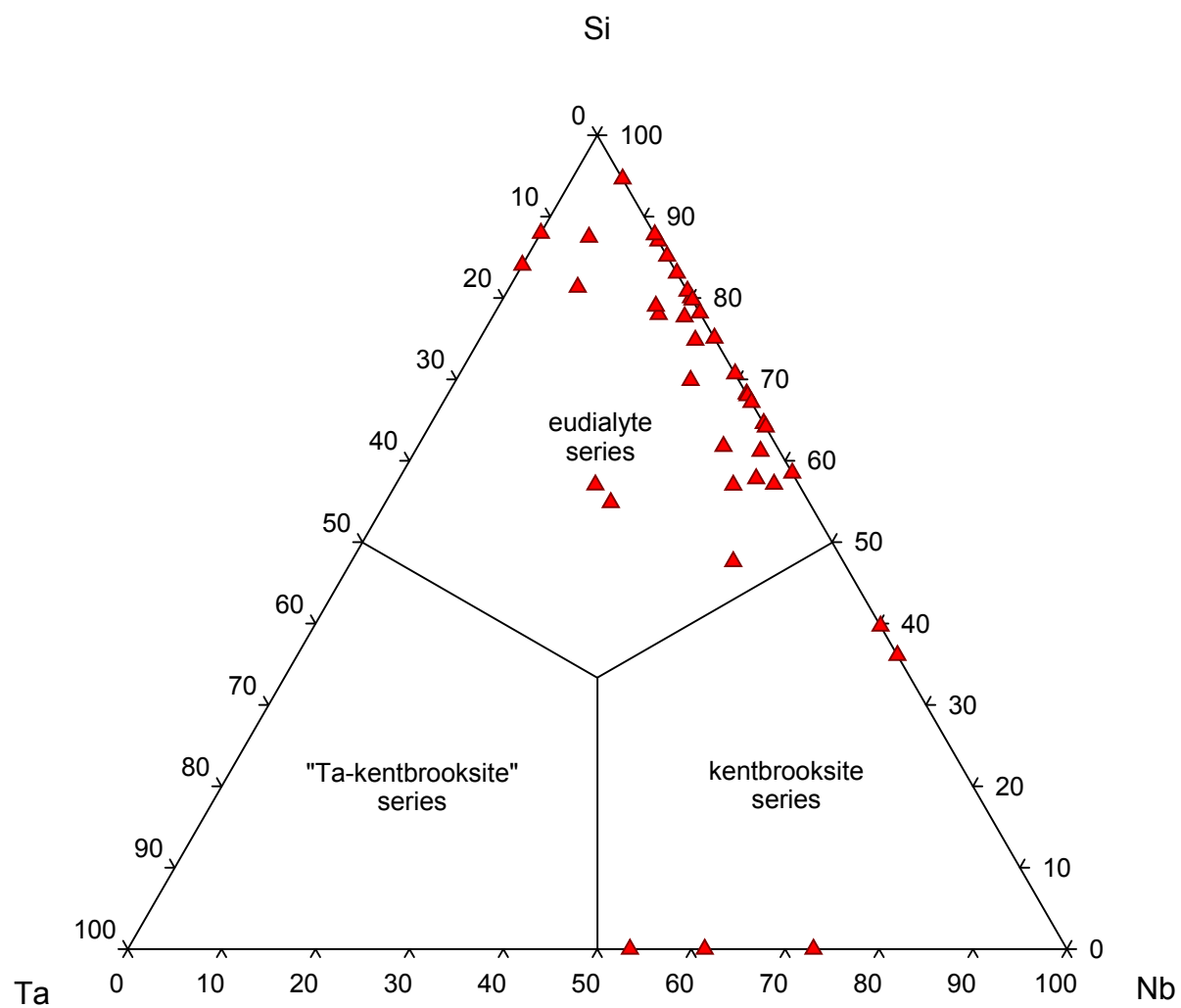


FIGURE 120 – Relative site-occupancy of  $M(3)$  by Si, Nb, and Ta in eudialyte group minerals with Si, Nb, or Ta dominant – Eudialyte Syenite (Tice 2009)

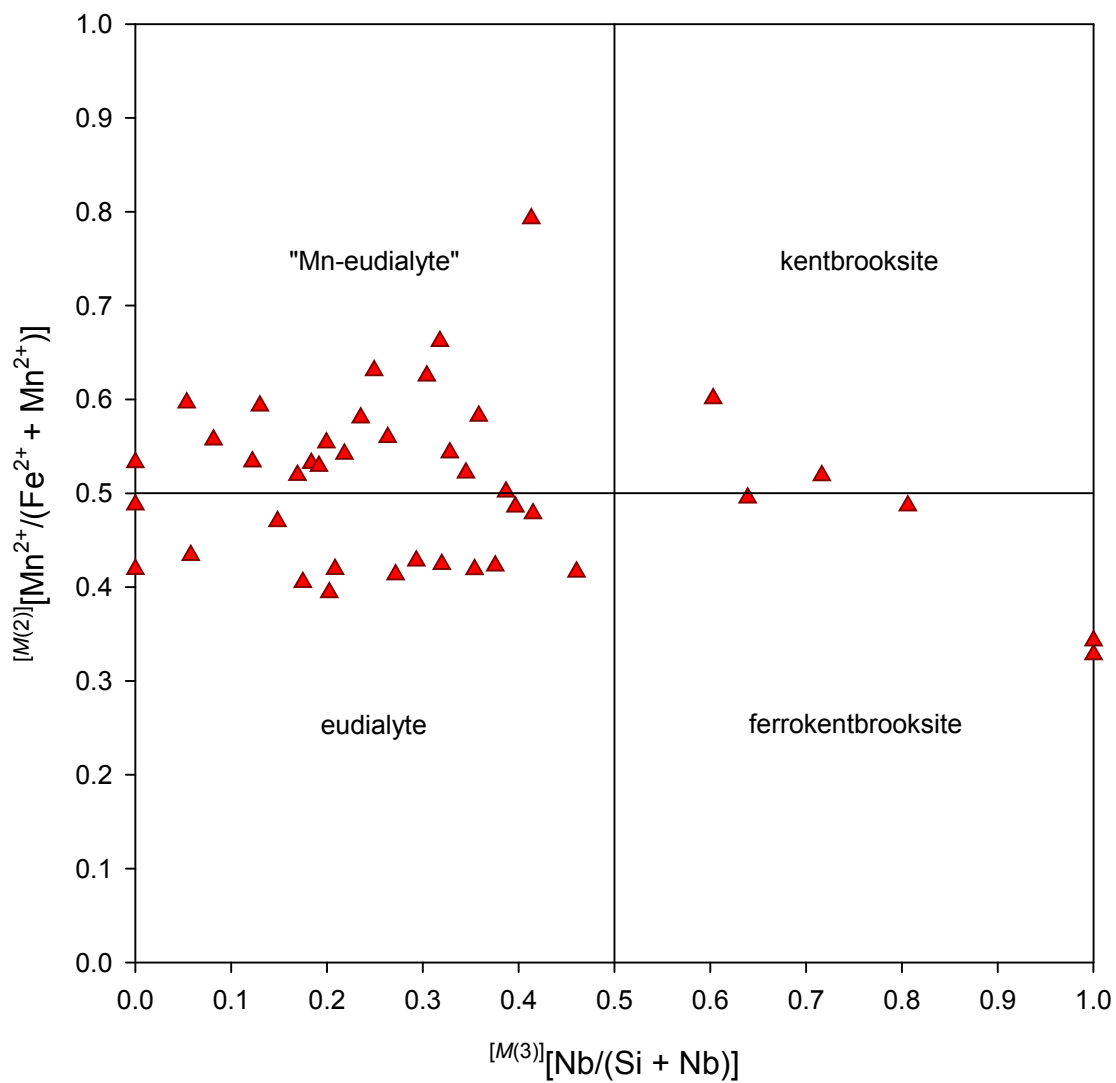


FIGURE 121 – Site-occupancy of  $M(2)$  versus  $M(3)$  and resulting speciation in eudialyte group minerals from the eudialyte and kentbrooksitite series – Eudialyte Syenite (Tice 2009)

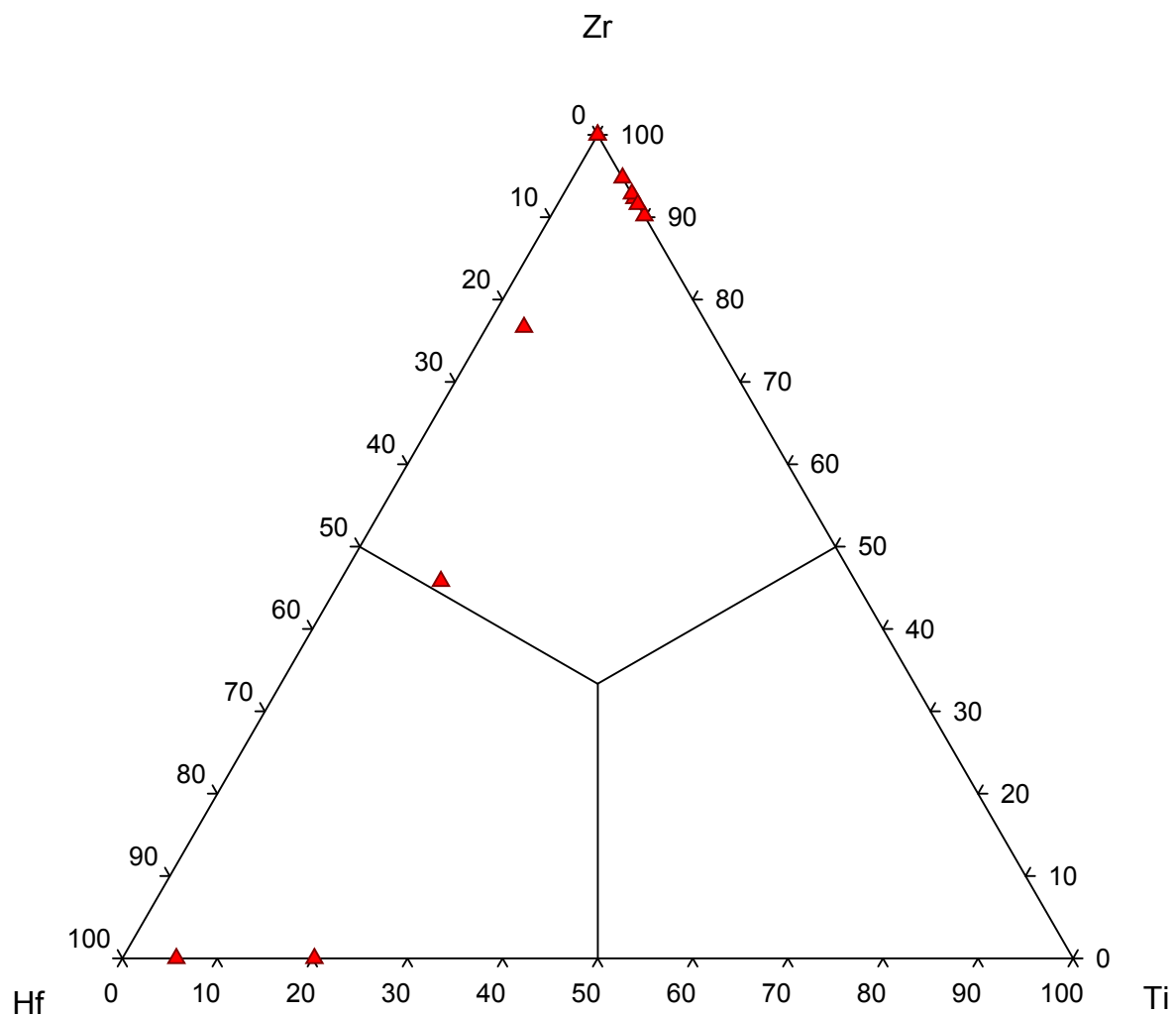
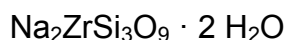


FIGURE 122 – Relative site-occupancy of  $M(3)$  by Zr, Ti, and Hf in eudialyte group minerals with Zr, Ti, or Hf dominant – Eudialyte Syenite (Tice 2009)

### ***Gaidonnayite***



#### *Eudialyte Syenite*

Gaidonnayite occurs as a rare mineral in the eudialyte syenite, where it is seen as subhedral prismatic crystals to 30  $\mu\text{m}$  in length. It is found associated with a eudialyte group mineral, fluorite, and manganoan pectolite. Gaidonnayite is one of several sodium zirconosilicates that occur at Mont Saint-Hilaire. Therefore, identification was founded, but not based, on an initial EDS spectrum to determine the general chemistry. Final identification was made in the petrographic microscope (biaxial negative,  $\delta = 0.026$ ).

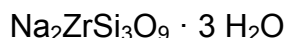
#### *Annite Lamprophyre*

Gaidonnayite is present as a trace mineral in the annite lamprophyre, although it is very abundant locally. It occurs as subhedral to euhedral prismatic crystals to 5 mm in length, these crystals being arranged in sprays of subparallel individuals. Euhedral octahedra of pyrochlore are embedded in several individuals of gaidonnayite. Gaidonnayite is one of several sodium zirconosilicates that occur at Mont Saint-Hilaire. Therefore, identification was founded, but not based, on an initial EDS spectrum to determine the general chemistry. Final identification was made in the petrographic microscope (biaxial negative,  $\delta = 0.026$ , striations visible along prisms). Representative analyses of gaidonnayite are listed in TABLE 47. The gaidonnayite compositions are sodium-deficient, owing to beam-sensitivity, and are overall rather free of trace elements, but they exhibit remarkable and consistent enrichment in Zn, up to 6.30 wt.% ZnO.



TABLE 47 – Representative electron microprobe analyses of gaidonnayite – Annite Lamprophyre

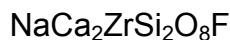
Lithology:	<i>Annite Lamprophyre</i>						
Sample:	<i>MSH-B-6</i>						
Target:	<i>7b</i>	<i>7c</i>	<i>8d</i>	Target:	<i>7b</i>	<i>7c</i>	<i>8d</i>
SiO <sub>2</sub> (wt.%)	51.56	54.03	50.37	<i>Cations</i>			
TiO <sub>2</sub>	0.08	0.07	0.01	Si	3.120	3.190	3.121
ZrO <sub>2</sub>	35.30	36.14	33.31	Ti	0.004	0.003	0.000
Al <sub>2</sub> O <sub>3</sub>	0.08	0.06	1.25	Zr	1.041	1.040	1.006
Sc <sub>2</sub> O <sub>3</sub>	na	na	na	Al	0.006	0.004	0.091
REE <sub>2</sub> O <sub>3</sub>	0.00	0.04	0.06	Sc	na	na	na
La <sub>2</sub> O <sub>3</sub>	0.00	0.04	0.06	REE	0.000	0.001	0.001
Ce <sub>2</sub> O <sub>3</sub>	0.00	0.00	0.00	Fe <sup>2+</sup>	0.005	0.006	0.014
FeO <sub>tot</sub>	0.10	0.11	0.27	Mn <sup>2+</sup>	0.001	0.004	0.006
MnO	0.03	0.07	0.12	Mg	0.000	0.002	0.001
MgO	0.00	0.02	0.01	Zn	0.282	0.272	0.223
ZnO	6.30	6.25	4.88	Ca	0.020	0.016	0.045
CaO	0.30	0.25	0.68	Ba	na	na	na
BaO	na	na	na	Na	0.705	0.450	0.630
Na <sub>2</sub> O	6.01	3.93	5.25	K	0.002	0.000	0.001
K <sub>2</sub> O	0.02	0.00	0.02				
SUM	99.80	100.98	96.21	Normalized to 9 oxygen <i>apfu</i> na = not analyzed			

***Hilairite******Annite Lamprophyre***

Hilairite has been tentatively identified as a trace mineral in the annite lamprophyre, as subhedral, prismatic crystals to 0.75 mm in length, associated with natrolite, aegirine, calcioancylite-(Ce), and annite. Like other sodium zirconsilicates in this study, identification was founded, but not based, on an initial EDS spectrum. Final identification was based on examination in the petrographic microscope (uniaxial,  $\delta = 0.010$ ). A representative analysis of hilairite is listed in TABLE 48. Hilairite was sodium-deficient, owing to beam-sensitivity, but the analyses show an enrichment in Zn, similar to that in gaidonnayite, up to 5.75 wt.% ZnO.

TABLE 48 – Representative electron microprobe analysis of hilairite – Annite Lamprophyre

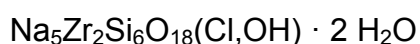
Lithology:	<i>Annite Lamprophyre</i>		
Sample:	<i>MSH-B-6</i>		
Target:	<i>12h</i>	Target:	<i>12h</i>
SiO <sub>2</sub> (wt. %)	51.07	<i>Cations</i>	
TiO <sub>2</sub>	0.05	Si	3.059
ZrO <sub>2</sub>	36.71	Ti	0.002
Al <sub>2</sub> O <sub>3</sub>	0.08	Zr	1.072
Sc <sub>2</sub> O <sub>3</sub>	na	Al	0.006
REE <sub>2</sub> O <sub>3</sub>	0.02	Sc	na
La <sub>2</sub> O <sub>3</sub>	0.02	REE	0.001
Ce <sub>2</sub> O <sub>3</sub>	0.00	Fe <sup>2+</sup>	0.007
FeO <sub>tot</sub>	0.13	Mn <sup>2+</sup>	0.004
MnO	0.07	Mg	0.006
MgO	0.07	Zn	0.254
ZnO	5.75	Ca	0.004
CaO	0.06	Ba	na
BaO	na	Na	0.897
Na <sub>2</sub> O	7.73	K	0.001
K <sub>2</sub> O	0.01		
SUM	101.76	Normalized to 9 oxygen <i>apfu</i> na = not analyzed	

***Låvenite******Nepheline Melasyenite***

Låvenite has been tentatively identified as a rare mineral in the nepheline melasyenite. It was found as a euhedral, prismatic crystal, 25 µm wide by 75 µm long, included by orthoclase. It was also found as a subhedral, prismatic crystal, 50 µm wide by 100 µm long, included by nepheline. This second crystal itself encloses a minuscule specimen of titanite and is associated with annite, apatite, aegirine-augite, and a crystal tentatively identified as thorianite. Identification was on the basis on EDS analysis, optical properties ( $\delta = 0.007$ ), and electron microprobe analysis. A representative analysis of låvenite is listed in TABLE 49. Låvenite was slightly sodium-deficient, owing to beam-sensitivity.

TABLE 49 – Representative electron microprobe analysis of lävenite – Nepheline Melasyenite

Lithology:	<i>Nepheline Melasyenite</i>		
Sample:	<i>MSH-B-8</i>		
Target:	<i>4h</i>	Target:	<i>4h</i>
SiO <sub>2</sub> (wt. %)	31.46	<i>Cations</i>	
TiO <sub>2</sub>	1.13	Si	1.898
ZrO <sub>2</sub>	25.33	Ti	0.051
Al <sub>2</sub> O <sub>3</sub>	0.12	Zr	0.745
Sc <sub>2</sub> O <sub>3</sub>	na	Al	0.008
REE <sub>2</sub> O <sub>3</sub>	0.00	Sc	na
La <sub>2</sub> O <sub>3</sub>	na	REE	0.000
Ce <sub>2</sub> O <sub>3</sub>	0.00	Fe <sup>2+</sup>	0.053
FeO <sub>tot</sub>	1.05	Mn <sup>2+</sup>	0.090
MnO	1.76	Mg	0.002
MgO	0.02	Zn	0.000
ZnO	0.00	Ca	2.089
CaO	32.32	Ba	na
BaO	na	Na	0.729
Na <sub>2</sub> O	6.23	K	0.005
K <sub>2</sub> O	0.06		
SUM	99.47	Normalized to 8 oxygen <i>apfu</i> na = not analyzed	

***Petarasite******Annite Lamprophyre***

Petarasite is a trace mineral in the annite lamprophyre, in which petarasite individuals are found in quantity in a characteristic association with apatite. The petarasite is present as subhedral prismatic to anhedral crystals to 0.5 mm in length. Petarasite was identified primarily by its EDS signature, which shows Na, Zr, and Si with Cl, but without Ca, Fe, or Mn, thus differentiating the analysis from the eudialyte group. Examination in the petrographic microscope supports the EDS identification (biaxial,  $\delta \approx 0.035$ ). Representative analyses of petarasite are listed in TABLE 50. The petarasite compositions are seriously sodium-deficient, owing to beam-sensitivity, and exhibit substantial enrichment in Zn, up to 6.88 wt.% ZnO.

TABLE 50 – Representative electron microprobe analyses of petarasite – Annite Lamprophyre

Lithology:	<i>Annite Lamprophyre</i>		
Sample:	<i>MSH-B-6</i>		
Target:	<i>4c</i>	<i>4d</i>	<i>4ma</i>
SiO <sub>2</sub> (wt.%)	52.38	53.77	50.77
TiO <sub>2</sub>	0.02	0.03	0.03
ZrO <sub>2</sub>	39.11	38.27	38.06
Al <sub>2</sub> O <sub>3</sub>	0.01	0.01	0.01
Sc <sub>2</sub> O <sub>3</sub>	na	na	na
REE <sub>2</sub> O <sub>3</sub>	0.05	0.06	0.07
La <sub>2</sub> O <sub>3</sub>	0.05	0.06	0.07
Ce <sub>2</sub> O <sub>3</sub>	0.00	0.00	0.00
FeO <sub>tot</sub>	0.34	0.31	0.36
MnO	0.35	0.32	0.31
MgO	0.01	0.03	0.03
ZnO	5.50	4.50	6.18
CaO	0.16	0.16	0.16
BaO	na	na	na
Na <sub>2</sub> O	2.44	1.76	4.58
K <sub>2</sub> O	0.16	0.11	0.15
SUM	100.64	99.36	100.73

Target:	<i>4c</i>	<i>4d</i>	<i>4ma</i>
<i>Cations</i>			
Si	6.263	6.415	6.146
Ti	0.001	0.003	0.003
Zr	2.280	2.226	2.247
Al	0.002	0.002	0.001
Sc	na	na	na
REE	0.002	0.003	0.003
Fe <sup>2+</sup>	0.033	0.030	0.036
Mn <sup>2+</sup>	0.035	0.032	0.032
Mg	0.002	0.006	0.006
Zn	0.485	0.397	0.553
Ca	0.021	0.021	0.021
Ba	na	na	na
Na	0.566	0.408	1.074
K	0.024	0.017	0.023
Normalized to 18 oxygen <i>apfu</i> na = not analyzed			

***Zircon******Type 2 Nepheline Leucosyenite***

Zircon occurs as a trace mineral in the Type 2 nepheline leucosyenite, in which it is present as clusters and individuals of euhedral to subhedral dipyramidal crystals, individually to 300  $\mu\text{m}$  diameter. These crystals are found in association with sodalite pseudomorphs after nepheline, natrolite, and microcline. Identification was made on the basis of EDS analysis, supported by examination in the petrographic microscope (uniaxial positive,  $\delta \approx 0.030$ ).

### *Feldspar-Aegirine Dikes*

Zircon occurs as a rare mineral in the feldspar-aegirine dikes. It is found as a skeletal, euhedral prismatic crystal 1.5 mm wide by 2.5 mm long. Forms present are the tetragonal prism {010} and the tetragonal dipyrmaid {011}. Zircon from the feldspar-aegirine dikes is intergrown with microcline and associated with aegirine and pyrochlore. Identification was made on the basis of EDS analysis, supported by examination in the petrographic microscope (uniaxial positive,  $\delta = 0.035$ ).

### *East Hill Suite Zirconosilicates*

#### *Paragenesis*

The East Hill suite presents a complex picture of zirconosilicate paragenesis (Table 51). As crystallization proceeded, zirconosilicate stability oscillated back and forth between alkaline or alkali zirconosilicates and zircon. The evanescent appearance of calcium zirconosilicates in the nepheline melasyenite was followed by zircon in the nepheline leucosyenite, alkali (Na and

TABLE 51 – Paragenesis of zirconosilicates – East Hill suite

<i>X-Zr-silicate</i> <i>X = ?</i>	<i>Mineral(s)</i>	<i>Nepheline</i> <i>Melasyenite</i>	<i>Nepheline</i> <i>Leucosyenites</i>	<i>Eudialyte</i> <i>Syenite</i>	<i>Feld.-Aeg.</i> <i>Dikes</i>	<i>Annite</i> <i>Lamprophyre</i>
none	zircon					
Ca	calciohilairite					
	lāvenite					
Na/Ca	eudialyte group					
Na	catapleiite					
	gaidonnayite					
	hilairite					
	petarasite					

Na/Ca) zirconosilicates in the eudialyte syenite, zircon in the feldspar-aegirine dikes, and finally, sodium zirconosilicates in the annite lamprophyre. This sequence overall reflects the alkaline chemical evolution of the East Hill suite, with Ca-rich minerals followed by those increasing in Na content; however, the interspersed zircon indicates that other factors played a part.

The nepheline melasyenite contains only a minimal quantity of calcium zirconosilicates, but their presence indicates that zirconosilicates saturated in the East Hill suite magma early in the crystallization sequence. High temperature magmas that crystallize an alkaline zirconosilicate (Figure 123, path B<sub>1</sub>), rather than zircon, must contain relatively low concentrations of zirconium. (Marr *et al.* 1998)

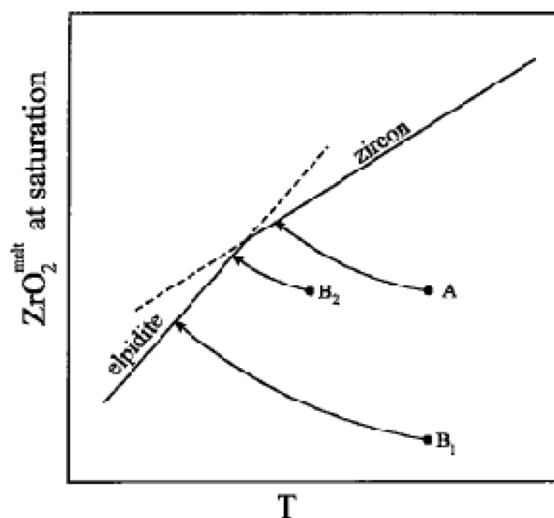


FIGURE 123 – Schematic cooling paths in  $[\text{ZrO}_2]$ – $T$  space for three peralkaline magmas. Magma A crystallizes zircon; magmas B<sub>1</sub> and B<sub>2</sub> crystallize elpidite,  $\text{Na}_2\text{ZrSi}_6\text{O}_{15} \cdot 3 \text{H}_2\text{O}$ . Cooling paths assume equal Zr solubility. (Marr *et al.* 1998)

Field evidence indicates that the nepheline leucosyenites began crystallizing before the nepheline melasyenite had completely solidified, suggesting similarly high emplacement temperatures. Therefore, the subsequent crystallization of zircon in the nepheline leucosyenite could be explained simply by an increase in the Zr content of the melt (Figure 123, path A). Nepheline geothermometry and sulfide assemblages indicate that the eudialyte syenite

crystallized at lower temperatures than the nepheline mela- and leucosyenites. As an increase in zirconium concentration in the melt shifted the cooling path for the nepheline leucosyenite magma, this decrease in temperature could explain the return to alkali zirconosilicate crystallization in the eudialyte syenite (Figure 123, path B<sub>2</sub>).

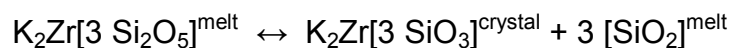
A complication comes with the reappearance of zircon in the feldspar-aegirine dikes. By this point in the emplacement of the East Hill suite, magma temperatures would seem to be too low to stabilize zircon at the high zirconium concentration that existed during feldspar-aegirine dike crystallization. Another complication is that zircon is merely present as a rare mineral, whereas the feldspar-aegirine dikes have the highest whole-rock Zr content in the East Hill suite. This latter point is easily accounted for, as feldspar-aegirine dike clinopyroxene is the most Zr-rich in the East Hill suite; however, this compounds the question of why zircon saturated again with why aegirine outcompeted zircon for zirconium.

One facet of the solution to these questions is likely the influence of oxygen fugacity. Decreasing oxygen fugacity promotes zirconosilicate crystallization and, in particular, inhibits the crystallization of alkali zirconosilicates. Low  $f_{O_2}$  favors 8-coordinated Zr in the melt, which translates into lower zircon solubility. (Farges *et al.* 1994) As the oxygen fugacity in the East Hill suite fell during crystallization, the zircon saturation surface shifted to lower temperatures and concentrations of Zr, facilitating the crystallization of late-stage zircon. In contrast, Zr is 6-coordinated in clinopyroxene; therefore, low oxygen fugacity should inhibit Zr uptake by clinopyroxene, but both low  $f_{O_2}$  and high-Zr aegirine are the case in the feldspar-aegirine dikes; so another factor must be at work.

The most likely influence is that of alkalis. Increasing alkalis in a peralkaline melt also increases Zr solubility. (Watson 1979; Watson & Harrison 1983) Furthermore, most Zr in such

melts is 6-coordinated (Farges 1989; Farges *et al.* 1991), which is advantageous to the crystallization of high-Zr clinopyroxene. Similarly, increasing alkalis increases the proportion in the melt of non-bridging oxygens, to which <sup>vi</sup>Zr preferentially bonds. (Linthout 1984; Farges *et al.* 1991 & 1994) At the extreme of this effect, due to their exceptionally high alkali content, agpaitic melts may exclude zircon, altogether. (Lazutkina *et al.* 1980) Obviously, the feldspar-aegirine dikes are not zircon-free, implying that the effects of low oxygen fugacity on Zr coordination were not entirely offset by those of elevated alkalis.

The final consideration in this paragenesis is the third appearance of alkali zirconosilicates in the East Hill suite, in the annite lamprophyre. Total alkalis, oxygen fugacity, and zirconium concentration are all very similar between the feldspar-aegirine dikes and the annite lamprophyre, so yet another factor must have influenced zirconosilicate crystallization, saturating the melt in alkali zirconosilicates rather than zircon. In the East Hill suite, whole-rock silica content was relatively high in the nepheline melasyenite and fell to a local minimum in the Type 2 nepheline leucosyenite; it increased to roughly the same level as in the nepheline melasyenite through the eudialyte syenite and the feldspar-aegirine dikes; and then it fell precipitously in the annite lamprophyre. Silica activity plays a role in situating the saturation surfaces of zirconosilicates by influencing the solubility of zirconium. In low-silica peralkaline melts, such as those in the East Hill suite, increasing silica increases the solubility of Zr by favoring the formation of alkali-zirconosilicate complexes over the crystallization of stable alkali zirconosilicate phases, such as wadeite (Marr *et al.* 1998):



Obviously, an increase in silica activity drives the reaction to the left, promoting the retention of Zr in the melt.



The high silica in the nepheline melasyenite would have helped retain Zr in the melt, accounting for its minimal zirconosilicate mineralization. Similarly, the decline in silica into the Type 2 nepheline leucosyenite and the annite lamprophyre could help explain the appearance of zircon and sodium zirconosilicates, respectively, by contributing to the saturation of the melt in Zr. This same effect is likely the reason for abundant alkali zirconosilicates in the annite lamprophyre. The high alkalis promoted an abundance of  $^{vi}\text{Zr}$  in the melt and countered the promotion of  $^{viii}\text{Zr}$  by low oxygen fugacity; also, whole-rock Zr content is the second highest in the East Hill suite, yet still three times higher than that in the eudialyte syenite, thus elevating the saturation of the melt in zirconosilicates. On top of these factors, the drastically reduced silica content in the annite lamprophyre would have driven the crystallization of alkali zirconosilicates.

One factor that has not been addressed yet is the influence of halogens on zirconium in the East Hill suite melt. Unlike its effect in granitic melts, fluorine tends to reduce Zr solubility in peralkaline melts due to competitive complexing of F by alkalis that reduces the availability of F to Al and Zr. (Mysen & Virgo 1985; Kohn *et al.* 1991; Schaller *et al.* 1992; Keppler 1993; Linnen 1998; Marr *et al.* 1998; Linnen & Keppler 2002) Chlorine is the dominant halogen in the East Hill suite, and its behavior is not nearly as well-understood as that of fluorine. Similar to fluorine, however, chlorine is empirically known to reduce the solubility of Zr in peralkaline melts. (Marr *et al.* 1998)

The whole-rock chlorine content in the East Hill suite is highest, by 1 to 2 orders of magnitude, in the nepheline leucosyenites. This is, however, largely due to the incorporation of Cl by nepheline altering to sodalite, which was a subsolidus reaction. Looking at it another way, Cl was not necessarily more abundant in the leucosyenites during crystallization. On the contrary, what is more likely, is that Cl was tied up in melt complexes and magmatic fluids and

became more abundant in the melt as crystallization of the entire suite progressed. The early syenitic lithologies contain a relatively small proportion of primary Cl-bearing phases, which would have concentrated Cl in the residual melt. This means that the syenoid melts that crystallized the eudialyte syenite, the feldspar-aegirine dikes, and the annite lamprophyre would have been enriched in Cl, decreasing the solubility of zirconium, and promoting the crystallization of abundant zirconosilicates.

#### *Zinc in Annite Lamprophyre Zirconosilicates*

Gaidonnayite, hilairite, and petarasite from this lithology exhibit consistently high Zn contents, at least 5 wt.% and up to nearly 7 wt.% ZnO. PIILONEN *ET AL.* (2000) found that similarly high Zn content is found in some niobokupletskite from pegmatites in the East Hill suite, although the enrichment is systematically variable. In East Hill suite niobokupletskite, Zn content correlates negatively with zinc mineralization, namely wurtzite, as opposed to sphalerite, and genthelvite,  $\text{Zn}_4\text{Be}_3(\text{SiO}_4)_3\text{S}$ . Zinc-free niobokupletskite occurs with wurtzite and genthelvite, whereas niobokupletskite from wurtzite- and genthelvite-free assemblages contains up to 4.31 wt.% ZnO. They concluded that the sulfur fugacity was not only too low ( $f_{\text{S}_2} < 10^{-10}$  bar) to stabilize sphalerite but also that sulfur fugacity was even lower in some portions of the pegmatites, precluding the crystallization of a sulfur-bearing Zn phase and sending Zn into niobokupletskite. High-Zn zirconosilicates in the annite lamprophyre, however, are associated with sulfide minerals, including sphalerite. The sulfur fugacity in the annite lamprophyre was clearly sufficiently high to stabilize sphalerite. This suggests either that there was sufficient Zn to go into both a sulfide phase and the zirconosilicates or that zirconosilicates do not compete for Zn in the same manner as niobokupletskite.

## OTHER SILICATES

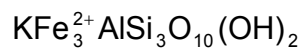
### *Almandine*



#### *Type 2 Nepheline Leucosyenite*

Almandine is found as a trace mineral in the Type 2 nepheline leucosyenite. It has been found in two occurrences. The first is a subhedral equant crystal measuring approximately 1 mm in diameter. It is dark blood red in color. The second is a group of discrete anhedral masses, each measuring between 20-50  $\mu\text{m}$  in maximum dimension. Both forms are found in association with sodalite pseudomorphs after nepheline, albite, and aegirine-augite. The latter are found in intimate contact with the aegirine-augite. Identification was on the basis of physical properties (color and form), EDS analysis, and optical properties (isotropic). Electron microprobe analyses yielded low totals (approximately 87 %), probably due to beam-scatter from fracturing. The analyses do, however, indicate limited solid-solution with spessartine, with up to 1.49 wt.% MnO.

### *Annite*



#### *Nepheline Melasyenite*

Annite is a minor mineral in the nepheline melasyenite, in which it occurs as dark brown to black, subhedral (sometimes craggy) books to 1 mm in diameter. In hand specimen, these books present a bronzy, submetallic luster on their basal cleavage surfaces. In thin section, the annite exhibits little to no zonation, though it is pleochroic, following the scheme:  $X$  = straw yellow to amber;  $Y$  = pale mint green, olive green, dark forest green;  $Z$  = olive green. In the

nepheline melasyenite, annite is associated with aegirine-augite, augite, hastingsite, magnetite, taramite, and titanite. In particular, in association with aegirine-augite, fluorapatite, hastingsite, magnetite, pyrite, and titanite, annite occurs in mafic stringers. Furthermore, annite may poikilitically enclose clinopyroxene and *vice versa*.

Representative analyses of annite are listed in TABLE 52. Annite from the nepheline melasyenite is magnesian, with some compositions plotting near the phlogopite boundary (Figure 127). These compositions follow a trend line of increasing Fe/Mg and  $\text{Fe}^{3+}/\text{Al}$ , heading towards the boundary with tetra-ferri-annite. The ferric to ferrous iron ratio was estimated from wet-chemical analysis of annite from the annite lamprophyre, as insufficient material could be gathered from the nepheline melasyenite. It is possible, even probable, that the annite from the nepheline melasyenite is less enriched in ferric iron than that from the annite lamprophyre. This would not affect speciation, though, and should merely be kept in mind. Annite compositions are aluminous, containing an average of 11.90 wt.%  $\text{Al}_2\text{O}_3$  and up to 12.99 wt.%  $\text{Al}_2\text{O}_3$ . Annite has high concentrations of cerium, up to 1.02 wt.%  $\text{Ce}_2\text{O}_3$ , and titanium, up to 3.11 wt.%  $\text{TiO}_2$ . Other important trace elements include manganese, up to 1.59 wt.%  $\text{MnO}$ , zinc, up to 1.06 wt.%  $\text{ZnO}$ , and zirconium, up to 1.03 wt.%  $\text{ZrO}_2$ .

#### *Feldspar-Aegirine Dikes*

Annite is found as a trace mineral in the feldspar-aegirine dikes. It occurs as subhedral crystals to 300  $\mu\text{m}$  in diameter and 250  $\mu\text{m}$  in thickness. They are pleochroic, following the scheme: *X* = red orange, *Z* = nearly opaque, dark red brown. No crystals were oriented appropriately to measure the color associated with *Y*. Annite is associated with albite, microcline, natrolite, and hematite. Identification was on the basis of EDS and EMP analyses,

TABLE 52 – Representative electron microprobe analyses of annite – Nepheline Melasyenite

Lithology:	<i>Nepheline Melasyenite</i>		
Sample:	<i>MSH-B-8</i>		
Target:	<i>15b</i>	<i>19f</i>	<i>21d</i>
SiO <sub>2</sub> (wt. %)	36.43	35.35	36.08
TiO <sub>2</sub>	2.97	2.91	3.11
ZrO <sub>2</sub>	0.00	0.01	0.00
P <sub>2</sub> O <sub>5</sub>	na	na	na
Al <sub>2</sub> O <sub>3</sub>	11.37	11.41	11.77
Sc <sub>2</sub> O <sub>3</sub>	na	na	na
REE <sub>2</sub> O <sub>3</sub>	0.54	0.57	0.74
La <sub>2</sub> O <sub>3</sub>	na	na	na
Ce <sub>2</sub> O <sub>3</sub>	0.54	0.57	0.74
FeO <sub>tot</sub>	29.38	28.09	29.01
MnO	1.48	1.53	1.51
ZnO	0.73	0.62	0.43
CaO	0.00	0.29	0.05
BaO	na	na	na
MgO	6.83	6.96	7.09
Na <sub>2</sub> O	0.48	0.38	0.59
K <sub>2</sub> O	8.75	8.21	8.72
Cl	0.51	0.38	0.41
F	0.72	0.72	0.60
O≡Cl	-0.12	-0.09	-0.09
O≡F	-0.30	-0.30	-0.25
SUM	99.76	97.02	99.75
Normalized to 22 cations na = not analyzed OH site-occupancy calculated by difference Fe <sup>3+</sup> estimated by wet-chemical analysis			

Target:	<i>15b</i>	<i>19f</i>	<i>21d</i>
<i>T-site Si<sub>3</sub></i>			
Si	2.717	2.703	2.685
<sup>iv</sup> Al	0.283	0.297	0.315
<i>T-site Al</i>			
<sup>iv</sup> Al	0.716	0.730	0.717
Fe <sup>3+</sup>	0.242	0.237	0.238
<sup>iv</sup> Ti	0.042	0.033	0.044
<i>M-site</i>			
<sup>vi</sup> Al	0.000	0.000	0.000
<sup>vi</sup> Ti	0.124	0.135	0.129
<sup>vi</sup> Zr	0.000	0.000	0.000
Fe <sup>3+</sup>	0.000	0.000	0.000
Fe <sup>2+</sup>	1.591	1.559	1.567
Mg	0.759	0.793	0.786
Mn <sup>2+</sup>	0.093	0.099	0.095
Zn	0.040	0.035	0.023
<sup>vi</sup> □	0.393	0.379	0.399
<i>I-site</i>			
Ba	na	na	na
Ca	0.000	0.024	0.004
Na	0.070	0.056	0.085
K	0.832	0.800	0.828
<i>A-site</i>			
Cl	0.064	0.049	0.052
F	0.170	0.175	0.142
OH	1.766	1.777	1.806

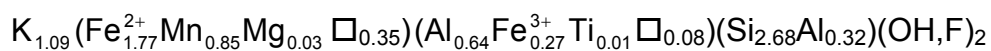
supported under the petrographic microscope (habit, pleochroism, and twinkling extinction).

Representative analyses of annite are listed in TABLE 53. Annite from the feldspar-aegirine dikes is near end-member annite, as it contains virtually no magnesium (Figure 127). There is no real trend in the analyses towards another end-member, except perhaps a slight shift towards tetra-ferri-annite. The ferric to ferrous iron ratio was determined from wet-chemical analysis of annite from the annite lamprophyre, as insufficient material could be gathered from the feldspar-

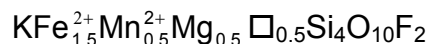
TABLE 53 – Representative electron microprobe analyses of annite – Feldspar-Aegirine Dikes

Lithology:	<i>Feldspar-Aegirine Dikes</i>						
Sample:	<i>MSH-B-3</i>						
Target:	<i>17a1</i>	<i>17a2</i>	<i>18a</i>	Target:	<i>17a1</i>	<i>17a2</i>	<i>18a</i>
SiO <sub>2</sub> (wt.%)	33.03	33.57	32.64	<i>T-site Si<sub>3</sub></i>			
TiO <sub>2</sub>	0.80	2.01	0.21	Si	2.706	2.663	2.685
ZrO <sub>2</sub>	0.00	1.51	0.00	<sup>iv</sup> Al	0.294	0.337	0.315
P <sub>2</sub> O <sub>5</sub>	0.06	0.03	0.06	<i>T-site Al</i>			
Al <sub>2</sub> O <sub>3</sub>	9.06	9.47	9.85	<sup>iv</sup> Al	0.581	0.549	0.640
Sc <sub>2</sub> O <sub>3</sub>	0.00	0.00	0.00	Fe <sup>3+</sup>	0.326	0.304	0.269
REE <sub>2</sub> O <sub>3</sub>	0.00	0.00	0.00	<sup>iv</sup> Ti	0.049	0.120	0.013
La <sub>2</sub> O <sub>3</sub>	na	na	na	<i>M-site</i>			
Ce <sub>2</sub> O <sub>3</sub>	0.00	0.00	0.00	<sup>vi</sup> Al	0.000	0.000	0.000
FeO <sub>tot</sub>	36.04	34.67	29.60	<sup>vi</sup> Ti	0.000	0.000	0.000
MnO	5.52	5.56	12.23	<sup>vi</sup> Zr	0.000	0.058	0.000
ZnO	0.00	0.00	0.00	Fe <sup>3+</sup>	0.000	0.000	0.000
CaO	0.04	0.05	0.15	Fe <sup>2+</sup>	2.144	1.997	1.767
BaO	0.12	0.10	0.05	Mg	0.052	0.044	0.033
MgO	0.43	0.38	0.27	Mn <sup>2+</sup>	0.383	0.374	0.852
Na <sub>2</sub> O	0.00	0.11	0.00	Zn	0.000	0.000	0.000
K <sub>2</sub> O	10.44	10.85	10.41	<sup>vi</sup> □	0.421	0.526	0.348
Cl	0.00	0.00	0.00	<i>I-site</i>			
F	0.00	0.00	0.00	Ba	0.004	0.003	0.002
O≡Cl	0.00	0.00	0.00	Ca	0.003	0.004	0.013
O≡F	0.00	0.00	0.00	Na	0.000	0.016	0.000
SUM	95.53	98.29	95.47	K	1.091	1.098	1.092
Normalized to 22 cations na = not analyzed OH site-occupancy calculated by difference Fe <sup>3+</sup> estimated by wet-chemical analysis				<i>A-site</i>			
				Cl	0.000	0.000	0.000
				F	0.000	0.000	0.000
				OH	2.000	2.000	2.000

aegirine dikes. Based on the comparable iron crystal chemistry of other ferrous/ferric minerals (*e.g.* clinopyroxene), however, this ratio is likely a good proxy for that of the feldspar-aegirine dikes. It is silica-deficient, but it is not aluminous, owing to a high iron content (up to 36.04 wt.% FeO). Annite from the feldspar-aegirine dikes contains prodigious amounts of manganese, averaging 7.77 wt.% and containing up to 12.23 wt.% MnO. This results in the formula,



This composition contains a large montdorite component. Montdorite is not an end-member mica group species, but is an intermediate, currently valid, species between annite-phlogopite and a hypothetical Mn-dominant end-member. (Rieder *et al.* 1998) Montdorite itself has the ideal formula,



Titanium and zirconium are also present in significant quantities, up to 2.01 wt.% TiO<sub>2</sub> and 1.51 wt.% ZrO<sub>2</sub>, respectively.

### *Annite Lamprophyre*

Annite is the most common mineral in the annite lamprophyre, constituting about 65% of the modality. It occurs as euhedral, equant to short prismatic books to 4 mm diameter and 6 mm length. In hand specimen, most crystals are so dark as to appear black, though some are perceived as having a very dark brown or brownish-green color. In thin section, the crystals of annite are seen to be strikingly zoned and strongly pleochroic, as is consistent with lamprophyric annite. The pleochroism follows the scheme: *X* = amber, orange, red-orange; *Y* = pale mint green, light forest green, yellow-green, tan; *Z* = amber, greenish-amber, amber green, medium forest green, dark forest green. It is not readily possible to associate particular *Y* colors with *X* or *Z* colors, but *X* and *Z* colors appear in common pairs (*X* & *Z*): amber & amber, amber & greenish-amber, orange & amber green, red-orange & medium forest green. Thus, *X* and *Z* colors match one another in terms of their intensity.

Representative analyses of annite are listed in TABLES 54 & 55. The analyses are of six zones from a single crystal of annite. Annite from the annite lamprophyre is solidly annitic in chemistry, with compositions plotting nearly in the center of the annite field (Figure 127). There

TABLE 54 – Representative electron microprobe analyses of annite – Annite Lamprophyre

Lithology:	<i>Annite Lamprophyre</i>					
Sample:	<i>MSH-B-6</i>					
Target:	3(1)	3(2)	3(3)	3(4)	3(5)	3(6)
SiO <sub>2</sub> (wt.%)	36.01	34.58	35.12	36.20	36.37	34.67
TiO <sub>2</sub>	2.34	0.87	0.86	0.95	2.56	0.85
ZrO <sub>2</sub>	0.04	0.00	0.04	0.00	0.09	0.15
P <sub>2</sub> O <sub>5</sub>	0.00	0.00	0.00	0.00	0.00	0.00
Al <sub>2</sub> O <sub>3</sub>	9.41	9.13	9.08	9.42	9.43	8.68
Sc <sub>2</sub> O <sub>3</sub>	na	na	na	na	na	na
REE <sub>2</sub> O <sub>3</sub>	0.00	0.00	0.01	0.18	0.12	0.12
La <sub>2</sub> O <sub>3</sub>	0.00	0.00	0.01	0.18	0.12	0.12
Ce <sub>2</sub> O <sub>3</sub>	0.00	0.00	0.00	0.00	0.00	0.00
FeO <sub>tot</sub>	29.15	29.62	32.40	32.50	26.57	32.97
MnO	3.44	4.54	3.21	4.04	4.35	5.31
ZnO	1.23	0.68	1.04	0.81	0.53	0.61
CaO	0.00	0.00	0.01	0.00	0.00	0.00
BaO	na	na	na	na	na	na
MgO	5.91	4.94	5.32	5.40	6.20	3.89
Na <sub>2</sub> O	0.24	0.34	0.20	0.30	0.30	0.29
K <sub>2</sub> O	10.40	9.21	10.49	10.75	9.88	10.42
Cl	0.00	0.00	0.00	0.00	0.00	0.00
F	0.65	0.70	0.83	0.82	0.95	0.81
O≡Cl	0.00	0.00	0.00	0.00	0.00	0.00
O≡F	-0.27	-0.30	-0.35	-0.35	-0.40	-0.34
SUM	98.53	94.30	98.25	101.03	96.96	98.43
Normalized to 22 cations na = not analyzed OH site-occupancy calculated by difference Fe <sup>3+</sup> estimated by wet-chemical analysis						



TABLE 55 – Site-occupancies of annite from TABLE 54 – Annite Lamprophyre

Lithology:	<i>Annite Lamprophyre</i>					
Sample:	<i>MSH-B-6</i>					
Target:	3(1)	3(2)	3(3)	3(4)	3(5)	3(6)
<i>T-site Si<sub>3</sub></i>						
Si	2.745	2.781	2.730	2.734	2.791	2.726
<sup>iv</sup> Al	0.255	0.219	0.270	0.266	0.209	0.274
<i>T-site Al</i>						
<sup>iv</sup> Al	0.589	0.646	0.562	0.573	0.644	0.531
Fe <sup>3+</sup>	0.245	0.263	0.278	0.271	0.225	0.286
<sup>iv</sup> Ti	0.134	0.053	0.050	0.054	0.130	0.050
<i>M-site</i>						
<sup>vi</sup> Al	0.000	0.000	0.000	0.000	0.000	0.000
<sup>vi</sup> Ti	0.000	0.000	0.000	0.000	0.017	0.000
<sup>vi</sup> Zr	0.001	0.000	0.001	0.000	0.004	0.006
Fe <sup>3+</sup>	0.000	0.000	0.000	0.000	0.000	0.000
Fe <sup>2+</sup>	1.613	1.729	1.828	1.782	1.481	1.882
Mg	0.671	0.592	0.616	0.608	0.710	0.456
Mn <sup>2+</sup>	0.222	0.309	0.211	0.259	0.283	0.353
Zn	0.069	0.041	0.060	0.045	0.030	0.036
<sup>vi</sup> □	0.423	0.329	0.283	0.306	0.476	0.267
<i>I-site</i>						
Ba	na	na	na	na	na	na
Ca	0.000	0.000	0.001	0.000	0.000	0.000
Na	0.036	0.052	0.031	0.043	0.045	0.045
K	1.011	0.945	1.040	1.036	0.967	1.045
<i>A-site</i>						
Cl	0.000	0.000	0.000	0.000	0.000	0.000
F	0.156	0.179	0.203	0.197	0.230	0.201
OH	1.844	1.821	1.797	1.803	1.770	1.799
Normalized to 22 cations na = not analyzed OH site-occupancy calculated by difference Fe <sup>3+</sup> estimated by wet-chemical analysis						

is only a slight trend towards tetra-ferri-annite, as Fe/Mg increases faster than  $\text{Fe}^{3+}/\text{Al}$ ; the ferrous/ferric ratio was determined colorimetrically using the metavanadate technique of WILSON (1960). It is silica-deficient, but not aluminous, owing to a high content of magnesium and iron (up to 7.27 wt.% MgO and 34.41 wt.% FeO, respectively). Manganese contents are significant, averaging 4.10 wt.% and up to 6.15 wt.% MnO. Titanium content is high, up to 2.56 wt.%  $\text{TiO}_2$ . Other important trace elements are zinc, up to 1.32 wt.% ZnO, and zirconium, up to 0.99 wt.%  $\text{ZrO}_2$ .

Ternary plots of common chromophoric elements ( $\text{Fe}^{3+}$ ,  $\text{Mn}^{2+}$ , and  $\text{Ti}^{4+}$ ) against pleochroic colors for the three indicatrices (Figures 124 to 126) reveals no relationship between the relative content of these elements and color zonation in annite. Since ferric iron content of the annite was determined as an average of several whole crystals, the  $\text{Fe}^{3+}/\text{Fe}^{2+}$  ratio is fixed for all analyses, hence for all zones in a given crystal. It is possible that  $\text{Fe}^{3+}$  actually varies from zone to zone, and exchanges such as  $\text{Fe}^{3+} \leftrightarrow \text{Al}$  or  $\text{Fe}^{2+} + \text{Ti}^{4+} \leftrightarrow \text{Fe}^{3+} + \text{Ti}^{3+}$  may be responsible for changes in color and pleochroism between zones in a given crystal.

#### *East Hill Suite Annite*

Similarly to the amphibole group (Pe-Piper 1988; Mitchell 1990), there exists a positive correlation between Mg content in micas and magmatic oxygen fugacity. (Wones & Eugster 1965) Mica in the East Hill suite rests entirely within the annite field (Figure 127). Most compositions have a  $X_{\text{Fe}^{3+}}$  between 0.20 and 0.35, but  $X_{\text{Fe}^{2+}}$  varies more substantially, from 0.65 to nearly 1.00 from the nepheline melasyenite to the feldspar-aegirine dikes. This prominent increase in  $X_{\text{Fe}^{2+}}$  shows that the  $f_{\text{O}_2}$  – T trend of decreasing oxygen fugacity that

amphibole chemistry demonstrated to have commenced in the nepheline melasyenite continued through the crystallization history of the East Hill suite.

Increasing oxygen fugacity has been implicated in increasing  $X_{\text{Fe}^{3+}}$  in biotite. (Wones & Eugster 1965; Redhammer *et al.* 1993)  $X_{\text{Fe}^{3+}}$  in annite in the East Hill suite increases slightly, concurrently with a larger proportional increase in  $X_{\text{Fe}^{2+}}$ ; however, if an increase in  $f_{\text{O}_2}$  were

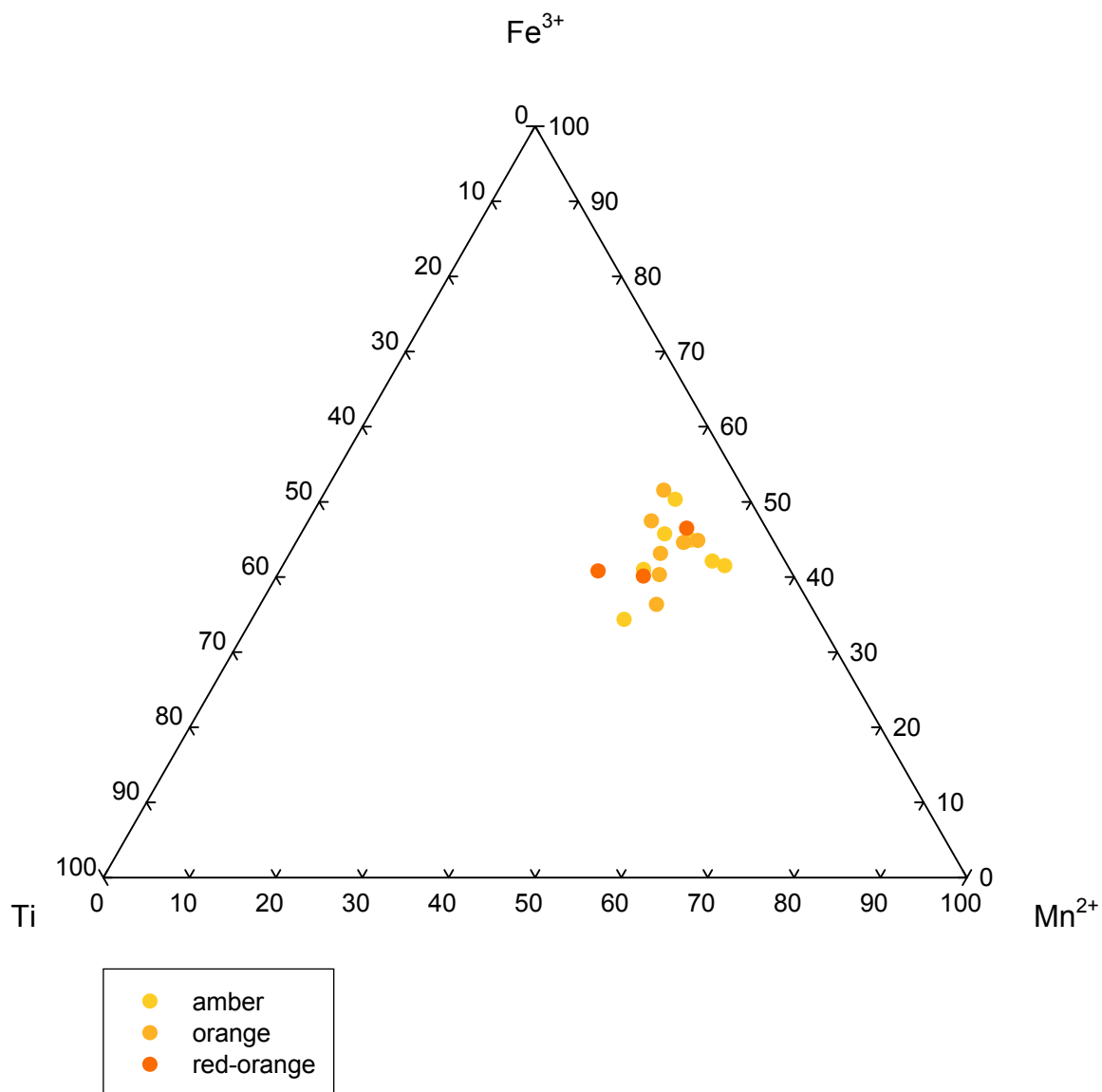


FIGURE 124 – Annite  $X$ -indicatrix pleochroism – Annite Lamprophyre

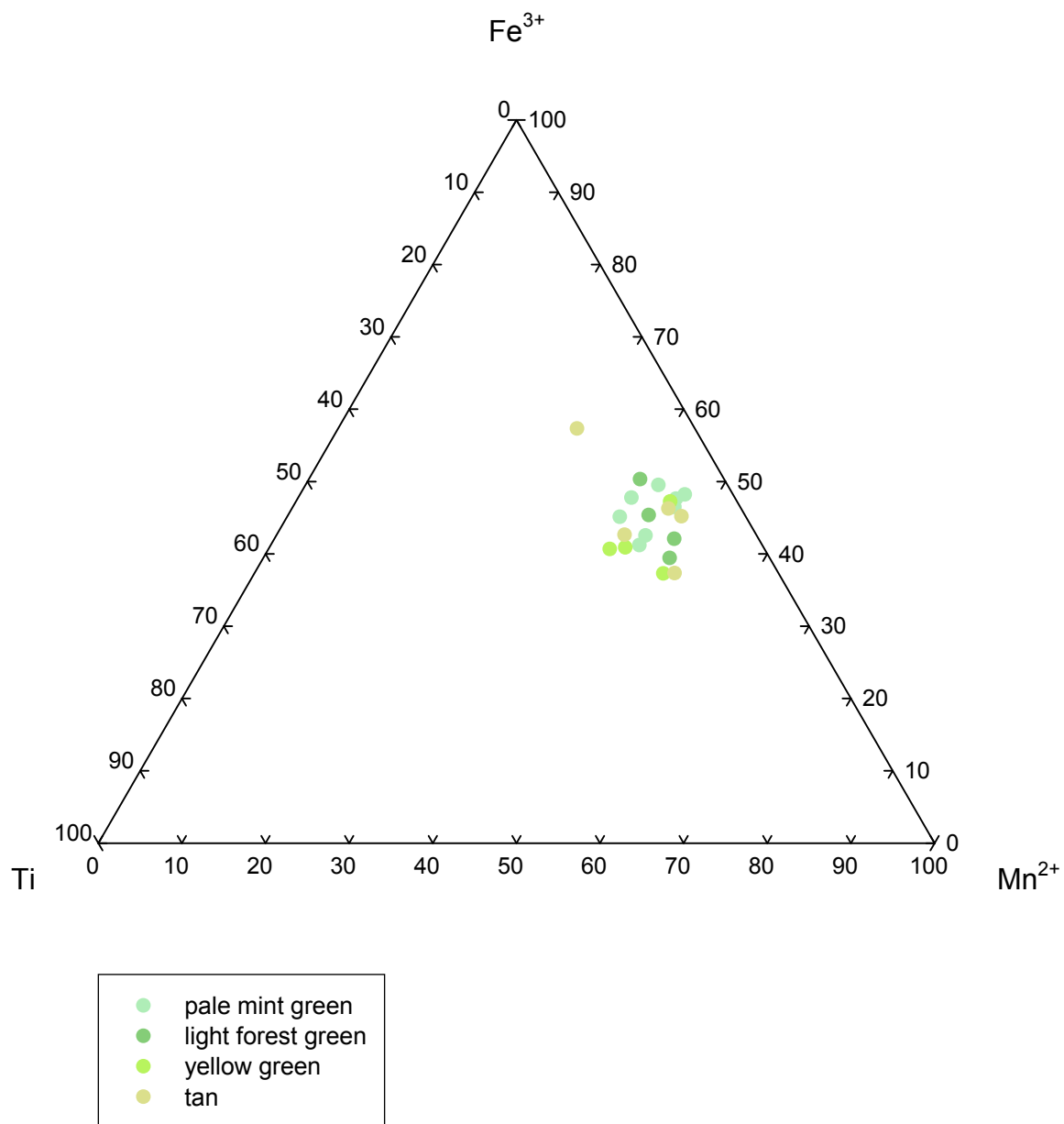


FIGURE 125 – Annite *Y*-indicatrix pleochroism – Annite Lamprophyre

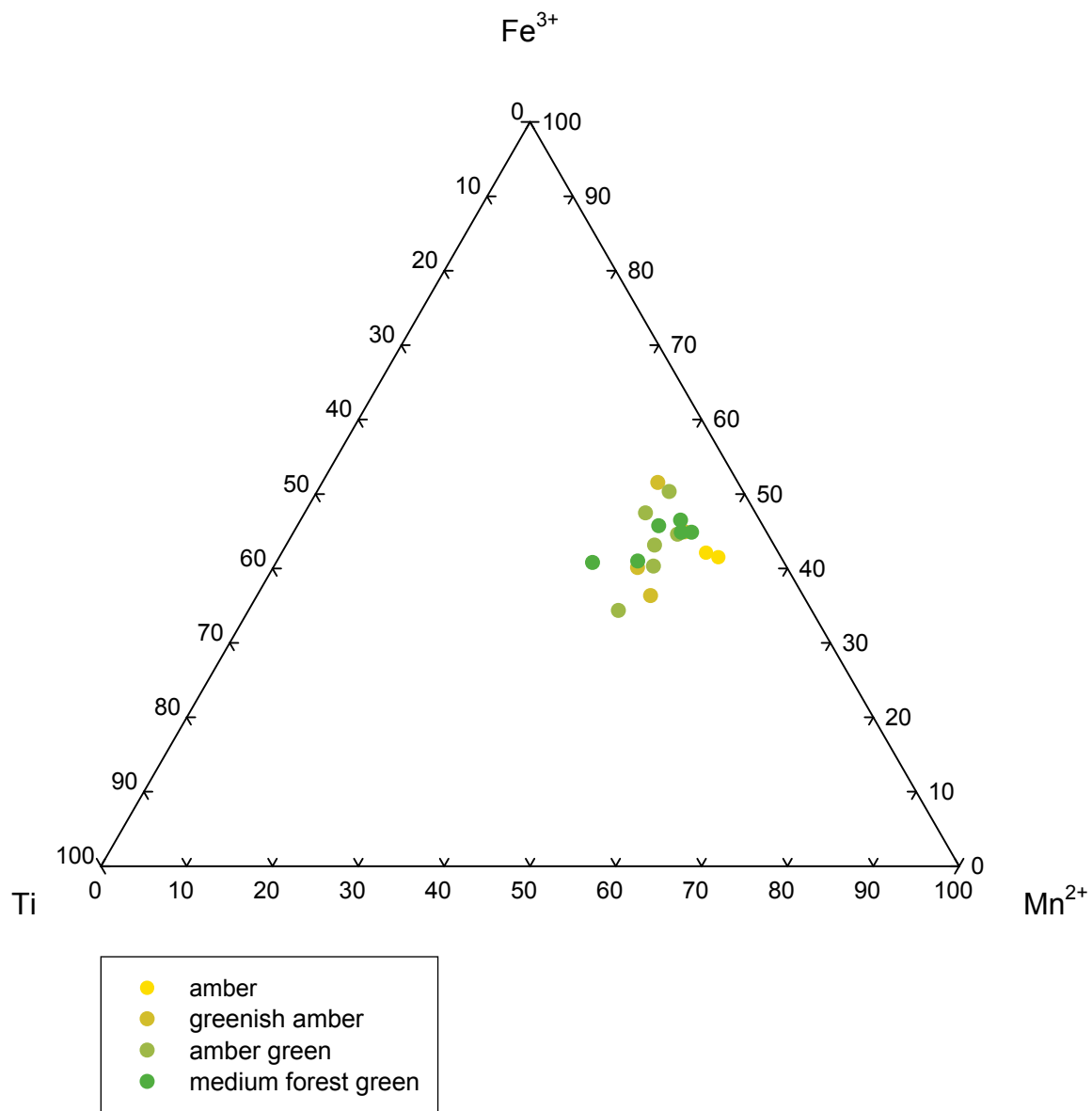


FIGURE 126 – Annite Z-indicatrix pleochroism – Annite Lamprophyre

responsible for the increased  $X_{\text{Fe}^{3+}}$ , that would contradict the decrease in oxygen fugacity indicated by the increase in  $X_{\text{Fe}^{2+}}$ . A clue as to what is driving the change in  $X_{\text{Fe}^{3+}}$  may be found in a comparison of  $^{\text{iv}}\text{Fe}^{3+}$  and  $^{\text{iv}}\text{Al}$  (Figure 128). In amphiboles,  $\text{Fe}^{3+}$  substitution follows two principal routes, a dehydrogenation reaction in which ferrous iron is oxidized to ferric iron:



and simple substitution with aluminum,  $\text{Fe}^{3+}\text{Al}_{-1}$ . (Clowe *et al.* 1988) Among a number of possible mechanisms, these two operate in micas, as well. (Feldstein *et al.* 1996) In the nepheline melasyenite,  $^{\text{iv}}\text{Fe}^{3+}$  increases with almost perfect parity with the *apfu* decrease in  $^{\text{iv}}\text{Al}$ . This implies that increasing  $\text{Fe}^{3+}$  in annite in the nepheline melasyenite is not driven by oxidation of  $\text{Fe}^{2+}$ .

Annite is a late-crystallizing mineral in the nepheline melasyenite, and the pattern of ferric iron and aluminum is consistent with the oxygen environment late in the crystallization of the nepheline melasyenite, in which amphiboles had already switched over from the dehydrogenation reaction to Al substitution. In the feldspar-aegirine dikes and the annite lamprophyre, the trend of  $^{\text{iv}}\text{Fe}^{3+}$  does not reflect substitution for Al but neither does the  $\text{Fe}^{3+}$  content vary significantly. The slight increase in  $X_{\text{Fe}^{3+}}$  in these lithologies may be associated with the increased availability of  $\text{Fe}^{3+}$  resulting from the elevated magmatic alkalinity that drove the increase in aegirine content in clinopyroxene, or it may reflect the more oxidizing conditions that existed near the end of crystallization of the East Hill suite.

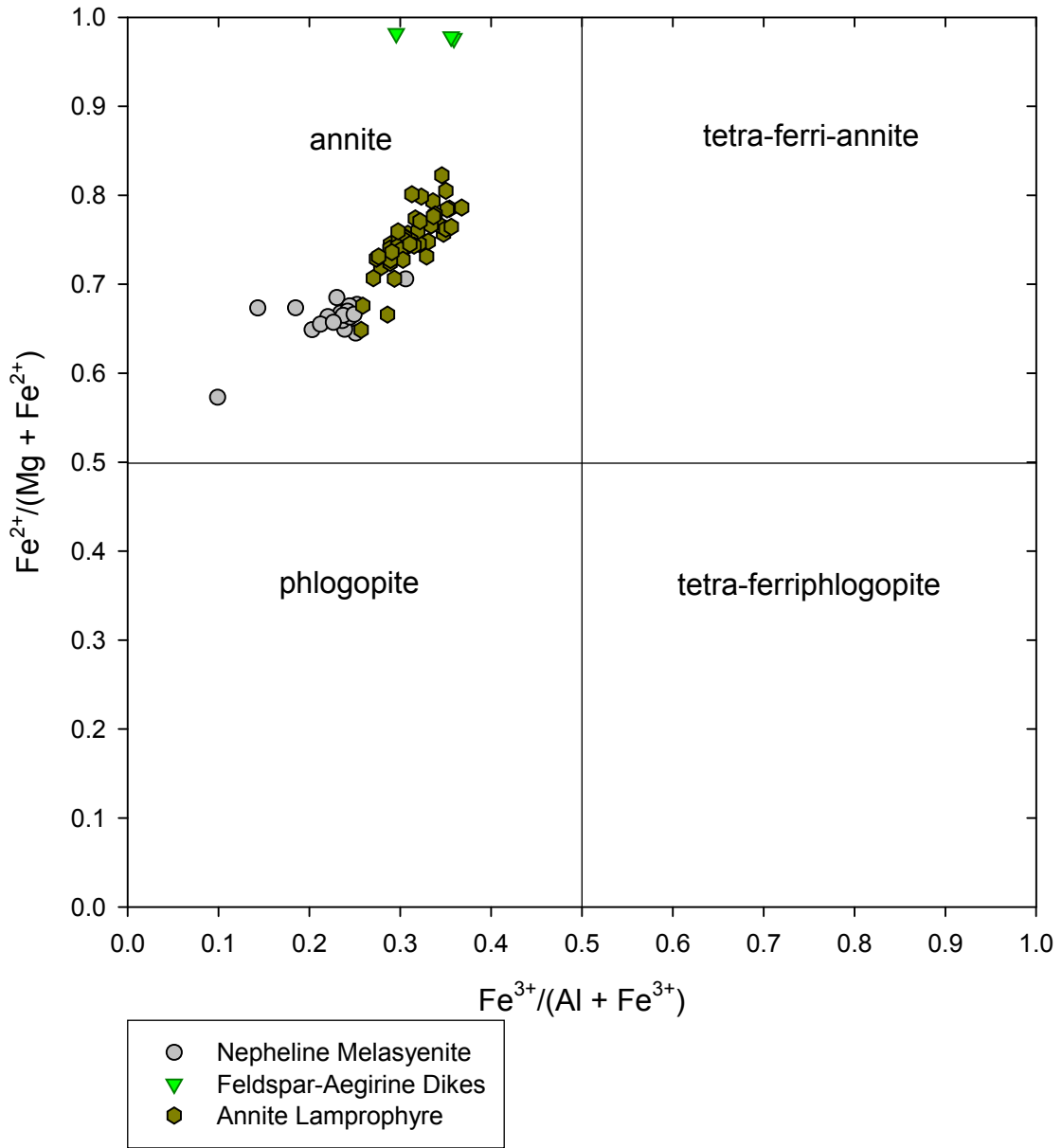


FIGURE 127 – Annite compositions – East Hill suite. Nomenclature after RIEDER *ET AL.* (1998).

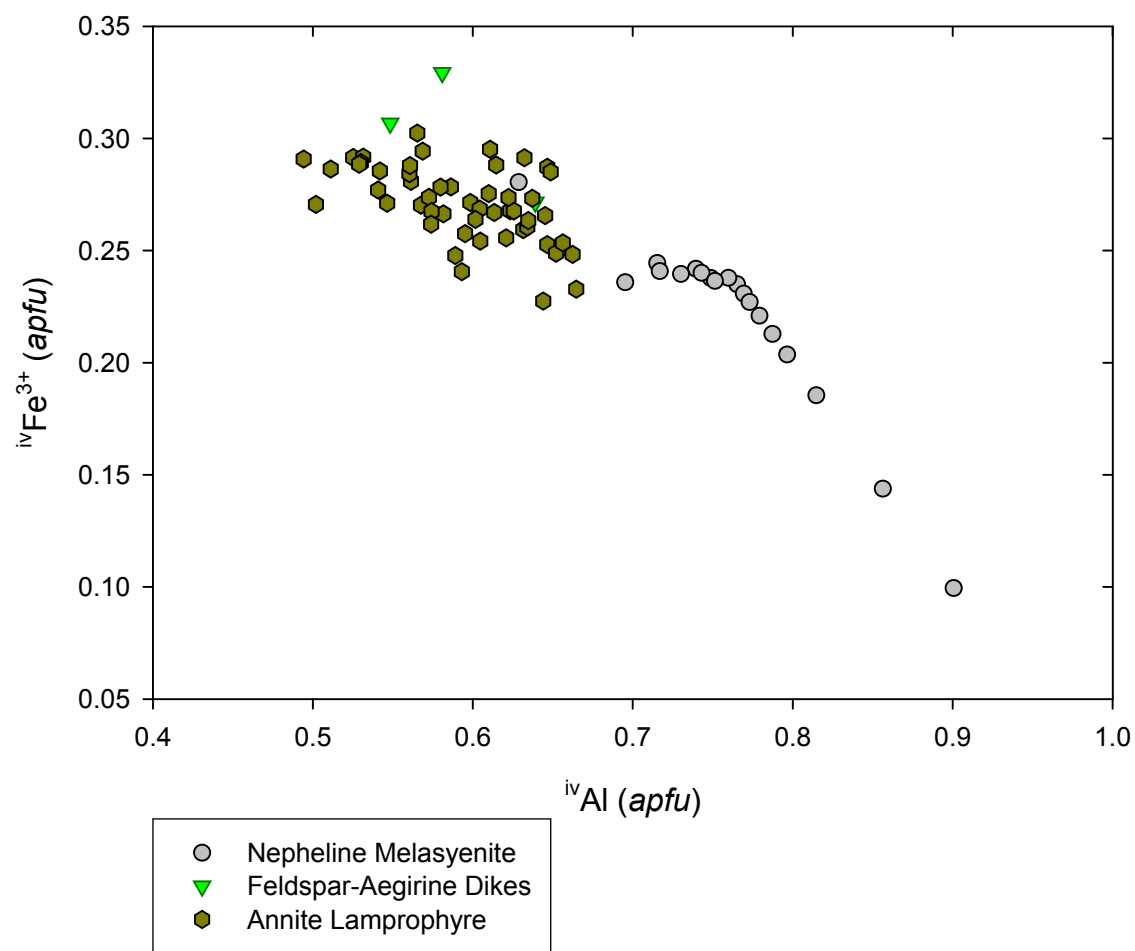


FIGURE 128 –  $ivFe^{3+}$  versus  $ivAl$  in annite – East Hill suite



In addition to pointing to decreasing  $f_{O_2}$ , an increase in annite content also indicates cooling. (Wones & Eugster 1965) Crystallization temperature is also positively correlated to Ti content. (Robert 1976; Trønnes *et al.* 1985) In the East Hill suite, the pattern of temperature decrease indicated by Mg content is supported by negative correlation between Ti and  $X_{Fe^{2+}}$  (Figure 129). The data suggest that the annite lamprophyre and the feldspar-aegirine dikes may have crystallized over a similar temperature range.

HENRY *ET AL.* (2005) propose a geothermometer based on Ti in biotite for use in ilmenite- or rutile-bearing, graphitic, peraluminous metapelites, and they caution that using the geothermometer in systems lacking the appropriate mineral assemblage may lead to substantial errors. In fact, application of their geothermometer to biotite in the feldspar-aegirine dikes and the annite lamprophyre resulted in a wide range of absurd temperatures. The nepheline melasyenite, however, is both ilmenite-bearing and borderline peraluminous, and the geothermometer yielded a reasonable range of estimated crystallization temperatures for annite. Most temperatures clustered between 475 and  $525 \pm 24^\circ\text{C}$ ; some suspect estimates were in the 325-350°C range.

Annite from the East Hill suite exhibits an iron-enrichment trend from the nepheline melasyenite through the annite lamprophyre into the feldspar-aegirine dikes (Figure 130). The annite compositions from the annite lamprophyre lie slightly off the trend line that would connect the annite compositions from the nepheline melasyenite and the feldspar-aegirine dikes. This may reflect a different source magma for the annite lamprophyre, as also suggested by whole-rock geochemistry. Excluding the annite lamprophyre, the annite compositions indicate a positive correlation between annite iron content and degree of magmatic evolution.

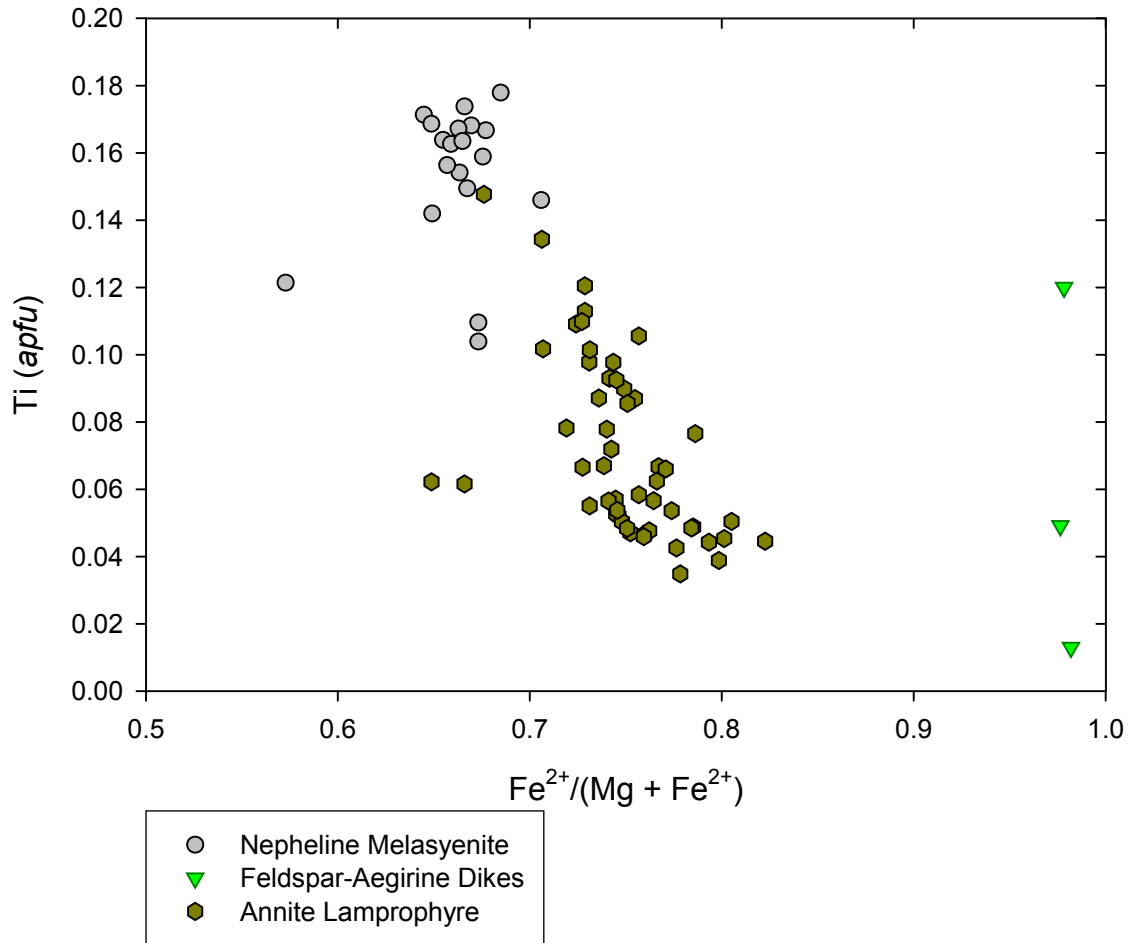


FIGURE 129 – Ti versus  $X_{\text{Fe}^{2+}}$  in annite – East Hill suite

Among compared nepheline syenite complexes (Figure 130), the trend of East Hill suite annite compositions best follows those from Oslo and South Greenland, although East Hill suite annite is less aluminous than that from those localities. Actual compositions are more similar to those from Chilwa or Magnet Cove, though more aluminous. Comparison of the Al content of East Hill suite annite with that of Ti and  $\text{Mn}^{2+}$  revealed covariation of all three elements. EBY *ET AL.* (1998) suggest that this indicates that the annite more likely inherited its aluminum content from the magma, rather than subsequent metasomatism.

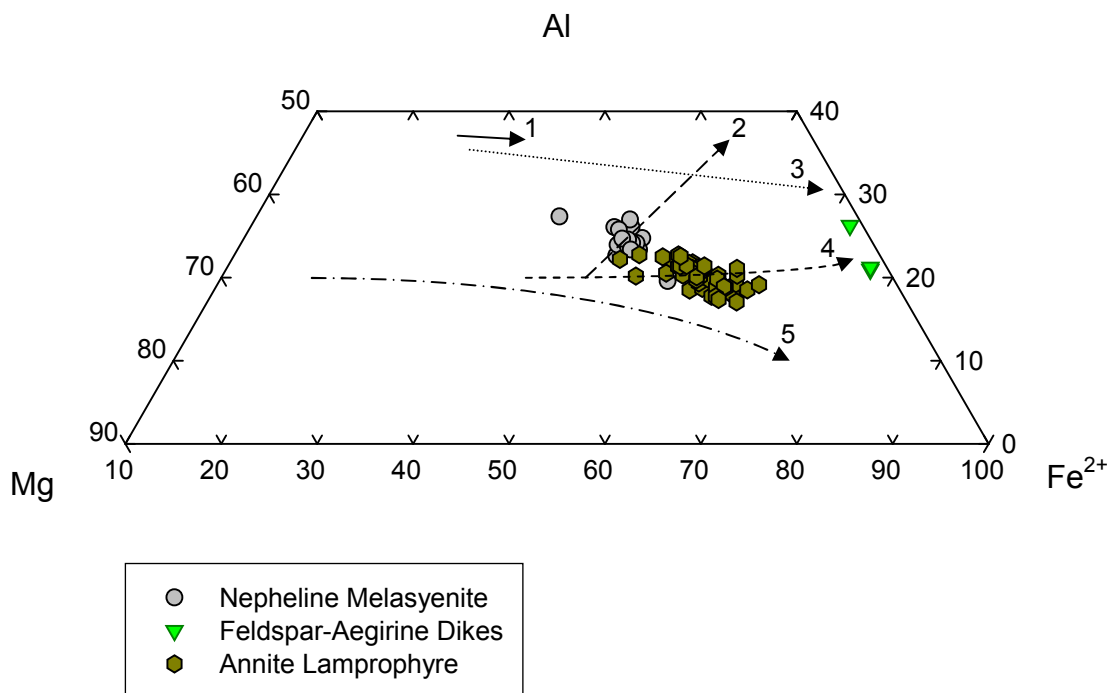


FIGURE 130 – Annite enrichment trend in the East Hill suite, compared to enrichment trends from other nepheline syenite complexes. (1) Oslo rift, Norway (Andersen & Sørensen 1993), (2) Kasungu-Chipala, Ilomba & Ulindi, Malawi (Eby *et al.* 1998), (3) Igdlersfjalsalik, South Greenland (Finch 1995), (4) Junguni, Chilwa Alkaline Province, Malawi (Woolley & Platt 1988), (5) Magnet Cove, Arkansas Alkaline Province, Arkansas (Flohr & Ross 1990).

Both Ti and Al (Figures 129 & 131) decrease with increasing  $X_{\text{Fe}^{2+}}$ , although it is unclear as to which path the evolutionary trend follows. Owing to the disposition of the data points, it is possible to lay a best-fit curve through both the nepheline melasyenite and annite lamprophyre data or both the nepheline melasyenite and the feldspar-aegirine dike data, leaving the remaining lithology in each case as an outlier. Independent evidence from whole rock analyses, however, suggests that the annite lamprophyre is that which should be the outlier. In contrast, Mn increases with increasing  $X_{\text{Fe}^{2+}}$  (Figure 132), and all three mica-bearing lithologies lie along a common trend line.

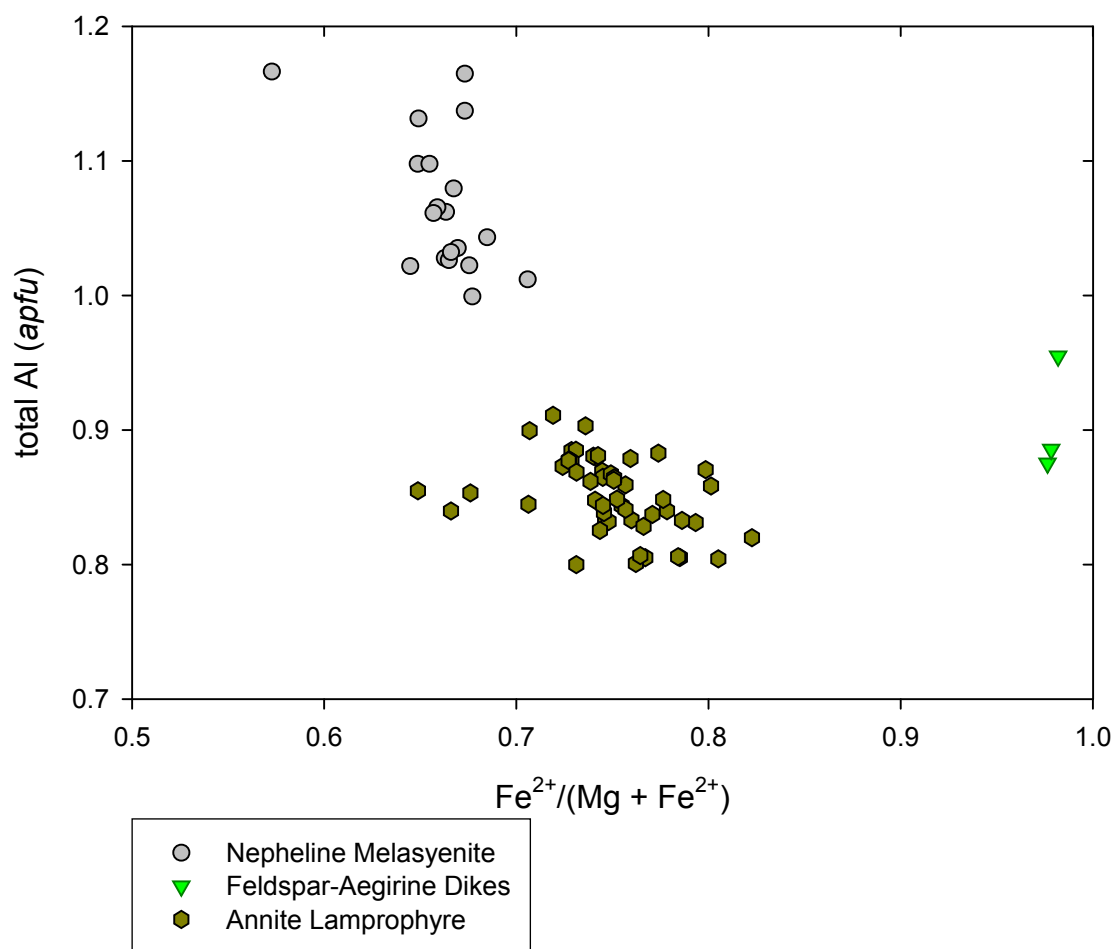


FIGURE 131 – Total Al *versus*  $X_{\text{Fe}^{2+}}$  in annite – East Hill suite

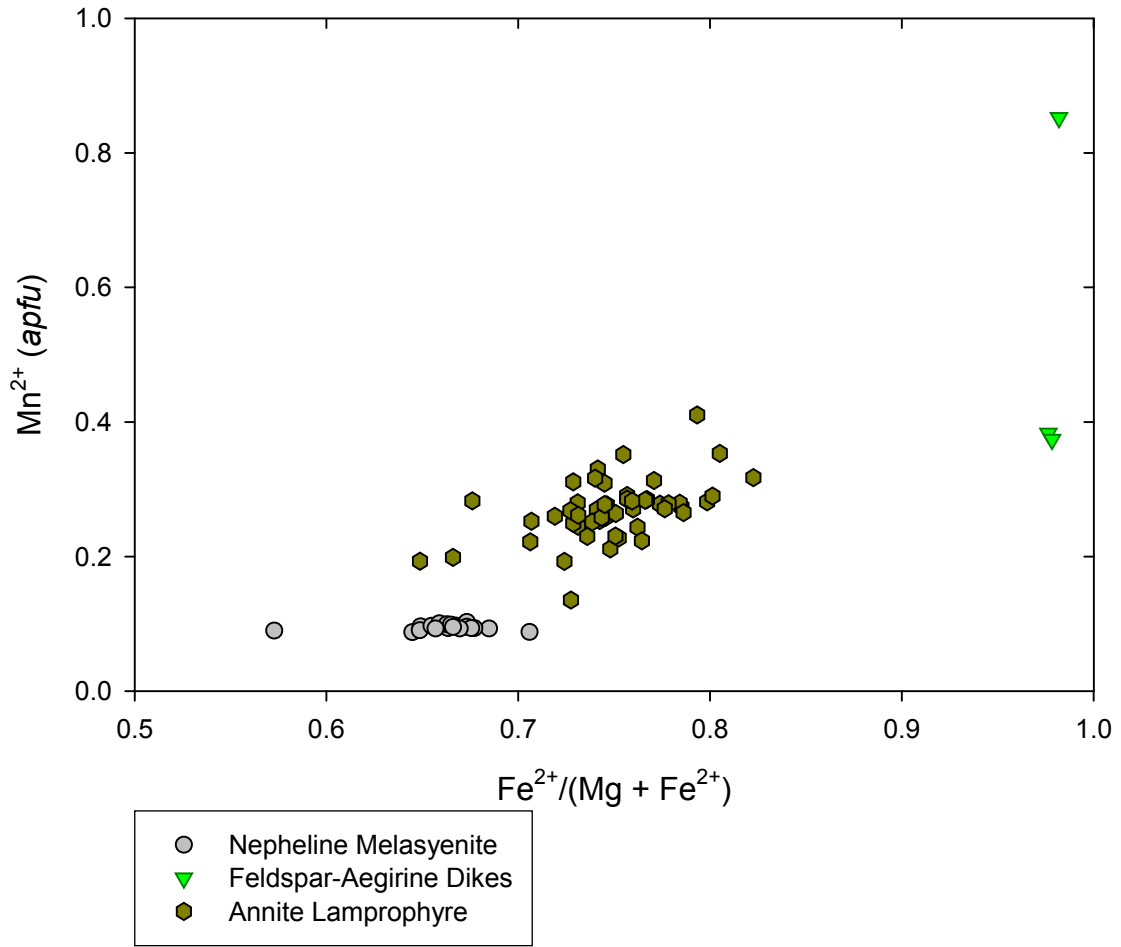


FIGURE 132 –  $\text{Mn}^{2+}$  versus  $X_{\text{Fe}^{2+}}$  in annite – East Hill suite

### ***Pectolite-Sérandite Series***

Pectolite,  $\text{Na}(\text{Ca}, \text{Mn}^{2+})_2\text{Si}_3\text{O}_8(\text{OH})$

Sérandite,  $\text{Na}(\text{Mn}^{2+}, \text{Ca})_2\text{Si}_3\text{O}_8(\text{OH})$

#### *Type 1 Nepheline Leucosyenite*

Members of the pectolite-sérandite series are found as trace minerals in the Type 1 nepheline leucosyenite, as rose pink to salmon, anhedral to subhedral, platy crystals to 2 mm in maximum dimension. They are opaque to translucent with a pearly luster and are associated with clinopyroxene, potassium feldspar, natrolite, fluorapatite, arsenopyrite, and sphalerite.

#### *Type 3 Nepheline Leucosyenite*

Sérandite is a trace mineral in the Type 3 nepheline leucosyenite. It occurs as anhedral to subhedral, bladed crystals to 25  $\mu\text{m}$  long, associated with aegirine, included by sodalite pseudomorphs after nepheline. It is also associated with calcite and fluorite, with sodalite pseudomorphs after nepheline.

#### *Eudialyte Syenite*

Sérandite occurs as a minor mineral in the eudialyte syenite, associated with aegirine, alkali feldspar, and natrolite. Sérandite is seen as equant stacks of platy, subhedral crystals to 1 cm in maximum dimension, with individual crystals to 4 mm (Figure 133). The sérandite exhibits prominent basal cleavage and has a pearly to vitreous luster. Most individuals are pale pink in color, although some may be yellow, brown, or colorless. A representative analysis of sérandite is listed in TABLE 56.

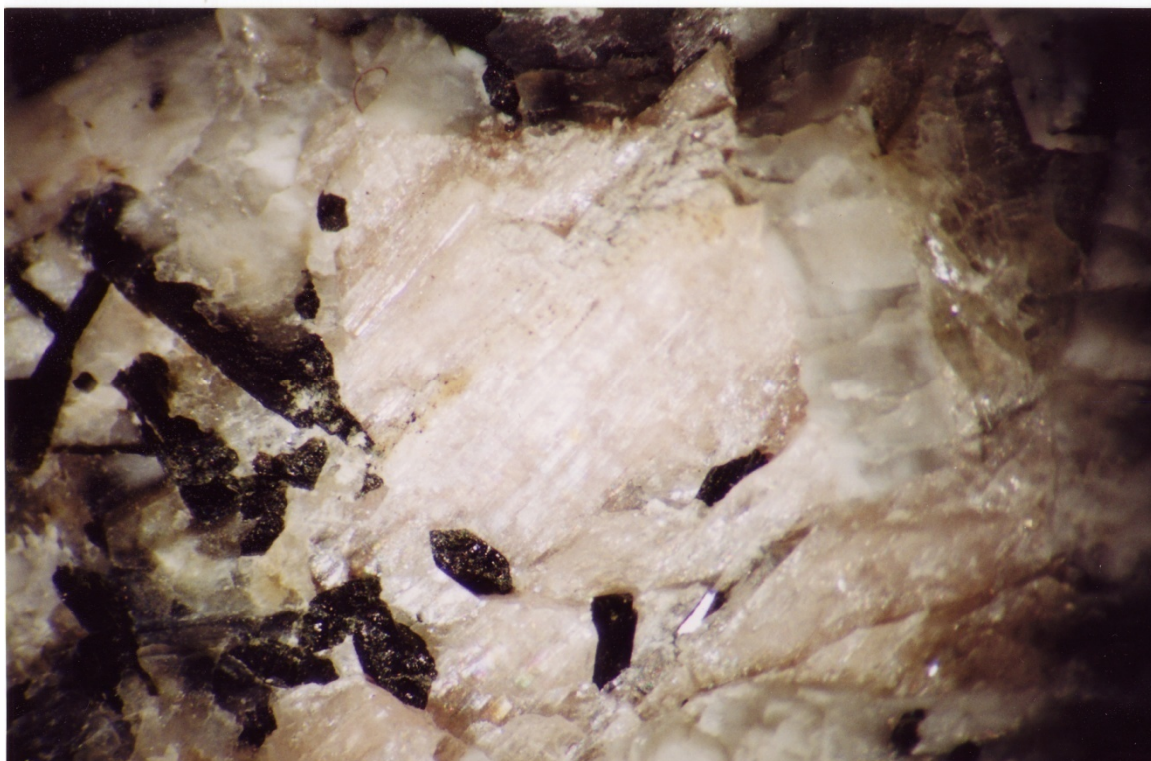
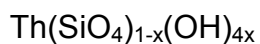


FIGURE 133 – Sérandite, associated with aegirine (black), alkali feldspar, and natrolite – Eudialyte Syenite (12x)

TABLE 56 – Representative electron microprobe analysis of sérandite – Eudialyte Syenite

Lithology:	<i>Eudialyte Syenite</i>		
Sample:	<i>MSH-B-1</i>		
Target:	<i>1e</i>	Target:	<i>1e</i>
SiO <sub>2</sub> (wt. %)	51.22	<i>Cations</i>	
Al <sub>2</sub> O <sub>3</sub>	0.02	Si	3.008
FeO <sub>tot</sub>	1.12	Al	0.001
MnO	25.35	Fe <sup>2+</sup>	0.055
MgO	0.05	Mn <sup>2+</sup>	1.261
ZnO	na	Mg	0.004
CaO	10.22	Zn	na
BaO	na	Ca	0.643
Na <sub>2</sub> O	9.11	Ba	na
K <sub>2</sub> O	0.00	Na	0.000
H <sub>2</sub> O*	2.55	K	1.038
SUM	99.64	OH	0.999
*H <sub>2</sub> O calculated to yield best combination of charge-balance and 1 OH <i>pfu</i>		Normalized to 9 oxygen <i>apfu</i> na = not analyzed	

### *Thorogummite*



#### *Type 2 Nepheline Leucosyenite*

Thorogummite has been tentatively identified as a rare mineral in the Type 2 nepheline leucosyenite. It occurs as an anhedral mass to 5  $\mu\text{m}$  in diameter. Identification was primarily based on EDS analysis.

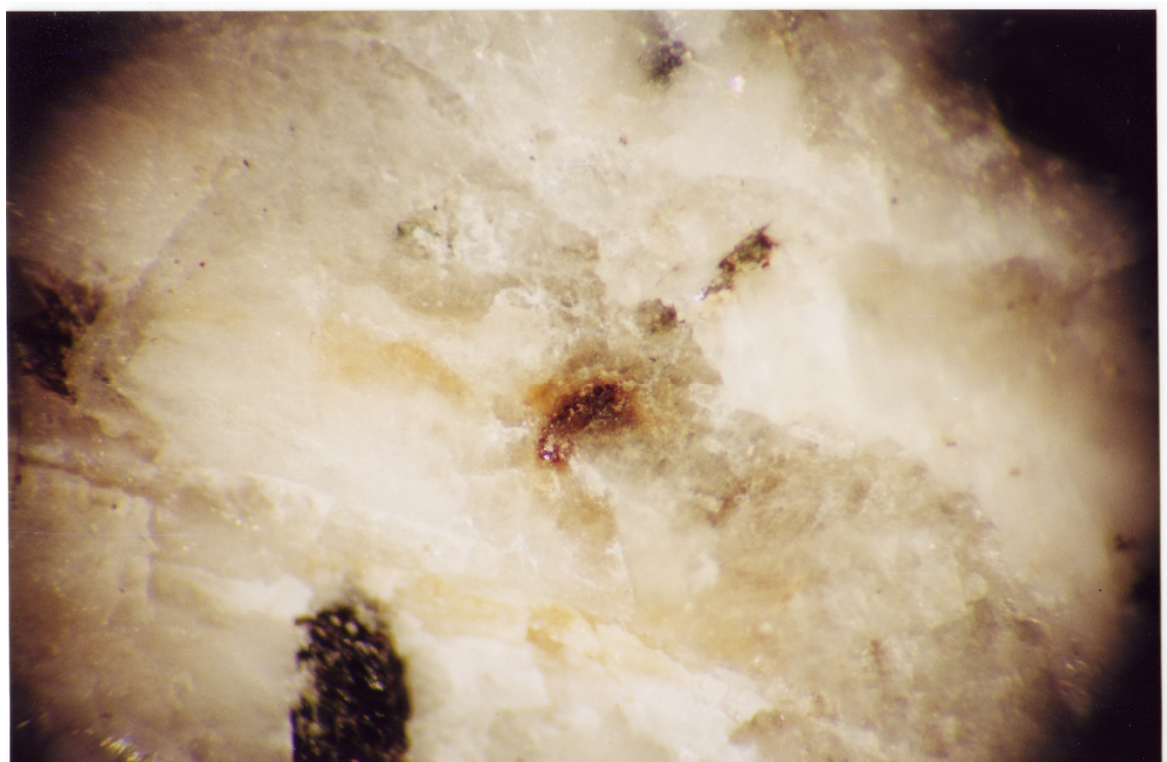


FIGURE 134 – Thorogummite (?) associated with alkali feldspar and natrolite – Eudialyte Syenite (30x)

#### *Eudialyte Syenite*

Thorogummite has been tentatively identified as a rare mineral in the eudialyte syenite. It is seen in certain vugs as irregular masses, approximately 100  $\mu\text{m}$  in diameter (Figure 134), associated with alkali feldspar and natrolite. In thin section, it appears amber in color, with a



granular appearance, and it is associated with ancylite-(Ce), with or without apatite. It is also seen as a 10  $\mu\text{m}$  bleb associated with pyrochlore. In both cases, identification is primarily based on EDS analysis, but this evidence is supported by physical similarity of the specimen, in terms of color, luster, form, and association, to previously documented occurrences of thorogummite at Mont Saint-Hilaire (Mandarino & Anderson 1989).

#### UNIDENTIFIED PHASES

##### ***Ca-Zr Silicate***

Occurs in the Type 3 nepheline leucosyenite as subhedral, perhaps fibrous, crystals, apparently growing across a 10  $\mu\text{m}$ -wide fracture in natrolite after sodalite after nepheline. Chemical components were determined by EDS analysis. The estimated birefringence is 0.007, which is too low for any known Ca-Zr silicates from Mont Saint-Hilaire. The EDS analysis also yields Na and Nb signals; this may indicate an admixture of a Na-Nb silicate or oxide, although such known minerals are also poor matches based on optical properties. Not enough data could be collected on this sample to make a tentative identification.

##### ***Ce-dominant Ca-REE Carbonate***

Occurs in the Type 3 nepheline leucosyenite as anhedral to subhedral equant crystals to 15  $\mu\text{m}$ , included by aegirine. Chemical components were determined by EDS analysis. This could be any one of several minerals, including synchysite-(Ce) and parisite-(Ce), both of which are common with respect to accessory minerals at Mont Saint-Hilaire.

### ***Ce-dominant Ca-REE Phosphate #1***

Occurs in the Type 1 nepheline leucosyenite as an amber to brown, blebby aggregate 50  $\mu\text{m}$  in diameter. The apparent birefringence is 0.007, but this could be slightly artificially low owing to the small size of the specimen. Chemical components were determined by EDS analysis. The only Ca- and Ce-bearing phosphate currently known in the East Hill Suite is brockite,  $(\text{Ca,Th,Ce})\text{PO}_4 \cdot \text{H}_2\text{O}$  (Mandarino & Anderson 1989), but note that this mineral does not have cerium as an essential constituent and that it is likely to contain thorium, an element that did not show up in EDS analysis, at the same time. Furthermore, brockite is white and has a birefringence of 0.015. Therefore, it does not seem likely that the unidentified phase is brockite. This may represent a new mineral at Mont Saint-Hilaire.

### ***Ce-dominant Ca-REE Phosphate #2***

Occurs in the Type 3 nepheline leucosyenite as colorless, subhedral hexagonal crystals to 7  $\mu\text{m}$  in maximum dimension, with most individuals measuring between 2 and 5  $\mu\text{m}$  in maximum dimension. These crystals are present at the interface between microcline and natrolite after sodalite after nepheline. The apparent birefringence is 0.007, although the small size of the specimens almost certainly skews this to the low side. Compensating for thickness, this could represent a birefringence as high as 0.025. EDS analysis also yielded a Th and a U signal. Brockite,  $(\text{Ca,Th,Ce})\text{PO}_4 \cdot \text{H}_2\text{O}$ , is a reasonably good guess as to the identity of this phase. It has the correct chemistry, color, and morphology, and its birefringence (0.015) is in the potential range for this specimen, taking into account a thickness correction. There is not enough data, however, for a confident identification.

### *Na-Zr Silicate*

Occurs in the Type 1 nepheline leucosyenite as aggregates of bladed crystals that appear colorless in thin section. Birefringence is estimated to be approximately 0.014. The individual crystals are up to 50  $\mu\text{m}$  in length with various aspect ratios. The aggregates are associated with aegirine-augite and occur at the margin of altered sodalite pseudomorphs after nepheline, adjacent to microcline and intergrown with natrolite. Chemical components were determined by EDS analysis.

A number of Na-Zr silicates occur in the East Hill Suite: catapleiite,  $\text{Na}_2\text{ZrSi}_3\text{O}_9 \cdot 2 \text{H}_2\text{O}$ ; elpidite,  $\text{Na}_2\text{ZrSi}_6\text{O}_{15} \cdot 3 \text{H}_2\text{O}$ ; gaidonnayite,  $\text{Na}_2\text{ZrSi}_3\text{O}_9 \cdot 2 \text{H}_2\text{O}$ ; hilairite,  $\text{Na}_2\text{ZrSi}_3\text{O}_9 \cdot 3 \text{H}_2\text{O}$ ; parakeldyshite,  $\text{Na}_2\text{ZrSi}_2\text{O}_7$ ; petarasite,  $\text{Na}_5\text{Zr}_2\text{Si}_6\text{O}_{18}(\text{Cl},\text{OH}) \cdot 2 \text{H}_2\text{O}$ ; and terskite,  $\text{Na}_4\text{ZrSi}_6\text{O}_{15}(\text{OH})_2 \cdot \text{H}_2\text{O}$ . (Mandarino & Anderson 1989) Owing to similarities in stoichiometry, it is not meaningful to try to distinguish these species solely on the basis of estimated Na:Zr:Si ratios from an EDS analysis. Petarasite, however, can be eliminated immediately, based on EDS analysis, as the unidentified phase does not have a Cl signal in its EDS spectrum.

Catapleiite ( $\delta = 0.036$ ), gaidonnayite ( $\delta = 0.026$ ), and parakeldyshite ( $\delta = 0.043$ ) have birefringences that are too high, and terskite ( $\delta = 0.008$ ) has a birefringence that is too low. Elpidite ( $\delta = 0.012$ ) and hilairite ( $\delta = 0.013$ ) are the best possibilities. These two minerals can be readily distinguished, in general, based on other optical properties, in that elpidite is biaxial positive and hilairite is uniaxial negative. The specimen, however, is too small to obtain a suitable interference figure.

Elpidite typically forms bladed crystals; hilairite crystals are usually more equant and prismatic. Although both may exhibit similar habits, based on this property, elpidite is the more likely candidate, but there is not enough evidence for confident identification.

## DISCUSSION

### VARIATION IN MAGMATIC EXTENSIVE PARAMETERS

#### *Oxygen Fugacity*

Although the East Hill suite is the focus of this study, crystallization at Mont Saint-Hilaire commenced with the gabbros of the Sunrise and Pain de Sucre suites. (Greenwood & Edgar 1984; Gilbert & Foland 1986) Spinel and apatite were the first minerals to crystallize, followed semi-contemporaneously by ilmenite and titanomagnetite. Ilmenite-magnetite geochemistry indicates subsolidus equilibration over a temperature range of 560-775°C, with  $f_{O_2}$  near the QFM buffer, which corresponds to a approximate oxygen fugacity range of  $10^{-18}$  to  $10^{-20}$  bar and decreasing with temperature. (Greenwood & Edgar 1984) CURRIE *ET AL.* (1986) essentially agree with the temperature range for the gabbro magnetite and the oxygen fugacity for the Sunrise suite, but they propose an oxygen fugacity of about  $10^{-24}$  bar for the Pain de Sucre suite. Olivine and clinopyroxene crystallized following ilmenite and titanomagnetite (Greenwood & Edgar 1984), and the olivine-clinopyroxene geothermometer indicates crystallization temperatures for these minerals around 1100°C for both gabbroic suites. (Currie *et al.* 1986)

The generally low oxygen fugacity of the East Hill suite is parenthetically touched upon by CURRIE *ET AL.* (1986), but their only estimate is from ilmenite-magnetite geochemistry from the nepheline melasyenite, for which their analyses calculate to approximately 575°C with an  $f_{O_2} \approx 10^{-22}$  bar, just below the QFM buffer and intermediate in oxygen fugacity to the gabbroic suites. Mineralogical and geochemical data from this study expands this view (Figure 135) Overall, mineral geochemistry from amphiboles, magnetite, and annite points to generally decreasing oxygen fugacity with cooling.

The Zr-in-sphene thermobarometer (Hayden *et al.* 2008) gives an approximate temperature range of  $700-950 \pm 20^\circ\text{C}$  at 1 kbar. Petrography shows that titanite is one of the first minerals to crystallize in the nepheline melasyenite; therefore, the East Hill suite magma intruded at nearly  $1000^\circ\text{C}$ . The presence of primary titanite indicates oxygen fugacity above the QFM buffer (Carmichael & Nicholls 1967), and the paragenetic immediacy of subsequent ilmenite-magnetite crystallization suggests that the titanite  $f_{\text{O}_2}$  was not far above QFM. This corresponds to an estimated emplacement oxygen fugacity of at least, but near,  $10^{-11.5}$  bar.

Ilmenite, magnetite, and clinopyroxene probably began to crystallize while titanite was still forming, probably still above  $900^\circ\text{C}$ . Amphibole followed clinopyroxene in the paragenesis, and amphibole includes subhedral magnetite. Therefore, magnetite and clinopyroxene had to have crystallized prior to amphibole. Temperature estimates from amphibole extend to as high as approximately  $875^\circ\text{C}$ , so magnetite and calcic clinopyroxene crystallization temperatures must be at least as high. More sodic pyroxenes in the nepheline melasyenite are observed to be later-formed, thus cooler. Also, acmitic pyroxene is only stable in the presence of water below about  $800^\circ\text{C}$  at 1 kbar. (Bailey 1969) Amphibole geochemistry points to decreasing oxygen fugacity with cooling down to about  $650^\circ\text{C}$ , when amphibole crystallization ceased.

Ilmenite-magnetite geochemistry indicates a temperature range of 600 to  $525^\circ\text{C}$  and an approximate range of  $f_{\text{O}_2}$  from  $10^{-22}$  to  $10^{-23.5}$  bar, decreasing with temperature. Considering the presumed magnetite crystallization temperature, based on paragenetic relationships, the geochemically-derived temperature range probably represents subsolidus equilibration. The transition in oxygen fugacity from the relatively high  $f_{\text{O}_2}$  of titanite crystallization to the lower  $f_{\text{O}_2}$  of magnetite equilibration requires the  $f_{\text{O}_2}$  – T path to be steep enough to cross the QFM buffer. Like amphiboles, specific oxygen fugacity data could not be derived from annite

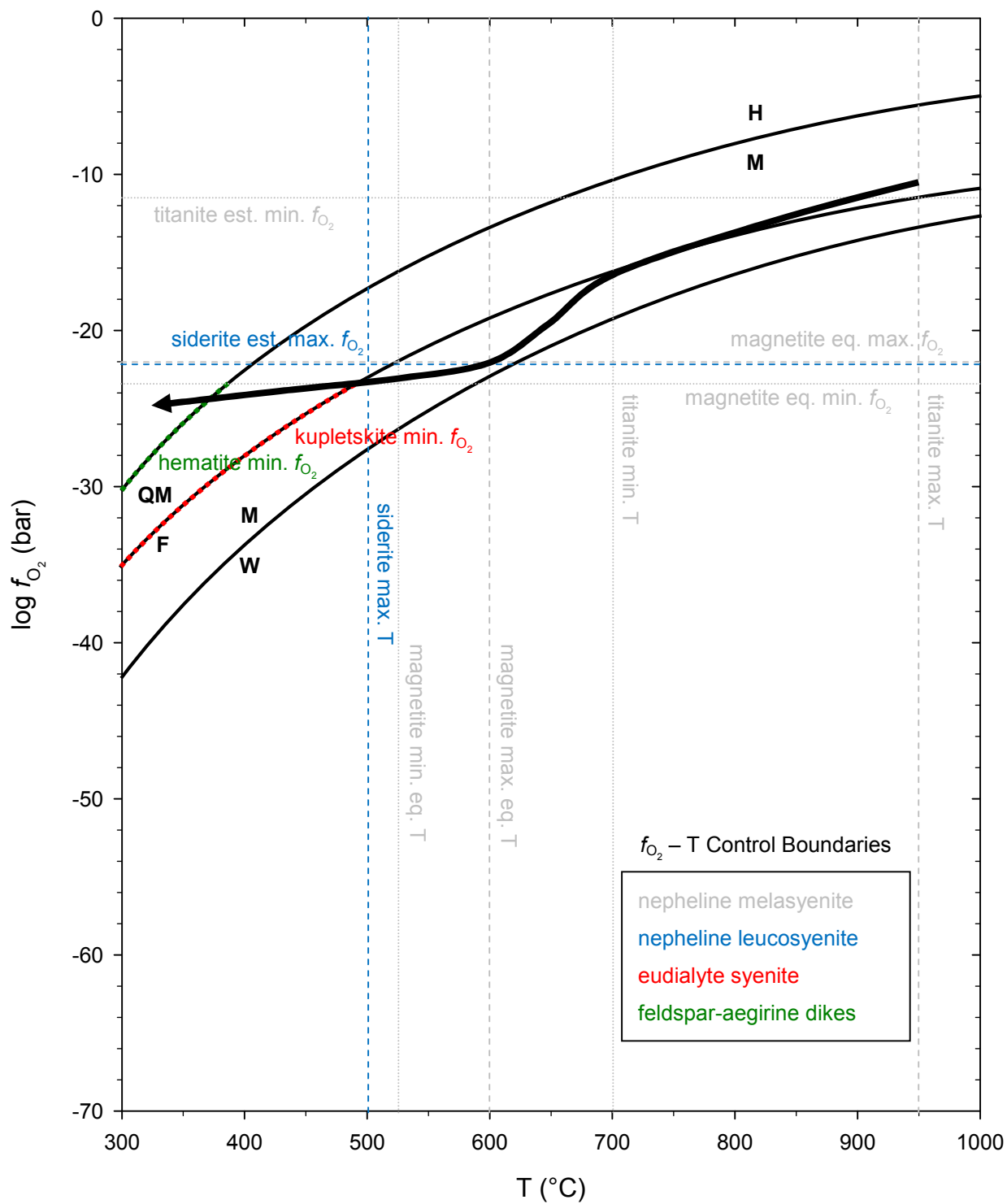


FIGURE 135 – Estimated oxygen fugacity *versus* temperature path for the East Hill suite. Upper  $f_{O_2}$  - T control boundaries are dashed; lower boundaries are dotted. Buffers after EUGSTER & WONES (1962).

compositions, but they also clearly point to a continued trend of decreasing oxygen fugacity.

Sphalerite yields an estimated  $f_{\text{O}_2}$  of  $10^{-22}$  bar.

In the Type 2 nepheline leucosyenite, siderite crystallized as a late-stage mineral, only stable below  $500^\circ\text{C}$  and an  $f_{\text{O}_2}$  of  $10^{-22}$  bar (Huebner 1969). Kupletskite also occurs as a late-stage phase in the Types 1 and 3 nepheline leucosyenite, as well as the eudialyte syenite.

Kupletskite defines the lower oxygen fugacity limit for these lithologies, as it decomposes to an aenigmatite group mineral below the QFM buffer. (Marsh 1975)

Crossing back over the QFM buffer demands that the  $f_{\text{O}_2}$  – T path levels out somewhat, although annite geochemistry from the feldspar-aegirine dikes and the annite lamprophyre indicates that oxygen fugacity continued to fall through these lithologies. The appearance of late-stage hematite in the feldspar-aegirine dikes marks the  $f_{\text{O}_2}$  – T path crossing the HM buffer.

### ***Sulfur Fugacity***

The extent of sulfide mineralization in the East Hill suite has been heretofore overlooked, and similarly, so, too, has been the variation in sulfur fugacity in the East Hill suite magma.

Control over the evolution of the  $f_{\text{S}_2}$  – T path was not as strong as over the  $f_{\text{O}_2}$  – T path, mainly due to the lack of sufficient analytical data to utilize sulfur geobarometers. However, the various sulfide mineral assemblages from the East Hill suite at least allow some bracketing of reasonable  $f_{\text{S}_2}$  – T ranges (Figure 136).

Pyrite followed magnetite in the nepheline melasyenite, commencing crystallization along with late-stage magnetite. Pyrite stabilizes below about  $750^\circ\text{C}$  at a maximum sulfur fugacity of approximately  $10^1$  bar. Pyrite coexisting with late-stage magnetite in the nepheline

melasyenite suggests crystallization temperatures from 600 down to 525°C over a possible  $f_{S_2}$  range of  $10^0$  to  $10^{-4}$  bar. (Whitney 1984) Hedenbergite stability relations in the nepheline melasyenite establish an upper limit of sulfur fugacity at  $10^{-0.6}$  bar at 500°C.

Sulfide mineralization in the East Hill suite was largely restricted to oxygen fugacities at or below the QFM buffer. This represents a thermal window between about 800 and 500°C (Figure 135). At emplacement, the East Hill suite magma crystallized a sulfide-free assemblage at a temperature of approximately 1000°C and an  $f_{O_2}$  of about  $10^{-10}$  bar. This corresponds to a maximum sulfur fugacity of  $10^0$  bar (Figure 136); however, due to the lack of sulfide minerals early in the crystallization history, there was no way to fix a firm sulfur fugacity minimum at these temperatures. The  $f_{S_2}$  – T path should enter the pyrite field near the temperature estimate for the onset of pyrite crystallization, 600°C, which corresponds to a sulfur fugacity of about  $10^{-2}$  bar. To reach this point, the path could follow one of two general routes; it could either begin at relatively low  $f_{S_2}$  and then travel to higher sulfur fugacities with cooling (Figure 136, solid path), or it could begin near its maximum and then trace a path of decreasing sulfur fugacity (Figure 136, dotted path).

Petrography reveals that magnetite first crystallized in the absence of sulfides, followed by a magnetite-sulfide association. The decreasing  $f_{S_2}$  path (dotted) enters the pyrrhotite stability field almost immediately after emplacement, which is inconsistent with observations. The increasing  $f_{S_2}$  path (solid) remains in the magnetite field down to about 850°C, which corresponds to oxygen fugacity just above the QFM buffer, consistent with the  $f_{O_2}$  conditions of sulfide mineralization. The initial increase in sulfur fugacity also makes sense in light of the absence of sulfur-bearing phases in the early nepheline melasyenite.





(FIGURE 136) Estimated sulfur fugacity *versus* temperature path for the East Hill suite. Upper  $f_{S_2} - T$  control boundaries are dashed; lower boundaries are dotted. Sulfide and magnetite stability fields after KRETSCHMAR & SCOTT (1976), WHITNEY (1984) & CHOI & YOUM (2000). Dashed-dotted isopleths represent the loci in  $f_{S_2} - T$  space of the magnetite-sulfide boundary at the indicated oxygen fugacities. (data from Whitney 1984) Magmatic  $f_{O_2}$  values as a function of T from FIGURE 135. The po-mt curve crossing these isopleths represents the boundary between the pyrrhotite and magnetite fields for the  $f_{O_2} - T$  path of the East Hill suite magma.

After entering the pyrrhotite field, sulfur fugacity increases with cooling at a lower rate than in the magnetite field, due to extraction of sulfur from the melt. At about 700°C, the  $f_{S_2} - T$  path begins a sharp turn towards lower sulfur fugacity. This corresponds to the sudden drop of oxygen fugacity across the QFM buffer, which allowed the development of abundant sulfide mineralization. Just below 650°C, the path enters the pyrite stability field, permitting the crystallization of pyrite and the transition of pyrrhotite to pyrite.

Once in the pyrite field, the  $f_{S_2} - T$  path is restricted to a route that stays close to the pyrite-pyrrhotite boundary. The presence of chalcopyrite in the eudialyte syenite establishes a maximum sulfur fugacity, as does the presence of arsenopyrite in the nepheline leucosyenite. The path must pass through the py + asp stability field before cooling far below 500°C; this corresponds to the reëmergence of the  $f_{O_2} - T$  path above the QFM buffer and the decline in sulfide mineralization. Sulfur fugacity remains important, however, as this portion of the path represents sulfate mineralization in the form of barite.

## *The Formal Concept of Alkalinity*

### *Overview*

Beginning with the first formal, modern studies of alkaline rocks—in particular, that of USSING (1912)—investigators have made efforts to develop a system of classification. Alkaline rocks, however, do not lend themselves well to categorization by simple modal proportions, in the manner of the Q-A-P-F diagrams of STRECKEISEN (1967). As BOWEN (1956, p. 234) put it, “The alkaline rocks constitute a group that is difficult to mark off sharply from their more abundant sub-alkaline relatives.” Alkaline rocks resist classification by conventional means because of their vast diversity of mineralogy and chemistry. The fundamental reason for this diversity is the broad range of whole-rock alkali metal content. Consequently, alkali metal content and alkaline mineralogy form the basis of the two main approaches to classification.

### *Geochemical Alkalinity*

The term *agpaitic* was originally used by USSING (1912) to refer to the Ilímaussaq complex, Greenland and has come to refer to any particularly alkaline rock. Numerous ratios of various combinations of alkali metals ( $\pm$  femic elements  $\pm$  alkaline earth metals) *versus* aluminum  $\pm$  silicon have been proposed to delineate the several species of alkaline rock. (Sørensen 1974) All of them, however, revolve around the concept of the agpaitic index or coefficient (Sørensen 1974; Khomyakov 1995), defined as,

$$\frac{\text{Na}_2\text{O} + \text{K}_2\text{O}}{\text{Al}_2\text{O}_3} = 1.0$$

in which the variables are the molecular proportions of the three oxides. Alkaline rocks whose bulk rock composition results in a value for the agpaitic index greater than 1.0 are referred to as

agpaitic; those whose agpaitic index is less than 1.0 are referred to as miaskitic. This division serves the same purpose in the alkaline rocks, as does the boundary between alkaline and calc-alkaline rocks in the greater universe of igneous rocks; it defines two broad groups of rocks that exhibit important genetic differences.

Agpaitic rocks are depleted in calcium and magnesium, are enriched in iron (often more so in ferric iron), contain elevated quantities of rare elements (*e.g.* Ce, Nb, Zr), and are characterized, provisionally, with important systematic exceptions (Khomyakov 1995), by a low content of CO<sub>2</sub>. Miaskitic rocks exhibit the opposite character in each of these four criteria (Sørensen 1974) and represent a transition between calc-alkaline and alkaline rocks.

### *Mineralogical Alkalinity*

Alkaline rocks are also be defined by their accessory mineral assemblage. Comparison of bulk rock chemistry with observed mineralogy reveals that particular minerals are typologically associated with particular ranges of agpaicity. SØRENSEN (1974) observed that agpaitic rocks are generally characterized by prominent high-alkali accessory minerals such as eudialyte, whereas miaskitic rocks contain corresponding low-alkali or alkali-free phases such as zircon.

KHOMYAKOV (1995) synthesized the results of his own work and presented a more formal and objective mineralogical basis for establishing agpaicity. His system recognizes the subjective relationship between mineralogy and alkalinity but classifies rocks by establishing an objective measure of mineral alkalinity. The alkalinity modulus,  $K_{\text{alk}}$ , is a gauge of the alkalinity of the chemical environment hosting a given phase and is calculated as,

$$K_{\text{alk}} = 100 \times \frac{x}{x + y + p}$$

from examination of the general formula of accessory amphoteric silicates,  $A_xM_ySi_pO_q$ , in which A = alkali metals, such as Na, and M = rare elements, such as Zr.

The alkalinity modulus defines five divisions of alkaline rocks based on the predominant agpaicity of their accessory minerals. As with the system of SØRENSEN (1974), miaskitic minerals (and rocks) are their own indivisible category, but agpaitic minerals are subdivided into four groups (Table 57). It is significant to mention, that KHOMYAKOV (1995) does not exclude secondary minerals from this scheme. Whereas the initial petrologic definitions for the rocks of this study were based, inasmuch as was feasible, on primary mineralogy, KHOMYAKOV (1995) rightly implies that the secondary minerals say as much about the ultimate chemical environment.

TABLE 57 – Mineralogical alkalinity & characteristic mineral assemblages (Khomyakov 1995)

<b>Agpaitic</b>	<i>Selected Characteristic Accessory Minerals</i>	<i>Selected Characteristic Rock-Forming Minerals</i>
hyperagpaitic $K_{alk} > 40\%$	olympite, vuonnemite, zirsinalite	<i>hackmanite</i> , riebeckite
highly agpaitic $35 < K_{alk} < 40\%$	astrophyllite, eudialyte, keldyshite	aegirine, analcime, sodalite
medium-agpaitic $25 < K_{alk} < 35\%$	gaidonnayite, hilairite, titanite	aegirine, arfvedsonite, nepheline
low agpaitic $15 < K_{alk} < 25\%$	lāvenite, pyrochlore, zircon	augite, katophorite, cancrinite
<b>Miaskitic</b>	<i>Selected Characteristic Accessory Minerals</i>	<i>Selected Characteristic Rock-Forming Minerals</i>
miaskitic $K_{alk} \leq 15\%$	allanite, fluorite, calcite	augite, hastingsite, albite

### *Geochemical Alkalinity of the East Hill Suite*

Calculated agpaitic indices (AI) for the East Hill Suite reveal both miaskitic and agpaitic lithologies (Figure 137). Although it occupies most of the volume of the East Hill suite, the nepheline melasyenite is the sole miaskitic rock, with AI = 0.79. The nepheline leucosyenites are much more alkaline than the other agpaitic lithologies, with AI = 1.43, 1.64, and 1.32 for Types 1, 2, and 3, respectively. The eudialyte syenite, feldspar-aegirine dikes, and annite lamprophyre are more moderately alkaline, with respective AI values of 1.16, 1.16, and 1.17.

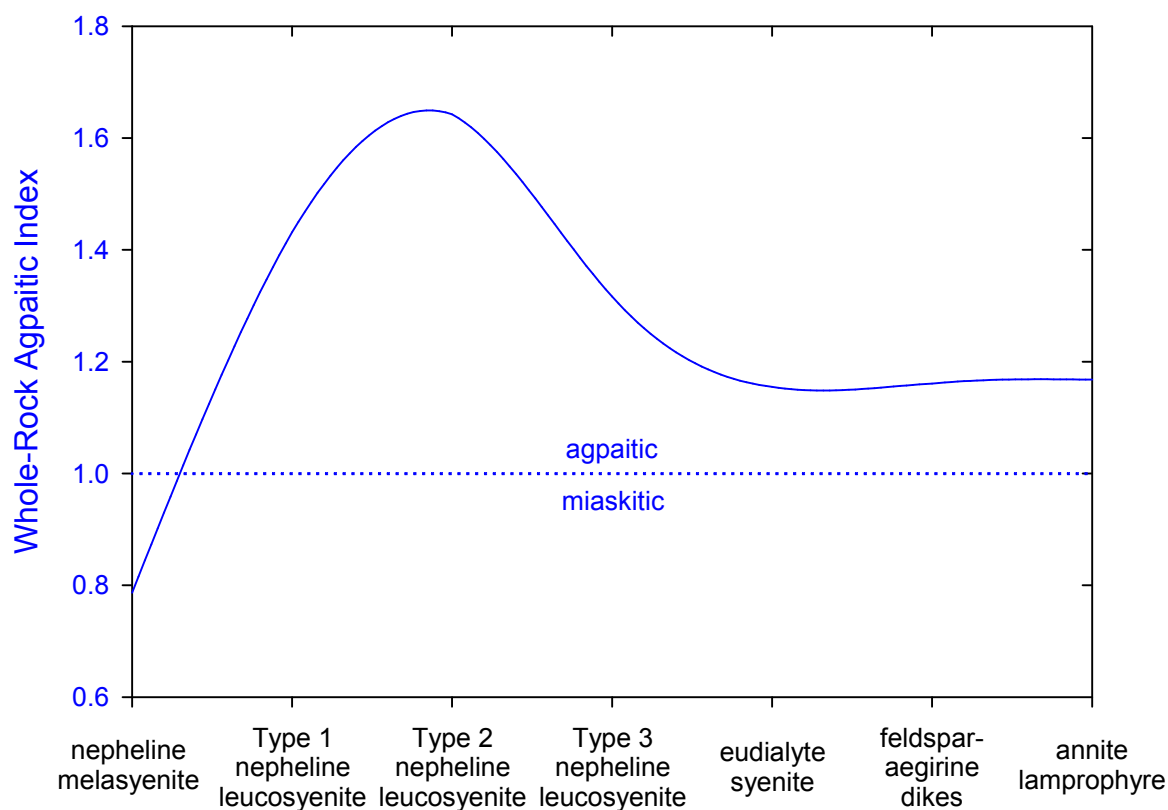


FIGURE 137 – Whole-rock agpaitic indices – East Hill suite

The plot of AI values takes the general form of a skewed bell curve. At first glance, it appears that the rock types are listed out of genetic order. Intuition suggests that agpaiticity

should continuously increase with magmatic evolution; in terms of a plot, it should appear as a more or less straight line or as a polynomial curve, either of which would have a positive slope.

The AI curve, however, does not follow this expected trend. The latter portion of it has a variously negative slope, and AI values reach a maximum before even the middle of the sequence. Prior to calculation of agpaitic indices, the lithologies were put in a sequence meant to represent their deduced order of crystallization, based on field relationships, geochemical data, and mineralogical observations. Considering this sound foundation for the original sequence, what could explain the resultant pattern of alkalinity?

KHOMYAKOV (1995) describes a phenomenon observed in pegmatites in the Khibina and Lovozero massifs that he refers to as the “alkalinity wave.” The concept of the alkalinity wave is that maximum alkalinity occurs in rocks formed during an intermediate stage of crystallization. The earliest- and latest-formed lithologies will be less agpaitic, if not miaskitic. The phenomenon is attributed to a build-up of alkali- and rare-element-rich mineralizing fluids that reaches its maximum influence during the middle of the sequence of crystallization.

The build-up of fluid is initiated by the formation of anhydrous phases in early stages of crystallization and peaks during some intermediate stage. KHOMYAKOV (1995) suggests that the alkalinity of this fluid is governed by the acid-base behavior resulting from temperature variation. At high temperature, normally-strong acids do not dissociate to nearly the degree seen at room temperature; thus, they behave as weak acids, and the melt is dominated by strong bases that are left unneutralized. With falling temperature, strong acids are permitted to dissociate more freely, neutralizing strong bases, and lowering the alkalinity of the melt.

This phenomenon, or at least the geochemical trappings thereof, appears to exist in the East Hill Suite, as well. Rock types that are clearly intermediate in terms of their crystallization

sequence, the nepheline leucosyenites, exhibit the highest degrees of agpaicity in the suite. The latest-formed rock types, the eudialyte syenite, the feldspar-aegirine dikes, and the annite lamprophyre, are much less agpaitic; and the earliest, the nepheline melasyenite, is, in fact, miaskitic. This suggests that alkali-rich fluids were active in the East Hill Suite, and that these fluids caused an enhancement of the agpaicity of the nepheline leucosyenites.

The alkalinity wave observed in the East Hill Suite is a large-scale phenomenon, whereas KHOMYAKOV (1995) describes the alkalinity wave as a characteristic of agpaitic pegmatites. Furthermore, all known references from the literature that refer to the alkalinity wave (*e.g.* Fersman 1937, 1958; Semenov 1972; Kogarko 1977; Borutsky *et al.* 1980; Pekov 1995) invoke it as a phenomenon that characterizes the transition of bulk-rock chemistry in the cadre and on the scale of pegmatites. This study of the East Hill Suite at Mont Saint-Hilaire may represent the first description of this phenomenon on the scale of an entire intrusive sequence.

### ***Mineralogical Alkalinity of the East Hill Suite***

#### *Overview*

Consistent with the data from agpaitic indices, from a mineralogical standpoint, the nepheline melasyenite is dominantly miaskitic, whereas the other lithologies are dominantly agpaitic (Table 58). Interestingly, cancrinite, natrolite, nepheline, and sodalite, while agpaitic minerals, are present in the nepheline melasyenite. Similarly, calcite, a miaskitic mineral, is present in all of the agpaitic rock types<sup>7</sup>, but it is not present in the one miaskitic lithology.

---

<sup>7</sup> This situation with calcite is, in fact, the exact opposite of the long-running view on its occurrence in alkaline rocks. HEINRICH (1966, p. 18) goes so far as to say, “Agpaitic rocks contain very little CO<sub>2</sub>, and accessory calcite is *absent* [italics added].” This has clearly been proven to be somewhat inaccurate, in that KHOMYAKOV (1995) reports calcite in more than minor quantities as a postmagmatic mineral from the Khibina massif, and calcite occurs, of course, in agpaitic rocks at Mont Saint-Hilaire.



TABLE 58 – Characteristic mineral assemblages – East Hill suite

	<i>nepheline melasyenite</i>	<i>nepheline leucosyenite (all Types)</i>	<i>eudialyte syenite</i>	<i>feldspar- aegirine dikes</i>	<i>annite lamprophyre</i>
<b>alumino- silicates</b>	<b>alkali feldspar</b> <i>cancrinite</i> <i>natrolite</i> <b>nepheline</b> <i>sodalite</i>	<b>alkali feldspar</b> <i>cancrinite</i> <i>natrolite</i> <i>nepheline</i> <b>sodalite</b>	<b>alkali feldspar</b> <b>natrolite</b> <b>sodalite</b>	<b>alkali feldspar</b>	<b>natrolite</b>
<b>amphibole group</b>	<b>hastingsite</b>	<i>arfvedsonite</i>	ferro- eckermannite	–	<i>riebeckite</i>
<b>pyroxene group</b>	<b>augite</b> <i>titanaugite</i>	<b>aegirine</b>	<b>aegirine</b>	<b>aegirine</b>	aegirine
<b>zircono-/ titano- silicates</b>	<i>ilmenite</i> titanite	<i>kupletskite</i> <i>pyrochlore</i> <i>zircon</i>	<i>catapleiite</i> eudialyte <i>gaidonnayite</i> <i>pyrochlore</i>	<i>pyrochlore</i>	<i>gaidonnayite</i> <i>petarasite</i> <i>pyrochlore</i>
<b>other minerals</b>	fluorapatite <i>magnetite</i>	<i>calcite</i> <i>fluorapatite</i>	<i>calcite</i> <i>fluorapatite</i>	<i>calcite</i>	<b>annite</b> <i>calcite</i> <b>fluorapatite</b>
<b>Major Minerals</b> , Minor Minerals, <i>Trace &amp; Rare Minerals</i> <i>Agpaitic Minerals</i> , <i>Miaskitic Minerals</i> , Unaffiliated Minerals Mineral affinities compiled from HEINRICH (1966), SØRENSEN (1974) & KHOMYAKOV (1995)					

Some factor causes this unexpected distribution of minerals. It is possible that the fundamental magmatic chemistry of the East Hill Suite is anomalous, in terms of agpaitic intrusive suites. This is probably at least partly true, in that calcite appears to be a primary, magmatic phase in some occurrences, even in the more evolved lithologies. A unique magma composition, however, does not explain all of the discrepancies. In particular, most of the minerals that are found outside of their expected agpaitic range occur as secondary minerals, suggesting a non-magmatic influence. The most obvious possibility, in terms of the compositions and modes of occurrence of these secondary phases, is the action of alkaline fluids, during or following crystallization.

## Pyroxene Alkalinity

Average alkalinity moduli,  $K_{\text{alk}}$ , were calculated for pyroxene group minerals from each lithology of the East Hill Suite (Figure 138). These range from a low of 8.33 for the nepheline melasyenite to a high of 23.43 for the annite lamprophyre. It is obvious from a brief examination of FIGURE 138, however, that the values are not evenly spread across this range. They rise sharply from that of the nepheline melasyenite and plateau to nearly constant values for the remaining lithologies. Clinopyroxene has a mathematical maximum  $K_{\text{alk}}$  value of 25.0, which represents pure end-member aegirine; thus, it is not possible for any clinopyroxene  $K_{\text{alk}}$  to be much more agpaitic than those represented in the more evolved lithologies of the East Hill Suite.

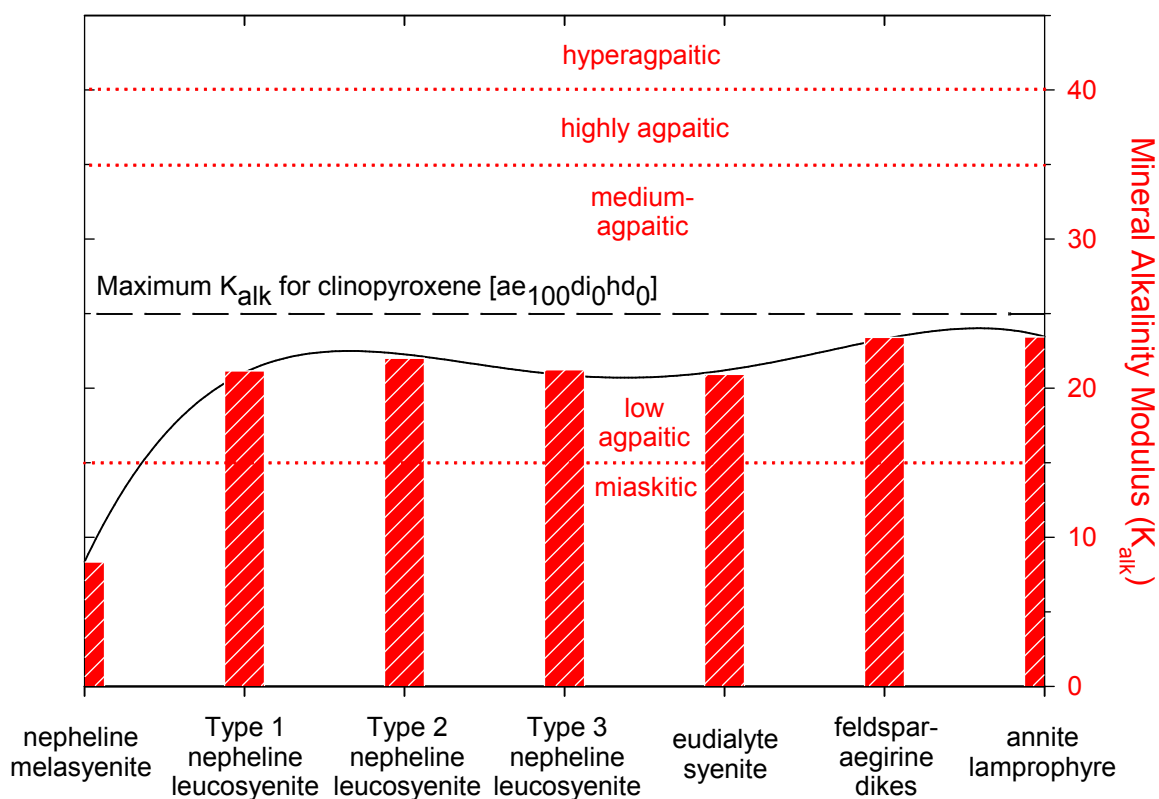


FIGURE 138 – Alkalinity moduli of pyroxene group minerals – East Hill suite

The results of the clinopyroxene alkalinity moduli calculations were then superposed on the agpaicity indices for the several lithologies of the suite (Figure 139). Here, something interesting reveals itself. There is good agreement between clinopyroxene alkalinity and whole-rock agpaicity for the nepheline melasyenite, the eudialyte syenite, the feldspar-aegirine dikes, and the annite lamprophyre, but there is a significant disparity between these measurements for the three nepheline leucosyenites. In fact, not only is the agreement between AI and  $K_{alk}$  better for the other lithologies, but their AI values plot lower, in every case, than their average clinopyroxene  $K_{alk}$  values. On the other hand, the AI for the nepheline leucosyenites plots substantially higher than the  $K_{alk}$  for their clinopyroxenes.

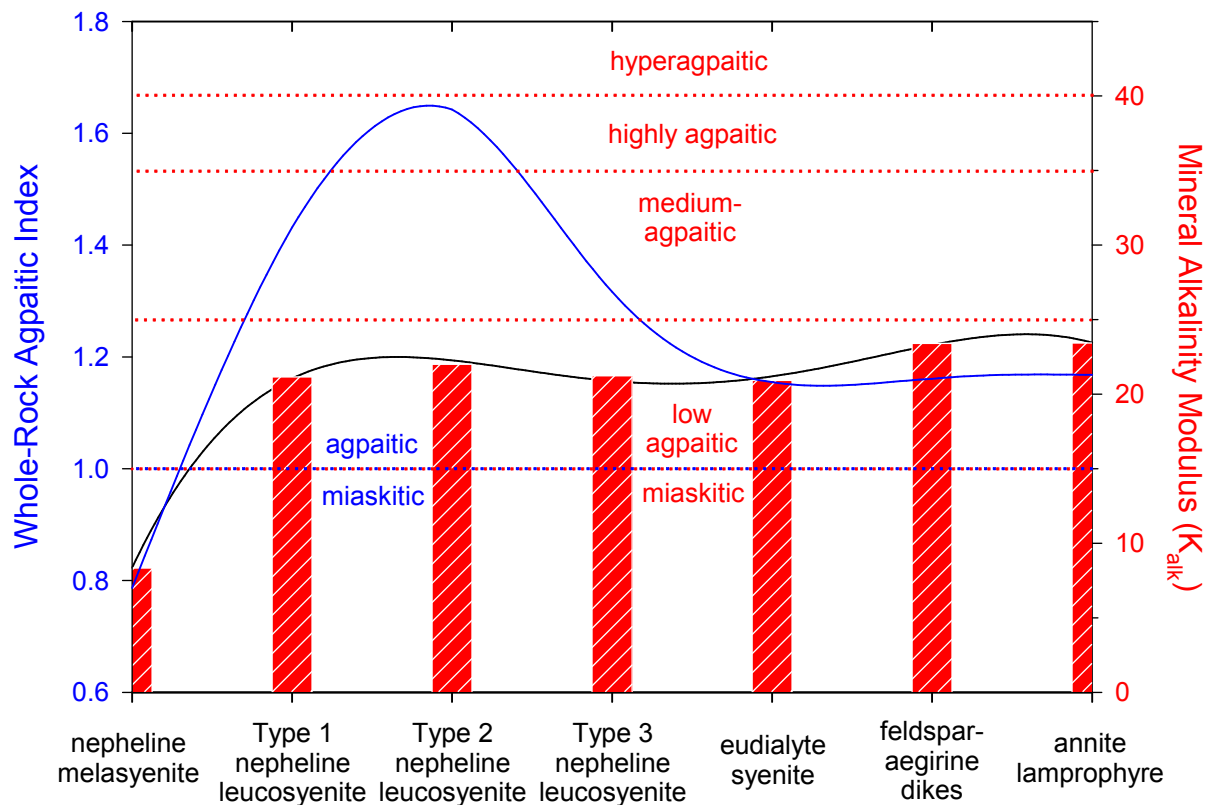


FIGURE 139 – Pyroxene alkalinity moduli compared with whole-rock agpaicity indices – East Hill suite

To phrase it a different way, the clinopyroxene from the nepheline leucosyenites is less alkaline than the rock, as a whole, whereas the clinopyroxene for the remaining lithologies is more alkaline than the rock, as a whole. More particularly, however, the clinopyroxene from the nepheline leucosyenites is, on average, less alkaline than the average from the other more-evolved lithologies (eudialyte syenite, feldspar-aegirine dikes, and annite lamprophyre), even though the nepheline leucosyenites are much more agpaite than these other lithologies.

All of this preceding analysis of clinopyroxene chemistry is, of course, run on the assumption that purely magmatic processes are in play. Although  $K_{alk}$  can never be higher than 25.0 for clinopyroxene, AI values for the nepheline leucosyenites should correlate, at least proportionally, with clinopyroxene  $K_{alk}$  values. So the clinopyroxene from the nepheline leucosyenites should have the highest average  $K_{alk}$  in the East Hill Suite, solely considering the action of magmatic evolution. As it does not, this, too, suggests that another mechanism is at work that has influenced the whole-rock chemistry of the East Hill Suite. Again, invoking alkaline fluids could account for the anomalous agpaite geochemistry.

## EVIDENCE FOR & BEHAVIOR OF ALKALINE FLUIDS

### *Introduction*

An analysis of the whole-rock agpaicity and the mineralogical alkalinity of lithologies in the East Hill Suite from this study suggests that several rock types were subjected to mineral reactions mediated by alkali-rich fluids. This suggestion is in concert with the concept of the alkalinity wave of KHOMYAKOV (1995). Alkaline fluids have played a role in other alkaline complexes, for example the Strange Lake complex, Labrador-Québec border (Salvi & Williams-Jones 1990) and Ilímaussaq, Greenland. At Ilímaussaq, Na- and Cl-rich fluids were involved in

late-stage hydrothermal mineralization and replacement reactions. (Markl & Baumgartner 2002)

In contrast, the Strange Lake magma is interpreted to have interacted with Ca-rich fluids, causing Ca-metasomatism, followed by low-salinity fluids that diluted and removed fluorine from the system, destabilizing rare-element complexes and causing rare-element mineralization. (Salvi & Williams-Jones 1990) Alkaline brine has been invoked to explain the abundance of sodalite in the East Hill suite (Currie *et al.* 1986); although there is no objection to the presence of alkaline fluids, there are mechanistic issues with their theory.

In addition to the patterns of geochemical and mineralogical alkalinity, there is ample mineralogical evidence that alkali-rich fluids also had a strong influence on the geochemistry and mineralogy of the East Hill Suite:

- 1) albitization of K-feldspar
- 2) corrosion of alkali feldspar, especially K-rich crystals
- 3) ubiquitous alteration of nepheline to form sodalite
- 4) alteration of nepheline to form cancrinite
- 5) subsequent alteration of sodalite to form natrolite
- 6) subsequent alteration of natrolite to form dawsonite
- 7) crystallization of siderite in void space following dawsonite
- 8) crystallization of rhodochrosite
- 9) late-stage alkali zirconosilicate mineralization
- 10) possible alteration of melilite to form natrolite + calcite

Furthermore, systematic variation in the nature of fluid-mediated mineralization points towards significant changes in fluid chemistry and the geochemical environment over time.

## ***Nepheline Alteration Reactions***

### *Nepheline → Sodalite*

CURRIE *ET AL.* (1986) propose the interaction of the East Hill suite magma with a Na- and Cl-rich brine to account for the general alkalinity of the suite and the abundance of sodalite. They suggest that the magma assimilated the brine, driving the crystallization of primary sodalite. Most sodalite in the East Hill suite, however, is subsolidus and secondary after nepheline. Upon initial examination, the Type 1 nepheline leucosyenite and eudialyte syenite appear to contain phenocrystic nepheline. Examination with the petrographic microscope and EDS analysis reveal, however, that over 90% of the nepheline in these rock types has been converted to colorless pseudomorphs of sodalite. This alteration is more obvious in the Type 2 and 3 nepheline leucosyenites, in which occur blue sodalite pseudomorphs after nepheline and purple *hackmanite* pseudomorphs after nepheline, respectively. In all cases, alteration proceeded from rim to core and, in some cases, was obviously fracture-controlled. This is consistent with a fluid-mediated reaction.

The alteration of nepheline to sodalite in the Type 1 nepheline leucosyenite is ideally effected as follows:

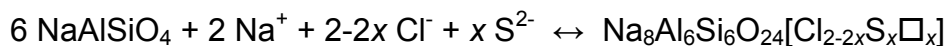


The product of this reaction is end-member sodalite, which is colorless. In reality, nepheline contains varying amounts of potassium:



which results in the release of potassium into the system. This may be a factor in the late-stage crystallization of astrophyllite group minerals.

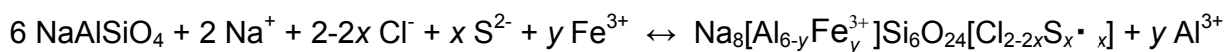
In the Type 2 nepheline leucosyenite, small quantities of sulfur may be inferred to have participated in the reaction; again, considering an ideal nepheline composition:



This inference arises from the blue color of the sodalite in the Type 2 nepheline leucosyenite.

Chemically, sodalite is a member of a class of compounds called ultramarines. In the ultramarines, sulfur radical anions act as chromophores; in particular, in sodalite,  $\text{S}_3^\cdot$  radicals produce the striking blue color that is familiarly associated with sodalite, although  $\text{S}_2^\cdot$  radicals, which are responsible for yellow coloration, are present in subordinate amounts. Experimental evidence suggests that up to about 40% of the anionic cage sites in the sodalite structure may be occupied by  $\text{S}_3^\cdot$  radicals, and that these radicals are supplied and replenished, if necessary, from a reservoir of  $\text{S}^{2-}$  anions. (Gobeltz-Hauteccœur *et al.* 2002)

*Hackmanite*, in the Type 3 nepheline leucosyenite, follows a similar reaction:



Notice the incorporation of iron. This follows the scheme proposed by PETERSON (1983) to account for the unusual photochromic behavior of *hackmanite*, and is supported by microprobe analyses of *hackmanite* by TICE (1995). Sulfur radical anions play a role in the color of *hackmanite*, as well. Photochromic behavior aside, the persistent reddish-purple color of *hackmanite* is probably due to a combination of  $\text{S}_3^\cdot$  and  $\text{S}_2^\cdot$  radicals, in combination with either  $\text{S}_4^\cdot$  or  $\text{S}_4^0$ , each of which produces a red color. (Clark & Cobbold 1978; Gobeltz-Hauteccœur *et al.* 2002)

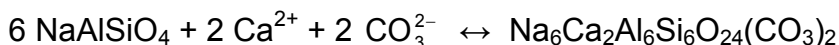
Note that although sulfur radicals may theoretically occupy a large proportion of anionic sites, very little sulfur, perhaps on the order of a few mole percent, is necessary to cause the transition to blue sodalite or *hackmanite*. Sodalite analyses from CURRIE *ET AL.* (1986), TICE

(1995), and this study were nearly sulfur-free. Low-S sodalite, however, doesn't necessarily indicate low-S or high-Cl brines, although there most certainly were brines. The lack of S in sodalite is due to scavenging by chalcophile elements, as revealed by the abundance of microsulfides.

Subtleties of sulfur chemistry aside, a common thread runs through each of these alteration processes, reaction of a sodium chloride-rich fluid with nepheline to form sodalite. Such reactions cause a greater proportional reduction in Cl content in the fluid than Na, thus increasing the Na/Cl ratio. An increase in Na/Cl results in a concomitant increase in pH due to an increase in the concentration of NaOH in the fluid. (Markl & Baumgartner 2002)

#### *Nepheline → Cancrinite*

Some nepheline in the nepheline melasyenite, as well as a very little in the nepheline leucosyenite, also altered to cancrinite:



Petrography and other mineral reactions suggest that the cancrinite reaction was subsequent to the sodalite reaction, reflecting a change in fluid chemistry.

#### *Sodalite → Natrolite*

Following conversion of nepheline to sodalite, some of this secondary sodalite was affected by hydrothermal fluids. White reaction rims of natrolite appear on pristine sodalite cores, along fractures, and lining cavities in sodalite pseudomorphs; some crystals are complete pseudomorphs of natrolite after sodalite. This is according to the following reaction:

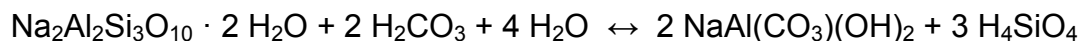




The formation of natrolite at the expense of sodalite or nepheline is favored by acidic conditions or by an increase in  $a_{\text{SiO}_2}$  in hydrothermal fluids. (Eitel 1964; Seyfried & Janecky 1985) Since the chlorination reaction that forms sodalite resulted in a decrease in the acidity of the alkaline fluids, natrolite crystallization probably indicates an increase in silica.

*Natrolite → Dawsonite & Late Carbonates*

Natrolite was followed by dawsonite in the sodalite pseudomorph reaction zones, according to the reaction:



As with the sodalite to natrolite reaction, the previous reactant is expelled; there, chloride exchanged for silica and, here, silica for carbonate. As the fluid chemistry changed, it became depleted in the earlier substance and enriched in the new. This favored partial dissolution of the last mineral formed and deposition of a new phase.

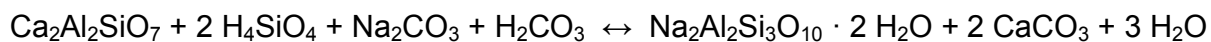
The increase in fluid carbonate concentration is also reflected in the crystallization of siderite within voids in the sodalite-natrolite-dawsonite reaction zones and the crystallization of rhodochrosite in miarolitic cavities and the annite lamprophyre. Crystallization of rhodochrosite may also indicate the development of more reducing conditions in the fluids. Under these circumstances, control of Mn mineralization shifts from increasingly soluble sulfides to carbonates. Iron sulfides are not so affected, however; so, the appearance of siderite must be due to increased carbonate activity. (Maynard 2003)

### ***Zirconosilicate Mineralization***

The East Hill suite is characterized by relatively abundant late-stage zirconosilicate mineralization, from the eudialyte syenite through the annite lamprophyre. Summarizing the previous discussion of zirconosilicate crystallization, Zr remained variably soluble in the melt as crystallization of the suite proceeded. The lack of Cl-bearing phases early in the East Hill suite increased the Cl content of the system, contributing to the decrease in the solubility of Zr (Marr *et al.* 1998) and promoting zirconosilicate mineralization. Alkali halide complexes probably played a role in this process, as well as in the nepheline-sodalite paragenesis. Nearly all East Hill sodalite, is subsolidus, secondary after nepheline, which means that the Cl was isolated until late in the crystallization history.

### ***Melilite Alteration***

The lamprophyre in the East Hill suite resembles an alnøite in all important respects except for the groundmass. The annite lamprophyre exhibits a natrolite-calcite groundmass, whereas alnøite *sensu stricto* is characterized by a melilite groundmass. Reaction of a silica- and carbonate-enriched fluid with melilite allows for the development of a natrolite-calcite assemblage according to the reaction:



Later stages of fluid evolution in the East Hill suite were marked by a transition from silica to carbonate chemistry. It is possible that the annite lamprophyre was originally an alnøite that took on its current assemblage due to alkaline fluid alteration.

## CONCLUSIONS

The East Hill suite comprises a series of miaskitic and agpaitic syenites that are genetically related by fractionation, as well as a lamprophyric unit that may represent its own pulse of magma. The first lithology to crystallize, the nepheline melasyenite, does not represent a substantial departure from the gabbroic rocks of the two precedent suites at Mont Saint-Hilaire and is rather primitive in comparison to the remaining rock types. Most lithologies are not especially silica-deficient; rather, they derive their typical alkaline mineralogy from high alkali content. The whole-rock alkaline profile of the suite was altered by the action of late-stage, Na-rich fluids that reversed more potassic unaltered chemistries, resulting in strongly Na-rich rocks. Due to their high nepheline content, the nepheline leucosyenites were startlingly enriched in alkalis even prior to the influence of these fluids. Whole-rock trace element geochemistry is dominated by Zr, Ce, and Y; however remarkable enrichments in Zn highlight a general enrichment in several chalcophile elements, notably Pb. Chlorine content is elevated, and so, too, is that of sulfur.

The mineralogy of the East Hill suite is characterized by transitions from calcium- to sodium-rich analogues of amphiboles, pyroxenes, titanosilicates, and zirconosilicates. Opaque minerals grade somewhat suddenly from an early oxide-dominant assemblage to a diffuse but pervasive presence of microsulfides throughout the remainder of the suite. Carbonates and sulfates became important closer to the end of crystallization.

Amphibole, iron-titanium oxide, titanite, and annite geochemistry outline a more complex oxygen fugacity history than previously recognized. The East Hill suite began crystallizing above the QFM buffer, precipitously fell below QFM and skirted MW before not only emerging above QFM but also above HM at the end of crystallization. Notably, this curve

represents a continuous decline in oxygen fugacity, which contradicts both intuition and previous suggestions that the rising dominance of aegirine was due to oxidation of pyroxene ferrous iron due to increasing oxygen fugacity. On the contrary, the rise of aegirine is a consequence of the increasing alkalinity of the melt. Unlike oxygen fugacity, sulfur fugacity initially rose before favorable oxidation conditions contributed to widespread microsulfide crystallization, which then drove a decline in sulfur fugacity with cooling.

Evidence suggests that previous statements regarding the presence of a NaCl-rich brine at Mont Saint-Hilaire are correct to the extent that they were present; however, the action of these brines has been shown to be quite different. Rather than being assimilated wholesale by the intruding magma and generating primary sodalite, chloride was isolated, probably as melt complexes, and only allowed to become reactive in the system in late-stage fluids that extensively altered nepheline to sodalite. These fluids exhibited systematic changes in chemistry, proceeding from chloride-rich, to silica- and then carbonate-rich, and left their mark on the suite in the form of numerous successions of and individual secondary phases.

Two issues have been avoided in this study, petrogenesis of the East Hill suite magma and the source of the alkaline fluids. These are neither settled questions nor are they unimportant; rather, they are beyond the scope of this work. They are, in particular, very important questions, and there has been no shortage of speculation and research on either subject. This study has revealed new information about the geochemistry of the East Hill suite magma and alkaline fluids that may help address the origins of this fascinating complex.

## REFERENCES

- AHRENS, L.H., PINSON, W.H. & KEARNS, M.M. (1952): Association of rubidium and potassium and their abundance in common igneous rocks and meteorites. *Geochimica et Cosmochimica Acta* **2**, 229-242.
- AIUPPA, A., ALLARD, P., D'ALESSANDRO, W., MICHEL, A., PARELLO, F., TREUIL, M. & VALENZA, M. (2000): Mobility of major, minor and trace metals during basalt weathering and groundwater transport at Mt. Etna volcano (Sicily). *Geochimica et Cosmochimica Acta* **64**, 1827-1841.
- AL'MYASHEVA, O.V., KORYTKOVA, E.N., MASLOV, A.V. & GUSAROV, V.V. (2005): Preparation of nanocrystalline alumina under hydrothermal conditions. *Inorganic Materials* **41**, 460-467.
- ANDERSEN, T. & SØRENSEN, H. (1993): Crystallization and metasomatism of nepheline syenite xenoliths in quartz-bearing intrusive rocks in the Permian Oslo rift, SE Norway. *Norsk Geologisk Tidsskrift* **73**, 250-266.
- ANDERSON, J.G. (1974): The Geology of Alángorssuaq, northern Nunarssuit complex, South Greenland. Ph.D. Thesis, University of Aberdeen, Aberdeen, United Kingdom.
- ANTHONY, J.W., BIDEAUX, R.A., BLADH, K.W. & NICHOLS, M.C. (2003): Handbook of Mineralogy, Volume V: Borates, Carbonates, Sulfates. Mineral Data Publishing, Tucson, Arizona.
- AOKI, K. (1964): Clinopyroxenes from alkaline rocks of Japan. *American Mineralogist* **49**, 1199-1223.
- APTED, M.J. & LIOU, J.G. (1983): Phase relations among greenschist, epidote-amphibolite, and amphibolite in a basaltic system. *American Journal of Science* **283A**, 328-353.
- ARMSTRONG, J. & BARNETT, R. (2003): The association of Zn-chromite with diamondiferous lamprophyres and diamonds: unique compositions as guide of the diamond potential of non-traditional diamond host rocks. *Extended Abstracts, 8<sup>th</sup> International Kimberlite Conference* **FLA 230**.
- ARZAMASTSEV, A.A., BEA, F., GLAZNEV, V.N., ARZAMASTSEVA, L.V. & MONTERO, P. (2001): Kola alkaline province in the Paleozoic: Evaluation of primary mantle magma composition and magma generation conditions. *Russian Journal of Earth Sciences* **3**, 1-32.
- \_\_\_\_\_, IVANOVA, T.N. & KOROBEINIKOV, A.N. (1987): Petrology of ijolite-urtite series of the Khibina alkaline massif and apatite-nepheline mineralization. Nauka, Leningrad.

- \_\_\_\_\_, YAKOVENCHUK, V., PAKHOMOVSKY, Y. & IVANYUK, G. (2008): The Khibina and Lovozero alkaline massifs: Geology and unique mineralization. 33 *International Geological Congress, Field Trip Guidebook Excursion 47*.
- BACK, M., GAULT, R. & RAMIK, R. (2006): Mont Saint-Hilaire Official Species List. (June 18, 2009) <http://www.saint-hilaire.ca/main/mindescr.htm>
- BAILEY, D.K. (1969): The stability of acmite in the presence of H<sub>2</sub>O. *American Journal of Science* **267-A**, 1-16.
- BAILEY, J.C., GWOZDZ, R., ROSE-HANSEN, J. & SØRENSEN, H. (2001): Geochemical overview of the Ilímaussaq alkaline complex, South Greenland. In *The Ilímaussaq alkaline complex, South Greenland: status of mineralogical research with new results*, H. Sørensen (ed.), *Geology of Greenland Survey Bulletin* **190**, 55-64.
- BANKS, N.G. (1982): Sulfur and copper in magma and rocks: Ray porphyry copper deposit, Pinal County, Arizona. In *Advances in Geology of Porphyry Copper Deposits, Southwestern North America*, S.R. Titley (ed.), University of Arizona Press, Tucson, Arizona, 227-257.
- BARKOV, A.Y., MARTIN, R.F., POIRIER, G. & MEN'SHIKOV, Y.P. (2000): Zoned tungstenian molybdenite from a fenitized megacryst in the Khibina alkaline complex, Kola Peninsula, Russia. *Canadian Mineralogist* **38**, 1377-1385.
- BARTON, J.C., TAYLOR, L.A. & CHOU, I.-M. (1982): The  $f_{O_2}$  – T and  $f_{S_2}$  – T stability relations of hedenbergite and hedenbergite-johannsenite solid solutions. *Economic Geology* **77**, 764-783.
- BARTON, P.B. & TOULMIN, P. (1966): Phase relations involving sphalerite in the Fe-Zn-S system. *Economic Geology* **61**, 815-849.
- BATES, R.L. & JACKSON, J.A. (eds.) (1980): *Glossary of Geology*. 2<sup>nd</sup> Edition. American Geological Institute, Falls Church, Virginia.
- BAU, M. (1996): Controls on the fractionation of isovalent trace elements in magmatic and aqueous systems: evidence from Y/Ho, Zr/Hf, and lanthanide tetrad effect. *Contributions to Mineralogy and Petrology* **123**, 323-333.
- BÉDARD, J.H.J. (1985): La pétrogenèse et les mécanismes de différenciation des magmas anorogéniques: exemples de la Gaspésie, de la Nouvelle-Angleterre et des Collines Montérégiennes. Doctoral Dissertation, Université de Montréal, Montréal, Québec, Canada.
- \_\_\_\_\_. (1988): Comparative amphibole chemistry of the Monteregian and White Mountain alkaline suites, and the origin of amphibole megacrysts in alkali basalts and lamprophyres. *Mineralogical Magazine* **52**, 91-103.

- BOL, L.C.G.M., ARIEJAN, B., SAUTER, P.C.C. & JANSEN, J.B.H. (1989): Barium-titanium-rich phlogopites in marbles from Rogaland, southwest Norway. *American Mineralogist* **74**, 439-447.
- BORUTSKY, B.E., ZABAVNIKOVA, N.I. & SOKOLOVA, M.N. (1980): The types of mineral associations as indicators of basicity of the mineral-forming medium of rocks of the alkaline complex. In *Geokhimiya. Mineralogiya: Mezhdunarodnyi geologicheskii congress, XXVI sessiya: Doklady sovetskikh geologov*, F.V. Chukrov & V.L. Barsukov (eds.), Nauka, Moscow, 191-199.
- BOWDEN, P. (1964): Gallium in younger granites of northern Nigeria. *Geochimica et Cosmochimica Acta* **28**, 1981-1988.
- BOWEN, N.L. (1956): *The Evolution of the Igneous Rocks*. Reprint of 1<sup>st</sup> Edition (1928). Dover Publications, Inc., New York.
- \_\_\_\_\_ & TUTTLE, O.F. (1950): The system  $\text{NaAlSi}_3\text{O}_8\text{--KAlSi}_3\text{O}_8\text{--H}_2\text{O}$ . *The Journal of Geology* **58**, 489-511.
- BROOKS, C.K. (1968): On the interpretation of trends in element ratios in differentiated igneous rocks, with particular reference to strontium and calcium. *Chemical Geology* **3**, 15-20.
- BURT, D.M. (1972): Mineralogy and geochemistry of Ca-Fe-Si skarn deposits. Ph.D. Thesis, Harvard University, Cambridge, Massachusetts.
- CANADIAN MINERALOGIST (2009): Search articles "hilaire". (June 18, 2009)  
<http://www.canmin.org/search.dtl>
- CARMICHAEL, I.S.E. & NICHOLLS, J. (1967): Iron-titanium oxides and oxygen fugacities in volcanic rocks. *Journal of Geophysical Research* **72**, 4665-4687.
- CARROLL, M.R. & RUTHERFORD, M.J. (1988): Sulfur speciation in hydrous experimental glasses of varying oxidation state: Results from measured wavelength shifts of sulfur X-rays. *American Mineralogist* **73**, 845-849.
- CASTET, S., DANDURAND, J.-L., SCHOTT, J. & GOUT, R. (1993): Boehmite solubility and aqueous aluminum speciation in hydrothermal solutions (90-350°C): Experimental study and modeling. *Geochimica et Cosmochimica Acta* **57**, 4869-4884.
- ČERNÝ, P., MEINTZER, R.E. & ANDERSON, A.J. (1985): Extreme fractionation in rare-element granitic pegmatites: selected examples of data and mechanisms. *Canadian Mineralogist* **23**, 381-421.
- \_\_\_\_\_, TRUEMAN, D.L., ZIEHLKE, D.V., GOAD, B.E. & PAUL, B.J. (1981): The Cat Lake – Winnipeg River and the Wekusko Lake pegmatite fields, Manitoba. *Manitoba Mineral Resources Division, Economic Geology Report* **ER80-1**.

- CHAI, L. & NAVROTSKY, A. (1994): Enthalpy of formation of siderite and its application in phase equilibrium calculation. *American Mineralogist* **79**, 921-929.
- CHAKHMOURADIAN, A.R. (2004): Crystal chemistry and paragenesis of compositionally unique (Al-, Fe-, Nb-, and Zr-rich) titanite from Afrikanda, Russia. *American Mineralogist* **89**, 1752-1762.
- \_\_\_\_\_ & ZAITSEV, A.N. (2002): Calcite-amphibole-clinopyroxene rock from the Afrikanda complex, Kola Peninsula, Russia: mineralogy and a possible link to carbonatites. III. Silicate minerals. *Canadian Mineralogist* **40**, 1347-1374.
- CHANG, Y.A. & AHMAD, N. (1982): Thermodynamic data on metal carbonates and related oxides. Metallurgical Society of AIME, Warrendale, Pennsylvania.
- CHARLES, R.W. (1975): The phase equilibria of richterite and ferrichterite. *American Mineralogist* **60**, 367-374.
- \_\_\_\_\_ (1977): The phase equilibria of the intermediate composition on the pseudobinary  $\text{Na}_2\text{CaMg}_5\text{Si}_8\text{O}_{22}(\text{OH})_2 - \text{Na}_2\text{CaFe}_5\text{Si}_8\text{O}_{22}(\text{OH})_2$ . *American Journal of Science* **277**, 594-625.
- CHEN, T.T. (1978): Colloform and framboidal pyrite from the Caribou deposit New Brunswick. *Canadian Mineralogist* **16**, 9-15.
- CHIPERA, S.J. & BISH, D.L. (1997): Thermodynamic modeling of zeolite stability. *Los Alamos National Laboratory* **LA-UR-97-2160**.
- CHOI, S.-G. & YOUM, S.-J. (2000): Compositional variation of arsenopyrite and fluid evolution at the Ulsan deposit, southeastern Korea: A low-sulfidation porphyry system. *Canadian Mineralogist* **38**, 567-583.
- CHURAKOV, S. (2001): Physical-chemical properties of complex natural fluids. Doctoral Dissertation, Technischen Universität Berlin, Berlin, Germany.
- CLARK, J.R. & PAPIKE, J.J. (1968): Crystal-chemical characterization of omphacites. *American Mineralogist* **53**, 840-868.
- CLARK, R.J.H. & COBBOLD, D.G. (1978): Characterization of sulfur radical anions in solutions of alkali polysulfides in dimethylformamide and hexamethylphosphoramide and in the solid state in ultramarine blue, green, and red. *Inorganic Chemistry* **17**, 3169-3174.
- CLARK, T.H. (1955): St. Jean-Beloeil Area: Iberville, St. Jean, Napierville-Laprairie, Rouville, Chambly, St. Hyacinthe, and Verchères Counties. *Québec Department of Mines, Geological Report* **66**.



- CLOWE, C.A., POPP, R.K. & FRITZ, S.J. (1988): Experimental investigation of the effect of oxygen fugacity on ferric-ferrous ratios and unit-cell parameters of four natural clin amphiboles. *American Mineralogist* **73**, 487-499.
- COTTON, F.A. & WILKINSON, G. (1980): Advanced Inorganic Chemistry. Wiley-Interscience, New York.
- COULSON, I.M. (2003): Evolution of the North Qôroq centre nepheline syenites, South Greenland: alkali-mafic silicates and the role of metasomatism. *Mineralogical Magazine* **67**, 873-892.
- \_\_\_\_\_ & CHAMBERS, A.D. (1996): Patterns of zonation in rare-earth-bearing minerals in nepheline syenites of the North Qôroq Center, South Greenland. *Canadian Mineralogist* **34**, 1163-1178.
- CURRIE, K.L. (1970): An hypothesis on the origin of alkaline rocks suggested by the tectonic setting of the Montereian Hills. *Canadian Mineralogist* **10**, 411-420.
- \_\_\_\_\_ (1983): An interim report on the geology and petrology of the Mont Saint Hilaire pluton, Quebec. *Geological Survey of Canada Paper* **83-1B**, 39-46.
- \_\_\_\_\_, EBY, G. & GITTINS, J. (1986): The petrology of the Mont Saint Hilaire complex, southern Quebec: An alkaline gabbro-peralkaline syenite association. *Lithos* **19**, 65-81.
- CZAMANSKE, G.K. (1974): The FeS content of sphalerite along the chalcopryrite-pyrite-bornite sulfur fugacity buffer. *Economic Geology* **69**, 1328-1334.
- DEARGOLLO, R. & SCHILLING, J.-G. (1978): Ge-Si and Ga-Al fractionation in Hawaiian volcanic rocks. *Geochimica et Cosmochimica Acta* **42**, 623-630.
- DECLERCQ, J., HELLEVANG, H. & AAGAARD, P. (2009): Dawsonite dissolution rate and mechanism at acidic and basic pH, implication for CO<sub>2</sub> sequestration. *International Conference on Deep Saline Aquifers for Geological Storage of CO<sub>2</sub> and Energy*.
- DEMIN, A.M. & KHITAROV, D.N. (1958): Geochemistry of potassium, rubidium and thallium in application to problems of petrology. *Geokhimiya* **6**, 721-734.
- DIETRICH, R.V. (1968): Behavior of zirconium in certain artificial magmas under diverse p-T conditions. *Lithos* **1**, 20-29.
- DOIG, R. & BARTON, J.M. (1968): Ages of carbonatites and other alkaline rocks in Quebec. *Canadian Journal of Earth Sciences* **5**, 1401-1407.
- DONALDSON, C.H. (1977): Kaersutite overgrowths on highly aluminous titanagite in the Quarsut sill. *Mineralogical Magazine* **41**, 297-300.

- DOWTY, E. & CLARK, J.R. (1973): Crystal structure refinement and optical properties of a  $\text{Ti}^{3+}$  fassaite from the Allende meteorite. *American Mineralogist* **58**, 230-242.
- DUGGAN, M.B. (1988): Zirconium-rich sodic pyroxenes in felsic volcanics from the Warrumbungle Volcano, Central New South Wales, Australia. *Mineralogical Magazine* **52**, 491-496.
- DYULGEROV, M.M. & PLATEVOET, B. (2006): Unusual Ti and Zr aegirine-augite and potassic magnesio-arfvedsonite in the peralkaline potassic oversaturated Buhovo-Seslavytzi complex, Bulgaria. *European Journal of Mineralogy* **18**, 127-138.
- EBY, G.N. (1984): Montereian Hills I. Petrography, major and trace element geochemistry, and strontium isotopic chemistry of the western intrusions: Mounts Royal, St. Bruno, and Johnson. *Journal of Petrology* **25**, 421-452.
- \_\_\_\_\_ (1985a): Montereian Hills II. Petrography, major and trace element geochemistry, and strontium isotopic chemistry of the eastern intrusions: Mounts Shefford, Brome, and Megantic. *Journal of Petrology* **26**, 418-448.
- \_\_\_\_\_ (1985b): Age relations, chemistry, and petrogenesis of mafic dikes from the Montereian Hills and younger White Mountain igneous province. *Canadian Journal of Earth Sciences* **22**, 1103-1111.
- \_\_\_\_\_ (1992): Chemical subdivision of the A-type granitoids: Petrogenetic and tectonic implications. *Geology* **20**, 641-644.
- \_\_\_\_\_ (2006): Carbonatites to alkali granites – Petrogenetic insights from the Chilwa and Montereian Hills – White Mountain igneous provinces. *Geological Association of Canada/Mineralogical Association of Canada, Joint Annual Meeting, Abstracts with Program*.
- \_\_\_\_\_, WOOLLEY, A.R., DIN, V. & PLATT, G. (1998): Geochemistry and petrogenesis of nepheline syenites: Kasungu-Chipala, Ilomba, and Ulindi nepheline syenite intrusions, North Nyasa alkaline province, Malawi. *Journal of Petrology* **39**, 1405-1424.
- EITEL, W. (1964): Silicate Science. *Silicate Science* **4**, Academic Press, University of Virginia, Charlottesville, Virginia.
- ENGELL, J. (1972): A closed system crystal-fractionation model for the agpaitic Ilimaussaq intrusion, South Greenland with special reference to the lujavrites. *Bulletin of the Geological Society of Denmark* **22**, 334-362.
- ERNST, W.G. (1962): Synthesis, stability relations, and occurrence of riebeckite and riebeckite-arfvedsonite solid solutions. *The Journal of Geology* **70**, 689-736.

- \_\_\_\_\_ & LIU, J. (1998): Experimental phase-equilibrium study of Al- and Ti-contents of calcic amphibole in MORB – A semiquantitative thermobarometer. *American Mineralogist* **83**, 952-969.
- EUGSTER, H.P. & WONES, D.R. (1962): Stability relations of the ferruginous biotite annite. *Journal of Petrology* **3**, 82-125.
- FARGES, F. (1989): Ordre local autour de Zr, Th et U dans des silicates amorphes: Minéraux métamictes et verres silicates. Thèse de l'Université Paris 7, Paris, France.
- \_\_\_\_\_, BROWN, G.E., JR. & VELDE, D. (1994): Structural environment of Zr in two inosilicates from Cameroon: mineralogical and geochemical implications. *American Mineralogist* **79**, 838-847.
- \_\_\_\_\_, PONADER, C.W. & BROWN, G.E., JR. (1991): Structural environments of incompatible elements in silicate glass/melts systems. I. Zr at trace levels. *Geochimica et Cosmochimica Acta* **55**, 1563-1574.
- FELDSTEIN, S.N., LANGE, R.A., VENNEMANN, T. & O'NEIL, J.R. (1996): Ferric-ferrous ratios, H<sub>2</sub>O contents and D/H ratios of phlogopite and biotite from lavas of different tectonic regimes. *Contributions to Mineralogy and Petrology* **126**, 51-66.
- FERGUSON, A.K. (1977): The natural occurrence of aegirine-neptunite solid solution. *Contributions to Mineralogy and Petrology* **60**, 247-253.
- \_\_\_\_\_ (1978): The occurrence of ramsayite, titan-låvenite and a fluorine-rich eucolite in a nepheline syenite inclusion from Tenerife, Canary Islands. *Contributions to Mineralogy and Petrology* **66**, 15-20.
- FERGUSON, J. (1964): Geology of the Ilímaussaq alkaline intrusion South Greenland, description of map and structure. *Meddelelser om Grønland* **172**, 1-82.
- \_\_\_\_\_ (1970): The differentiation of agpaitic magmas: The Ilímaussaq intrusion, South Greenland. *Canadian Mineralogist* **10**, 335-349.
- FERSMAN, A.E. (ed.) (1937): Minerals of the Khibina and Lovozero tundras. Akademiya Nauk SSSR, Moscow.
- \_\_\_\_\_ (1958): A contribution to the geochemistry of alkaline magmas. *Izbrannye trudy* **4**, 413-419.
- FINCH, A. (1995): Metasomatic overprinting by juvenile igneous fluids, Igdlersigalik, South Greenland. *Contributions to Mineralogy and Petrology* **122**, 11-24.
- FLEET, M.E. & PAN, Y. (1995): Crystal chemistry of rare earth elements in fluorapatite and some calc-silicates. *European Journal of Mineralogy* **7**, 591-605.

- FLEISCHER, M. & MANDARINO, J.A. (1995): Glossary of Mineral Species. 7<sup>th</sup> Edition. The Mineralogical Record, Inc., Tucson, Arizona.
- FLOHR, M.J.K. (1994): Titanium, vanadium, and niobium mineralization and alkali metasomatism from the Magnet Cove Complex, Arkansas. *Economic Geology* **89**, 105-130.
- \_\_\_\_\_ & ROSS, M. (1989): Alkaline igneous rocks of Magnet Cove, Arkansas: Metasomatized ijolite xenoliths from Diamond Jo quarry. *American Mineralogist* **74**, 113-131.
- \_\_\_\_\_ & \_\_\_\_\_ (1990): Alkaline igneous rocks of Magnet Cove, Arkansas: mineralogy and geochemistry of syenites. *Lithos* **26**, 67-98.
- FLOYD, P.A. (1977): Rare earth element mobility and geochemical characterisation of spilitic rocks. *Nature* **269**, 134-137.
- FRYKLUND, V.L., JR. & HOLBROOK, D.F. (1950): Titanium ore deposits of Hot Spring County, Arkansas. *Arkansas Resources and Development Commission Bulletin* **16**.
- FUHRMAN, M.L. & LINDSLEY, D.H. (1988): Ternary-feldspar modeling and thermometry. *American Mineralogist* **73**, 201-215.
- GAULT NATURE RESERVE (2007): Bibliography of past research. (June 18, 2009) <http://www.mcgill.ca/gault/research/bibliography/>
- GILBERT, L.A. & FOLAND, K.A. (1986): The Mont Saint Hilaire plutonic complex: occurrence of excess <sup>40</sup>Ar and short intrusion history. *Canadian Journal of Earth Sciences* **23**, 948-958.
- GIRET, A., BONIN, B. & LEGER, J.-M. (1980): Amphibole compositional trends in oversaturated and undersaturated alkaline plutonic ring-complexes. *Canadian Mineralogist* **18**, 481-495.
- GIUSEPPE, G., MAZZI, F. & TADINI, C. (1971): The crystal structure of eudialyte. *Tschermaks Mineralogische und Petrographische Mitteilungen* **16**, 105-127.
- GOBELTZ-HAUTECEUR, N., DEMORTIER, A., LEDE, B., LELIEUR, J.P. & DUHAYON, C. (2002): Occupancy of the sodalite cages in the blue ultramarine pigments. *Inorganic Chemistry* **41**, 2848-2854.
- GOLD, M. (1963): The relationship between the limestones and the alkaline igneous rocks of Oka and St.-Hilaire, Quebec. Doctoral Dissertation, McGill University, Montréal, Québec, Canada.

- GOLD, D.P., EBY, G.N., BELL, K. & VALLEE, M. (1986): Carbonatites, diatremes, and ultra-alkaline rocks in the Oka area, Quebec. *Geological Association of Canada, Mineralogical Association of Canada, Canadian Geophysical Union, Joint Annual Meeting, Ottawa '86, Field Trip Guidebook* **21**.
- GOLYSHEV, V.M., SIMONOV, V.I. & BELOV, N.V. (1971): Crystal structure of eudialyte. *Sov. Phys. Crystallogr.* **16**(1), 70-74.
- GOMES, C.D.B., MORO, S.L. & DUTRA, C.V. (1970): Pyroxenes from the alkaline rocks of Itapirapuã, São Paulo, Brazil. *American Mineralogist* **55**, 224-230.
- GRAPES, R., YAGI, K. & OKUMURA, K. (1979): Aenigmatite, sodic pyroxene, arfvedsonite and associated minerals from Morutu, Sakhalin. *Contributions to Mineralogy and Petrology* **69**, 97-103.
- GREENWOOD, R.C. & EDGAR, A.D. (1984): Petrogenesis of the gabbros from Mt. St. Hilaire, Quebec, Canada. *Geological Journal* **19**, 353-376.
- GRICE, J.D. & GAULT, R.A. (2006): Johnsenite-(Ce): A new member of the eudialyte group from Mont Saint-Hilaire, Quebec, Canada. *Canadian Mineralogist* **44**, 105-115.
- HAMILTON, D.L. (1961): Nephelines as crystallization temperature indicators. *The Journal of Geology* **69**, 321-329.
- HANNINGTON, M.D. & SCOTT, S.D. (1989): Sulfidation equilibria as guides to gold mineralization in volcanogenic massive sulfides; evidence from sulfide mineralogy and the composition of sphalerite. *Economic Geology* **84**, 1978-1995.
- HARRIS, C. & RICKARD, R.S. (1987): Rare-earth-rich eudialyte and dalyite from a peralkaline granite dyke at Straumsvola, Dronning Maud Land, Antarctica. *Canadian Mineralogist* **25**, 755-762.
- HART, S.R. & ALDRICH, L.T. (1967): Fractionation of potassium/rubidium by amphiboles: implications regarding mantle composition. *Nature* **155**, 325-327.
- HATCH, F.H., WELLS, A.K. & WELLS, M.K. (1972): Petrology of the Igneous Rocks. 13<sup>th</sup> Edition. George Allen & Unwin, London, England.
- HAWTHORNE, F.C., OBERTE, R., CANNILLO, E., OTTOLINI, L., ROELOFSEN, J.N. & MARTIN, R.F. (2001): Li-bearing arfvedsonitic amphiboles from the Strange Lake peralkaline granite, Quebec. *Canadian Mineralogist* **39**, 1161-1170.
- HAYDEN, L.A., WATSON, E.B. & WARK, D.A. (2008): A thermobarometer for sphene (titanite). *Contributions to Mineralogy and Petrology* **155**, 529-540.

- HEIER, K.S. (1962): Trace elements in feldspars – a review. *Norsk Geologisk Tidsskrift* **42**, 415-454.
- HEINRICH, E.W.M. (1966): The Geology of Carbonatites. Rand McNally & Company, Chicago.
- HELLEVANG, H. (2006): Interactions between CO<sub>2</sub>, saline water and minerals during geological storage of CO<sub>2</sub>. Doctoral Dissertation, University of Bergen, Bergen, Norway.
- \_\_\_\_\_, AAGAARD, P., OELKERS, E.H. & KVAMME, B. (2005): Can dawsonite permanently trap CO<sub>2</sub>? *Environmental Science and Technology* **39**, 8281-8287.
- \_\_\_\_\_, DECLERCQ, J. & AAGAARD, P. (2009): Why is dawsonite absent in CO<sub>2</sub> charged reservoirs? *International Conference on Deep Saline Aquifers for Geological Storage of CO<sub>2</sub> and Energy*.
- \_\_\_\_\_, KVAMME, B. & AAGAARD, P. (2004): Long term interactions between minerals and reactive fluids – Stability of dawsonite. *Proceedings of the Third Annual Conference on Carbon Capture and Sequestration DOE/NETL*, 1-7.
- HELZ, R.T. (1973): Phase relations of basalts in their melting range at P<sub>H<sub>2</sub>O</sub> = 5 kb as a function of oxygen fugacity. *Journal of Petrology* **14**, 249–302.
- \_\_\_\_\_, (1979): Alkali exchange between hornblende and melt: a temperature-sensitive reaction. *American Mineralogist* **64**, 953–965.
- HENDERSON, C.M.B. & EZEPUE, M.J. (1989): Marandguzi alkaline complex, Zimbabwe. In *Alkaline Rocks*, C. Leelanandam (ed.), *Geological Society of India Memoirs* **15**, Bangalore.
- HENRY, D.J., GUIDOTTI, C.V. & THOMSON, J.A. (2005): The Ti-saturation surface for low-to-medium pressure metapelitic biotites: Implications for geothermometry and Ti-substitution mechanisms. *American Mineralogist* **90**, 316-328.
- HOFMANN, A.W. (1988): Chemical differentiation of the earth: The relationships between mantle, continental crust, and oceanic crust. *Earth and Planetary Science Letters* **90**, 297-314.
- \_\_\_\_\_, (1997): Mantle geochemistry: the message from oceanic volcanism. *Nature* **385**, 219-229.
- \_\_\_\_\_, (2003): Sampling mantle heterogeneity through oceanic basalts: Isotopes and trace elements. In Treatise on Geochemistry, Volume 2: The Mantle and Core. H.D. Holland, K.K. Turekian & R.W. Carlson (eds.), Elsevier, 61-102.
- HORNG, W.S. & HESS, P.C. (2000): Partition coefficients of Nb and Ta between rutile and anhydrous haplogranite melts. *Contributions to Mineralogy and Petrology* **138**, 176-185.

- HORVÁTH, L. & GAULT, R.A. (1990): The mineralogy of Mont Saint-Hilaire, Quebec. *Mineralogical Record* **21**, 284-360.
- HSU, L.C. (1976): The stability relations of the wolframite series. *American Mineralogist* **61**, 944-955.
- \_\_\_\_\_ (1977): Effects of oxygen and sulfur fugacities on the scheelite-tungstenite and powellite-molybdenite stability relations. *Economic Geology* **72**, 664-670.
- HUEBNER, J.S. (1969): Stability relations of rhodochrosite in the system manganese-carbon-oxygen. *American Mineralogist* **54**, 457-481.
- HUGHES, J.M., ERTL, A., BERNHARDT, H.-J., ROSSMAN, G.R. & RAKOVAN, J. (2004): Mn-rich fluorapatite from Austria: Crystal structure, chemical analysis, and spectroscopic investigations. *American Mineralogist* **89**, 629-632.
- HUMPHRIS, S.E. & THOMPSON, G. (1978): Trace element mobility during hydrothermal alteration of oceanic basalts. *Geochimica et Cosmochimica Acta* **42**, 127-136.
- ISUK, E.E. & CARMAN, J.H. (1981): The system  $\text{Na}_2\text{Si}_2\text{O}_5$ - $\text{K}_2\text{Si}_2\text{O}_5$ - $\text{MoS}_2$ - $\text{H}_2\text{O}$  with implications for molybdenum transport in silicate melts. *Economic Geology* **76**, 2222-2235.
- JOHAN, Z. (1988): Indium and germanium in the structure of sphalerite: an example of coupled substitution with copper. *Mineralogy and Petrology* **39**, 211-229.
- JOHANNSEN, A. (1931): A Descriptive Petrography of the Igneous Rocks, Volume 1. Chicago University Press.
- JOHNSON, O., FERRARIS, G., GAULT, R.A., GRICE, J.D., KAMPF, A.R. & PEKOV, I.V. (2003a): The nomenclature of eudialyte-group minerals. *Canadian Mineralogist* **41**, 785-794.
- \_\_\_\_\_, GAULT, R.A., GRICE, J.D. & ERCIT, T.S. (1999a): Khomyakovite and manganokhomyakovite, two new members of the eudialyte group from Mont Saint-Hilaire, Quebec. *Canadian Mineralogist* **37**, 893-899.
- \_\_\_\_\_ & GRICE, J.D. (1999): The crystal chemistry of the eudialyte group. *Canadian Mineralogist* **37**, 865-891.
- \_\_\_\_\_, \_\_\_\_\_ & GAULT, R.A. (1999b): Oneillite: a new Ca-deficient and REE-rich member of the eudialyte group from Mont Saint-Hilaire, Quebec, Canada. *Canadian Mineralogist* **37**, 1111-1117.
- \_\_\_\_\_, \_\_\_\_\_ & \_\_\_\_\_ (2003b): Ferrokentbrooksite, a new member of the eudialyte group from Mont Saint-Hilaire, Quebec, Canada. *Canadian Mineralogist* **41**, 55-60.

- JONES, A.P. (1980): The petrology and structure of the Motzfeldt Centre, Igaliiko, South Greenland. Doctoral Dissertation, University of Durham, Durham, England.
- \_\_\_\_\_ & LARSEN, L.M. (1985): Geochemistry and REE minerals of nepheline syenites from the Motzfeldt Centre, South Greenland. *American Mineralogist* **70**, 1087-1100.
- \_\_\_\_\_ & PECKETT, A. (1980): Zirconium-bearing aegirines from Motzfeldt, South Greenland. *Contributions to Mineralogy and Petrology* **75**, 251-255.
- JUGO, P.J., LUTH, R.W. & RICHARDS, J.P. (2005): Experimental data on the speciation of sulfur as a function of oxygen fugacity in basaltic melts. *Geochimica et Cosmochimica Acta* **69**, 497-503.
- KAJIWARA, Y. (1971): Sulfur isotope study of the Kuroko-ores of the Shakanai No. 1 deposits, Akita Prefecture, Japan. *Geochemical Journal* **4**, 157-181.
- \_\_\_\_\_ (1973): A simulation of the Kuroko type mineralization in Japan. *Geochemical Journal* **6**, 193-209.
- \_\_\_\_\_ & DATE, J. (1971): Sulfur isotope study of Kuroko-type and Kieslager-type strata-bound massive sulfide deposits in Japan. *Geochemical Journal* **5**, 133-150.
- KATSURA, T. & NAGASHIMA, S. (1974): Solubility of sulfur in some magmas at 1 atm pressure. *Geochimica et Cosmochimica Acta* **38**, 517-531.
- KEPPLER, H. (1993): Influence of fluorine on the enrichment of high field strength trace elements in granitic rocks. *Contributions to Mineralogy and Petrology* **114**, 479-488.
- KHOMYAKOV, A.P. (1995): Mineralogy of Hyperagpaitic Alkaline Rocks. 1<sup>st</sup> English Edition. Oxford University Press, Oxford, England.
- \_\_\_\_\_, SØRENSEN, H., PETERSEN, O.V. & BAILEY, J.C. (2001): Naujakasite from the Ilímaussaq alkaline complex, South Greenland, and the Lovozero alkaline complex, Kola Peninsula, Russia: a comparison. In *The Ilímaussaq alkaline complex, South Greenland: status of mineralogical research and new results*, H. Sørensen (ed.), *Geology of Greenland Survey Bulletin* **190**, 95-108.
- KOCHHAR, N. (2000): Attributes and significance of A-type Malani magmatism, northwestern peninsular India. In Crustal Evolution and Metallogeny in the Northwestern Indian Shield, M. Deb (ed.), Alpha Science International, Pangbourne, England, 158-188.
- KOGARKO, L.N. (1977): Problems of the origin of agpaitic magmas. Nauka, Moscow.
- \_\_\_\_\_ & GULYAYEVA, L.A. (1965): Geochemistry of the halogens in the alkalic rocks of the Lovozero massif (Kola Peninsula). *Geokhimiya* **8**, 1011.



- KOHN, S.C., DUPREE, R., MORTUZA, M.G. & HENDERSON, C.M.B. (1991): NMR evidence for five- and six-coordinated aluminum fluoride complexes in F-bearing aluminosilicate glasses. *American Mineralogist* **76**, 309-312.
- KOJIMA, S. & SUGAKI, A. (1985): Phase relations in the Cu-Fe-Zn-S system between 500 degrees and 300 degrees C under hydrothermal conditions. *Economic Geology* **80**, 158-171.
- KOLBE, P. & TAYLOR, S.R. (1966): Major and trace element relationships in granodiorites and granites from Australia and South Africa. *Contributions to Mineralogy and Petrology* **12**, 202-222.
- KOROLEVA, N.N., KORMILITSYN, V.S. & KOTENEVA, YE.A. (1970): Colloform formations of galena in ores of Kan-i-Mansur polymetallic deposit of Karamazar area. *International Geology Review* **12**, 433-438.
- KOSTERIN, A.V., SHEVALEYEVSKII, I.D. & KIZYURA, V.E. (1964): Behavior of zirconium and hafnium in the pegmatites of the southern Stanovoi Range. *Geochemistry International* **1**, 989-993.
- KRETSCHMAR, U. & SCOTT, S.D. (1976): Phase relations involving arsenopyrite in the system Fe-As-S and their application. *Canadian Mineralogist* **14**, 364-386.
- KULLERUD, G. & YODER, H.S. (1959): Pyrite stability relations in the Fe-S system. *Economic Geology* **54**, 533-572.
- KUMARAPELI, P.S. (1970): Montereian alkalic magmatism and the St. Lawrence rift system in space and time. *Canadian Mineralogist* **10**, 421-431.
- \_\_\_\_\_ & SAULL, V.A. (1966): The St. Lawrence valley system: a North American equivalent of the East African rift valley system. *Canadian Journal of Earth Sciences* **3**, 639-659.
- KURTZ, A.C., DERRY, L.A. & CHADWICK, O.A. (2002): Germanium-silicon fractionation in the weathering environment. *Geochimica et Cosmochimica Acta* **66**, 1525-1537.
- LARSEN, E.S. & BUIE, B.F. (1938): Potash analcime and pseudoleucite from the Highwood Mountains of Montana. *American Mineralogist* **23**, 837-850.
- LARSEN, L.M. (1976): Clinopyroxenes and coexisting mafic minerals from the alkaline Ilímaussaq intrusion, south Greenland. *Journal of Petrology* **17**, 258-290.
- LAZUTKINA, L.N., KOGARKO, L.N. & KRIGMAN, L.D. (1980): Stability of zirconium minerals in alkali apatite magmas. *Geochemistry International* **17**(4), 83-86.

- LEAKE, B.E., WOOLLEY, A.R., ARPS, C.E.S., BIRCH, W.D., GILBERT, M.C., GRICE, J.D., HAWTHORNE, F.C., KATO, A., KISCH, H.J., KRIVOVICHEV, V.G., LINTHOUT, K., LAIRD, J., MANDARINO, J.A., MARESCH, W.V., NICKEL, E.H., ROCK, N.M.S., SCHUMACHER, J.C., SMITH, D.C., STEPHENSON, N.C.N., UNGARETTI, L., WHITTAKER, E.J.W. & YOUZHI, G. (1997): Nomenclature of amphiboles: Report of the Subcommittee on Amphiboles of the International Mineralogical Association, Commission on New Minerals and Mineral Names. *Canadian Mineralogist* **35**, 219-246.
- \_\_\_\_\_, \_\_\_\_\_, BIRCH, W.D., BURKE, E.A.J., FERRARIS, G., GRICE, J.D., HAWTHORNE, F.C., KISCH, H.J., KRIVOVICHEV, V.G., SCHUMACHER, J.C., STEPHENSON, N.C.N. & WHITTAKER, E.J.W. (2003): Nomenclature of amphiboles: Additions and Revisions to the International Mineralogical Association's 1997 Recommendations. *Canadian Mineralogist* **41**, 1355-1362.
- LEE, O.I. (1936): A new property of matter: Reversible photosensitivity in hackmanite from Bancroft, Ontario. *American Mineralogist* **21**, 764-776.
- LE MAITRE, R.W. (1989): A Classification of Igneous Rocks and Glossary of Terms: Recommendations of the International Union of Geological Sciences, Subcommission on the Systematics of Igneous Rocks. Blackwell Publishing, Oxford.
- LE ROEX, A.P. & LANYON, R. (1997): Isotope and trace element geochemistry of Cretaceous Damaraland lamprophyres and carbonatites, northwestern Namibia: Evidence for plume–lithosphere interactions. *Journal of Petrology* **39**, 1117-1146.
- LEV, S.M., MCLENNAN, S.M., MEYERS, W.J. & HANSON, G.N. (1998): A petrographic approach for evaluating trace element mobility in a black shale. *Journal of Sedimentary Research* **68**, 970-980.
- LINNEN, R.L. (1998): The solubility of Nb–Ta–Zr–Hf–W in granitic melts with Li and Li + F; constraints for mineralization in rare metal granites and pegmatites. *Economic Geology* **93**, 1013-1025.
- \_\_\_\_\_, & KEPPLER, H. (2002): Melt composition control of Zr/Hf fractionation in magmatic processes. *Geochimica et Cosmochimica Acta* **66**, 3293-3301.
- LINTHOUT, K. (1984): Alkali-zirconosilicates in peralkaline rocks. *Contributions to Mineralogy and Petrology* **86**, 155-158.
- LIU, J.G., KUNIYOSHI, S. & ITO, K. (1974): Experimental studies of the phase relations between greenschist and amphibolite in a basaltic system. *American Journal of Science* **274**, 613-632.
- LIU, J. (1997) High pressure phase equilibria involving the amphibolite–eclogite transformation. Doctoral Dissertation, Stanford University, Palo Alto, California.

- MANDARINO, J.A. & ANDERSON, V. (1989): Monteregian Treasures, The Minerals of Mont Saint-Hilaire, Quebec. Cambridge University Press, Cambridge, England.
- MANNING, D.A.C., HAMILTON, D.L., HENDERSON, C.M.B. & DEMPSEY, M.J. (1980): The probable occurrence of interstitial Al in hydrous, F-bearing and F-free aluminosilicate melts. *Contributions to Mineralogy and Petrology* **75**, 257-262.
- MANSKER, W.L., EWING, R.C. & KEIL, L. (1979): Barium-titanium biotites in nephelinites from Oahu, Hawaii. *Contributions to Mineralogy and Petrology* **64**, 156-159.
- MARINI, L. (2007): Geological Sequestration of Carbon Dioxide: Thermodynamics, Kinetics, and Reaction Path Modeling. *Developments in Geochemistry* **11**, Elsevier, Amsterdam.
- MARKL, G. & BAUMGARTNER, L. (2002): pH changes in peralkaline late-magmatic fluids. *Contributions to Mineralogy & Petrology* **144**, 331-346.
- MARKS, M. & MARKL, G. (2001): Fractionation and assimilation processes in the alkaline augite syenite unit of the Ilímaussaq intrusion, South Greenland, as deduced from phase equilibria. *Journal of Petrology* **42**, 1947-1969.
- MARR, R.A., BAKER, D.R. & WILLIAMS-JONES, A.E. (1998): Chemical controls on the solubility of Zr-bearing phases in simplified peralkaline melts and application to the Strange Lake intrusion, Quebec-Labrador. *Canadian Mineralogist* **36**, 1001-1008.
- MARSH, J.S. (1975): Aenigmatite stability in silica-undersaturated rocks. *Contributions to Mineralogy and Petrology* **50**, 135-144.
- MARTIN, D.J. (1984): Titanian aegirine in a teschenite sill. *Mineralogical Magazine* **48**, 529-531.
- MAYNARD, J.B. (2003): Manganiferous sediments, rocks, and ores. In Treatise on Geochemistry, Volume 7: Sediments, Diagenesis, and Sedimentary Rocks. H.D. Holland, K.K. Turekian & F.T. Mackenzie (eds.), Elsevier, 289-308.
- MCDONOUGH, W.F. (2001): The Composition of the Earth. In Earthquake Thermodynamics and Phase Transformations of the Earth's Interior. R. Teisseyre & E. Majewski (eds.), Academic Press, 3-23.
- MCHONE, J.G. & BUTLER, J.R. (1984): Mesozoic igneous provinces of New England and the opening of the North Atlantic Ocean. *Geological Society of America Bulletin* **95**, 757-765.
- \_\_\_\_\_ & MCHONE, N.W. (1993): Field guide to Cretaceous intrusions in the northern Taconic Mountains region, Vermont. *Vermont Geology* **7**, 1-27.

- MELCHER, F., OBERTHÜR, T. & RAMMLMAIR, D. (2006): Geochemical and mineralogical distribution of germanium in the Khusib Springs Cu-Zn-Pb-Ag sulfide deposit, Otavi Mountain Land, Namibia. *Ore Geology Reviews* **28**, 32-56.
- MIDDLEMOST, E.A.K. (1975): The basalt clan. *Earth Science Reviews* **11**, 337-364.
- MIELKE, J.E. (1979): Composition of the Earth's crust and distribution of the elements. In *Review of research on modern problems in geochemistry. International Association for Geochemistry and Cosmochemistry. Earth Science Series No. 16*, F.R. Siegel (ed.), UNESCO Report SC/GEO/544/3, Paris, 13-37.
- MILLER, D.M., GOLDSTEIN, S.L. & LANGMUIR, C.H. (1994): Cerium/lead and lead isotope ratios in arc magmas and the enrichment of lead in the continents. *Nature* **368**, 514-519.
- MITCHELL, R.H. (1980): Pyroxenes of the Fen alkaline complex, Norway. *The American Mineralogist* **65**, 45-54.
- \_\_\_\_\_ (1990): A review of the compositional variation of amphiboles in alkaline plutonic complexes. *Lithos* **28**, 135-156.
- \_\_\_\_\_ & BRUNFELT, A.O. (1974): Scandium, cobalt and iron geochemistry of the Fen alkaline complex, southern Norway. *Earth and Planetary Science Letters* **23**, 189-192.
- \_\_\_\_\_ & LIFEROVICH, R.P. (2004): Ecandrewsite-zincian pyrophanite from lujavrite, Pilanesberg alkaline complex, South Africa. *Canadian Mineralogist* **42**, 1169-1178.
- \_\_\_\_\_ & PLATT, R.G. (1978): Mafic mineralogy of ferroaugite syenite from the Coldwell alkaline complex, Ontario, Canada. *Journal of Petrology* **19**, 627-651.
- \_\_\_\_\_ & \_\_\_\_\_ (1982): Mineralogy and petrology of nepheline syenites from the Coldwell alkaline complex, Ontario, Canada. *Journal of Petrology* **23**, 186-214.
- \_\_\_\_\_ & VLADYKIN, N.V. (1996): Compositional variation of pyroxene and mica from the Little Murun ultrapotassic complex, Aldan Shield, Russia. *Mineralogical Magazine* **60**, 907-925.
- MIYAJI, F., KONO, Y. & SUYAMA, Y. (2005): Formation and structure of zinc-substituted calcium hydroxyapatite. *Materials Research Bulletin* **40**, 209-220.
- MIYASHIRO, A. (1978): Nature of alkalic volcanic rock series. *Contributions to Mineralogy and Petrology* **66**, 91-104.
- MORIMOTO, N. (1989): Nomenclature of pyroxenes. *Canadian Mineralogist* **27**, 143-156.
- \_\_\_\_\_ & KULLERUD, G. (1962): The Mo-S system. *Carnegie Institute Washington Year Book* **61**, 143-144.

- MORSE, S.A. (1970): Alkali feldspars with water at 5 kb pressure. *Journal of Petrology* **11**, 221-251.
- \_\_\_\_\_ (1982): Kiglapait geochemistry V: Strontium. *Geochimica et Cosmochimica Acta* **46**, 223-234.
- MURTHY, V.R. & GRIFFIN, W.L. (1970): K/Rb fractionation by potassium feldspars. *Chemical Geology* **6**, 265-271.
- MYSEN, B.O. & VIRGO, D. (1985): Structure and properties of fluorine-bearing aluminosilicate melts: the system  $\text{Na}_2\text{O}-\text{Al}_2\text{O}_3-\text{SiO}_2-\text{F}$  at 1 atm. *Contributions to Mineralogy and Petrology* **91**, 205-220.
- NAGASHIMA, S. & KATSURA, T. (1973): The solubility of sulfur in  $\text{Na}_2\text{O}-\text{SiO}_2$  melts under various oxygen partial pressures at 1100, 1250, and 1300°C. *Bulletin of the Chemical Society of Japan* **46**, 3099-3103.
- NASH, W.P. & WILKINSON, J.F.G. (1970): Shonkin Sag laccolith, Montana. I: Mafic minerals and estimates of temperature, pressure, oxygen fugacity, and silica activity. *Contributions to Mineralogy and Petrology* **25**, 241-269.
- NEUMANN, E.-R. (1980): Petrogenesis of the Oslo Region larvikites and associated rocks. *Journal of Petrology* **21**, 499-531.
- NIELSEN, B.L. & STEENFELT, A. (1979): Intrusive events at Kvanefjeld in the Ilímaussaq igneous complex. *Bulletin of the Geological Society of Denmark* **27**, 143-155.
- NIELSEN, T.F.D. (1979): The occurrence and formation of Ti-aegirines in peralkaline systems. *Contributions to Mineralogy and Petrology* **69**, 235-244.
- OBERTI, R., SMITH, D.C., ROSSI, G. & CAUCIA, F. (1991): The crystal-chemistry of high-aluminium titanites. *European Journal of Mineralogy* **3**, 777-792.
- OKADA, K., NAGASHIMA, T., KAMESHIMA, Y., YASUMORI, A. & TSUKADA, T. (2002): Relationship between formation conditions, properties, and crystallite size of boehmite. *Journal of Colloid and Interface Science* **253**, 308-314.
- OKAY, A.I. (1980): Sodic amphiboles as oxygen fugacity indicators in metamorphism. *The Journal of Geology* **88**, 225-232.
- OLIVO, G.R. & GIBBS, K. (2003): Paragenesis and mineral chemistry of alabandite ( $\text{MnS}$ ) from the Ag-rich Santo Toribio epithermal deposit, northern Peru. *Mineralogical Magazine* **67**, 95-102.
- O'NEILL, J.J. (1914): St. Hilaire (Beloeil) and Rougemont Mountains, Quebec. *Canada Department of Mines, Geological Survey Memoir* **43**.

- ORDÓÑEZ-CALDERÓN, J.C., POLAT, A., FRYER, B.J., GAGNON, J.E., RAITH, J.G. & APPEL, P.W.U. (2008): Evidence for HFSE and REE mobility during calc-silicate metasomatism, Mesoarchean (~3075 Ma) Ivvisaartoq greenstone belt, southern West Greenland. *Precambrian Research* **161**, 317-340.
- OYARZUN, R., MÁRQUEZ, A., LILLO, J., LÓPEZ, I. & RIVERA, S. (2001): Giant versus small porphyry copper deposits of Cenozoic age in northern Chile: adakitic versus normal calc-alkaline magmatism. *Mineralium Deposita* **36**, 794-798.
- PALACHE, C., BERMAN, H. & FRONDEL, C. (1966): The System of Mineralogy of James Dwight Dana and Edward Salisbury Dana, Yale University 1837-1892—Volume 1. 7<sup>th</sup> Edition, 8<sup>th</sup> Printing. John Wiley & Sons, Inc., New York.
- PAN, Y & FLEET, M.E. (1996): Intrinsic and extrinsic controls on the incorporation of rare-earth elements in calc-silicate minerals. *Canadian Mineralogist* **34**, 147-159.
- PARSONS, I. (1978): Feldspars and fluids in cooling plutons. *Mineralogical Magazine* **42**, 1-17.
- \_\_\_\_\_ & BROWN, W.L. (1988): Sidewall crystallization in the Klokken intrusion: Zoned ternary feldspars and coexisting minerals. *Contributions to Mineralogy and Petrology* **98**, 431-443.
- PE-PIPER, G. (1988): Calcic amphiboles of mafic rocks of the Jeffers Brook plutonic complex, Nova Scotia, Canada. *American Mineralogist* **73**, 993-1006.
- PEARCE, J.A. & NORRY, M.J. (1979): Petrogenetic implications of Ti, Zr, Y, and Nb variations in volcanic rocks. *Contributions to Mineralogy and Petrology* **69**, 33-47.
- PEARCE, N.J.G. (1989): Zirconium-bearing amphiboles from the Igaliko Dyke Swarm, South Greenland. *Mineralogical Magazine* **53**, 107-110.
- PEKOV, I.V. (1995): Moraesite from the alkaline pegmatite of Lovozero Massif, Kola Peninsula. In Ural'skiy Mineralogicheskiy Sbornik, No. 5, B.V. Chesnokov (ed.), Rossiyskaya Akademiya Nauk, Ural'skoye Otdeleniye, Institut Mineralogii, Miass, Russian Federation, 256-260.
- PETERSON, R.C. (1983): The structure of hackmanite, a variety of sodalite, from Mont Saint-Hilaire, Quebec. *Canadian Mineralogist* **21**, 549-552.
- PHILPOTTS, A.R. (1970): Mechanisms of emplacement of the Monteregian intrusions. *Canadian Mineralogist* **10**, 395-410.
- \_\_\_\_\_ (1976): Petrography of Mounts Saint-Bruno and Rougemont. *Québec Ministère des Richesses Naturelles, Rapport ES-16*.

- PIILONEN, P.C., LALONDE, A.E., McDONALD, A.M. & GAULT, R.A. (2000): Niobokupletskite, a new astrophyllite-group mineral from Mont Saint-Hilaire, Quebec, Canada: Description and crystal structure. *Canadian Mineralogist* **38**, 627-639.
- \_\_\_\_\_, \_\_\_\_\_, \_\_\_\_\_, \_\_\_\_\_ & LARSEN, A.O. (2003): Insights into astrophyllite-group minerals. I. Nomenclature, composition and development of a standardized general formula. *Canadian Mineralogist* **41**, 1-26.
- \_\_\_\_\_, McDONALD, A.M. & LALONDE, A.E. (1998): The crystal chemistry of aegirine from Mont Saint-Hilaire, Quebec. *Canadian Mineralogist* **36**, 779-791.
- PLATT, R.G. (1996): Nepheline syenite complexes—an overview. In Undersaturated Alkaline Rocks: Mineralogy, Petrogenesis, and Economic Potential, R.H. Mitchell (ed.), *Mineralogical Association of Canada Short Course* **24**, 63–99.
- \_\_\_\_\_, & WOOLLEY, A.R. (1986): The mafic mineralogy of the peralkaline syenites and granites of the Mulanje complex, Malawi. *Mineralogical Magazine* **50**, 85-99.
- POLI, S. (1993): The amphibolite-eclogite transformation: an experimental study on basalt. *American Journal of Science* **293**, 1061–1107.
- POULIOT, G. (1962): The thermal history of the Monteregian intrusives based on a study of the feldspars. Doctoral Dissertation, McGill University, Montréal, Québec, Canada.
- POULSON, S.R., KUBILIUS, W.P. & OHMOTO, H. (1991): Geochemical behavior of sulfur in granitoids during intrusion of the South Mountain batholith, Nova Scotia, Canada. *Geochimica et Cosmochimica Acta* **55**, 3809-3830.
- \_\_\_\_\_, & OHMOTO, H. (1990): An evaluation of the solubility of sulfide sulfur in silicate melts from experimental data and natural samples. *Chemical Geology* **85**, 57-75.
- POWELL, M. & POWELL, R. (1977): A nepheline–alkali feldspar geothermometer. *Contributions to Mineralogy and Petrology* **62**, 193-204.
- PRESNALL, D.C. (1995): Phase Diagrams of Earth-Forming Minerals. In Mineral Physics and Crystallography: A Handbook of Physical Constants, American Geophysical Union, Washington, D.C., 248-268.
- PROWATKE, S. & KLEMME, S. (2005): Effect of melt composition on the partitioning of trace elements between titanite and silicate melt. *Geochimica et Cosmochimica Acta* **69**, 695-709.
- RAJASEKARAN, P.K. (1968): Mineralogy and petrology of nepheline syenite in Mont Saint Hilaire, Quebec. Doctoral Dissertation, McGill University, Montréal, Québec, Canada.

- RANLØV, J. & DYMEK, R.F. (1991): Compositional zoning in hydrothermal aegirine from fenites in the Proterozoic Gardar Province, South Greenland. *European Journal of Mineralogy* **3**, 837-853.
- RASTSVETAeva, R.K. & ANDRIANOV, V.I. (1987): New data on the crystal structure of eudialyte. *Dokl. Akad. Nauk SSSR* **293**, 1122-1126 (in Russian).
- \_\_\_\_\_, & BORUTSKII, B.E. (1988): Crystal chemical peculiarities of eudialyte proceeding from new structural data. *Mineral. Zh.* **10**, 48-57 (in Russian).
- \_\_\_\_\_, & GUSEV, A.I. (1988): Crystal structure of eucolite. *Sov. Phys. Crystallogr.* **33**(2), 207-210.
- \_\_\_\_\_, SOKOLOVA, M.N. & BORUTSKII, B.E. (1990): Crystal structure of potassium oxonium eudialyte. *Sov. Phys. Crystallogr.* **35**(6), 814-817.
- REDHAMMER, G.J., BERAN, A., DACHS, E. & AMTHAUER, G. (1993): A Mössbauer and X-ray diffraction study of annites synthesized at different oxygen fugacities and crystal chemical implications. *Physics and Chemistry of Minerals* **20**, 382-394.
- RIEDER, M., CAVAZZINI, G., D'YAKONOV, Y.S., FRANK-KAMENETSKII, V.A., GOTTARDI, G., GUGGENHEIM, S., KOVAL, P.V., MÜLLER, G., NEIVA, A.M.R., RADOSLOVICH, E.W., ROBERT, J.-L., SASSI, F.P., TAKEDA, H., WEISS, Z. & WONES, D.R. (1998): Nomenclature of the micas. *Canadian Mineralogist* **36**, 905-912.
- ROBERT, J.L. (1976): Titanium solubility in synthetic phlogopite solid solutions. *Chemical Geology* **17**, 213-227.
- ST. JULIEN, P. & HUBERT, C. (1975): Evolution of the Taconian orogen in the Quebec Appalachians. *American Journal of Science* **275-A**, 337-362.
- SALVI, S. & WILLIAMS-JONES, A.E. (1990): The role of hydrothermal processes in the granite-hosted Zr, Y, REE deposit at Strange Lake, Quebec/Labrador: Evidence from fluid inclusions. *Geochimica et Cosmochimica Acta* **54**, 2403-2418.
- SATO, T. (1977): Kuroko deposits: their geology, geochemistry and origin. In Volcanic Processes in Ore Genesis. I.G. Gass (ed.), Geological Society of London Special Publication **7**, 153-161.
- SCHAIRER, J.F. (1950): The alkali feldspar join in the system  $\text{NaAlSiO}_4\text{--KAlSiO}_4\text{--SiO}_2$ . *The Journal of Geology* **58**, 512-517.
- SCHALLER, T., DINGWELL, D.B., KEPPLER, H., KNÖLLER, W., MERWIN, L. & SEBALD, A. (1992): Fluorine in silicate glasses: a multinuclear nuclear magnetic resonance study. *Geochimica et Cosmochimica Acta* **56**, 701-707.



- SCHROLL, E. (1999): Germanium: Element and geochemistry. In Encyclopedia of Geochemistry, C.P. Marshall & R.W. Fairbridge (eds.), Kluwer Academic Publishers, Dordrecht, Germany, 307-308.
- SCHUCKER, D.E. & FOLAND, K.A. (1992): Mesozoic igneous intrusions in New England and Québec: implications from lead (Pb) isotopes on petrogenesis and mantle sources (Ascutney Mountain, VT; Mont Saint-Hilaire, Québec; Pliny Complex, NH). Doctoral Dissertation, Ohio State University, Columbus, Ohio.
- SCHWARTZ, A., TAUBER, A. & SHAPPIRIO, J.R. (1967): The growth of gamma-MnS crystals in sodium silicate gels. *Materials Research Bulletin* **2**, 375-380.
- SCOTT, S.D. & BARNES, H.L. (1971): Sphalerite geothermometry and geobarometry. *Economic Geology* **66**, 653-669.
- SEEWALD, J.S. & SEYFRIED, W.E., JR. (1990): The effect of temperature on metal mobility in subseafloor hydrothermal systems: constraints from basalt alteration experiments. *Earth and Planetary Science Letters* **101**, 388-403.
- SEMENOV, E.I. (1972): Mineralogy of the Lovozero alkaline massif. Nauka, Moscow.
- SEVEROV, E.A. & VERSHKOVSKAYA, O.V. (1960): The behavior of gallium during the process of albitization of granitoids. *Dokl. Acad. Sci. USSR, Earth Sci. Sect.* **135**, 1096-1097.
- SEYFRIED, W.E., JR. & DING, K. (1993): The effect of redox on the relative solubilities of copper and iron in Cl-bearing aqueous fluids at elevated temperatures and pressures: An experimental study with application to subseafloor hydrothermal systems. *Geochimica et Cosmochimica Acta* **57**, 1905-1917.
- 
- \_\_\_\_\_ & JANECKY, D.R. (1985): Heavy metal and sulfur transport during subcritical and supercritical hydrothermal alteration of basalt: Influence of fluid pressure and basalt composition and crystallinity. *Geochimica et Cosmochimica Acta* **49**, 2545-2560.
- SHAND, S.J. (1943): Eruptive Rocks; Their Genesis, Composition, Classification, and their Relation to Ore Deposits, with a chapter on Meteorites. Revised 2<sup>nd</sup> edition. Hafner Publishing Co., New York.
- SHARP, Z.D., ESSENE, E.J. & KELLY, W.C. (1985): A re-examination of the arsenopyrite geothermometer: Pressure considerations and applications to natural assemblages. *Canadian Mineralogist* **23**, 517-534.
- SHAW, C.S.J. & PENCZAK, R.S. (1996): Barium- and titanium-rich biotite and phlogopite from the Western and Eastern Gabbro, Coldwell alkaline complex, northwestern Ontario. *Canadian Mineralogist* **34**, 967-975.

- SIEDNER, G. (1965): Geochemical features of a strongly fractionated alkali igneous suite. *Geochimica et Cosmochimica Acta* **29**, 113-138.
- SIIVOLA, J. & SCHMID, R. (2009): Recommendations by the IUGS Subcommission on the Systematics of Metamorphic Rocks: Web version 01.02.07. (November 02, 2009) [http://www.bgs.ac.uk/scmr/docs/papers/paper\\_12.pdf](http://www.bgs.ac.uk/scmr/docs/papers/paper_12.pdf)
- SIMON, G., KESLER, S.E. & ESSENE, E.J. (1997): Phase relations among selenides, sulfides, tellurides, and oxides. II. Applications to selenide-bearing ore deposits. *Economic Geology* **92**, 468-484.
- SINKANKAS, J. (1961): Natrolite from Houdaille Industries quarry, Bound Brook, Somerset County, N.J.. *American Mineralogist* **46**, 1195-1197.
- SIRBESCU, M. & JENKINS, D.M. (1999): Experiments on the stability of cancrinite in the system  $\text{Na}_2\text{O}-\text{CaO}-\text{Al}_2\text{O}_3-\text{SiO}_2-\text{CO}_2-\text{H}_2\text{O}$ . *American Mineralogist* **84**, 1850-1860.
- SMITH, J.V. (1974): Feldspar Minerals, Volume 2, Chemical and Textural Properties. Springer-Verlag, New York.
- SOBOLEV, V.S., BAZAROVA, T.Y. & KOSTYUK, V.P. (1974): Inclusions in the minerals of some types of alkaline rocks. In The Alkaline Rocks, H. Sørensen (ed.), John Wiley & Sons, New York, 389-401.
- SOOD, M.K. (1981): Modern Igneous Petrology. John Wiley & Sons, New York.
- SØRENSEN, H. (1974): Alkali syenites, feldspathoidal syenites, and related lavas. In The Alkaline Rocks, H. Sørensen (ed.), John Wiley & Sons, New York, 22-52.
- SPEAR, F.S. (1981): An experimental study of hornblende stability and compositional variability in amphibolite. *American Journal of Science* **281**, 697-734.
- SPENCER, K.J. & LINDSLEY, D.H. (1981): A solution model for coexisting iron-titanium oxides. *American Mineralogist* **66**, 1189-1201.
- STEPHENSON, D. (1972): Alkali clinopyroxenes from the nepheline syenites of the South Qôroq center, south Greenland. *Lithos* **5**, 187-201.
- \_\_\_\_\_ & UPTON, B.G.J. (1982): Ferromagnesian minerals in a differentiated alkaline complex: Kûngnât Fjeld, South Greenland. *Mineralogical Magazine* **46**, 283-300.
- STORMER, J.C., JR. (1983): The effects of recalculation on estimates of temperature and oxygen fugacity analyses of multicomponent iron-titanium oxides. *American Mineralogist* **68**, 586-594.

- STRECKEISEN, A. (1967): Classification and nomenclature of igneous rocks. *Neues Jahrbuch Miner. Abh.* **107**, 144-240.
- \_\_\_\_\_. (1976): To each plutonic rock its proper name. *Earth Science Reviews* **12**, 1-33.
- STURCHIO, N.C., MUEHLENBACHS, K. & SEITZ, M.G. (1986): Element redistribution during hydrothermal alteration of rhyolite in an active geothermal system: Yellowstone drill cores Y-7 and Y-8. *Geochimica et Cosmochimica Acta* **50**, 1619-1631.
- SUGIURA, T. (1968): Bromine to chlorine ratios in igneous rocks. *Bulletin of the Chemical Society of Japan* **41**, 1133-1139.
- SUITCH, P.R., LACOUT, J.L., HEWAT, A. & YOUNG, R.A. (1985): The structural location and role of  $\text{Mn}^{2+}$  partially substituted for  $\text{Ca}^{2+}$  in fluorapatite. *Acta Crystallographica* **B41**, 173-179.
- SUN, S.S. & McDONOUGH, W.F. (1989): Chemical and isotopic systematics of oceanic basalts; implications for mantle composition and processes. In Magmatism in the Oceanic Basins. A.D. Saunders & M.J. Norry (eds.), Geological Society of London Special Publication **42**, 313-345.
- SWEENEY, R.E. & KAPLAN, I.R. (1973): Pyrite framboid formation: laboratory synthesis and marine sediments. *Economic Geology* **68**, 618-634.
- TAIT, K.T., SOKOLOVA, E., HAWTHORNE, F.C. & KHOMYAKOV, A.P. (2003): The crystal chemistry of nepheline. *Canadian Mineralogist* **41**, 61-70.
- TAPPERO, R., D'ARCO, P. & LICHANOT, A. (1997): Electronic structure of  $\alpha$ -MnS (alabandite): an *ab initio* study. *Chemical Physics Letters* **273**, 83-90.
- TARDY, Y. & NAHON, D. (1985): Geochemistry of laterites, stability of Al-goethite, Al-hematite, and  $\text{Fe}^{3+}$ -kaolinite in bauxites and ferricretes: an approach to the mechanism of concretion formation. *American Journal of Science* **285**, 865-903.
- TAYLOR, S.R., DUNCAN, A.R., EWART, A., KAYE, M. & WHITE, A.J.R. (1969): Genetic significance of Co, Cr, Ni, Sc and V content of andesites. *Geochimica et Cosmochimica Acta* **33**, 275-286.
- \_\_\_\_\_, EMELEUS, C.H. & EXLEY, C.S. (1956): Some anomalous K/Rb ratios in igneous rocks and their petrological significance. *Geochimica et Cosmochimica Acta* **10**, 224-229.
- TICE, P.E. (1995): Paragenesis of a nepheline-sodalite syenite pegmatite dike, Mont Saint-Hilaire, Québec, Canada. Honours Undergraduate Thesis, McGill University, Montréal, Québec, Canada.

- \_\_\_\_\_ (2009): Mineralogy of eudialyte group minerals from the East Hill Suite of the Mont Saint-Hilaire alkaline plutonic complex, including an alternative site-assignment algorithm & a proposed classification system. Master of Science Thesis, University of New Orleans, New Orleans, Louisiana.
- \_\_\_\_\_ & MARTIN, R.F. (1996): A model for the formation of “line rock” in a sodalite-nepheline syenite pegmatite dike on Mont Saint-Hilaire. *Geological Association of Canada/ Mineralogical Association of Canada Joint Annual Meeting, Abstracts with Program*.
- TIEPOLO, M., OBERTI, R. & VANNUCCI, R. (2002): Trace-element incorporation in titanite: constraints from experimentally determined solid/liquid partition coefficients. *Chemical Geology* **191**, 105-119.
- TILLEY, C.E. (1954): Nepheline-alkali feldspar paragenesis. *American Journal of Science* **252**, 65-75.
- TRACY, R.J. & ROBINSON, P. (1977): Zoned titanian augite in alkali olivine basalt from Tahiti and the nature of titanium substitutions in augite. *American Mineralogist* **62**, 634-645.
- TREIMAN, A.H. & ESSENE, E.J. (1984): A periclase-dolomite-calcite carbonatite from the Oka complex, Quebec, and its calculated volatile composition. *Contributions to Mineralogy and Petrology* **85**, 149-157.
- TRØNNES, R.G., EDGAR, A.D. & ARIMA, M. (1985): A high pressure–high temperature study of TiO<sub>2</sub> solubility in Mg-rich phlogopite: Implications to phlogopite chemistry. *Geochimica et Cosmochimica Acta* **49**, 2323-2329.
- TROPPER, P., MANNING, C.E., ESSENE, E.J. & KAO, L.-S. (2000): The compositional variation of synthetic sodic amphiboles at high and ultra-high pressures. *Contributions to Mineralogy and Petrology* **139**, 146-162.
- TSUKADA, T., SEGAWA, H., YASUMORI, A. & OKADA, K. (1999): Crystallinity of boehmite and its effect on the phase transition temperature of alumina. *Journal of Materials Chemistry* **9**, 549-553.
- UPTON, B.G.J., STEPHENSON, D. & MARTIN A.R. (1985): The Tugtutôq older giant dyke complex: mineralogy and geochemistry of an alkali gabbro-augite-syenite-foyaite association in the Gardar Province of South Greenland. *Mineralogical Magazine* **49**, 623-642.
- USSING, N.V. (1912): Geology of the country around Julianehaab, Greenland. *Meddelelser om Grønland* **38**, 1-376.
- VARET, J. (1969): Les pyroxènes des phonolites du Cantal (Auvergne, France). *Neues Jahrbuch Mineral., Monatshefte*, 174-185.

- VLASOV, K.A. (1966): Geochemistry and Mineralogy of Rare Elements and Genetic Types of Their Deposits. I. Geochemistry of Rare Elements. Israel Program for Scientific Translation, Jerusalem.
- VREDENBURG, E. (1904): Elæolite and sodalite-syenites in Kishengarh State. *Records of the Geological Survey of India* **31**, 43.
- WANG, Y., LI, J., LU, J. & FAN, W. (1982): Geochemical mechanism of Nb,Ta-mineralization during the late stage of granite crystallization. *Geochemistry Beijing* **1**, 175-185.
- WATSON, E.B. (1979): Zircon saturation in felsic liquids: experimental results and applications to trace element geochemistry. *Contributions to Mineralogy and Petrology* **70**, 407-419.
- \_\_\_\_\_ & HARRISON, T.M. (1983): Zircon saturation revisited: Temperature and composition effects in a variety of crustal magma types. *Earth and Planetary Science Letters* **64**, 295-304.
- WEAVER, S.D., BRADSHAW, J.D. & ADAMS, C.J. (1991): Granitoids of the Ford Ranges, Marie Byrd Land, Antarctica. In Geological Evolution of Antarctica, J.W. Thomson & J.A. Crame (eds.), Cambridge University Press, Cambridge, England, 345-352.
- WEBBER, K.L., FALSTER, A.U., SIMMONS, W.M.B. & FOORD, E.E. (1997): The role of diffusion-controlled oscillatory nucleation in the formation of line rock in pegmatite-aplite dikes. *Journal of Petrology* **38**, 1777-1791.
- WHALEN, J.B., CURRIE, K.L. & CHAPPELL, B.W. (1987): A-type granites: geochemical characteristics, discrimination and petrogenesis. *Contributions to Mineralogy and Petrology* **95**, 407-419.
- WHITNEY, J.A. (1984): Fugacities of sulfurous gases in pyrrhotite-bearing silicic magmas. *American Mineralogist* **69**, 69-78.
- WILKINSON, J.F.G. & HENSEL, H.D. (1994): Nephelines and analcimes in some alkaline igneous rocks. *Contributions to Mineralogy and Petrology* **118**, 79-91.
- WILLIAMS, J.F. (1891): Magnet Cove Rock – Leucite Syenite Dike Rock. In *Annual Report of the Geological Survey of Arkansas for 1890. Volume II: The Igneous Rocks of Arkansas*, J.C. Branner, State Geologist (ed.), 267-277.
- WILSON, A.D. (1960): The micro-determination of ferrous iron in silicate minerals by a volumetric and colorimetric method. *Analyst* **85**, 823-827.
- WILSON, A.E. (1964): Geology of the Ottawa-St. Lawrence Lowland, Ontario and Quebec. *Geological Survey of Canada Memoir* **241**.
- WILSON, M. (1989): Igneous Petrogenesis. George Allen & Unwin, London.

- WINTSCH, R.P. & ALEINIKOFF, J.N. (2005): Foliation development and reaction softening by dissolution and precipitation in the transformation of granodiorite to orthogneiss, Glastonbury complex, Connecticut, U.S.A. *Canadian Mineralogist* **43**, 327-347.
- WONES, D.R. & EUGSTER, H.P. (1965): Stability of biotite: experiment, theory, and application. *American Mineralogist* **50**, 1228-1272.
- WOOLLEY, A.R. & PLATT, R.G. (1988): The peralkaline nepheline syenites of the Junguni intrusion, Chilwa province, Malawi. *Mineralogical Magazine* **52**, 425-433.
- WORKMAN, R.K. & HART, S.R. (2005): Major and trace element composition of the depleted MORB mantle (DMM). *Earth and Planetary Science Letters* **231**, 53-72.
- WRIGHT, T.L. (1968): X-ray and optical study of alkali feldspar: II. An X-ray method for determining the composition and structural state from measurement of 2 $\theta$  values for three reflections. *The American Mineralogist* **53**, 88-104.
- XU, T., APPS, J.A. & PRUESS, K. (2005): Mineral sequestration of carbon dioxide in a sandstone–shale system. *Chemical Geology* **217**, 295-318.
- YAGI, K. (1966): The system acmite–diopside and its bearing on the stability relations on natural pyroxenes of the acmite–hedenbergite–diopside series. *The American Mineralogist* **51**, 976-1000.
- \_\_\_\_\_ & ONUMA, K. (1967): The join  $\text{CaMgSi}_2\text{O}_6$ – $\text{CaTiAl}_2\text{O}_6$  and its bearing on the titanaugites. *J. Fac. Sci. Hokkaido University, Ser. IV* **13**, 463-483.
- YANG, C. & HESSE, R. (1991): Clay minerals as indicators of diagenetic and anchimetamorphic grade in an overthrust belt, external domain of southern Canadian Appalachians. *Clay Minerals* **26**, 211-231.
- YODER, H.S., JR., STEWART, D.B. & SMITH, J.R. (1957): Ternary feldspars. *Carnegie Institute Washington Year Book* **56**, 206-214.
- \_\_\_\_\_ & TILLEY, C.E. (1962): Origin of basalt magmas: an experimental study of natural and synthetic rock systems. *Journal of Petrology* **3**, 342-532.
- YUND, R.A. & KULLERUD, G. (1966): Thermal stability of assemblages in the Cu-Fe-S system. *Journal of Petrology* **7**, 454-488.
- ZACCARINI, F., GARUTI, G., ORTIZ-SUAREZ, A. & CARUGNO-DURAN, A. (2004): The paragenesis of pyrophanite from Sierra de Comechingones, Córdoba, Argentina. *Canadian Mineralogist* **42**, 155-168.
- ZAITSEV, A.N. (1996): Rhombohedral carbonates from carbonatites of the Khibina massif, Kola Peninsula, Russia. *Canadian Mineralogist* **34**, 453-468.

- 
- \_\_\_\_\_ & CHAKHMOURADIAN, A.R. (2002): Calcite-amphibole-clinopyroxene rock from the Afrikanda complex, Kola Peninsula, Russia: mineralogy and a possible link to carbonatites. II. Oxysalt minerals. *Canadian Mineralogist* **40**, 103-120.
- ZANGOOL, A. (2003): Magmatic evolution and subsolidus alteration of annite in nepheline syenites, Mont Saint-Hilaire, Quebec. Doctoral Dissertation, McGill University, Montréal, Québec, Canada.
- ZHAO, D., ESSENE, E.J. & ZHANG, Y. (1999): An oxygen barometer for rutile-ilmenite assemblages: oxidation state of metasomatic agents in the mantle. *Earth and Planetary Science Letters* **166**, 127-137.
- ZHAO, Z.-F., ZHENG, Y.-F., CHEN, R.-X., XIA, Q.-X. & WU, Y.-B. (2007): Element mobility in mafic and felsic ultrahigh-pressure metamorphic rocks during continental collision. *Geochimica et Cosmochimica Acta* **71**, 5244-5266.

## VITA

Peter Edward Tice was born on September 4, 1972 in Princeton, New Jersey. In July of 1977, his family and he moved to Wyomissing, Pennsylvania, a small semi-agricultural town in Pennsylvania's Amish and German region. The move brought him much closer to the Appalachian Mountains and fed his burgeoning interest in rocks and minerals, which was supported by his maternal grandfather, Ed Stepnowski, Sr., an avid collector of minerals from the Franklin, New Jersey mines. Following his high school graduation in 1989, he moved to Montréal, Québec, where he attended McGill University.

At McGill University, Peter's geology curriculum gave him a rigorous exposure to all major fields of geology. While deriving a great deal of pleasure from each of his classes, it did not take long for him to focus in on mineralogy & petrology, especially igneous petrology, as his favorites. During his last year at McGill, he worked with Dr. Robert F. Martin on an Honours Undergraduate Thesis concerning the mineralogy and petrology of a pegmatite dike at Mont Saint-Hilaire. Peter graduated from McGill in 1995 with a B.Sc. in Geology and an American History minor.

Seeking to maintain his course of education in the fundamental principles of mineralogy and igneous petrology, he moved to New Orleans to work with Dr. Wm. B. "Skip" Simmons, Jr. and Mr. Alexander Falster at the University of New Orleans. Following nine consecutive years in university, Peter found himself needing a break and spent a nearly a year between 1998 and 1999 in Greenville, South Carolina. Although he was variously employed as a car salesman, a waiter, a bartender, and a chef, he still found the time to head into the local mountains to collect and study minerals. He returned to the University of New Orleans in September, 1999.



Peter and his wife evacuated from Hurricane Katrina on August 27, 2005. Watching the television news, it soon became apparent that they would not be returning to New Orleans in the near future, and with a baby on the way, they resettled in Austin, Texas.

To make ends meet, Peter worked at the second largest Home Depot in the United States, where, after only six months, he became the assistant supervisor of the Garden department. In the meantime, he took evening and weekend classes in teacher certification, and was hired in July, 2007 by the San Marcos, Texas school district to teach high school science.

Peter is currently a science teacher at the Phoenix Academy, teaching biology, chemistry, physics, and earth science to at-risk students in 9<sup>th</sup> through 12<sup>th</sup> grades. He was recently honored by being selected for the second time as a participant in *Project Flowing Waters*, an NSF-funded science-teaching consortium between the San Marcos Consolidated Independent School District and Texas State University that seeks to develop innovative methods of science education that give students more exposure to real-world science investigation and more insight into their local geology and environment. He also serves as a campus technologist, the campus representative to the District Education Improvement Committee, the campus representative of the National Education Association, and is the Vice-President of the San Marcos Education Association. Peter is also the coach for the St. James School 4<sup>th</sup> & 5<sup>th</sup> grade mathematics team.

Peter received his Master's degree in Geology in the summer of 2009 and his Doctorate in Geology in the summer of 2010. He plans to continue his research into alkaline complexes, mineralogy, and magmatic processes as a university professor.